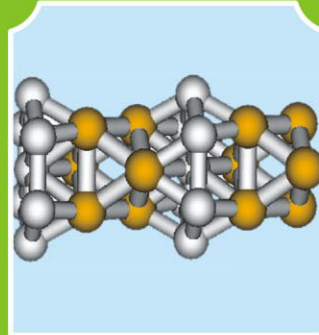
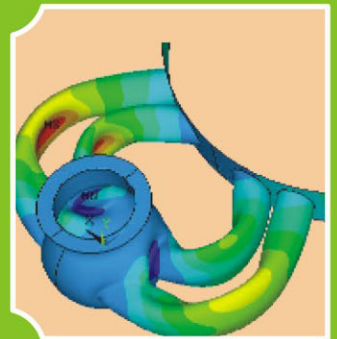
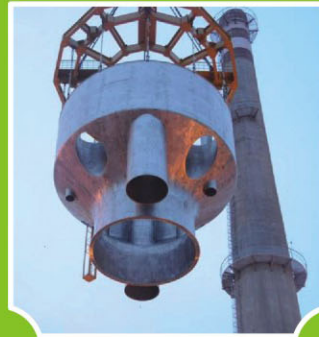


# INDIRA GANDHI CENTRE FOR ATOMIC RESEARCH

2010



## ANNUAL REPORT



Government of India  
Department of Atomic Energy  
Indira Gandhi Centre for  
Atomic Research  
Kalpakkam 603 102

# IGCAR

2010

## INDIRA GANDHI CENTRE FOR ATOMIC RESEARCH

### ANNUAL REPORT



Government of India  
Department of Atomic Energy  
Indira Gandhi Centre for  
Atomic Research  
Kalpakkam 603 102



*“Actions today mould our tomorrows”*

*- Indira Gandhi*



*“... The relative role of indigenous science & technology and foreign collaboration can be highlighted through an analogy. Indigenous science & technology plays the part of an engine in an aircraft, while foreign collaboration can play the part of a booster. A booster in the form of foreign collaboration can give a plane an assisted take-off, but it will be incapable of independent flight unless it is powered by engines of its own. If Indian industry is to take-off and be capable of independent flight, it must be powered by science & technology based in the country ...”*

**- Homi Jehangir Bhabha**



*“There is a totality about modernisation, and in order to gain confidence, we must experiment with our resources even at the risk of failure. There is a need for a constant interplay between basic sciences, technology, industrial practice and management, if economic progress is to result from the activity undertaken.”*

**- Vikram Sarabhai**

## Editorial Committee

### Chairman

Dr. P. R. Vasudeva Rao

### Convener

Dr. M. Sai Baba

### Members :

Dr. C. Anand Babu  
 Dr. N.V. Chandrasekhar  
 Dr. C. Mallika  
 Dr. D. Ponraju  
 Dr. Saroja Saibaba  
 Dr. C.V. Srinivas  
 Shri R.V. Subba Rao  
 Kum. S.Usha  
 Shri K. A.Venkatesan  
 Dr. Vidya Sundararajan

### Address for Correspondence

Dr. P. R. Vasudeva Rao  
 Chairman, Editorial Committee  
 Director, Chemistry Group  
 Indira Gandhi Centre for Atomic Research  
 Kalpakkam - 603 102

Phone : +91-44-2748 0229 / 0222  
 Fax : +91-44-27480222 / 0065  
 Email : vasu@igcar.gov.in  
 dcg@igcar.gov.in  
 Website : www.igcar.gov.in

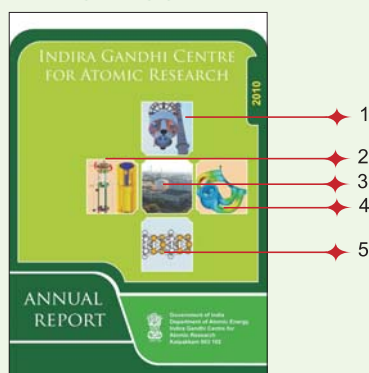
### Published by:

Scientific Information Resource Division  
 Indira Gandhi Centre for Atomic Research  
 Kalpakkam - 603 102

# CONTENTS

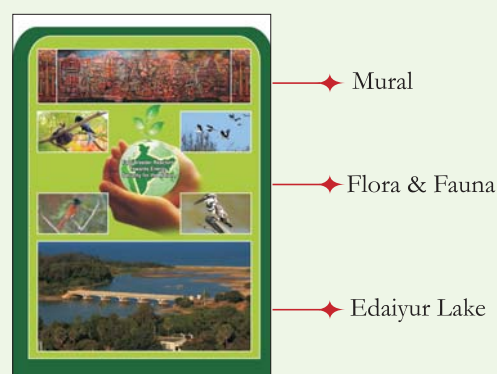
Foreword	
Editorial	
I. Fast Breeder Test Reactor	1
II. Prototype Fast Breeder Reactor	19
III. R&D for Fast Breeder Reactors	47
IV. Fuel Cycle	105
V. Basic Research	143
VI. Infrastructure Facilities	183
VII. Awards / Publications / News & Events / Organisation	193

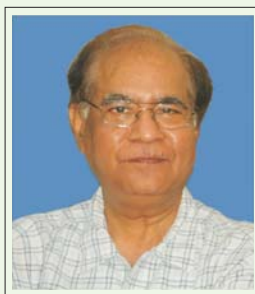
### FRONT COVER



1. Erection of inner vessel of Prototype Fast Breeder Reactor
2. 3D model of fresh subassembly transport cask of Prototype Fast Breeder Reactor
3. Fast Breeder Test Reactor
4. Layout optimisation of primary pipe of Commercial Fast Breeder Reactor
5. Structure of the FePt nanowire obtained from ab-initio calculations

### BACK COVER





## Foreword

I am delighted to write the Foreword for the Annual Report 2010. This report showcases the achievements of the Centre in diverse and interlinked fields within the ambit of basic sciences like physics, chemistry, biology, engineering and technology.

Fast Breeder Test Reactor, which is the flagship of our Centre, has completed 16<sup>th</sup> irradiation campaign and is poised for operating at higher power levels. The reactor continues to operate efficiently with greater availability. The life extension studies carried out have concluded that FBTR can be operated for ten more effective full power years. It is an international benchmark that about 1000 pins of carbide fuel have been irradiated to a burn-up of 155 GWd/t (one subassembly has reached a burn-up of 165 GWd/t), without any clad breach. The fuel cycle has been closed with the loading of the fuel in to FBTR, containing plutonium obtained from spent fuel discharged from FBTR reprocessed in CORAL facility. Our emphasis would continue to utilize CORAL facility as a test bed for R&D in reprocessing in addition to utilising it for reprocessing fuel discharged from FBTR. KAMINI continued to operate efficiently while meeting the demands of the strategic sector.

The year 2010 has seen considerable progress on the construction front of Prototype Fast Breeder Reactor. The test fuel bundle of PFBR in FBTR has reached a burn-up of 112 GWd/t. Both the main vessel and the reactor vessel have been positioned inside the civil structure. IGCAR continues to provide the inputs towards design, R&D, regulatory review and manufacturing of crucial components and testing large components in sodium facilities, designed and built for the purpose. Many important regulatory clearances have been obtained towards the construction. Having fulfilled the task of providing R&D inputs for PFBR, we are engaged in design of advanced fast reactors with higher burn-ups, advanced fuels and structural materials, which would ensure enhanced performance with innovative design, robust safety and improved economy.

We continue to focus on structural design optimization, development of new devices and sensors, modeling and simulation studies towards the development of safety grade decay heat removal system, advanced sodium pumps, centrifugal extractors, robotic sampling system and remote handling gadgets etc. On the materials front, we have made progress towards development of novel structural materials with improved properties, oxide dispersion strengthened ferritic alloys, reduced activation ferritic/martensitic steels, achieving tunable thermal properties of the nano fluids, architecturing of nano coatings for unique performance, room temperature ionic liquids, alternate extractants, supercritical fluid separations etc. We are continuing our work towards development of superior processes for uranium exploration, non-destructive evaluation, minor actinide partitioning, pyrochemical reprocessing and waste management technologies.

We have been successful in meeting the quality of human resources through Training School, Homi Bhabha National Institute and encouraging collaborations with eminent institutions and organizations in India and worldwide.

The environment, safety, infrastructure development, township development, medical facilities and school education are other areas of focus that has received much of our attention. Our townships have become greener and environmentally friendly towards enhancing the quality of life. We have also focused on the neighbourhood with respect to education (skill sets), health care, hygiene, awareness, etc.

I would like to compliment the new editorial team (Dr. M. Sai Baba, Dr. Vidya Sundararajan, Dr. Saroja Saibaba, Shri R.V. Subba Rao, Dr. C. Anand Babu, Kum. S. Usha, Dr. C. Mallika, Dr. N.V. Chandrasekar, Dr. D. Ponraju, Shri K.A. Venkatesan and Dr. C.V. Srinivas) steered by Dr. P.R. Vasudeva Rao, Director, Chemistry Group for bringing out the report comprehensively in line with the established traditions of quality and aesthetics. I also appreciate colleagues from Scientific Information Resource Division, Shri Gaddam Pentaiah and Shri A. Rangarajan for their contributions and efforts.

I see immense challenges and opportunities to ensure targeted performance of Prototype Fast Breeder Reactor with targeted performance parameters, the design and development of FBRs-1 and 2, closing of the Fuel Cycle for Fast Reactors with benchmarks specifications.

We have to continue to improve on successes through holistic approaches integrating science with technology missions, improving townships, neighbourhood, environment with ethics and equity and the most important continue to build capacity, capability and eminence of the Centre.

This is the last Annual Report with me as the Director of Indira Gandhi Centre for Atomic Research. I wish to thank my colleagues and you who supported me in the endeavours to make my work meaningful and enjoyable. I am confident that journey of 'Excellence with Relevance' would continue with rigour and vigour in the Centre as it discovers new challenges and opportunities.



**Baldev Raj**

*Director, IGCAR*

## Mission of IGCAR

- ★ To conduct a broad based multidisciplinary programme of scientific research and advanced engineering development, directed towards the establishment of the technology of Sodium Cooled Fast Breeder Reactors (FBR) and Associated Fuel Cycle Facilities in the Country
- ★ The development and applications of new and improved materials, techniques, equipment and systems for FBRs
- ★ To pursue basic research to achieve breakthroughs in Fast Reactor Technology

## Vision

To be a Global Leader in Sodium cooled Fast Breeder Reactor and Associated Fuel Cycle Technologies by 2020



## Editorial

It is a great privilege to prepare and edit the Annual Report of a Centre like Indira Gandhi Centre for Atomic Research, which has a unique blend of mission oriented and basic research programmes and a vibrant atmosphere for R&D. A perusal of the Annual Report of 2009 and the current report for the year 2010, clearly brings out the continuity of the momentum of R&D in the centre, with the consolidation of research in continuing programmes and the initiation of several new R&D programmes as in the previous years. FBTR has continued to be a vital R&D tool for demonstration of several new technologies related to the fast reactor programme, validation of the design and performance of equipment and for providing valuable operating experience and feedback to the designers. The fact that the operating life of the reactor could be extended for a further period of ten effective full power years augurs well for the fast reactor programme of the country. The PFBR construction is in an advanced stage and the Centre has met all essential R&D commitments towards the PFBR. However, a few R&D programmes have been continued to provide inputs towards the smooth installation of equipments and commissioning of subsystems for PFBR. One example of such an activity is the 3D visualization for walk through of PFBR nuclear buildings and the animation of the fuel handling systems. The main focus of the R&D programmes is now shifting towards series of commercial fast reactors that could follow the PFBR. Efforts towards enhancing the safety and economics of Fast Breeder Reactors are well illustrated by the number of articles that have appeared in this report on this subject. This includes development of advanced design of the reactor components and testing facilities and materials for the fast reactors and advanced elements of fuel cycle, as well as basic research for supplementing and augmenting the understanding of behaviour of the materials and processes and to develop new materials and processes. Setting higher targets for the burn-up to be reached by the fuel, has for instance, encouraged the development of advanced clad materials such as the oxide dispersion strengthened ferritic-martensitic steel. The experience in the development of materials has also contributed to the development of Reduced Activation Ferritic Martensitic steel for the fusion programme. The report also contains articles on several interesting activities that would have societal applications such as development and demonstration of SQUID based magnetocardiography systems and detection of diabetic neuropathy using infrared thermal imaging.

With the successful functioning of the BARC Training School at IGCAR and the flourishing of the Homi Bhabha National Institute and the periodic enhancement in the strength of research scholars in the Centre, there has been a significant growth in the range, content and quality of the R&D programmes in the Centre. This is particularly true in areas related to basic research on materials and fuel cycle and also with respect to other domains such as safety research and reactor design.

The Editorial Committee is thankful to all the authors who have contributed interesting articles highlighting the above achievements. The new Editorial Committee put in intense efforts to have peer review of the articles and multiple stages of editing to ensure that the articles are readable and at the same time comprehensive. We have also retained the overall structure of the report and appearance as in previous years. We welcome inputs from readers both with respect to the quality of presentation and technical content therein.

I personally thank the members of the Editorial Committee and in particular Dr. M. Sai Baba for his laudable efforts to bring out a quality product. I particularly thank the hard work put in by colleagues of SIRD, especially Shri G. Pentaiah and Shri A. Rangarajan, in expediting the publication. The Editorial Committee is indebted to Dr. Baldev Raj, Director, IGCAR whose motivation and guidance has helped us to bring out the publication as always in the first quarter of the year and at the same time maintaining high quality and standards.

A handwritten signature in blue ink, appearing to read 'P.R. Vasudeva Rao'.

**(P.R. Vasudeva Rao)**  
Chairman, Editorial Committee  
Director, Chemistry Group



# CHAPTER I

## Fast Breeder Test Reactor

## I.1 Highlights of 16<sup>th</sup> Irradiation Campaign

FBTR completed the 16<sup>th</sup> irradiation campaign at 18 MWt in October 2010 and is poised for the 17<sup>th</sup> campaign at higher power levels (22.5 MWt).

While the major mission of the 16<sup>th</sup> irradiation campaign was to complete the irradiation of PFBR test fuel subassembly, the other goals were

- Continuing the irradiation of structural materials (D9 & SS)
- Obtaining operational experience with the modified steam generator orifices and
- Testing of in-core detector of PFBR

Reactor start-up was initiated on December 25, 2009 after completion of the modifications for replacement of the spring loaded orifice assemblies of the steam generator water tubes by modified welded assemblies. Start-up had to be aborted as reactivity anomaly with respect to the calculated value was observed indicating reduction in the shutdown margin. Two MOX subassemblies in the fourth ring were shifted to the periphery to restore the shutdown margin as per the technical specification limit.

After detailed analysis and obtaining safety clearances, reactor was started on February 11, 2010. Initially, the reactor was operated at 90% of the target power of 18 MWt, to monitor the steam generator steam outlet temperatures. After review of the data on steam generator parameters by Safety Committee, reactor power was raised to the target power (18 MWt) on 7<sup>th</sup> April. On 17<sup>th</sup> May, the PFBR test subassembly reached the burn-up of 100 GWd/t. The campaign

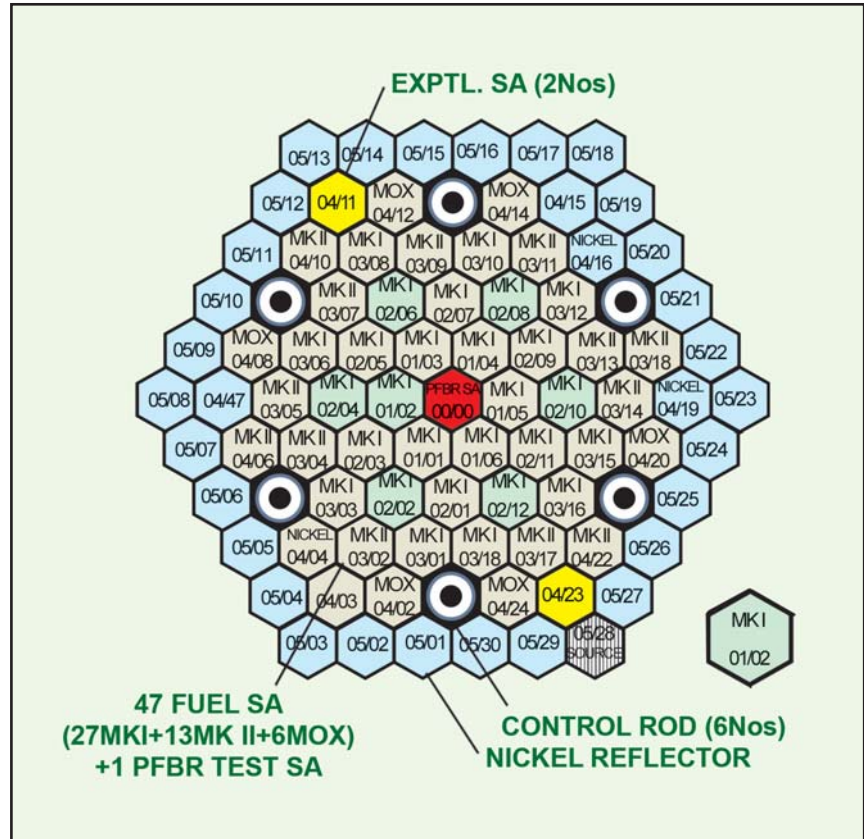


**Fig. 1** Core of FBTR for 16<sup>th</sup> irradiation campaign

was ended on 22<sup>nd</sup> October when the PFBR test subassembly attained a peak targeted burn up of 112 GWd/t. Steam temperatures from the steam generator tubes and feed water flow through the steam generator modules were regularly monitored and found to be alright. The reactor was operated at maximum power of 18 MWt with 47 fuel subassemblies (Figure 1) for 2367 hours (~ 99 days) with high power operation of 2204 hours (~92 days).

The reactor inlet sodium temperature was 658 K and the maximum outlet temperature of sodium from the reactor was 743 K. The corresponding steam temperature was 721 K. Central subassembly outlet temperature and feed water temperature were 788 K and 468 K respectively and steam pressure was 11.96 MPa. During the high power operation

turbine-generator was synchronized to grid, producing a maximum power of 3.2 MWe. The cumulative thermal energy developed was ~38 GWh and electrical energy developed was 4.9 million units. Performance of the reactor, heat transport systems and auxiliary systems was satisfactory.

The replacement of spring loaded orifices of steam generator tubes with modified type assemblies was effective in yielding the desired improvement of equalizing the outlet steam temperatures of all the four modules.

Irradiation of structural materials (D9 and SS) in the 5<sup>th</sup> ring is continuing. During this campaign, PFBR in-core neutron detector was tested at 16.2 MWt and 400 kWt with the detector in the experimental canal. The 400 kWt testing was carried out

at 673 K isothermal sodium temperature. As a part of this testing, flux measurement by foil irradiation and gamma measurement using high temperature gamma detector inside the reactor just above the central subassembly also carried out.

The reactor was in fuel handling state for about 30 days in August to September for measuring the bowing of subassembly heads using the core coordinate measurement device as part of the investigations to analyse the possible causes for the shutdown margin anomaly observed in the beginning of the campaign.

With the completion of PFBR test fuel irradiation, the linear heat rating of Mark I subassembly is no longer governed by the PFBR test subassembly and the peak rated Mark I subassembly can operate at its design operating linear heat rating. Analysis by design group with rationalised hot spot factors indicates that it is now possible to raise the operating linear heat rating of fresh MK-I fuel to 375 W/cm as against 320 W/cm specified earlier. Also, it will be possible to raise the linear heat rating to 400 W/cm after a burn-up of 500 MWd/t itself, (earlier, this limit was 35000 MWd/t). The analysis is carried

out for an inlet temperature of 673 K. Reactor power for this linear heat rating will be 22.5 MWt. SARCOP clearance has been obtained for the higher linear heat rating. Histograms giving details of the 16<sup>th</sup> irradiation campaign are shown in Figure 2.

It is planned to start the 17<sup>th</sup> irradiation campaign shortly with a core of 48 fuel subassemblies (27 MK-I, 13 MK-II & eight MOX fuel). With an inlet temperature of 673 K, the reactor outlet will be close to 773 K. The turbine-generator power will be ~6 MWt; FBTR will be able to export power to IGCAR power distribution system.

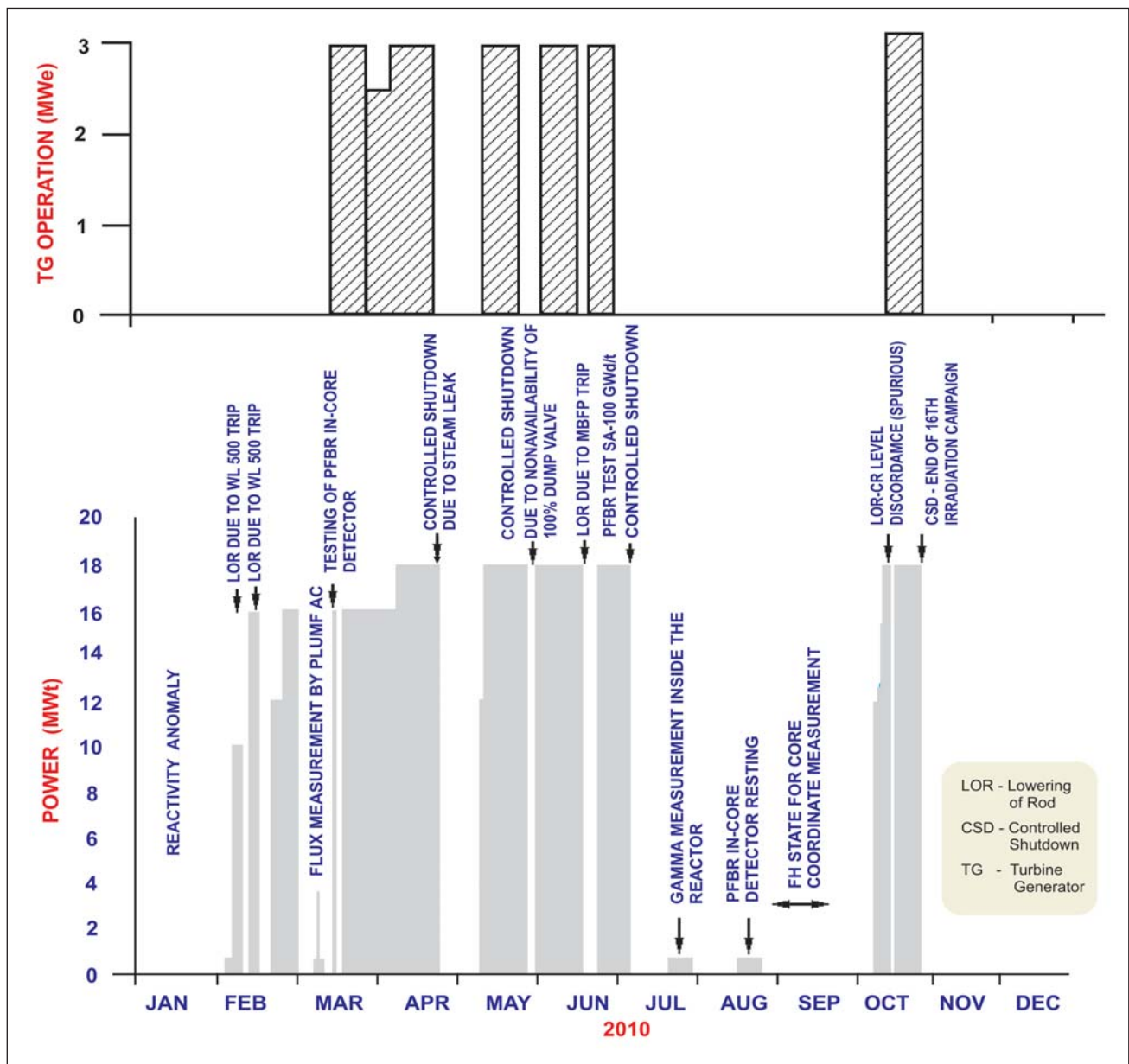


Fig. 2 Histogram of 16<sup>th</sup> campaign

## I.2 Testing of In-core Detector of PFBR in FBTR

The neutron flux in PFBR in the detector location in control plug varies over more than nine decades. High temperature fission chambers in the control plug periphery integrated with wide range channels (Pulse-Campbell) monitor the flux in all states of the reactor with a good overlap. Towards this requirement, detectors and channels are being developed at Electronics Division, BARC. Electronics Division has designed and developed high temperature fission chambers of 0.2 cps/nv sensitivity, required for PFBR. Prototypes were fabricated and tested at APSARA reactor, to ensure the functionality of the detectors. To test high temperature fission chambers for the intended range of neutron flux, temperature and gamma field expected in PFBR, it was planned to test them in FBTR. It was decided to put one High Temperature Fission Chamber in the experimental canal (in-vessel) and another chamber in the detector pit E5 (outside) location. The in-vessel high temperature fission chamber is expected to see a neutron flux of  $\sim 10^{10}$  nv, gamma field of  $\sim 10^6$  R/h and a maximum temperature of 753 K. The outside high temperature fission chamber is placed in the same location as that of FBTR detectors, where neutron flux of  $\sim 10^{10}$  nv, gamma field of  $\sim 10^4$  R/h

and a maximum temperature of 353 K are expected.

These high temperature fission chambers were tested in thermal column of APSARA at ambient temperature up to  $8 \times 10^7$  nv in pulse and Campbell modes of operation, and fission chambers were also checked in APSARA shielding corner with a special arrangement to provide an ambient temperature upto 853 K, and neutron flux up to  $8 \times 10^7$  nv in pulse and Campbell modes of operation. Performance of the high temperature fission chambers was found to be satisfactory. The detectors were tested in FBTR in March 2010. During the testing in FBTR, the detectors underwent simultaneously all the three conditions of high neutron flux, gamma field and high temperature. Both high temperature fission chambers were connected to identical preamplifiers, pulse and Campbell electronic instrument channels. It was also aimed to characterize the Pulse and Campbell performances of high temperature fission chambers against standard RTC fission chamber with a sensitivity of 1 cps/nv.

For installing the in-vessel detector in the reactor in the experimental canal, a special assembly of 6 meter length containing inner detector holder with neutron and gamma

shielding and outer assembly was designed and fabricated (Figure 1). In pulse mode of operation, high temperature fission chamber at experimental canal exhibited nonlinearity due to the vicinity of auxiliary Sb-Be neutron source. The Campbell signal was measured in the neutron flux range of  $3 \times 10^5$  to  $3 \times 10^{10}$  nv. As expected, the temperature at the high temperature fission chamber in the experimental canal varied as per operational power of reactor. Hence at low power up to 10 kWt, a temperature of 453 K only could be achieved. As HV applied to high temperature fission chambers started coming down at higher neutron fluxes, Campbell channel was switched off at 6 MWt. As the power was raised to 16 MWt, the temperature seen by the high temperature fission chambers increased to 745 K. Performance of the high temperature fission chambers in the detector pit was as expected and showed a neutron sensitivity of  $\sim 0.17$  cps/nv. After the high temperature fission chamber was operated at full power level of 16 MWt at 745 K with neutron flux  $> 10^{10}$  nv and gamma field of  $> 10^6$  R/h, pulse distortion was observed at HV of 400 V. However,

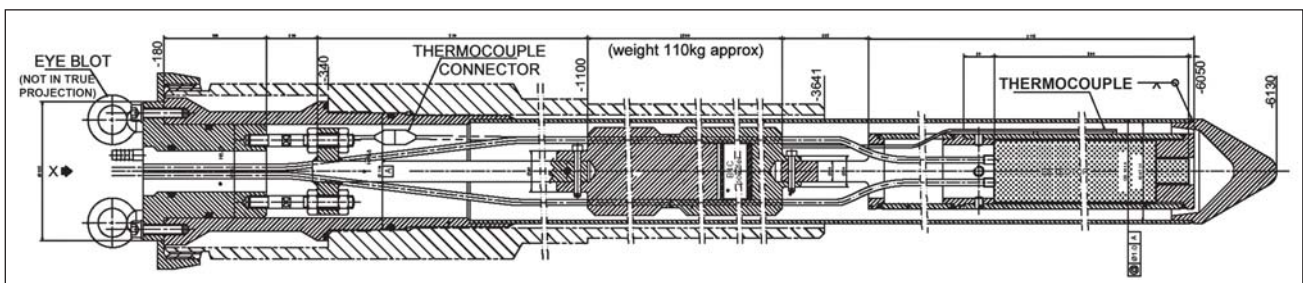
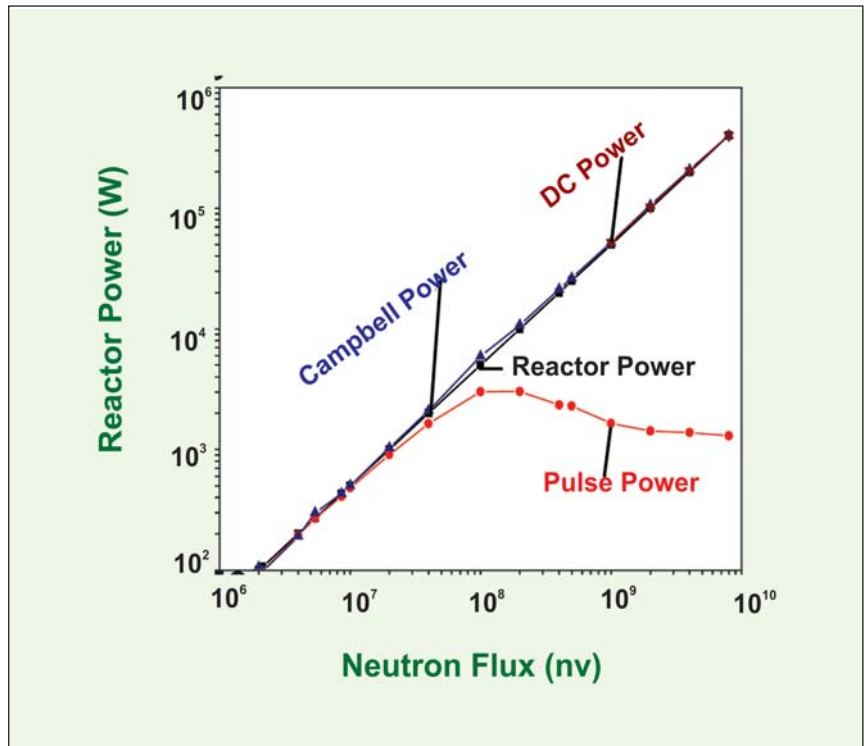


Fig. 1 Sectional view of prototype fast breeder reactor incore detector holder assembly

pulse shape did not get disturbed up to 360 V. In experimental canal high temperature fission chamber-01 sees high neutron flux at shut down due to the presence of the auxiliary neutron source. Hence high temperature fission chamber-01 is placed in experimental canal operated in pulse mode of operation from  $1 \times 10^3$  to  $2 \times 10^7$  nv where it shows good accuracy and linearity. It also showed good accuracy and linearity in Campbell signal from  $1 \times 10^5$  to  $8 \times 10^9$  nv. Performance tests will be continued in FBTR with the intended values of neutron flux and gamma field for other high temperature fission chambers being fabricated by ECIL.



**Fig. 3** Output signals of HTFC-01 in experimental canal in FBTR

The experiment was repeated in August 2010 to investigate the cause for the distortion in the shape of the neutron pulses. Detector and electronics set up (Figure 2) were tested for their performance with suitable discriminator bias and HV level in the reactor containment building using pulse generator.

Subsequently, the high temperature fission chamber-03 detectors along with a standard RTC fission chamber was lowered into the E5 detector pit of FBTR and high temperature fission chamber-01 was lowered into the experimental canal. The reactor was subsequently started with optimum HV and discriminator bias

setting and pulse counts. Campbell outputs were recorded at different reactor power levels along with the temperature for all the detectors from shutdown to 400 kWt at an isothermal temperature of 673 K. Output signals of high temperature fission chamber-01 located in the experimental canal are shown in Figure 3.

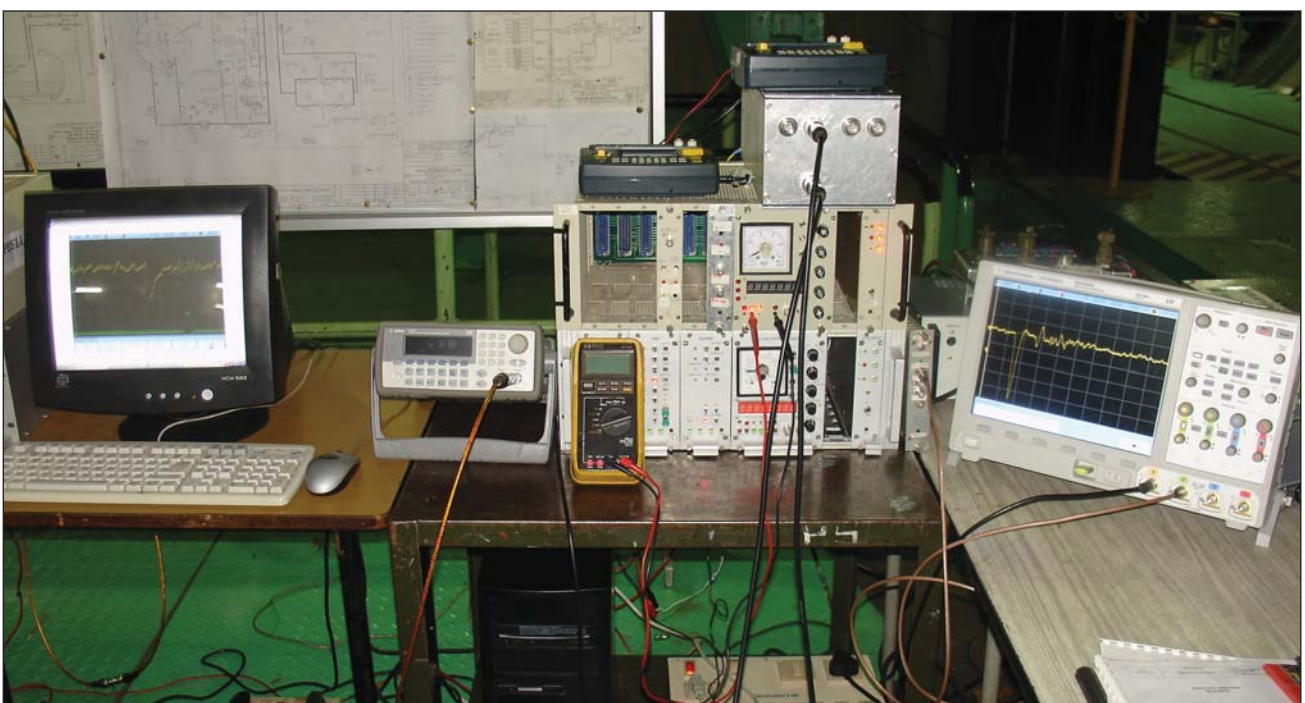


**Fig. 2** Detector electronics inside reactor containment building

### I.3 Realizing the Target Linear Power for FBTR Mixed Carbide Fuel

FBTR core consists of 70 % PuC-30 %UC (MK-1), 55 % PuC- 45 %UC (MK- 2) & 44% PuO<sub>2</sub>- 56 % UO<sub>2</sub> (MOX) sub-assemblies (SA). Height of core in MK-1 & MK-2 subassemblies are 320 mm in length and in MOX subassembly, the core length is 430 mm. MK-1 fuel is designed to operate at 400 W/cm peak linear power. The entire core subassembly is aligned with each other at their middle. Coolant enters the subassembly from the bottom of the subassembly. For proper flow zoning, flow control devices are kept at the bottom of the handling head for MK-1 & MK-2 subassembly and at the bottom of the foot for MOX subassembly.

At present, reactor is operating at 18 MWt capacity with 46 driver fuel SA consisting of 27 MK-1, 13 MK-2 & 6 MOX SA and 1 test PFBR fuel subassembly. Nickel reflector subassembly surrounds this fuel subassembly. The present core configuration is shown in Figure 1. Flow through various subassemblies is controlled to obtain near uniform temperature at the core exit and also to maximize temperature at core exit.

MK-1 fresh fuel was designed to operate at a peak linear heat rating

of 320 W/cm with an inlet temperature of 607 K. However, to increase the steam outlet temperature to the desired rating of around 773 K, three tubes in each of the four modules in the steam generator have been plugged. This would result in the increase in the reactor inlet temperature of sodium to 673 K. A study has been carried out to find out the effect of this increase in the inlet temperature on the allowable peak linear power (ALP) of the fuel. Towards this, hotspot factors have been rationalized based on the experiences gained from FBTR operation and in line with international experience.

In general, the tolerances specified on the fabrication of components facilitate good recovery but form a source of uncertainty. Similarly, properties of material and also the experimental results are predicted with an error band and form a source of error. Also, to avoid spurious SCRAM, flexibility is given to operators resulting in operational uncertainty. Uncertainties related to fabrication are grouped under statistical category while the rest are treated as direct factors.

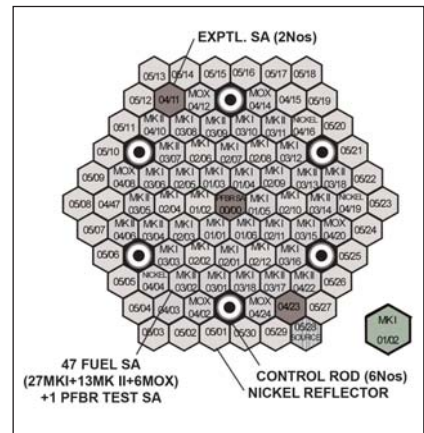
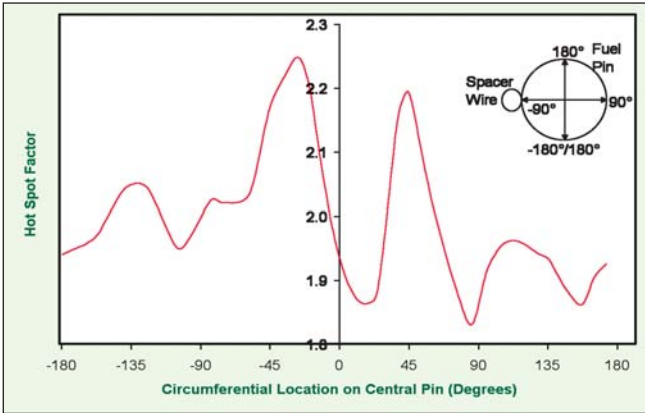


Fig. 1 Core configuration for 16<sup>th</sup> campaign

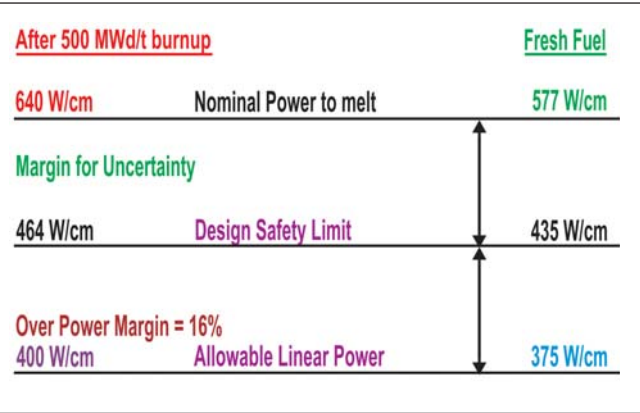
In the earlier treatment before rationalization, fissile enrichment and linear mass have been separately treated. In the present evaluation, they have been combined together as fissile mass as they both represent the same. Similarly, before rationalization, gap conductance is treated as a direct factor. Truly, this uncertainty arises due to the tolerance allowed on the clad ID and pellet OD. Hence, it is decided to treat this uncertainty as a statistical uncertainty in line with its nature. A similar treatment was given to this uncertainty in JOYO. Also, the effect of spacer wire on the variation in the clad outer temperature has been analyzed using CFD. This variation results in a hotspot and is shown in Figure 2 and this has been adopted as the hotspot factor. Besides, before rationalization, pin pitch was considered. The same has been renamed as channel in the present study and in the evaluation of uncertainty and statistical nature of the tolerances on the dimension like pin pitch, clad OD and spacer OD have been considered. Further, in the present study, film heat transfer coefficient uncertainty is taken as

Table 1 : Comparison of hotspot factors before & after rationalization

Temp Rise across	Clad mid - wall temperature Studies		Fuel Centre DSL Studies	
	After	Before	After	Before
Channel	1.1387	1.1795	1.1279	1.1795
Film	2.1667	2.7759	1.2301	1.5750
Clad	1.3197	1.4259	1.2136	1.3131
Gap			1.2597	1.4839
Fuel			1.2256	1.3298



**Fig. 2** Hotspot factor due to circumferential temperature distribution



**Fig. 3** Design safety limit on linear power

10% based on lower uncertainties on physical properties of sodium and high flow rate envisaged for the high power operation as against 30 % taken in the earlier study. In the earlier study, power related uncertainties like channel & linear power have been assumed whereas in the present study they have been rationalized based on their evaluation parameters.

Thermal balance or absolute power calibration uncertainty had been duplicated with local power and channel power uncertainties in the earlier study which has now been corrected. Besides, it has also been treated as a part of over power margin uncertainty in FBTR. Hence, the contribution of this towards uncertainty is treated as nil and the hotspot factor is taken as 1 and is hence removed from the list of hotspot factors. Similarly, reactor

inlet temperature is now termed as coolant temperature measurement uncertainty to take care of variation in both the inlet and outlet temperature of the coolant.

Rationalization resulted in a significant reduction in the hotspot factors and a comparison is made with the factors before rationalization in Table 1. The confidence level in the prediction is 99.7 %.

With these hotspot factors and with the PIE data on fuel cracking, fission gas release & fuel swelling allowable, linear power for operation at beginning of life and burnup required to reach its target rating (400 W/cm) and flow required have been determined. The design criteria followed is that at 116 % power fuel centerline temperature under hotspot condition shall be less than its melting point of 2123 K and clad

mid- wall temperature under hotspot condition shall be < 973 K. From the analysis, it is observed that MK-1 fuel can be operated at 375 W/cm at beginning of life and could be raised to 400 W/cm in about 3 days (500 MWd/t burnup) as shown in Figure 3 and could sustain the 400 W/cm power till it is discharged at 155 GWd/ t burnup. Temperature distributions in fuel pin at beginning of life and at 500 MWd/t burnup are shown in Figures 4a and 4b.

The study has helped in not only increasing the beginning of life power to 375 W/cm from the existing 320 W/cm but also reducing the conditioning period to reach its target rating of 400 W/cm to 500 MWd/t from about 35 GWd/t burnup. A flow of 3.2 kg/s is required to maintain clad mid-wall temperature below 973 K.

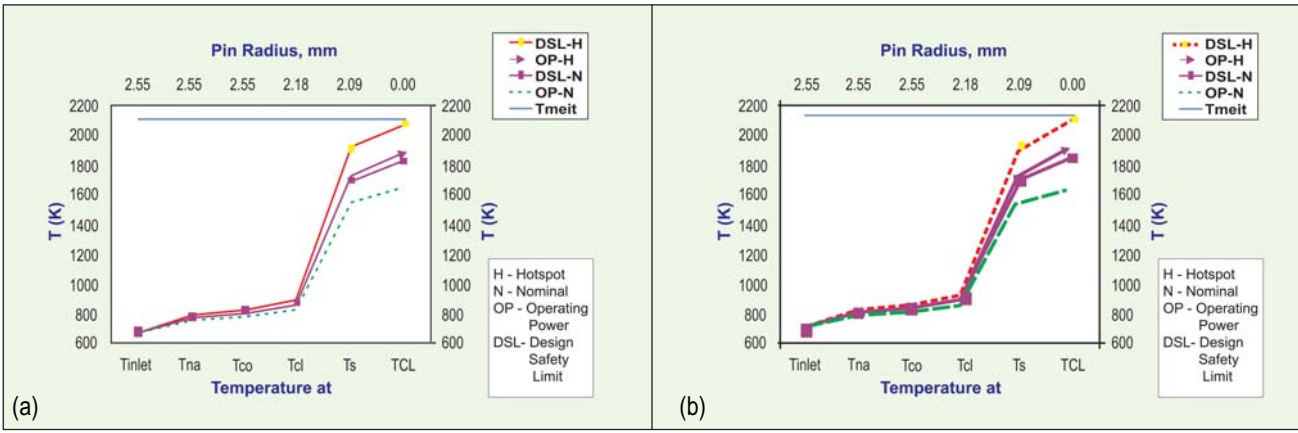


**Fig. 4** Temperature distribution for (a) Fresh fuel (b) At 500 MWd/t

## I.4 Irradiation of Prototype Fast Breeder Reactor Test Fuel Subassembly

FBTR reached a major milestone in October 2010 when the irradiation of the PFBR test fuel was completed. The irradiation of the MOX fuel simulating the PFBR fuel composition commenced in the year 2003 with 11<sup>th</sup> irradiation campaign.

PFBR is designed with a mixed oxide fuel of plutonium and natural uranium of two different compositions viz. 21% and 28 % of PuO<sub>2</sub> for the two enrichment zones. The fuel is designed to operate at a peak linear heat rating (LHR) of 450 W/cm and target burn-up of 100 GWd/t. The flux in FBTR core is  $2.3 \times 10^{15}$  n/cm<sup>2</sup>/s, whereas the flux in PFBR is  $8 \times 10^{15}$  n/cm<sup>2</sup>/s. To achieve the linear heat rating of 450 W/cm with the lower flux in FBTR, the PFBR test fuel is enriched with <sup>233</sup>U, thus retaining the chemical composition as in PFBR fuel. Typical fuel composition of the pellets of the PFBR test subassembly is 29% PuO<sub>2</sub>, 38% oxide of <sup>233</sup>U and balance 33% oxide of natural uranium. The composition has been designed such that when the high-grade MK-I fuel in the first ring is operating at a peak linear heat rating of 320 W/cm, the test subassembly will have a peak linear heat rating of 450 W/cm at the core centre.

Figure 1 gives the details of the PFBR test subassembly. This has 37 pins of 6.6 mm OD and 5.7 mm ID, same as that of PFBR fuel pins. On either side of the fuel pin bundle, steel rods are used as reflectors. The fuel pellet has 5.52 mm OD with a central hole of  $\phi$ 1.6 mm. Active fuel column length

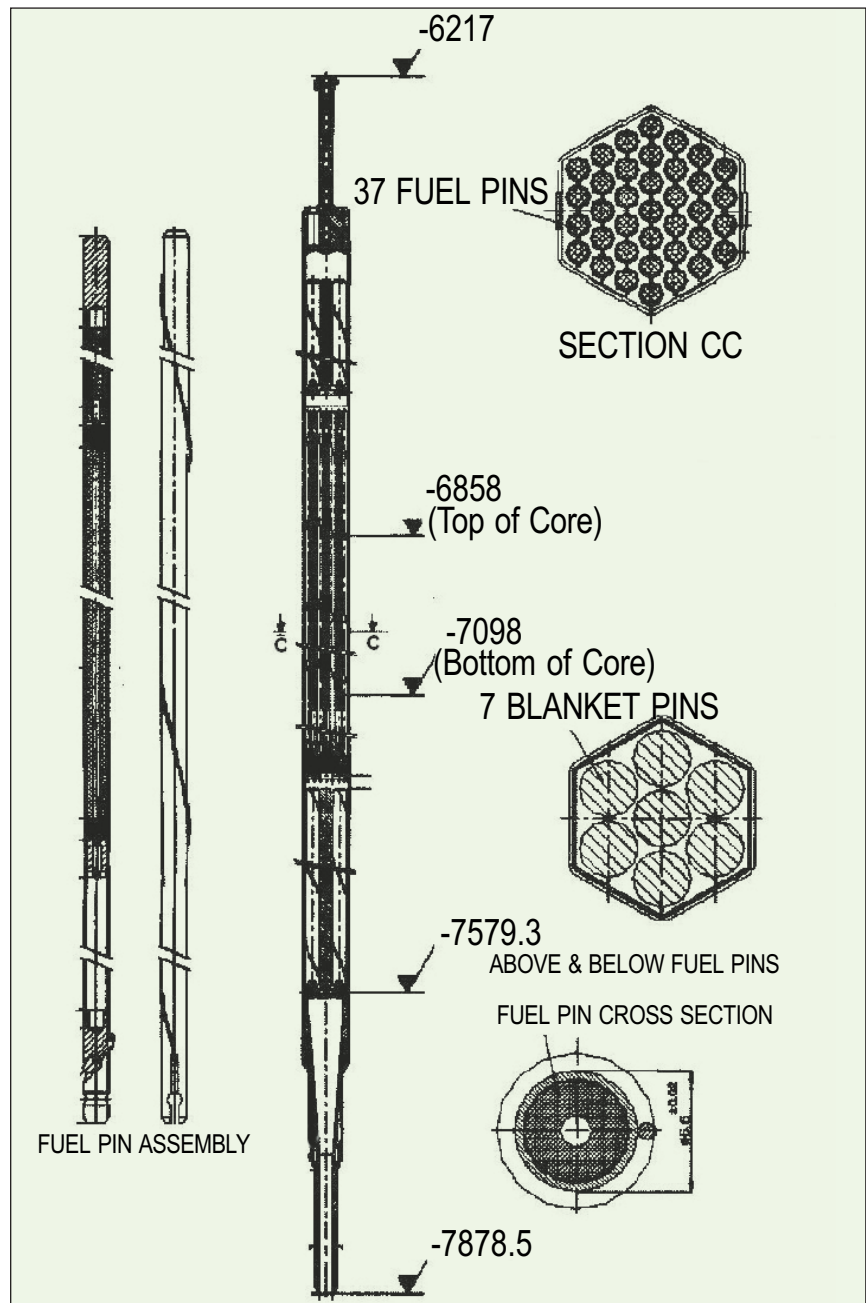


**Fig. 1** Prototype fast breeder reactor test fuel subassembly

is 240 mm as against 320 mm for FBTR carbide fuel. Top of the fissile column is level with the top of the core (-6858 mm). The pin has two classes of pellets- class A pellets with a linear mass of 2.18 g/cm and class B pellets with a lower linear mass of 2.11 g/cm. Class B pellets are loaded at the top 1/3<sup>rd</sup> of the fissile column. The test subassembly generates

350 kWt at 450 W/cm. Accordingly, the subassembly has been fitted with a zone IV orifice. In addition, the steel reflector pin dimensions are slightly different from standard FBTR blanket pin dimensions in order to modify the hydraulic characteristics of the subassembly as required. The clad and wrapper are made of cold worked D9 alloy.

While it is possible to operate at the required linear heat rating in FBTR and reach the target burn-up, displacement per atom (dpa) and clad damage fraction (cdf) corresponding to the target burn-up in PFBR cannot be simulated in FBTR fully due to the lower flux. For the operating parameters of FBTR, the clad damage fraction that can be achieved will be about 0.12 as against the PFBR design clad damage fraction of 0.3. However, the irradiation will help in understanding the behaviour of the MOX fuel per-se. Since  $^{233}\text{U}$  will be used in the third stage of India's nuclear energy programme, the irradiation is expected to provide some useful and valuable insights into its behaviour as well. Initially, the

subassembly was intended to be irradiated upto a peak burn-up of 100 GWd/t at a reactor inlet temperature of 653 K.

Irradiation of this sub-assembly was carried out in six irradiation campaigns starting from 11<sup>th</sup> campaign. During this period, the core progressively evolved from 39 fuel subassembly core to 47 in the 16<sup>th</sup> campaign. During the 11<sup>th</sup> to 14<sup>th</sup> campaigns the reactor was operated with inlet sodium temperature of 620 K only. In the last two campaigns the reactor inlet temperature was raised to about 653 K by blanking three out of seven tubes in all the four SG modules. Based on the lower operating inlet temperature during the earlier

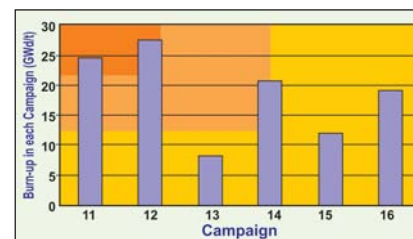


**Fig. 2** Peak burn-up logged in each campaign

campaigns, the burn-up limit was raised to 112 GWd/t. Peak burn-up logged in each campaign is shown in Figure 2. The revised target burn-up was reached at the end of 16<sup>th</sup> irradiation campaign. After in-core cooling for about three months, when the decay heat reaches 200 watt, the subassembly will be discharged and sent to hot cells for post-irradiation examination.

## 1.5 Gamma Dose Measurements in the Central Canal Plug above Fuel Sub-assembly Head in FBTR

High temperature in core fission detectors to be used in PFBR for monitoring the neutron flux at various stages are being developed indigenously. As these detectors are exposed to high temperatures (around 845 K) and high gamma fields of  $5 \times 10^5$  R/h, the performance of the detectors have to be tested. These detectors were tested in BARC at high temperature and high gamma field independently. FBTR is chosen to be a suitable place to test the detectors at high temperature and gamma field.

Gamma fields in FBTR were earlier theoretically calculated. The gamma field in FBTR has two major components, one due to sodium activation gammas and the other coming from the core. The gamma

coming from the latter is composed of capture gammas and fission gammas. The sodium activation is mainly from  $^{24}\text{Na}$  activity.  $^{24}\text{Na}$  has a half life of 15 hours and the activity saturates after a few half lives. However, core gammas are directly proportional to the reactor power. Hence, the total gamma activity in the detector has a component which depends on the reactor power and reactor operation history.

In order to obtain the contribution from core gammas, 2D coupled neutron gamma transport calculations were performed using the transport code DORT with IGCS3 cross section set. This cross section set has 175 neutron groups and 42 gamma groups. FBTR is modeled in RZ geometry extending up to the

reactor vault radially and top shield axially (relevant part of the model for this is shown in Figure 1). Though major sodium activity is produced in the core, as sodium is circulated in the reactor, sodium activity gets uniformly mixed. The sodium activity is calculated in two steps. In the first step sodium activation throughout the core is calculated using the neutron flux distribution. Making use of this activity, average specific sodium activity is calculated. The distributed gamma source is calculated using this specific activity and smeared sodium distribution in the reactor. Using this source distribution and 42 group gamma cross sections, two dimensional gamma distribution is calculated again with DORT code. Total gamma distributions from the core and

sodium activation gammas are given in Figures 2 and 3.

As the calculated gamma flux has inherent error due to the approximations in the reactor modeling and errors and uncertainties in the data used, it was felt necessary to measure the gamma field before the HTFC is tested and measure the gamma dose distribution in central canal location and extrapolate in the experimental canal using the calculation. A miniature high temperature gamma detector was used to measure the gamma dose distribution. This detector was earlier calibrated in a standard gamma field. The efficiency of the detector was found to be  $3.7 \times 10^{-14} A/(R/hr)$ . A special plug was designed to load the detector in the central canal location. This special arrangement is shown in Figure 4.

In order to get the sodium activation gamma component, the reactor was

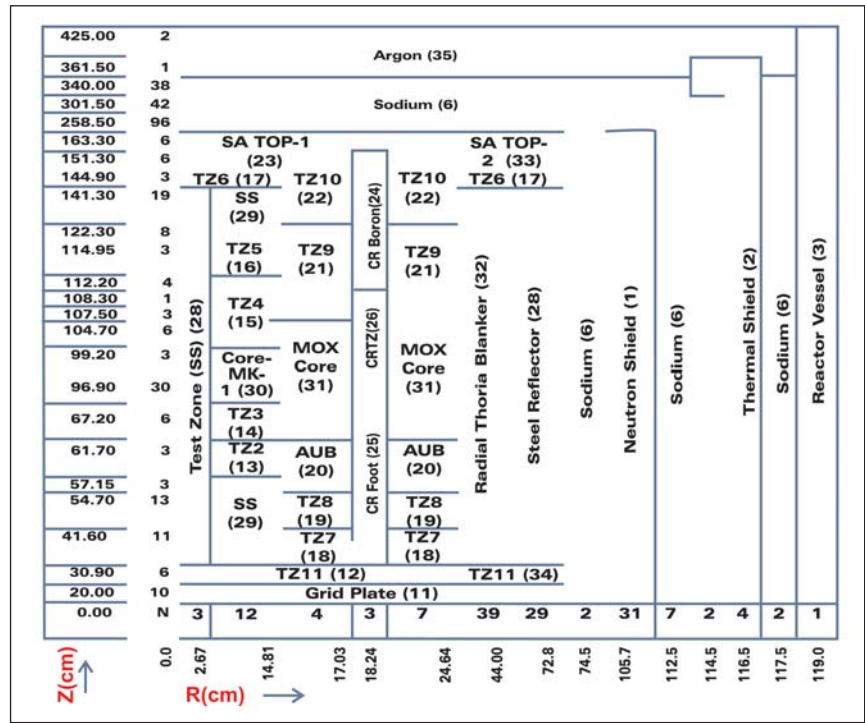


Fig. 1 2D R-Z calculation model of FBTR (Numbers in brackets denote region numbers)

operated for nearly three weeks so that sodium activity is saturated. Then the reactor was shut down, to avoid core gammas. The miniature gamma detector was loaded in the

reactor and gamma field was measured at various axial positions of the detector. Table 1 gives a comparison of the measured activity of the sodium activation gammas

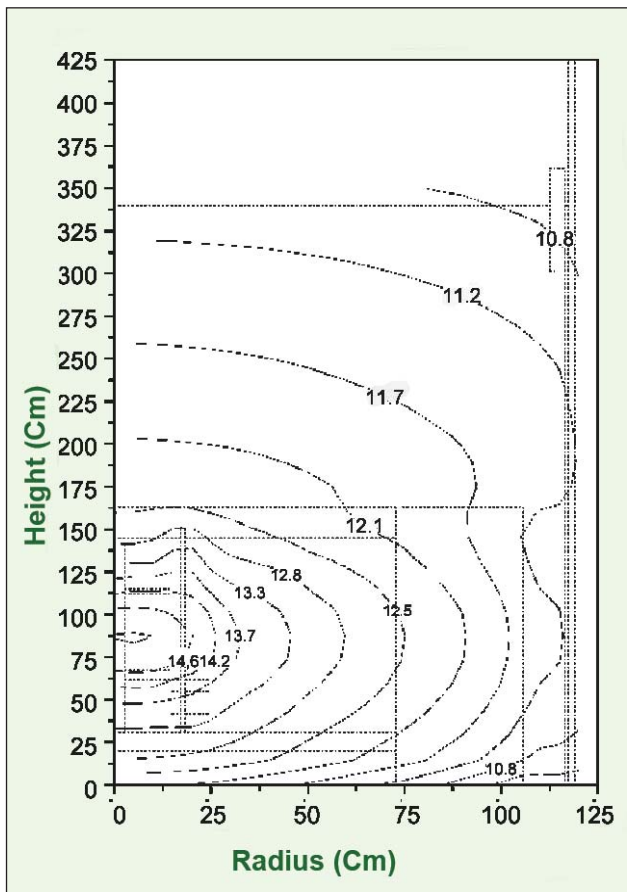


Fig. 2 Core gamma contours

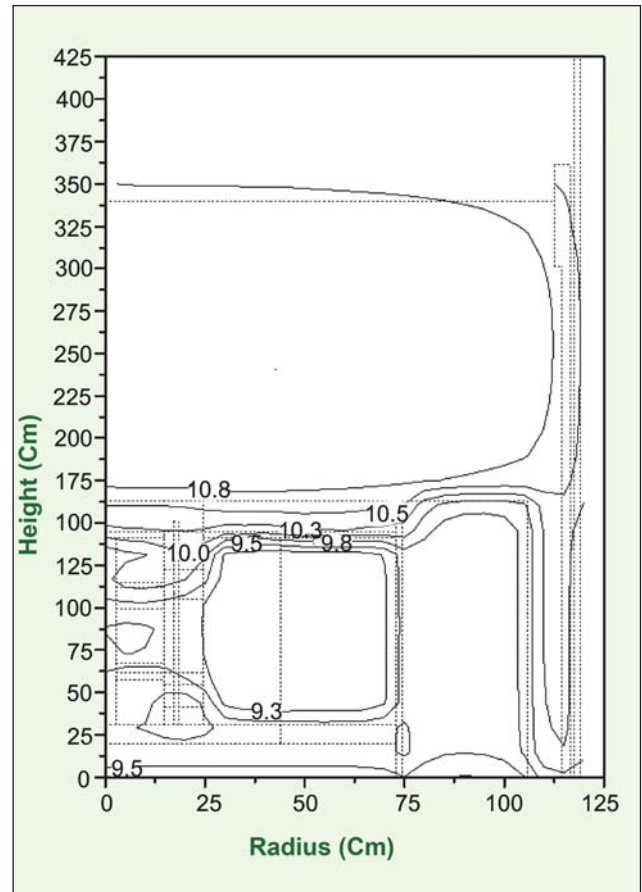
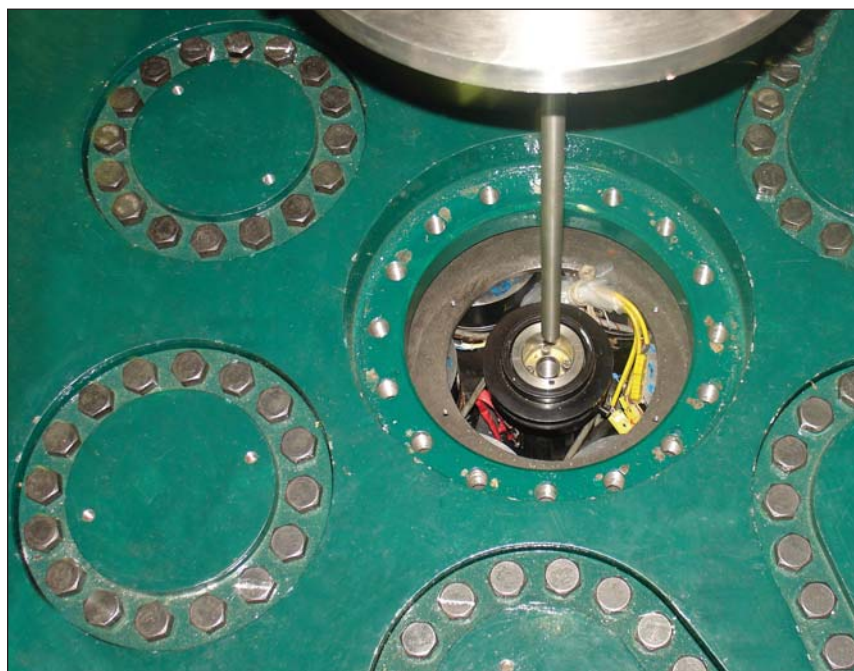


Fig. 3 Activation gamma contours

and the calculated values. The reactor was kept shut down for six days so that sodium activity decayed fully. Then reactor was made critical and reactor power was stabilized at various power levels, and gamma field was measured at each power level at different axial locations. Table 2 gives the measured gamma fields at various locations and the comparison of measured and calculated core gamma fields. Measurements show that core gamma activity is proportional to power. The C/E ratios determined were found to be very good considering the errors in the modeling, data uncertainties and experimental errors.



**Fig. 4** Gamma detector being loaded into the central canal plug

Table 1 : The ratio of experimental to calculated values of Gamma Dose Rates (R/h) at different elevations in FBTR- Central Canal (Sodium Activation Gammas)				
Elevation (mm)	Distance from the grid plate (-7850 mm)	Gamma dose rate (R/h) x 10 <sup>5</sup>		
		Experimental	Calculated	Ratio
-6160	1690	1.47	1.05	1.40
-5960	1890	1.31	1.29	1.01
-5760	2090	1.67	1.37	1.22
-5560	2290	0.66	1.40	0.47
-5360	2490	0.99	1.40	0.71
-5160	2690	0.56	1.39	0.40

Table 2 : The ratio of experimental to calculated values of Gamma Dose Rates (R/h) at different elevations in FBTR- Central Canal (Core Gammas)				
Elevation (mm)	Distance from the grid plate (-7850 mm)	Gamma dose rate (R/h) x 10 <sup>4</sup>		
		Experimental	Calculated	Ratio
-6160	1690	35.0	15.3	2.29
-5960	1890	18.8	7.37	2.55
-5360	2490	6.36	3.26	1.95
-4760	3090	1.59	1.27	1.25
-4450	3400	0.86	0.57	1.50

## 1.6 Major Refurbishment of Plant Systems of FBTR

FBTR has completed 25 years of successful operation in this year. Over the years, several modifications and refurbishments were done on the plant systems to sustain their availability, correction of latent deficiencies and for performance improvement. Some of the major refurbishments completed recently are discussed below.

### Erection and commissioning of new above ground fire water system

The fire water system of FBTR caters to the fire water requirements of the plant. It also acts as an alternative cooling water source for the emergency diesel generator sets. This system experienced frequent failures owing to leaks developing in the underground portion. The

underground network was made of Cast Iron (CI) pipes with lead caulked joints. Because of ageing and fatigue, the pipe lines started leaking. Locating and repairing the failed pipe laid underground was found to be extremely difficult and time consuming. Moreover any leak or repair in this system results in depressurization and draining of the

entire system as there are no isolation valves in the ring main for isolation of leaky segments. Non-availability of fire water system violates the relevant clauses of FBTR technical specifications, as it is a critical safety system. Hence, it was decided to have a new ring main eliminating the observed deficiencies of the present underground system.

The new ring main of FBTR-RML complex is fabricated with carbon steel pipes of complete welded design. The lines are laid above ground and the portions at the road crossings are routed through underground concrete trenches. 70% of the pipe line is located on the terrace of FBTR-RML complex making it freely accessible for operation and maintenance. The system has a 250 NB header at the discharge of the fire water pumps branching into two 200 NB pipe line which surrounds the FBTR-RML complex. Isolation valves are provided at suitable locations to divide it into two segments in case requirement arises for attending any fault in a particular segment. The fire water supply to the respective buildings and fire hydrants located outside the building are provided through landing valves in the down comers tapped from the main header located at the terrace. Vents and drains are provided with isolation valves for filling and draining the system. The entire above ground ring main was hydro tested at 1.37 MPa. After thoroughly flushing the lines, the new system was commissioned with the existing two 50% capacity fire water pumps.

**Replacement of main boiler feed water pump**

The steam water system has two French make Main Boiler Feed Water Pumps (MBFP) which are multistage, high temperature pumps

rated for 77 t/h flow at 1770 mlc head. These pumps experienced several failures during steam water system transients mainly due to the low NPSH margin. Moreover, owing to non-availability of spares for the imported pump, one of these pumps was replaced in 1997 by a KSB make pump. The KSB pump with improved NPSH margin has a trouble free performance for the past 13 years. Since the 2<sup>nd</sup> imported pump had seized twice during steam water system transients, a new KSB make pump was procured with identical specifications as that of the first pump. The pump was erected with partial base frame supplied by KSB on the existing grouted base frame of the original pump. During erection, major deviation in pump level and insufficient contact area in the support legs were observed. The base frame was further machined and the pump legs and seating pads were scrapped to achieve the required level, horizontality and contact area. The pump was aligned with gear box and motor. The suction, discharge, leak off and

recirculation lines were modified to suit the new pump. Trial run and endurance run with cold water and hot run were carried out. The hydraulic and mechanical performance was evaluated to be satisfactory.

**Erection and commissioning of new roof exhausters**

The ventilation of service building where Ward Leonard drives and Diesel Generator sets were located is done by fresh air supply from supply fans located at DM water plant and through a set of roof exhausters. All the three roof exhausters became inoperable and could not be repaired due to ageing and related problems. Their non-availability was seriously affecting the ventilation of this area especially during summer season. New roof exhausters were procured, installed and commissioned successfully.

**Refurbishment of steam generator and turbine data logger**

During the 15<sup>th</sup> irradiation campaign, steam temperature differences were observed among the steam

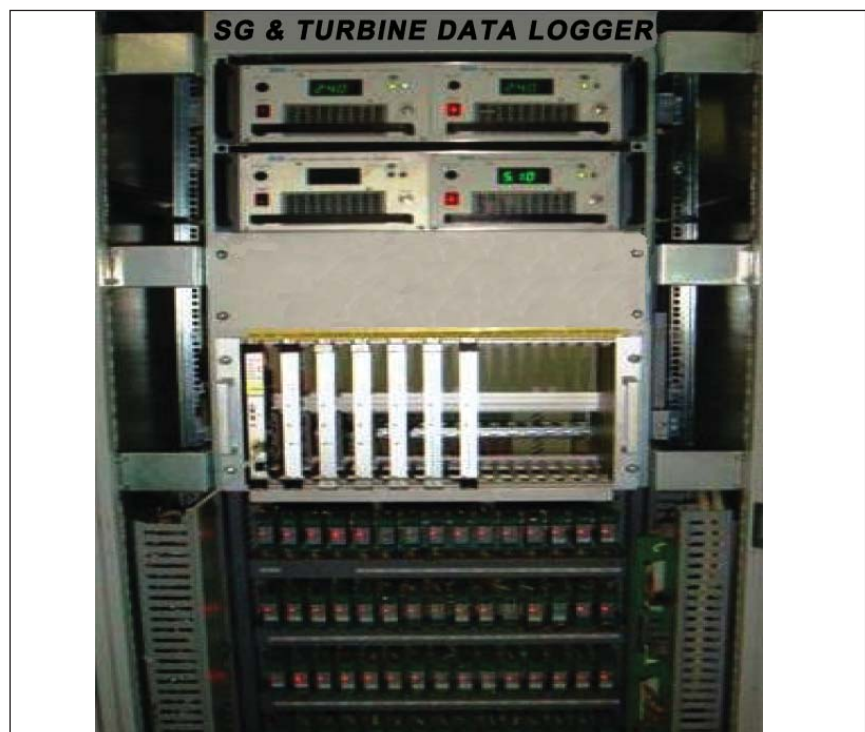


*Fig. 1 Steam generator and turbine data logger*

generator tubes. Investigation revealed the dislodgement of orifice assemblies. The orifice assemblies were replaced by welded design. In order to monitor the steam generator data on-line, a new industrial PC based steam generator and turbine data logger system was installed and commissioned in place of the obsolete system having only some limited features. (Figure 1) The new system also meets the additional requirements of monitoring the module and tube temperatures of steam generator after blanking of three out of seven tubes to reach near design temperature. It also monitors the parameters of steam turbine and its auxiliary systems. Apart from these analog signals, the data logger also processes digital inputs and provides outputs for alarm annunciation. The system records turbine lock out and unit lock out conditions as and when they occur and this data is very helpful for the post event analysis in case of any turbine trip. It also generates digital outputs for alarms for cold end  $\Delta T$  between sodium outlet and feed water inlet, sodium outlet of two steam generator modules of the same loop, steam sub header of two steam generator modules of the same loop and between steam sub header of two loops in steam generator.

The system has been developed with the following features:

- \* Receives eighty numbers of analog and seventeen numbers of digital input signals and generate ten numbers of digital outputs for initiating control room alarms apart from the analog outputs.
- \* Accomplishes Data logger functions in two newly installed panels (one for housing all the

hardware like CPU card, I/O cards, redundant power supplies, isolation amplifiers, etc., and the other for housing the industrial PC based data server, GUI and HMI) located in Central Data Processing System.

- \* The system consists of isolation amplifiers suitable for resistance, current, high or low level voltage and digital input signals to be monitored. Redundant power supply units are provided to cater to the power supply requirements of the hardware.
- \* Mimic dynamic flow sheets, trend logging of signals etc., are incorporated in the GUI for better representation.
- \* Provisions are available to take print out of log and the flow sheets along with signal values.

The new system was commissioned in March, 2010 and is in continuous service since then. The system could deliver the relevant data related to steam generator and turbine parameters for review and analysis during the high power operation.

### Commissioning of new dedicated chillers

Chilled water is sourced from centralised water chilling plant (CWCP) cooled air handling units to meet the air conditioning requirement of FBTR. Two 113 TR Frick make (1974 model, Freon-22) chillers had been provided in FBTR for emergency loads whenever there is an interruption of chilled water supply from CWCP. Even though the refrigeration requirement was estimated to be 470 TR, over the years, there was a gradual degradation in the air conditioning of



**Fig. 2** 350 TR centrifugal chiller

the plant due to insufficient quantity and the high inlet temperature of chilled water supplied from CWCP. The standby chillers also could not be run in parallel with CWCP as the water flow through the evaporators was inadequate resulting in tripping of these chillers on low suction pressure. Moreover, the chillers had to be discarded because of ageing and non-availability of Freon-22 beyond 2010. Hence, a decision was taken to have adequate capacity of dedicated chillers for FBTR and to discard the existing obsolete Frick chillers with the state of art energy efficient chillers. Accordingly, one 350 TR (Figure 2) (centrifugal type- Macquay make) and two 150 TR (screw type- Kirloskar make) chillers were procured and installed. A separate cooling water system consisting of three pumps (two in service and one standby) and a cooling tower of 650TR capacity was provided. The screw chillers and two cooling water pumps were provided with emergency power supply. Normally the centrifugal chiller and one screw chiller will be in service. In case of grid failure, two screw chillers will cater to the emergency chilled water loads.

The chillers were erected and commissioned successfully. All the chillers are available and are operated depending on the chilled water requirements of the plant.

## I.7 Gamma Scanning of Irradiated FBTR Fuel Pins

Gamma scanning has been carried out for the first time on irradiated FBTR fuel pins that have seen a peak burn-up of 155 GWd/t. It is one of the important techniques used for nondestructive examination of irradiated fuel pins for understanding the in-reactor fuel behavior, especially the fission product distribution. The gamma scanning system established in the Radiometallurgy Laboratory (RML) consists of a collimator and turret assembly, automated gamma scanning bench, detector assembly with nuclear electronics and computer hardware and software.

The collimator-turret assembly is housed in a circular opening in the 1200 mm thick concrete front wall of the hot cell. Lead shielding is provided in the turret assembly to compensate for the shielding loss created by the opening in the cell wall. The turret incorporates four collimators with different slit dimensions. The turret is mounted on ball bearings to facilitate rotation around its horizontal axis, to position the desired collimator slit in front of the fuel pin. Each collimator has a primary segment made of an alloy of tungsten-copper-nickel (density 17.1 g/cc) and a coarse secondary segment made of lead. The



Fig.1 Collimator-turret assembly

collimators facilitate a small and well defined region of the fuel pin to be seen by the gamma detector. Figure 1 shows collimator turret assembly with high purity germanium detector.

A new computer controlled four axes gamma scanning bench was designed, fabricated and commissioned inside the hot cells with provision for precisely positioning and aligning the fuel pin (irradiated) through X,Y,Z &  $\theta$  movements. This bench is modular in construction and has linear motion (LM) guides with ball screws and stepper motors. Figure 2 shows the gamma scanning bench.

Detector assembly is based on high purity germanium detector which has a resolution better than 1.8 keV at 1.33 MeV. The output pulses from the detector are amplified and fed to the multichannel analyzer for



Fig.2 Four axis gamma scanning bench

obtaining the gamma spectrum. Nuclear electronics such as high voltage supply, spectroscopy amplifier and multichannel analyzer are integrated in a PC with appropriate software for analysis.

Gamma scanning of irradiated fuel pins after a burn-up of 155 GWd/t gave valuable information on the fission product redistribution along the length of the fuel pin. The results were also used to estimate the active fuel column length and the axial flux profile along the fuel column. Figures 3 and 4 shows the axial distribution profile of Cesium ( $^{137}\text{Cs}$ ) and Ruthenium ( $^{106}\text{Ru}$ ) flux profile respectively. Clear evidence of axial migration and deposition of cesium was observed from gamma scanning. The fuel column length estimated from gamma scanning is in good agreement with radiography results.

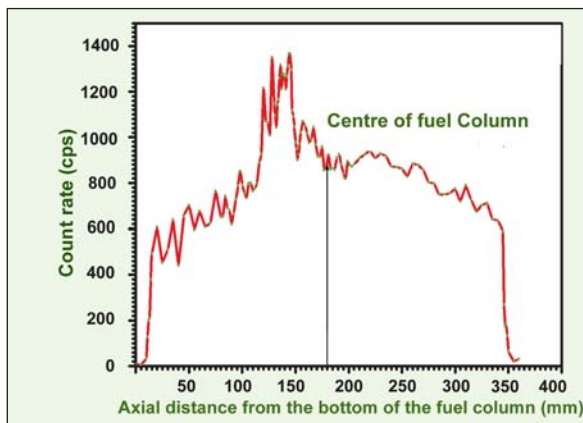


Fig. 3 Axial distribution of  $^{137}\text{Cs}$

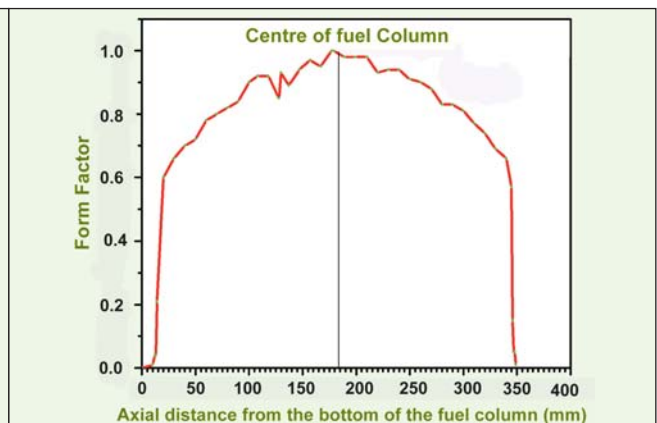


Fig. 4 Axial flux profile of  $^{106}\text{Ru}$

## I.8 Assessment of Mechanical Property Changes of FBTR Grid Plate Material

The performance of the grid plate which supports the core subassemblies is one of the factors considered for extending the life of FBTR. The grid plate of FBTR (SS 316) operating at a temperature of about 623 K experiences a cumulative neutron dose of a few displacement per atom (dpa) over its life time. As a part of the programme on assessment of irradiation induced degradation of FBTR grid plate, an accelerated irradiation test was performed in FBTR to characterize its mechanical property changes.

The experimental subassembly used for this test consisted of an irradiation capsule with five compartments in which pre-fabricated miniature tensile and disc specimens of FBTR grid plate material (SS 316) were stacked (Figure 1a). The experimental assembly was irradiated in the 4<sup>th</sup> ring of FBTR for duration of 58.18 effective full power days during the 14<sup>th</sup> irradiation campaign. The temperature of the irradiation was around 623 K and the accumulated displacement damage ranged from about 1.08 dpa to a maximum of 2.57 dpa at the center of the capsule.

The irradiated experimental subassembly was received in hot

cells of Radio Metallurgy Laboratory (RML) and dismantled using laser cutting to retrieve the irradiated tensile and disc specimens. Remote tensile tests were carried out on the irradiated tensile specimens at temperatures of 298, 623 and 673 K using a universal testing machine (Figure 1b) installed in the hot cells. As conventional or readily available grips did not exist for ambient / elevated temperature tests of miniaturized tensile specimen (12.7 mm gage length, 3 mm gage width, 1 mm thick), considerable efforts went into development of miniaturized wedge type grips and accessories for carrying out the remote tensile tests.

The stress-strain curves of irradiated SS 316 tested at 623 K are shown in Figure 2. It can be seen that the irradiated SS 316 undergoes an increase in yield strength and ultimate tensile strength with respect to the unirradiated values for all the dpa conditions.

Up to 1.08 dpa, this hardening results in negligible changes in uniform elongation. Above 1.08 dpa, the increase in yield strength is considerably higher than the increase in ultimate tensile strength.

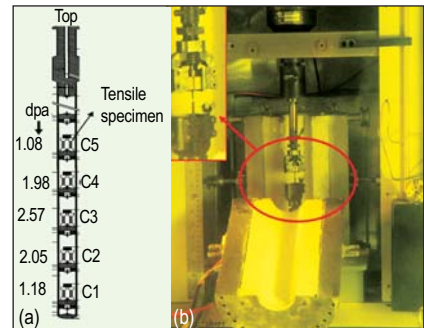


Fig. 1 (a) Schematic of the irradiation capsule (b) Remote tensile testing machine inside the hot cells

The narrowing of the difference between yield strength and ultimate tensile strength with increase in dpa results in the reduction of uniform elongation to about 20% for the specimen irradiated to 2.57 dpa. The trends in the yield strength, ultimate tensile strength and % uniform elongation of irradiated SS 316 tested at 623 K are shown in Figure 3. The effect of low dose neutron irradiation on the material property is considered in the design standard of FBR structural materials by limiting the accumulated neutron irradiation to maintain ductility above 10 %. A uniform elongation of above 20% at test temperatures of 301 K, 623 K and 673 K of SS 316 indicates retention of adequate ductility in SS 316 grid plate of FBTR for an accumulated fast neutron dose of 2.57 dpa.

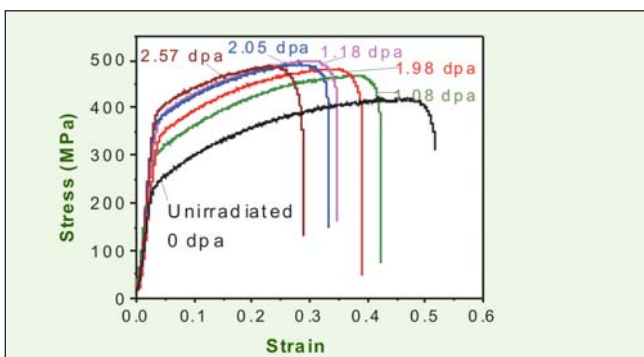


Fig. 2 Stress-strain curves of SS316 irradiated to various displacement damages and tested at 623 K

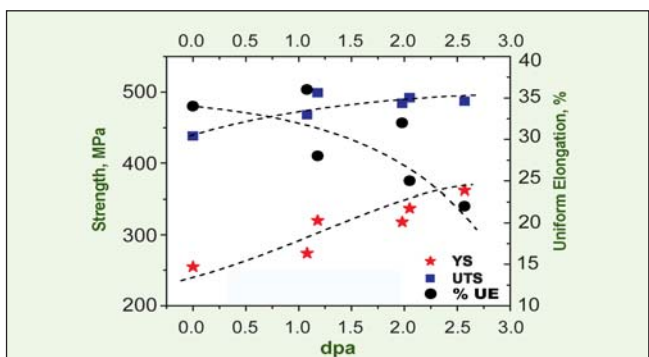


Fig. 3 Trends in yield strength, ultimate tensile strength and % uniform elongation of irradiated SS 316 tested at 623 K as a function of dpa

## I.9 Diverse Utilization of KAMINI Reactor

**K**AMINI Reactor is a unique  $^{233}\text{U}$  fuelled, light water moderated, natural convection cooled and beryllium oxide reflected 30 kWt research reactor. KAMINI Reactor houses two irradiation sites: Pneumatic Rabbit Fast Transfer System (PFTS) and Thimble locations (North and South) for activation analysis experiments and three beam tubes to extract the neutron beams at the core-reflector for neutron radiography of active as well as non-active components and for radiation physics experiments. Over the years, KAMINI has been utilized for activation analyses, shielding experiments and neutron radiography of fuel pins from FBTR and pyro-devices used in ISRO satellite launch vehicles (Figures 1 and 2).

In recent times, the usage of KAMINI has been extended for additional applications. Neutron radiography of macro electric mechanical pressure sensors (MEMS) from LPSC, Bangalore which are used for positioning the satellite, were tested at south beam tube for assessing the capabilities to withstand neutron irradiation for extended mission in outer space. KAMINI was also utilised for testing, calibration, evaluation and acceptance tests of various types of proto type neutron detectors developed by BARC and various other types of regular detectors manufactured by ECIL, Hyderabad for different reactors in India. The detectors were tested at a flux level of about  $10^{10}$  to  $10^{11}$  nv and gamma field of  $10^5$  R/h up to the



**Fig. 1** Pyro bolt cutter

maximum power level of 30 kWt just outside the core reflector assemblies.

The newly developed boron coated parallel plate gamma compensated ionization chambers (neutron sensitivity  $1.57 \times 10^{-14}$  A/nv) developed by BARC for use in thermal reactors was tested by placing them in the reactor. These detectors were assembled in a IS grade aluminium dry tube fixture of 4 meter length (Figure 3).

Vanadium type self powered neutron detectors (SPND) (Figure 4) with the sensitivity of  $3 \times 10^{-21}$  A/nv used for flux mapping in PHWRs were tested at a flux level of  $10^{11}$  nv. The response of 22 numbers of such detectors was assessed by placing the detectors adjacent to the core at axial reflector block-II location. Two long length of Inconel SPNDs



**Fig. 3** Compensated ion chamber being loaded into reactor through a dry tube



**Fig. 2** Pyro explosive transfer assembly

developed for use in 700 MWt reactors and traveling in-core probe (TIP) detectors with a sensitivity of  $1 \times 10^{-17}$  A/nv used for cross calibration of localised power range monitoring (LPRM) in Tarapur reactors were also tested for acceptance.

IS grade aluminium dry tube assembly of 4 meter length in sections with bent (avoiding streaming) was fabricated for testing ionization type neutron detectors. As the removal of lengthy dry tube assembly and retrieving the detector from it requires more time and man power, a permanent straight dry tube fixture with shielding arrangement is being planned for testing these detectors on regular basis. It is also planned to test proto type neutron detectors of PFBR in KAMINI reactor.



**Fig. 4** Assembly of self powered neutron detectors

## I.10 Comparison of Neutron Attenuation Measurements between Advanced Shield Material Ferro Boron and $B_4C$ in KAMINI Reactor

Theoretical studies have shown that use of ferro boron has the potential of improving economics and reduction of volume of shields of fast reactor core shielding. Experimental measurements of the neutron attenuation in the material were carried out using the neutron beam of KAMINI reactor whose spectrum is fairly similar to the neutron spectrum incident on the shields in PFBR. Experimental measurements were also carried out in boron carbide powder for comparison. The ferro boron samples contained 11.8 and 15% of boron. The bulk density of both the samples is  $3.8 \text{ g/cm}^3$ . The experiment was conducted by stacking the ferro boron filled in the five aluminium boxes in front of south end neutron beam. The various activation foils were fixed in between the boxes filled with ferro boron at required distances. The foils become activated when subjected to neutron flux and the measurements of their activities at different depths in the shield material were obtained using high purity germanium co-axial and planar detector based gamma ray spectrometers. Analysis of the measured reaction rates were carried out and neutron attenuation characteristics obtained.

In the first experiment, five aluminium boxes of two different sizes such as  $300 \times 150 \times 50 \text{ mm}$  and  $300 \times 150 \times 60 \text{ mm}$  filled with ferro boron of 11.8% boron was used. The overall thickness of the shield model



**Fig. 1** Arrangement of ferro boron filled boxes and foil holders at south beam of KAMINI

was 335 mm. As shown in Figure 1, the boxes were stacked in the south end beam path with the help of a specially designed stand. In the first phase, irradiation of indium, gold, manganese-copper, cadmium and rhodium foils were carried out. In the second phase platinum, manganese-copper foils and NaCl pellets were used. A total of 30 foils were used for six different irradiation locations in the first phase of irradiation. In the second phase 18 foils were used. In the second and third experiments ferro boron of 15% boron and boron carbide powder were used respectively. In case of ferro boron of 15% boron, 29 foils were used at six different locations in the first phase of irradiation and 18 foils were used in the second phase. In the third experiment, 25 foils were used for five different irradiation locations in the first phase of irradiation with  $B_4C$  powder. In the second phase, 10 foils and 10 pellets were used. The foils were so

selected that their combined sensitivities covered the energy spectrum from thermal, epithermal to fast neutron region. The design of foil holders is such as to facilitate proper positioning of foils in the middle of the beam path. In all the experiments the irradiation of foils were carried out at reactor power of 25 kW.

Rhodium and platinum foils were also counted in NaI (TI) detector with anticoincidence shielding. All foils were counted after sufficient delay to have dead time errors  $<3 \%$ . The reduction factors were obtained in the activation gold, manganese and copper represented thermal and epithermal flux attenuation where as indium, hafnium and rhodium represented the fast neutron reduction. Backscattered contributions are seen for thermal and epithermal reaction rates. This is mainly due to reflection of neutrons, which increases the values of the thermal neutron fluxes at the last location. However effect

**Table 1: Ratios between measured reaction rates of different locations at 25 kW (L1, L2,... represent locations)**

Thickness (cm)	Attenuation of Au (n,γ) reaction			Attenuation of Mn (n,γ) reaction			Attenuation of In (n,n) reaction		
	FeB (11.8 %)	FeB (15 %)	B <sub>4</sub> C	FeB (11.8 %)	FeB (15 %)	B <sub>4</sub> C	FeB (11.8 %)	FeB (15 %)	B <sub>4</sub> C
0 (L1/L1)	1.00	1.00	1.00	1.00	1.00	1.00	1.00	1.00	1.00
0.5 (L1/L2)	73.83	88.43	158.96	55.57	74.82	180.08	1.43	1.38	1.54
12.5 (L1/L3)	346.58	367.86	683.15	365.53	448.08	1161.61	2.89	2.88	3.55
19.5 (L1/L4)	909.64	924.27	1647.25	1086.55	1235.38	2744.32	6.63	6.81	8.98
26.5 (L1/L5)	1649.26	1711.89	426.29	2164.60	2185.26	759.77	14.95	16.33	26.45
33.5 (L1/L6)	376.74	361.10	-	435.24	520.29	-	39.92	42.91	-

of reflection on the threshold reaction rates of indium and rhodium are not appreciable. The attenuations of the measured reaction rates in cases of ferro boron of 11.8% and 15% boron as well as boron carbide are given in Table 1.

Figures 2a and 2b give the comparison of attenuation in ferro boron of 11.8% as well as 15% of boron and B<sub>4</sub>C powder as a function

of thickness for Au(n, γ) and Cu (n, γ) reactions. From the figures attenuations of Au(n, γ) and Cu (n, γ) over 20 cm of B<sub>4</sub>C is approximately 1.5 to 2.5 times more than ferro boron. It should be noted that ferro boron has only 11.8 % to 15 % of boron as compared to 78% boron in B<sub>4</sub>C. Figures 3a and 3b give similar comparison in ferro boron of 11.8% as well as 15% boron and B<sub>4</sub>C powder

as a function of thickness for In(n,n') and Hf(n,n') reactions. With regard to these reaction rates representing fast fluxes, attenuations are more or less the same in the cases of Indium and hafnium up to a thickness of 26.5 cm. The measurements and analysis have shown that ferro boron is a good alternative shield material for future breeder reactors.

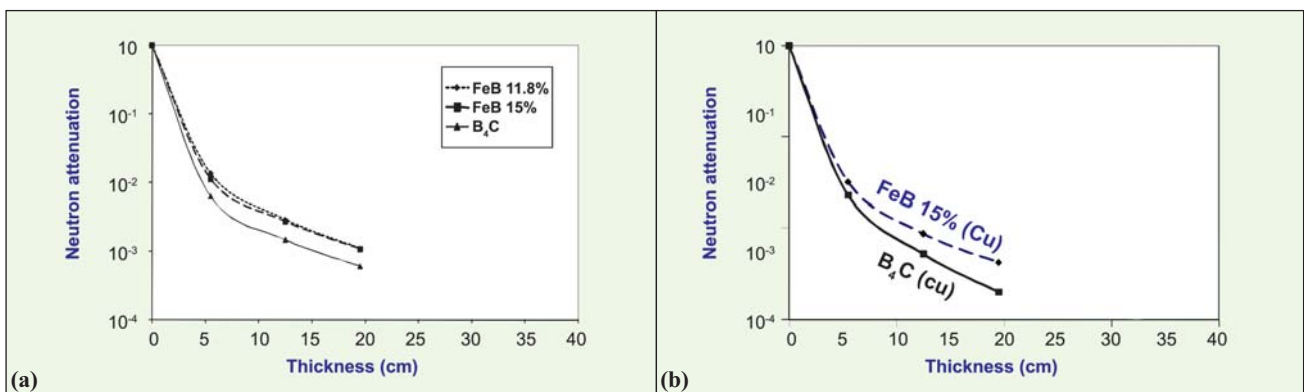


**Fig. 2** Comparison between attenuations in B<sub>4</sub>C powder and ferro boron as a function of thickness for (a) Au(n, γ) reactions (b) Cu(n, γ) reactions.

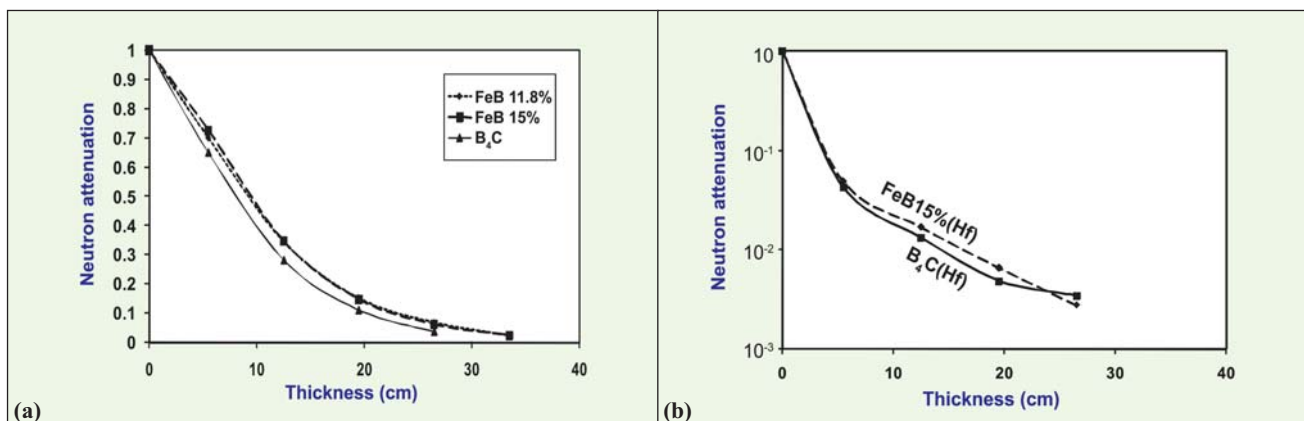


**Fig. 3** Comparison between attenuations in B<sub>4</sub>C powder and ferro boron as a function of thickness for (a) In(n, n') reactions (b) Hf(n, n') reactions



## CHAPTER II

## Prototype Fast Breeder Reactor

## II.1 Construction Status of Prototype Fast Breeder Reactor

The entire civil structural works of electrical building 1&2, control building, radioactive waste building, fuel building, steam generator building 1 & 2 have been completed. The peripheral buildings surrounding nuclear island connected building (NICB), namely service water pump house, Horton spheres, ventilation stack, diesel generator buildings and service building have been completed.

Subsequent to erection of safety vessel and main vessel in reactor vault, the next major milestone achieved was the erection of thermal baffle. Thermal baffle is to provide annular passage for the cold sodium, which is circulated to cool the main vessel and bring down the temperature during the normal operation of the reactor. It is made up of stainless steel SS316LN with two concentric shells of diameter 12.44 meter and 12.67 meter respectively with a height of 5 meter.

Further, the grid plate which holds the fuel sub-assemblies was



**Fig. 1** Erection of thermal baffle

integrated with primary pipe and erected inside main vessel. Subsequently another major milestone, the erection of inner vessel which serves as a leak resistant barrier between the hot and cold sodium of primary sodium inside the reactor, was also achieved. It is made up of stainless steel SS316LN and consists of a lower and upper cylindrical shell of diameter 12 meter

with a height of 11 meter joined together by a conical shell called Redan.

The next major milestone achieved was the erection of roof slab. Roof slab forms the top cover for main vessel and supports major components. Roof slab weighing about 230 MT is a box type structure made of carbon steel plates of diameter 12 meter with a height of 1.5 meter interconnected by radial stiffeners and cylindrical shells for the various component penetrations.

One thousand four hundred seventy tones of sodium has been transferred to the storage tanks positioned at the raft level.

The construction of indoor Gas Insulated Switchyard (GIS) has been completed & pre-commissioning works are under progress.

Manufacture of major components like additional inclined fuel transfer machine, steam generator, large rotating plug and small rotating plug,



**Fig. 2** Erection of grid plate assembly



**Fig. 3** Erection of inner vessel



**Fig. 4** Erection of roof slab

cold trap have been delivered at the site.

Conventional system equipments like compressors and air receivers for compressed air generation system, air handling units and chillers for air conditioning and

ventilation system, diesel generators have been erected in position.

Conduit laying for lighting and power cables, tele-communication cables, plant annunciation control cables, Fire detection system in Nuclear Island connected Building are in progress.

The construction of simulator building (for training & licensing of operators) was completed and the erection works for simulator control room panels, plant computers and local control centre computers has been completed.



**Fig. 5** Overall view of nuclear island connected building

## II.2 Erection of Key Reactor Assembly Components of Protoype Fast Breeder Reactor

After the construction of reactor vault, erection of the major components of PFBR reactor assembly has been started one by one. Erection of each reactor assembly component is unique and involves many challenges. It is required to handle many heavy & large vessels with thin slender structure and large diameter box type structured components. The components are required to be lowered within the restricted space available due to their optimised geometry and size towards saving cost. Stringent erection tolerances were specified to facilitate safe reactor operation, higher burn-up, proper fuel handling and in-service inspection, etc. and to prevent any mechanical interaction during all operating conditions.

A dedicated approach was followed towards realising the erection goals. For handling heavy components, a new heavy duty crane, the largest in the country, was acquired from Germany. Comprehensive analyses were made to design and develop

the handling spiders, structures and tools. Full scale mock-ups were carried out to simulate the possible wind load conditions, as-built dimensions of the components and close clearances involved. Extensive tests were conducted to qualify the handling frames and tools. Prior to erection of each key component, the sequence of activities to be followed was firmed up and important checklists were finalised through a series of dedicated brain storming discussions among IGCAR, BHAVINI and industry.

Safety vessel (Ø13.5 m, height 13 m, weight 150 t) was the first component to be erected. Having delicate thermal insulation panels mounted all around the vessel and small gap available between the vessel and reactor vault, safety vessel was erected inside the vault with much dedicated efforts (Figure 1). Core catcher (Ø7.6 m, height. ~1 m and weight 22 t) and core support structure (Ø7.8 m, height 1.6 m and weight 45 t) were integrated with main vessel at site assembly shop. From the site assembly shop, main vessel

integrated with core support structure, (total weight ~205 t) supported on base frame was moved to the crane using trolleys. A specially designed lifting frame with 24 arms (Figure 2) was used for lifting and lowering main vessel inside safety vessel (Figure 3). The lifting frame was rested on supports placed over reactor vault top keeping a specified gap between safety vessel and main vessel at bottom location. Support bracket was welded around main vessel and the load was transferred to 126 numbers of vertical tie rods extending from reactor vault. After this, thermal baffle was lowered inside (Figure 4) and integrated to main vessel by welding.

Grid plate (Ø6.8 m, height 1 m and weight 80 t) was integrated with primary pipes and spherical headers in a clean room at site. Then grid plate was lowered successfully inside the main vessel (Figure 6) and bolted to the core support structure flange holes. Further, after ensuring the space available between the spherical header support and



Fig. 1 Safety vessel erection inside reactor vault

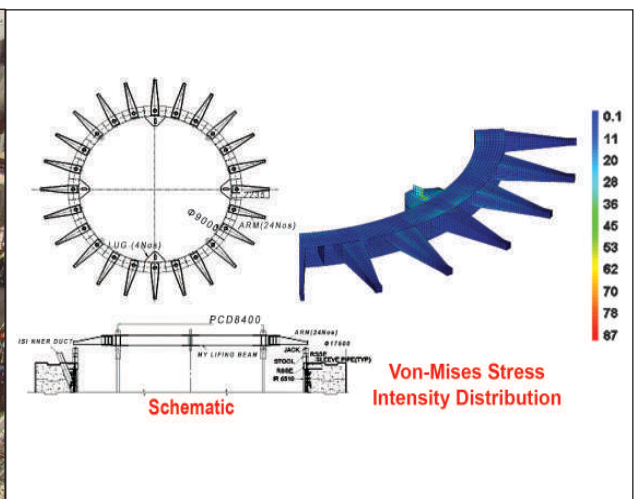


Fig. 2 Main vessel lifting frame



**Fig. 3** Erection of main vessel along with core catcher and core support structure

**Fig. 4** Erection of thermal baffle

matching support plate on the core support structure, thicknesses of the spacer plates were adjusted by machining, inserted into their respective places and fastened to facilitate free sliding of spherical header in case of differential thermal expansion during reactor operation. The achieved flatness and verticality have been checked and ensured. Mounting of grid plate on the core support structure respecting the stringent erection tolerances is an important milestone achieved towards success of the project.

Inner vessel (Ø12.2 m, height 9.1 m and weight 65 t) was erected over grid plate inside main vessel and bolted to the grid plate. For handling the vessel, a novel method was employed that minimised the time taken for engaging and disengaging the fixtures and erection and prevented any adverse / heavy loading on the vessel. The bolt holes of grid plate and core support structure and that of grid plate and inner vessel have exact matching, which is an engineering achievement. The weld joint between roof slab and main vessel (RS – MV) is the most critical joint in achieving the required dimensions which have far reaching implications in ensuring the safe and

satisfactory operation of the reactor. For this, a full scale mock-up that simulated all the site conditions and

constraints has been successfully carried out within a short period of time. Through this mock-up, the

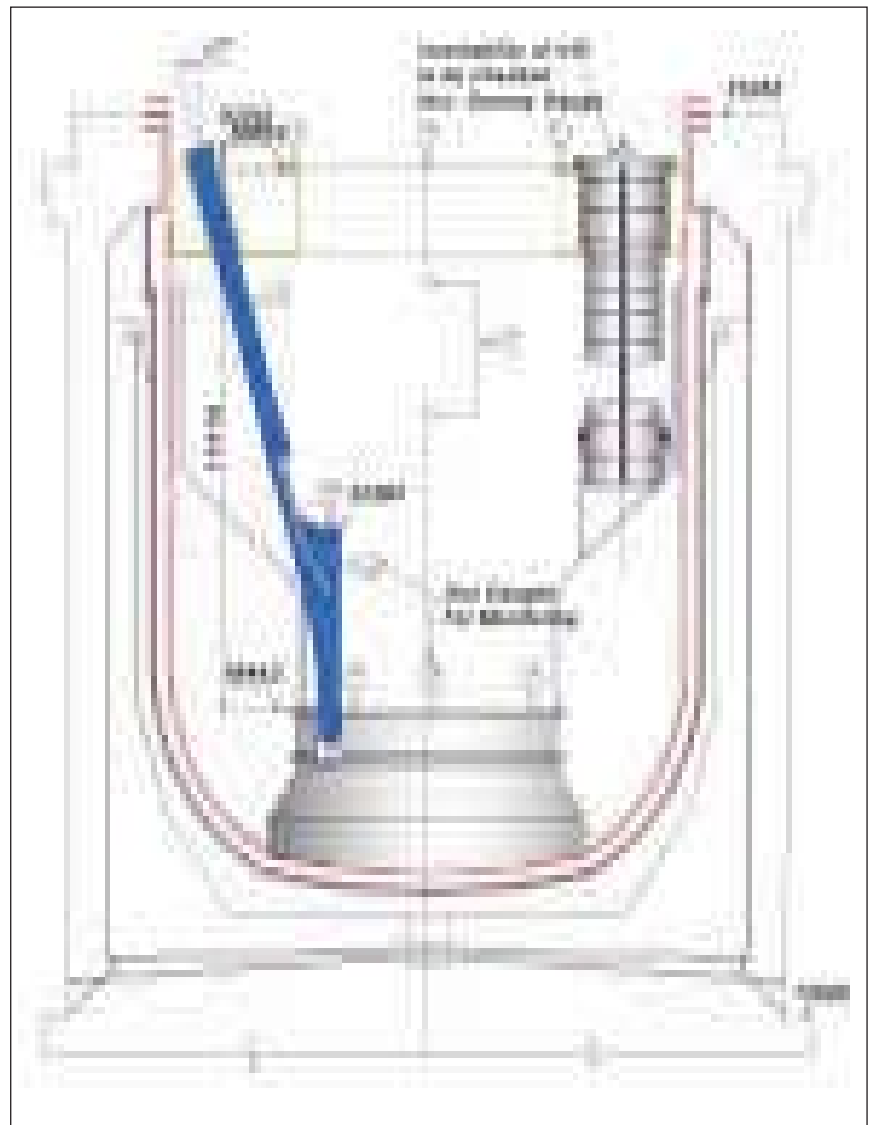


**Fig. 5** Inspection scheme during fit-up and welding of roof slab and main vessel joint

mismatch correction methodology, suitable weld configuration in the presence of constraints, welding procedure, job movement arresting system etc., have been established.

As the roof slab supports all the components which enter the main vessel, the vertical heights and alignment between the support flanges and the corresponding components within main vessel become the important design requirements to be met. Prior to erection

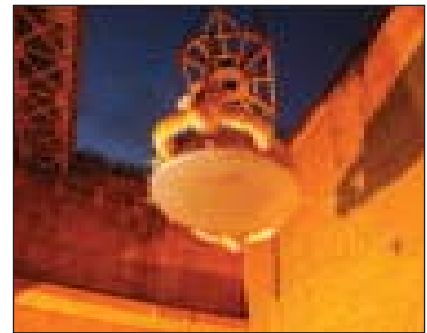


**Fig. 6** Erection of grid plate along with primary pipe

of roof slab (Ø 12.9 m, height 3.4m and weight ~235 t) and integration with main vessel, towards ensuring fool proof methodology to achieve the specified

dimensions and the functional aspects, step by step procedure to be followed and the scheme for inspection (Figure 5) have been formulated.

### II.3 Beginning-of-life Gap Closure Behaviour of Experimental Prototype Fast Breeder Reactor Mixed Oxide Fuel Pin

The Prototype Fast Breeder Reactor (PFBR) will use mixed oxide fuel with two different PuO<sub>2</sub> compositions, 21 ± 1 % and 28 ± 1 % for the two enrichment zones. The fuel pellets are of annular type designed to operate at a peak linear heat rating (LHR) of 450 W/cm. The fabrication tolerances in the fuel pellet dimensions may result in higher fuel-clad-gap during the fabrication of the fuel pin. Hence, linear power of fresh fuel will be limited to 400 W/cm in the initial phase. Subsequent to the restructuring of the pellet by swelling and cracking resulting in reduction of fuel-clad gap during this phase, LHR will be enhanced to the rated power of 450 W/cm.

To evaluate the beginning-of-life gap-closure behaviour and to arrive at the required duration of pre-conditioning of fresh fuel, an experimental MOX fuel pin of PFBR fuel composition (U<sub>0.71</sub>Pu<sub>0.29</sub>)O<sub>2</sub> was irradiated in FBTR for a duration of 14 days

(burn-up ~ 2600 MWd/t) in an irradiation capsule at a maximum linear power of 400 W/cm. This fuel pin has a fissile column length of 240 mm. The fuel pin was extracted from the capsule in the hot cells of Radiometallurgy laboratory for post irradiation examination (PIE). The fuel pin was sectioned at five axial locations along the length of the fuel column and remote metallography was carried out on these sections.

Fuel-clad radial gap was estimated from the metallographic images at the cut circumferential locations in the fuel-clad cross-sections. The average radial gap was calculated and compared with that of the unirradiated fuel pin. The typical photomosaic of the fuel pin cross-section at the centre of the fuel column (120 mm from the top of the fuel column) is shown in Figure 1. The photomicrograph shows the presence of a few radial cracks. It also reveals that the fuel-clad gap has

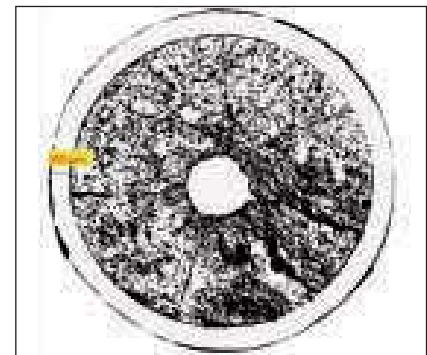


**Fig. 1** Photomosaic of fuel pin cross-section at the centre of the fuel column

reduced considerably from the pre-irradiation radial gap of around 75-110 micrometers to around 13 micrometers throughout the fuel column length after irradiation for 14 days. Cracking of the pellets and relocation of the fuel has resulted in reduction of fuel-clad gap. The early closure of the fuel-clad gap is a valuable feedback indicative of the optimum preconditioning period required for the fresh fuel before enhancing the linear heat rating to the design value.

## II.4 Qualification Testing of PFBR Transfer Arm in Air

**T**ransfer arm is the in-vessel fuel handling machine of PFBR. The machine was indigenously designed and manufactured. The machine which is 23.4 meter in height, weighs 23 tonnes and consists of several parts operating with close tolerances makes assembly, disassembly and modifications a challenging task.

The outer tube is a critical component of the gripper assembly which is responsible for hoisting and lowering the fuel sub assembly from and into the core. During the initial functional testing in air, the machine developed problem resulting in scoring of the outer surface of the outer tube which is a composite assembly of pipes of a total length of ~ 14.5 meter and 137 mm in diameter. As a result of the scoring the component was jammed in its mating part and the testing had to be stopped. The machine was then disassembled and

the problem was analyzed. The design and materials were modified suitably and later validated in a mock up testing. After completion of the mock up tests, the modifications were implemented in the prototype (Figure.1).

A modified grid plate arrangement consisting of six sub-assembly sleeves and a port for locating transfer pot was fabricated in carbon steel and assembled in large component test rig (Figure 2). The transfer pot was suspended by its rollers on guides and supported on columns. The elevation of the top of the subassemblies mounted on the grid plate was 22,400 mm. The transfer arm was assembled above the grid plate with the oval shield plug bottom flange at an elevation of 30,035 mm. Above arrangements have been made equivalent to the reactor conditions.

Tests were conducted with a mock core consisting of six straight subassemblies (each of 4.5 meter in height and 260 kg weight) arranged in a hexagonal pattern and a bowed (53 mm) sub assembly in the centre to test smooth operation of transfer arm in adverse condition. The testing consisted of lifting the sub assembly, rotating the machine, lowering the sub assembly into the Transfer Pot, and then reversing these steps to lower the sub assembly back into the mock core.

One cycle of operation involved gripping the sub assembly from the central location in grid plate, raising the sub assembly by 406 meter, rotating transfer arm by ~ 87° in order to align the subassembly over the



**Fig. 1** Transfer arm under assembly

transfer pot and lowering by 4.6 meter in order to rest the sub assembly inside the transfer pot. The testing was done at the gripper hoist speed of 30 mm/s.

The air tests were trouble free and the stipulated requirement of two hundred cycles of testing of the gripper assembly was successfully completed. This has increased confidence in the performance of the machine which is now being readied for sodium testing.



**Fig. 2** Grid plate arrangement with six subassembly sleeves

## II.5 Performance Evaluation of Diverse Safety Rod Drive Mechanism for Prototype Fast Breeder Reactor

**P**rototype Fast Breeder Reactor (PFBR) is equipped with two independent, fast acting and diverse shutdown systems. The absorber rod of the first system is called Control and Safety Rod (CSR) and of the second system is called Diverse Safety Rod (DSR). The respective drive mechanisms are called Control and Safety Rod Drive Mechanism (CSRDM) and Diverse Safety Rod Drive Mechanism (DSRDM). There are nine number of CSRDMs and three number of DSRDMs in Prototype Fast Breeder Reactor.

Full scale prototypes of both CSRDM and DSRDM were manufactured and subjected to extensive testing, including performance testing and endurance testing, in argon and in sodium under simulated operating conditions.

After successful completion of the assembling at manufacturer's site, all the mechanisms were transported to IGCAR. Figures 1 and 2 show the photographs of upper and lower parts of DSRDM-1. All the mechanisms are stored in 'ARDM storage facility' in Large Components Test Rig (LCTR) of Engineering Hall-III. Care is taken to prevent the entry of foreign particle and to prevent the corrosion of the mechanism.

All functional tests in air are carried out in dedicated test centres maintaining controlled environment, meeting the interface dimensions of CSRDM / DSRDM.



**Fig. 1** Lower part of DSRDM-1

Site testing of all the three numbers of Diverse Safety Rod Drive mechanism was completed successfully. All the functional checks which characterize the performance of the mechanism such as frictional force measurement, torque measurement, translation characteristics, inter seal leak rate



**Fig. 2** Upper part of DSRDM-1

measurement, electromagnet minimum holding current measurement, EM response time measurement etc. were carried out and the test results were found to be satisfactory.

After the site testing, DSRDM was cleared for erection in PFBR. In addition, the base line data was generated for future use.

## II.6 Manufacture and Functional Testing of Primary Side of Inclined Fuel Transfer Machine

Inclined fuel transfer machine (IFTM) (Figure 1) is one of the critical machines of the fuel handling system. It is used in Prototype Fast Breeder Reactor to transfer spent fuel subassemblies from the in-vessel transfer post located in the periphery of the reactor core to the ex-vessel transfer post located in fuel building. In the reverse direction, the spent fuel is replaced by fresh fuel. The machine was designed jointly by BARC and IGCAR.

The machine consists of two legs, the primary side provided within the reactor containment building and the secondary side located in fuel building. The primary leg includes the primary tilting mechanism, primary ramp, shield plug, gate valve, bellows and interconnecting piece. The secondary leg consists of secondary ramp, secondary tilting mechanism, gate valve and inter-connecting piece. The rotatable shield leg interconnects the primary and secondary legs and includes a rotary support table supporting on a slewing ring. The transfer of the subassemblies is carried out in a sodium filled pot to ensure removal of the decay heat of the spent fuel subassemblies. The pot moves on rollers over rails provided on both the legs. Hoisting of the pot is done using a welded link chain moving over a sprocket. The primary/secondary tilting mechanism serve to tilt the pot from vertical to 17/23° inclination. Location and orientation of the rails within individual components and relative alignment of rails between

components are kept within precise requirements in order to ensure smooth movement of the pot.

The manufacture and testing strategy of the fuel transfer machine involves two phases. In Phase I, the primary ramp and primary tilting mechanism are manufactured first, tested and installed in the reactor matching with the sequence of reactor assembly components. In Phase II, an additional primary ramp and primary tilting mechanism is manufactured for use along with other Inclined Fuel Transfer Machine components for integrated assembly and testing. Testing in air and sodium is planned to be carried out before erection in the reactor.

Manufacture of Phase I of inclined fuel transfer machine was completed at M/s MTAR, Hyderabad. The overall assembly (Figure 2) is 20 meter in height, 4.5 m in width and weighs 30 tonne. The major challenges were controlling distortion of rails during hardfacing using colmonoy and meeting the tolerances, profiling of the sprocket groove to ensure smooth release of chain and kinematic design modifications to ensure smooth and noise free movement of pot. The challenges were successfully overcome and functional testing of the assembly for twenty cycles were successfully carried out. It will be re-assembled at large component test rig at IGCAR and will be tested in air & sodium before despatch to BHAVINI.

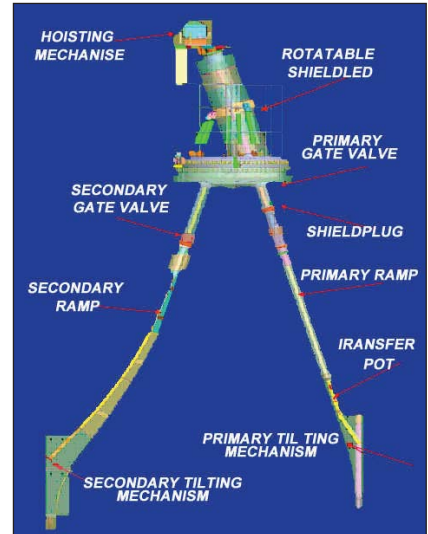


Fig. 1 Inclined fuel transfer machine



Fig. 2 Inclined fuel transfer machine assembly at M/s MTAR

## II.7 Design, Development and Manufacture of Small and Large Rotatable Plugs for Prototype Fast Breeder Reactor

### Design challenges

Small & large rotatable plugs (SRP & LRP) are the two important components of Top Shield (Figure 1) in PFBR. They provide shielding against gamma & thermal radiation as well as facilitate in-vessel fuel handling operation in combination with transfer arm. Conceived as large diameter box structures measuring  $\phi 6.9$  m, 1.8 m height to give high rigidity with minimum weight, the natural frequency is kept above 20Hz in order to avoid peak in-floor response spectra and the relative horizontal / vertical movement between top shield and core top during SSE is limited to 25 mm /  $< 0.5$  \$ reactivity insertion. From the functional requirements of the control plug and transfer arm (TA), which are supported on small rotatable plug, the deflection / rotation of large & small rotatable plug (due to thermal and mechanical loads) are restricted to control the misalignment between absorber rod and their drive mechanism and lateral displacement between transfer arm centre line and subassembly at the subassembly top level. The box structure is fabricated from special grade carbon steel (A48P2) to ensure

that it is free from lamellar defects and the thicknesses of plates used is restricted to 20 mm to avoid post weld heat treatment of completed large/ small rotatable plug owing to its large diameter.

A warm roof concept ( $T \sim 383$  K) was chosen to avoid deposition of sodium in the annular gaps at component penetrations. Air in a closed loop is used for cooling the bottom plate and the vertical shells of the penetrations. The hot air after cooling the bottom plate and penetration shells is used to heat the top plate so that the desired  $\Delta T$  between the top & bottom plates is achieved.

To enable rotation of these plugs, the same are mounted over large diameter bearings measuring  $\sim \phi 6.6$  m &  $\phi 4.4$  m (Figure 2). These bearings are provided with in-built gears to drive the same. Subsequent to difficulty in importing, these bearings were indigenously designed with axial/radial run-out of 0.4/0.8mm and 0.25/0.5mm in large and small rotatable plug respectively. The gears were designed to transmit huge torque required for rotating the plugs.

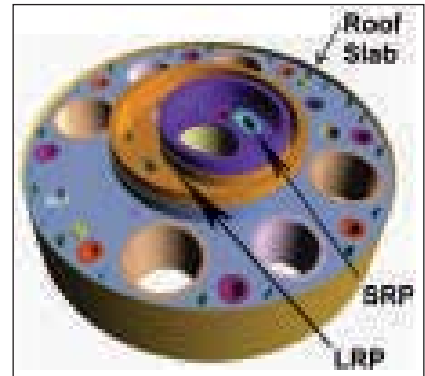


Fig. 1 Top view of top shield assembly

To avoid effect of backlash between gears over the measurement of plug position, the encoder and synchro are mounted over a specially designed anti-backlash gear arrangement. The final assembly and welding of various subassemblies were planned beforehand through 3D CAD modeling (Figure 3).

Inflatable seals along with back-up seals are provided between stationary and rotating parts to achieve required leak-tightness. To reduce the frictional resistance during rotation, the inflatable seals as well its mating sealing surface are provided with teflon coating ( $50 \mu\text{m}$  thickness).

### Manufacturing challenges

Due to stringent design requirements and large size as well as extensive

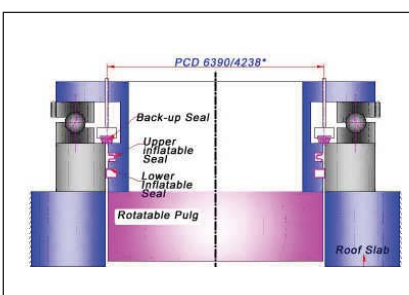


Fig. 2 Sealing & bearing arrangement for rotatable plugs

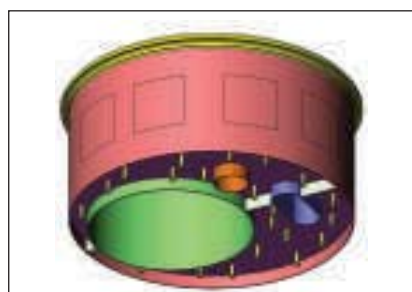


Fig. 3 3D CAD model of small & large rotatable plugs



Fig. 4 Large diameter bearing



Fig. 5 Teflon coating of SRP-BSR ring



Fig. 6 Backup seal test rig



Fig. 7 Assembly of small rotatable plugs within large rotatable plugs

welding involved in fabrication, there were several challenges as listed below during manufacture of box structures.

- \* Achieving the dimensions within the tolerances specified based on functional aspects.
- \* Ensuring proper weld fit-up between large size fabricated shells.
- \* Ensuring the soundness and quality of welds.
- \* Meeting the interface requirements with other components.
- \* Integration of plug assembly, support arrangement and seals.
- \* Performance testing of seals and bearings.

Based on the functional requirements such as reducing the radiation streaming gaps, ensuring structural rigidity under buckling, optimization of size etc., tight fabrication tolerances are specified for the rolled and welded penetration shells as well as manufactured structures. Achieving the dimensions within the specified tolerances was a challenge from the fact that the structures are to be fabricated completely by welding of rolled shells and plates. The problems faced during manufacture were overcome

through extensive study, analysis and mock-ups. Through well coordinated effort, the large diameter bearings were realised based on the indigenous design (Figure 4). Teflon coating of large diameter rings was carried out which was most challenging. Due to large size of forgings over which teflon is to be coated, distortion of the rings during heating/cooling is one of the primary concerns which was taken care through adequately, supporting the ring and controlling the heating and cooling rates (Figure 5). Back-up seals are one of the most challenging to be realized. Detailed and elaborate works were carried out to develop these seals indigenously. Room temperature and elevated temperature leak tests were carried out on  $\phi 1\text{m}$  sample seals (Figure 6) and after confirming that sample seal meets the functional requirements, reactor size seals measuring

$\phi 6.4\text{ m}$  &  $\phi 4.4\text{ m}$  were manufactured. Assembly of all the components and fixing of seals were carried out to perfection without any problems through coordinated efforts (Figure 7).

Performance tests of small and large rotatable plugs like leak testing of seals, positioning accuracy of the drive system, torque estimation for drives, run-outs in large bearings, end limit switch activation for plug rotation etc. were carried out to ensure that the design objectives were met. The leak testing was carried out with seals inflated to 70 kPa (g) pressure whereas the interseal space was pressurized to 25 kPa (g). Considering the overwhelming dimensions of the seals tested ( $\phi 6.4\text{m}$  &  $\phi 4.24\text{m}$ ), and the negligible quantity of argon required per day to meet the requirements, the observed leak rates (Table 1) are very much acceptable.

Table 1: Results of leak testing	
Region	Observed leak rate across seals (std.cc/s)
LRP Back-up seal and lower inflatable seal	0.28
LRP Back-up seal and upper inflatable seal	0.3
SRP Back-up seal and lower inflatable seal	0.16
SRP Back-up seal and upper inflatable seal	0.12

## II.8 Demonstration of Indigenous Manufacturing Capability of Sodium Pumps for 500 MWe Prototype Fast Breeder Reactor

**D**esign, selection of materials and manufacturing technology for the sodium pumps differs to a large extent from the conventional pumps as sodium pumps operate at high temperature (673 K) and handle sodium. Chemically reactive nature of sodium requires an inert atmosphere above the sodium free surface. This requirement makes the sodium pumps to be necessarily designed vertical. Pumps are of single stage type with low suction pressure (characteristic of pool type breeder reactors) driven by variable speed drive system to operate at required speed for various reactor power level. It is also equally important that careful choice of materials for the various components of the pump is made. Austenitic stainless steel (SS 304 LN) is chosen as the principal material, in view of its good high temperature mechanical properties, compatibility with liquid sodium, good weldability, availability of design data and satisfactory experience in the use of these steels in fast reactors all over the world. The manufacturing technology for these pumps involves high degree of skill for manufacture of precision tolerance stainless steel

components with sophisticated heat treatment and hard facing technologies and manufacturing of high quality large SS castings. The main features of primary sodium pump (PSP) and secondary sodium pump (SSP) are identical like mechanical centrifugal, vertical type with free sodium surface having argon cover gas. The seals and bearing systems are also similar in nature. The salient characteristics of sodium pumps are indicated in Table 1.

One of the major challenging areas in the manufacture is fabrication of long shaft (Figure 1) and its heat treatment with minimum dimensional distortion. The shaft is a stepped one, made of three forged pieces welded together i.e., two solid end pieces joined with a central hollow tube. As the shaft has to operate under close running clearance at the bottom bearing level, it is machined (Figure 2) to high standards with tight tolerances (concentricity between bearing support locations to be 50 microns).

Similarly, the welding process for joining the three parts of the shaft must ensure that the distortion is kept to a bare minimum as no machining on the hollow part and no straightening of the shaft are permitted after welding. To minimize shrinkage and distortion during welding, a weld joint design with zero root gap and a backing centering ring (hollow) configuration was adopted. To relieve the residual stresses and maintain the dimensional stability of

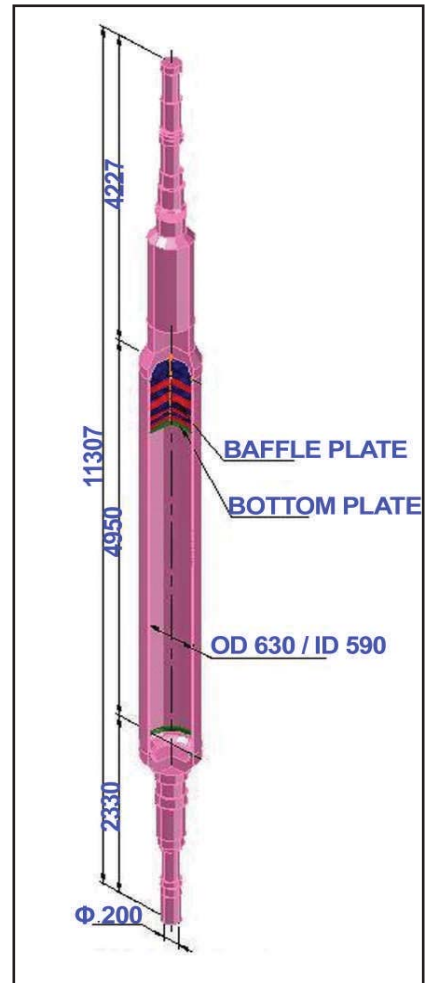


Fig. 1 Shaft of primary sodium pump

the shaft during operation, the shaft is stress relieved as per code requirements in specially built vertical furnace with controlled atmosphere of argon plus 10% hydrogen (to avoid any scale formation).

After the finish machining, balancing of the shaft with all rotating components to G0.4 grade accuracy of ISO 1940 was challenging due to large length and overhang. The other challenge is to achieve a crack free colmonoy deposition of hard facing on the surfaces of hydrostatic bearing journal and bush with 1 mm (min.) thickness and 45 HRC

Table 1: Characteristics of pump		
Parameter	PSP	SSP
Flow (m <sup>3</sup> /s)	4.13	3.34
Head (m)	75	65
Speed (rpm)	590	900
Motor power	3600	2700
Flow halving time (s)	8	4
Diameter (mm)	630/590	300/270
Length(m)	11.3	5.6



**Fig. 2** Machining of primary sodium pump shaft

hardness value. The spherical shell of SSP is made of rolled and pressed plates welded together with controlled sequence to minimize distortion (Figure 3).

A large weight SS casting with ASTM quality level 2 (no cracks, hot tears, inserts and mottling) with stringent surface finish (better than 6.3 microns in accessible areas to minimize erosion due to even mild cavitation or pitting) is also made for the impeller for the first time in the country.

Apart from good radiographic quality, castings are required to meet specific chemical composition, mechanical properties and delta ferrite content.

Adequate care is given for draining of sodium (during removal of the pump for maintenance) by selecting smooth geometry for sodium wetted parts.

Performance testing of pumps include testing in water at different speeds to monitor the hydraulic

(head, capacity and efficiency), mechanical behaviour (vibration, noise) and cavitation free operation of the pump in a test loop at manufacturers site. Design of the test set up is in conformance with Hydraulic Institute Standards. During the pump performance testing, the oil cooling circuit of mechanical seals and bearings also will be evaluated. Finally endurance test for 50 hours is planned at the nominal running speeds of respective pumps.

The whole exercise has demonstrated the capability of manufacturing large components indigenously for the sodium pumps with stringent manufacturing requirements.

Initial trial run of first SSP was completed and the pump is ready for endurance testing.

Operating experience of pumps in the fast reactors worldwide including FBTR (~1.5 lakhs hour operation of pumps) has proved the reliable

operation of the component. Adoption of nearly similar design concept for sodium pumps for Prototype Fast Breeder Reactor underscores this reliable performance.

The challenges, largely due to size and weight, and the experience gained during various stages of design and manufacture are useful towards optimization and improving the design of sodium pumps for future reactors.



**Fig. 3** Secondary sodium pump spherical shell under manufacture

## II.9 Vibration Measurement of Subassembly using Ultrasonic Technique

Low induced vibration of subassemblies in PFBR is not desirable as it can cause failure of the fuel element clad tubes due to fatigue, wear and vibration induced fretting. Excessive vibration will also cause reactivity fluctuations, rattling and power control problems. During commissioning of PFBR, it is required to measure the vibration of subassembly in sodium in isothermal condition at 493 K. It is difficult to carry out such measurement under sodium, using conventional accelerometers. Development of ultrasonic technique for the vibration measurement of sub-assemblies in PFBR is under progress.

Ultrasonic sensor operating in pulse-echo mode is used to detect the movement of subassembly in the experiment carried out in which ultrasonic sensor is mounted near the target (subassembly surface) and the time delay between the transmitted pulse and reflected echo is used to calculate the distance between the sensor and the target. The movement of the target (subassembly) will cause a variation in the time delay, which will be a representation of the subassembly movement. An electro-dynamic exciter attached to the subassembly is used to excite the subassembly with known frequency and amplitude during experiments in water. For validating the results obtained from ultrasonic technique, a linear variable differential transformer (LVDT) and an accelerometer attached on the subassembly, were used as the

reference sensors. Figure 1a shows instrumentation schematic employed.

A test setup was made up of stainless steel, simulating the geometrical arrangement as in PFBR. Perspex embedded SS window was assembled in the test section to view the movement of top end of subassembly during measurements. Ultrasonic sensor is kept immersed in water near top of the subassembly and it is fired continuously with different pulse repetition frequencies. Using electro-dynamic exciter, subassembly is excited and experiments were conducted with different excitation frequencies and amplitudes. Experiments were repeated with different pulse repetition frequencies to study the effect of signal distortion. The output signal from the ultrasonic equipment and reference linear variable differential transformer were recorded and analyzed.

Signal processing technique to extract the vibration signal from the

ultrasonic pulse-echoes has been developed in LabVIEW. Filtering and smoothing of the signal has been carried out and the frequency and amplitude of the vibration has been measured from the vibration signal. The amplitude and frequency of vibration of subassembly measured using ultrasonic technique was found to be matching well with the reference signal from linear variable differential transformer. Figure 1b shows the reference signal recorded from the linear variable differential transformer for an excitation frequency of 2 Hz and amplitude 0.5 mm (peak to peak) and Figure 1c shows the signal extracted from the ultrasonic sensor. The measured frequency of vibration and amplitude is 2.04 Hz and 0.51 mm peak to peak.

Analysis of the experimental result indicates the overall error is less than 3%. The developed technique proved to be a potential and promising non-destructive evaluation method for vibration measurement under sodium.

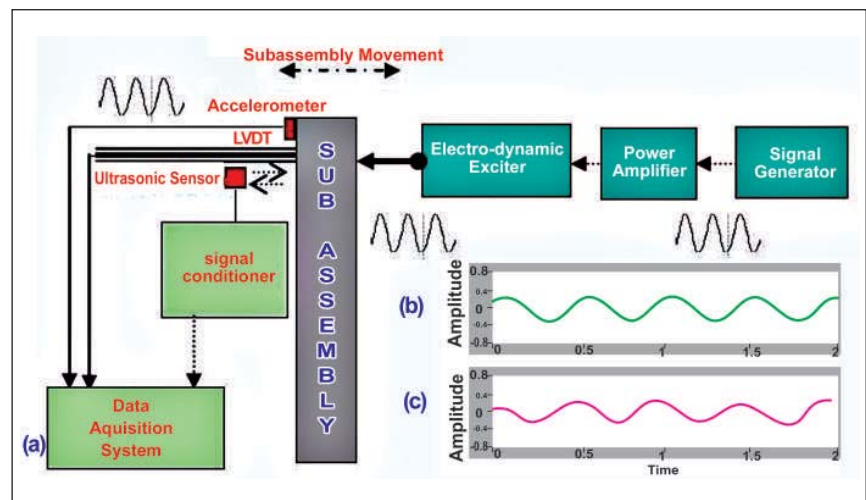


Fig. 1 (a) Instrumentation schematic with (b) Linear variable differential transformer reference signal and (c) Vibration time waveform extracted from ultrasonic pulse-echo signals

## II.10 Development of Methodology for Non-destructive Assessment of Integrity of PFBR Steam Generator Shell Welds

The inner shell of the PFBR steam generator (SG) is made in two halves (modified 9Cr-1Mo steel) and welded axially throughout the length and circumference at four locations. During circumferential welding of the steam generator shells, defects such as arc strike on the tube wall, spatter of weld metal and fusion of weld root with tubes might form due to the narrow gap (3 to 5 mm) between the shell and the peripheral steam generator tubes. Presence of such defects, especially fusion, would adversely affect the in-service performance of the steam generator. Hence, it is essential to inspect the peripheral tubes after circumferential welding for detection of defects using nondestructive evaluation (NDE) techniques. There is no standard guideline or technique available for nondestructive detection of such defects.

Nondestructive evaluation techniques for detection of such welding defects should be chosen such that they are sensitive, reliable, fast and implementable in the shop floor. In the shop floor conditions, the peripheral steam generator tubes can be accessed for inspection from the inner side of the tube or from the outer surface of the shell. Remote field eddy current (RFEC) technique, developed for in-service inspection of steam generator tubes, is suitable for this application for inspection from the tube side.

In order to understand the remote field eddy current and ultrasonic signals due to welding defects calibration, specimens simulating the actual shell welding conditions have been fabricated. Low, medium and high levels of arc strike, spatter and fusion have been created in a 2 meter long steam generator shell sector with a circumferential weld by systematically varying the welding parameters.

Testing of calibration specimens revealed that the characteristics of the signals due to arc strike and spatter type of welding defects were nearly identical, found different for fusion and support structures. This difference in signature of signals can be effectively utilized for automated classification using K-means clustering algorithm.

Ultrasonic testing of calibration specimens revealed single back wall echo, when there was no fusion, and two back wall echoes when there was fusion. In order to further

understand the ultrasonic A-scan signals of fusion type defects, numerical simulation has been carried out using CIVA software which works on semi-analytical formulation. The model predicted A-scan signals have been found to be in good agreement with the experimental signals. Thus, the simulation study has given confidence that ultrasonic technique can be used for unambiguous identification of fusion type of weld defects.

Combining remote field eddy current and ultrasonic techniques, a methodology has been developed for reliable detection of welding defects. The methodology which was implemented at L&T, Powai (Figure 1) essentially involves using remote field eddy current technique for detection and classification of all types of welding defects in peripheral steam generator tubes and ultrasonic technique to ascertain the fusion type of defects. The



Fig. 1 Inspection of SG-A at the manufacturer's site

methodology consists of the following steps:

- (a) Remote field eddy current testing of steam generator tubes and storing of the horizontal and vertical voltage signals
- (b) Automated detection of signal peaks above the threshold level (amplitude of signal from defect of depth 5% wall thickness that is acceptable) using peak finding algorithm
- (c) Classification of peak amplitude into arc strike and spatter, fusion and support structures using K-mans algorithm
- (d) Identification of regions corresponding to fusion type indications
- (e) Ultrasonic testing from shell side to confirm fusion

The methodology has been validated using steam generator tubes having an acceptable defect and without defects. Remote field eddy current testing of the tube with defect resulted in an indication which, as expected, has been classified into Cluster I, corresponding to arc strike and spatter that are acceptable.

During the actual implementation, a flexible remote field eddy current probe with 25 m long nylon conduit has been specifically developed for this purpose. A total of 144 peripheral tubes have been tested using remote field eddy current technique in four steam generators (36 tubes in each).

The methodology has not detected any fusion like indication, thus

qualifying the welding procedure employed for circumferential welding of shells. A photograph of inspection carried out on SG-A is shown in Figure 1. Typical RFECD signals of one of the SG tubes are shown in Figure 2. The remote field eddy current signals detected by the automated peak finding algorithm are marked as circles. The clustering algorithm has classified the peak detected indications into support structures (Cluster III).

Remote field eddy current testing revealed that the tubes are free from welding defects. Thus, implementation of the methodology has also resulted in ensuring the structural integrity of the steam generator.

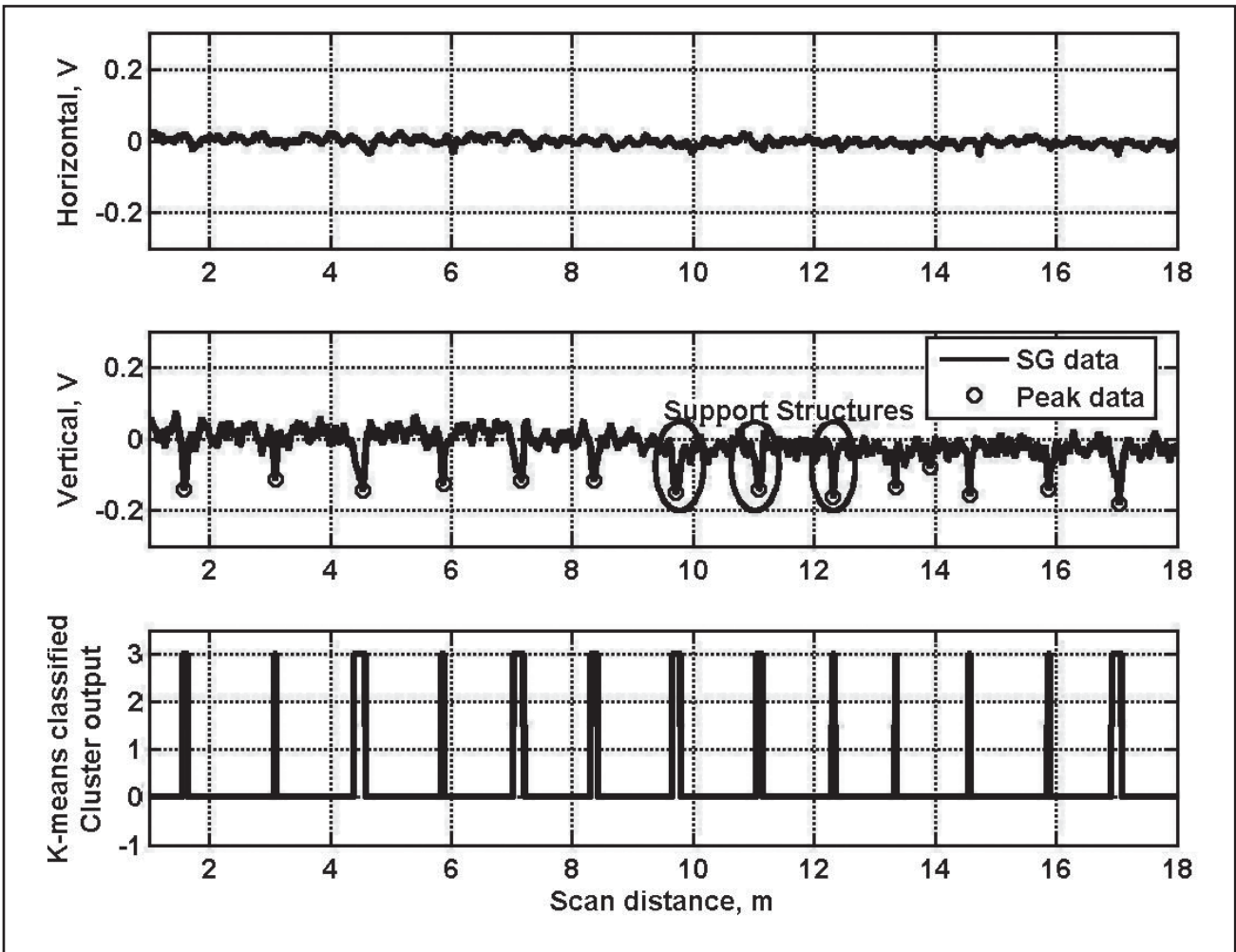


Fig. 2 Remote field eddy current signals from one steam generator tube and the K-means classified output

## II.11 Development of Ultrasonic Technique for Detection of Subassembly Protrusion in Prototype Fast Breeder Reactor

**P**rotrusion of any subassembly from the normal level in PFBR is detected using ultrasonic technique. This becomes essential because visual inspection of subassemblies under sodium is not possible due to its opacity.

The ultrasonic under sodium scanner manufactured for PFBR was tested in water and later in sodium in a one meter diameter vessel in Engineering Hall-3. The distance of the head of the subassembly from the ultrasonic under sodium scanner is 5.4 meter in liquid sodium environment in PFBR. Experiments at National Institute of Ocean Technology (NIOT), Chennai were conducted in water at an equivalent distance of 9.2 meter as the velocity of sound is different in sodium (2500 m/s) and water (1500 m/s).

The set up consists of a water tank (16m long X 9m wide X 7m deep) with two moving platforms that are capable of moving entire length of the tank (Figure 1). The trolleys are provided with arrangements for mounting the transducer and the target and provided with drive to move the transducer/target in X, Y, Z and  $\theta$  directions. Suitable arrangement was made to fix the transducer and the target in the moving mechanism as shown in Figure 2.

The target distance was varied from a minimum of four meters to a maximum of eleven meters. The high temperature ultrasonic transducer with MI cable was mounted on fixed platform.

The target plate of size 100 X 100 mm was mounted in the movable platform. A one MHz transducer was used in tone burst mode. Both the transducer and the target were immersed to a depth of two meters in water. 400 V peak to peak with 15 cycles sine wave excitation was given to the transducer and the echo from the target at different distances from four meters to eleven meters was recorded as shown in Figure 3. The excitation voltage was limited to 400 V to ensure safe operation of the transducer.

The results confirm that it is possible to detect targets upto a distance of eleven meter (against the requirement of 9.2 meter) in water using the in-house transducer with tone burst pulser.



Fig.1 Water tank with moving platform



Fig. 2 Transducer with fixing arrangement

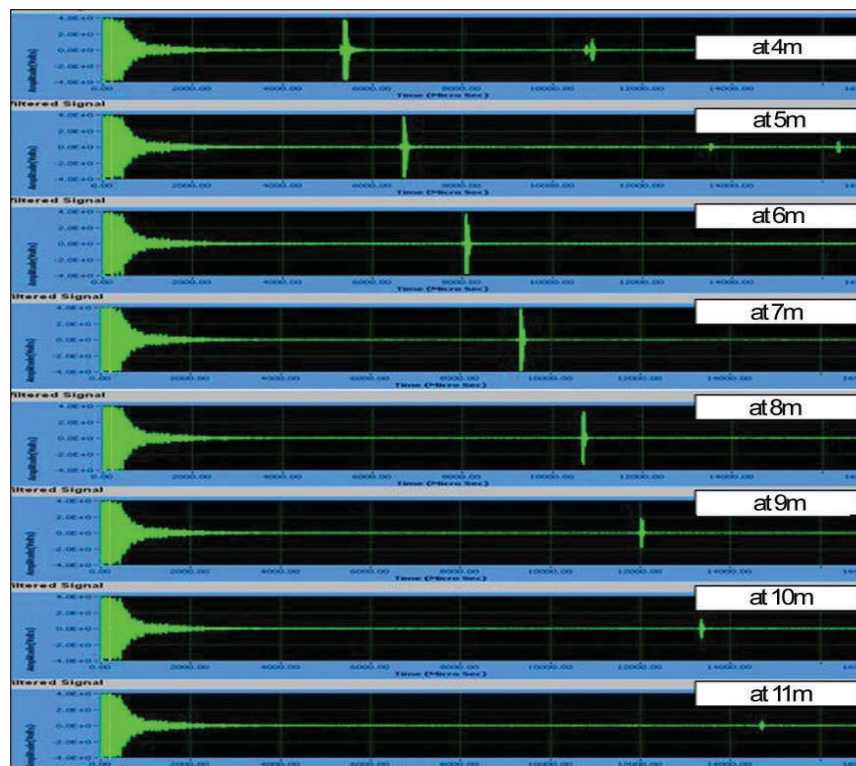


Fig. 3 A scan wave form showing echo from the target at various distance using tone burst pulser

## II.12 Manufacture and Preliminary Tests of the Prototype Fast Breeder Reactor - In-service Inspection System: Experiences to Date

The main vessel and reactor roof slab confine the primary coolant and cover gas with any associated radioactivity in PFBR. In addition to continuous surveillance during reactor operation, periodic inspection of main vessel and safety vessel of PFBR shall be carried out during the reactor shutdown conditions.

The annular inter-space between the main vessel and the safety vessel is about 300 mm and this inter-space is used to gain access for carrying out the inspection. The main vessel-safety vessel inter-space is filled with nitrogen, and the inspection campaign is to be conducted in a leak-tight manner maintaining the integrity of this atmosphere. The temperatures would be 423 K during the planned ISI campaigns and hence the devices need to be operated remotely in this environment with limited access. A comprehensive in-service inspection (ISI) system for carrying out inspection tasks has been designed and the system is in the advanced stage of development. The critical locations identified for inspection are the dissimilar weld, in-situ weld, core support structure welds ultrasonic test and the surfaces of the main vessel and safety vessel by visual examination.

The comprehensive ISI system, as designed, primarily consists of two devices – Main ISI device and DISHA. Main ISI device is a 4-wheeled vehicle which roams the inter-space over the main vessel - safety vessel surface. The latter device utilizes the anti-convection barrier (ACB) as a pathway to move around and inspect

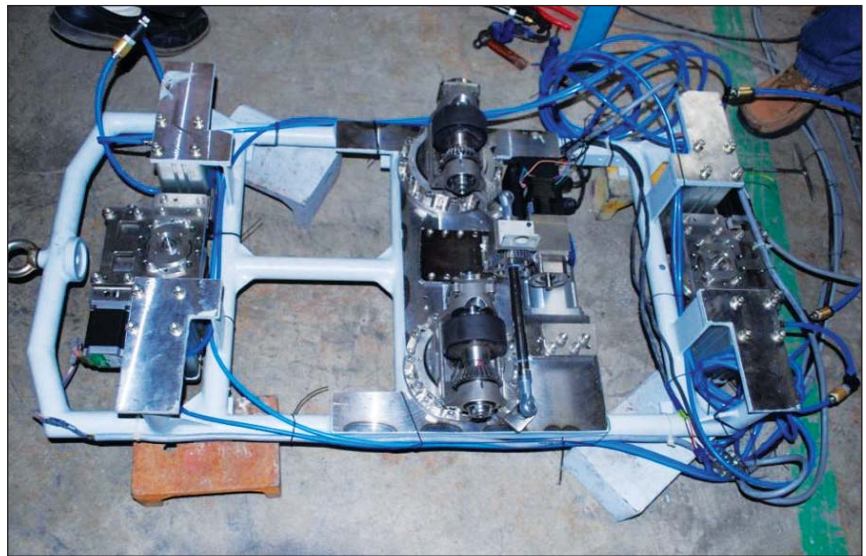


Fig. 1 Drive transmission layout of the main ISI device

the dissimilar weld and the in-situ weld. The associated chambers – the airlock chamber (ALC) and the plug handling chamber (PHC) provide leak tight handling and housing for the inspection devices and shielding cum sealing plugs, respectively. Six ISI openings at the top of the reactor vault provide access to the inter-space for deploying the vehicles. The modules for visual examination and ultrasonic test form the payloads on both the devices.

The room temperature experimental prototypes validated the inherent design principles. This led to a manufacturing schedule for making high temperature versions of the two devices with cooling of the visual examination modules in an encasement with nitrogen. The design for the main ISI device has been enhanced with two end wheels fitted with pneumatic cylinders and two base wheels arranged in such a way that two wheels are resting on

the main vessel and other two wheels are resting on the safety vessel which enable clamping of the device between the main vessel and safety vessel surfaces in the inter-space. The traction motor is attached to the middle wheels. A common steering has been provided on the middle wheels, with a floating link with individual steering on the end wheels. Figure 1 shows the main ISI device with its transmission layout.

The preliminary room temperature test run and trials were successfully carried out at the manufacturing site (Figure 2) on mild steel surface. Individual pressure regulators were used for varying the pressure of the air delivery to the actuators. Weight of the basic device without payloads is 90 kg. The vehicle was tested with 41 kg payload, for vertical and traverse movement. These tests revealed that reliable operation of the device hinges critically on the wheel linings used. High temperature



**Fig. 2** Room temperature mock-up tests of the main ISI device on mild steel surface



**Fig. 3** Room temperature tests of the main ISI device on SS 304

testing of wheel liners at Automotive Research Association of India, Pune provided an insight into the behaviour of elastomeric lining materials at various loads. Fluorocarbon and hydrogenated nitrile butadiene rubber were both used as test candidates for the lining material. A grooved VITON® wheel lining gave the desired friction gripping on mild steel surfaces without bulging and tearing. Tests being conducted on SS 304 surfaces are shown in Figure 3. Interestingly, traction results on SS 304 are excellent and the integrity of the linings did not deteriorate as in the case of mild steel surfaces. Subsequent tests were successful for the main ISI device with payloads in its ability to move over the simulated thermocouple covers on main vessel side and Ø8 mm mutual induction cable cover on safety vessel side. The room temperature mock-up test facility forming a sector of the main vessel and safety vessel is being fabricated (Figure 4) which will be utilized for validation of the devices and associated handling systems. Petals of knuckle and

crown regions have been made of mild steel to demonstrate the capability and understanding of the manufacturer's comprehension.

A high temperature (423 K) test chamber has been fabricated which will be used to validate the device assembly and the choice of its subsystems for high temperature operation. High temperature stand-alone tests of the traction motor and the steering motor (with compressed air cooling) were successful, thus justifying the selection of the motors.

Customized slip-skid sensors have been successfully developed and tested and are ready for integration with the main ISI device. It is also imperative to optimize the pneumatic tubing and electrical/ electronic wiring and plan the routing accordingly. A customized heat exchanger has been fabricated for cooling the nitrogen which is used for cooling the cameras and motors on board the ISI device. Software for the operation of the ISI devices is under development. Prototyping experience has provided lot of inputs while formulating the architecture of the software.

Visual examination camera has been customized and tested at room temperature with satisfactory results. High temperature tests are due once the heat exchanger is operational.

The trials and experimentation at the manufacturing site has revealed quality information for ensuring the development of a robust system. High temperature test and validation of the integrated system will be taken up shortly followed by comprehensive testing and validation in the mock-up test facility. The benchmark trials will be finally conducted in the reactor.



**Fig. 4** Test petals of the room temperature mock-up test facility

## II.13 Enrichment of Boron Isotopes by Ion Exchange Chromatography using Weak Base Fine Resin

Boron has been enriched using ion exchange chromatography process in the enrichment plant. In this process, HCl is used as the displacing agent and NaOH as regenerant with strong base anion resins having size of 0.3-1.2 mm. The equilibrium time for attaining 65% enrichment in  $^{10}\text{B}$ , which is the requirement for control rod material of PFBR was observed to be 48 months. Later, a technology was developed using strong base fine resin (75-150  $\mu\text{m}$  particle size) which reduces the equilibration time to twelve months. Both these technologies were transferred to Heavy Water Board and are being operational in various commercial scale plants. Further to reduce equilibration time and cost, a process has been developed using weak base anion resin. This process uses DM water as eluent and there is no

consumption of acid or alkali compared to the other two process mentioned above.

Bench scale experiments have been carried out for isotopic separation of  $^{10}\text{B}$  from natural boric acid mixture using weak base anion exchange resin. DM water was used as a displacing agent and higher enrichment was observed when compared to using strong base anion resin and  $\text{HNO}_3$  as displacing agents. Based on encouraging results, a new pilot scale setup was designed and fabricated to conduct the experiments.

Experiments are being conducted in pilot plant having six numbers of columns in series of six meter height water as shown in Figure 1. Columns are packed with the weak base fine resin (75-150  $\mu\text{m}$  diameter). Resin was pre-treated and converted into



**Fig. 1** Pilot plant set-up for  $^{10}\text{B}$  enrichment

free base form ( $\text{OH}^-$ ) by passing NaOH solution and washed with DM water. Three columns were equilibrated with required normality of boric acid solution. The boric acid band was eluted with DM water and the  $^{10}\text{B}$  isotope was found to be enriched at the rear end of the ion exchange column.

It was planned to conduct experiments with 0.1 and 0.2 N boric acid feed concentrations, and results are given in Figure 2.

From these experimental results, it was concluded that when feed boric acid solution concentration increases beyond 0.2 N, enrichment level to the corresponding number of cycles decreases but quantity increases. The equilibration time to reach 65%  $^{10}\text{B}$  is about one month. This new process significantly reduces the equilibration time and overall cost. Further, experiments are planned to be carried out in pilot plant to optimize parameters.

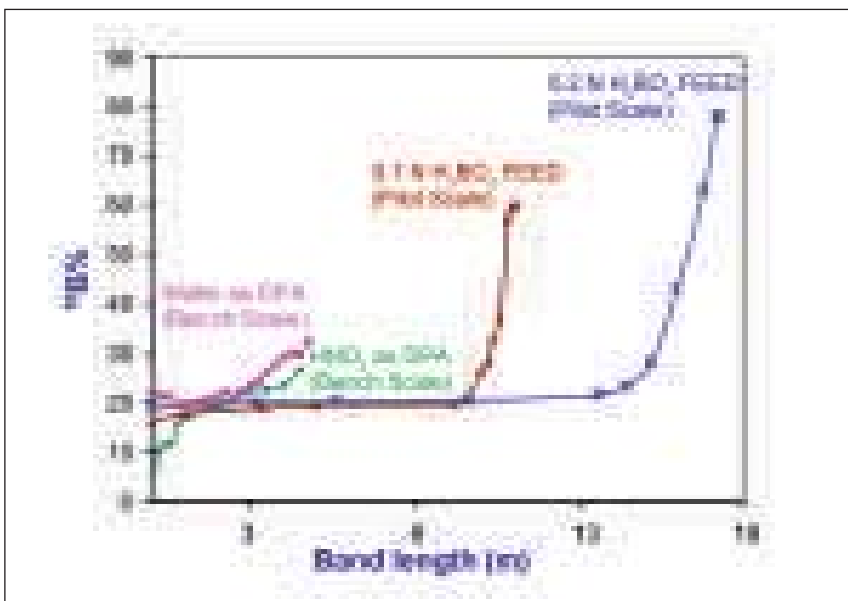


**Fig. 2** Comparison of  $^{10}\text{B}$  enrichment using water on weak and  $\text{HNO}_3$  on strong base anion resins in bench scale as displacing agents and 0.1 and 0.2N  $\text{H}_3\text{BO}_3$  feed concentration on WBA in pilot scale

## II.14 I&C for Failed Fuel Location System of Prototype Fast Breeder Reactor

It is necessary to design a system for identifying failed fuel subassembly in the core for early detection of clad failure. In case of direct contact between fuel and coolant i.e. wet rupture results in release of both gaseous and solid fission products including delayed neutron precursors into the coolant. Solid fission products such as  $^{140}\text{Ba}$ ,  $^{140}\text{La}$ ,  $^{134}\text{Cs}$ ,  $^{137}\text{Cs}$  and  $^{95}\text{Zr}$  radio-nuclides are released into the coolant that can be detected by means of delayed neutron precursors in sodium coolant using in-vessel high temperature fission chambers. Bulk DND system is connected to the reactor protection logic. Upon detection of failed fuel, in order to locate the fuel subassembly in which fuel failure occurred, 198 subassemblies are to be scanned. This is done with three numbers of failed fuel location modules operating simultaneously, each catering to 66 fuel subassemblies. Failure of fuel pin in central fuel subassembly is detected by indirect method and is inferred when there is no indication from any other fuel subassembly.

Sodium sampling sleeves, concentric over each thermocouple tube sheath, are positioned above the top of each fuel subassembly. The sampling tubes from the sleeves are routed to the base plate of the selector valve of failed fuel location modules. Selector valve with the help of motor drive, positions the outlet tube to any one of the 66 inlet sampling tubes. An optical encoder attached to the shaft of the selector valve monitors the position of the selector valve. ADC electromagnetic conduction pump is used to pump the sodium from the outlet of the

selected assembly to the sodium capacity (Figure 1).

An electromagnetic flow meter is provided at the outlet of the sodium capacity to monitor the flow of sodium. Neutron detectors ( $^{10}\text{B}$  coated proportional counters) are provided around the capacity in moderator block, to detect any neutron flux in the sodium sample, due to the fission products, which are delayed neutron emitters. The sampled sodium is returned to the pool. In order to reduce temperature difference between hot pool sodium and the sodium returning from sampling tube and to avoid high temperature at detector location, the sodium capacity is wrapped with thermal insulation. Heaters are provided to maintain a minimum temperature of 423 K for sodium in the capacity and sampling pipe.

Temperature is monitored on sodium capacity flow meter and sodium-piping, near seals and in moderator. Lead is provided as gamma shield around the capacity to reduce gamma activity. Drive shaft of the selector valve is rotated by a positional drive system with an encoder. It comprises of permanent magnet DC servo motor, servo controller and encoder.

Rotation of the selector valve permits sequential monitoring of each fuel subassembly outlet for the presence of delayed neutrons due to failure of fuel pin. Graphical user interface (GUI) and positional drive system control software are designed to operate in sequential mode and in random mode, specifying the angle or fuel subassembly.

Under normal conditions, the system is operated once in a week, otherwise

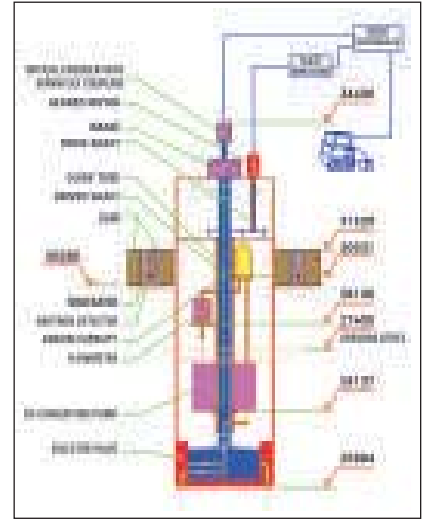


Fig. 1 Schematic diagram of FFLM

the system is maintained in poised state for the startup. When 'Bulk DND' signal actuates SCRAM, the reactor is restarted by inhibiting 'Bulk DND' signal and operated at 20% Pn to identify the location of the failed FSA using failed fuel location modules. Total scanning time is approximately eight hours. Each failed fuel location module instrumentation consists of the following:

- Selector Valve mechanism
- DC Conduction EM pump
- EM Flow Meter
- Heaters
- Pump Power Supply
- Positional Drive System
- Neutron Detectors
- I&C Panel

The instrumentation and control is provided in signal processing cabinets (SPC) in RCB-LCC1. Electronics and control for the sensors (heater, flow meter, thermocouples), positional drive system, along with interlocks (pump control logic), alarms, displays and testing facilities are provided in these signal processing cabinets.

## II.15 3D Visualization for Walkthrough of Fast Breeder Reactor Nuclear Buildings and Fuel Handling System Animation

The Prototype Fast Breeder Reactor consists of Nuclear Island Connected Buildings (NICB) and conventional systems buildings. Using the advanced visualization centre 3D plant walkthrough of all the buildings of NICB has been done. Walkthrough for Reactor Containment Building, Steam Generator Building, Fuel building, Control Building, Electrical Building and Radioactive Waste Building has been generated. The walkthrough helps in interference check between various systems and space constraints for operation and maintenance of the plant. A virtual human being was 3D modeled and has been animated for walkthrough of these buildings. The buildings consist of 3D components of various equipments, piping, heating and ventilation ducts, electrical cable trays, civil structures and steel structures. All the building walkthrough have been ported to the advanced visualization centre facility for visualizing in a fully immersive 3D environment (Figure 1).



Fig. 1 Walkthrough of virtual human in reactor containment building

### Animation of fuel handling system

This system consists of the following sub systems namely: fresh subassembly storage bay, fresh subassembly transport cask, fresh subassembly transfer gripper, and Fresh sub assembly inspection facility, nitrogen filling facility, fresh subassembly transfer chamber, fresh subassembly entry port, fresh subassembly cell transfer machine and fresh subassembly preheating

facility. The above mentioned sub systems were 3D modeled component wise, then assembled the various components with suitable textures, lighting properties and material properties. Finally the 3D subsystem has been animated based on their working principle and ported to advanced visualization centre for fully immersive 3D viewing. 3D views of various fuel handling sub systems are shown in the respective Figures 2a to d.

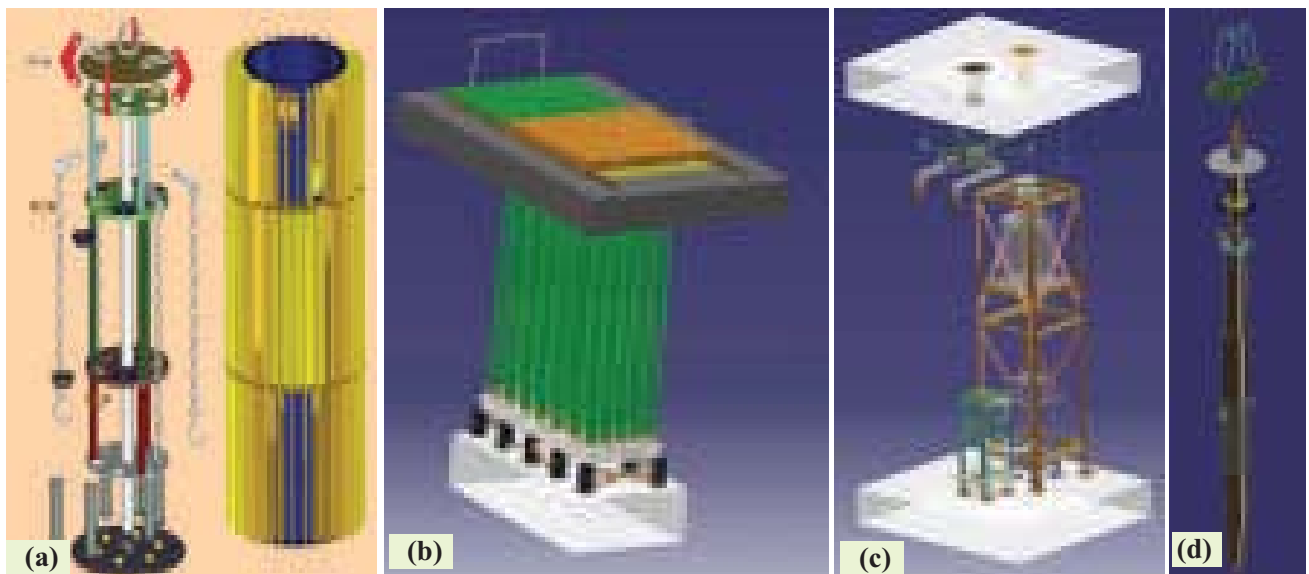


Fig. 2 3D model of fresh subassembly (a) Transport cask (b) Storage bay (c) Inspection facility (d)TA gripper

## II.16 Fault Tolerant Real Time Computer System for Primary Sodium Main Circuit of Prototype Fast Breeder Reactor

The entire primary sodium main circuit is contained in a single large vessel called main vessel. An inner vessel is provided between the core and the main vessel. The function of the inner vessel is to separate the hot and cold pool sodium. There are two primary sodium pumps and four intermediate heat exchangers in the primary sodium system. The main vessel is surrounded by safety vessel to contain the sodium if it leaks from the main vessel. Primary sodium main circuit transfers the heat generated in the core to the secondary sodium circuit and decay heat removal circuit through heat exchangers, maintaining safe operating temperature of core subassemblies and main vessel. Primary sodium pump oil cooling circuit is used to cool the bearings and mechanical seals of the primary sodium pump. Oil is used as the coolant.

In PFBR signals of primary sodium pump 1 (PSP1), intermediate heat exchangers 1 and 2 and pump oil cooling circuit of PSP1 are terminated at RCB LCC1 and the signals of primary sodium pump 2, Intermediate heat exchangers 3 and 4 and pump oil cooling circuit of PSP2 are terminated at RCB LCC3. These signals are safety class 2 signals. Hence dual redundant VME bus based real time computer (RTC) systems with switch over logic system (SOLS) is the configuration selected for these systems.

### Hardware configuration

Each RTC system consists of VME bus based 68020 CPU card, analog Input cards, digital Input cards and relay output cards. SOLS consists of switch over logic card and O-ring logic cards. Inputs from continuous level probes, discontinuous level switches and RTD inputs are connected to both the RTC systems. Both the RTC systems receive process thresholds and alarm thresholds from process computer (PC) of Distributed Digital Control System using TCP/IP protocol. Both the RTC systems scan the physical inputs, do the validation check of each analog input, process the inputs, generate outputs for interlocks and window alarm annunciation and also generate soft outputs. Software cycle time is 5 seconds. Interlock output is generated to trip the EM pump of primary sodium purification circuit based on 2/3 logic, when main vessel sodium level goes beyond the specified value. Interlock output is also generated to trip the oil pumps (part of pump oil cooling circuit) and primary sodium pumps based on 2/3 logic, when the oil outlet temperature and inlet pressure goes beyond specified value. Physical outputs from RTC systems are connected to O-ring logic card of SOLS. Both the RTC systems check the healthiness of all the cards present in the system and generate healthiness output to SOLC. If both the RTC systems are healthy then SOLC routes RTC1 outputs to plant. If RTC1 fails, then

RTC2 outputs are routed to the plant. If both the RTC system fail then fail safe outputs are routed to the plant. Figure 1 shows the configuration of primary sodium main system mounted in a 36U cabinet with analog and digital input/output simulators.

### Software development & testing

Software for primary sodium main circuit was developed by following well defined software development methodology. Waterfall model was selected for software development, because of its simplicity, ease of Verification and Validation (V & V) and tracking and control on deliverables across lifecycle. AERB safety guide SG/D-25 was followed in all phases of software development. Computer Aided Software Engineering (CASE) tools were extensively used at various phases.

System Requirements Specifications (SyRS) document was prepared as per IEEE standard 1233. Software Requirements Specifications (SRS) document was prepared as per IEEE standard 830 following the SyRS.



Fig. 1 Primary sodium main cabinet (SPCrb102 & 103)

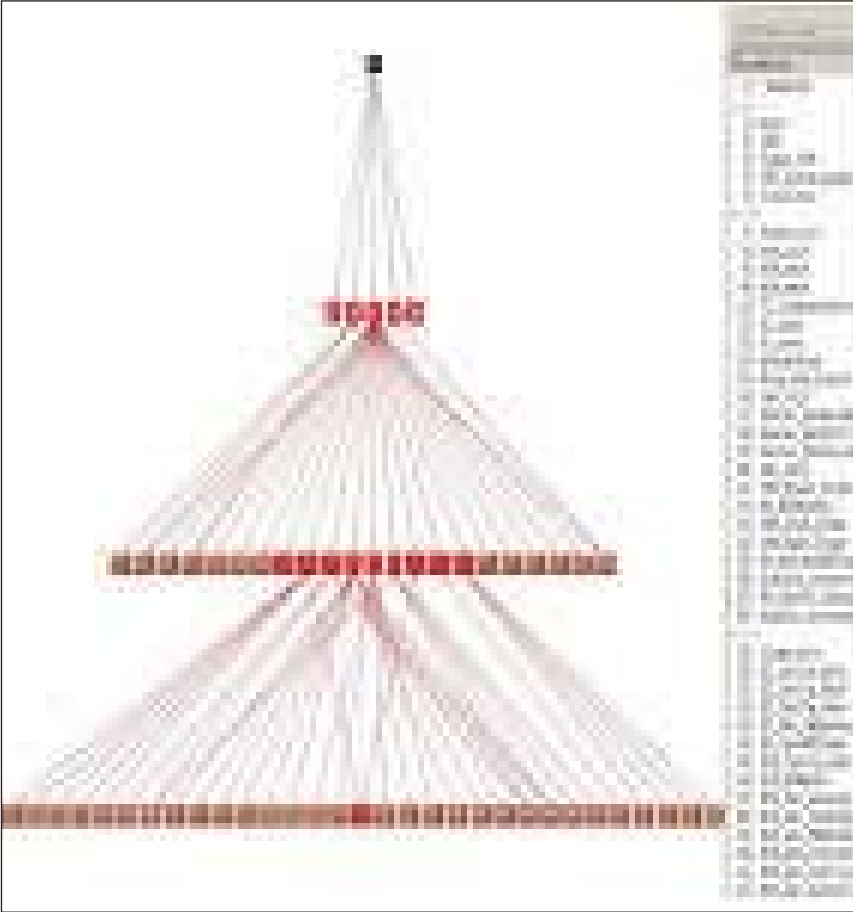


**Fig. 2** Static call graph

These requirements were captured using Teleology DOORS CASE tool and the traceability between SyRS and SRS was established. SDD document was prepared as per IEEE standard 1016 (which follows the SRS) and stored in Teleology DOORS CASE tool. Context diagram, data flow diagram, state

transition diagram, state event matrix, structure chart and flow chart were prepared using Software through Pictures/ Structured Environment (StP/SE) tool. Traceability between SRS and SDD was established. Software was developed in C language using Tasking C cross compiler for 68K

processor and fused into EPROM of both the CPU cards. Developed code was checked for Motor Industries Software Reliability Association (MISRA) 'C' compliance using LDRA tool. This tool was also used to generate various software metrics and software quality aspects like maintainability, testability and analysability. Static call graph generated by LDRA is shown in Figure 2.

Software was thoroughly tested by simulating field inputs. Hardwired inputs were connected to AI cards and DI cards of both the RTC systems and process thresholds and alarm thresholds were received from PC. Different combinations of inputs were given and corresponding outputs were monitored. Soft outputs and data were sent to PC (where all plant information are stored), SC2 display station and LCC display station using TCP/IP protocol. Further these data were displayed in GUI display stations. GUI display of analog & digital inputs and relay outputs developed using Qt in Linux platform. Functionalities of the system were successfully demonstrated in the laboratory.

## II.17 Real Time Measurement of Free Level Oscillations in 1/4<sup>th</sup> Models of PFBR using Pulsating Conductance Monitoring Device

**A** high resolution PC-based level monitoring device using pulsating sensor with complete instrumentation and software package has been developed in-house in order to capture any

minor change in liquid level in a large liquid pool during sudden fluctuations. The probe consisting of a pair of stainless steel (SS) wires of appropriate geometry fixed onto a vertical rectangular shaped teflon

plate forms a conductance cell while placing it into a conducting liquid. When the conductance probe is dipped in the water pool upto a fixed height of the sensing part one can get a fixed conductance value at a

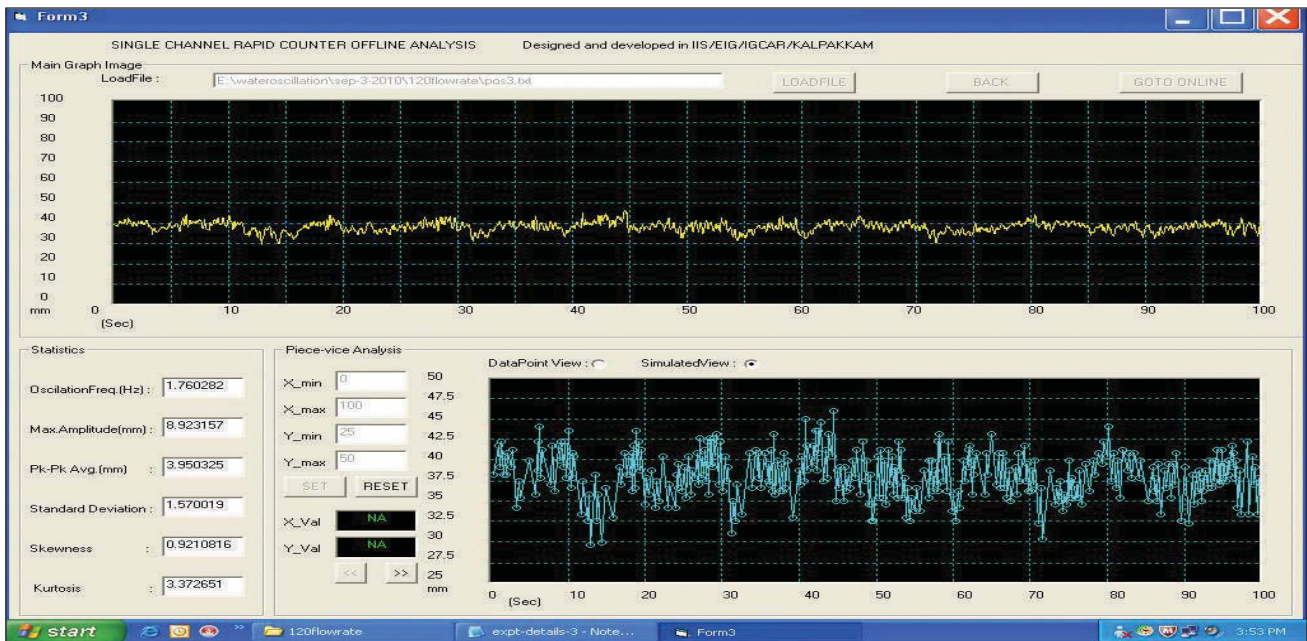


**Fig. 1** A typical online plot of free surface oscillations of the water pool with respect to time in a particular location of the simulated test facility

given temperature. If the water level is allowed to fluctuate due to any external means the level of water sensed by the electrodes will either increase or decrease which, in turn, will alter the initial conductance of water. Hence if the shift in conductance is captured quickly, it will be possible to measure the amplitude of oscillations. With this simple concept a PC based plug-and-play type stand alone real time system with very little auxiliary hardware has been developed for real time determination of water level oscillations in a large water pool. The data acquisition system was made using visual basic. The digital pulses as the primary signal which is generated by direct conversion of conductance to frequency with the help of a laboratory made typical logic gate oscillator (LGO) are communicated to PC directly through its serial port without any add-on card. The pulse frequency is directly related to the height of water level in mm. The relation between pulse frequency and height was established by appropriate calibration and it was fed to the system software to give

direct information of height of water level. After a detailed investigation in laboratory the measurement facility was deployed for rapid monitoring of liquid level oscillations in the 1/4<sup>th</sup> scale model of PFBR, a simulated facility to study hydrodynamic and flow induced vibrations in liquid sodium pool of PFBR. The probe was mounted at different locations in the water pool. At various flow rates the measurements were taken at nine locations. Three independent measurement campaigns were conducted. During measurement, pool temperature was progressively increased which affected the height of measurement. Hence, appropriate measures were adopted for correction in height of liquid level.

The salient features of this measurement device are

- (i) graphic display of real time change in liquid level
- (ii) counting in every 20 ms interval with acceptable precision (RSD <3%)
- (iii) provision for back ground correction

- (iv) height correction due to change in water temperature
- (v) computation of amplitude and frequency of oscillations, online statistics in measurement and
- (vi) continuous measurement without any constraint in time limit etc.

The measurement was conducted for a period of 100 seconds at each location. A typical online plot in a particular location of one of the measurement campaigns is shown in Figure 1 and the photograph of simulated facility during measurement is shown in Figure 2. The present work provided useful information for assessment of appropriate design which would be adopted in the PFBR.



**Fig. 2** Photograph of the simulated test facility

## II.18 Software Development for Prototype Fast Breeder Reactor Control Systems with Safety Critical Application Development Environment CASE Tool

**S**oftware Development Methodology is a framework that is used to structure, plan and control the process of developing software for any application. The I and C systems of PFBR are classified as safety-critical systems, safety-related systems and non-nuclear safety systems. Most of these are computer based systems that are indigenously developed. The control software for PFBR control systems, namely, Control and Safety Rod Drive Mechanism, Diverse Safety Rod Drive Mechanism, Transfer Arm, Spent subassembly Storage Bay Transfer Machine are developed using software development methodology and international standards have been adopted for enhancing the software quality and reliability.

The computer based control systems are dual redundant Real Time Computers (RTC) with VME bus based Motorola 68020 CPU card, digital / analog, Input / output (I/O) cards and process oriented I/O cards such as synchrony to digital converter card, optical encoder interface card, etc. These dual RTC systems send their healthy status to Switch over Logic System, which routes the healthy RTC's output to the plant. RTC systems scan all the inputs, process these data with the fused software, updates the output and send all the data to the centralized process computer of Distributed Digital Control System using TCP/IP protocol in a particular cycle interval repeatedly. These data are logged

in the process computer and displayed in various display stations for the information and action of operators. The system hardware and software are designed and completely tested for quality and reliability.

Software life cycle depicts the significant phases involved in the development of software. For the above said control systems, waterfall life cycle model is employed, which is a sequential development approach. AERB/SG/D-20 and D-25 guidelines have also been followed for software development of computer based control systems.

### Computer aided software engineering (CASE) tools

The use of CASE tools for the development of software along the life cycle improves software quality, system simulation, performance analysis, maintainability, traceability to requirements, impact analysis, automatic report generation, etc. Different CASE tools have been applied along the steps of software life cycle. One of the important CASE tools used for software development is Safety Critical Application Development Environment suite, which is a certified software factory. The software design flow using safety critical application development environment is shown in Figure 1. The requirements of the system were modeled, which is provided with powerful module libraries that simplify intricate operations and manipulations.

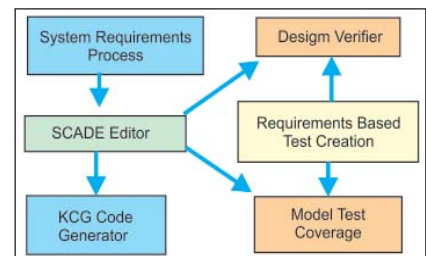


**Fig. 1** Safety critical application development environment design flow

The model was then simulated in batch mode or interactive mode, by creating test scenarios using simulator of the suite. The results were checked against the desired results as per the requirements specification. Model Test Coverage tool was used to analyse the structural coverage of the model for all the requirements. Design verification tool was used to verify the design for safety critical properties of the system. It uses formal verification techniques to verify the design with respect to safety critical properties of the system. After confirming the functional correctness of the model, KCG was used to generate C code for the model. KCG is qualified to DO 178-B, level-A.

The generated C code is certifiable to IEC 61508. The generated C code was deployed in the hardware and the system was tested for their functional requirements. RM Gateway was used to create traceability links between system requirements, SCADE model and test plans. The CASE tools have been applied successfully to develop reliable software for the PFBR control systems and they are being tested in the laboratory.

## II.19 Development and Qualification Testing of Safety Logic Systems for PFBR

PFBR is provided with two independent fast acting shutdown systems, viz., SDS-1 and SDS-2 to initiate safety action against various design basis events. For SDS-1, Safety Logic with Fine Impulse Test System (SLFIT) is used and for SDS-2, Pulse Coded Safety Logic System (PCSL) is used. The Safety Logic systems are responsible for initiating safety action after performing 2/3 voting of triplicate SCRAM parameters. The safety logic systems need to undergo stringent qualification tests, before being deployed in the reactor.

The SLFIT receives SCRAM signals from neurotic, thermal, pump speed, power to flow ratio (P/Q) and delayed neutron detection systems. SLFIT system consists of two major blocks, viz., safety logic and fine impulse test logic. The fine impulse test (FIT) logic periodically monitors the healthiness of safety logic, thus ensuring its availability. In the event of FIT logic detecting an unsafe fault in the safety logic, operator is alerted for taking necessary action.

The PCSL receives SCRAM signals from thermal, P/Q and delayed neutron detection systems. The PCSL system consists of two major blocks, viz., the core logic and diagnostic logic. The core logic employs a dynamic logic, which is fail-safe. The diagnostic logic is used to detect faults in the core logic and annunciate them. In this case, follow up action by operator is not required as core logic is fail-safe.

SLFIT and PCSL systems employ design diversity to guard against common mode failures. The diversity is achieved at design level by using static logic levels for normal

operation of the SLFIT system and dynamic coded pulses in PCSL system. Additionally, devices used for implementation are of different technologies and from different manufacturers.

PCSL system was tested with 3 numbers of electro-magnet (EM) coils. The EM coils have to operate at 823 K in reactor, which is a unique requirement for PFBR. Hence, the EM coils were kept in an oven at 823 K under inert atmosphere created by purging argon to avoid corrosion of the EM coils. The system was tested continuously for long duration successfully to ensure the robustness of the system.

Subsequently, a set of qualification tests was carried out to ensure that the safety logic systems are fit for deployment in the reactor. 100 hours burn-in test was carried out first to ensure that system performs its intended function at room temperature. During burn-in test, the normal operation of the system, safety action and annunciations at various stages were monitored. Post burn-in functional checks were also carried out to ensure there were no deviations/ degradation in the system's performance.

Subsequently, EMI/EMC testing (Figures 1 and 2) was carried out to ensure the system performs its intended function in the presence of



Fig. 2 Radiated susceptibility testing of PCSL system



Fig. 1 Pulse magnetic field testing of SLFIT System

electrical disturbances, which occur in the operating environment. EMI/EMC tests were carried out as per IEC-61000 standards. The safety logic systems successfully passed radiated emission, radiated susceptibility, electrical fast transient, surge, ring wave, damped oscillatory, pulse magnetic field and electro-static discharge tests.

Temperature is a major cause for the failure of electronic systems. Hence the safety logic systems need to be qualified for operation at extreme ambient temperature, which arises due to failure of air-conditioning system. So, dry heat testing of the safety logic systems were performed for 4 hours operation at 318 K and 4 hours operation at 328 K successfully as per IS-9000 standard in a walk-in chamber (see in Figure 3).



Fig. 3 Dry heat testing of SLFIT system inside walk in chamber

## II.20 Environmental and EMI/EMC Qualification of Remote Terminal Units for PFBR

Seven different Remote Terminal Units (RTU) i.e., 16Ch Leak Detector Input, 16Ch Thermocouple Input, 16Ch Analog Input, 30Ch Digital Input, 16Ch Relay Output, Combination of 16Ch Digital Input-16Ch Relay Output and Combination of 16Ch Digital Input-8Ch Analog Input-8Ch Relay Output have been designed and developed as shown in Figure 1 for Instrumentation and Control of Safety Class 2 (IB) and Non-Nuclear Safety systems of PFBR. RTU is a microcontroller based single board computer used to detect sodium leak from SPLD type of leak detector, measure surface temperature of sodium pipelines from K-type thermocouples, acquire analog/digital signals from level probes/limit switches and send digitized data packets over ethernet to the nearest LCC and also generates control outputs in the form of potential free contacts in all states of the reactor. RTUs are designed to operate in the extreme field condition of plant, so as to reduce the cabling from large number of surface thermocouples and SPLD type of sodium leak detectors. RTUs were subjected to environmental qualification as per the test procedure provided at the

test facility available at EIG and EMI/EMC qualification as per the test procedure provided at SAMEER, Chennai.

### Environmental qualification

Two sets from each type of RTU boards were assembled on 19" 6U card frame as shown in Figure 2a. Power supply for the operation of RTU boards, field interrogation voltage and various simulator signals were kept outside the chamber. The performance of RTU boards were monitored by a specially designed GUI runs on PC which in turn is connected to all the Ethernet ports of RTU boards. Tests like Dry Cold (IS 9000 Part II Section 4), Dry Heat (IS 9000 Part III Section 5), Temperature Cycling (IS 9000 Part XIV Section 2) and Damp Heat (IS 9000 Part V Section 1) were conducted on RTU boards.

### EMI/EMC qualification

Two boards from each of seven types of RTUs along with two redundant power supplies, two ethernet switches and three fan modules were assembled inside a 27U high cabinet for the EMI/EMC qualification at SAMEER, Chennai as shown in Figures 2b and 2c. The performance of RTU boards were

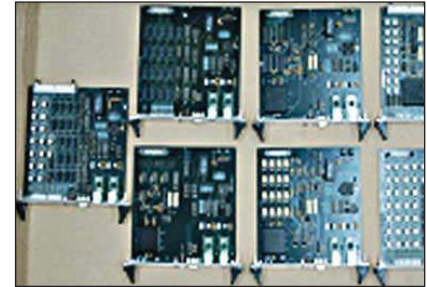
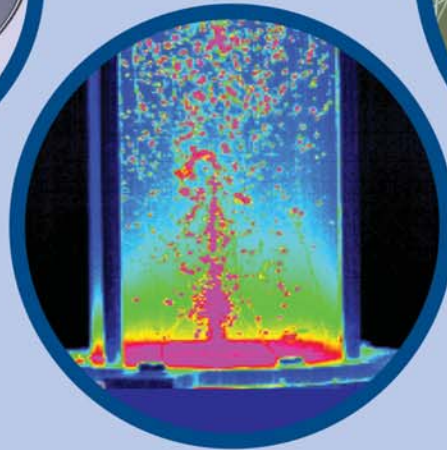


Fig. 1 Seven different RTU boards

monitored by a specially designed GUI runs on PC which in turn connected to all the Ethernet ports of RTU boards. Tests like Conducted Emission (CISPR11/22-Class A), Radiated Emission (CISPR11-Class A), Harmonic Current Emission (IEC 61000-3-2), Radiated Susceptibility (IEC 61000-4-3), Electrostatic Discharge Immunity (IEC 61000-4-2), Power Frequency Magnetic Field (IEC 61000-4-8), Pulse Magnetic Field (IEC 61000-4-9), Voltage Dips and Interruption (IEC 61000-4-11), Damped Oscillatory (IEC 61000-4-12), Ring Wave Immunity (IEC 61000-4-12), Harmonics – Inter harmonics & Low frequency Immunity (IEC 61000-4-13), Voltage Fluctuation Immunity (IEC 61000-4-14), Variation of Power Frequency (IEC 61000-4-28) Electrical Fast Transient Immunity (IEC 61000-4-4), High Energy Surge Immunity (IEC 61000-4-5) and Conducted RF Immunity (IEC 61000-4-6) were conducted on RTU cabinet.



Fig. 2 (a) Environmental qualification RTU boards at our Centre (b) & (c) EMI/EMC qualification of RTU cabinet at SAMEER, Chennai



## CHAPTER III

Research &  
Development  
for FBRs

### III.1 Innovative Design and Safety Features of Commercial Fast Breeder Reactors

Towards techno economic demonstration of the sodium cooled fast reactor (SFR) technology, design and development of an industrial scale prototype fast breeder reactor (PFBR) of 500 MWe has been completed by IGCAR. The construction of PFBR is currently in the final stage. Beyond PFBR, it is planned to construct six 500 MWe reactors by adopting twin unit concept, among which one twin unit would be built at Kalpakkam. Many innovative design and safety features and design optimization require to be incorporated for improved economy and enhanced safety.

The rich experience from design, manufacture and erection of PFBR components, international experience and trends would be taken into account in the design of future commercial fast breeder reactors (CFBR). At the same time, some of the proven concepts and choices made for PFBR are retained in the design. The innovative design features and improvements conceived for the reactor assembly of CFBR are shown in Figure 1.

The use of integral control plug with small rotatable plug, reduction of the gaps between the flanges in view of different levels of flanges taking the advantage of the dome shaped roof slab, machining of penetration shells in roof slab, reduction in the annular gaps between inner vessel & thermal baffles and thermal baffle & main vessel based on the experience gained from PFBR component manufacture altogether yield the net

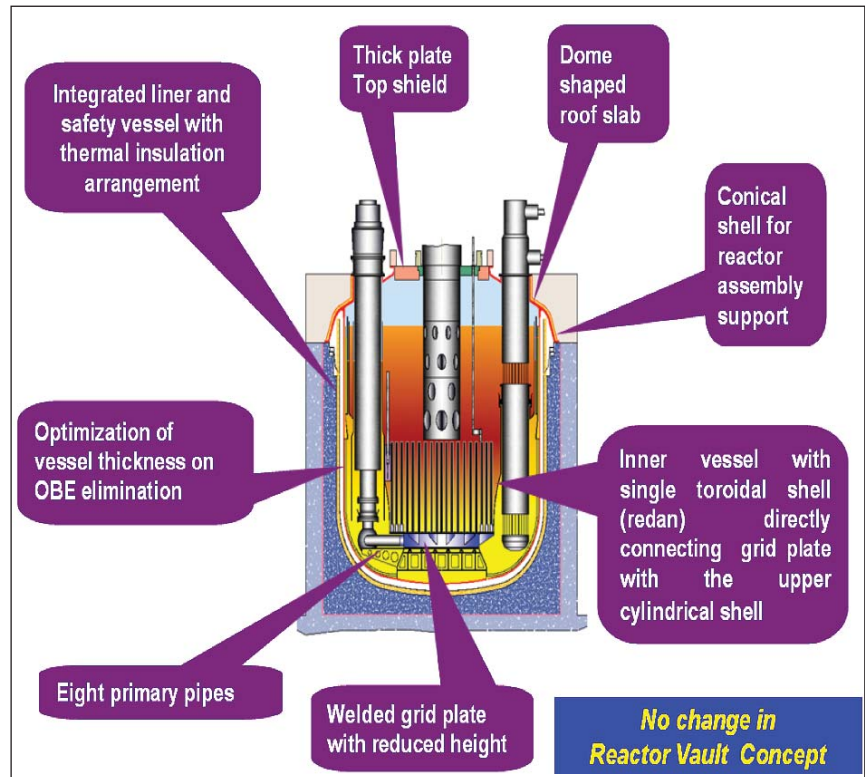


Fig. 1 Major improvements introduced in CFBR reactor assembly

reduction of pitch circle diameter of pump/IHX to 9.4 meter, thereby the reduction of main vessel diameter from 12.9 to 12.1 meter.

Eight primary pipes with reduced size are provided (four in PFBR) to increase safety margin in case of only pipe rupture event. With the increase in number and reduction in size of primary pipes, the grid plate height is reduced. Also, sleeves are

provided in grid plate only for subassemblies that require forced cooling and for few rows of shielding subassemblies. For other shielding subassemblies, spigots are provided that are welded to top plate. With this arrangement the diameter of grid plate shell and bottom plate are reduced (Figure 2). The net reduction in weight of grid plate is more than 50%.

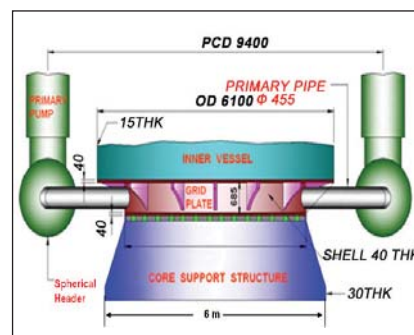


Fig. 2 Welded grid plate with improved design features

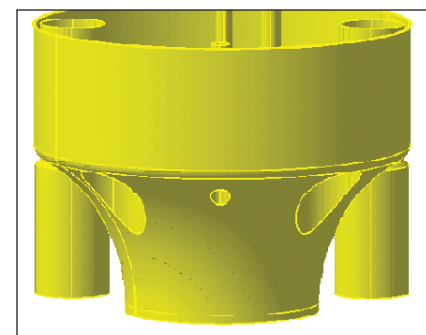


Fig. 3 Inner vessel with single toroidal redan

As the grid plate shell diameter is reduced, the core support structure diameter is also reduced. To account for this, the shape of dished end and the triple point location where core support structure transmits the loads to main vessel is optimised with respect to buckling and plastic collapse failure modes, apart from limiting the vertical displacement to 3 mm from vibration considerations. Shape of inner vessel also has been optimised with reduced upper shell diameter and single toroidal redan (Figure 3), which results in higher buckling strength reduced thickness and hence reduced weight.

Other features are dome shaped roof slab with conical skirt support under compression, thick plate under compression, thick plate concept for rotatable plugs, integrated control plug and small rotatable plug, embedded safety vessel, in-vessel primary sodium purification system, reduction of vessel thicknesses by making OBE an inspectable after earthquake, optimum shielding with advanced shielding materials such as ferro boron, use of SS304LN in place of SS316LN for cold pool components and piping. Three steam generator modules per loop with increased tube length of 30 meter, enhancement of design life to 60 years from 40 years, reduced construction time of 5 years against 7.5 years for PFBR and enhanced burn-up to 200 GWd/t to be achieved in stages. Total saving in reactor assembly structural material other than core is 25%.

Fuel handling scheme is revised by eliminating the IFTM. Instead, a straight pull machine and two

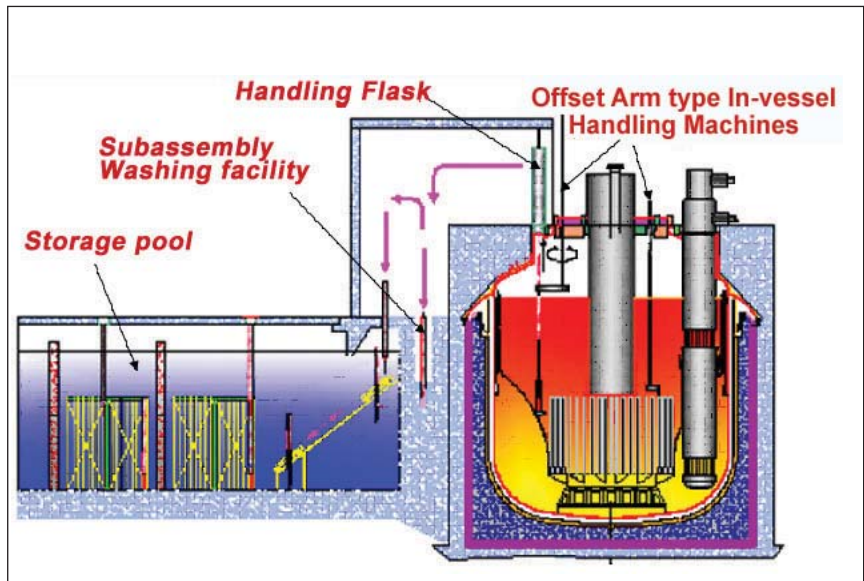


Fig. 4 Revised fuel handling scheme for CFBR

transfer arms as indicated in the Figure 4 (improved fuel handling system) are proposed for CFBR.

To enhance the reliability of shutdown systems of future FBRs by one order of magnitude compared to that of PFBR, active and passive features are introduced in shutdown

mechanisms. To minimize the failure and to ensure ultimate shutdown of the reactor, liquid poison injection system is conceptualized (Figure 5). The possible failures modes of the existing systems have been analyzed and based on this, directions for enhancing the reliability have been arrived at.

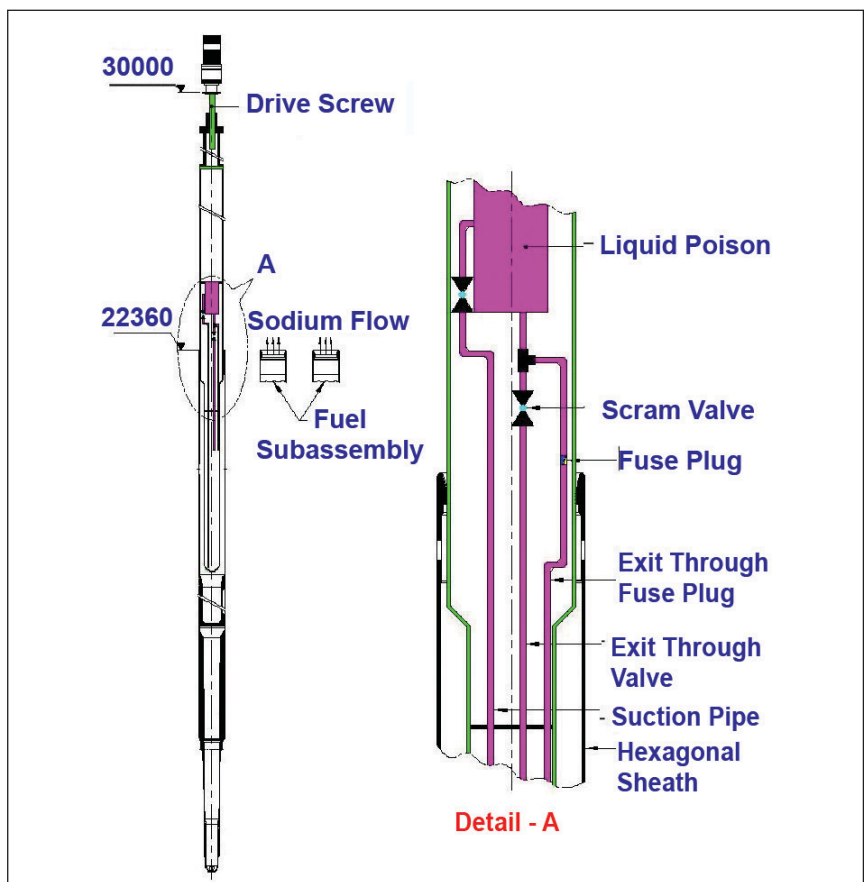


Fig. 5 Ultimate shutdown system

### III.2 Structural Design Optimisation of Reactor Assembly Components of Commercial Fast Breeder Reactors

The reactor assembly components of commercial fast breeder reactors were conceptualised with many innovative design and safety features to improve economy and enhanced safety. The diameter of main vessel, thermal baffles and inner vessel has been reduced. The number of primary pipes has been increased from four to eight with reduced size, which provides enhanced safety margin in case of one pipe rupture event. With this modification, the height of the grid plate has been reduced. Also, by introduction of spigots welded to top plate of grid plate to support most of the shielding subassemblies instead of sleeves, the diameter of grid plate shell and bottom plate are reduced.

Inner vessel upper shell diameter is reduced and its redan is of single toroidal shape as compared to conical shape in PFBR. This improves the buckling strength, reduces thickness and in turn weight of inner vessel. Roof slab has been made dome shaped with a conical

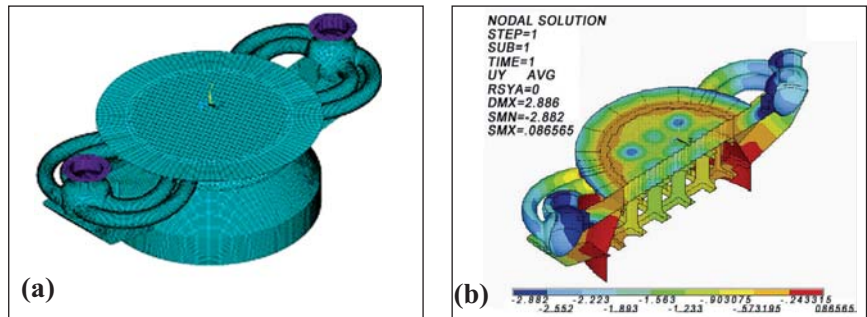


Fig. 2 Grid plate along with core support structure and primary pipe (a) FE model (b) Displacement plot

skirt support which is in compression under the reactor assembly load.

Subsequent to the conceptual improvements, structural design optimisation of the components has been carried out through in-house and collaborative projects. Some of the results are discussed below.

With the reduced shell diameter of grid plate, the overall dimensions of core support structure (CSS) are also reduced, which calls for revision of location of the triple point, where the core support structure transmits the load including its self weight to main vessel. The shape of the dished end and the triple point location were optimized with respect to buckling and plastic collapse failure modes, apart from limiting the vertical

displacement to 3 mm from vibration considerations. The optimized shape has three portions viz. knuckle, crown and a frustum of conical shell in-between with a triple point location diameter of 6 meter (Figure 1). The thicknesses of cylindrical shell, knuckle, crown, cone and triple point location have been arrived as 20, 25, 20, 25 and 35 mm respectively. This reduced thicknesses (compared to PFBR main vessel) combined with the reduction in the diameter contribute significantly to weight reduction.

For the loads due to weight of core subassemblies and inner vessel and pressure head of sodium, the slope limits for grid plate along with core support structure are  $5 \times 10^{-4}$  and  $8 \times 10^{-4}$  radians respectively at the

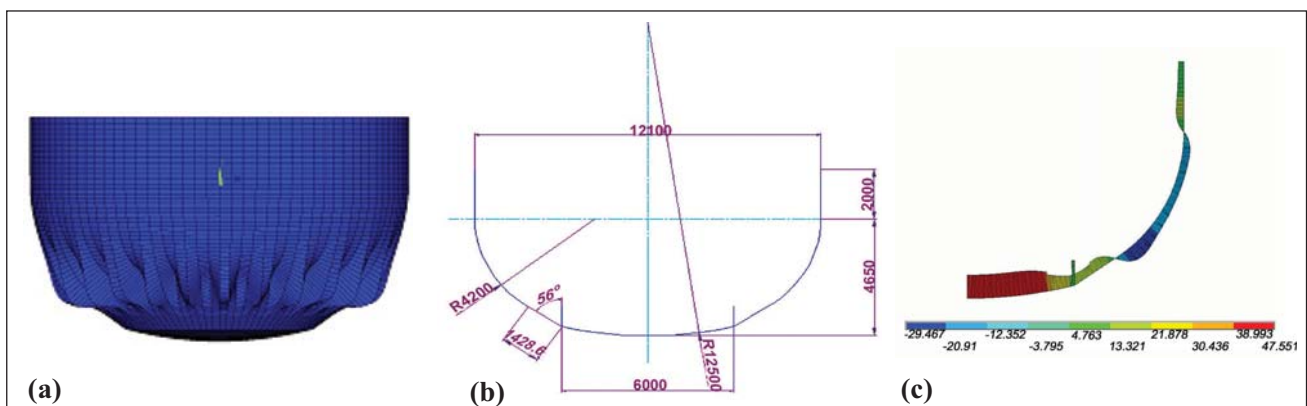
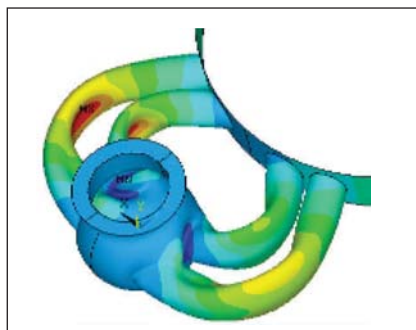


Fig. 1 Optimisation of bottom dished end of main vessel (a) Buckling mode shape (b) Optimised geometry (c) Hoop stress



**Fig. 3** Layout optimisation of primary pipe

locations of CSR/DSR subassembly and other subassembly (except shielding subassembly). The deflection limit is 3 mm at the centre of grid plate. During optimisation process (Figure 2), the thicknesses of top and bottom plates and shell of grid plate as well as number of stiffeners and number and locations of intermediate supports were varied as parameters. Also, the number and layout of stiffeners, thicknesses of plates and shells of core support structure were used as parameters. The perforated top and bottom plates of grid plate were modelled as equivalent solid plate with modified Young's modulus and Poisson's ratio. The optimised thickness of top and bottom plates and shell of grid plate is 40 mm each and that of parts of core support structure is 30 mm. A 3 x 3 square grid stiffener layout is selected for the central square grid region in core support structure. There is a weight saving of 55% for grid plate and 33% for core support structure compared to PFBR. Primary pipe layout has been optimised as shown in Figure 3.

Inner vessel has been analysed (Figure 4) for pressure load due to differential level between hot & cold pools and thermal load including through-thickness thermal gradient. The optimised thickness of 15 mm is arrived at for the single toroidal redan, with respect to buckling mode

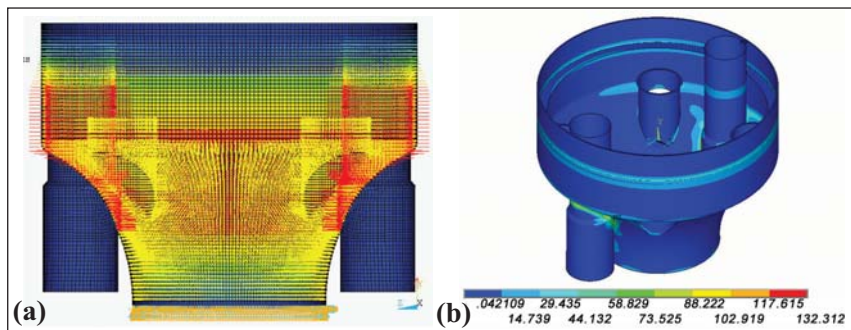


**Fig. 4** Optimisation of inner vessel (a) FE model with boundary conditions (b) Overall Von-Mises stress

of failure (20 mm in case of PFBR). The weight saving is about 12%.

The proposed dome shaped roof slab is a stainless steel structure (SS 304LN) which provides support for all the components entering the main vessel. The important components are primary sodium pumps, intermediate heat exchangers (IHX), decay heat exchangers, large rotatable plug (LRP), in-vessel primary sodium purification systems, fuelling machine etc. The primary loading on the structure is dead weight of components supported over it. The entire load of main vessel along with that of its internals and sodium is transferred to roof slab at tri-junction which is specially made from forged sectors. In addition, the temperature gradient across thickness causes thermal stresses in the structure. During handling of components like primary pump and intermediate heat exchangers, additional maintenance load resulting from handling flask need to be considered. During seismic events, the additional load resulting from seismic excitation need to be accounted appropriately. The basic thickness of structure varies from 60 to 80 mm for dome where as it is 20-30 mm for penetration shells (Figure 5).

Analysis of dome structure was carried out under normal load

conditions to meet the design requirements of maximum deflection of 3 mm (Figure 6) at inner edge and maximum global Von-Mises stress of 129 MPa at 473 K. Further, the slope of support flanges for major components like pump, IHX and LRP need to be restricted to ensure the verticality of components within acceptable limits. The model is meshed with shell elements having six DOFs. Several geometrical features like radial stiffeners, circumferential stiffeners between penetration shells, gussets for penetration shells etc. were added to the basic structure to increase the rigidity of the dome and in-turn to reduce the central deflection. The air cooling system is integrated over the top surface of the dome so that the stiffening effect of the same is also accounted in the analysis. Due to change in the concept, the net reduction in the weight of the roof slab will be ~80 tonnes which is around 35% of present roof slab.

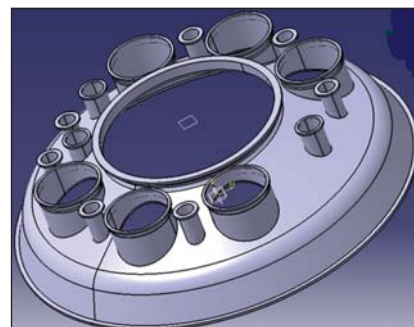


**Fig. 5** Dome shaped roof slab with conical support skirt

### III.3 An Innovative Design of Flow Zoning Devices using Computational Fluid Dynamics for Fast Breeder Reactors

Reactor core of PFBR consists of different subassemblies (SA) like fuel, blanket, control rod etc. since the radial power profile across the core section is not uniform, judicious allocation of flow to various zones should be made for getting a higher mean outlet temperature from the core and to limit the maximum cladding temperature to design value. It is also required to keep the temperature difference between the adjacent subassemblies within the acceptable limits for the structural integrity of the upper core structure from thermal striping consideration. Hence, in order to obtain uniform outlet temperature, the reactor core has been grouped into fifteen flow zones. Out of this fifteen flow zones there are seven zones covering fuel subassemblies, three zones for blanket subassemblies, two storage and one each for control rod, reflector, and shielding. Allocation of required flow rate to different zones will be done by putting a suitable pressure drop device (or flow restricting device) at the inlet of the subassemblies. The requirement of the flow and pressure drop are such that the simple orifice plates with single hole or multi holes will not be

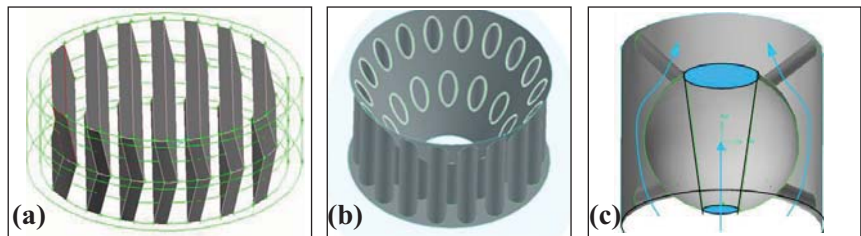


Fig.1 (a) Slit orifice (b) Cone orifice (c) Ball orifice

suitable candidates as they cannot meet both pressure drop and cavitation requirements especially for fuel zones. Hence a special honeycomb geometry orifice plates were developed for usage in PFBR. However for future FBRs it was felt prudent to improvise the design of the present set of pressure drop devices so as to enhance the anticavitation performance. Based on detailed computational fluid dynamic (CFD) studies, three different options were chosen namely slit orifices, cone orifices and Ball orifices. Figures 1a to 1c show these three different designs.

Out of the above three designs cone type design is more promising, because of its advantages like meeting the pressure drop requirement by one assembly and minimizing cavitation effects. This geometric configuration also allows the choice of a single type of design

for flow allocation. CFD analysis was carried out to optimize its geometry to ascertain its hydraulic performance. Cone type orifices were attempted first for Zone 4 which has sodium flow rate of 34.1 kg/s. Figure 2 shows the comparison of velocity and pressure profile for cone type orifices with respect to present design honeycomb type orifices (64% flow area). It can be seen that cone type orifices result in more smooth profile and thus enhances the anti-cavitation performance.

Cone orifices with varying porosities were inserted inside the foot to achieve the desired value of 22 mNa column. From analysis, it was observed that the cone assembly having porosity of 66% (having central hole diameter of 30mm and outer hole diameter of 15 mm) was closer to the required value with a pressure drop of 23.2 mNa column.

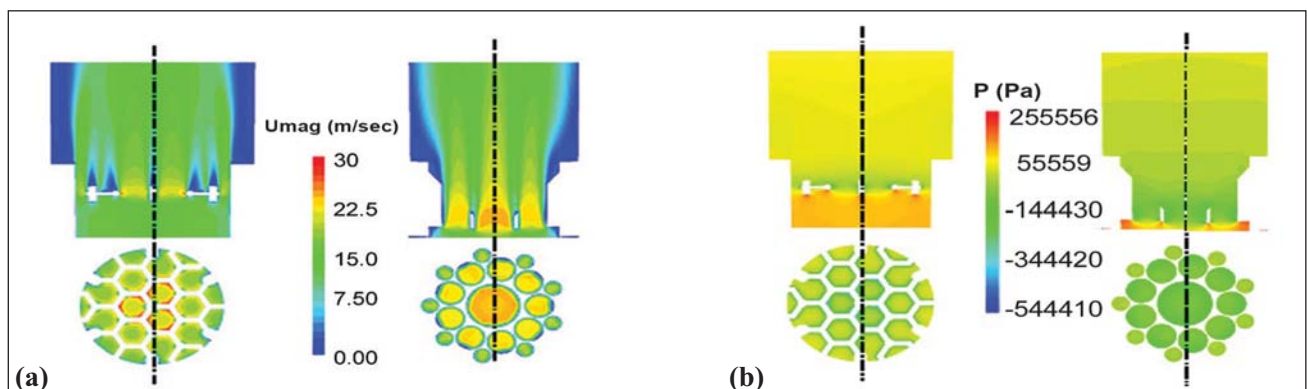
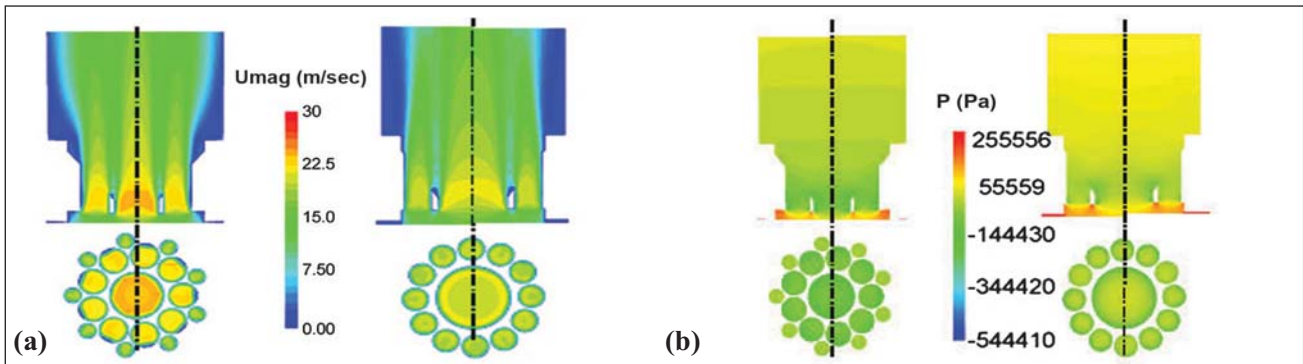


Fig. 2 Comparison of honey comb type and cone type orifice (a) Velocity profile (b) Pressure profile



**Fig. 3** Cone type orifice (64% opening and 66% opening area) (a) Velocity profile (b) Pressure profile

Anti-cavitation performance was also found to be better than present orifice design. Pressure and velocity profile

for both these cases are compared in Figure 3. Design for other fuel zones are in progress. Similarly

design for all other zones is being carried out and experimental verification of this orifice is planned.

### III.4 Reliability Study of Modified Core Temperature Monitoring System for Future FBRs

For monitoring the adequacy of core cooling in PFBR, temperatures at the coolant outlets of all fuel sub-assemblies and coolant inlet of the core are measured. It provides signals for protection of the reactor from various incidents like sub-assemblies partial flow blockage, primary pump speed reduction, transient over power and power failure. Due to large number of thermocouple signals to be processed, computer based core temperature monitoring is designed to generate trip signals for parameters like abnormal increase in mean temperature across the core, deviation of the temperature reading in sub-assemblies outlet from the expected value and abnormal increase in temperature across the central sub-assemblies. The instrumentation scheme consists of two mineral insulated stainless steel sheathed, ungrounded K-type thermocouples at the outlets of each fuel subassemblies (except central subassemblies) and a few blankets

subassemblies at 210 locations and three thermocouples at central sub-assemblies location. The signals from all the thermocouples are signal conditioned, electronically multiplied into three, isolated and fed to three different Real Time Computers (RTC).

Triple modular redundancy is provided at the processing level but dual redundancy at the sensor level. This leads to interlinking of redundant loops to perform safety action. To achieve complete independence, a schematic with three thermocouples per subassemblies is proposed for future series of FBRs with each Real Time computers receiving an independent but single temperature signal of every subassembly outlet (Figure 1). The former scheme has the advantages of reduced number of thermocouples and flexibility for the computer to compare the readings from two redundant thermocouples to check their concurrence, but the redundant loops are interlinked and are prone

to simultaneous failures. The latter has the advantage of complete independence, reduced computer hardware, reduced cabling and a better balance between spurious trips and safety actions. The system being safety class-1, comparative reliability study is carried out between the PFBR scheme and the proposed scheme to gain insight into the merits/demerits of proposed system from reliability stand point.

Fault trees are built and probability to fail upon demand is estimated for both the schemes. Since availability of the reactor is of paramount importance from the economic perspective, spurious trip rate is also estimated. Failure rates for electronic hardware and computer boards are calculated based on parts stress method. Failure rate of thermocouples are derived from FBTR operating experience since similar thermocouples are used in the test reactor. Constant failure rate is assumed since all the electronic hardware undergoes burn in tests.

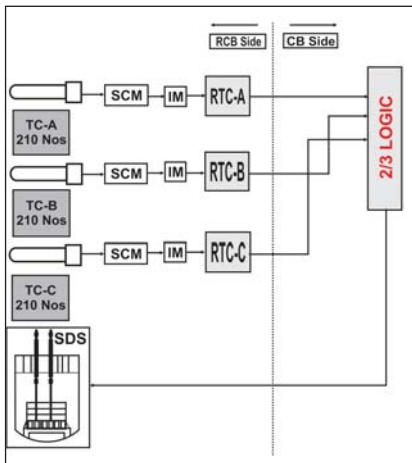


Fig. 1 Proposed architecture for core temperature monitoring system

The computer system is designed with diagnostic features like watch dog timer to detect software and CPU failures, relay read back facility in digital output boards and reference value check in analog input cards. In view of this, 50% of the failures are conservatively assumed to be unsafe. Common cause failures between redundant components are taken into account using Beta factor method.

Intelligent algorithm embedded in the computer software poses modeling challenges. The computers perform a software validity check of the

thermocouple readings and rejects meaningless readings. Some instances of validity check are the subassemblies coolant outlet temperature is to be greater than the reactor inlet temperature, reactor coolant inlet temperature is to be greater than the melting point of sodium, when two redundant outlet subassemblies differ by 5 K, the lower reading is to be rejected, when two redundant reactor inlet sub-assemblies differs by 5 K, the higher reading is to be rejected etc. To accommodate this intelligence, estimation is repeated for the cases of varying fault coverage factors for thermocouple failures. Fault coverage of one means every possible thermocouple failure will be detected by the computer leading to rejection of the reading or tripping the reactor forcefully.

The central subassembly is not protected by a thermo well (to reduce its response time); its stainless steel sheath is directly exposed to flowing sodium and has higher chances of failure. Hence the central subassemblies thermocouple is found to dominate

the reliability figures thus masking the real advantage of the proposed system. The study is extended by incorporating six thermocouples in central subassemblies, two each for a computer. The proposed system then is found to have significant reduction in failure probability upon demand.

The PFBR scheme uses 2 out of 2 logic to process redundant signals from the same subassemblies. This is because 1 out of 2 logic is expected to produce unacceptable spurious trips. 2 out of 3 voting is applied on the SCRAM signals from individual computers. In the proposed scheme, since each computer receives just one thermocouple reading, individual SCRAM is based on the single reading and 2 out of 3 voting is applied upon the individual SCRAM signals. Due to this arrangement, the spurious trip rate is expected to be marginally increased and is proved from the reliability results. The study helped in concluding to adopt the proposed system for future FBRs. The study also helped in gaining a greater insight into the system for further improvements.

### III.5 Design of Steam Generator for Commercial Fast Breeder Reactors

The operating experience of fast reactors worldwide has highlighted the need for reliable performance of steam generator as it is one of the most critical components deciding the plant availability. Based on design, development and manufacturing experience from steam generator of 500 MWe prototype fast breeder reactor (PFBR) and also from

reassuring operational feedback from steam generator test facility (SGTF) and FBTR, the concept of integral once-through steam generator with mod. 9Cr-1Mo steel as principal material of construction is retained for CFBR.

For CFBR which is being designed for 60 years plant life, the present design of PFBR steam generator is reassessed and optimised based on

manufacturing experiences gained with focus on improved economics and enhanced safety. Some of the key aspects like optimization of tube size, selection of tube length and number of steam generator modules per secondary sodium loop are discussed below.

Tube size for sodium heated steam generator is decided based on the economics, manufacturability, bore

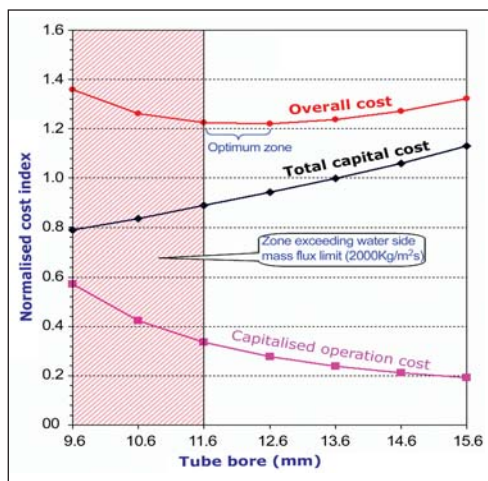


Fig. 1 Tube size optimisation studies

weldability, NDE and ISI requirements. Detailed optimization study is carried out taking the capital and pumping costs amortized over design life of 60 years. It is observed that the optimum zone lies between 11.6 and 12.6 mm (Figure 1). Based on the fact that for the 12.6 mm tube ID, manufacturing (Internal bore weld and X-ray radiography tools) and inspection technologies (Eddy current probe) are already established for PFBR, the same is recommended for CFBR steam generator.

For a given tube size, selecting a particular tube length is of great importance to ensure the heat removal performance of steam generator. A longer tube is preferred to reduce the number of tube to tube sheet joints as the joints are the potential locations for failure highlighted through the international operating experiences as well. The failure of such weld joints would lead to ingress of high pressure/temperature water/steam into sodium resulting in exothermic sodium-water reaction. Further, it is observed that manufacturing schedule of steam generator is largely influenced by the number of tube to tube sheet joints and hence, it is preferable to reduce their number. The tube length as a

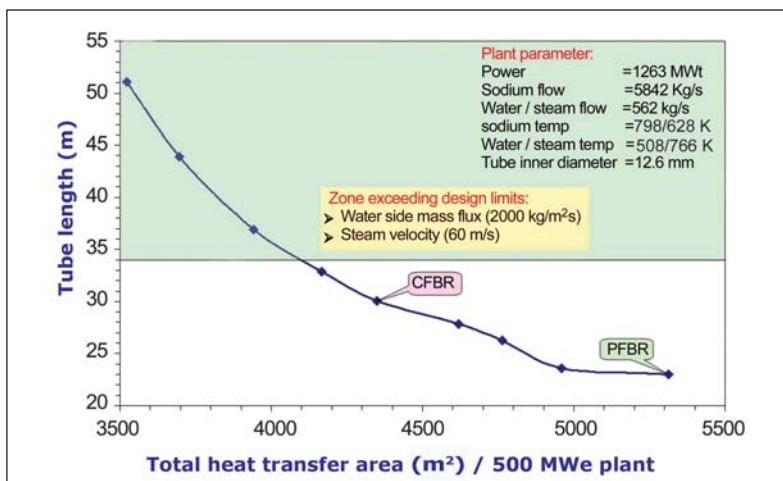


Fig. 2 Heat transfer area required vs tube length

function of heat transfer area, related to number of tube to tube-sheet joints is presented in Figure 2. It is observed, for the given plant parameters and tube size, the maximum tube length of 34m could be used beyond which the design limits would be exceeded.

Owing to the constraints in manufacture of tubes, the PFBR steam generator was designed with a tube length of 23 m. However, for CFBR, a tube length of 30 m is judged to be the preferable choice taking into consideration the reduction in number of tube to tube sheet joints by ~40%, which offers

enhancement of safety and also reduction in number of modules per secondary loop which leads to reduction in manufacturing schedule and overall cost. Hence, the same is chosen for CFBR.

Detailed optimization studies are carried out for 3, 4 & 5 steam generator modules per loop, taking into consideration overall effect of capital cost, operating cost, outage cost and construction schedule. The studies indicate that reduction in number of modules (from 4 SG/loop in PFBR to 3 SG/loop for CFBR) results in considerable reduction in

Table 1: Comparison of CFBR SG with PFBR Stream generator		
Description of steam generator	CFBR	PFBR
Thermal power per SG (MW)	210.5	157.9
No. of steam generators/plant	6	8
Design life (Years) / Cap. factor	60 / 85%	40 / 75%
Tube length (m) / No. of tubes	30 / 433	23 / 547
Tube size (ID / thk.) (mm)	12.6/2.4	12.6/2.3
Pitch (mm)	32.4	32.2
Shell inner diameter (mm)	736	831
Effective heat transfer area (m <sup>2</sup> )	710	652
Water side mass flux (kg/m <sup>2</sup> s)	1735	1030
Steam outlet velocity (m/s)	29.8	17.8
Tube side pressure drop (bars)	7.20	2.80
Shell side pressure drop (bars)	1.4	0.8
Critical heat flux (ID) (kW/m <sup>2</sup> )	566	579
Peak heat flux (ID) (kW/m <sup>2</sup> )	836	694
Total number of tube to tube sheet joints required	5196	8752
Specific steel consumption (T/MWe)	~0.598	~0.756

total module cost leading to associated reduction in manufacturing schedule. It also leads to corresponding reduction in length of sodium and water/steam piping, number of rupture discs and isolation valves, number of hydrogen in-sodium detection systems, instrumentation and heating arrangement leading to reduction in accessories cost, reduced number of outages and compact layout. Hence, the design with 3 modules / loop concept for the two loop design is found to be optimal for CFBR. The

choice leads to reduction of ~23% in capital cost of steam generator and ~27% in overall cost including accessories as compared with PFBR.

With the 30m long steam generator, the total number of steam generator modules required for the twin units of CFBR would be 6 x 2 +1 (spare).

The process design of steam generator is evolved with the plant parameters, respecting limits on water side mass flux (2000 kg/m<sup>2</sup>s) based on rippled magnetite

formation, maximum steam velocity (60 m/s) based on erosion consideration, maximum heat flux (725 kW/m<sup>2</sup>) to reduce risk of water side corrosion effects and avoiding unstable flow regimes throughout the range of operation of steam generator. Literature survey indicates that these limits are applicable to 2¼ Cr-1Mo steels and choice of the same for modified 9Cr-1Mo steel is conservative. The results of process design of CFBR steam generator are indicated in Table I in comparison with that of PFBR steam generator.

### III.6 Permissible Temperature in FBR Vault Concrete

Presently AERB-SG-CSE-1 and ACI 349-06 limit the temperature in safety related structural concrete up to 338 K for normal operation or any other long term purpose. The temperature shall not exceed 366 K for local areas like penetrations. Possible increase of these limits result in significant relief in design of biological cooling system and savings in its principal and running cost. Data and information available in literature particularly by USNRC on ageing effects of long-term temperature in concrete are studied. Experimental results obtained from collaborative project with IIT-Madras show that permissible temperature in FBR vault concrete during normal and

SGDHR conditions can be increased from the present limits. Literature study confirms that degradation of mechanical properties of normal strength concrete tested at cold as well as hot conditions are not significantly affected by long term moderate temperature up to 383 K exposures.

The collaborative studies concluded the following: Mechanical and physical properties of unsealed, unconfined stress free normal strength concrete specimens exposed to elevated temperatures similar to reactor vault conditions and tested at room temperature show that degradation of properties at steady state exposure of 348 K is similar to that of 338 K and the

degradation observed at 363 K is within the design limits of mechanical properties specified by AERB-SG-CSE-1 (Figure 1). Also degradation was within the limit for the specimens subjected to temperature cycles as concrete exposed to temperatures during reactor life time (Figure 2). The degraded properties are 115% higher than that of specified characteristic limits of 28 days cured concrete by AERB standards, important criteria which is recommended by USNRC.

Hence, steady state temperature at normal operation condition can be increased to 348 K and therefore at SGDHR condition the temperature can be increased up to 368 K. This results in substantial reduction in the design cost of biological cooling system as well as in the running cost of the cooling system. Degradation of mechanical properties of vault concrete due to long term steady state and scale down thermal cycles simulated for a period of 40 years reactor life shows that the temperature can be permitted up to 348 K at normal operations and up to 368 K at SGDHR conditions safely.

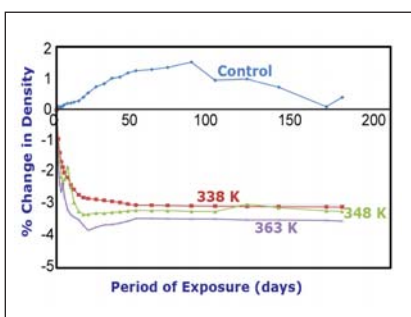


Fig. 1 Loss of moisture at steady state temperature

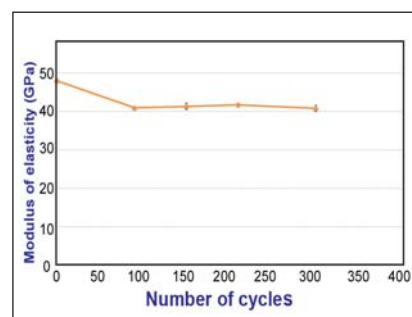


Fig. 2 Degradation of modulus of elasticity at cyclic exposure

### III.7 Numerical and Experimental Studies on the Performance of Thermal Baffles in Sodium Heated Steam Generator

Different transients in a power plant will induce thermal and mechanical loading to the components of the power plant. The mechanical damage due to the thermal transients will be much severe in sodium environment compared to the conventional heat transport systems as the change in temperature of the fluid will transmit to the structure much quickly in sodium environment. It is therefore necessary to have preventive mechanism to protect the thick parts of the sodium components from the severe thermal shock. Tube sheets of the steam generator are one of the components which undergo severe thermal shocks during operational transients. These also experience high differential temperature of 120 degree across the thickness during steady state operation. In order to protect the steam generator (SG) tube sheets from high temperature gradient during normal operation as well as during transient conditions, thermal baffle assemblies are provided near both top and bottom tube sheet regions.

In the steam generator, heat exchange takes place from sodium which enters at 798 K and leaves at 628 K to the water/steam which enters at 508 K and leaves at 766 K. These operating temperatures give a differential temperature of 120 degree across bottom tube sheet of steam generator. Figure 1 shows the schematic of steam generator tested in SGTF. Performance testing of thermal baffles was carried out in this 19 tube model of the sodium heated once through steam generator which has completed 5000 hours of high

temperature operations. The arrangement of thermal baffles in the model steam generator is similar to that of prototype fast breeder reactor steam generator. Four numbers of baffles are provided above the bottom tube sheet. Same arrangement of thermal baffles exists below the top tube sheet of steam generator. The 8 mm thick thermal baffles are made of Mod 9Cr-1Mo steel which is the material of construction of the tube, tube sheet and shell of steam generator. The gap between the baffles is 6 mm. Figure 2 shows the details of steam generator bottom tube sheet and thermal baffle arrangement.

Among all the enveloping incidents the incident of loss of feed water flow to the steam generator will result in the maximum temperature variation in the steam generator. In case of loss of feed water flow incident, the hot sodium at 798 K from the oil fired sodium heater, the heat source in the facility, will flow through the steam generator and these results in thermal shock to the thick components like bottom tube sheet. The effect of this incident on the bottom tube sheet of steam generator was studied by computation and experiments.

The heat conduction study was carried out with a finite element model of bottom tube sheet and thermal baffles assembly. 30° sector of the tube sheet and thermal baffles assembly is taken for the analysis as the assembly is symmetrical for 30° sector. The temperature distribution on the SG bottom tube sheet derived by the calculations using finite element analysis model is given in Figure 3.

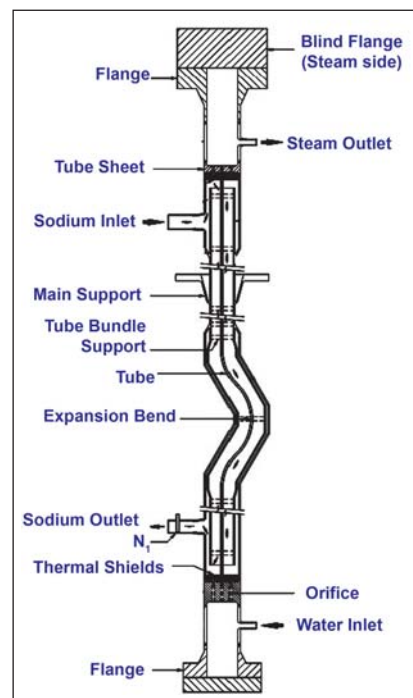


Fig. 1 Schematic of steam generator

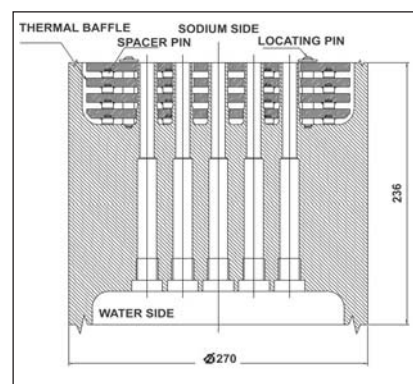


Fig. 2 Details of steam generator bottom tube sheet

From the results it can be observed that the temperature variation in tube sheet is gradual and the tube sheet is not exposed to high temperature gradient. The maximum temperature reached by the tube sheet is 578 K and the same is felt in the tube sheet and shell fillet portion. A temperature difference of 120 degree in the process fluids gives a temperature difference of 70 degree in the thick tube sheet. Still, the wall of the tube portions which is just outside the

thermal baffle will be exposed to a temperature difference of 120 degree approximately.

Sequence of incidents during loss of feed water flow is as follows

- i. Steam generator is operating at rated parameters at time  $t = 0$
- ii. Boiler feed pump trips and feed water flow to steam generator stops.
- iii. Oil fired heater trips as safety action
- iv. Sodium pump continues to operate at rated flow

A three dimensional transient thermal analysis was carried out to derive the thermal response of tube sheet and baffle assembly when it is exposed to a cyclic sodium temperature variation followed by loss of feed water flow incident. The same finite element model used for static thermal analysis was also used for transient studies. The temperature profile obtained from static thermal analysis was given as the initial condition for the transient study. Tube sheet temperature at top surface and bottom surface is plotted with sodium temperature in Figure 4a.

From the results it can be seen that the maximum amplitude of temperature oscillation at tube sheet top surface is around 61 degree with a time period of 9 minutes compared to the amplitude of 170 degree in sodium temperature. Tube sheet bottom surface temperature is rising slowly without any oscillations. The analysis shows that temperature drops in 8 mm thick thermal baffle is four times more than in the 6 mm sodium gap. This is basically due to high thermal conductivity of sodium compared to modified 9Cr-1Mo steel. The amplitude of the temperature oscillation is less for the thermal baffles near to the tube sheet compared to the upper ones.

During the experimental study, at steady state operation of the steam generator at 5.5 MWt power condition, the sodium outlet temperature was measured as 617 K and the feed water inlet temperature was measured as 506 K. The tube sheet top surface temperature was measured as 575 K. The observed temperature drop of 42 degree across the thermal baffle arrangement was in close agreement with the computed value. With steam generator operating at steady state with rated power (5.5 MWt) and rated parameters, feed water supply to the steam generator was stopped. After the loss of feed water incident the sodium temperature at the SG bottom increased from 617 to 771 K in 150 seconds. This is an increase of 154 degree in bottom thermal shield sodium temperature within 150 seconds at a rate of 62 K/min followed by the loss of feed water incident. But at the same time the increase in the temperature observed at the top surface of the bottom tube sheet was 90 degree, that is from 575 to 665 K in 240 seconds. The corresponding rate of temperature rise is 22.5 K/min. Further both the shield predicted temperature drop of 50 degree across the thermal baffles and tube sheet temperature profiles and their trends are similar. Temperature variations of sodium above bottom thermal baffle and tube sheet surface temperature after loss of feed water incident are shown in Figure 4b.

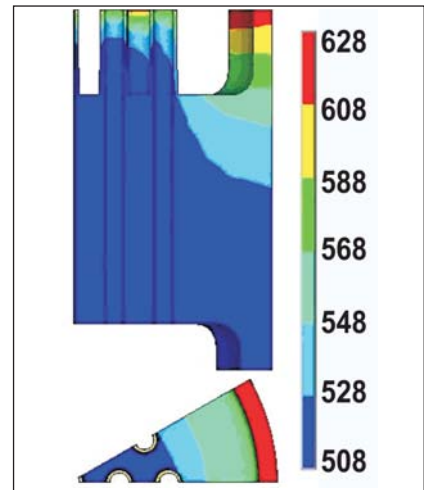


Fig. 3 Temperature distribution of steam generator bottom tube sheet under normal operating conditions.

The experimentally observed thermal characteristic of the steam generator bottom tube sheet thermal baffle arrangement is in line with the numerically predicted characteristics. The amplitude of the sodium temperature oscillation and the tube sheet top surface temperature oscillations were in close agreement. The actual rate of temperature rise of sodium and tube sheet is less than the rate predicted by the numerical simulations.

This is mainly due to the cooling of sodium caused by the evaporation of stagnant residual water present in the feed water system followed by the drop in feed water pressure. Thus it is confirmed that thermal loading on tube sheet during steady state operating conditions and transient conditions are adequately taken care of by the thermal shields.

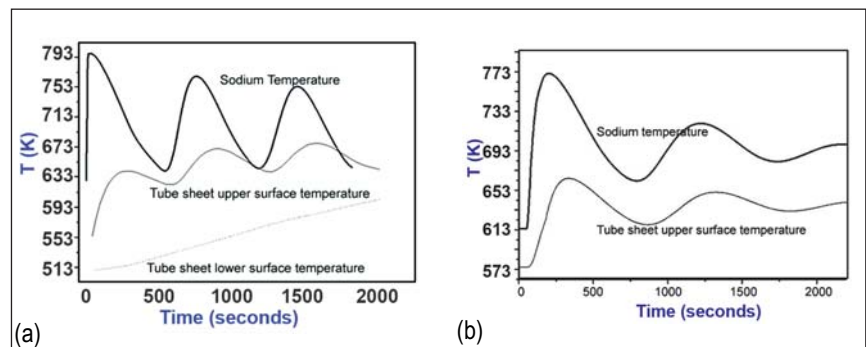
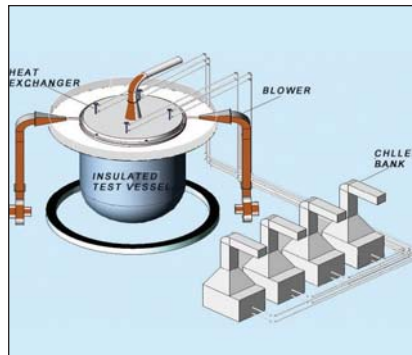


Fig. 4 Bottom tube sheet temperature variations followed by loss of feed water flow to SG – (a) Obtained by numerical simulations (b) Experiments

### III.8 Experimental and Numerical Simulation Studies on Post Accident Heat Removal Condition in Sodium Cooled Fast Reactor

In fast reactor safety, post accident heat removal assessment assumes importance to ensure integrity of structural components. It is essential to demonstrate the passive built-in heat removal capabilities in the event of a core disruptive accident. In order to accomplish this objective, a dedicated post accident thermal hydraulics (PATH) facility has been designed, constructed and commissioned. It consists of (1:4) scaled major internals of the bottom of the reactor to investigate heat removal by the natural circulation with water as working fluid. Schematic and pictorial views of the PATH facility are shown in Figures 1 and 2.

The objectives of experimental programme are investigation of continuous heat removal capability of core catcher plate through natural convection with scaled reactor internals and generate data for validation of mathematical models developed. Water is used to simulate the natural convection characteristics



**Fig. 1** Schematic of the post accident thermal hydraulics facility



**Fig.2** Pictorial view of the post accident thermal hydraulics facility

of sodium. Variable speed air blower system with symmetric pipe inlet at six points at top of the water surface is provided to simulate heat extraction at any desired level. Two 1:4 decay heat exchanger model of type-A has been designed, fabricated and installed. To establish the natural convection flow pattern generated under steady or transient conditions, complete temperature mapping of the system at different locations is required. About 90 thermocouples and 20 RTDs were used to get complete temperature profile.

In phase-I studies, a transient heating run has been completed at

12 kW input thermal source power with 500 mm opening in the cover plate and top surface of water initially open to ambient air environment. Temperatures were measured in various locations with a sampling time of 10 seconds continuously up to 100 hours. Temperature profiles along the central axis of the vessel for different lapsed time interval were obtained. Fitted spatial distributions of the recorded temperature at different times (30, 50, 80 and 100 hours) are presented in Figure 3. Overall heat loss from the surfaces of test vessel and water surface inclusive of conductive, radiative and water evaporative was also obtained to account for heat balance.

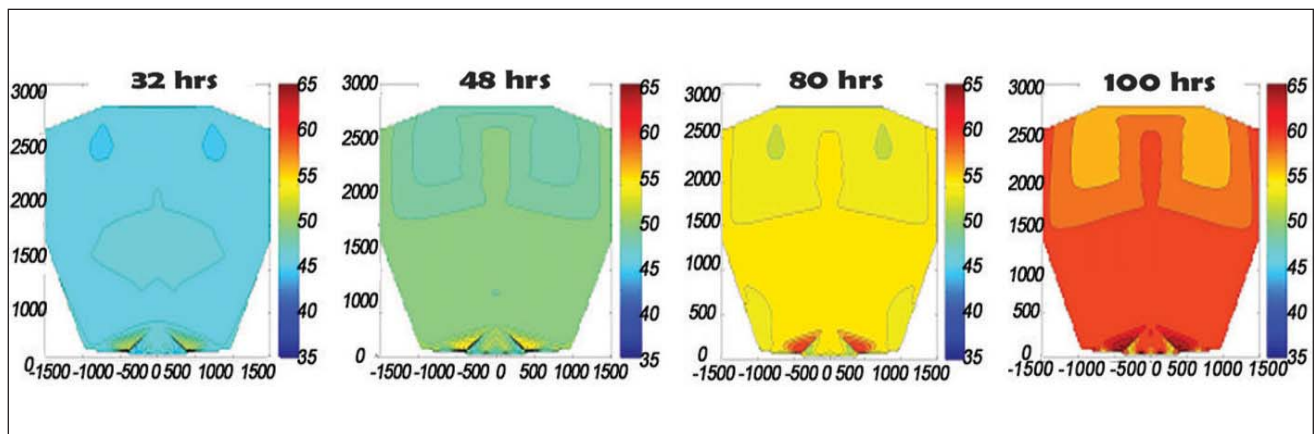


**Fig. 3** Fitted spatial distributions of the recorded temperature at different times

### III.9 Technology Development of Thick Plate Welding for the Top Shield Concept of CFBR

Current design for PFBR has a box type structure for top shield. The height of top shield of PFBR is 1800 mm to meet the structural as well as shielding requirements. The top shield is comprised of small rotatable plug (SRP), large rotatable plug (LRP) and roof slab. They consist of top and bottom plates interconnected with radial stiffeners and shells for component penetrations. In order to meet the shielding requirements, concrete is filled inside top shield box structure (Figure 1). The interconnection of the various plates, shells and stiffeners resulted in numerous T-type weld joints which are inherently susceptible to lamellar tearing. Though the material of construction was carbon steel AFNOR A48P2 with guaranteed through thickness (short transverse) ductility, the problem of lamellar tearing was encountered during the manufacturing process. This resulted in increase in manufacturing time due to the remedial measures taken. Therefore, for future FBR (CFBR), thick plate concept is conceived for small rotatable plug and large rotatable plug. Consequently, the only type of weld required will be butt weld between sectors of thick plates and the possibility of lamellar tearing will be eliminated. Furthermore,

ASTM A516 Grade 65 material can be used instead of the special material A48P2. This adoption would further lead to the following advantages. The component penetrations will be machined and hence the annular gaps will be less than 5 mm (compared to ~20 mm in case of PFBR). This will drastically reduce the complementary shielding requirement above small rotatable plug and large rotatable plug. Annular gaps less than 5mm will also result in substantial reduction of cellular convection in the annular gaps and hence less circumferential temperature asymmetry and reduced thermal stresses. Smaller annular gaps also mean less deposition of sodium aerosols in the gaps and less amount of sodium ejected into the top shield in the unlikely event of core disruptive accident. Furthermore, the reduction in annular gaps will contribute towards reduction in top shield/main vessel diameter. The schematic of thick plate small rotatable plug and large rotatable plug for CFBR is depicted in Figure 2. In order to determine the thickness required for small rotatable plug and large rotatable plug of CFBR, finite element analysis was performed considering both structural and thermal loads. The thickness

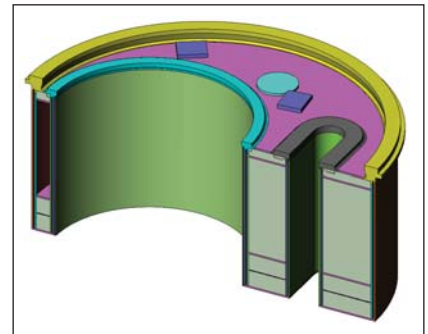


Fig. 1 Box type SRP of PFBR (cut-section)

requirement is governed by the consideration of rigidity rather than that of strength. The deflection contours for large rotatable plug and small rotatable plug are shown in Figures 3 and 4 respectively. The thickness of small rotatable plug and large rotatable plug required is 300 and 500 mm respectively. However, for future 1000 MWe metallic fuel FBRs, it is anticipated that the thickness required will be of the order of 800 mm.

If conventional (wide angle) grooves are employed for butt welding of plates of such large thickness, there are certain drawbacks as given below. The edge preparation for welding requires huge amount of material to be removed by machining and equivalent amount has to be filled by depositing weld metal. This is a wasteful endeavour.

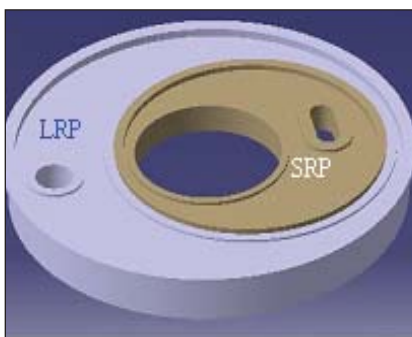


Fig. 2 Thick plate SRP & LRP of CFBR

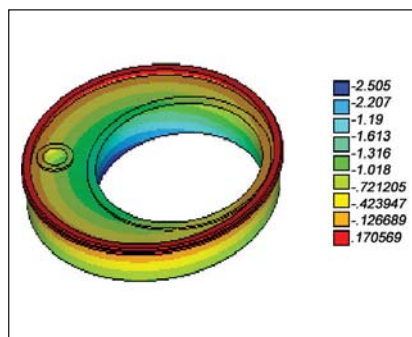


Fig. 3 Deflection contour of thick plate LRP

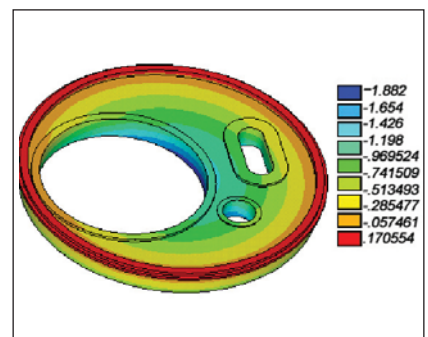


Fig. 4 Deflection contour of thick plate SRP

Furthermore, depositing the weld requires excessive heat input. This will result in low strength and toughness of the weld metal. These drawbacks can be overcome if narrow gap welding technique is adopted for thick plates. Therefore, a program was initiated for the development of narrow gap welding technology of 800 mm thick welds of ASTM A516 Gr. 65 plates. Narrow Gap Welding utilises weld groove preparation having very small included angle (less than  $4^\circ$ ) in contrast to the conventional weld grooves (U and V types). The advantages of the Narrow Gap Welding technique compared to the conventional groove welds are as follows. Smaller cross-section of the weld groove requires less filler material and less heat input during welding. This resulted in reduction of residual stresses and less distortion due to low heat input and smaller volume of molten weld metal. High quality of the weld is obtained as a result of low heat input, extremely narrow heat affected zone (HAZ) and fine grained weld metal. Therefore improved fracture toughness and fatigue strength of the

welded joint is realised. The aforementioned advantages are more pronounced in case of welding very thick plates as is the case for fabrication of thick plate rotatable plugs. Small rotatable plug and LRP are Class-1 components being part of the primary leak tight boundary of the reactor assembly. Therefore, the technical specification for technology development was prepared after considering the requirements of RCC-MR, ASME Sec III-NB and PFBR specifications for small rotatable plug and large rotatable plug.

A narrow groove of  $2^\circ$  included angle was used for the weld edge preparation. Figure 5 shows the welding set-up at L&T, Hazira where the work was carried out. Traditionally submerged arc welding (SAW) is used for welding thick plates because of the higher weld metal deposition rates compared to other arc welding processes. A schematic of the completed narrow gap weld is shown in Figure 6. Before carrying out welding of actual plates, mock-up welding was conducted. Three mock-up welds were made.

During the course of mock-up welding, valuable experience was gained regarding the shrinkage behaviour of narrow gap welds, effect of precambering and stiffeners / restraints. Three welds were carried out after mock-up welding. Repair procedures were also demonstrated for the welds both for defects at the end of the plate and the defects near the middle of the plate. For repair, narrow groove similar to that used for original welding was used (Figure 7). This minimised the volume of base metal and previously deposited weld metal to be removed for repair.

The welds have successfully passed all the non-destructive examination (NDE) and destructive testing requirements of the technical specifications. The NDE carried out on the welds include hot magnetic particle examination at mid-weld height and liquid penetrant examination and ultrasonic examination of completed weld. The successful development of thick plate narrow gap welding technology has given confidence to incorporate thick plate design for small rotatable plug and large rotatable plug in CFBR.

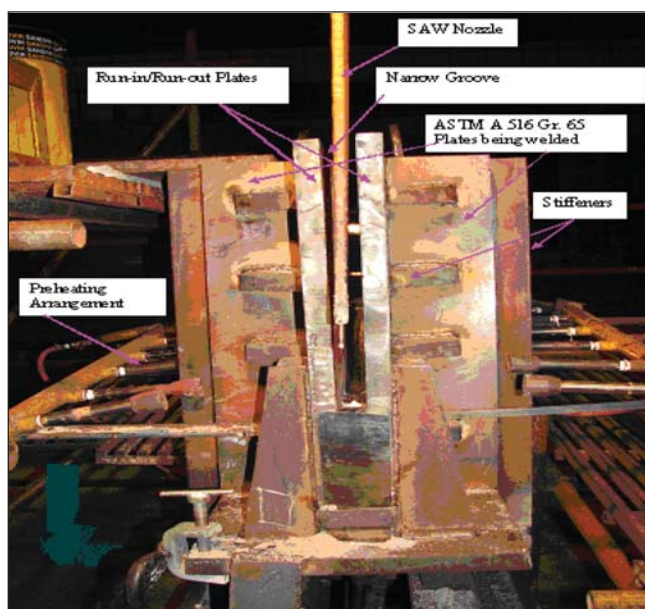


Fig. 5 SAW set-up for NGW of 800 mm thick welds

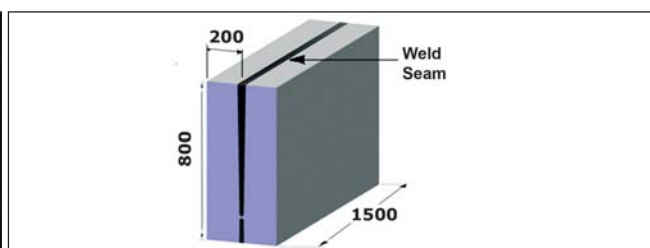


Fig. 6 Schematic of 800 mm thick narrow gap weld



Fig. 7 Narrow groove for repair

### III.10 A Design Approach for Establishing Creep Strength Reduction Factor for Repair Welds for Fast Reactor Fuel Pins End Plug

Structural reliability for fast reactor components is governed by robustness of weld design, since the welds are unavoidable and they are weak links in the structures. Based on vast experience gained through construction of 500 MWe Prototype Fast Breeder Reactor (PFBR), it is possible to develop robust design rules for the welds with specified number of repair, with respected to fuel pin end plug welding. In order to recommend the robust design rules for repaired welds for the consideration of inclusion in the future design code (RCC-MR 2007), extensive test data on fuel pin end plug welds with variable number of welds repairs (up to 4 repairs) are being generated, providing biaxial stresses.

#### Experimental work

An experiment has been conducted to obtain the creep strength reduction factor of weld and its variation with number of weld repairs.

#### Innovative ideas in the experiment

Experiment is conducted for 36 pins with variable number of weld repairs at a time to reduce scattering. Biaxial stresses are provided within the pins. Time to rupture of the pins is reduced by providing high temperature and pressure, so that the experiment can be completed within a short time.

#### Experiment

The experimental set up consists of a pressure chamber where a pressure of 200 bar (20 MPa) is maintained. 36 fuel pins of 1 meter length, 6.6 mm outer diameter, 0.45 mm wall thickness are taken in the set up. The pins in the experiment are hollow, giving provision for the pressure in the pressure chamber to directly act on the walls of the pins, thus providing biaxial stresses on the pins. The pressure chamber is filled with argon and is pressurized to 200 bars.

The set up is placed in a furnace of 10 KW capacity as shown in Figure 1.

A nichrome heating element is present around the surface of the furnace which is operated using PID controller with an accuracy of one degree. Six thermocouples (K-type) positioned very close to the welds are used to monitor the temperature. The top of the fuel pins is at the centre of the furnace as the maximum temperature is seen at the middle portion of the furnace. The furnace is thoroughly insulated.

Pressure is periodically monitored using analog pressure gauge (bourdon pressure gauge) so that any drop in pressure, which shows either a leak or rupture in any of the fuel pins is noticed. The time to rupture is noted and the experiment is continued after removing the ruptured pin and thoroughly welding the hole.

#### Observations from the experiment

The ruptured fuel pins are shown in Figure 1 and it is observed that the crack initiates at the weld and rupture takes place at the HAZ (heat affected



Fig. 1 Investigation of creep strength reduction factor for fuel pin end plugs: (a) Fuel pins welded to pressure chamber, (b) Pressure chamber enclosed in a furnace and (c) Ruptured fuel pins

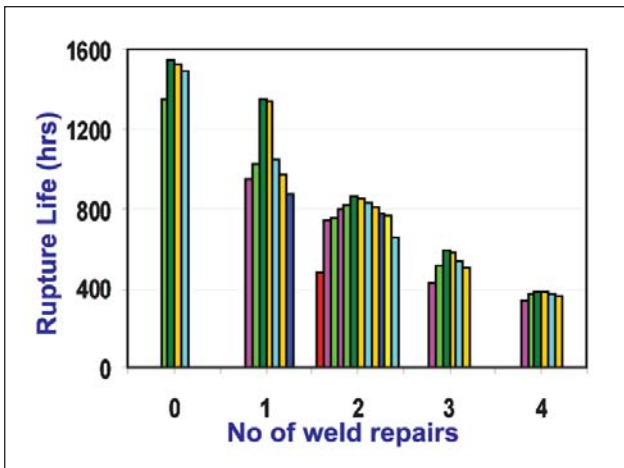


Fig. 2 Rupture life of fuel pins obtained from the experiment

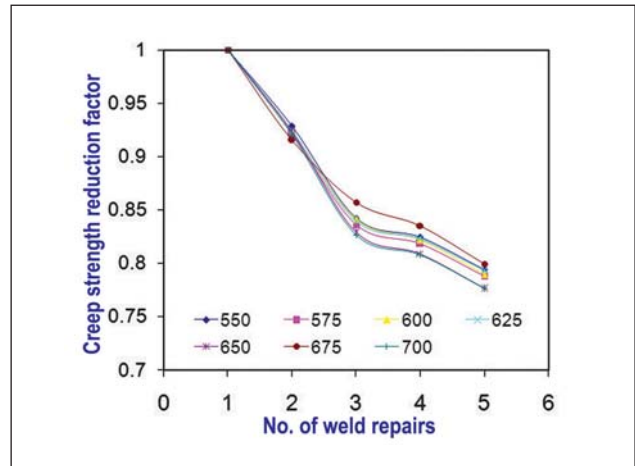


Fig. 3 Creep strength reduction factor ( $J_r'$ ) curve recommended

zone) of the end plug. Time to rupture keeps on decreasing as the number of weld repairs increased, i.e. those fuel pins with more number of repairs has lower creep rupture life when compared with those having lower number of repairs.

### Procedure to obtain creep strength reduction

- Time to rupture obtained from the experimental results (Figure 2) is used to obtain the average stress to rupture for each specimen from the average stress to rupture curve given in RCC-MR Section 1- Subsection Z (A3).
- It is multiplied with  $J_r$  (RCC-MR Section 1- Subsection Z, table A9.1J.3) to get stress to rupture on welding. This accounts for decrease in strength of the material on welding once.
- The stress to rupture for the specimen at '0' repair which ruptures first is taken to be the minimum stress to rupture. It means the pins are supposed to fail at this minimum stress.
- The strength reduction factors were then determined by dividing this minimum stress to rupture with the rupture stress of that specimen.
- The minimum of these factors for each case of repair is taken as the creep strength reduction factor and the factors are tabulated at different temperatures.

This procedure is followed for all the cases at 723, 748, 773, 798, 823, 848, 873, 898, 923, and 848 K by obtaining the time to rupture at all these temperatures using Larson Miller Parameter.

### Establishment of creep strength reduction factor

The minimum of all the factors obtained by applying the design procedure is taken to be the creep strength reduction factor (termed as  $J_r'$ ) for that particular number of weld repairs at that particular temperature. The decrease in creep strength reduction factor with increase in temperature and number of repairs can be observed in Figure 3.

### Procedure to use the results

- Fuel pin with 'n' repairs at a given temperature and applied stress (S) is considered.
- Get  $J_r$  from Table A9.1J.3 in RCC-MR
- Get the corresponding factor ( $J_r'$ ) from the curve recommended.
- Determine equivalent stress ( $S'$ ) =  $S / (J_r' * J_r)$

- Get time to rupture at  $S'$  from average stress to rupture curve from RCC-MR.

### Major observations

The weld-repair process changes the metallurgical properties of the material, thus decreasing the strength and rupture life. The acceptance of such repairs has to be seen carefully towards minimizing multiple handling of fissile material. Thus, the factors have been recommended from which the reduction of rupture life on increasing the number of repairs can be used for the generic sodium cooled fast reactor applications.

Regarding fuel pins, even after four repairs, the reduced life is greater than the life decided by the dilation, irradiation creep and swelling which occurs at the middle portion of the central fuel column. However, as a part of best practices, the weld repair has to be restricted to one or maximum two.

### Further works

The experiment will be repeated at different pressures and temperatures and the calculations will be obtained to get the creep strength reduction factor at different temperature and stresses, so that the tables thus obtained can be recommended in RCC-MR to account for the reduction of creep strength when there are weld repairs.

### III.11 Coupled Thermal Hydraulic Analysis of Safety Grade Decay Heat Removal System

One of the most important tasks in the successful design of a nuclear reactor is the demonstration of safe and reliable decay heat removal. Demonstrating this with the help of experiments is very expensive and time consuming. On the other hand, demonstrating this with the help of numerical models require confidence in the analysis and models used, which when established can be improved by solving benchmark problems. To arrive at an international benchmark for decay heat removal studies, a collaborative project titled, "Integrated Approach for the Modeling of a Safety Grade Decay Heat Removal System for Liquid Metal Reactors" was started. Total six agencies were participating in this project, viz., (i) IAEA, (ii) IGCAR, India, (iii) IPPE, Russian Federation, (iv) CIAE, China, (v) JRC, European Commission and (vi) KAERI, Republic. of Korea, India playing the leading role for this project.

The project was aimed at analyzing the Safety Grade Decay Heat Removal System (SGDHRS) under natural convection condition including the effect of Inter-Wrapper Flow (IWF). In this study, the hot and cold pools along with core, control plug, intermediate heat exchangers (IHX) and grid plate were analyzed

in 3-Dimensions with suitable porous body models and coupled with one-dimensional models of SGDHRS and secondary sodium system. The problem is of multi-scale in nature because of narrow IWF gaps (~3.4 mm) compared to pool diameter of 12 m and height of 10 m. Because of complexity of the problem, each country has followed different approach by simplifying the problem without diluting the important features.

IGCAR has modeled complete (360°) hot and cold pools with detailed core model representing each subassembly (SA). Unstructured finite volume mesh was used and the number of cells was ~700,000. Code in-built wall functions were used to account heat transfer and pressure drop for IWF. A commercial Computational Fluid Dynamic (CFD) code has been used for transient 3-dimensional simulations. Figures 1 and 2 show the CFD mesh adopted in the analysis. Each subassembly is surrounded by 6 cells of IWF. Power generated in a subassembly is taken as average power generated by a subassembly in that zone. Secondary sodium circuit is modeled by one dimensional conservation equations of mass, momentum and energy accounting for buoyancy effects by Boussinesq approximation.

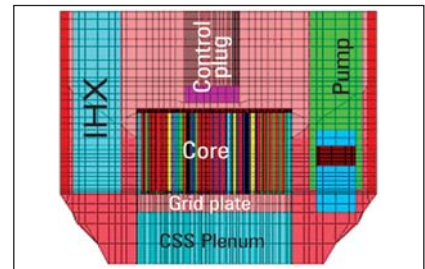


Fig. 1 Vertical section of CFD mesh used in the couple analysis

In this one Dimensional model, steam generator is modeled as a simple heat exchanging pipe. The secondary sodium system model is dynamically coupled with the CFD code. Decay heat exchanger (DHX) is externally coupled with 1-D model of Safety Grade Decay Heat Removal System for calculating heat transfer to it.

Six different cases were studied by the participants to assess the effect of inter-wrapper flow heat transfer, secondary sodium inventory, delay in opening of dampers, ambient air temperature variation and replacement of sodium in the intermediate circuit of SGDHRS by Na-K. Figure 3 shows the temperature distribution in primary sodium system at various instants following station blackout event. It can be seen that hot pool is stratified during natural convection flow condition. One of the critical parameters of interest during SGDHR conditions with core under

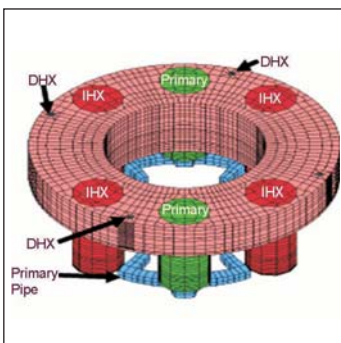


Fig. 2 Mesh for hot pool along with pump, IHX and DHX

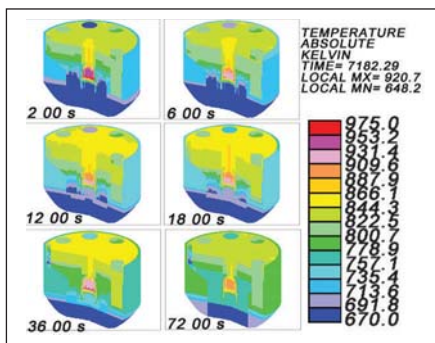


Fig. 3 Instantaneous temperature field in primary sodium system

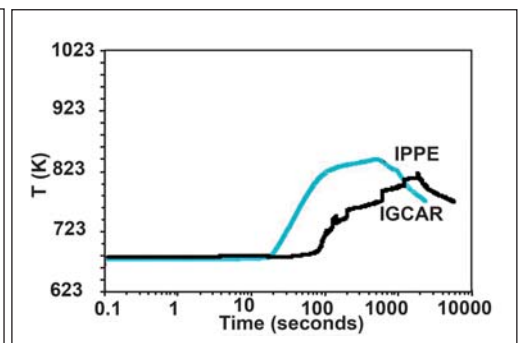


Fig. 4 Predicted evolution of storage subassembly sodium outlet temperature

natural convection is storage subassembly sodium outlet temperatures. Figure 4 shows the evolution of storage subassembly sodium outlet temperature following station blackout, predicted by IGCAR against that predicted by IPPE-Russia. Considering the complexity in the modeling, the comparison is satisfactory.

Comparing the results of various cases studied it was established that the delay in initiation of safety grade decay heat removal system, replacement of intermediate sodium in safety grade decay heat removal system with Na-K and decrease in AHX air inlet temperature do not alter the primary temperatures significantly.

The secondary sodium inventory plays an important role in reducing primary temperatures by  $\sim 50$  K. The effect of IWF heat transfer on primary temperatures was found to be limited to about 20 K in the fissile core and 50 K in the blanket zone. It was also concluded that the 1-D models are conservative.

### III.12 Hydraulic Studies in the Inlet Plenum of Steam Generator for Development of an Optimal Flow Distribution Device

Steam generator (SG) in liquid metal cooled fast breeder reactor (LMFBR) produces steam by transferring the heat from the liquid metal sodium to high pressure water flowing through the tubes. Steam generator is a shell and tube type of heat exchanger. Hot fluid enters the shell of the steam generator through a side nozzle. It rises up in the annular space, enters into the window of tube bundle and flows down. The non uniformity of flow and temperature distribution in the inlet plenum results in the flow induced vibration of the tube bundles and in the degradation of the heat transfer performance. Flow distribution in steam generator involving measurements in experiments and analysis using computational models have been studied. The experiments involve the measurements of radial and axial velocity by using ultrasonic velocity profiler (UVP). Experiments have been carried out to study the flow distribution in 1/5<sup>th</sup> scale model of inlet plenum of 500 MWe steam generator (Figure 1). The kinematic similarity is ensured between the 1/5<sup>th</sup> scale model and full scale steam generator by keeping the Reynolds number in the inlet nozzle above 50000.

Experiments were performed for two types of configurations namely:

- 1) Disc and doughnut baffle type of flow distribution devices and 2) Combined configuration of disc and doughnut baffle and porous shell. Radial velocity is measured along the window height at different circumferential as well as axial positions. The CFD simulations were carried out for the different types of configurations like the basic configuration (without any flow distribution devices) and for the different geometries of the flow distribution devices. The radial velocity plot as a function of the window height for different tangential positions for the basic configuration is shown in Figure 2. This study has helped to characterize the distribution of liquid sodium in the inlet plenum of the steam generators. The combined



Fig. 1 1/5<sup>th</sup> scale model of the steam generator inlet plenum

configuration of disc and doughnut baffle and porous shell as flow distribution devices have been found to achieve uniformity in the distribution of liquid sodium. Figure 3 shows the comparison of the radial velocity profile along the window height for the various combinations of the devices.

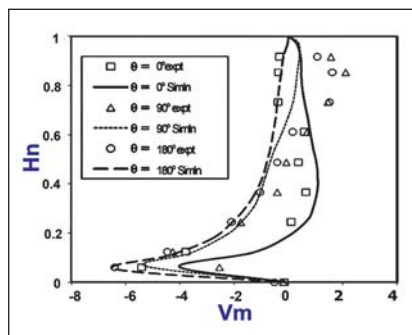


Fig. 2 Radial velocity plots for the basic configuration

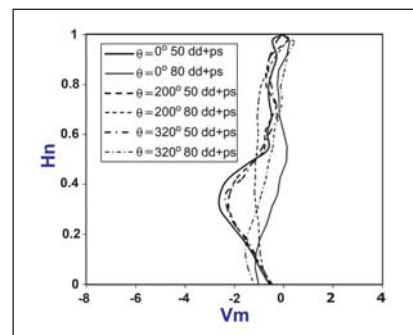


Fig. 3 Comparison of radial velocity profile along the window height

### III.13 Development of Thermal Mixers for the Secondary Circuit of FBR

The sodium streams of different temperatures get mixed at Tee joints in the secondary circuit of PFBR. The thermal mixing of sodium streams in the vicinity of the structural components can lead to the thermal fatigue failure of the component, which necessitates study of phenomena in detail.

R&D of thermal Tee mixers is being carried out in collaboration with Institute of Chemical Technology, Mumbai. Initially computational fluid dynamic (CFD) analysis was employed to simulate the thermal mixing phenomena which was validated by published benchmark results. Subsequent to this, the Tee joints of PFBR geometry were simulated and validated by experimental results. The flow velocity and temperature in selected plane of the model were measured by hot film anemometer, constant temperature anemometer and constant current anemometer module. Figure 1 shows the hot film anemometer probe arrangement in the model.

The mean normalized temperature profile and normalized RMS value of temperature fluctuations are shown in Figures 2a and 2b respectively for a velocity ratio of 0.5 between cold and hot jet.

It can be seen from these figures that the computational fluid dynamic prediction is in fair agreement with

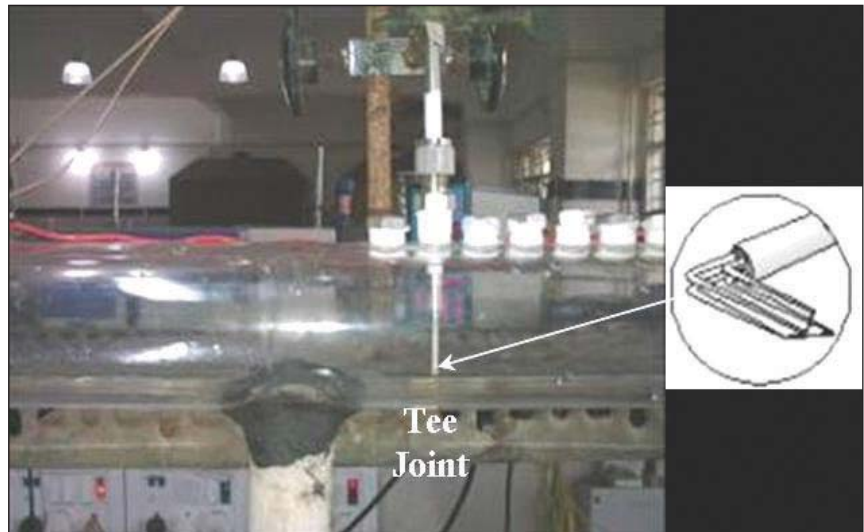


Fig.1 Experimental model

the experimental measurement. Subsequent to this, the validated computational fluid dynamic technique was used to develop thermal mixers in Tee joints. These mixers help to reduce temperature fluctuation near the wall of Tee junction. A design of such mixer is shown in Figure 3. The contour plot of RMS temperature fluctuation near the inner wall of the Tee joint with and without mixer is shown in Figure 4.

It can be seen from this figure that the thermal mixers can reduce the temperature fluctuation significantly and the zone where maximum fluctuation takes place is away from the wall thus reducing the thermal load on the structure. The validation of the mixer design is carried out by conducting experiments in water.

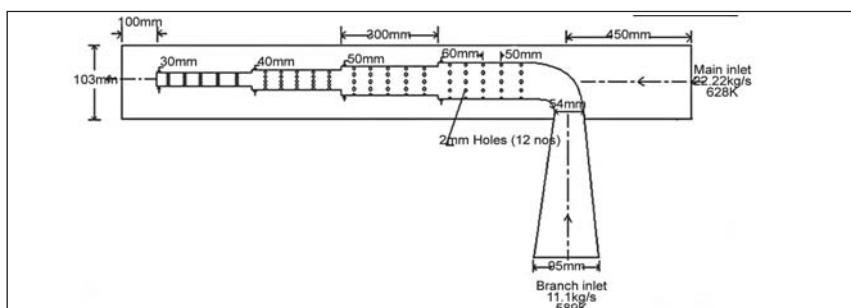


Fig. 3 Schematic of thermal mixer

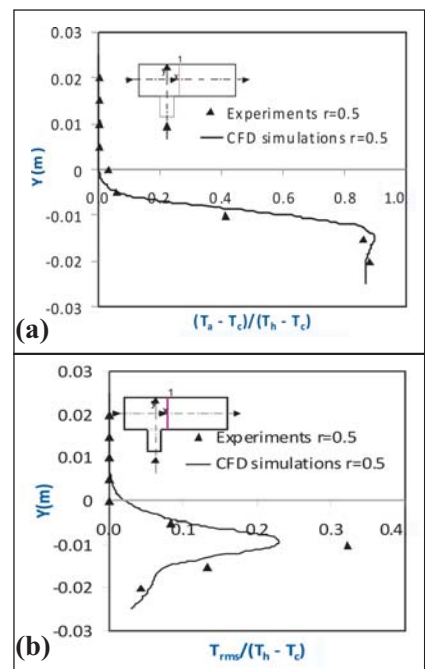


Fig. 2 (a) Normalized temperature distribution (b) Normalized rms of temperature fluctuation

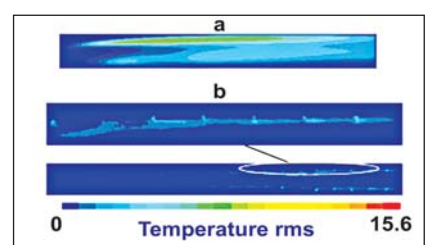


Fig. 4 Temperature fluctuation with and without mixer (a) Tee without Mixer (b) Tee with Mixer

### III.14 In-situ Calibration of Permanent Magnet Flow Meters using Noise Analysis Technique

The performance of permanent magnet flow meters used in fast breeder reactors can be degraded because of radiation and high temperature sodium environment. Accordingly, drift of output voltage affect its stability. Since it is difficult to remove the meter, it is desirable to calibrate the meter at appropriate time intervals for ensuring accuracy and stability from the sodium system. Noise analysis technique has been developed for the in-situ calibration.

Permanent magnet flow meter output signal consists of a D.C. signal (proportional to flow) over which a fluctuating component is superimposed. This fluctuation is due to the turbulence conditions existing in the region of the magnetic field. The fluctuating component occurring at any instant at the upstream electrode pair of the flow meter takes a finite time to reach the downstream electrode pair of flow meter, which can be obtained using the cross correlation signal analysis technique. As the distance between the electrode pair and pipe diameter are known, flow rate can easily be estimated.

Cross correlation is a signal processing technique that measures the degree of the similarity of two waveforms. For two time signals,

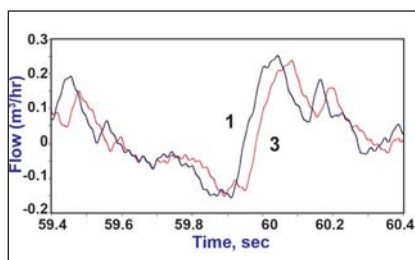


Fig. 2 Shift in the time signals (Electrode pair 1 &3) [Flow 35m<sup>3</sup>/h]

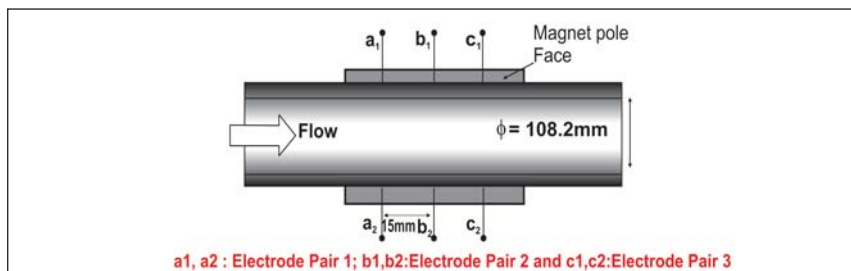


Fig. 1 Configuration of permanent magnet flow meter

say,  $x_1(t)$  and  $x_2(t)$ , cross correlation function is defined as

$$R_{xy}(\tau) = \frac{1}{T} \int_0^T x_1(t)x_2(t - \tau) dt$$

Where, T is sample size and  $R_{xy}(\tau)$  is obtained by shifting the  $x_2(t)$  along the time axis and calculating the integral of their product at each position. When  $x_1(t)$  is equal to  $x_2(t)$  after a time shift  $\tau$ , the product gives large contribution to integral and the peak value of cross correlation  $R_{xy}(\tau)$  corresponds to the delay of  $x_2(t)$  with respect to  $x_1(t)$ .

Experiments were carried out with permanent magnet flow meter in steam generator test facility (SGTF), which is installed in the sodium outlet line of steam generator. Three pairs of electrodes are provided in the flow meter with 15 mm distance between electrode pairs (Figure 1). The voltage fluctuations from two pairs of electrodes were acquired for estimating the cross correlation function and measurements were carried out for sodium flow varying

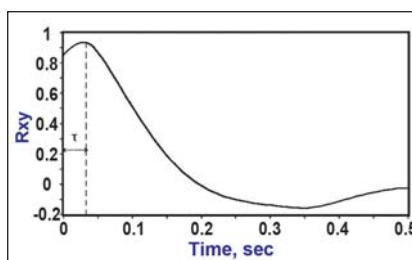


Fig. 3 Cross correlation function,  $Q = 35.24 \text{ m}^3/\text{h}$ ,  $\tau = 28.81 \text{ ms}$

from 25m<sup>3</sup>/hr to 105m<sup>3</sup>/hr. The signals acquired were filtered and analyzed. Figure 2 shows the typical time domain signals from the electrode pairs  $a_1$ - $a_2$  &  $c_1$ - $c_2$  for a sodium flow of 35.24 m<sup>3</sup>/hr. Typical cross correlation function is presented in Figure 3.

From the transit time, flow through the pipe is calculated using diameter of the pipe and the electrode distance. Figure 4 shows the calibration curve obtained using cross correlation technique, using the signals from electrode pairs ( $a_1$ - $a_2$ ) and ( $c_1$ - $c_2$ ). Flow rate estimated using cross correlation ( $Q_c$ ) was compared with that of flow rate calculated from DC voltage of permanent magnet flow meter ( $Q_v$ ) and the accuracy of cross correlation technique was found to be within  $\pm 5\%$ . This noise analysis technique is very promising and can be used for in-situ calibration of permanent magnet flow meters in FBRs.

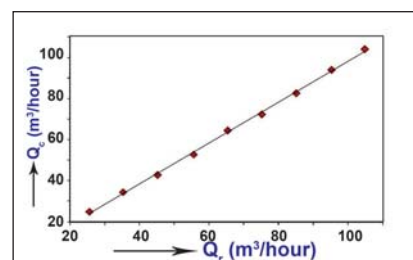


Fig. 4 Calibration curve (Electrode pair  $a_1$ - $a_2$  &  $c_1$ - $c_2$ )

### III.15 Development of Active Magnetic Bearing for Centrifugal Sodium Pump

The rotor assembly of the primary and secondary centrifugal sodium pumps of PFBR is supported by hydrostatic bearings in sodium and the same is supported by Kingsbury type thrust bearing and a radial sleeve bearing above the cover gas space. The bearings above the cover gas space are cooled by means of a dedicated oil circuit. Although the system is equipped with engineered features and safe operational procedures to avoid oil leakage into liquid sodium, there were instances in nuclear reactors of oil leakage into the primary circuit that have resulted in extended shutdowns.

One way to eliminate oil leakages is by replacing existing oil cooled bearings with active magnetic radial and thrust bearings. These bearings have several additional advantages over conventional bearings viz. (i) no mechanical wear (ii) built-in condition monitoring (iii) adaptive vibration control etc.

A collaborative work with M/s National Aerospace Laboratories (NAL), Bengaluru was initiated for the development of radial and thrust active magnetic bearings to suit a small vertical centrifugal sodium pump. The shaft of the existing pump was modified to suit the radial and thrust active magnetic bearings which replaced the tapered roller bearings in the original pump.

The vertical centrifugal sodium pump for which the active magnetic bearings is developed is a radial flow pump with the following rating: capacity = 50 m<sup>3</sup>/h, head = 22.5 m, N = 2900 rpm and specific

speed = 33 m/h. It consists of a top suction radial flow impeller and axial diffuser assembled inside a vertical pump tank. The tank is provided with a side inlet and vertical downward outlet. A free liquid level is provided in the pump tank and the free surface is topped by argon cover gas. Liquid entering the pump at the side is discharged to the vertical downward pipe by the rotating impeller. The high pressure region downstream of the pump impeller is sealed from the low pressure liquid in the pump by means of a labyrinth joint.

The rotating assembly is supported in sodium by means of a six pocket hydrostatic bearing and above the cover gas space by means of conventional oil cooled angular contact ball bearings. A pair of mechanical seals is employed for sealing. The lower mechanical seal prevents the leakage of cover gas to the atmosphere and the upper mechanical seal prevents the leakage of the cooling and lubricating oil to the atmosphere. The oil is used for cooling / lubricating the top bearings and mechanical seal.

The upper portion of the pump shaft was modified to suit the radial and thrust active magnetic bearings. The system was then integrated with the pump hydraulics. The active magnetic bearings system (Figure 1) consists of

- (i) Active magnetic radial bearing
- (ii) Radial retainer/auxiliary bearing
- (iii) Active magnetic thrust bearing
- (iv) Thrust retainer/auxiliary bearings.

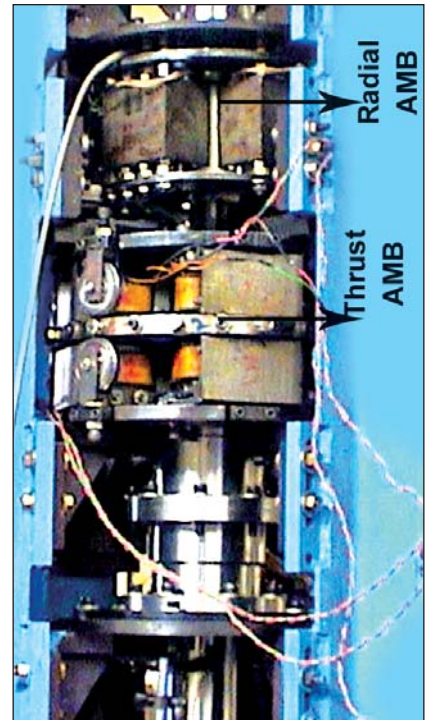


Fig. 1 Thrust and radial active magnetic bearings

The rotor assembly was first tested in air at NAL. The rotor was supported at the bottom by ball bearings (instead of the in sodium hydrostatic bearing) and operated at various speeds up to the rated speed.

The system was then re-assembled at FRTG in a water loop (Figure 2). The pump was assembled with the hydrostatic bearing and mechanical seal assembly and operated successfully up to the rated speed of 2900 rpm.



Fig. 2 Pump test loop

### III.16 Heat Transport in Safety Grade Decay Heat Removal Circuit in Sodium Loop under Steady State Natural Circulation Condition

To study the thermal hydraulic behavior of Safety Grade Decay Heat Removal (SGDHR) system of PFBR, a scaled down model of the circuit in sodium, SADHANA (Safety GrAde Decay HeAt removal circuit in NAtrium) was commissioned in Engineering Hall III. This facility is a 1:22 scaled model designed on Richardson number similitude. The capacity of SADHANA loop is 355 kW and the height difference between the thermal centers of sodium to sodium decay heat exchanger (DHX) and sodium to air heat exchanger (AHX) is 19.5m.

Sodium in test vessel-IV (TV-IV), which simulates the hot pool of PFBR, is heated by immersible electrical heaters. This heat is transferred to the secondary sodium through decay heat exchanger. The secondary sodium gets circulated in the secondary loop by the buoyancy head developed in the loop due to the temperature difference in hot and cold legs of the loop. The heat from secondary sodium circuit is ejected to the atmosphere through the air heat exchanger. A 20 meter high chimney develops the air flow required to transfer the heat from secondary sodium to the atmosphere through air heat exchanger. Figure 1 shows the isometric view of the experimental facility and Table 1 gives its comparison with PFBR SGDHR system. The SADHANA Facility simulates the exact inlet and outlet temperature of DHX and AHX of

SGDHR system of PFBR. The Inlet and outlet temperature of Sodium in DHX is 575 K & 768 K and the Inlet and Outlet temperature of Sodium in AHX is 768 K & 575 K. The design temperature of test vessel, secondary sodium loop and related equipments are 873 K. The facility (Figure 2) was commissioned and has completed around 2500 hours of high temperature operation.

The operation of the experimental system was highly stable and there was no fluctuation in sodium temperature or sodium flow during the steady state conditions. At 823 K sodium pool temperature, 6.7m<sup>3</sup>/h sodium flow was induced in the secondary loop with a Decay heat exchanger outlet temperature of 793 K and air heat exchanger outlet temperature of 590 K. For this condition the power consumed was 425 kW from the sodium pool as against the rated capacity of 355 kW thereby removing 19.4% more power than its design value. Further the experiment was done at different sodium pool temperatures till the cold leg temperature reduces to below 473 K. A correlation for the mean difference in temperature between hot and cold leg as a function of the mass flow rate induced in the secondary loop was found to be  $\Delta T = 81.38W^{1.83}$  with a regression coefficient of 0.996.

Figure 3 plots the mean temperature difference as a function of flow rate for the different pool temperatures. The developed sodium mass flow

Parameters	SGDHR of PFBR	Model
Working fluid	10	Sodium
Heat removal capacity(MW)	8	0.355
Height between thermal center(m)	41	19.5
Inside diameter of intermediate loop pipe (mm)	200	52.48
Richardson number, Ri	15.66	16.67
Euler's number, Eu	14.13	15.36
Reynolds's number, Re	734422	124712
Sodium velocity (m/s)	1.2	0.78
Sodium mass flow rate (kg/s)	32.42	1.45

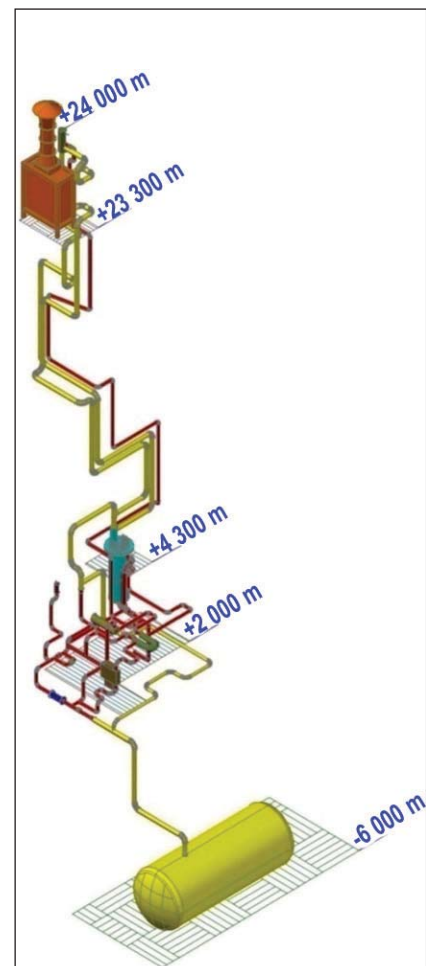


Fig. 1 Isometric view of SADHANA facility



Fig. 2 View of SADHANA facility

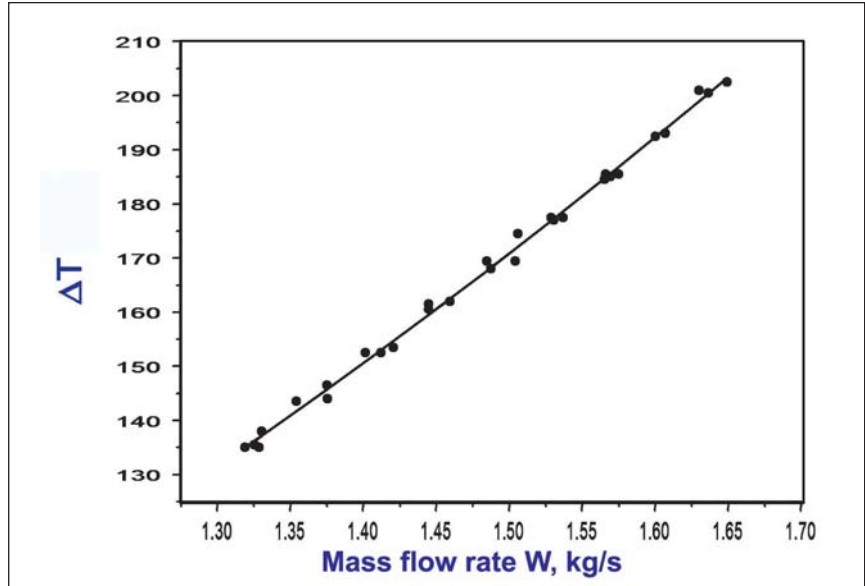


Fig. 3 Plot of differential temperature in hot and cold legs with respect to the mass flow rate of sodium

rate in the secondary loop for different sodium pool temperature is plotted in Figure 4 along with the fitted trend line. The sodium flow established in the secondary loop is 11.6% more than the performance of DHX and AHX and were in expected lines. When the sodium pool was at 823 K temperature, the heat transported by DHX to the secondary was 424.7 kW by heating the sodium from 589 K to 792 K. This gave a hot end  $\Delta T$  of 31 K. 410.0 kW of heat was ejected from the secondary sodium through AHX to the atmosphere. This brought down the secondary sodium temperature

from 790 K at AHX inlet to 594 K at AHX outlet. 14.7 kW of heat loss is estimated in the pipe lines due to surface losses.

During these experiments the sodium temperature in the pool was measured at different elevations with bare thermocouples. These readings gave an idea of stratified sodium layers in the test vessel. The readings of these bare thermocouples have been plotted with respect to the distance from free sodium level Figure 5.

Experiments were conducted to evaluate the transient response of

the system when the dampers opened suddenly with the temperature of the sodium pool maintained constant. From the experiments it has been established that the full sodium flow is achieved in approximately nine minutes, with a damper opening time of 70 seconds.

The performance of the experimental system is satisfactory and it meets all the design requirements. Natural convection in sodium circuit was demonstrated in SADHANA, thereby experimentally validating the passive decay heat removal system of PFBR.

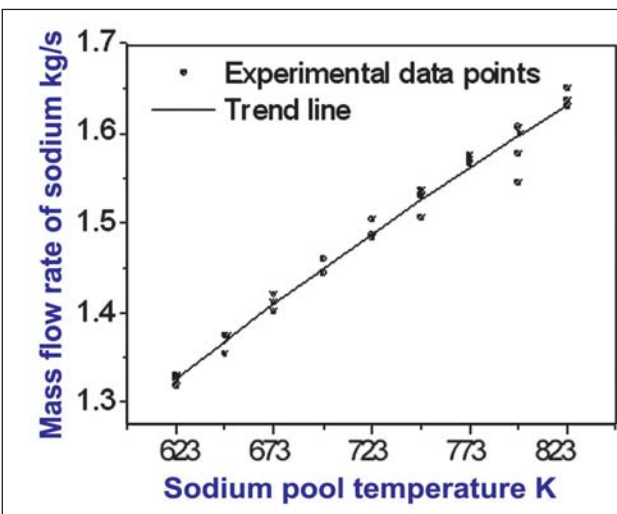


Fig. 4 The mass flow rate in secondary loop of SADHANA for different sodium pool temperature

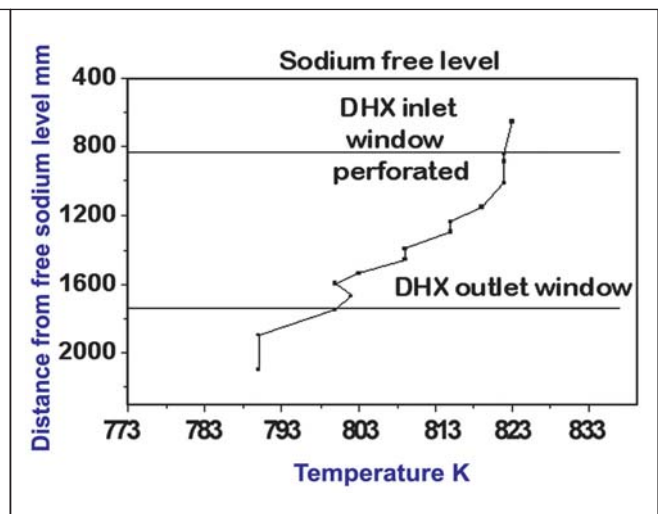


Fig. 5 Variation of sodium pool temperature along the height at 823 K sodium pool temperature

### III.17 Development of High Temperature Pre-Pressurised Capsule and Integrity Testing of Non-Instrumented Gas-Gap Sub Capsule

Pressurised capsules have been developed to generate the irradiation creep data by subjecting them to the stress conditions prevailing in the reactor components, mainly the fuel cladding tube. Pressurised capsule is a closed tube filled with inert gas at high pressure having end plugs welded to both of its ends. One of the end plugs has passage for filling inert gas (argon and helium) and an arrangement to seal this passage after filling of the gas. Pressurised capsules are compact in size and occupy less space in the irradiation capsule during testing in FBTR. Normally gasket made of copper is used in the sealing arrangement of the pressurised capsule. However, the pressurised capsule with copper gasket cannot maintain its leak tightness at temperatures above 723 K. For irradiation creep testing of the clad tubes at higher temperatures, it was planned to use gaskets made of stainless steel, which required several trials with different conical angles and different torques. Experiment was carried out to assess the ability of stainless steel gasket to hold the internal pressure of the capsule without any leak and the ability of the welds to hold the end plug integral with tube.

A total of six pressurised capsules were fabricated and each capsule was exposed at different temperatures from 773 to 973 K in an electrical furnace for 120 hours. The weight of the capsules was measured before and after exposing them to test temperatures. No difference in weight was observed ensuring the leak tightness of the pressurised capsules fabricated using stainless steel gaskets until 973 K. It was also

**Table 1: Details of experimental parameters of pressurised capsules with stainless steel gasket (Duration of testing in furnace is 120 hours)**

Sample No.	Test temperature (K)	Pressure at room temperature (bar)
1	773	75
2	823	65
3	873	45
4	923	25
5	973	15

noticed that the welds were intact without appearance of any defect. Table 1 shows the details of experimental parameters. The filling pressures at higher temperatures have been reduced in line with the reduced creep rupture strength of the material at higher temperatures.

The sealed subcapsule of a high temperature gas-gap irradiation capsule contains structural material specimens immersed in static sodium with top portion filled with argon. The subcapsules are arranged inside the irradiation capsule with different compositions of argon and helium mixture filled in the annular space between each subcapsule and the irradiation capsule. Different high temperatures can be attained during irradiation of the specimens placed in the subcapsules based on the gap thickness and type of gas mixture filled in the annular space. Irradiation temperatures in the range of 673-873 K can be achieved. The sub-capsule is made of Type 316 stainless steel tube closed at the ends by end plugs. The dimensions of a subcapsule are: OD-16 mm, wall thickness- 0.75 mm and overall length –97 mm. One of the end plugs of the subcapsule has a threaded bore with a small hole to fill liquid sodium in the subcapsule. Sodium is filled upto a height of 82 mm in an inert atmosphere glove box under

slight positive pressure of argon gas. The remaining unfilled portion is occupied by argon. The passage is sealed with a screw, and a cap is welded over the screw using laser welding technique. Figure 1 shows a typical sub capsule.

In order to verify the leak tightness of the subcapsule filled with sodium, a subcapsule was fabricated, encapsulated in a quartz tube under negative inert atmosphere and then exposed in an electrical furnace to various temperatures from 573 to 973 K for a minimum of 30 hours at each temperature. The capsule after exposure to different temperatures was checked for defects by visual method under magnification and no defect was observed. No change in weight was also noticed. The capsule was then checked by helium leak test method for leak tightness. The capsule was found to maintain its integrity without any leak upto the test temperature of 973 K.

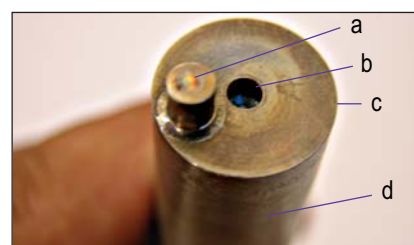


**Fig. 1** Typical subcapsule (a) Cover cap (b) Laser weld joint (c) Intermediate plug (d) TIG welded joint.

### III.18 Design of Spatially Hyper Redundant Robotic Systems - for Complex Tasks

**S**patial Hyper Redundant (SHR) robots are robots having controllable degrees of freedom more than the actual degrees of freedom. Their highly articulated structures make them well suited for niche applications, such as inspection and operation in highly constrained environments.

There are two very important aspects considered while designing these kinds of robots. The first is an efficient joint with two degrees of freedom on rotation and secondly the intelligent control system for the gaits. Unlike other robots, the complexity is primarily on the controlling of sixteen actuators /motors for a minimum eight segmented robot. In order to reduce the cables and wiring system, a Controller Area Network (CAN) protocol is adapted over the RS-485 bus to transmit the data for all the actuators through two wires. Master-slave controllers are used to completely control the robot. The master processes the gait and communicate through the controller area network bus and the slaves receive the command and actuate the motors.

It is always a challenge for the designers to keep the weight of the system as low as possible. Two designs

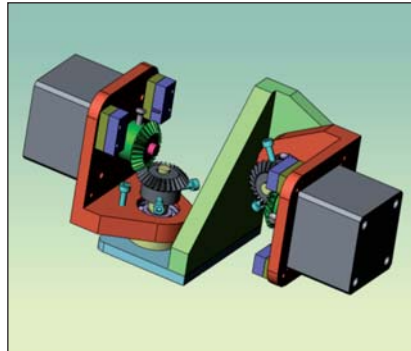


Fig. 1 Motors in the joint

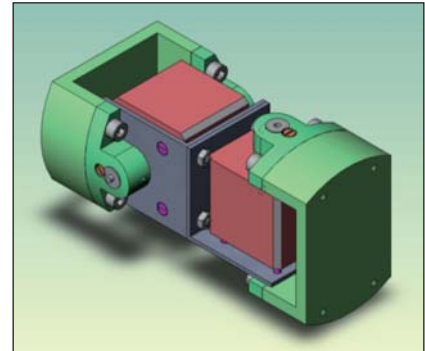


Fig. 2 Motors in the link



Fig. 3 SHR with eight link

have been evolved, one with actuators in the system and another with actuators in the base and power transmitted through the cables. The former one has the option of being autonomous and being commanded from a computer which simulates the gait. The later one has the option of being used as a specialized end effector which can be mounted on autonomous vehicles to carry out inspections and also to perform specialized intricate functions in the most constrained task spaces. Figure 1 shows the snake type of robotic joint with motors being fixed inside the links and a power transmission effected .

Figure 2 shows another type having the actuators mounted right on the joint itself which reduces the weight of the overall system thereby lessening the torque demand. The overall SHR robotic system is shown in Figure 3.

The cable driven spatial hyper redundant robotic system is designed to have a ball socket arrangement as that of the human backbone. Figure 4 shows one segment where the cables are terminated in four perpendicular axes. The cables are not shown in the figure. The springs help actuators to return back the discs to normal state when the loads/tension in the

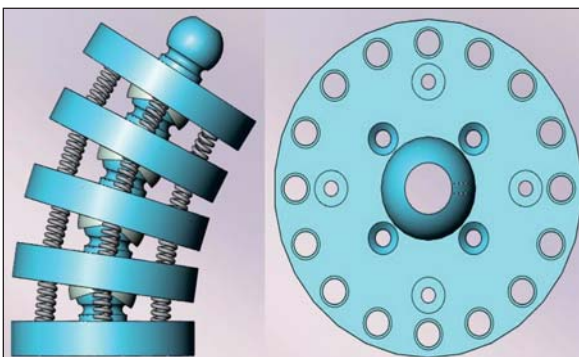


Fig. 4 CAD model of one segment of SHR

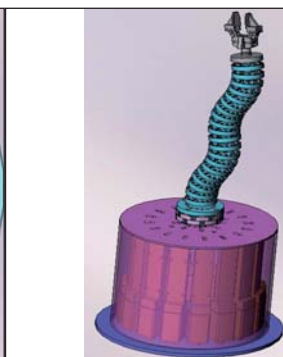


Fig. 5 3D-CAD model of the SHR with 16 linear actuators at the base



Fig. 6 Discs assembled

wires are removed. By developing appropriate load/tension on the wires through linear actuators, the segment can be made to bend. Similarly each of the segments can be bent to reach the end effector to any arbitrary position in the space.

Similarly, four such segments with each segment having four discs are designed to form the full length of the manipulator. The linear actuators are all stacked at the base as shown in Figure 5 and the pulley arrangement routes the cable lessening the friction during the operation. A central hole is provided in the discs to route various cables for powering the LED lights and the camera at the end effector. Sensors can be mounted to see the participation of the discs in forming the right curvature while making the end effector reach the desired coordinates. Figure 6 shows seven discs fabricated and assembled. The discs are free to

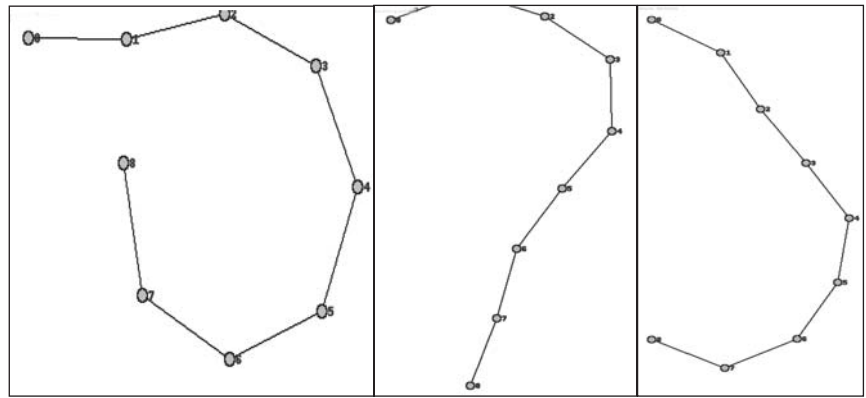


Fig.7 Genetically evolved SHR shapes

move in the ball socket joint. As the controllable degrees of freedom are higher in these hyper redundant systems, an attempt is made to simulate a two dimensional SHR robotic system with eight joints with one degree of freedom in each joint.

Genetic Algorithm (GA) has been used to evolve the link angles thereby doing a heuristic search with the constraints applied to ensure that the end effector reaches the desired target location. Figure 7 shows the

mathematically modeled links which are 100 mm each reaching the desired coordinates. The GA is simulated through the PYTHON code. The angles are the chromosomes and the survival of the fittest is considered to reproduce a few generations to evolve the spatial states of the spatial hyper redundant robotic system. Figure 7 shows the various desired end effector reaches for which the link angles are obtained using the Genetic Algorithm.

### III.19 Development of Eddy Current Technique to Measure Weir Overflow Height in Main Vessel Cooling Circuit of Prototype Fast Breeder Reactor

The main vessel in PFBR houses the entire primary sodium system. The inner vessel, which holds hot pool sodium, divides the sodium into hot pool and cold pool. In order to keep the main vessel below the creep regime (723 K), the same is cooled by diverting 400 kg/s of cold sodium from core support structure. The cold sodium enters the outer annulus, formed by the main vessel and the outer baffle (known as feeding plenum) through pipes, where it flows upwards to the free surface cooling the main vessel. From the feeding plenum, it falls

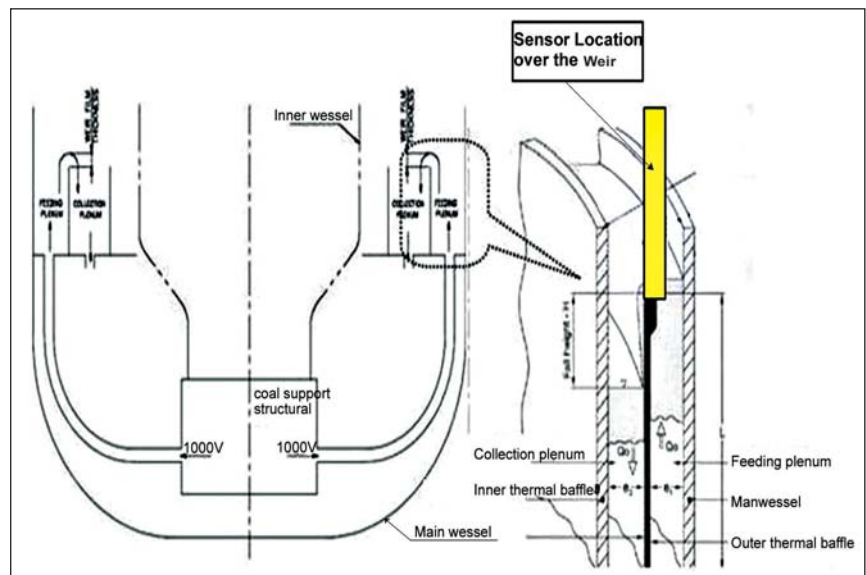


Fig.1 Schematic of main vessel cooling system

freely into the inner annulus (known as collection plenum) from where it enters the cold pool via orifices attached to the bottom of the restitution plenum (Figure1).

The sodium film height over the weir crest is a function of reactor power and varies from 15.5 mm at 28 % of reactor power to 26.90 mm at 100% of reactor power. Non-uniform weir flow height will result in non-uniform cooling of main vessel which may cause a tilt in main vessel. Hence, detection of weir flow height is an important parameter which requires development of sensor to detect weir overflow height. In order to achieve this objective an eddy current based sensor is under development.

To get the profile of the weir film height throughout the periphery of the main vessel cooling system, a number of sensors are placed diametrically opposite. Each sensor consists of one primary and one secondary winding. The primary winding is excited by a constant current source and its magnetic field induces a voltage in the secondary winding. When conducting sodium is in the vicinity of the windings eddy currents are induced in sodium which



Fig. 2 (a) Fabricated sensor using mineral insulated cable (b) Experimental test facility for sodium testing of weir film thickness sensor

reduces the secondary winding voltage. The reduction in voltage is proportional to the level of the sodium. Sodium weir overflow height can be evaluated by processing the output signal from sensors placed diametrically opposite above the weir.

The winding of the sensor was made from SS sheathed mineral insulated cable (Figure 2a) of 1mm OD. Sensor was positioned inside a 16 mm OD and 1 mm thick pocket. The primary winding of the sensor was excited by an alternating current of 100mA amplitude. The total length of sensor is 70 mm and the winding length is 60 mm.

For testing this weir film thickness in sodium, Test Pot-2 of SILVERNIA

sodium loop of Hall-1 was used (Figure 2b). During testing the sodium level was kept fixed and the sensor pockets were moved manually one by one to create a difference in sodium level seen by the two sensors and thus simulating the variation in film thickness.

Figures 3a and 3b give the output of the Sensor -1 and Sensor-2 sodium respectively. From the sodium test results, it can be seen that the sensor is able to detect the presence of sodium outside the pocket and the variation in sensor voltage with sodium level is nearly linear in the required range. The present tests are based on two sensors, which confirm the feasibility of this technique.

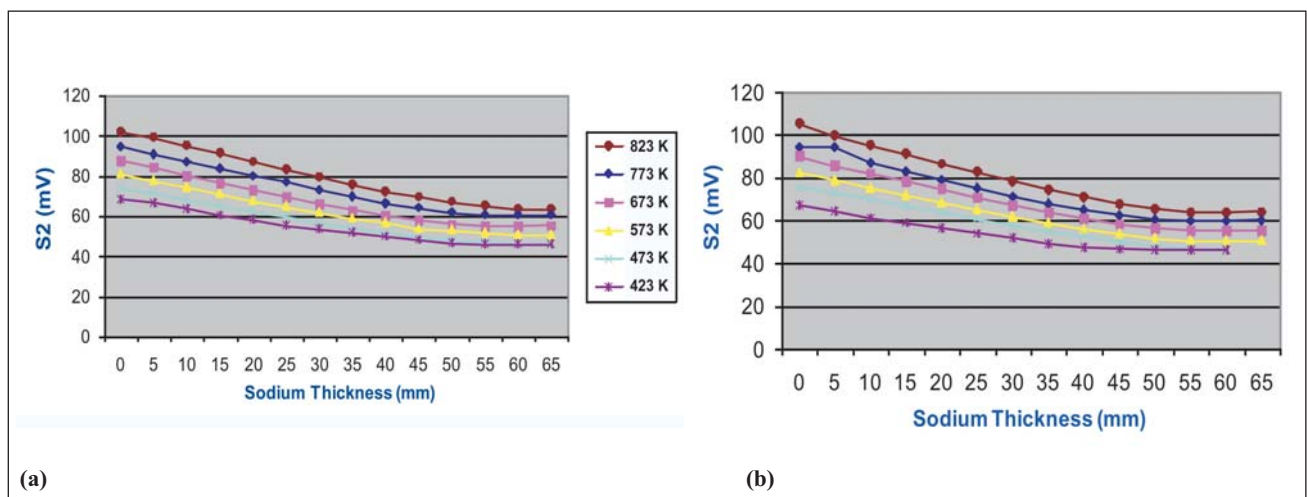


Fig. 3 Voltage vs sodium thickness of (a) Sensor 1 and (b) Sensor 2

### III.20 Development of Ultrasonic Waveguide for High Temperature Application

High temperature sodium immersed ultrasonic transducers are limited to temperatures of about 573 K. As a consequence, the ultrasonic imaging device can only be used in the reactor during shutdown. A device is needed for operating in sodium up to 773 K or higher. For a reactor designer, however, an immersed transducer is not necessarily an ideal device, because its reliability is uncertain, waveguides are the viable alternative to immersed transducers. The advantages are their relative simplicity, reliability and the fact that the source of sound can be located in a hospitable environment. The design and experiments with a new type of waveguide, a thin SS strip in which ultrasound is transmitted by a special type of guided Lamb wave is described below.

Lamb wave mode was chosen because it offers the advantage of propagating long distances both in the waveguide and liquid. This wave will detect immersed subassemblies and give information back to the source. The  $A_0$  Lamb wave mode was selected based on the high output of plane displacement component of the mode. The phase and group dispersion curves for a traction-free SS316 plate are shown in Figure 1. A suitable working point for generation of  $A_0$  mode was selected as 1.6 MHz-mm where the thickness of the SS 316 is 1.6 mm and frequency is 1 MHz. By sending angle beam longitudinal waves from a PZT crystal of dimension 76x12x2 mm placed on an Aqualene wedge ( $V=1521\text{m/s}$ ) with  $37^\circ$  inclination

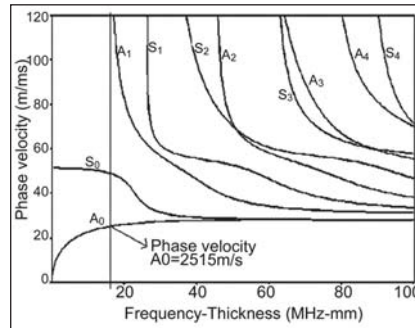


Fig. 1 Phase and group dispersion curve for SS

attached to the wave guide,  $A_0$  lamb wave modes ( $v_{ph}=2515\text{m/s}$ ) are generated as shown in Figure 2.

The region where lamb waves leak out into the fluid is the most critical part of the waveguide. Here mode conversion occurs from Lamb waves to compression waves in the adjacent fluid. The geometry of the region where Lamb waves leak out should be so designed that the emitted beam in liquid propagates with the least half beam angle. The design process includes determination of three parameters of the wave guide namely Length of leakage ( $L$ ), angle of curvature ( $\psi$ ) and angle of bend ( $\theta$ ) as shown in Figure 3. It was found that the variation of half beam angle is negligible after a leakage length of 30 mm and hence the leakage length was fixed to be 30mm. The variation

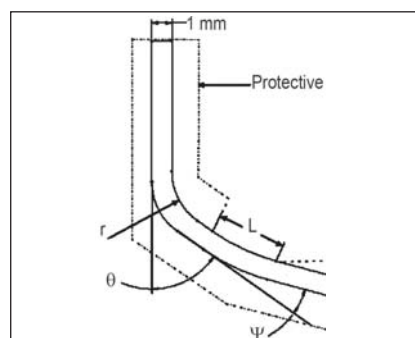


Fig. 3 Wave guide design

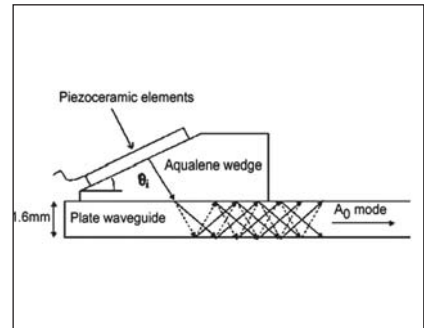


Fig. 2 Generation of Lamb wave

of half beam angle with angle of curvature was studied and observed that at  $4^\circ$ . The side lobes have least intensity, which implies that the sensitivity of measurement is highest at this value. It can be seen that the angle of leakage for a curvature of  $4^\circ$  is  $32.8^\circ$ . The plate has to be bent by an angle equal to the angle of leakage to keep the propagating beam horizontal in water.

To prevent mode conversion from taking place immediately as the strip waveguide enters the liquid, the waveguide is enclosed within a tube until the required point of emission is reached. The end of the encapsulating tube is drawn to such a size that its inner diameter matches the strip width. The tube is then cut to a shape to reveal the strip to the medium. The strip is in place by a seam weld along its edges. The



Fig. 4 Encapsulated (for 1m) wave guide with 10 m long strip

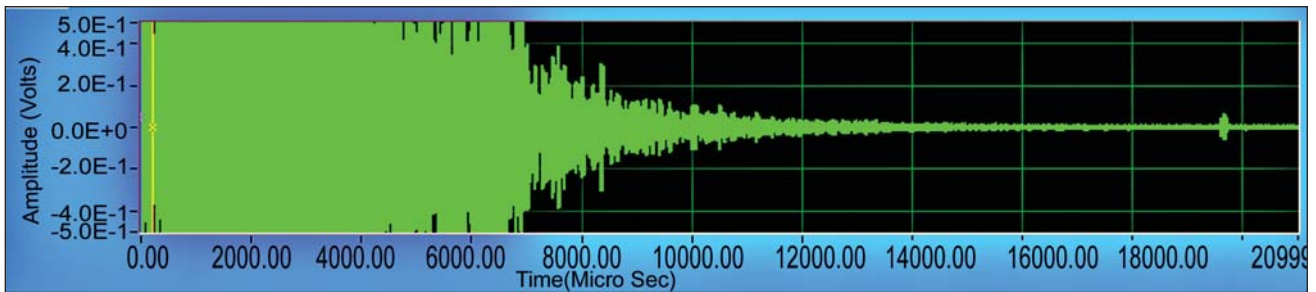


**Fig. 5** A-scan data from cylindrical target

immersed portion of the wave guide is designed such that only one face of the strip waveguide touches the liquid, thereby providing single beam as shown in Figure 4.

Experiments were carried out in water and a 1 MHz tone burst ultrasonic signal was generated using Ritec system (RPR 4000 pulser receiver) outside the hostile

environment and transmitted to the area of interest using waveguide that is 10 meter long of thickness 1.6 mm. This wave guide was tested in National Institute of Ocean Technology (NIOT) placing the 100 mm cylindrical target at a distance of 10 meter in water.

A 10 meter long SS316 waveguide for water was designed and operated

at a frequency of 1 MHz. The test was conducted in water and the results are compared with immersed transducer. With increased gain and power the echo was received from the target at a distance of 10 meter using waveguide. The waveguide can be used as an alternative to immersed transducers for reactor environment, however, this called for dimensional changes.

### III.21 Out-of-pile Test towards Development of Instrumented Irradiation Capsule

The data on the fuel centre line temperature at different linear powers will be useful in raising the power level of the reactor without exceeding the safety limits. Fuel pin parameters such as final fission gas pressure, irradiation creep, swelling etc. can be measured during post irradiation examination but fuel pin centerline and surface temperature can be measured online only.

It is planned to develop an instrumented fuel irradiation capsule to measure the centre line temperature of fuel and surface temperature of clad of a fast reactor test fuel pin in FBTR.

The out-of-pile test is designed to simulate the main features of IFI capsule. A heater pin has been used in the out-of-pile experiment to

function as a fuel pin. However, the linear power of a fuel pin cannot be simulated since the linear power of commercially available electrical heater pins of 8 mm diameter is in the range of 10 W/cm at 230 volt as compared to linear powers of 200 to 450 W/cm of fast reactor fuel pin. Three numbers of chromel-alumel (type – K) thermocouples have been attached on the surface of heater pin to measure the pin surface temperature. High temperature thermocouple that will be required to measure the center temperature of fuel pin is not used to measure the centre temperature of the heater pin because of complexity of introducing the thermocouple into sealed electrical heater pin. The heater pin is kept in a tube of dimensions 20 mm OD and

18 mm ID (modified equipment holder well / irradiation capsule) drilled with flow holes on its surface. Heater pin cable and thermocouples were routed through intermediate plugs and micro-brazed with the plugs to have leak tight joints as in the case of instrumented fuel irradiation capsule. This arrangement was loaded in the IF-1300 test rig at Hall-2 of Fast Reactor Technology Group.

IF-1300 test rig consists of FBTR test special subassembly (IF-1300) with dummy fuel pins, coolant (demineralised water) in the flow loop, pump and associated instrumentation.

During the experiment, the flow rate of the pump was varied from 0 kg/s (stagnant condition) to 2.81 kg/s (nominal flow rate of FBTR to

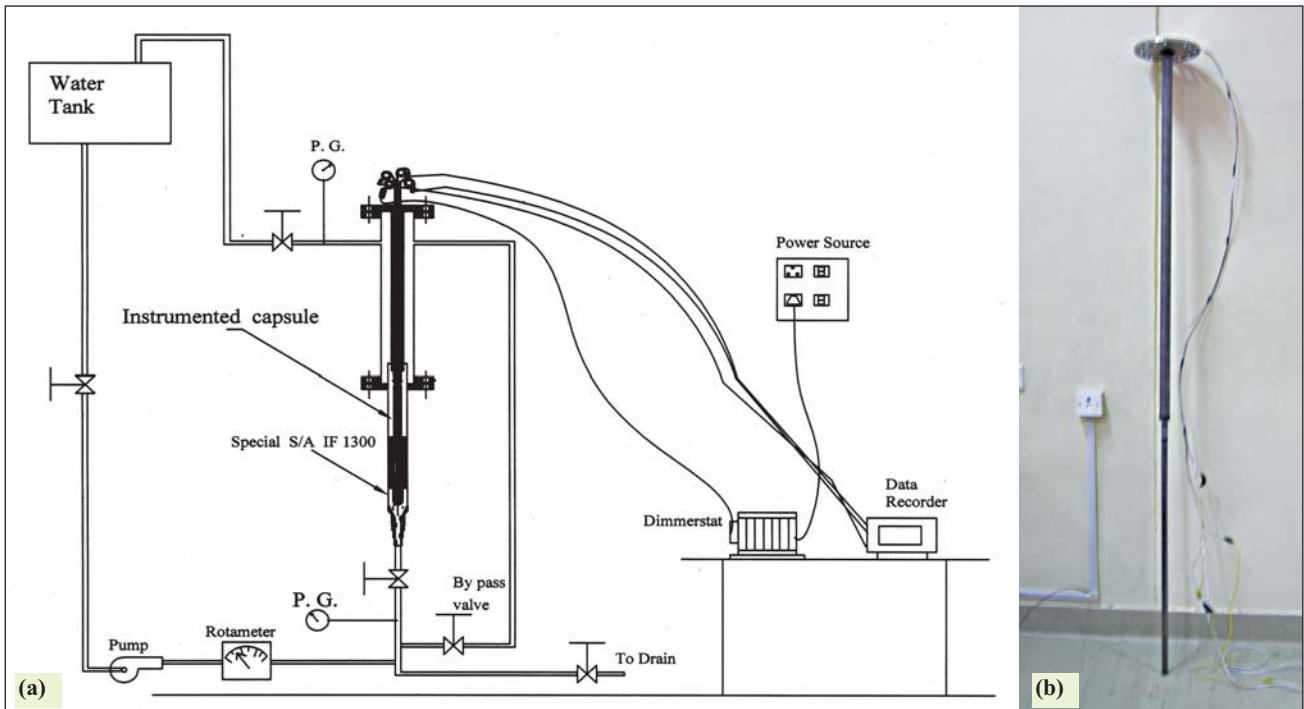


Fig. 1 (a) Sketch showing the flow test rig and (b) Test instrumented capsule

simulate Reynolds number). Inlet temperature of coolant (water) was maintained at 307 K and it was monitored by resistance temperature detector. Flow rate was measured using water collection tank and stopwatch. 1.5 mm OD stainless steel sheathed K-type thermocouples were used to monitor the surface temperature of heater pin and outlet temperature of water and these were recorded using data acquisition system. Figure 1 shows the sketch of the flow test rig and the test instrumented capsule.

Using dimmerstat, voltage was kept constant at 230 V in both types of

flow rates (0 and 2.81 kg/s) and heater pin power at that voltage was 500 watt. Maximum temperatures recorded near the surface of heater pin at different flow rates are shown in Figures 2 and 3. From Figure 2, it can be seen that when power of heater pin was raised to 500 watt, there was sudden rise in temperature in the case of stagnant condition; however in case of water flow rate of 2.81 kg/s, heat generated by heater pin is removed by the coolant and there is no considerable rise in temperature (Figure 3).

In the case of stagnant condition, experimental run was carried out for

24 minutes, until the temperature reached 355 K from the initial temperature of 307 K. In the case of flow rate of 2.81 kg/s, experimental run was carried out for 110 minutes and the temperature reached during this period was observed to be 313 K from the initial temperature of 307 K. This observed rise in temperature of 6 K is due to combination of heat generated by the heater pin and running of the centrifugal pump.

This experimental work reveals the ruggedness of the test instrumented capsule and establishment of online measurement of temperature in a test loop at different flow conditions.

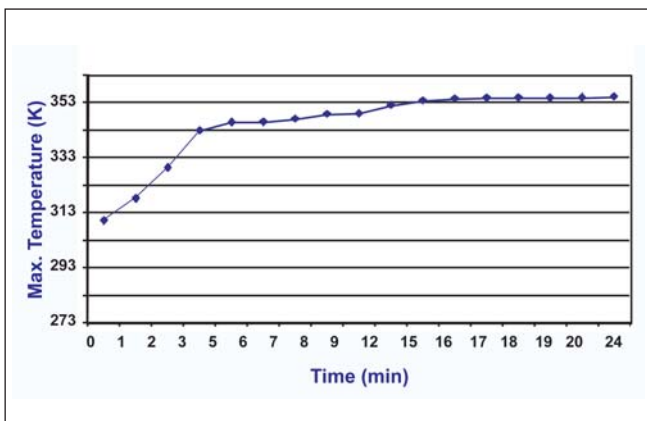


Fig. 2 Variation of maximum temperature with time at flow rate of 0 kg/s (Stagnant condition)

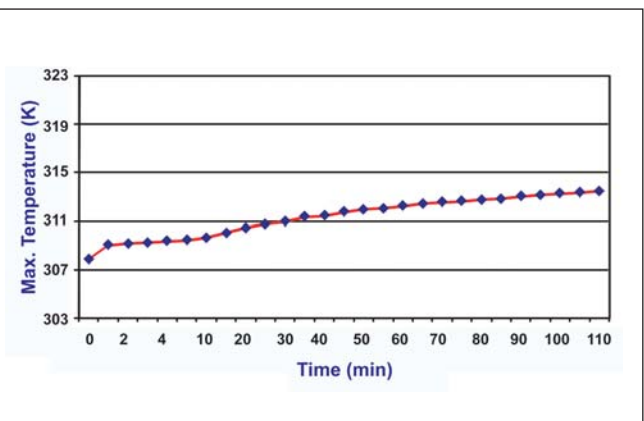


Fig. 3 Variation of maximum temperature with time at flow rate of 2.81 kg/s (simulation of FBTR flow)

## III.22 Real-Time Detection of Leak in Sodium Circuits using Fiber Optic Sensors

Potential regions of leakage in sodium circuits of FBRs are near welds, high stress areas and thin sections subjected to thermal shock. Wire type leak detectors and spark plug type leak detectors are used as the primary leak detectors in single wall pipe lines of secondary sodium circuits. The secondary leak detection system is sodium aerosol based global leak detectors which samples air from the ambient and passed through the sensor. Most of these techniques cannot detect location of the leak. A new sodium leak detection system using fiber optic sensor is tested to measure the change in temperature during the sodium leak. The most important advantage of fiber optic sensor over all other types of sensor is that it provides sensing over the entire length of the fiber. Also, the measurand is coded with the spatial information. In addition, optical fiber sensors are immune to electromagnetic interference, chemically inert, and amenable for long transmission distances.

The feasibility of using Raman Distributed Temperature Sensor (RDTS) for sodium leak detection is demonstrated in the test section-2 (Horizontal TS) of LEENA facility. Also, the fiber laying methodology is optimized and the dynamic response of the sensor to the sodium leak is evaluated.

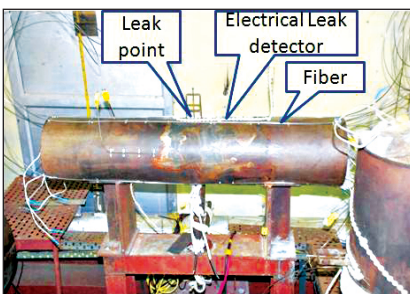


Fig. 1 Optical fiber sensor laid on the pipe surface

Test section-2 of LEENA Facility consists of horizontal pipeline of length 1000 mm and diameter 210 mm size. It is provided with a leak simulator at the top through which controlled leak is created.

Required temperature for the experiment is maintained with the help of surface heaters provided inside the test section. A wire type leak detector is provided near the leak simulator to detect the starting of the sodium leak. Heaters, thermocouples and insulation were provided over the test section.

A polyamide coated fiber encased in SS capillary tube was used as the optical fiber sensor deployed on the surface of the test pipe and across the cross section of the insulation. The capillary tube containing the fiber is fixed on the pipe using metal shims (Figure 1). Care is taken not to introduce undue stress on the fiber. The RDTS with polyamide coated fiber sensor encased in SS capillary is able to monitor temperature upto 623 K with a spatial resolution of 1 m and temperature resolution of 1 K. The rise in the temperature seen by the fiber sensor placed in the insulation around the pipe, due to leaking sodium, is an indicator of the leak.

There are 16 fiber sensors deployed over TS-2. Six of these sensors are placed on the outer surface of the pipe section, along the axis at different

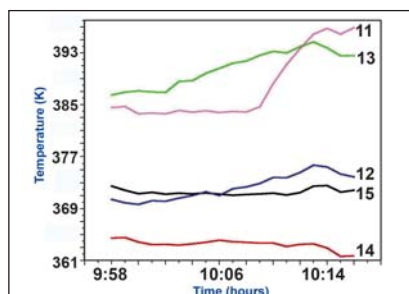


Fig. 2 Response of temperature during leak at first insulation layer

sectors around the pipe section. This is followed by an insulation layer surrounding the pipe over the sensors. Five more sensors are placed on this insulation layer along different sectors. This is surrounded by a second insulation layer, the final set of five sensors placed on this insulation layer. The pipe section along with insulation is encapsulated with aluminum clad. The liquid sodium temperature was maintained at 623 K during leak.

Typical dynamic response of the sensors to the leak, with time is shown in Figure 2. The temperature rise seen by the fiber sensor on contact with hot liquid sodium is the indicator of sodium leak. In general the temperature rise is followed by the falling temperature after reaching a maximum. It may be observed that each of the sensors sees temperature rise at different instances. This is because, leaking sodium, as it percolates across the insulation or drips along the surface of the pipe comes in contact with each of the fiber sensors at different circumferential positions at different times. The time delay seen by each sensor placed in specific sector around the pipe section has been used to reconstruct the temporal sequence of the leaking and percolating sodium.

This is verified subsequently by observing the sodium leak while removing the insulation layer by layer (Figure 3).



Fig. 3 Glass wool sticking to the surface of the pipe indicating the sodium leak track

### III.23 Settlement for Core Debris on the Core Catcher based on Simulation Tests with Woods Metal in Water

In the event of postulated transient over power and transient under flow without protective emergency safety actions, Core Disruptive Accident (CDA) takes place. During Core Disruptive Accident, high pressure-high temperature-molten fuel gets exposed to the surrounding coolant and structural material. The molten core debris comes and settles on to the core catcher plate. The decay heat generated in the debris needs to be removed by natural convection of coolant surrounding the debris to avoid further damage to the core catcher. To understand the dislocated melt dispersion and subsequent debris settling behavior an experimental set up (Figure 1) to melt woods metal (Bi 50% Pb 25% Sn 12.5% & Cd 12.5 %) and melting point of 345 K and pour arrangement in the water is manufactured and installed. Woods metal is chosen because woods metal and liquid uranium dioxide's physical properties (density, surface tension and kinematic viscosity) are similar. It facilitates investigations encompassing both hydrodynamic and boiling fragmentation processes.

The set up consists of a simple, innovatively designed SS furnace cum melt release system and a transparent test vessel of dimension 80 X 80 X 125 cm, which hold water in which the melt is released through a nozzle of 15 mm diameter. Few experimental runs were carried out with 2 kg woods metal heated to 473 K and water heights of 230, 340, 454, 590 and 845 mm to assess relative bed forming characteristics. High speed imaging at 500 fps has

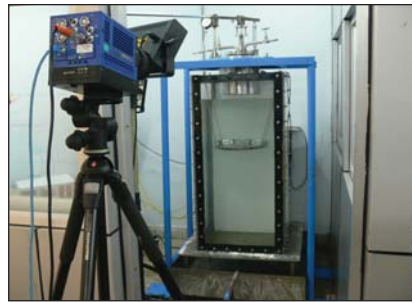


Fig. 1 Experimental set up for melting Woods metal

been taken to measure front velocity, jet instability and subsequent spreading in the collector plate. A geometrically scaled (X16) core catcher plate with chimney height and chimney top are used as collector plate. Thermocouples were positioned down the stream to monitor the melt steam temperature just after release and the melt impact temperature on to the chimney to evaluate the state of the melt at the collector plate. With water depth of ~ 230 mm the melt remained in liquid state on reaching the collector plate. The stream dispersed and the shattered droplets re-fused to form a solidified debris bed (Figure 2). Temperature data recorded are shown in Figure 3a. For water depths

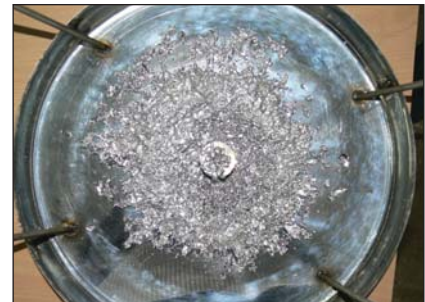


Fig. 2 Debris bed obtained for 230 mm depth

of 340, 454 and 590 mm, a small solidified debris heap was seen over and around the chimney with fine particles sprayed all over the collector plate. Typical high speed images obtained for 340 mm water depth case is given in Figure 3b. With 800 mm water depth effective melt dispersal was observed with no debris deposit on top of the chimney.

These tests provided better insight into the complex phenomena and the data generated will be useful for validation of numerical predictions. Conclusion based on these results may help to validate the core catcher incorporated in PFBR for accommodating core debris representing larger number of melted subassemblies subsequent to severe accident.

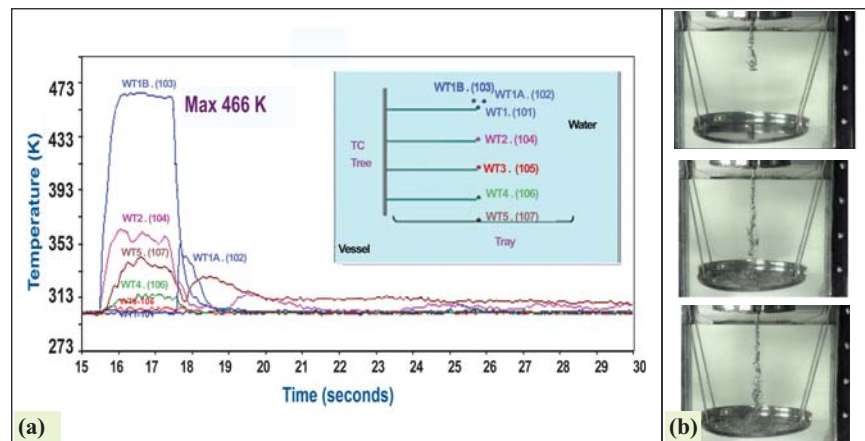


Fig. 3 (a) Temperature signals recorded during 230 mm water depth (b) High speed images during descending phase for 340 mm water depth

### III.24 Development of a Temperature Sensitive Magnetic Switch for Diverse Safety Rod Mechanism for Fast Breeder Reactors

PFBR employs a Diverse Safety Rod Drive Mechanism (DSRDM) for an emergency shutdown of the reactor. The DSRDM, located just above the core, comprises of an electromagnet that holds the Diverse Safety Rod (DSR). The reactor shutdown is enabled by de-energising the electromagnet that causes the DSR to drop into the core. To enhance the reliability of the DSRDM, a temperature sensitive magnetic switch (TSMS) is being developed for incorporation in the DSRDM. In the temperature sensitive magnetic Switch, the electrical switching is enabled by de-magnetisation that occurs when the temperature exceeds the Curie temperature of the magnetic component in the temperature sensitive magnetic switch. Design considerations require the magnetic component to have a Curie temperature of 893 K. Also desirable, in the component, is a low magnetic remanence and a small coercivity. For efficient and reliable switching, a magnetic susceptibility that drops sharply at the Curie temperature is essential.

Initial investigations were centred about obtaining an alloy with the

required Curie temperature. It was found that no composition in the well known Iron-Nickel binary system had a high enough Curie temperature. However, addition of cobalt to a range of the nickel-iron alloys was found to increase the Curie temperature. Based on laboratory melts (of 5 grams) using high purity starting materials, it was determined that the ternary alloy of composition (wt %) of 50Ni-37Fe-13Co has a Curie temperature of around 893 K.

While the Curie temperature is decided by the material chemistry, other magnetic properties, such as permeability, coercivity and remanence, strongly depend on the processing parameters. To obtain the temperature sensitive magnetic Switch component, which is tubular in shape, the processing of the alloy ingot by hot forging followed by extrusion route was tried. However, during hot forging employed to break up the cast structure of the ingot, the ingot cracked extensively making it impractical to proceed further by this route. Temperature sensitive magnetic switch components machined from the ingots too did not

have the required magnetic properties. Based on the reports in literature that exposure to oxygen at elevated temperatures is deleterious to the magnetic properties in soft magnetic materials, the process route was changed, and it was decided to obtain the component by investment casting with melting and pouring being carried out in vacuum followed by finish machining. This technique has proved to be successful. Figure 1 shows the Magnetisation (M) versus Magnetic Field (H) curves obtained with a Vibrating Sample Magnetometer (VSM) using samples from the investment casting. The absence of hysteresis at room temperature as well as at 873 K is a remarkable feature of the material and the method used to process it. The sharp transition in magnetisation at the Curie temperature shown in Figure 2, indicates the high degree of homogeneity of the sample. Magnetic Induction (B) versus Magnetic field (H) measurements using ring specimens (also obtained from the investment casting), shown in Figure 3, indicates the excellent magnetic properties of the bulk material.

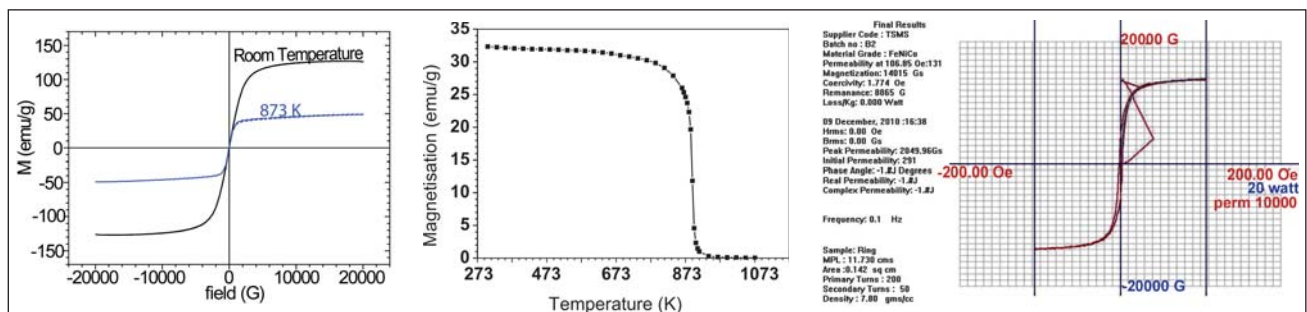


Fig. 1 Magnetisation vs. magnetic field (M-H) hysteresis curves of investment cast nickel-iron-cobalt alloy determined using a vibrating sample magnetometer

Fig. 2 Variation in magnetisation with temperature of investment cast nickel-iron-cobalt alloy determined using a vibrating sample magnetometer at 500 Oe field

Fig. 3 Variation in magnetic induction with field (hysteresis) determined using a ring specimen

### III.25 Development of Remotely Operable Diameter Measuring System

The data on irradiation behaviour of the indigenously developed D9 alloy is being generated by carrying out irradiation experiments in FBTR. The irradiation creep behavior of D9 alloy needs to be generated for the conditions of stresses and temperatures to which it will be subjected to in the reactor. Pressurised capsule technique is widely used to obtain irradiation creep data as it simulates the biaxial stress conditions of the fuel pin cladding. Pressurised capsules of D9 alloy have been developed and are currently being irradiated in FBTR at about 653 K to generate baseline irradiation creep data at lower temperature. Pressurised capsules will be exposed to irradiation at high temperatures using gas-gap type irradiation capsules in FBTR. Increase in diameter of pressurised capsules due to irradiation is expected to be in the range of 5 to 30 micrometers.

A highly accurate remotely operable diameter measuring (RODM) system has been developed to measure the diameter of pressurised capsules after irradiation in the hot cells of Radiometallurgy Laboratory, IGCAR. The system makes use of either an optical micrometer or two linear variable differential transformers (LVDTs) to continuously acquire the diameter along the length of the capsules. Figure 1 shows the schematic view of a pressurised capsule before and after irradiation.

In remotely operable diameter measuring system, a high precision self centered 3-jaw mechanical chuck with stepping motor is provided to hold, index and rotate the irradiated pressurised capsule. X-stage is provided to scan the pressurised

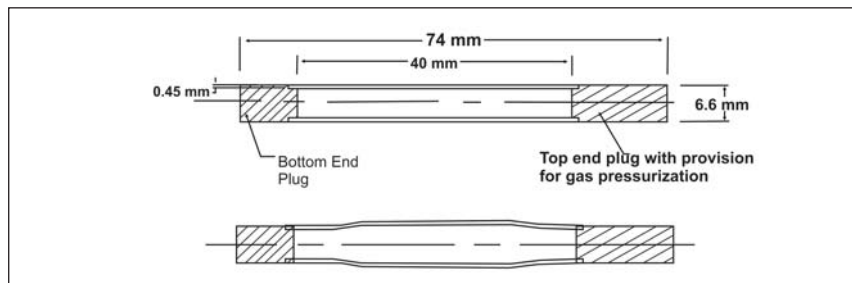


Fig. 1 Schematic view of the pressurised capsule before and after irradiation

capsule along its length. Using a charge coupled device (CCD) micrometer or a pair of linear variable differential transformers, the diameter of pressurised capsule can be measured. To achieve precise positioning, stepper motors with rotary encoders are provided in the X-stage and the chuck. Many contact or non-contact types of sensors were considered. Out of them, charge coupled device based optical micrometer has been selected due to its very fine resolution, high repeatability ( $\pm 0.15$  micron), easy operation and maintenance-free design (no moving parts). Charge coupled device micrometer module has a measuring head (transmitter and receiver). Uniform and stable light emitted from a gallium nitride (GaN) green light emitting diode (LED) passes through a tele-centric optical system and is received by an HL- charge coupled device. When the sample is loaded on the system its lateral dimension obstructs the green light from LED to the charge coupled device. The charge coupled device micrometer-controller (kept in operating area outside the hot cells) determines the diameter of the sample at the particular location by analysing the amount of green light reaching the charge coupled device.

Since there is no experience or literature available about effect of radiation dose on this type of system,

a linear variable differential transformer based set up has been installed as a standby to charge coupled device based optical micrometer. Linear variable differential transformer based set up has been selected since this system meets all the functional requirements and there is experience of using them in the hot cells. Differential linear variable differential transformer probes (knife edge type) have been used to make contact with the specimen at diametrically opposing positions to measure the difference in the diameter of the specimen.

The diameter measurements will be made at three to five locations spaced 5mm apart along the specimen length, and at 0, 45, 90, 135, 180, 225, 270 and 315 degree rotations with respect to the index mark for each axial position.

Figure 2 shows the view of charge coupled device based optical micrometer module and linear variable differential transformer module.

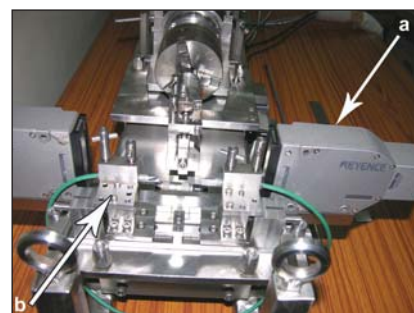


Fig. 2 CCD based (a) Optical micrometer module and (b) LVDT module

### III.26 Co-agglomeration studies of Sodium Aerosols with Fission Product Aerosols in a Closed Vessel

In the case of core disruptive accident (CDA) condition of sodium cooled fast reactors, the Reactor Containment Building (RCB) is bottled up with large amount of sodium aerosols along with fuel and fission product aerosols. The environmental source term depends on the quantity of aerosols released, which in turn depends on quantity of aerosols that remain suspended and leak rate. The sodium aerosols are generated by the combustion process resulting in micrometer range while, fuel and fission product aerosols are generated by vaporization condensation route resulting in nanometer range.

When a system of aerosols with disparate flow regimes are suspended in reactor containment building, the particle collision frequency functions between (i) sodium and sodium, (ii) fission products and fission products and (iii) sodium and fission products and subsequent changes in number concentration and mass concentrations are essential to model the aerosol settling pattern. The longer the time as the aerosols remain suspended in RCB volume, the more would be the environmental source term that leads to higher radiological impact.

Taking into account the above facts in our study, aerosols of sodium, non-radioactive fission products cerium oxide ( $CeO_2$ ), strontium peroxide ( $SrO_2$ ), and the mixtures of sodium with non-radioactive fission products [ $CeO_2+Na$  and  $SrO_2+Na$ ] were generated and the aerosol characteristics were studied. The study includes (i) the initial size distribution of sodium,  $CeO_2$  and  $SrO_2$  aerosols, (ii) the behaviour of suspended mass concentration as a function of time and (iii) behaviour of suspended number concentration as a function of time. It is to be noted at this point, though the radioactive species are present in the reactor containment building volume, the physical characteristics such as initial size distribution is not expected to change for non radioactive surrogates. The mass concentration studies are carried out by taking the mass ratio of fission product aerosols to sodium aerosols at 1:10, in accordance with EFR source term. Time evolution of number concentration measurements were carried out separately taking care of particle concentration limit, detection limit and avoiding bias due to mass concentration studies.

Experiments were carried out in the Aerosol Test Facility (ATF), which

mainly consists of an aerosol chamber of volume one cubic meter, a sodium combustion cell for the production of sodium aerosols, a 25 kW thermal plasma torch for the production of non-radioactive fission product aerosols and various aerosol measurement apparatus connected through sampling ports fitted with nozzles. The sampling is carried out as real time measurements.

About 5-10 grams of sodium is heated up to 823 K, under the argon environment. The hot sodium is ignited by exposing it to air, after flushing out the argon. By combustion, sodium oxide aerosols are formed in the combustion cell and get filled into the aerosol chamber and its diagnostic ports. The combustion cell is isolated after two minutes so that sodium aerosols are bottled-up in the aerosol chamber. About 5 g of  $SrO_2$  and  $CeO_2$  powders were pelletized and rigidly fixed in to the wire feeder tube and kept in front of the plasma flame. The pellets were melted and evaporated and re-condensed to produce aerosols in the chamber. The initial size distribution (CMD) of the sodium aerosols generated by combustion route is determined to be

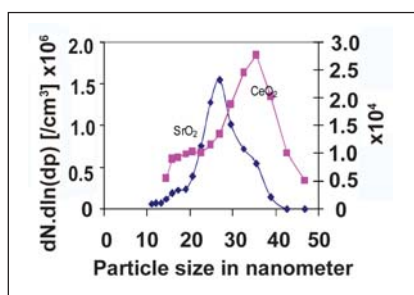


Fig. 1 Initial size distribution of  $SrO_2$  and  $CeO_2$  aerosols

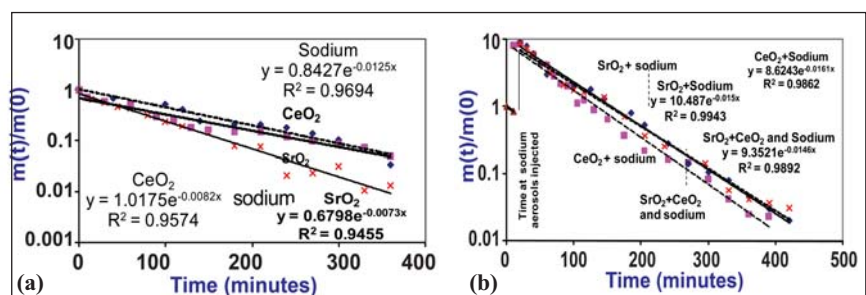


Fig. 2 Suspended mass concentration of (a) Sodium and (b) Fission product aerosols

0.923  $\mu\text{m}$  with geometric standard deviation (GSD) of 1.2 (The initial count-size distribution for  $\text{SrO}_2$  and  $\text{CeO}_2$  aerosols are determined to be 27 nm with  $\text{GSD} \approx 1.1$  and 32 nm with  $\text{GSD} \approx 1.2$  respectively (Figure 1). It is observed that the size distribution is uni-model and confirmed that sodium combustion aerosols are in micrometer range, while  $\text{SrO}_2$ ,  $\text{CeO}_2$  aerosols produced by vaporization and condensation route are in nano-meter range.

The normalized suspended mass concentration of aerosols of  $\text{SrO}_2$ ,  $\text{CeO}_2$  and sodium as a function of time is shown in Figure 2a. It is observed that the suspended mass concentration of sodium aerosols decreases at a faster rate than  $\text{SrO}_2$  and  $\text{CeO}_2$  aerosols. The size of the sodium aerosols grows both by physical (Brownian coagulation) and chemical (formation of hydroxide and carbonate) processes. The size of  $\text{SrO}_2$  and  $\text{CeO}_2$  aerosols grows only by Brownian coagulation. The sodium aerosols become larger at a faster rate and the larger sized sodium aerosols undergo faster gravitational settling than  $\text{SrO}_2$  and  $\text{CeO}_2$  aerosols. The suspended aerosol mass concentration of mixed

aerosols was measured as a function of time (Figure 2(b)). The collision frequencies among sodium aerosols and sodium with  $\text{CeO}_2$  or  $\text{SrO}_2$  aerosols are much higher than that of the collision frequencies among the fission product aerosols (the small particles have high Brownian diffusivities). Also the large sized sodium aerosols undergo gravitational agglomeration with smaller sized fission product aerosols. Hence, the combined effect would dominate and the particles settle together. Thus the behavior of aerosol governs the behavior of suspended aerosols.

The depletion of number concentration is measured for sodium,  $\text{SrO}_2$ ,  $\text{CeO}_2$  and mixed aerosols. Figures 3a, 3b and 3c show the depletion of number concentration pattern for sodium,  $\text{CeO}_2$  and mixed aerosols of sodium and  $\text{CeO}_2$  as average gas volume per particle ( $1/N$ ) versus time respectively. It is observed from the figures that the rate of change of gas volume per particle exhibit two regions (two different slopes). The first region for  $\text{CeO}_2$  lasts up to 70-80 minutes (Figure 3b), while for sodium aerosols it lasts only up to

Table 1 Gas volume per particle vs time		
Aerosols	Time	K
Na	30	$4 \times 10^{-15}$
$\text{CeO}_2$	80	$7 \times 10^{-16}$
$\text{Na} + \text{CeO}_2$	20	$6 \times 10^{-15}$

30 minutes (Figure 3a). Then they exhibit a steep decrease in the number concentration for both the aerosols. The  $\text{CeO}_2$  aerosols are in the free molecular regime having high Brownian diffusivities and target areas for collisions are very small while sodium aerosols are already in the continuum regime and collision frequency function is large. These smaller particles undergo coagulation till their size becomes sufficient enough for gravitational settling, whereas the size of the sodium aerosols increases at a faster rate, (both by physical and chemical process), resulting steeper slope than expected in the normal Brownian coagulation for nano-sized aerosols.

The net coagulation frequency function for the first region is obtained by fitting the value of  $1/N$  versus time in a straight line fit as given in table 1.

The coagulation frequency function for sodium aerosols is found to be one order higher than that of  $\text{CeO}_2$  aerosols. In the second region the rate of change in gas volume per particle is rapid where the gravitational settling / sedimentation begin to dominate.

Thus experimental results suggest that in the fast reactor CDA scenario, the sodium aerosol behavior governs the overall behavior of suspended aerosols of fuel and fission products. The initial size distribution of sodium aerosols is very critical in deciding the behavior of suspended aerosol system.

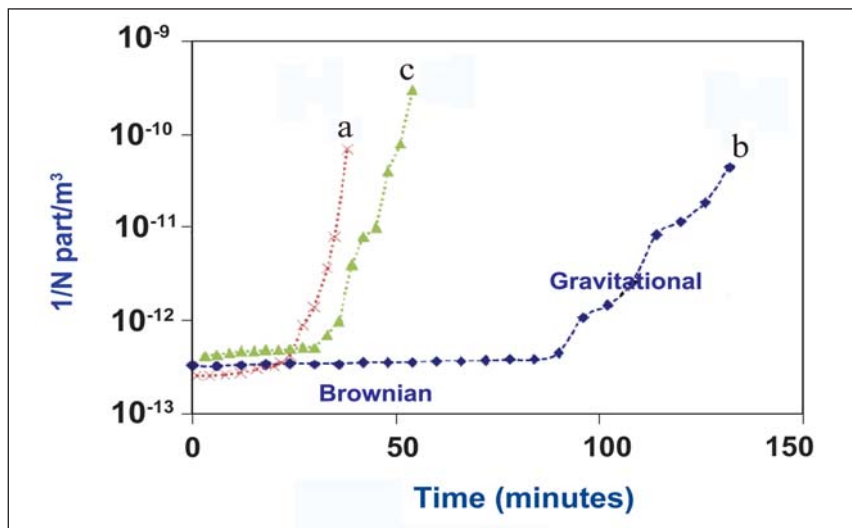


Fig. 3 Average gas volume ( $1/N$ ) vs Time (a) Sodium aerosols (b)  $\text{CeO}_2$  aerosols (c)  $\text{CeO}_2$ -Na aerosols

### III.27 High Temperature Metallurgical Compatibility with SS304L Steel and Phase Stability of Indigenously Developed Ferro Boron

The feasibility of using a commercial grade Ferro-boron (Fe -15 to 17 wt% B) alloy as an alternate shielding material in the outer subassemblies of future Indian fast reactors is studied. From shielding physics point of view, the study suggested that it is possible to use Ferro - boron as shielding material, provided its metallurgical and chemical compatibility with the SS 304L steel clad and liquid sodium at typical operating conditions are satisfactory. It is necessary to characterize the thermal stability and the nature of the metallurgical interaction of Fe-B alloy with the 304L clad, at typical service and also at higher temperatures.

The chemical composition of the alloy taken for this study is Fe-15.4B-0.3C-0.89Si-0.17Al-0.006S-0.004P-0.003O (wt.%). The XRD profile indicates the presence of two boride phases, orthorhombic FeB phase(major) and tetragonal boride Fe<sub>2</sub>B phase(minor). Additional phases like boro-cementite of Fe<sub>3</sub>(B,C) stoichiometry and cubic Fe<sub>23</sub>(B,C)<sub>6</sub> type carbides are also detailed.

The metallurgical compatibility of stainless steel was carried out in the temperature range of 823-1073 K and an interaction time of up to about 5000 hours. The experimental setup (Figure 1) consists of a cylindrical cavity made of 304L stainless steel into which the Fe-B alloy powder is loaded and gently compacted by the 304L plunger that is screwed down from the top. A number of such Fe-B loaded diffusion jigs have been

made, which are then exposed to different temperatures in a muffle furnace for different durations of time. In Figure 2, the microstructural development across the reaction interface for various time durations at a typical test temperature of 973 K is illustrated. In general, the diffusion layer consists of parallel tracks of fine intermetallic boride particles, embedded in the steel matrix. The hardness of the borided layer region on 304L stainless steel is found to be very high, of the order of 1600 VHN.

In Figure 3, the variation of the reaction layer depth with temperature and time is presented in the form of x<sup>2</sup> versus time plot, x stands for the

Table 1: Variation of reaction layer depth (m) with time (h) and temperature (T)						
hours	40	200	600	1000	2000	5000
T						
823 K	4	9.2	15	20	27	43
973 K	15	22	30	45	52	82
1073 K	18	27	40	49.5	65	101

reaction layer depth and time t. In Table 1, the data on variation of observed reaction layer thickness with time at three different temperatures 823, 973 and 1073 K are listed. The x<sup>2</sup> versus time data has been fitted by using the following equation:

$$x^2 = k(T) t.$$

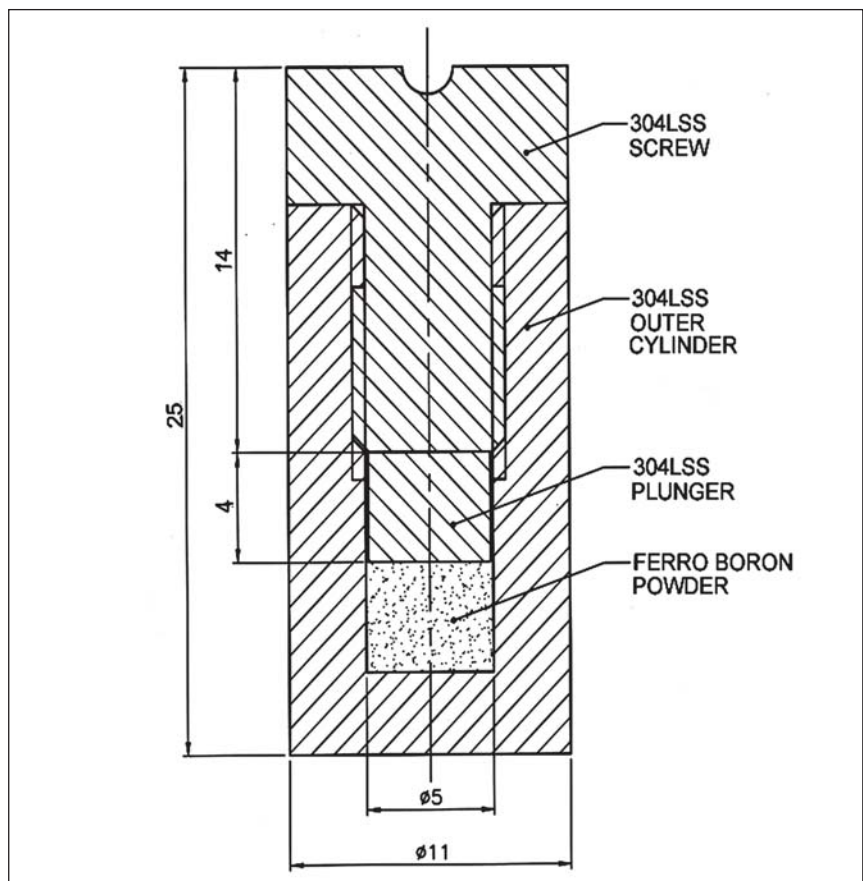


Fig. 1 Schematics of diffusion jig

The linear behavior given in Eq. (1) is usually interpreted as supportive of the operation of bulk diffusion as the probable rate controlling step. The rate constant  $K$  is usually represented by the Arrhenius form  $k(T) = k_0 \exp(-Q/RT)$ ;  $k_0$  is the pre-exponential factor and  $Q$  is the apparent activation energy for the overall reaction at the interface. In Figure 4, the variation of  $\ln\{k(T)\}$  with  $1/T$  is presented. The effective activation energy  $Q$  estimated from the slope of the linear correlation turns out to be  $57.7 \text{ kJ mol}^{-1}$ . The second set of data is shown as dotted line in Figure 5. The value for  $Q$  obtained in the latter case is found to be  $59.3 \text{ kJ mol}^{-1}$ .

In Figure 5, the DSC thermogram obtained during heating of Fe-B alloy to its melting range, followed by cooling to room temperature is shown. With this background and with the help of Fe-B binary phase diagram the different thermal arrests witnessed in Figure 5 may be interpreted in the following manner.

- (i) Curie temperature ( $T_c$ ) signifying magnetic to nonmagnetic transformation of  $\text{Fe}_2(\text{B},\text{Si})$  phase is found to be  $988 \text{ K}$ .
- (ii) Dissolution of borocementite  $\text{Fe}_3(\text{B},\text{C})$  and cubic  $\text{Fe}_{23}(\text{B},\text{C})_6$  mixed borocarbide phases in matrix occurs at about  $1377 \text{ K}$ .
- (iii) Dissolution of the lower boride phase,  $\text{Fe}_2(\text{B},\text{Si})$  and the

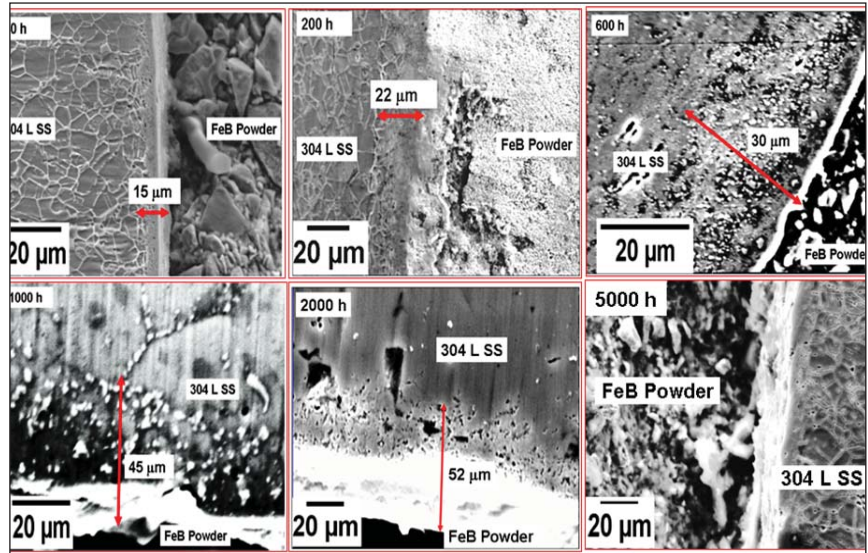


Fig. 2 Microstructural collage of the reaction layer formed at the interface of SS 304 L and Fe-B powder at 973 K

formation of the first traces of liquid phase is found to occur at  $1500 \text{ K}$ . However, it must be remembered that in the present case of multi component Fe-B alloy, the dissolution of lower boride occurs over a narrow temperature range and besides is also initiated at a lower temperature.

- (iv) The full melting of higher boride  $\text{Fe}(\text{B},\text{Si})$  begins at  $1632 \text{ K}$ . It is almost completed at  $1723 \text{ K}$ . It must however be mentioned that the Fe-B alloy used in the present study is actually a multi-component system, containing especially about  $0.3 \text{ wt. \% C}$  and  $0.89 \text{ wt. \% Si}$ . At present, very few experimental high temperature phase equilibria

data exist for Fe-B-Si-C quaternary system, especially around high boron and low carbon side. The phase changes that are witnessed during heating are essentially repeated in the cooling cycle, with some under cooling effects. The melting enthalpy estimated for Fe-B alloy is found to be  $1115 \pm 20 \text{ kJ.kg}^{-1}$ .

The novel significance of this study is as follows:

- (i) Metallurgical compatibility of FeB alloy with SS 304 L steel shows that it can be used very safely under typical service conditions.
- (ii) The DSC characterization of FeB alloy shows that it is well stable under typical service temperature condition.

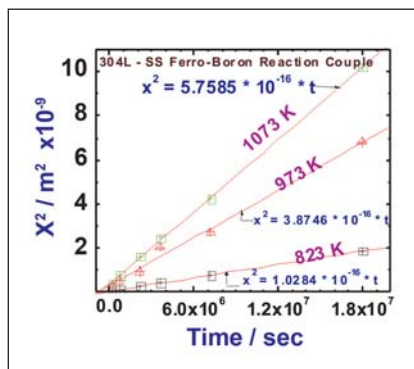


Fig. 3 Time - temperature variation of the reaction layer depth with time

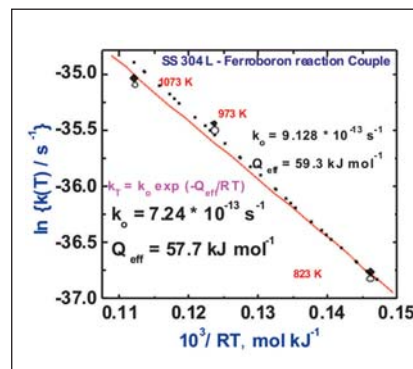


Fig. 4 Variation of the reaction constant  $k(T)$  with temperature

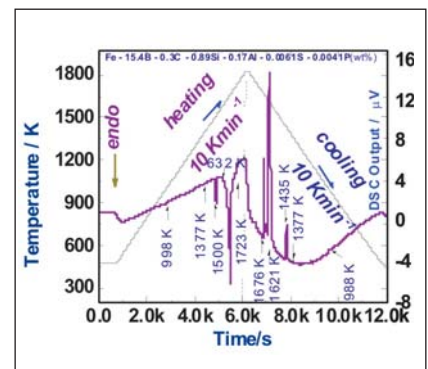


Fig. 5 DSC Thermogram of Fe-B alloy obtained during heating and cooling at the rate of  $10 \text{ Kmin}^{-1}$

### III.28 Tensile, Creep, Thermomechanical Fatigue and Corrosion-Fatigue Behaviour of 316L(N) Stainless Steel

#### Universal Scaling of the Work Hardening Parameters for Type 316L(N) Stainless Steel

An interesting inter-relationship has been obtained between the work hardening parameters, associated with the validity of Hollomon ( $\sigma = K_1 \varepsilon^{n_1}$ ) and Ludwigs ( $\sigma = K_1 \varepsilon^{n_1} + \exp[K_2 + n_2 \varepsilon]$ ) equations describing tensile flow behaviour in 316L(N) SS for wide range of strain rates and temperatures. This is observed as a linear correlation between normalized strength parameters i.e., strain hardening coefficients ( $K_1/\mu$  and  $K_3/\mu$ ) and transition stresses ( $\sigma_{1L}/\mu$  and  $\sigma_{2L}/\mu$ ) and respective strain parameters i.e., strain hardening exponent ( $n_1$  and  $n_3$ ) and transition strains ( $\varepsilon_{1L}$  and  $\varepsilon_{2L}$ ) independent of strain rate and temperature as shown in Figure 1. It is important to mention that 316L(N) SS exhibits three distinct temperature regimes in the variation of yield and ultimate tensile

strengths and uniform elongation with temperature; a gradual decrease from room temperature to 523 K followed by peaks/plateaus at intermediate temperatures due to occurrence of dynamic strain ageing and a rapid decrease in the recovery dominant high temperature regime. At high temperatures, 316L(N) SS obeys Hollomon power law relation. Large positive stress deviation from the Hollomon equation at low strains, due to dominating planar slip, facilitated application of Ludwigs equation appropriately at room and intermediate temperatures. Like the variations in yield and ultimate tensile strengths and uniform strain with temperature, the work hardening strength parameters ( $K_1/\mu$ ,  $K_3/\mu$ ,  $\sigma_{1L}/\mu$  and  $\sigma_{2L}/\mu$ ) and strain parameters ( $n_1$ ,  $n_3$ ,  $\varepsilon_{1L}$  and  $\varepsilon_{2L}$ ) exhibited three temperature regimes characterised by a gradual decrease from room temperature to 523 K followed by peaks/plateaus at intermediate

temperatures and a rapid decrease at high temperatures. The linear correlation obtained between strength and strain parameters as shown in Figure 1 can be ascribed to be a consequence of universal scaling; one obtained between strength parameters and ultimate tensile strength, and the other between strain parameters and uniform plastic strain. The origin of the inter-relation between strength and strain parameters (Figure 1) can also be traced back to the linear correlation observed between true ultimate tensile strength and true uniform strain irrespective of strain rate and temperature dependent deformation mechanisms.

#### Extrapolation of creep-rupture life to sixty years

Increasing the reactor design life to 60 years is a viable option for improving the economy of sodium Cooled Fast Reactors (SFRs). In this

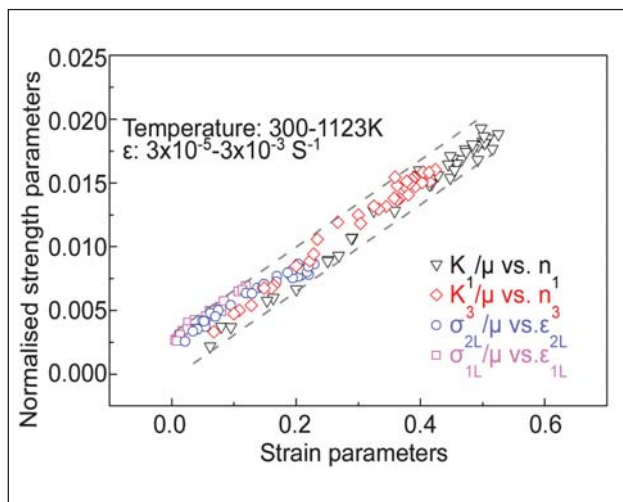


Fig. 1 Variations of normalised strain hardening coefficients and normalised transition stress values with respective strain hardening exponents and transition strains at different strain rates and temperatures

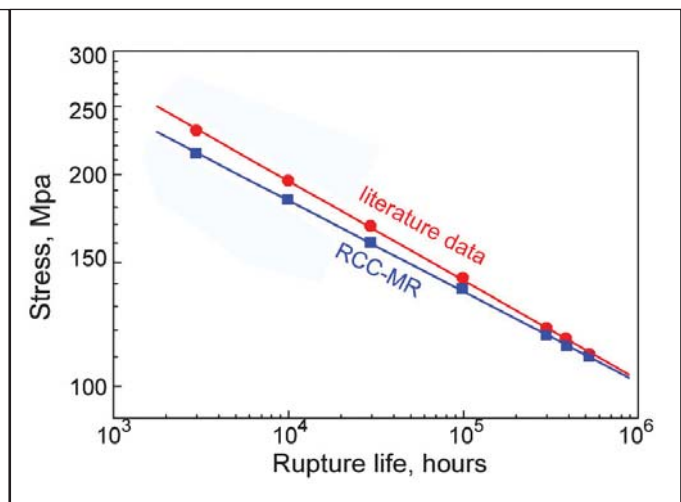


Fig. 2 Comparison of average stress-rupture data obtained from RCC-MR with that predicted from literature data using Larson-Miller parameter approach at T=873 K

context, it is proposed to design the future SFRs in India for 60 years lifetime ( $5.3 \times 10^5$  hours). Presently, RCC-MR design code provides design curves up to  $3 \times 10^5$  hours. An attempt has been made to assess the stress-rupture values for 316L(N) SS corresponding to sixty years design life. Creep-rupture data up to about 60,000 hours available in the literature has been used for the analysis which was based on Larson-Miller Parameter expressed as

$$LMP = T(C + \log t_r),$$

where  $T$  is temperature in Kelvin,  $t_r$  is the rupture life in hours and  $C$  is a material parameter. The optimum value for  $C$  was determined ( $C=20$ ) using third degree polynomial. Using the best fit polynomial equation, the average stress values for 60 years duration at 773, 823 and 873K were estimated. The creep rupture life data provided in the RCC-MR code was also used for the extrapolation. Design code recommends linear extrapolation as a straight line passing through the last two data points. The predicted average stress-rupture values at sixty years obtained using the literature data were higher than the values obtained using code data. Comparison of average stress-rupture values at 873 K obtained from analyses of literature and RCC-MR data clearly established that RCC-MR average stress data remained conservative in the temperature range 773-873 K even upto 60 years (Figure 2).

### Improving creep performance using A-TIG welding process

Type 316 L(N) SS weld joint of seven mm thickness was made by single pass A-TIG welding process developed in-house. The residual stresses in the weld joint were found to reduce by 75% and weld distortion by 33% as compared to that of weld

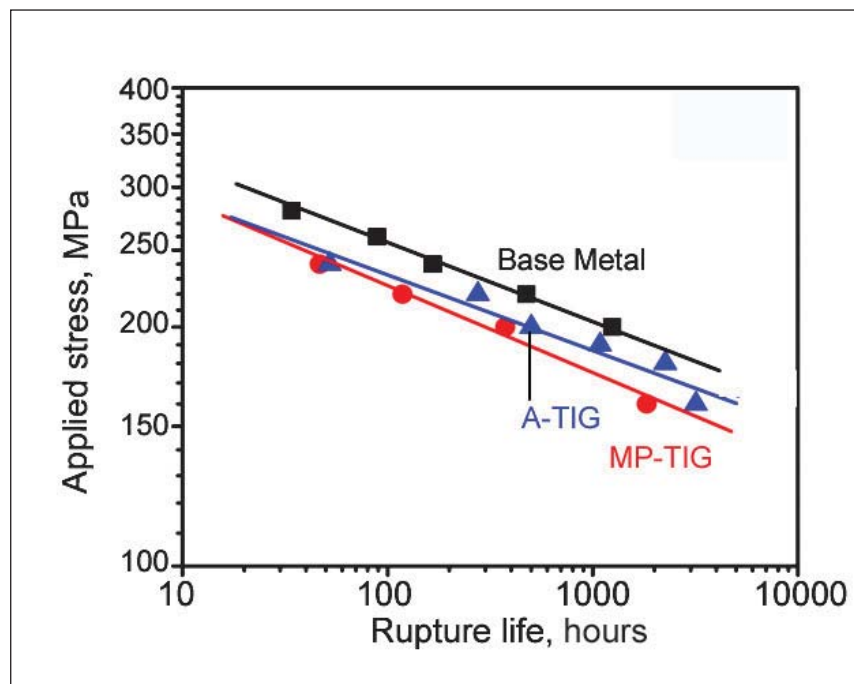


Fig. 3 Comparison of creep-rupture behaviour of base metal 316L (N) SS with A-TIG and MP-TIG weld joints at  $T=923$  K

joints made by other arc welding processes. High temperature performance of the A-TIG weld joint was assessed by evaluating the creep-rupture behaviour at 923 K and the performance was compared with that of the base metal and the multipass TIG weld joint. The variations of rupture life with applied stress for the base metal and the weld joints at 923 K are shown in Figure 3. Both the weld joints possessed lower creep rupture life than the base metal. The A-TIG weld joint had significantly higher rupture life than the multi-pass TIG joint especially at lower applied stresses. The enhanced creep-rupture life of A-TIG weld joint has been attributed to the coarse grain microstructure in the weld metal caused by higher peak temperature during A-TIG welding and the lower  $\delta$ - ferrite content. The above microstructural features resulting by welding process caused reduced creep cavitation which in turn delayed the onset of tertiary stage of creep deformation. A-TIG weld joint was found to exhibit

significant improvement in performance in terms of reduced residual stresses and distortion, matching tensile strength and ductility and enhanced creep rupture life in comparison to that of multipass TIG weld joint.

### Thermomechanical fatigue life

Structural components of sodium cooled fast reactors are subjected to cyclic mechanical loads that occur in combination with periodic temperature variations. Thermal stresses arise due to temperature gradients over the component during heating and cooling, associated with the startup/shutdown operations. The term thermomechanical fatigue (TMF) describes fatigue under simultaneous action of both temperature and mechanical strain. Isothermal low cycle fatigue (IF) tests performed at the maximum temperature ( $T_{max}$ ) of the expected TMF loading cycle are traditionally used as a basis for life estimation, in view of the experimental complexity associated with TMF testing.

Typically, designers use isothermal fatigue properties at the peak temperature of the design cycle to estimate the fatigue life of the component with an implicit assumption that this would yield a conservative lower bound value for the TMF life. However, many materials have yielded poor lives under TMF conditions. The TMF behaviour of 316L(N) SS was evaluated under in-phase (IP) and out-of-phase (OP) cycling conditions employing different temperature domains. Tests were performed under a mechanical strain control mode, at a fixed strain rate of  $6.4 \times 10^{-5} \text{ s}^{-1}$  and a strain amplitude of  $\pm 0.4\%$ . It was noticed that TMF life in OP cycling is lower than that in the IP tests in the low temperature regimes, whereas in the creep temperature domain, the IP tests yielded lower lives. Combined influence of creep and oxidation contributed to life reduction in IP tests when the peak temperature of cycling was above 873 K. IF tests carried out at the  $T_{\text{max}}$  of TMF cycles generally yielded lower fatigue lives in comparison with those obtained under TMF conditions. However, the

difference in fatigue lives between the isothermal and TMF lives was seen to diminish with increase in the peak temperature of TMF cycling, as presented in Figure 4. The variations in cyclic lives under TMF and isothermal fatigue conditions were seen to result in a crossover, rendering IP TMF more deleterious compared to IF cycling, at  $T_{\text{max}} > 650$ . The above life variation was seen to be associated with the dynamic strain ageing effects occurring in the intermediate temperature range.

#### Effect of Nitrogen Content on Stress Corrosion Cracking and Corrosion Fatigue Behaviour

The stress corrosion cracking and corrosion fatigue behaviour of 316L(N) SS have been studied with different nitrogen contents, namely 0.07 and 0.22 wt.% in a boiling solution of 5M NaCl + 0.15M  $\text{Na}_2\text{SO}_4$  (pH = 1.3). Corrosion fatigue tests were carried out at a stress ratio of 0.5 and a frequency of 0.1 HZ; the stress corrosion cracking experiments were performed using the constant load technique at a load equal to 70% yield stress. Open circuit potential was monitored with

respect to time during the stress corrosion cracking and corrosion fatigue tests. The potential at the time of cracking was taken as the critical cracking potential. Corrosion fatigue test results indicated better corrosion fatigue resistance for 316L(N) SS containing 0.22 wt. % nitrogen as compared to 316LN SS containing 0.07 wt. % nitrogen at all values of mean stress (Figure 5). The number of cycles to failure decreased with increasing mean stress for both the stainless steels. Both the stainless steels did not show any fatigue limit. Stress corrosion cracking tests indicated an increase in stress corrosion cracking resistance of type 316LN stainless steel as nitrogen content increased from 0.07 wt.% to 0.22 wt.%. The improvement in stress corrosion cracking and corrosion fatigue resistance was attributed to improved passivity with increasing nitrogen content. X-ray photoelectron spectroscopic studies indicated that the nitrogen and molybdenum contents in the passive film increased with increasing nitrogen content.

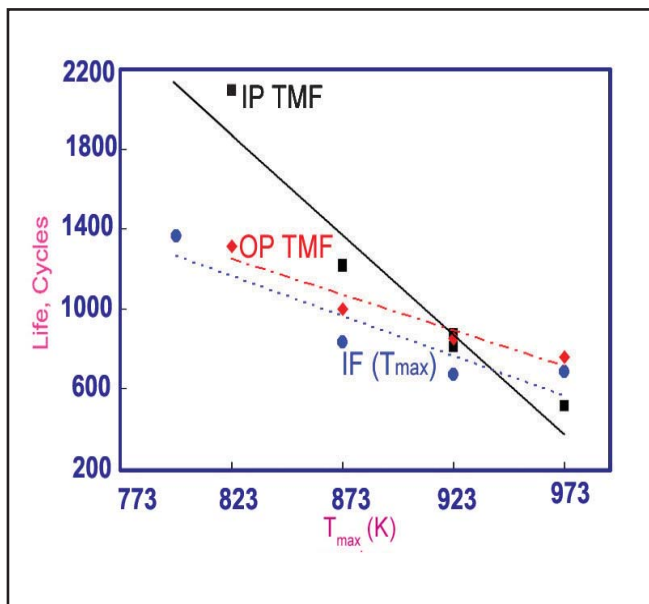


Fig. 4 A comparative plot of the cyclic lives obtained in TMF (IP and OP) and IF cycling at  $T_{\text{max}}$ .

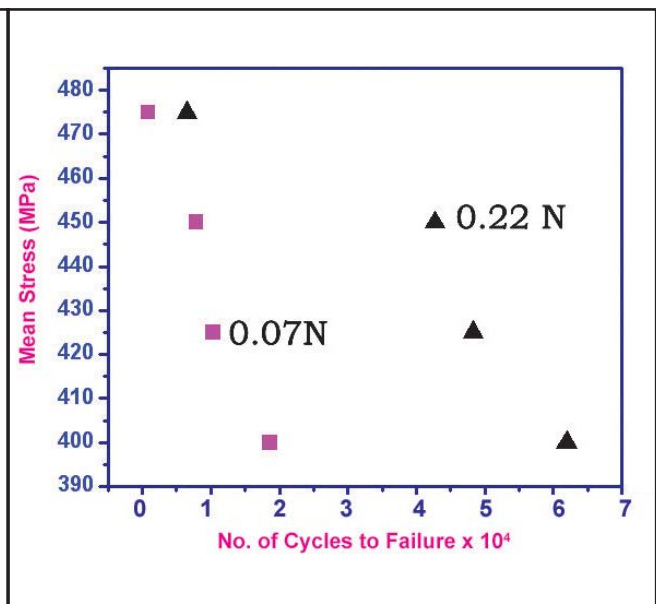
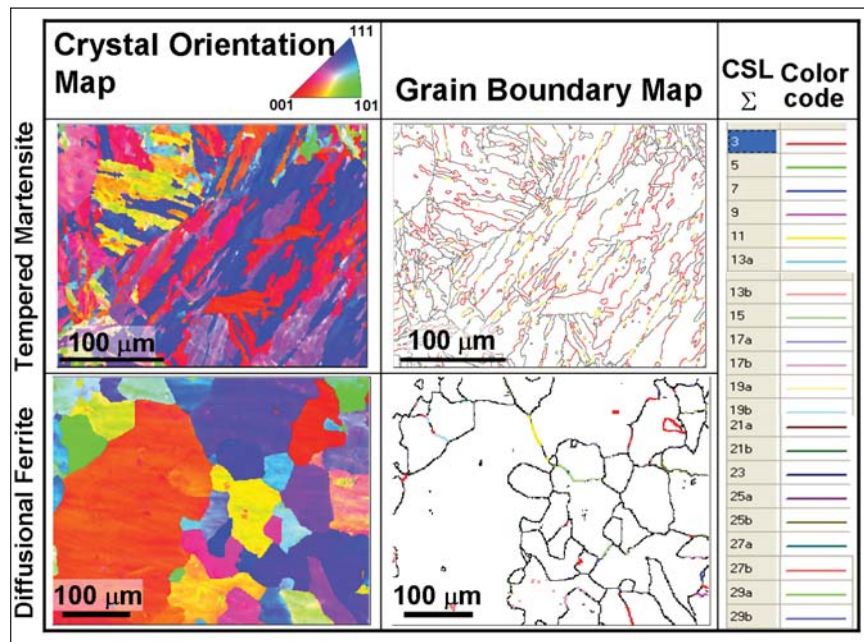


Fig. 5 Effect of nitrogen on corrosion fatigue resistance of type 316LN austenitic stainless steel.

### III.29 Studies on Grain Boundary, Fracture, Creep, Sodium Compatibility and Alloy Modification of Modified 9Cr-1Mo Steel

Modified 9Cr-1Mo steel is the material of construction for steam generators and candidate material for wrapper and clad tubes of future Indian sodium cooled fast breeder reactors (SFR). Creep strength and sodium compatibility are properties that are important for steam generators and fracture toughness and resistance to embrittlement are critical for use of this material as wrapper and clad tubes. Besides these studies, attempts to improve the Type IV cracking resistance of the weld joints of this alloy by controlled addition of boron have been successfully carried out.

Ductile-to-brittle transition phenomena observed in all ferritic steels, including modified 9Cr-1Mo steels can be aggravated by embrittlement that can arise due to long-term exposure to high temperature and irradiation environments. Embrittlement is associated with the segregation of impurities (such as S, P, Sb etc.) and precipitation of brittle phases (like  $\text{Fe}_2\text{Mo}$ ) at high-energy boundaries, leading to decrease of grain boundary cohesive strength and consequent intergranular brittle fracture. Coincidence Site Lattice (CSL) boundaries represent 'special' boundaries with low interfacial energy, as a finite fraction (denoted by  $1/\Sigma$ ) of extended lattice points of the two neighboring crystallite grains coincide. Effect of heat treatment, which in turn determine the mode of phase transformation ( military/ diffusional) of high-temperature austenite phase, on the fraction of CSL boundaries formed in this steel was evaluated using SEM-EBSD



**Fig. 1** EBSD results of the two types of microstructures in 9Cr-1Mo steel. The type of crystallographic plane aligned with the sample surface is depicted in the crystal orientation map. The different types of coincidence site lattice boundaries have been color coded in the grain boundary map

(Scanning Electron Microscopy-Electron Back Scattered Diffraction) technique. Figure 1 shows the EBSD results of the microstructure obtained upon 'Normalising & Tempering' treatment (Tempered Martensite) and 'Isothermal Annealing' treatment (Diffusional Ferrite). Crystal orientation map depicts the crystalline plane which is aligned with the sample surface. The martensitic mode of phase transformation ensued in a characteristic sub-structure of martensite crystallites, whereas the diffusional transformation resulted in polygonal ferrite grains. The different CSL ( $\Sigma$ 3-29) and the non-CSL boundaries (black lines) for the two microstructures have been depicted in the grain boundary map. The amount of  $\Sigma$ 3-29 CSL boundaries in the tempered martensite (33%) is higher compared to the diffusional ferrite (11%).

To study the cleavage fracture of modified 9Cr-1Mo steel, a procedure to estimate crack arrest toughness ( $K_{1A}$ ) from the small size pre-cracked Charpy specimens has been developed.  $K_{1A}$  is being proposed as a characteristic material toughness below which cleavage fracture does not occur. Crack arrest length is an important parameter that needs to be determined from the tests carried out in the ductile-brittle transition temperature (DBTT) regime for estimating  $K_{1A}$ . In the absence of microstructural signature on the fracture surface, estimation of crack arrest length is not easy. Hence, an analytical procedure known as 'Key curve' method is used for this purpose. The 'Key Curve' expression correlates load (P), ligament length (b) and plastic displacement or total displacement (d), which are the three variables in a fracture mechanics test.

$$P = B^* W^* (b/W)^\eta * H (d/W)$$

Where B – thickness, W- width,  $\eta$  eta factor.  $\eta = 2$  for a Charpy specimen.

The challenge was in obtaining the required parameters for the 'Key Curve' expression from the Charpy impact test. This was done successfully from the load-displacement curves recorded during the tests conducted at temperatures 243, 250 and 253 K for modified 9Cr-1Mo steel in the normalized and tempered condition, which exhibits typical cleavage fracture in this temperature regime. Figure 2 shows a typical load-displacement curve, which displays minimum plasticity at the initial stage, followed by cleavage fracture, crack arrest and finally plastic deformation till the end. The plot displays the crack arrest phenomenon which is the arrest in load drop above zero level at cleavage fracture. As the specimens display minimal plasticity before cleavage fracture, total displacement has been used as the variable for the key curve analysis employed in this study. The load – displacement pairs between yield point and peak load before cleavage fracture have been fitted to the key curve expression to obtain the constants of this equation. In the key curve equation,  $H(d/W)$  has been expressed as a power law. The fitted key curve is applied to the load–displacement pair at crack arrest or at final fracture to obtain the ligament length, and hence, the crack arrest length or final crack length. This method requires the unbroken final crack length for validation. However for the main tests conducted at 243, 250 and 253 K, the specimens fully fractured during the course of the tests causing non-availability of the unbroken final crack length. Hence, tests were conducted at higher temperatures in the DBTT regime of the material. In these verification tests, the

specimens did not fully fracture during the course of the tests, and hence, the unbroken final crack length was available for validation of this method. The verification tests displayed load-displacement records similar to those of the main tests. The final crack length calculated by the key curve method was in close agreement to the optically measured final crack length for all the verification tests justifying the validity of this method for the calculation of crack arrest length in the main tests of this study. Successful validation of this method was also demonstrated for the steel subjected to 5 and 10% cold work.

Effect of flowing sodium on mod.9Cr-1Mo steel was studied by exposing this material in normalized and tempered condition (N&T) to flowing sodium in a bi-metallic sodium loop for a time duration of up to  $3 \times 10^5$  hours at 798K. The results of tests conducted on sodium exposed mod. 9Cr-1Mo steel samples were compared with those of thermally aged and N&T steel of 1.6 mm thickness. Microstructure and EDX analysis did not reveal any significant changes at the surface. An increase in hardness up to about  $70 \mu\text{m}$  depth was observed on sodium exposure. This was attributed to surface carburization. No significant changes were observed in yield stress, ultimate tensile stress and ductility when compared to the N&T and thermally aged condition. The impact energy values decreased on sodium exposure vis-a-vis normalized and tempered steel. However, impact energy values of sodium exposed material did not differ from that of thermally aged steel, indicating that the changes in impact properties were attributed to thermal aging effects. No significant changes were observed in mechanical properties of mod.9Cr-1Mo steel between 16000

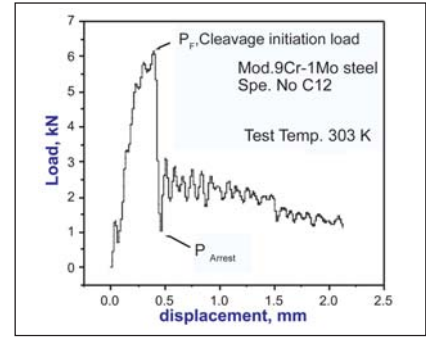


Fig. 2 Load Vs Displacement plot showing crack arrest load

hours (reported earlier) and 30000 exposures.

There are strong economic reasons for increasing the design life of SFRs to 60 years. However, this needs reliable long-term creep-rupture data for mod. 9Cr-1Mo steel, the major structural material for steam generator components of SFRs. Presently, RCC-MR, the design code available for SFRs provides design curves up to  $3 \times 10^5$  hours (~35 years). An attempt has been made to assess the stress-rupture values for mod. 9Cr-1Mo steel corresponding to 60 years design life using experimental creep-rupture data up to about  $1.28 \times 10^5$  hours, available in the literature. Stress-rupture values for 60 years design life have been determined from extrapolation using Larson-Miller Parameter expressed as

$$LMP = T(C + \log t_r),$$

where T is temperature in K,  $t_r$  is the rupture life in hours and C is a material parameter and an optimum value of  $C = 31$  was obtained. Using the best fit polynomial equation, the average stress values for 60 years duration at 773, 823 and 873K were evaluated. In addition to Larson-Miller parameter approach, artificial neural network (ANN) has been trained with available literature data and subsequently used for creep-rupture life extrapolation. RCC-MR stress-rupture values for 60 years at 773,

823 and 873K were also determined by linear extrapolation as a straight line passing through the last two data points, as suggested in the design code.

The average stress-rupture values for 60 years- $5.25 \times 10^5$  hours predicted from literature data using LMP approach, ANN method and RCC-MR for mod. 9Cr-1Mo steel (extrapolated to linear fit) are given in Table 1. The average stress values predicted from LMP and ANN methods are nearly equal. The predicted average stress-rupture values obtained from literature data are higher than that obtained from the design code RCC-MR. Comparison of average stress-rupture values at 823 K obtained from literature and RCC-MR for different durations is shown in Figure 3a, as an example. It can be clearly seen (Table 1 and Figure 3a) that RCC-MR average stress data remains conservative in the temperature range at 773-873 K.

In order to study the effect of boron in improving the resistance of the weld joint to Type IV cracking, properties of the base metal, weld joints and simulated HAZs of two heats of mod. 9Cr-1Mo steels, one with controlled addition of boron (P91B) and other without boron (P91) were examined. Both the base metals are subjected to two different normalising (1323 K/1h and 1423 K/1h) heat treatments followed by tempering (1033 K/3h). The grain sizes for P91 (19  $\mu\text{m}$ ) and P91B (28  $\mu\text{m}$ ) base metals after the normalising treatment at 1323 K were not much

different. In contrast grain sizes for these two steels after normalising treatment at 1423 K were found to be 130 and 250  $\mu\text{m}$ , respectively. From the results of tensile tests conducted on specimens with various heat affected zones simulated by heating them to peak temperatures in the range of 1073-1273 K and cooling rapidly, it is found that tensile behaviour for different HAZs simulated in boron containing steel is similar while that of boron free steel varied widely. It was also observed that the deformation behavior of HAZs (simulated) specimen is more uniform for coarse grained (high normalizing temperature) material than the other. As a result of reduced strength gradient in the HAZ, creep strength of weld joint of boron containing 9Cr-1Mo steel is found to be much better than that of the boron free steel. Creep test carried out at 873 K at stress levels of 80, 100 and 120 MPa for these steel weld joints are shown Figure 3b. The figure also reveals that the effect of prior austenite grain size of the base metal on the creep strength of the weld joint is more significant for boron containing steel (P91BH) (arrow indicate test are in progress) than for boron free steel (P91H).

Improved performance of the weld joints of the boron containing 9Cr-1Mo steel is attributed to the better stability of the HAZ microstructures of this steel than that of boron free steel. Prior austenite grain size is

Table 1: Predicted values corresponding to rupture life of 60 years			
T in K	Average stress MPa using		
	LMP	ANN	RCC-MR
773	210	214	199
823	131	132	126
873	74	74	69

more or less retained in different parts of the HAZ in spite of the difference in the thermal cycles experience by these different zones. This is in contrast to the wide variation in the prior austenite grain size observed in different parts of HAZ of boron free steel. Figure 4 compares the microstructures in the intercritical HAZ of boron containing 9Cr-1Mo steel and boron free steel.

The uniform microstructure of the HAZ with similar deformation behavior significantly brings down the localized deformation in the fine grained/inter critical HAZs of the boron containing steel compared to those observed in the boron free steel. Further, at high temperature boron distributes more uniformly and enhances its utility in stabilizing the microstructure.

These results clearly show the possibility of designing high Cr ferritic steels with controlled addition of boron to improve the resistance of this steel to Type IV cracking. With this improvement, it should be possible to increase the upper limit for design temperature for this class of steel for fossil power applications.

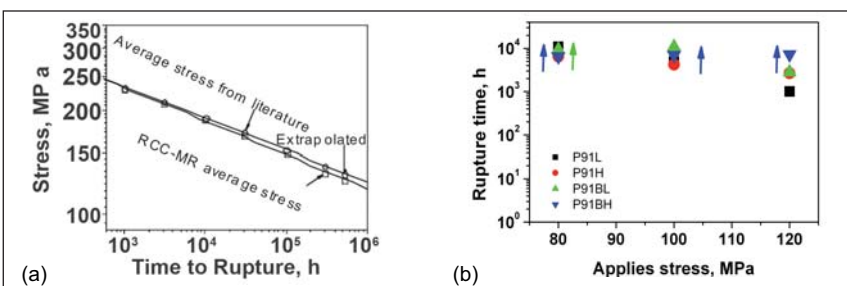


Fig. 3 (a) Comparison of average stress-rupture data obtained from RCC-MR with that predicted using Larson-Miller parameter approach for modified 9Cr-1Mo steel (b) Variation in rupture life vs. applied stress for different weld joints

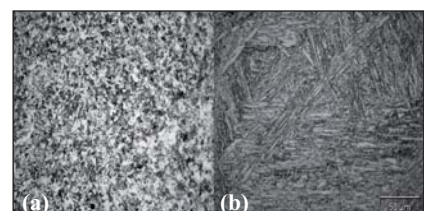


Fig. 4 Microstructure of inter critical heat affected zone of (a) P91 and (b) P91B weld joint prepared from 1423 K/1h normalised and 1033 K 3h tempered steels

### III.30 Development and Characterisation of Oxide Dispersion Strengthened 9Cr Ferritic/Martensitic Clad Tubes

The inherent superior void swelling resistance of ferritic/martensitic steels upto 200 dpa has made the 9-12Cr steels attractive for clad tubes of future Fast Breeder Reactors. However, their low creep strength at temperatures above 873 K restricts their application, and oxide dispersion strengthening is found to be a promising means of extending the creep resistance of the ferritic/martensitic (F/M) steels beyond 923 K without sacrificing the inherent advantages of high thermal conductivity and low swelling of ferritic steels.

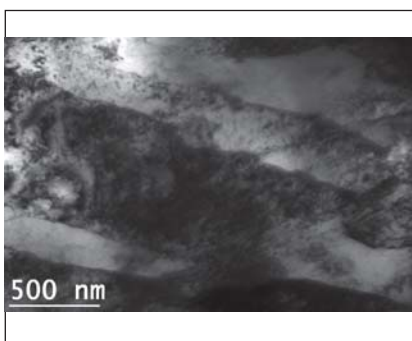
In Fe-9Cr-2W-0.1C-0.2Ti-0.35 Y<sub>2</sub>O<sub>3</sub> oxide dispersion strengthened (ODS) F/M steel, the superior properties are achieved by refinement of Y<sub>2</sub>O<sub>3</sub> (~ 30nm) to finer sizes (~ 5nm) with the formation of complex oxides (Y<sub>2</sub>Ti<sub>2</sub>O<sub>7</sub> / Y<sub>2</sub>TiO<sub>5</sub>) through interaction with Ti. A complex powder metallurgy route followed by hot and cold mechanical process steps is adopted to produce the clad tubes. Pre-alloyed powders of the steel and nano size Y<sub>2</sub>O<sub>3</sub> particles

were processed in a high energy attritor mill in argon atmosphere. The mixed powder is canned in mild steel can, degassed and sealed. The sealed cans are upset to compact the powder into canned billet. The upset billets are machined to remove the mild steel can. The billets were hot extruded to produce rods. Mother tubes were prepared by drilling the extruded rods with minimum concentricity. Clad tubes were produced by cold drawing (pilgering) of the mother tube with intermediate softening heat-treatments. The clad tubes were finally subjected to normalizing and tempering heat treatments in inert atmosphere. Clad-tubes with 6.6 mm outer diameter, 0.45 mm thickness and upto 4500 mm length have been successfully produced.

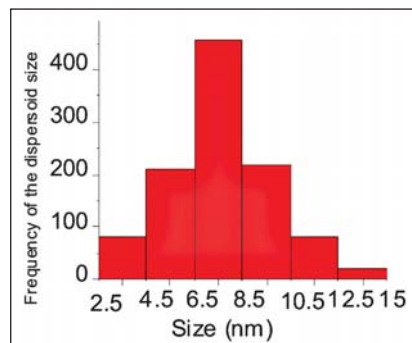
The tubes are characterised during each stage of the fabrication in order to optimize the process parameters. The tubes have been characterised for matrix texture, microtexture, dispersoid size, spatial distribution and phase content.

Figure 1 shows the micro-structure of a section of the final tube demonstrating a fairly uniform distribution of dispersoids within the matrix. Histogram of the size distribution (maximising at 7 nm) is shown in Figure 2. Careful measurements on high resolution TEM micrographs enabled the identification of the dispersoid phase under certain imaging conditions. A typical example of this is shown in the high-resolution micrograph in Figure 3. The central region of the image shows lattice planes of a dispersoid particle with a plane spacing of 0.30 nm that can be identified with the (222) planes of Y<sub>2</sub>O<sub>3</sub>. In summary, the required microstructure consisting of tempered martensite with fine and uniform dispersion of yttria-based dispersoids were observed in the finished clad tubes.

Figure 4 shows the EBSD orientation map of the ferrite grains from a section of the final tube. The random color distribution in this map along with nil pole concentration in the pole



**Fig. 1** Bright field micrograph showing fine martensitic lath in matrix of the final tube



**Fig. 2** Dispersoid size distribution in the matrix of the final tube

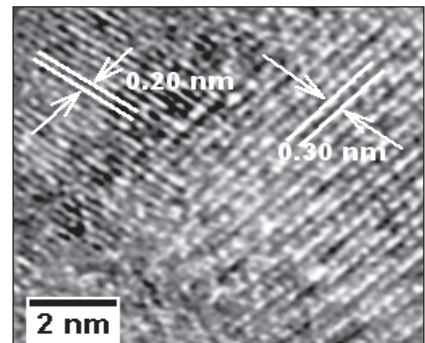


**Fig. 3** Lattice fringe from the dispersoid-matrix interface where 0.20nm spacing correspond to (110) of Fe and 0.30nm spacing is from (222) of Y<sub>2</sub>O<sub>3</sub>

figure shown in the inset of this figure are indicative of absence of texture in this material. Such randomly oriented ferrite grains is considered to be a positive attribute since anisotropy in properties is undesirable from application point of view. The clad tubes are developed in close collaboration with ARCI and NFC, Hyderabad.

The creep rupture strength of the developed 9Cr-ODS clad tube at 973 K is shown in Figure 5. The developed steel has creep rupture strength much superior than the modified 9Cr-1Mo although less than that of the austenitic alloy D9. Efforts have been initiated to increase creep rupture strength of 9Cr-ODS by

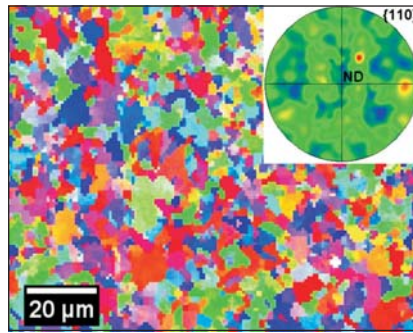


**Fig. 4** EBSD orientation map of a section of ODS tube showing random orientation of grains, confirmed by the corresponding  $\{110\}$  pole figure shown in its inset

increasing the  $Y_2O_3$  content and by refining the particles. Creep tests on 9Cr-ODS clad tube having 0.34 wt.%  $Y_2O_3$  is in progress. Initial results shows that the relatively long-term creep rupture strength of

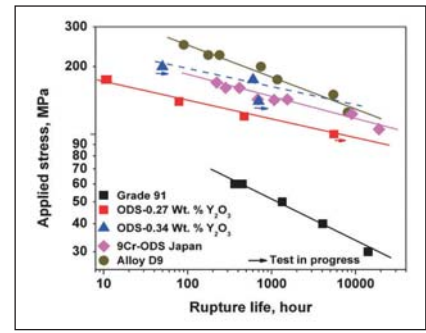


**Fig. 5** Comparison of creep rupture lives of developed 9Cr-ODS clad tubes with alloy D9 clad tube and modified 9Cr-1Mo steel at 973 K

the ODS steel is expected to be as good as alloy D9. Thus, this material is very promising as a clad material to increase the fuel burn-up to around 200 GWd/t.

### III.31 The Evaluation of Tribological Properties of Nuclear Grade Steel P91

**T**ribo-fatigue wear is attributed to generation of micro- events in a thin surface layer, resulting in destruction of tribo- layers where as fretting and delamination gives rise to catastrophic failure. In a tribo- system, frictional energy is dissipated through the tribo-surfaces. Some of this energy gets dissipated into a thin superficial layer, resulting in plastic deformation, phase transformation, diffusion, material losses by tribo-fatigue, and strain gradients from the surface. As a result the topography, microstructure and physical properties change continuously during tribo- sliding, until, at steady state, a surface layer is developed.

Modified 9Cr-1Mo steel (P91) used in steam generator of fast breeder reactors encountering contact with NiAl based alloy coating undergoes

flow induced vibration which leads to deformation induced material damage. The contacting materials can experience microscale sliding between each other which can also cause the fatigue induced wear.

To gain insight into micro- scale wear phenomena, tribological properties of P91 steel sliding with a 100Cr6 steel ball was investigated at 2N load and 1 cm/s sliding speed in ambient condition.

The results of the tribological tests are shown in Figure 1. These tests were interrupted at various sliding distances to observe the wear mechanism and extent of deformation that occurred in wear scars. Initially at 0.3 m of sliding distance the value of coefficient of friction increases monotonically to 0.6 prior to sharp decrease to 0.51. After

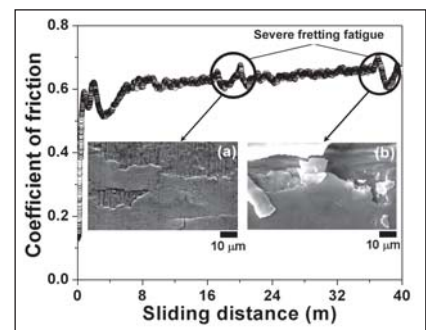


**Fig. 1** Coefficient of friction of P91 steel as a function of sliding distance

covering 2 meter of distance the value of coefficient of friction increases to 0.64 and reduces to a lower value of 0.53 at the end of sliding distance. After interruption at sliding distance of 4.5 meter, the same trend was observed as in 2 meter of sliding distance. Sharp increase in coefficient of friction (0.75) at sliding distance of 0.05 m followed by a rapid decrease to 0.51 at a

sliding distance of 0.1 meter was obtained. After 20 meter of sliding distance, the average value of coefficient of friction was found to be 0.65. Despite the use of similar material and loading conditions, distinctly different values of coefficient of friction manifest with variation in sliding distance. Severe fretting fatigue of surface morphologies of wear tracks are shown in Figure 1. These images were extracted at sliding distance of 20.13 m and 37.57 m as seen in (a) and (b), respectively, where coefficient of friction were found to be unstable. Raman peaks were found at 214  $\text{cm}^{-1}$  and 280  $\text{cm}^{-1}$  with weak evolution of 402  $\text{cm}^{-1}$  and 486  $\text{cm}^{-1}$  in the wear scans as shown in Figure 2a and 2b. These correspond to formation of  $\alpha\text{-Fe}_2\text{O}_3$  (hematite) phase. These peaks broaden and their intensity decline with increase in sliding distance.

Peaks also slightly shifted to higher wave number 221  $\text{cm}^{-1}$  and 293  $\text{cm}^{-1}$  as shown in Figures 2c and 2d. The broad peak at 671  $\text{cm}^{-1}$  was found for (Figures 2b to 2d) tracks, although it depicts comparatively lower intensity. This peak corresponds to formation of  $\text{Fe}_3\text{O}_4$  (magnetite) phase. The broad peaks around 393  $\text{cm}^{-1}$  in Figure 2a, 399  $\text{cm}^{-1}$  in Figure 2b, 408  $\text{cm}^{-1}$  in Figure 2c and 406  $\text{cm}^{-1}$  in Figure 2d were observed which also represent formation of  $\text{Fe}_2\text{O}_3$  phase. For higher sliding distance, these peaks shift to higher wave numbers. At the surface of the material, the  $\text{Fe}_2\text{O}_3$  peak is found to be very weak. It was found that the change in friction was caused by formation and tearing of oxide layer on the sliding surface. The deformation, spallation and phase formation of oxide layer composed of  $\text{Fe}_2\text{O}_3$  and  $\text{Fe}_3\text{O}_4$

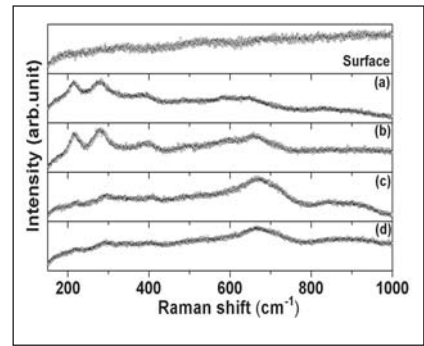


**Fig. 2** Raman shift of wear scars at sliding distance (a) 0.3 m (b) 2 m (c) 4.5 m and (d) 40 m

influences friction properties of steel. The adhesive failure of the surface oxide layer was the principal wear mechanism at shorter sliding distances. But at higher sliding distances, fretting failure of oxide layer dominated. The oxide layer  $\text{Fe}_3\text{O}_4$  was dominant for longer sliding distances. This renders it difficult to break down. Hence, a stabilized value of coefficient of friction manifests.

### III.32 Pilot Plant Study on Sodium Cleaning for Prototype Fast Breeder Reactor Reusable Components

During the operation of sodium cooled fast reactors, a thin layer of sodium gets adhered onto the surface of steel components, which are in prolonged physical contact with liquid sodium at elevated temperatures. Some of these components need to be taken out for periodic maintenance or replacement. Careful handling and safe cleaning procedures need to be adopted to avoid any possible violent reaction with moisture and oxygen present in ambient air. This could lead to damage to material and the operating personnel. In addition, the radiation dose due to the deposited sodium in the case

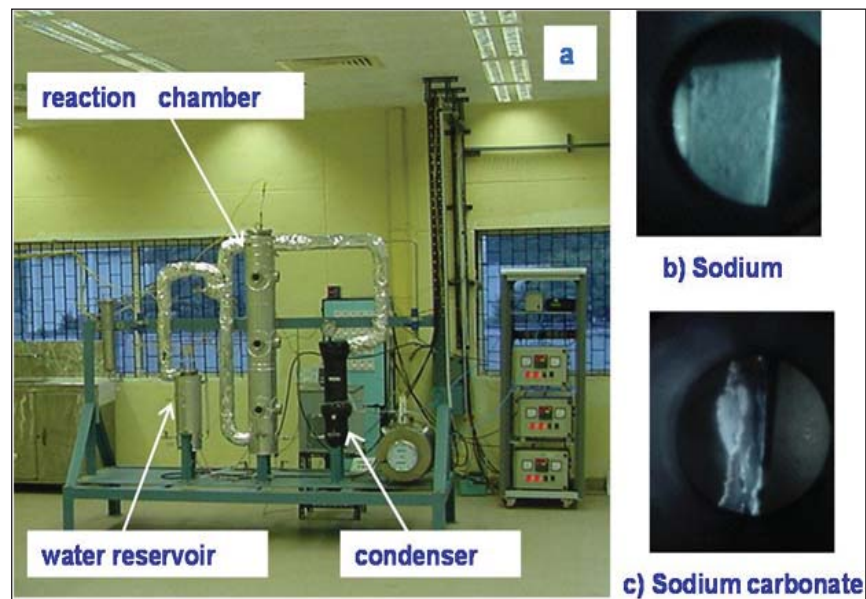


**Fig. 1** Photograph of (a) Pilot plant facility for sodium cleaning (b) Sodium (c) Carbonates of sodium

of primary components need to be addressed. Generally, water vapour-nitrogen (WVN) process is being employed for sodium cleaning of large components. In this method, any incomplete washing leaves residual sodium hydroxide on the component surface which can cause caustic stress corrosion cracking and inter-granular attack on the sensitized surfaces. To overcome this, water vapour-CO<sub>2</sub> (WV-CO<sub>2</sub>) process has been planned for cleaning sodium from the reusable large components of PFBR. Unlike WVN process, the product formed in WV-CO<sub>2</sub> process is a mixture of sodium carbonate and sodium bi-carbonate. As these carbonates are less alkaline they do not cause corrosion problems to the structural material. A pilot plant was constructed to study the above process and experiments have been carried out to optimize the process parameters such as gas flow rate, temperature and humidity.

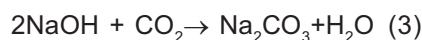
### Features of pilot plant

The photograph of pilot plant is shown in Figure 1a. The plant consists of three main components namely water reservoir, reaction chamber and condenser vessel. The unique features of this plant are i) a CO<sub>2</sub> re-circulating system in the reaction chamber for effective and economical use of the gas, ii) sensors to monitor and control moisture and CO<sub>2</sub> levels in the reaction chamber, iii) sensor for monitoring the hydrogen gas evolved during cleaning process at the outlet of pilot plant to prevent any untoward increase of hydrogen concentration beyond the lower explosive limit in air, iv) wet test meter for measuring gas flow rate and total volume of gas passed at the exit of reaction chamber, v) pressure relief systems at reaction

chamber and water reservoir to vent the gas in the event of accidental increase in pressure. The reaction chamber has a provision for filling up with water to wash the components after converting sodium to sodium compounds. Heaters are provided for drying the components after cleaning and washing as well as to avoid any condensation of water vapour during the sodium cleaning process. Three sets of viewing ports are available on the cleaning chamber for physical examination of components during the cleaning process.

### Theoretical background

In WV-CO<sub>2</sub> process, the sodium reacts with water vapour instantaneously forming sodium hydroxide as shown in reaction 1. The sodium hydroxide thus formed, reacts with carbon dioxide forming a mixture of sodium bicarbonate and sodium carbonate as shown in the following reactions 2 and 3.



### Cleaning process

Sodium wetted stainless steel specimens were cleaned by WV-CO<sub>2</sub> process in the pilot plant. This was carried out by bubbling CO<sub>2</sub> gas through the water reservoir at 343 K and allowing the water vapour to react with sodium in the reaction chamber. Cessation of hydrogen gas generation during cleaning process indicates the completion of sodium-water reaction. During the cleaning process, the sodium gets converted to carbonates of sodium without leaving behind any residual sodium hydroxide. The typical thickness of reaction product formed is about 15-20 mm for a

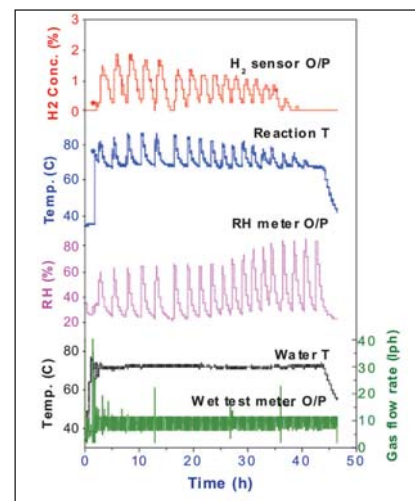


Fig. 2 Monitoring of process parameters as a function of time during sodium cleaning

initial sodium thickness of 2 mm. Photographs of sodium sample before and after the reaction are shown in Figure 1 b and 1c. It is seen that the carbonate layer is highly porous in nature which helps the water vapour to reach the underlying sodium and react further for complete removal of sodium.

After completion of reaction, the reaction chamber was filled with water to dissolve the carbonates of sodium adhering onto the surface of the specimen. The specimen was dried by maintaining the reaction chamber at 423 K for 8 hours under vacuum to take up further microstructural examination.

Figure 2 shows typical parameters such as temperature of water reservoir and sodium wetted specimen, relative humidity in reaction chamber, gas flow rate and hydrogen concentration at the exit monitored and recorded as a function of time. From Figure 2, the following inferences are made. The peaks of temperature and hydrogen level are due to the repeated introduction of moisture into reaction chamber till complete conversion of sodium to its carbonates. The concentration of hydrogen formed during the reaction and the resultant

temperature rise are controlled well within the safety limits by regulating the moisture level in the reaction chamber. The volume of hydrogen gas evolved as a function of time during sodium cleaning process is shown in Figure 3.

The completion of washing of the specimen was ensured by testing the effluent solution using pH indicator.

Volumetric analysis of the effluent showed that the product formed during cleaning process contains more of sodium bicarbonate thus indicating that the reaction 2 is more favourable under the cleaning procedure employed. The sodium content estimated from the effluent by Atomic Emission Spectroscopy (AES) and that from stoichiometric calculation based on reaction 1 are in good agreement. Typical values obtained are summarized in Table 1.

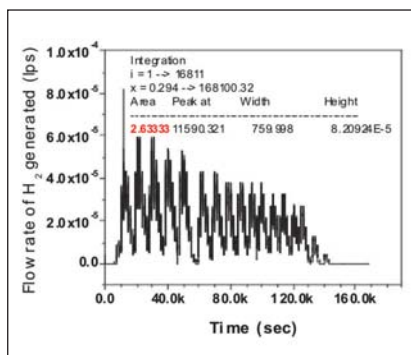


Fig. 3 Flow rate of hydrogen generated

The sodium cleaning experiments carried out in the pilot plant showed that the cleaning process can be carried out in a controlled manner by manipulating the introduction of moisture into the reaction chamber. The chemical analysis of the reaction product showed that the conversion of sodium hydroxide to a mixture of sodium bicarbonate and sodium carbonate was complete. This shows that the WV-CO<sub>2</sub> process can eliminate the possible caustic corrosion that would occur in presence of residual

Table 1: Quantity of sodium estimated		
Weighing (g)	Effluent (AES) (g)	H <sub>2</sub> sensor O/P (g)
4.4	4.4	4.3
4.6	4.6	4.9
4.6	4.8	5.2

sodium hydroxide as in the case of WVN process. Monitoring hydrogen sensor output gives information on reaction progress, completion as well as quantity of sodium adhered on the component. The in-house developed proton exchange membrane based hydrogen sensor is well suited for this purpose. The WV-CO<sub>2</sub> process is well suited for safe and effective cleaning of large reusable components taken out from sodium circuits of fast reactors.

### III.33 Application of PEM based Hydrogen Sensor during Fast Reactor Component Cleaning and Studies on Hydrogen Removal using PEM based Electrochemical Burner

#### Application of proton exchange membrane based hydrogen sensor (PEMHS) during fast reactor component cleaning

Sodium gets adhered to the reactor components during their life in the fast reactor and is required to be removed before commencement of maintenance activities.

Water vapour-carbon dioxide process is the method adopted for sodium removal from reusable components. In this method, sodium

reacts with water vapour carried by gaseous carbon dioxide. Hydrogen is produced during the cleaning process. Since hydrogen forms an explosive mixture with air beyond concentration limit of 4%, monitoring it in the gas mixture during cleaning is required before being let out to the atmosphere. Monitoring hydrogen also gives an estimate on the progress of the cleaning process.

The total amount of sodium removed during the cleaning process can be estimated from the amount of

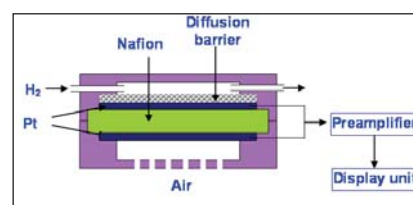


Fig. 1 Schematic of the hydrogen sensor

hydrogen released and from knowledge of the stoichiometry of the reaction between moistened carbon dioxide and sodium.

A fuel cell based amperometric hydrogen sensor (PEMHS), H<sub>2</sub>/Pt//nafion//Pt/O<sub>2</sub>, has been developed

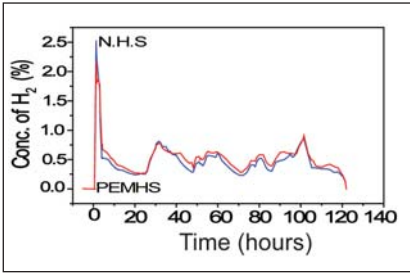


Fig. 2 Hydrogen monitoring during sodium cleaning of under sodium ultra sonic scanner

and tested for the purpose. The sensor operates in fuel cell mode and uses nafion as proton conducting electrolyte. Platinum is used as electrodes and a mechanical barrier limits the supply of hydrogen at the sensing electrode. A schematic of the sensor is shown in Figure 1. Platinum is deposited on nafion by decal method which involves a transfer printing procedure. The counter electrode is exposed to air and the sensor functions as a self breathing device. The hydrogen sensor operates in amperometric mode and the limiting current is linearly dependent on the concentration of hydrogen at the sensing side. The sensor is compact and is provided with a display unit developed indigenously that directly displays the hydrogen concentration. Being an indigenously developed device, it is possible to make the sensor with required dynamic range and sensitivity so as to be suitable for the application.

The sensor was tested for performance in a simulated sodium cleaning experiment in the laboratory and later made use of for hydrogen monitoring

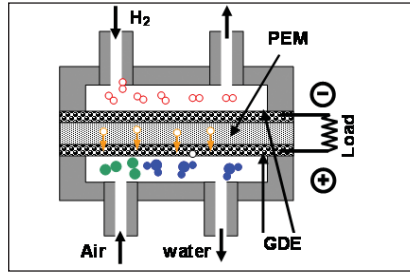


Fig. 3 Schematic of fuel cell

during sodium removal from reactor components subjected to in-sodium testing.

Under sodium ultra sonic scanner (USUSS) is one of the important components of PFBR that has to be tested and qualified in sodium. After in sodium functionality test, sodium sticking to the surface of the component had to be removed. PEM based H<sub>2</sub> sensor (PEMHS) was made use of for monitoring hydrogen released during sodium cleaning along with a commercially available sensor.

Figure 2 shows the responses of PEM sensor and a commercial sensor during sodium removal by H<sub>2</sub>O/CO<sub>2</sub> process. Both sensors responded similarly confirming the reliability of the PEM sensor. The sensor clearly indicated the variation in hydrogen concentration during increase and decrease of relative humidity of the CO<sub>2</sub>/H<sub>2</sub>O mixture. Thus the suitability of the sensor for field applications and specifically for sodium cleaning was demonstrated.

**Studies on hydrogen removal using proton exchange**

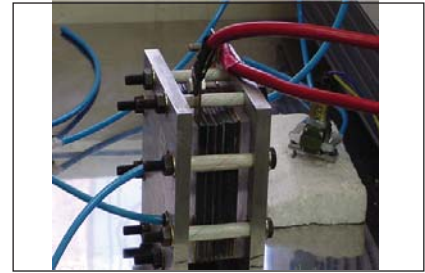


Fig. 4 Fuel cell stack with four cells

**membrane based electrochemical burner**

Hydrogen released during sodium cleaning can be safely removed by electrochemical oxidation using electrochemical burner. It is an electrochemical device that can be used for safe removal of H<sub>2</sub> even in inert medium, a modified fuel cell. Schematic of the fuel cell used as burner is shown in Figure 3. H<sub>2</sub> containing gas stream is sent at the anode side of the fuel cell. H<sub>2</sub>O is produced at cathode side by electrochemical reaction of hydrogen in gas stream and oxygen from air. Unlike a catalyst re-combiner, mixing of O<sub>2</sub> & H<sub>2</sub> is not required.

Studies were carried out using modified fuel cells made in-house and also using commercially available fuel cell stacks. Figure 4 is a photograph of proton exchange membrane based mini fuel cell stack that was made in-house. The membrane electrode assembly in the fuel cell was made using nafion 115 as proton conducting electrolyte. Diffusion electrodes consisting of carbon cloth containing platinum electro-catalysts was pressure

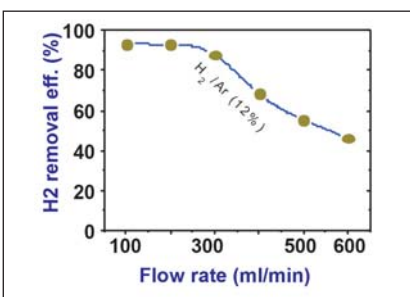


Fig. 5 Hydrogen removal using single fuel cell stack

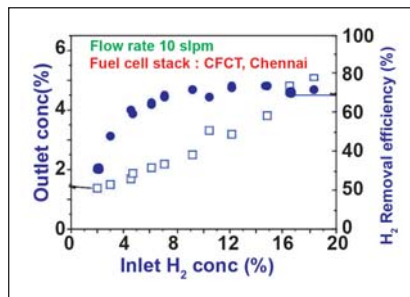


Fig. 6 Efficiency of electro chemical burner for hydrogen removal

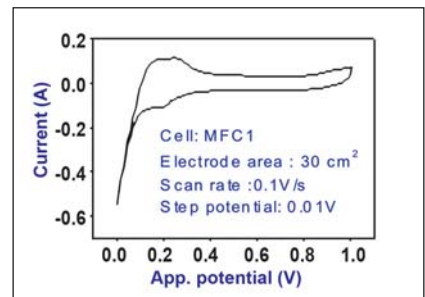


Fig. 7 Cyclic voltammogram of single fuel cell

bonded on either sides of the nafion membrane. The membrane electrode assembly consisting of nafion sandwiched between the diffusion electrodes was placed between two bipolar plates. Studies were conducted for hydrogen removal using single PEM fuel cell for understanding the hydrogen removal efficiency as a function of flow rate, platinum loading etc. Figure 5 shows the variation of

hydrogen removal efficiency as a function of flow rate for a gas mixture of  $H_2/Ar$ . Figure 6 shows the variation of hydrogen removal efficiency as a function of hydrogen concentration for a mini fuel cell stack. Electrochemical active area (ECA) is the area available at the interface for electrochemical reaction. High electrochemical active area facilitates higher reaction rate. Electrochemical active area of

membrane electrode assembly was measured by cyclic voltammetry as shown in Figure 7 and was found to be in required range. The hydrogen chemisorption surface area (CSA) is a parameter that determines the performance of the electrocatalyst that was used for making membrane electrode assembly. The CSA was determined using Temperature Programmed Desorption Reduction and Oxidation (TPDRO) equipment.

### III.34 Studies on the Oxidation and Ignition of Electrodeposited Boron

High-density boron carbide pellets containing boron enriched in  $^{10}B$  (65 at %) will be used in the control rods of the Indian prototype fast breeder reactor (PFBR). These high density boron carbide pellets are prepared by reacting elemental boron (produced through molten salt electrolysis method) with graphite.

Boron undergoes oxidation to form boric oxide a thermodynamically stable compound by the following reaction:  $4B + 3O_2 \rightarrow 2B_2O_3$ . Information on the mechanism and kinetics of oxidation of elemental boron is required for establishing a procedure for the safe handling of elemental boron in air. It is also essential to identify those conditions which favour ignition of boron powder and a study was undertaken using thermogravimetric and differential thermal analyzer to obtain the test results.

It was observed that ignition temperature ( $T_{ig}$ ) was affected by partial pressure of oxygen, particle size of the boron powder and heating

rate. Boron powder with a mean particle size of about  $10 \mu m$  was found to be susceptible to ignition in oxygen even at 783 K. In general, the susceptibility to ignition was found to vary inversely with the degree of crystallinity. Presence of carbon was found to retard the oxidation of boron and raise the ignition temperature. Powder with finer particles provides greater surface area and is thus more reactive. Boron powder of lower size fraction reacts faster and gets ignited at a relatively lower temperature. The

study indicated that boron powder with particle size less than  $32 \mu m$  could be handled safely without the risk of ignition up to 783 K in air. These observations confirm that the oxidation of the boron powder at room temperature is a kinetically hindered process.

The oxidation kinetics (both isothermal and non isothermal) was studied by heating boron powder in a stream of oxygen. Mechanistic interpretation of the oxidation reaction was done using model fit

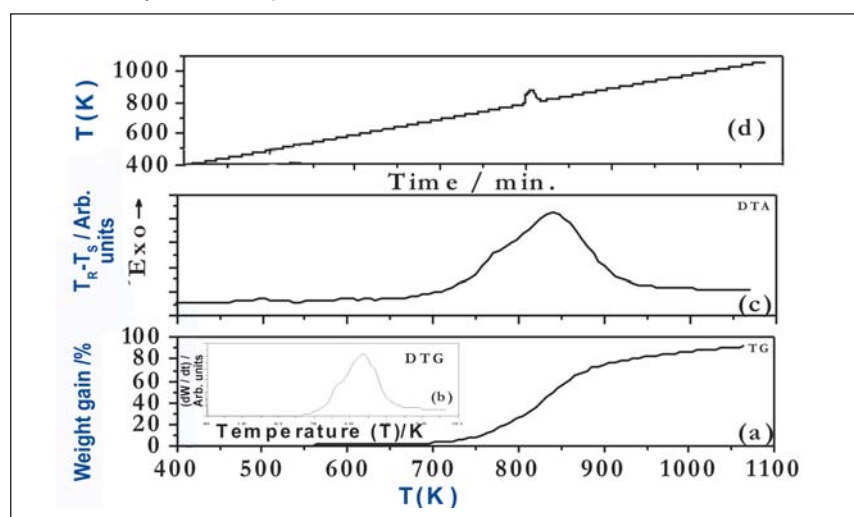
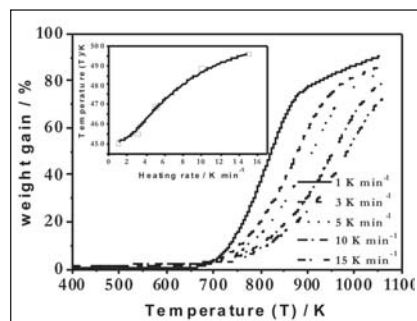


Fig. 1 Thermal analysis curves for the oxidation of electrodeposited boron powder (a) Thermogravimetry (b) Derivative thermogravimetry (c) DTA (d) Temperature vs time

method. Model free isoconversional method was used to derive the kinetic parameters. Typical thermal analysis curves [thermogravimetry (TG), derivative thermogravimetry (DTG), differential thermal analysis (DTA)] and sample temperature vs. time curve for the oxidation of electrodeposited boron powder are shown in Figure 1. The sample was heated from 393 to 1073 K in the flowing stream of oxygen gas at a heating rate of 5 K min<sup>-1</sup>. The TGA curve shown in Figure 1a clearly indicates that there was no measurable weight gain up to 700 K, beyond which a sudden increase in weight due to oxidation of boron powder is observed. The weight gain due to oxidation process continued to increase rapidly till temperature reaches 900 K. At temperatures above 900 K, the oxidation was found to be very sluggish due to slow rate of increase in weight with temperature. From the TGA curve, it is also clear that the observed weight gain is only ~80-90 % and the theoretical weight gain (111% per mol of boron, weight gain calculated from the balanced chemical reaction  $4B + 3O_2 = 2B_2O_3$ ) was not achieved in the temperature range of the present study. Though the thermogravimetry curve (Figure 1a) shows a single plateau which is indicative of single step oxidation reaction yet derivative thermogravimetry curve (Figure 1b, shown as inset) shows that the oxidation reaction is not a single step process but a two step process. The rate of oxidation is slow till 730 K and later rapid oxidation of the boron is observed which involves ignition reaction also. The exothermic peak (Figure 1c) obtained in the DTA curve and the sample temperature vs. time curve (Figure (1d)) shows the exothermic nature of the process.



**Fig. 2** Weight gain as a function of temperature at various heating rates. Inset: Onset temperature as function of heating rate

With the help of coupled evolved gas analysis (EGA) technique, it was confirmed that there was no loss in weight due to vaporization of  $B_2O_3$  (molecular weight ~ 69.6 g) formed during the oxidation of boron under experimental conditions. As theoretical weight gain was not achieved in the present study, for the convenience of calculation, the weight obtained after the completion of the thermogravimetry experiment was taken as the final weight gain ' $w_T$ ' for the oxidation reaction and the fraction of the boron oxidized ' $\alpha$ ', was evaluated by the relation

$$\alpha = \frac{w_T - w_i}{w_T - w_i}$$

where  $w_i$ ,  $w_T$  and  $w_t$  weights correspond to initial, final and intermediate weight respectively.

The variation of percentage gain in weight with temperature of oxidation of electrodeposited boron powder at various heating rates is shown in Figure 2. The curve for electrodeposited boron indicates that the observed weight gain is dependent on the rate of heating. A weight gain of ~ 90 % was observed when boron powder was heated at a rate of 1 K min<sup>-1</sup> while ~ 72 % weight gain was observed when sample was heated at 15 K min<sup>-1</sup>. Theoretical weight gain was not achieved in the temperature range and heating rate employed in the present study. This indicates that

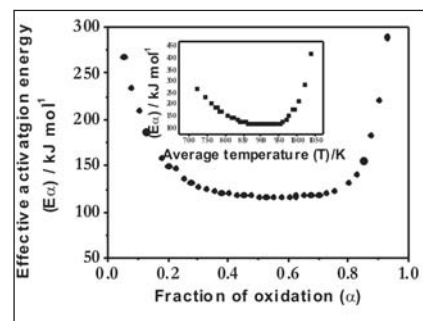


**Fig. 3** A plot of  $E_\alpha$  as a function of  $\alpha$  for electrodeposited boron powder. A plot of  $E_\alpha$  as a function of average temperature is shown as an inset

the reaction products formed during the oxidation reaction had a retarding effect on the progress of the oxidation reaction. The percentage weight gain is higher for lower heating rate and vice versa. This is due to better equilibration of the sample with temperature at lower heating rates. The variation of onset temperature of oxidation reaction with heating rate is shown as an inset in Figure 2. This shows that onset temperature of oxidation reaction increases with increase in heating rate.

The effect of temperature (due to change in heating rate) on the activation energy can be obtained by model free isoconversional methods like Kissinger-Akahir-Sunose (KAS) which takes the form:

$$\ln \frac{\beta_i}{T_{\alpha,i}^2} = \text{const} - \frac{E_\alpha}{RT_{\alpha,i}}$$

where the subscript 'i' denotes the various heating rates. The slope of the plot  $\ln \frac{\beta_i}{T_{\alpha,i}^2}$  vs  $1/T_{\alpha,i}$  gives the value of the effective activation energy  $E_\alpha$ . The plot of  $E_\alpha$  as a function of  $\alpha$  is shown in Figure 3. The variation of effective activation energy,  $E_\alpha$  with  $\alpha$  can be divided into three regions. For the first region  $\alpha = 0$  to 0.2, the  $E_\alpha$  decreases with  $\alpha$ . For the second region  $\alpha = 0.2$  to 0.8,  $E_\alpha$  remains constant and for the third region  $\alpha = 0.8$  to 1  $E_\alpha$  increases with  $\alpha$ . The change of  $E_\alpha$  with average temperature is shown as an inset in

Figure 3. The decrease in the value of  $E_a$  with temperature (up to  $\alpha = 0.2$ ) indicates that the oxidation rate increases with increasing temperature. The oxidation process of electrodeposited boron consists of formation of  $B_2O_3$  nuclei, growth of nuclei and diffusion of oxygen through the  $B_2O_3$  layer. During the initial stage of oxidation, the process is dominated by both nucleation and growth of  $B_2O_3$  phase (formation of  $B_2O_3$ ). Hence the activation energy decreases with the fraction. and growth of  $B_2O_3$  phase (formation of  $B_2O_3$ ). Hence the activation energy decreases with the fraction oxidized

as well as with temperature. For  $\alpha = 0.2$  to 0.8, the activation energy remains almost constant indicating that competing processes such as nucleation, growth, sintering, contracting area and volume which may have different activation energy and the effective activation energy does not change with temperature and  $\alpha$ . The complex nature of the mechanism of oxidation can be sorted out only by model fit approach. Beyond this  $\alpha$  value, the activation energy increases with  $\alpha$ , which indicates that there are parallel reaction occurring during oxidation. These parallel reactions could be

diffusion of oxygen through the product layer, sintering along with crystallization of the product. The activation energy,  $E_a$  for the oxidation process ( $\alpha$  range 0.2 to 0.8) was found to be  $122 \pm 7$  KJ mol<sup>-1</sup>.

The oxidation of boron is a complex process which involves several competing mechanisms. Among these, nucleation and growth, contracting area and volume and three dimension diffusion are important. Rapid oxidation of boron starts after 700 K hence electrodeposited boron can be handled safely without the risk of oxidation during production and processing.

### III.35 Computational Intelligence Models for Fast Reactor Systems

Nuclear Power Plant is a very complex system consisting of many subsystems like neutronics, heat transport, steam-water and fuel handling systems. As these sub-systems are interrelated any malfunction in one of the subsystems affects the other. It is feasible to implement intelligent systems in the form of neural network, data mining, expert system etc. for modeling and diagnosis in the real time artificial neural network. Neural network modeling is a data driven technique which is a powerful tool for identification of relevant physical parameters and more advantageous compared to the traditional methods of plant diagnostics. The main objective of our work is to develop neural network models for prediction of reactor system parameters under steady-state and transient conditions and detection of occurrence of any anomalies/events in different reactor

sub-systems. Process modeling and events identification with artificial neural network models have been successfully applied to following fast reactor subsystems.

#### Model for prototype fast breeder reactor neurotic system

A multi-layer feed-forward neural network model with back-propagation learning algorithm has been developed in order to estimate the reactor power based on the control rod positions which are used

to regulate the reactor power. The network model has ten input nodes representing nine control rod positions with a bias. The output layer has one output node representing the neurotic power. Fine tuning of the network to find optimal parameters has been carried out with different trials. The network has been trained comprehensively and the results have been validated and found to be accurate. The output can be obtained faster compared to conventional point kinetics model.

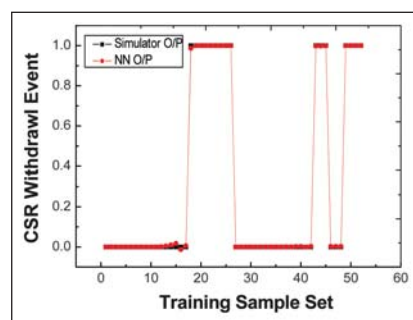


Fig. 1 Training outputs for the model

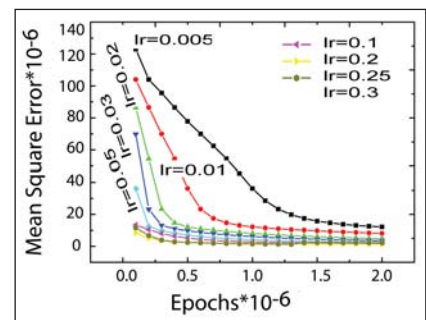


Fig. 2 Fine tuning of ANN model with different learning rates

**Event identification for neutronics system**

Using a 3-layer ANN, the characteristics of neurotic subsystem of PFBR has been modeled to identify the occurrence of uncontrolled withdrawal of control rod event. Taking into consideration the influence on this particular event, the process parameters are properly selected and a range of data is generated for the parameters using the thermal hydraulics safety analysis code and based on event analysis report of PFBR. 53 samples for training and 5 distinct test samples were used for validation. Training outputs are shown in Figure 1. The results obtained from the ANN model during its validation are accurate and satisfactory.

**Modeling intermediate heat exchanger at steady state and transient conditions**

The process modeling of sodium-sodium (Na-Na) intermediate heat exchanger (IHX) of fast breeder test reactor has been done with multilayer perceptions network. The input layer consists of five input nodes (including bias) and they are primary inlet temperature, primary flow, secondary inlet temperature and secondary flow. The output layer consists of two outputs,

primary outlet temperature and secondary outlet temperature. Initially the training data for the model have been generated based on theoretical calculations. Further the IHX steady state (safety critical and safety related) data of FBTR has been taken in real time from central data processing system and the network is modeled for prediction of primary and secondary outlet temperature. The results obtained are accurate and satisfactory in both the above mentioned cases.

Also the IHX model has been enhanced to study its behavior under specific transient conditions. The quadratic upstream interpolation for convective kinetics code (QUICK) data has been taken both in steady state and transient state for modeling the neural network.

The outlet temperatures of heat exchanger during severely unbalanced flow conditions have been evaluated and results show that the ANN model developed is accurate and fast in estimating the outlet temperatures for the given transient conditions. Figure 2 shows the error margin achieved for different learning rates and Figure 3 shows the training outputs for secondary sodium outlet temperature.

**Event identification for primary sodium system**

ANN based computational intelligence model has been developed for primary sodium pump trip event identification in primary sodium system of PFBR. All the relevant parameters including pump speed ( $N_p$ ), central subassembly outlet temperature ( $\theta_{CSA}$ ) and central subassembly temperature rise ( $\Delta\theta_{CSA}$ ), which cause the occurrence of the event, have been taken as input for the neural network model and its output indicates the occurrence or non-occurrence of the particular event to be identified. The neural network is trained with the data from simulator and safety analysis report and after extensive training the model can promptly detect the occurrence of the pump trip event during the operation. Figure 4 shows the actual outputs obtained along with desired values after training.

Our future work involves expanding the scope of the existing models to identify various events associated with different sub-systems of fast reactors in an integrated way and also apply different ANN algorithms in modeling and event identification for comparison study.

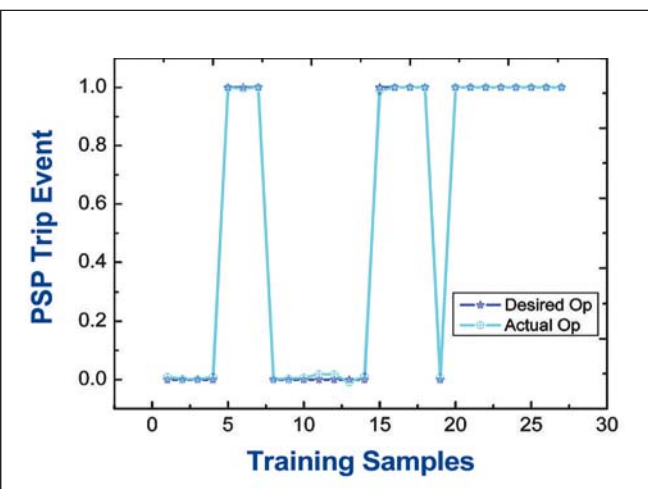
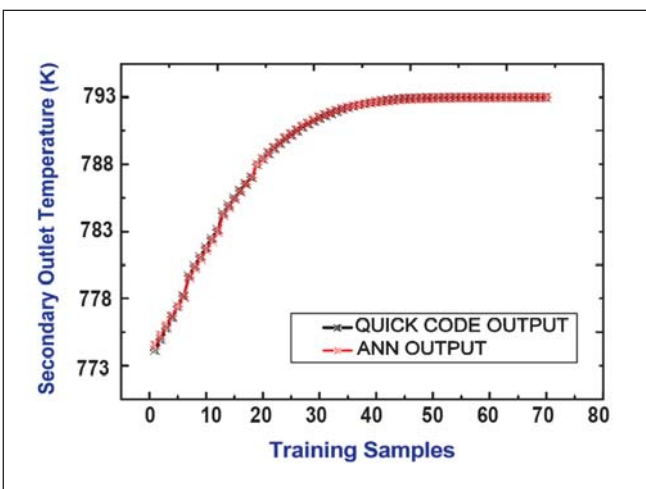


Fig. 3 Regression analysis of secondary Na outlet temperatures (Training)

Fig. 4 Training outputs with the desired o/p

### III.36 Experimental Studies on Sodium Jet Fires based on Small Scale Simulation Tests

Experimental studies on sodium jet fires based on small scale simulation tests are being carried out. Small sodium combustion set up consisting of a small sodium vessel where few gram of sodium is melted and quartz glass chamber where sodium is burnt is fabricated and installed to conduct experiments. Figure 1 shows the schematic of the set up. Experiments are planned to understand science of

- \* Sodium jet fire combustion
- \* Particle distribution during jet fire
- \* Effect of sodium temperature, oxygen, moisture and inert gas on percentage of sodium combustion.
- \* Effect of sodium jet fire on cable insulation

\* Study of fire extinguisher on sodium jet fire etc.

Experiments are conducted with loading few grams of sodium in the vessel and heating it to the desired temperature. The system is pressurized to desired pressure using argon and then the molten sodium is ejected to the combustion chamber. Combustion is done in glass chamber with facilities of burning sodium. High speed visualisation is carried out using optical and IR cameras to understand combustion phenomena. Figures 2a and 2b indicates image taken by optical camera and IR camera during sodium jet fire experiment.

Analysis using NACOM code was carried out for the combustion of 10 gram sodium in closed glass chamber of the set up to evaluate maximum gas temperature and pressure. Temperature & pressure plots obtained during experiment is shown in Figure 3 and particle size distribution obtained is shown in Figure 4. It is observed that the measured temperature and pressure are less compared to analysis. Some of the salient results obtained during initial

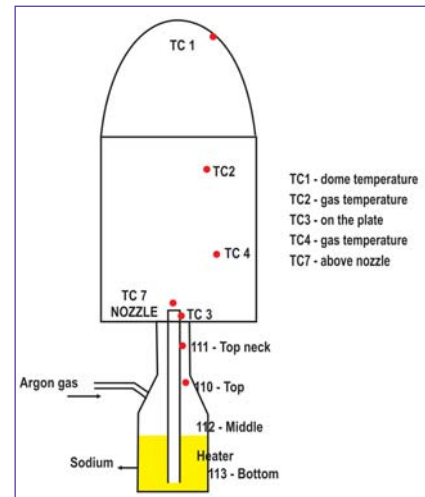


Fig. 1 Schematic of the small sodium combustion set up

few tests are as follows. It is observed that burning is effective with smaller particles. Impingement of jets on the solid objects such as pipes breaks the sodium jet into finer particles, which in turn enhances the effective burning. Temperature rise in the ambient is delayed and highly attenuated. Test with extinguisher powder on spray fire indicated that the kinetics of extinguishment action is much slower than the rate of sodium combustion. All these data are being accumulated by various tests for deriving fundamental understanding of sodium spray fire. In future more tests will be conducted to understand various other aspect of sodium jet fire.

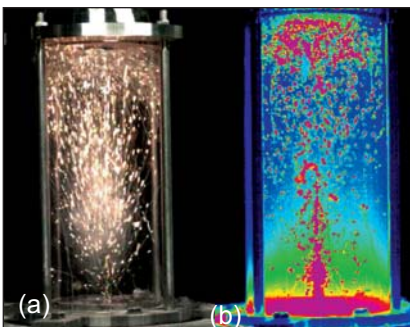


Fig. 2 (a) Sodium spray fire (b) Optical and IR photo of sodium burning

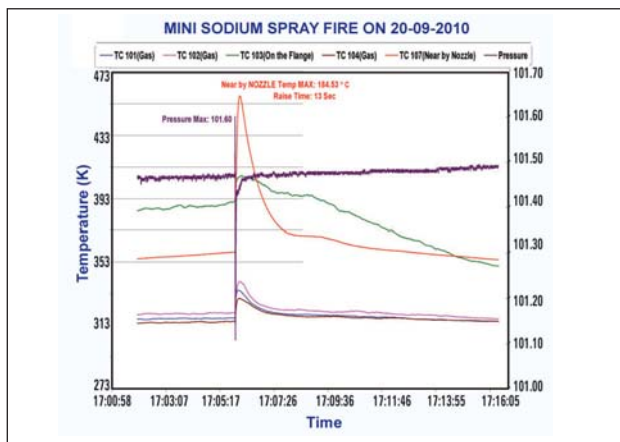


Fig. 3 Temperature record

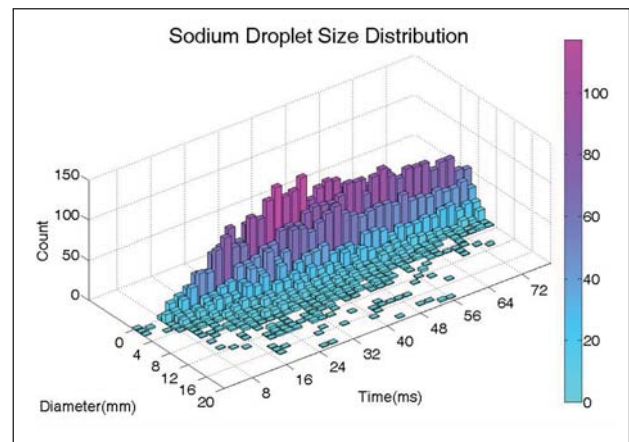


Fig. 4 Particle size distribution

### III.37 Experimental Deployments of Wireless Sensor Networks

Wireless Sensor Networks have been identified as one of the few emerging technologies and are composed of hundreds of tiny sensor nodes, which can sense, compute and communicate in wireless mode. Even though these nodes (Figure 1) can function autonomously, they work together in collaboration.

Since the sensor nodes are functioning in collaboration with each other as a whole network, it provides redundancy, fault tolerance and reliability compared to simple point to point communication.

#### Node developments

The off-the-shelf wireless sensor nodes are not suitable for reactor applications as they have limited scope and are not for industrial environment. Hence, the sensor nodes have been designed and developed in-house. Node development involves the design of hardware boards and the development of protocol stack for the functioning. The required nodes

are of two types namely edge nodes, which will be at the periphery to collect sensor data and cluster heads, which will group the information collected and forwards to the base station. ARM7 architecture based LPC21xx microcontroller + X Bee radio has been used for the low end node design. The cluster head nodes are designed with CORTEX-M3 architecture based LPC17xx microcontroller + AT86RF230 radio. Both nodes operate at 2.4 GHz ISM band and follow the wireless sensor networking standard ZigBee / IEEE 802.15.4.

#### Experimental deployments

Before placing the nodes in the reactor environment, wireless sensor networks have been established in various labs to test and validate the design of the nodes to prove the robustness.

**Temperature monitoring at SADHANA loop:** Safety grade Decay Heat removal loop in NAntrim

(SADHANA) facility, FRTG, IGCAR is a 335 KW sodium test facility to study the safety grade decay heat removal of PFBR. When the loop is in operation, it is necessary to continuously monitor the temperature at chimney outlet (11<sup>th</sup> floor) and chimney inlet (5<sup>th</sup> floor) from the control room (2<sup>nd</sup> floor). The wireless sensor network has been set up in 2.4GHz with the antenna transmission power of 3dbm (Figure 2). The sensors at inlet and outlet have been wirelessly connected to control for continuous data monitoring in the interval of 1 minute. The collected data is being stored in the database for further processing.

**Sodium leak detection at INSOT:** At IN Sodium Test (INSOT) facility, FRTG, two numbers of test sodium loops are established for creep and fatigue testing. Each loop has nearly 140 sodium leak detectors connected to the control room. As an experimental setup, 9 numbers of

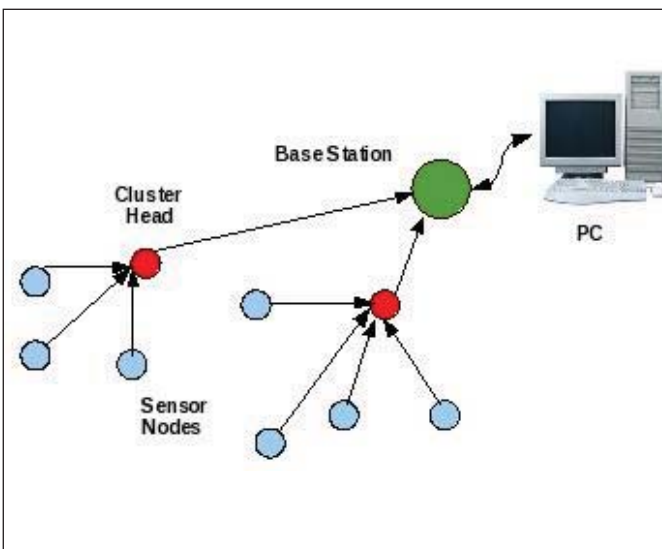


Fig. 1 Typical wireless sensor network



Fig. 2 Wireless sensor network node at SADHANA loop, FRTG



**Fig. 3** Wireless sensor network node at INSOT, FRTG

leak detectors distributed across three floors have been connected to wireless sensor nodes and the data being received at the control for every 5 seconds (Figure 3). The display at the base station in the control room is providing the four conditions namely: Leak, Healthy, Cable Open and Cable Short.

**Experiments at reactor containment building, FBTR**

Towards the implementation of wireless sensor networks at nuclear reactors, a test setup has been done

at FBTR, IGCAR (Figure 4). Initially the feasibility of wireless communication across Reactor Containment Building wall has been tested using different radios (RF230, X-bee, X-bee pro, Wi-Fi Access Points) with different power levels. Based on the observations, wireless sensor network has been established with few numbers of non nuclear safety signals connected to nodes placed inside RCB. The signals were successfully measured in the control room.

**Temperature monitoring of cluster room, CD**

The 128 node cluster at Computer Centre needs constant temperature and humidity monitoring since the heat generated, if not cooled properly may trip the whole system. Hence wireless sensor network has been established using IRIS nodes, which has Amiga 128 microcontroller with RF230 radio (Figure 5). The data received by the base station is made available to the operators.

**Radiation monitoring at radio chemistry laboratory:**

Wireless sensor network was established with 10 numbers of IRIS nodes for gamma radiation monitoring at RCL. To check the strength of radio signal across the shield, the recommended source <sup>137</sup>Cs, source strength of 9.9 µCi, has been kept with WSN nodes inside the mini hot cell with the glass shield of 400 mm and lead brick of 200 mm thickness. The radiation strength was measured and successfully transmitted to outside. The same experiment was repeated for hot cell with 1.5 meter thick concrete and the transmission was also successful.

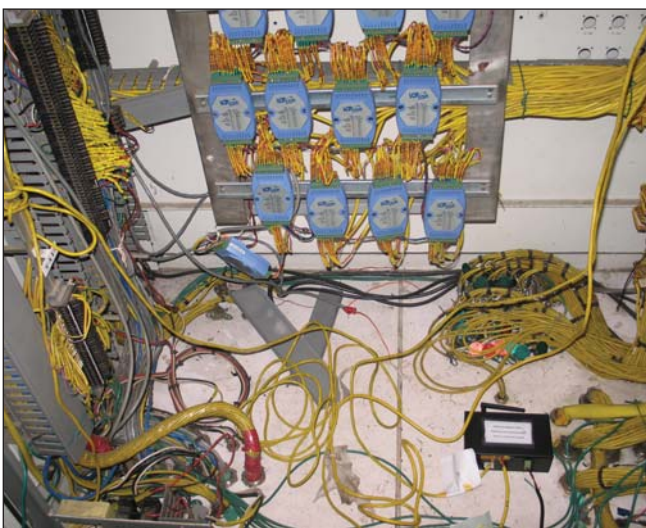


**Fig. 4** Wireless sensor network node at FBTR

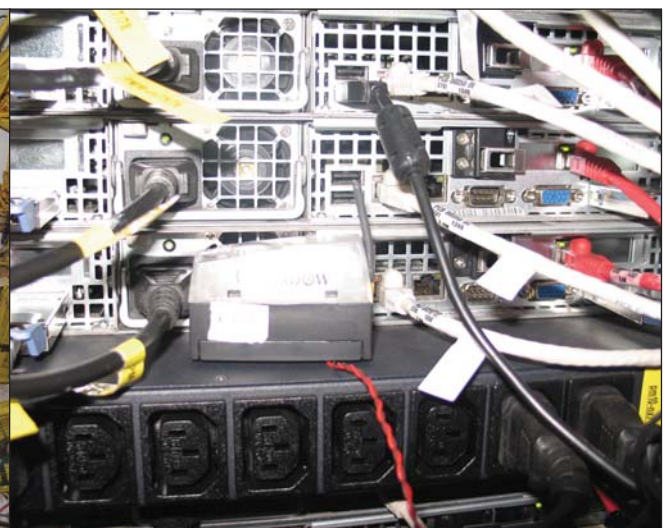


**Fig. 5** Wireless sensor network node at cluster room, computer division



# CHAPTER IV

## Fuel Cycle

## IV.1 Fast Reactor Fuel Cycle Facility

Detailed design of the Fast Reactor Fuel Cycle Facility (FRFCF) to close the fuel cycle of Prototype Fast Breeder Reactor (PFBR) is in progress. The work is being piloted by IGCAR with technical support from Bhabha Atomic Research Centre and Nuclear Fuel Complex. A preparatory project for development of site infrastructure and engineering of FRFCF is nearing completion. Approval of Atomic Energy Regulatory Board for the site of FRFCF has been obtained. Basic infrastructure like approach roads, construction power supply system, workshop, central stores, and construction office space have been created at the site to reduce the lead time required to commence the construction work once the financial sanction for FRFCF Project is available. Review of the preliminary

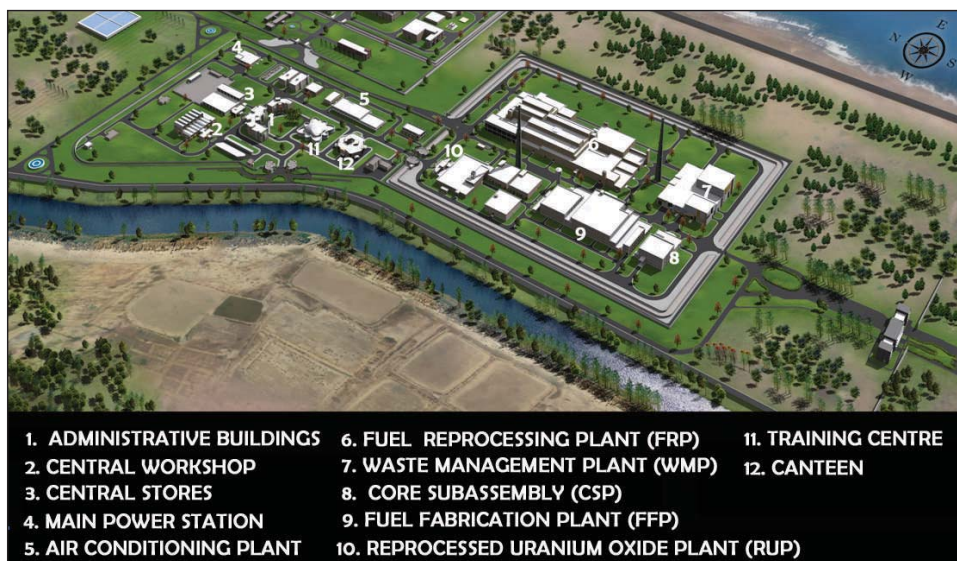


**Fig. 1** Perspective view of the fast reactor fuel cycle facility

safety analysis report by Project Design Safety Committee for FRFCF and specialist working groups is in progress. Detailed Project Report for FRFCF is prepared and the project proposal has been submitted for obtaining financial sanction. Approval of Atomic Energy Commission for the

proposal has been obtained. The proposal is being processed for approval by the Cabinet. Construction work on the project will commence during the year 2011. A perspective view of the fast reactor fuel cycle facility is given in Figure 1.

## IV.2 Single Pin Chopper– Analysis of Cutting Tool using Finite Element Method

Single pin chopper (SPC) is used for the chopping of irradiated fuel pins into small pieces of 25-32 mm length. A typical single pin chopper is being used successfully for several reprocessing campaigns of FBTR spent fuel which has seen a maximum burn-up of 155 GWd/t. The chopper cutting tool (which has been in service for many years) should possess significant fatigue strength and impact toughness to withstand service impact loads for its mechanical design. In order to predict the life of cutting tool, analysis was done using finite

element methods which revealed that the bending stress induced in the tool is very high at shank. The corresponding tool life is about 14000 cycles.

Finite element analysis was carried out to explain the high stresses identified and modifications were made, in order to improve its life. The results revealed that a sudden change in cross section along its depth occurs, where the tool is fixed in the tool holder, leading to the stress concentration, and betrayed characteristics of fatigue. This indicates that bending stresses

present in the cutting tool were localized at the shank portion. In the absence of other defects, these bending stresses would cause one side of the cutting tool to be in tension and the other in compression, which

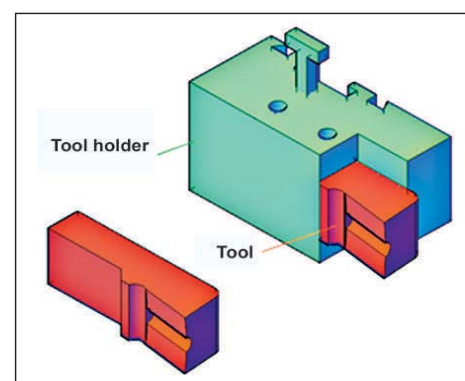


**Fig. 1** Geometric model of modified cutting tool

may lead to fatigue starting on the tension side. The cutting tool geometry (Figure 1) was modified to have better resistance to the bending stresses and improvement in the wear resistance to avoid the blunting of the tool. The modified SPC will be used in the pilot plant - CORAL of DFRP.

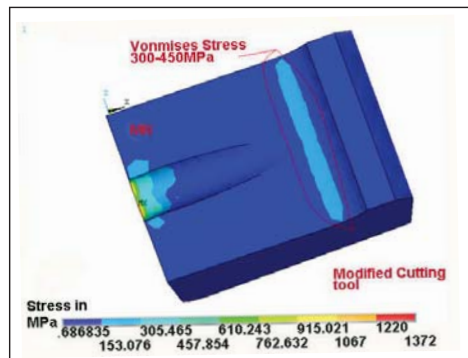


Fig. 2 Von Mises stress distribution for modified chopper cutting tool

Von-Mises stress distribution for modified chopper cutting tool is shown in Figure 2. Figure 3 gives the distribution of bending stress for the cutting tool along its length from cutting edge. Stress concentration areas and discontinuities are

minimized in the modified tool to reduce the localized stresses. Rigidity is increased by providing additional back support. Considering both fatigue as well as wear and tear,

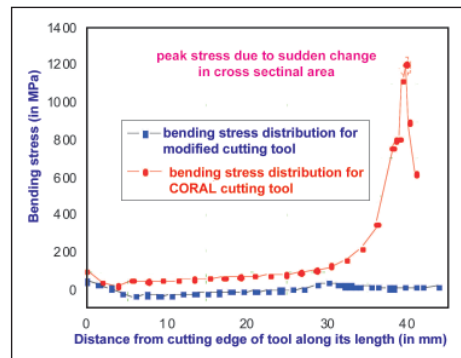


Fig. 3 Bending stress distribution for cutting tool along its length from cutting edge

the tool is predicted to have a life of  $10^5$  cycles which is an order of magnitude higher than the value for compact facility for reprocessing of advanced fuel's (CORAL) cutting tool.

### IV.3 Design of High Capacity Centrifugal Extractors

Large volume annular centrifugal extractors are required in high throughput reprocessing plants as well as in other industries. These centrifugal extractors (CE) are designed in the Reprocessing Group of IGCAR. The typical assembled view of a centrifugal extractor is given in Figure 1. The design of these extractors depends upon the critical speeds. As a rule of thumb, the critical speed should be at least 20% more than the operating speed to ensure safe operations.

The mechanical design of the centrifugal extractor assembly takes

into account wall thickness of rotating bowl, stresses at the junction of shaft and plate, fatigue design of drive shaft for rotating bowl, design of baffles inside the rotating bowl and dynamic model analysis of the rotating bowl. Wall thickness of the rotating bowl was designed based on maximum circumferential stresses and maximum radial stresses developed in a rotating bowl due to its self mass rotation and maximum circumferential stresses developed due to liquid centrifugal forces. The stress intensity induced at the wall thickness of rotating bowl is less than

the allowable membrane stress limit. The rotating bowl of centrifugal extractors was modeled axisymmetrically, meshed with element types Quad-42 (Quadrilateral 4 node) and 3D mass 21 element by using finite element software. In addition to self mass of rotating bowl, mass of baffle plates and processing liquid was lumped at key points of axisymmetric model using 3D mass 21 element.

Finite element analysis was also carried out to evaluate the junction stress between shaft and plate during static and operating

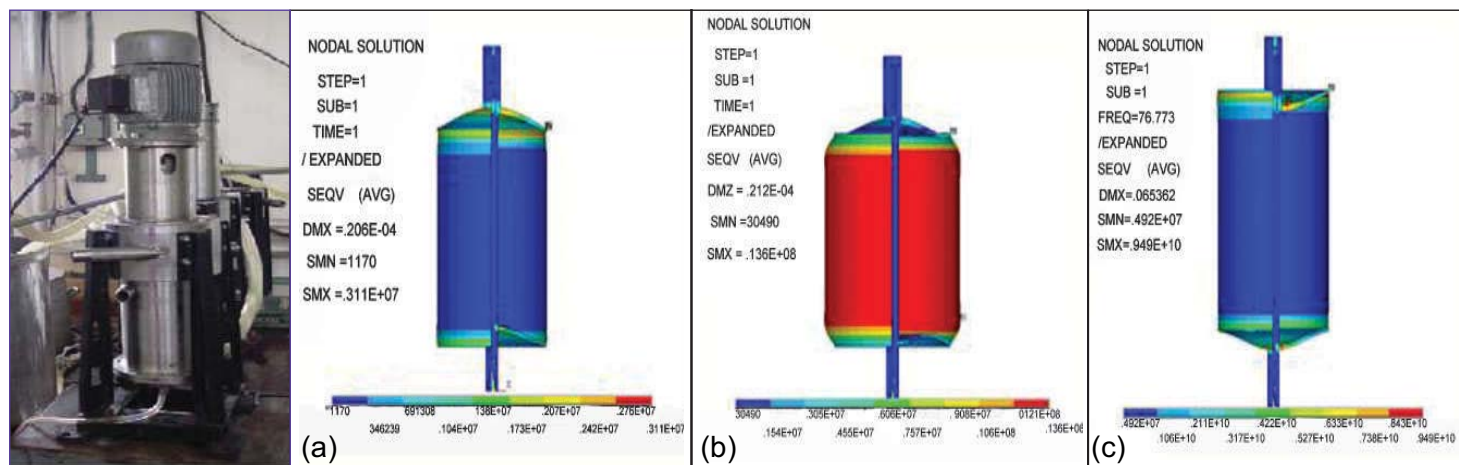


Fig. 1 Assembled view of centrifugal extractors Fig. 2 Junction stress under (a) Static condition (b) Operating condition and (c) 4 mode 1 (longitudinal mode)

conditions. Its stress distribution is shown in Figures 2a and 2b. The fatigue life at the junction between shaft and plate is infinite since the value for half of the difference between maximum Von-Mises stress at the junction during static and operating condition is less than the endurance strength.

The design of drive shaft at the top and bottom sides of rotating bowl was carried out based on the starting torque required. Finally, from the operational point of view, hollow shaft

was taken at the upper side and solid shaft was taken at lower side and inside of the rotating bowl. The fatigue life of both solid and hollow shafts is infinite due to the maximum shear stresses induced during starting and operating conditions. Four numbers of baffles located inside the rotating bowl were designed based on the angular force acting on baffles due to liquor when the bowl starts rotating.

For safe operation of rotating bowls, it is recommended that the operating

speed should not exceed 80% of the first critical speed to avoid lock-in phenomenon. Dynamic model analysis was carried out to find out the natural frequencies at different mode shapes. The first mode is the longitudinal mode which is shown in Figure 2c and its natural frequency was found to be well above its operating speed. Hence, the bowl is operated well below the first critical speed (sub critical speed) to limit the large whirl amplitudes and the rotating bowl is found to be dynamically stable.

## IV.4 Design of a Robotic Sampling System for the Analytical Cell of Demonstration FBR Fuel Reprocessing Plant (DFRP)

Automated sampling and analysis of process solution in FBR fuel reprocessing plants is a step towards complete plant automation. In this direction, prototypes developed for pilot plant (CORAL) have been of a great learning experience. Development of a remote sampling system for DFRP analytical cell, shown in Figure 1, has been taken up. Design of robotic sampling system is completed and manufacture of the system has been taken up. This system was designed with modular features for remote assembly and disassembly.

The DFRP analytical cell has two compartments namely, upper and lower for sampling and analysis of process solutions respectively. The analytical cell is vertically mirrored side by side and the automation covers the whole cell. Sixty sampling

points are provided in the sampling cell to collect samples from various process pipe lines. Twenty sampling points are located within the range of the viewing windows and are accessible to both methyl sulfonyl methane (MSM) as well as sample handling robot (SHR). Remaining sampling points are accessible only to the SHR. Most of the cell volume is occupied by all the sampling lines brought from various process pipelines into the sampling cell which poses one of the prime constraints besides the necessity of remote serviceability of the system in the reigning radioactive environment with nitric acid fumes.

The robotic sampling system consists of modules namely, SHR shown in Figure 2, capping/decapping robot (CDR) and pipette robot (PPR).

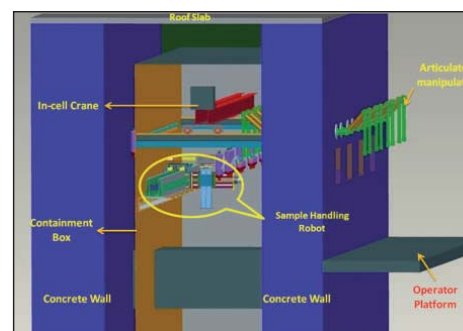
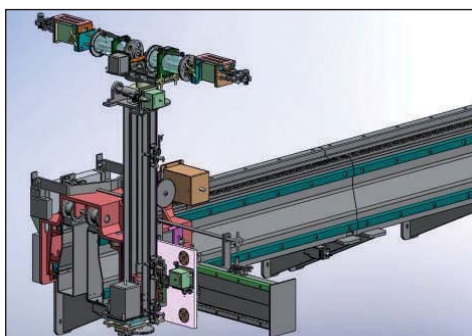
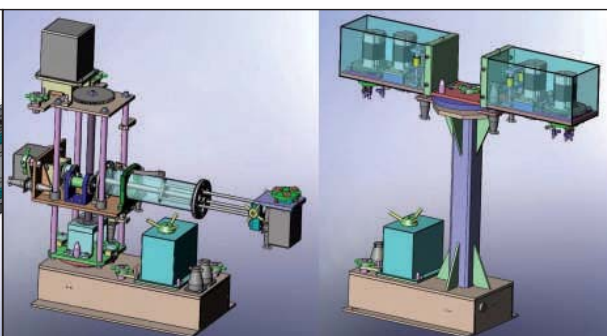


Fig. 1 CAD model of analytical cell

In view of the nature of the work space of the cells, a Cartesian configuration has been chosen for the sample handling robot with X, Y, and Z axes to cover 6000 X 700 X 400 mm. Additionally, a rotational axis ( $\theta$  -about Z-axis) with two redundant Y-axes was attached to  $\theta$ -axis, which gives extended reach along Y-axis as well as precise movement to reach the target position with gripper. The X-axis is positioned along the 6000 mm dimension of the cell and Y-axis along the 700 mm dimension. The



**Fig. 2** CAD model of sample handling robot



**Fig. 3** CAD model of CDR showing cap handling and bottle handling modules

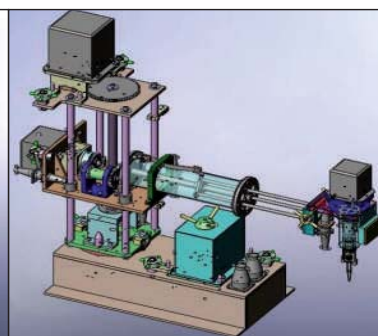


**Fig. 4** CAD model of PPR

X-axis rail is a critical component of the sample handling robot. It is a long translation stage with double rails supported on custom-designed girders made of SS 304 for rigidity and precise motion. Counterweights are provided to offset the cantilever effects of Y-axis translation stage with gripper. Salient design feature of the sample handling robot is that remote assembly and disassembly is possible for maintenance of all axes using the in-cell crane and methyl sulfonyl methane of the sampling cell. The gripper can handle a payload of 5 kgf. The function of sample handling robot is to collect empty sample bottle from the user-defined location on the storage rack kept inside the cell and transport the sample bottle to the pre-defined sampling point. Subsequently, the sample can be collected by piercing the bottle using the Z-axis travel and bring back the sampled bottle to the storage rack. The sampled bottle can subsequently be transported to the analytical cell by using in-cell crane facility as and when required.

Lower compartment of the analytical cell is the region, where analytical operations such as collecting sample (in the range of 50–1000  $\mu$ l) and dispensing the sample in analytical stations, cleaning and disposing of waste - are carried out. These operations are done by capping / decapping robot and Pipette Robot

with the assistance of methyl sulfonyl methane. Capping / decapping robot (shown in Figure 3) is a cylindrical robot made in two major modules namely bottle handling module and cap handling module. Bottle handling module assists in transporting the filled sample to capping / de-capping module to do capping / de-capping operation based on the analytical cycle. Cap handling module has two identical cap handling units placed 180° apart, facilitating dual purpose of reduced cycle time and redundancy. Each cap handling unit is capable of handling of both inner and outer caps.

The pipette robot is also a cylindrical robot (shown in Figure 4) similar to bottle handling module of CDR with the pipette head attached to it in place of bottle gripper. Payload capacity of PPR at fully extended condition is 2 kgf. Both CDR and PPR have a base rotation ( $\theta$ ) of  $\pm 330^\circ$ , vertical (z) travel of 0–200 mm, radial (r) travel of 150 mm and pipetting range of 50–1500  $\mu$ l. The complete sampling system is controlled by PLC based control system. Stepper motors are used for all the axes of sampling system to have precise motion in open loop control to limit the electronic devices inside the cell environment.

Dedicated application-specific software is being developed with complete security features, three

layer administrative privilege and system operation / configuration rights and safety interlocks.

A dedicated status monitoring and control screen has been incorporated to monitor the erroneous operations/operator violations which are simultaneously logged in the database for review. It has provision to send real-time message to the administrative authority as and when the events take place. The sampling operations can be executed either through pendant or man-machine-interface (MMI). Both modes of operation have lead-through teaching facility as well as auto mode execution. In teach mode operation, provision is made such that each instruction will be executed only on receiving operator's acknowledgment. This feature facilitates the operator to make any correction for any over or under shoot while teaching. Each operation and sample movements are logged on to the database which can be used later for analysis, report generation, etc.

The system is in the advanced stage of manufacturing and many of the modules have been completed. The integrated system will be tested in a mock-up, simulating the cell dimensions for demonstrating the functioning of the system including remote assembly and disassembly in modules.

## IV.5 Development of Motors for Centrifugal Extractors in Hot-cell

Centrifugal extractors (CE) employed in the aqueous reprocessing of spent fuels of fast breeder reactors are driven by electrical motors. The rotors and stators of these motors, made from stampings of silicon steel are exposed continuously to radiation and vapour of 4 M nitric acid in the plant. Owing to the vapour phase corrosion of the rotors, the corrosion products formed were found to cause increased friction. To protect the motor components from radiation and corrosion, polyetheretherketone, PEEK coating was chosen as it is a high performance thermoplastic having a radiation resistance of 10 MGy. It possesses excellent strength, stiffness, long-term creep and fatigue properties in addition to its high abrasion and cut-through resistance, low coefficient of friction and it is resistant to a wide range of chemicals at elevated temperatures. The linear aromatic PEEK family consists of repeated monomers of ether and ketone, responsible for high performance properties with respect to mechanical, thermal, chemical, etc.,

Radiation tolerance of PEEK was evaluated by exposing sheets of PEEK to gamma rays up to 12 MGy and comparing the mechanical properties as a function of radiation dose. Figure 1 shows the percentage decrease in the elongation at break owing to degradation. The elongation at break had decreased only to about 50% of its original value at 10 MGy. Further, PEEK coated samples when irradiated up to 10 MGy were observed to have good adherence

without any swelling. Hence, PEEK coating was tried on the motor components of CE.

Prior to coating, the rotor was machined to accommodate PEEK in order to maintain the final air gap between the coating and stator as 100 µm. The coating thickness was measured to be 80 to 90 µm. The hardness value determined was 80 to 84 Shores D. The electrical resistivity, surface resistivity was measured to be  $10^{11}$  to  $10^{12}$  ohm/sq. For evaluating the performance of coating in the plant, the coated rotor was fixed in the stator of the motor and the centrifugal extractor was run with nitric acid which simulates the operating conditions of the plant. After the test, the rotor was removed from the centrifugal extractor's motor and the condition of coating was evaluated. There was no change in the thickness of coating and no swelling/blister formation was observed. Figure 2 gives the photographs of the coated rotors before and after testing under actual condition in the plant. Hardness and surface resistivity values did not alter after exposure to acid vapour. The adherence of PEEK coating on the rotor was found to be satisfactory, as there was no peeling of the coated layer. It is ascertained that the PEEK coating on the surface of the rotor had enabled to give adequate protection to the motors of centrifugal extractors against corrosion. As the performance of the motor is also dependent on the air gap between the rotor and stator, motor load tests were conducted to assess the performance degradation due to

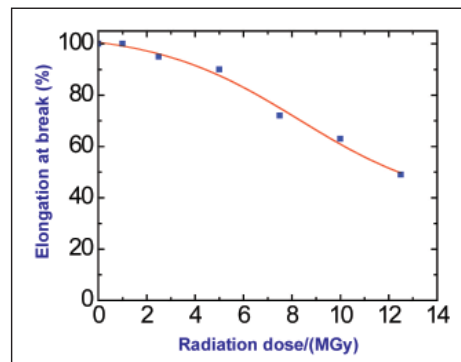


Fig. 1 Elongation at break as a function of radiation dose

increased gap between rotor and stator by recording torque as a function of current as well as speed and the results are shown in Figure 3. The performance was not severely affected by increasing the gap. The current drawn at the operating conditions was found to increase marginally by 10 to 15% which is within acceptable limits.

The stators of assembled motors could not be coated by PEEK since most of the stator components in the motor assembly do not possess the thermal resistance to withstand the curing temperature of 663 K for PEEK coating. So, epoxy coating was tried and a thickness of 100 µm could be achieved. Powder coating

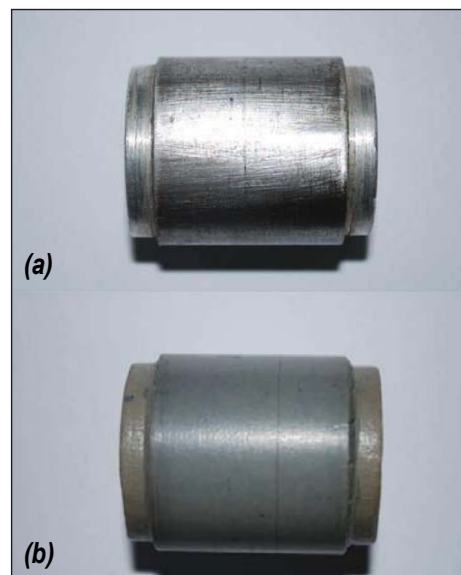


Fig. 2 Rotors with PEEK coating (a) Before testing and (b) After testing

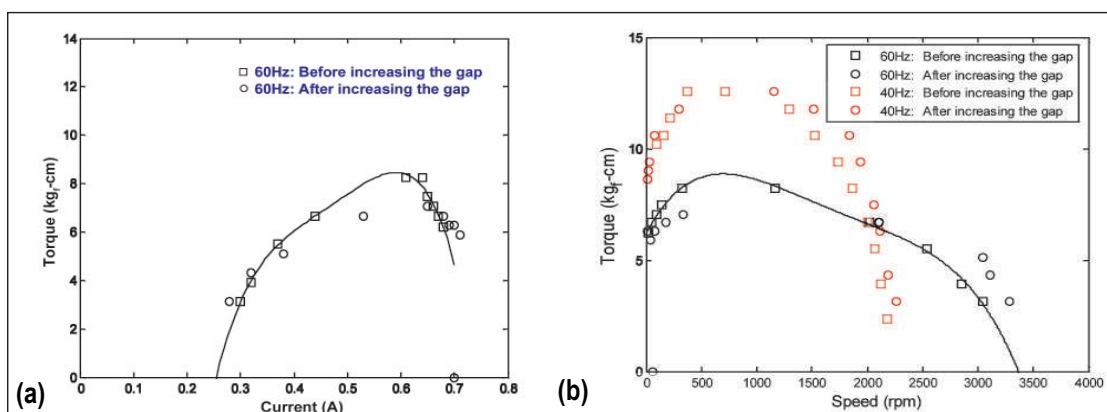


Fig. 3 Torque values as a function of (a) current and (b) speed

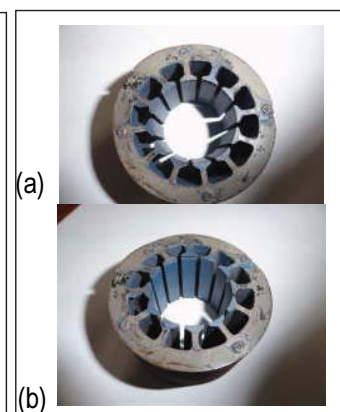


Fig. 4 Coated stators (a) before testing and (b) after testing

of the epoxy, tried on one stator yielded a thin film, which was found to be resistant to nitric acid vapour. As the PEEK coating tried before winding in the stator stack got delaminated after curing, fixtures were fabricated and PEEK coating was repeated. The laminated stack was intact with good chemical

resistance. Figure 4 (a) depicts a stator with PEEK coating and Figure 4 (b) shows the coated stator after testing under plant condition.

Performance of centrifugal extractors under severe conditions of acid vapour and radiant rays depends on the synergistic effect of the motor components rotor, stator and other

movable parts. Protecting the motor components of centrifugal extractors (which are prone to vapour phase corrosion) by way of coating with anticorrosive and radiation tolerant PEEK material would facilitate smooth functioning and enhancing the reliability and longer service life of centrifugal extractors.

## IV.6 Development of Remote Handling Gadgets for Improving Operational Performance of CORAL

Major considerations for designing hot cell system and equipment for remote operation and maintenance are equipment layout, availability of viewing space, interchangeability, modular construction, high reliability and robustness. Design and development of many remote operation equipment for alpha tight hot cells with all these constraints have been completed in CORAL during its large number of campaigns with FBTR spent fuel having burn-up up to 155 GWd/t.

The development of remote handling devices is of paramount importance in fast reactor fuel reprocessing plants, as it is extremely difficult to carry out contact maintenance, because of the high

radiation and contamination. Many gadgets are required which are amenable for operation using master slave manipulators and in-cell crane.

### Development of long airtight tong for master slave manipulator

Articulated master slave manipulator is one of the vital devices which substitutes the human arm for the application of handling radioactive materials behind thick shielding in the lead hot cells of nuclear industries to protect the personnel and environment from radiation and toxic hazards and aids in remote operation and maintenance of hot cell equipment. The master arm and slave arm are coupled to each other such that the position and direction of the two arms correspond to six

independent degrees of freedom, three of translation and three of rotation to access the end effector and a tong squeeze motion to grip items. The coupling between the two arms are bilateral with a mechanical advantage of 1:1.

With the present configuration the reach is 2 m<sup>3</sup> per pair, which is convenient to work in the hot cells. The in-cell crane is erected well above the reach of the articulated master slave manipulator. In case of any maintenance of in-cell crane, the reach of articulated master slave manipulator can be extended by attaching the long airtight tong (Figure 1) remotely and the maintenance can be carried out. Some of the in-cell equipment which are maintenance free, can also be

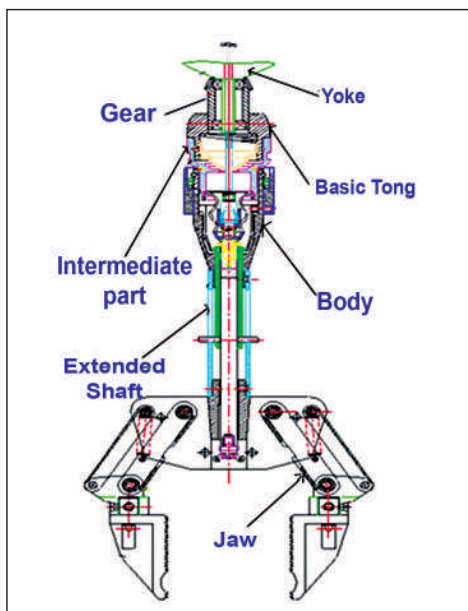


**Fig. 1** Schematic sketch of extended airtight tong

placed beyond the normal reach of the articulated master slave manipulator and if required, maintenance can be carried out with the aid of this tong. With the present design of airtight long tong, the reach is increased by about 30%.

**Maintenance of centrifuge at CORAL**

The centrifuge had posed various types of challenging maintenance requirements such as bearing failure of turbine, dislodging of bush and bearing acting as a vibration damper. In order to address such maintenance activities remotely, a typical stainless steel bearing puller for remote replacement of turbine bearing, special actuator (Figure 2) for remote replacement of quill shaft collet and

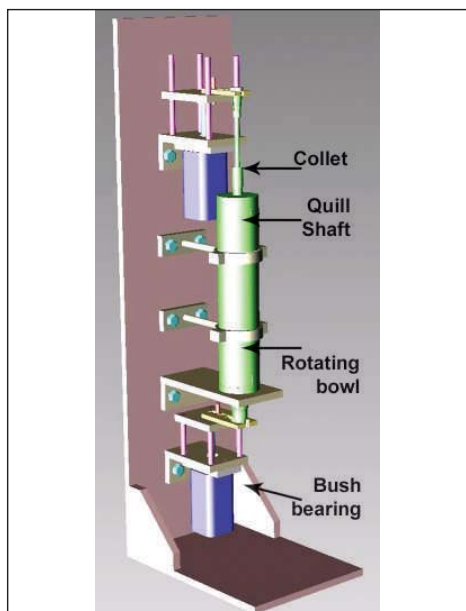


**Fig. 2** Centrifuge remote maintenance tool

viton bush had been developed. A typical in situ decontamination facility for rotating bowl cleaning was also developed and installed at CORAL.

**Remote maintenance of centrifugal extractor**

Centrifugal extractor is the heart of fast reactor fuel reprocessing facility. During the operation of different campaigns, a need was felt to introduce a component into the stationary bowl of the centrifugal extractor to improve the performance. For this, the rotating bowl along with motor assembly was removed with the aid of master slave manipulator, in-cell crane, pneumatic wrench and special gadgets. The component to be introduced was a thin spacer plate of thickness 3 mm.

The spacer was attached to the end of a specially designed tool, and was inserted into the stationary bowl and rotated remotely by the manipulator so as to match the stationary bowl vanes with the grooves of the spacer plate. Afterwards, with the assistance of the manipulator, the tool was unscrewed from the spacer plate and removed, allowing the plate to be positioned in the stationary bowl. In this way all the plates were placed successfully.

During the above remote operation, many challenges such as mismatching of vanes with the plate and falling of nuts into the stationary bowl etc., had been experienced and all were over come by using special gadgets remotely with the help of the manipulator. After this modification, substantial improvement was observed in the system.

In CORAL, there are two types of banks of centrifugal extractors (non interface and interface types) consisting of 16 stages. After a year and a half of operation, based on experience, it was decided to change one of the banks from one type to the other. With the aid of master slave manipulator, in-cell crane and special gadgets, all the 16 stages of rotating bowl assembly were remotely removed and bowls were replaced. Existing inter-phase airline to each stage was knocked-off

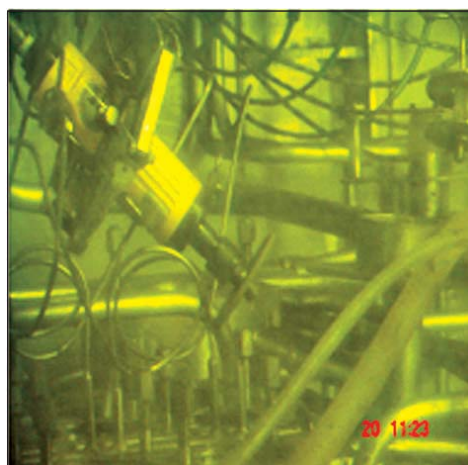


**Fig. 3** Centrifugal extractor bank inter-phase airline cutting remotely

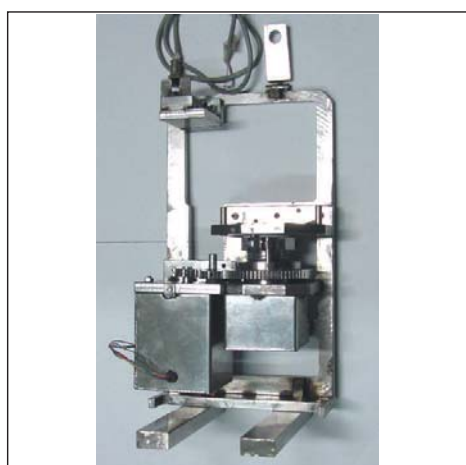


**Fig. 4** Centrifugal extractor dismantling equipment



**Fig. 5** Alpha bearing high active solid waste transfer system

remotely by using a pneumatic grinder with a cut off wheel shown in Figure 3. All the non interface rotating bowl assemblies were placed in the respective stages and tightened remotely by a pneumatic wrench and all the stages were found to run smoothly.

Highly active centrifugal extractor rotating bowl had to be dismantled for periodic maintenance of the motor. A novel automated dismantling equipment (Figure 4) was successfully

developed for assembling / disassembling of centrifugal extractor motor with rotating bowl remotely. By adopting this system at CORAL, contact maintenance could be avoided.

**Development of high active alpha bearing solid waste transfer system**

High active alpha bearing solid waste transfer system requires provision for alpha containment in addition to

provision of shielding for beta, gamma during transfer operations and should be amenable for both horizontal and vertical transfer. A novel system has been successfully designed for such applications (Figure 5). The advantage of this system is that both the outside surface of doors and the operating area will not be contaminated by alpha during transfer and also man Rem exposure will be negligible. The unit was demonstrated for its performance under plant conditions.

**IV.7 Fuel Pellet Defect Quantification**

During pellet fabrication, defects such as edge chip, surface chip and surface cracks are inevitable and due to these defects, the centerline temperature of the pellet rises more than that for defect free pellet which discourages the use of it in the reactor. To improve higher recovery, pellets with certain level of defects are accepted without compromising on the fuel performance and safety. It is hence required to quantify the acceptable level of defects which saves a lot of fissile material and thus the economy of operation. Besides, use of defective pellets necessitates in the introduction of some additional hotspot factors in the fuel

performance modeling. The main focus is to fit a new parameter which is dependent of the size and shape of the defect and to find the increase in the centerline temperature of the defective pellet in comparison with a normal pellet. Hence, a new parameter, defect factor,  $\zeta$ , which when applied on the temperature drop of a normal pellet, reflects the temperature increase due to a defect of any shape and size. Thus the defect factor can be used as an additional factor for fuel performance modeling.

Nominal centerline temperature for a normal pellet

$$T_{\text{centerline}} = T_{\text{Na}} + \Delta T_{\text{film}} + \Delta T_{\text{clad}} + \Delta T_{\text{gap}} + \Delta T_{\text{fuel}}$$

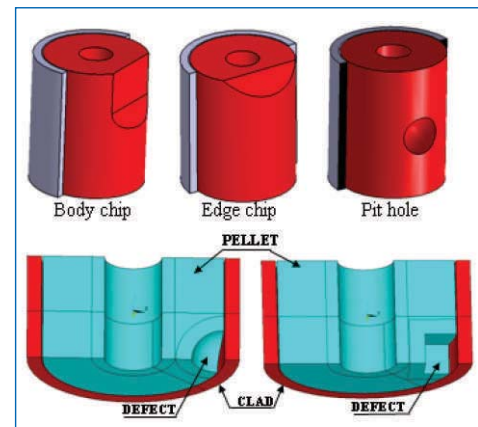


Fig. 1 Different types of defects and models

For a defective Pellet

$$T_{\text{centerline}} = T_{\text{Na}} + \Delta T_{\text{film}} + \Delta T_{\text{clad}} + \Delta T_{\text{gap}} + \Delta T_{\text{fuel}} * \zeta$$

Due to the defects, two effects are possible.

1. Loss of fissile material at the defect would reduce the power generation and reduce fuel centre temperature
2. Decrease in the fuel- clad gap conductance in the vicinity of the defect location resulting in higher local temperature

Owing the presence of defects in a pellet, the gap increases locally leading to reduced gap conductance. In the present analysis, different

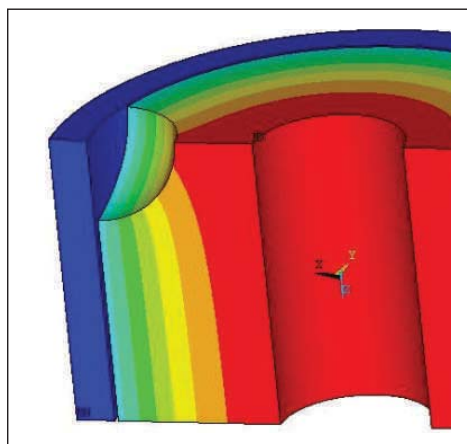


Fig. 2 Typical temperature profile in the defective pellet

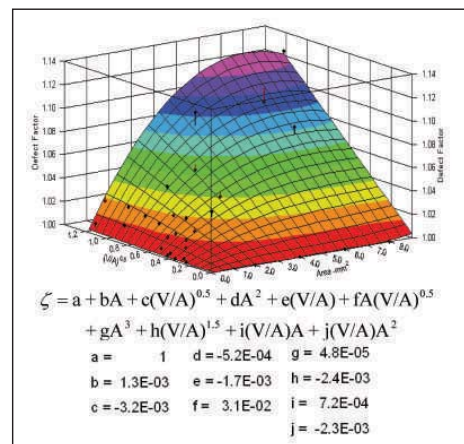


Fig. 3 Defect factor as a function of A & (V/A)<sup>0.5</sup>

types of defects are considered at beginning of life (BOL). For the purpose of analysis regular shaped defects are only considered. The different types of defects considered are hemi-spherical, cubical and conical. Figure 1 shows various possible defects considered in the model.

The increase in the defect size results in increase in centerline temperature and is a function of defect parameters such as opening area, volume of the defect and maximum depth of the defect. The typical temperature profile in a pellet with hemi-spherical defect is shown in Figure 2. To find out the rise in temperature of the pellet with defect, a factor  $\zeta$  is defined.

$$\zeta = \frac{\Delta T_{\text{Pellet with defect}}}{\Delta T_{\text{Pellet without defect}}}$$

It is expected that, with the increase in the defect size,  $\zeta$  centerline temperature also increases. Table 1 shows the temperature increase in the defective fuel as a function of defect dimensions and is compared with the defect free pellet. The thermal analysis for the defective pellet is extended for the defects with different aspect ratios. Regression analysis is done with defect dimensions and the  $\zeta$ . The defect factor variation as a function of area (A) and volume to area ratio (V/A)<sup>0.5</sup> is shown in Figure 3.

Table 1: Temperature rise as a function of the defect dimensions					
Defect Shape	Depth of Defect (mm)	Opening Area, A (mm <sup>2</sup> )	Volume, V (mm <sup>3</sup> )	Temperature Drop in the pellet (K)	Defect Factor $\zeta$
No Defect	-	-	-	1164	1.000
Hemi-sphere	0.2	0.126	0.017	1165	1.001
	0.3	0.283	0.057	1167	1.003
	0.5	0.785	0.262	1176	1.010
	0.7	1.539	0.718	1192	1.024
	1	3.142	2.094	1227	1.054
	1.5	7.069	7.069	1274	1.095
Cube	0.2	0.160	0.032	1165	1.001
	0.3	0.360	0.108	1168	1.003
	0.5	1.000	0.500	1185	1.018
	0.7	1.960	1.372	1214	1.043
	1	4.000	4.000	1275	1.095
	1.5	9.000	13.500	1309	1.125
Cone	0.2	0.126	0.008	1165	1.001
	0.3	0.283	0.028	1166	1.002
	0.5	0.785	0.131	1172	1.007
	0.7	1.539	0.359	1183	1.016
	1	3.142	1.047	1208	1.038
	1.5	7.069	3.534	1258	1.081

The defect factor variation with volume with constant opening area of defect is shown in Figure 4. The defect factor increases initially due to loss in the gap conductance and then decreases due to loss in the heat generation, because of the loss in fissile material. In Figure 5, the defect factor variation as a function of opening area with constant volume of defect is shown. It is observed that there is a continuous increase in the value of defect factor. The decreasing slope trend is due to the lesser effect of change in gap conductance as the depth of the defect is less. Also, it is observed that

the opening area of the defect predominantly affects the defect factor.

At the BOL, the peak operating power of the pellet is limited to 400 W/cm due to large gap drop. With development of crack and swelling of the fuel, the radial gap comes down and after about 3-5 days, the linear power could be raised to 450 W/cm. At 400 W/cm, the margin available at centerline temperature from melting is 101 K. After conditioning period, the gap will come down and then a margin of 83 degree is available. In any case, there is minimum margin of 80 degree

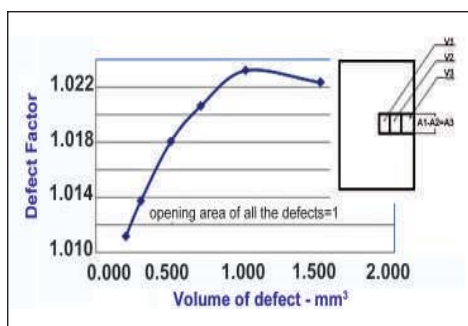


Fig. 4 Defect factor variation with volume of defect at constant surface opening area

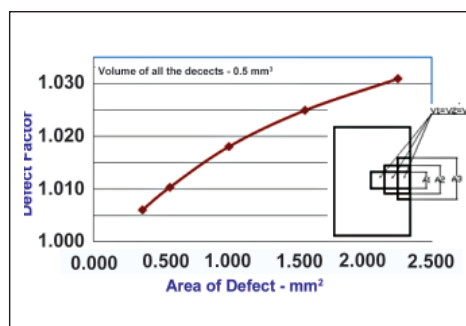


Fig. 5 Defect factor variation with surface opening area of defect at constant defect volume

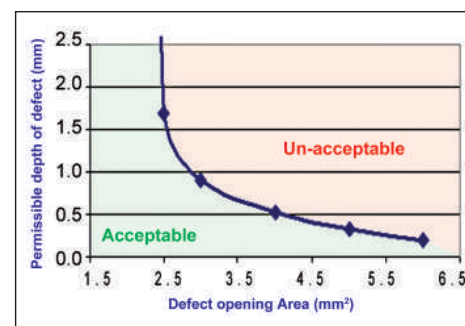


Fig. 6 Allowable defect depth as a function of opening area of the defect

is available which helps in loading the defective pellets. The depth of the permissible defect depends on the opening area. For an opening area of < 2.5 mm<sup>2</sup>, defect depth of any value can be allowed. But with increase in

the area of the defect, allowable defect depth will come down as shown in Figure 6. Hence, up to defect size of 5 mm<sup>2</sup> opening area which is 3% of the lateral surface area of the pellet, defect depths of 0.3 mm can be

allowed. This study has helped in not only determining the maximum allowable defect size from the point of view of thermal performance of the pellet but also in improving the recovery of the pellet.

## IV.8 Multiple Recycling of Fuel in PFBR in a Closed Fuel Cycle

FBR closed fuel cycle involves recycling of the discharged fuel, after reprocessing and refabrication. Our study in this regard for the PFBR indicates a comfortable feasibility of multiple recycling with self-sufficiency. The total inventory of Plutonium in the whole fuel cycle is conservatively estimated to be twice that of core. As the PFBR core has eight months cycle length and one-third core is discharged in every cycle, during the forty year life of the reactor ten reprocessing cycles are expected to occur. Estimations are done with the code ORIGEN2, using the most recent nuclear data, viz. ENDF/B-VII.0 and with the most recent specifications of the fuel composition. Ten refueling cycles are considered involving fuel recovery, cooling and refabrication, taking into account the mandatory requirement of conserving fuel worth and mass at every beginning-of-cycle. The

concept of <sup>239</sup>Pu reactivity equivalence (Table 1) is used to assess the fuel quality and to decide the plutonium fuel weight to be loaded to maintain reactivity. Plutonium as well as uranium recovery of 99.9% from the discharged fuel has been considered. In a cycle, the core subassembly is irradiated for 540 full-power-days (fpd), followed by an in-core cooling for 240 days, reprocessing time of 120 d and further delay of 120 d before refabrication, as schematically shown in Figure 1. For refabrication, the plutonium lost in a cycle is compensated for from that bred in axial and radial blankets caring to conserve fuel worth as at the beginning-of-life. This demands increased Pu inventory, to make up for the reactivity reduction due to accumulation of non-fissile plutonium nuclides viz. <sup>240</sup>Pu and

Nuclide	Eq'ce	Nuclide	Eq'ce
<sup>235</sup> U	0.78	<sup>240</sup> Pu	0.10
<sup>238</sup> U	0.06	<sup>241</sup> Pu	1.50
<sup>237</sup> Np	-0.20	<sup>242</sup> Pu	0.04
<sup>238</sup> Pu	0.58	<sup>241</sup> Am	-0.24
<sup>239</sup> Pu	1.00	<sup>242</sup> Am	2.94

<sup>242</sup>Pu. This increase is adjusted against by reducing uranium, however, the relative increase between consecutive cycles is seen to diminish with the cycle number, indicating saturation.

Among others, the study has brought out the importance of the resonance self-shielding effects in the cross-section averages used in the study. Average cross-section in an energy range is obtained with flux weighting to conserve the reaction rate in the

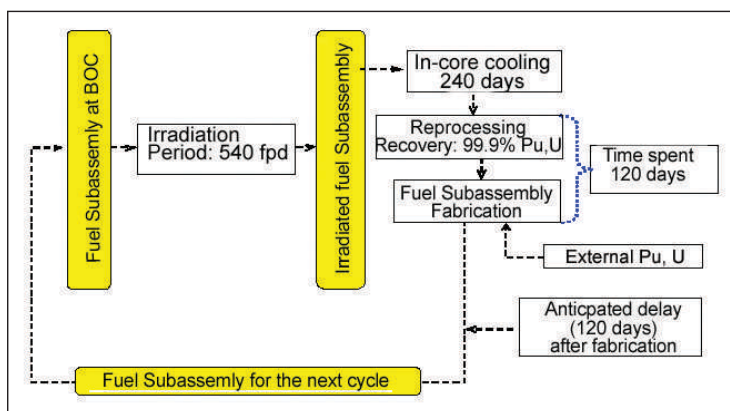
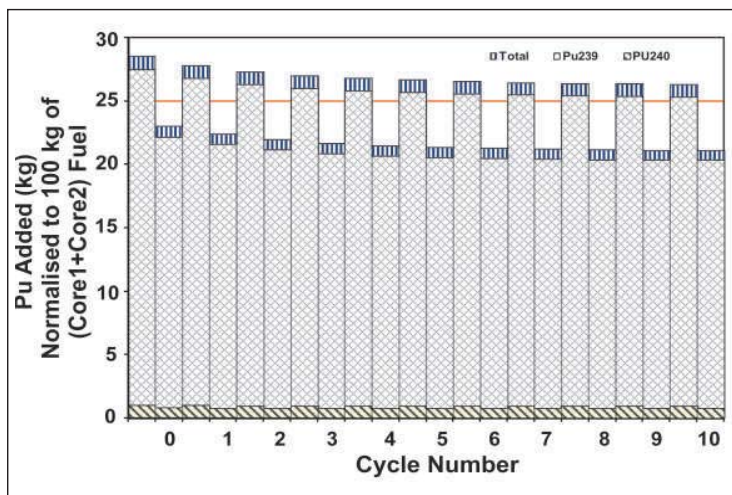
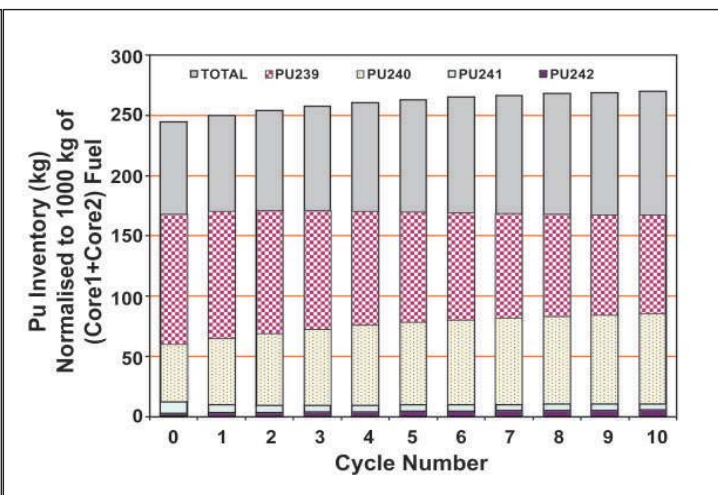


Fig. 1 Closed fuel cycle of one fuel sub-assembly

Region	Nuclide	Cross-section (b)		Ratio
		Unshielded	Self-shielded	
Core-1	<sup>238</sup> U	0.3590	0.3065	0.8537
	<sup>239</sup> Pu	0.5576	0.5399	0.9683
Core-2	<sup>238</sup> U	0.3260	0.2705	0.8298
	<sup>239</sup> Pu	0.4965	0.4707	0.9479
LAB	<sup>238</sup> U	1.0540	0.4303	0.4081
UAB	<sup>238</sup> U	0.7669	0.3864	0.5039
RB	<sup>238</sup> U	0.8365	0.3827	0.4575



**Fig. 2** Requirement of plutonium to be added from the radial blanket to maintain core reactivity



**Fig. 3** Plutonium inventory variation with recycling

range. Resonance self-shielding is caused by flux-depressions due to cross-section resonances of nuclides in the mixture affecting the average value. For a nuclide causing insignificant flux variations, self-shielding is irrelevant and it leads to unshielded average. Table 2 compares self-shielded and unshielded average capture cross-sections and their ratios, for uranium and plutonium in different regions, which shows that  $^{238}\text{U}$  capture suffers maximum self-shielding, with very pronounced effect in the (lower-axial, upper-axial and radial) blankets due to softer spectrum. This will have considerable influence on the

prediction of  $^{239}\text{Pu}$  production through breeding.

With respect to self-sufficiency, while self-shielded averages lead to a realistic prediction of bred fuel availability of 1.5 times the fuel needed in the core for replenishment in each cycle, unshielded averages over-estimate plutonium production. The estimates of plutonium added in each cycle to the recovered plutonium are shown in Figure 2, wherein the unshielded estimates are plotted adjacent to the self-shielded estimates. It is encouraging to note that the addition reaches

saturation almost from the fourth cycle for both the cases.

Figure 3 gives the plutonium inventory at beginning-of-cycle for each cycle, normalized to 1000 kg total fuel mass of both the cores taken together. Though the self-shielding affects the production in the blanket, the losses in the core, and the additions needed from the bred component, it has little influence on beginning-of-cycle inventories. The study indicates a comfortable feasibility of multiple recycling in PFBR, with the initial inventories stabilizing after a few cycles.

## IV.9 Demonstration of Minor Actinide Partitioning

**P**artitioning and transmutation (P&T) strategy is being proposed for the safe management of high level liquid waste (HLLW) in many countries. This method is based on the separation of trivalent actinides and long-lived radiotoxic fission products from HLLW and their transmutation into stable or innocuous products in advanced fast reactors. Partitioning of trivalent actinides from HLLW involves the

liquid-liquid extraction of both trivalent actinides and lanthanides followed by lanthanide-actinide separation. Several reagents such as the organophosphorous compounds, amides and diglycolamides have been proposed as potential candidates for actinide partitioning from HLLW. In TRUEX process, the trivalents (Ln(III) and An(III)) are selectively extracted in to a solution of tri-n-butylphosphate

(TBP), n-octyl (phenyl)-N, N-diisobutyl carbamoyl methyl-phosphine oxide (CMPO) in n-dodecane.

A method for partitioning of minor actinides from fast reactor (FR) fuel solution by using a solvent comprising 0.2 CMPO – 1.2 M TBP in n-DD is developed and subsequently demonstrated with fast reactor dissolver solution (155 GWd/t) using a novel 16-stage ejector mixer settler in hot cells.



**Fig. 1** Experimental setup in hot cell used for minor actinides partitioning

For this purpose, the dissolver solution was obtained by the dissolution of FBTR fuel (100 g), irradiated to the burn-up of 155 GWd/t (cooling period 2 year) in 11.5 M nitric acid in hot cell. Cesium, plutonium and uranium present in the dissolver solution were removed, prior to minor actinide partitioning, by using ammonium molybdophosphate impregnated XAD-7 (AMP-XAD), methylated poly(4-vinylpyridine) (PVP-Me), and macroporous bifunctional phosphinic acid (MPBPA) resins respectively.

Initially, cesium was removed, from the dissolver solution to minimize the occupational exposure and lower the degradation of processing materials. About 99.9% of cesium was removed during this process. About 94% of plutonium was recovered and quantitative removal of uranium was

achieved using MPBPA resin. The effluent thus obtained was used as a feed for minor actinide partitioning.

Prior to the demonstration run, batch studies were carried out with the feed solution (feed for MA partitioning). The trivalents from the loaded organic phase were back extracted using 0.1 M citric acid in 0.1 M  $\text{HNO}_3$ . It was observed that the quantitative extraction and stripping of Ln(III) and An(III) from other fission and corrosion products was achieved in five and seven contacts respectively.

Extraction of lanthanides (+3 state) and actinides (+3, +4 and +6 states) by CMPO-TBP solvent was performed in a counter current mode using a novel 16-stage ejector mixer settler installed in hot cell. The experimental setup used for minor actinides partitioning is shown in Figure 1. The system was operated

for ~7 hours and steady state was attained in four hours. The lanthanides and actinides were back extracted from the loaded organic in a counter current extraction process using the same mixer settler in a separate run. The stripping formulation is composed of 0.1 M citric acid and 0.1 M  $\text{HNO}_3$ . The results confirmed the quantitative separation and recovery (>99%) of trivalents (Am(III)+ Ln(III)) from the fuel solution.

Lanthanides were extracted in six stages and stripped in ten stages using the citric acid formulation. Nearly 20 – 25 % of radio ruthenium was carried to lean organic and it, therefore, calls for the cleanup of the solvent before recycling. The results accomplished from this demonstration run and the experience gained in hot cell

operation provide the impetus to employ CMPO-TBP solvent for partitioning of minor actinide from HLLW. However, more studies such as the co-extraction and stripping behaviour of other elements are needed for the success of partitioning and transmutation technology.

Chemical characterization of a typical high active liquid waste is necessary for characterizing the high-level liquid wastes which would be of similar in chemical nature and concentration levels. Characterization of this type of waste is a challenging task of determining various elements and radionuclides present in a complex mixture of multi-elemental matrix. Depending upon the type of fuel employed for irradiation, the composition of high level waste is different. There are several factors that affect the composition of the high level waste viz. the burn-up of the fuel, cooling time, materials for storage and efficiency of PUREX process, additives employed during reprocessing etc. High-active liquid waste was received from the CORAL pilot plant. The concentration of nitric acid in this waste was determined by titration method.

The gamma emitting isotopes were assayed using HPGe detector coupled with multi-channel analyzer (MCA). Plutonium was estimated by solvent extraction with HTTA followed by the determination of alpha activity. Uranium was analyzed by both spectrophotometry and HPLC methods. U(VI) was separated from high active waste by solvent extraction procedure using 1.1 M TBP/n-DD and stripped with

dilute nitric acid. The separated uranium was estimated by Arsenazo (III) method and ICP-AES. Uranium was also estimated using high performance liquid chromatography developed in our group.

Neutron activation analysis (NAA) is a convenient and sensitive method ( $\sim 10^{-3}$   $\mu\text{g}$ ) for estimating neptunium. This method requires the separation of the target neptunium from other actinides such as plutonium and americium. This was achieved by the solvent extraction of Np(IV) from high active waste in 0.5 M TTA/xylene. The extraction efficiency was about 97%. The  $^{237}\text{Np}$  present in organic phase was irradiated at KAMINI. The activation product formed  $^{238}\text{Np}$  was monitored by the characteristic gamma emissions at 984 keV and 1028 keV. Under similar conditions  $^{237}\text{Np}$  standards were irradiated and the calibration graph was constructed.

The radioactivities of americium and curium were determined by alpha counting technique and alpha spectrometry. This waste was contacted with CMPO-TBP solvent and the alpha activity of the organic phase was measured. Some of the heavier lanthanides namely lanthanum, cerium, neodymium, europium, samarium and praseodymium were analyzed using HPLC technique. The mobile phase composed of 0.1 M HIBA + 0.015 M camphor sulphonic acid was passed to elute the lanthanides at 3.4 pH. The other elements present in this waste were determined by ICP-AES. The concentration/activity of elements determined hitherto are tabulated in Table 1.

**Table 1: Elemental and isotopic composition of high level waste (155 Gwd/t)**

Nitric acid		4.6 M
Elements		Concentration, $\mu\text{g/ml}$
Plutonium (TTA)		3.6
Uranium	i) Ars-III	222
	ii) ICP-AES	216
	iii) HPLC	234
Neptunium (NAA)		< 2
Lanthanum	i) HPLC	56
	ii) ICP-AES	61
Neodymium (HPLC)		162
Cerium	i) HPLC	87
	ii) ICP-AES	103
Praseodymium	i) HPLC	38
	ii) ICP-AES	43
Samarium	i) HPLC	38
	ii) ICP-AES	36
Europium	i) HPLC	3
	ii) ICP-AES	<5
Molybdenum (ICP-AES)		202 $\pm$ 20
Chromium (ICP-AES)		884 $\pm$ 80
Dysprosium (ICP-AES)		< 5
Iron (ICP-AES)		3602 $\pm$ 100
Gadolinium (ICP-AES)		< 5
Manganese (ICP-AES)		368 $\pm$ 30
Nickel (ICP-AES)		787 $\pm$ 70
Palladium (ICP-AES)		8.7 $\pm$ 1
Silver (ICP-AES)		<5
Strontium (ICP-AES)		32 $\pm$ 3
Ruthenium (ICP-AES)		82 $\pm$ 8
Zirconium (ICP-AES)		3 $\pm$ 1
Calcium (ICP-AES)		316 $\pm$ 30
Magnesium (ICP-AES)		20 $\pm$ 3
Sodium (ICP-AES)		16800
Elements		Activity, $\mu\text{Ci/ml}$
Am + Cm	i) CMPO - TBP	51
	ii) CMPO	71
	iii) alpha count	77
$\gamma$ -spectrum		
$^{60}\text{Co}$		16.3
$^{106}\text{Ru}$		698
$^{125}\text{Sb}$		43
$^{134}\text{Cs}$		121
$^{137}\text{Cs}$		4190
$^{144}\text{Ce}$		325
$^{154}\text{Eu}$		37.5

## IV.10 Development of Extractants for the Separation of Actinides and Lanthanides

Solvent extraction plays a major and irreplaceable role in the nuclear fuel cycle operations. Several extractants and flow sheets are being developed for the nuclear fuel cycle, in general, and fast reactor fuel reprocessing, in particular. Selection of the extractant with the desirable properties is an important issue with respect to the efficiency and economics of the solvent extraction process on commercial scale. Alternative extractants for fast reactor fuel reprocessing and novel extractants for the processing of waste solutions containing minor actinides and fission products have been developed. Flow sheets for fast reactor fuel reprocessing, minor actinide recovery, actinide-lanthanide (An/Ln) separation etc. are being developed at our Centre using various extractants.

Despite the overall success of TBP in various solvent extraction processes such as thermal reactor fuel reprocessing, thorium extraction, U/Th separation, Zr/Hf separation etc, it suffers from some limitations such as third phase formation, chemical and radiation degradation, aqueous solubility etc.

In an attempt to develop an alternative extractant for fast reactor fuel reprocessing, tri-n-amyl phosphate (TAP, the higher homologue of TBP) and some of its isomers such as tri-iso-amyl phosphate (TiAP) and tri-2-methylbutyl phosphate (T2MBP) have been explored as potential extractants. These trialkyl phosphates (TaIP) have high metal

TaIP	At 299 ± 1 K			1.1 M TaIP/ <i>n</i> -dodecane HNO <sub>3</sub> 303 K		
	Density (g/cm <sup>3</sup> )	Solubility of H <sub>2</sub> O in TaIP (mg H <sub>2</sub> O/l)	Aqueous solubility of TaIP (mg TaIP/l water)	$D_{Th(IV)}$ 5 M HNO <sub>3</sub>	$D_{U(VI)}$ 3 M HNO <sub>3</sub>	$D_{Pu(IV)}$ 3 M HNO <sub>3</sub>
TBP	0.976	67	388	3.96	24.5	15.0
TAP	0.954	40.6	19	4.09	29.7	17.0
TiAP	0.948	41.1	-	4.47	29.8	18.1
T2MBP	0.958	39.2	24	2.86	30.5	-

loading capacity without third phase formation in the extraction of Th(IV) and Pu(IV) as compared to TBP. Distribution ratios (D) for the extraction of actinide ions by these extractants are also comparable to that of TBP and are illustrated in Table 1. In addition to these advantages, the above-mentioned extractants have better physicochemical properties as compared to TBP and are shown in Table 1. Feasibility of using TAP for reprocessing applications has been demonstrated by continuous counter-current runs (extraction as well as stripping for U(VI) – HNO<sub>3</sub> – 1.1 M TAP/HNP system) using a 16 stage ejector mixer-settler (made up of a monolithic polypropylene block) under high solvent loading conditions. Demonstration of mixer-settler runs with U/Pu (PFBR fuel dissolver solution composition) – HNO<sub>3</sub> – 1.1 M TiAP/HNP system using a similar facility installed in a twin glove-box is underway.

In continuation of our activities on the development of new and novel extractants for actinides separation, efforts were made to explore other extractants in the organophosphorous

family. In this connection, dialkylalkyl phosphonates have been synthesized to employ the extractants with higher extraction ability as compared to TBP for specific applications (the basicity of the phosphoryl group can be enhanced by replacing the C-O-P group by a C-P group).

The homologues of dibutylalkyl phosphonates viz. dibutylbutyl phosphonate (DBBP), dibutylhexyl phosphonate (DBHeP) and dibutyloctyl phosphonate (DBOP) were synthesized by Michaelis Becker reaction and characterized. Figure 1 shows the extraction behaviour of uranium and plutonium as a function of nitric acid concentration by 1.1 M DBBP, 1.1 M

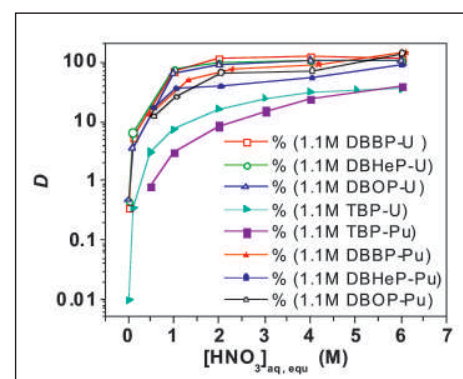


Fig. 1 Distribution ratio of U(VI) and Pu(IV) in various phosphonates at 303 K

**Table 2: Variation in the distribution ratio and separation factors as a function of [DTPA]; Organic phase: 0.1 M HDEHDGA/*n*-DD, Aqueous Phase: [DTPA] at pH=3, 298 K**

[DTPA], M	$D_{Eu}$	$D_{Am}$	$SF = \frac{D_{Eu}}{D_{Am}}$
0	298	$14.1 \times 10^1$	2.1
$10^{-5}$	27.6	$1.9 \times 10^{-1}$	145
$10^{-4}$	4.9	$6.5 \times 10^{-2}$	75
$1 \times 10^{-3}$	0.8	$1.7 \times 10^{-2}$	45
$5 \times 10^{-3}$	0.24	$2.5 \times 10^{-2}$	10

DBHeP and 1.1 M DBOP in *n*-dodecane as compared to TBP. The extraction of uranium and plutonium by phosphonates is higher than that of TBP. There is no third phase formation in the extraction of uranium by these phosphonates and the loading of the uranium in the organic phase is close to the theoretical value. Our studies revealed that DBHeP and DBOP are promising candidates for the preconcentration of uranium and plutonium from acidic media by extraction chromatography mode.

Glycolamic acids are promising candidates for the separation of lanthanides from aqueous medium. We have developed two glycolamic

**Table 3: Variation in the distribution ratios of  $^{152+154}Eu$  and  $^{241}Am$  as a function of pH at 298 K; Organic phase: 0.3 M SHDEHDGA/*n*-DD, Aqueous Phase: [HNO<sub>3</sub>]**

PH	$D_{Am}$	$D_{Eu}$	$SF = \frac{D_{Am}}{D_{Eu}}$
2.5	$8 \times 10^{-2}$	$7 \times 10^{-3}$	11
3.0	$17 \times 10^{-1}$	$12 \times 10^{-3}$	141
3.5	10	$2 \times 10^{-2}$	200

acids: di-2-ethylhexyldiglycolamic acid (HDEHDGA) and thio-di (2-ethylhexyl)diglycolamic acid (SHDEHDGA) for An/Ln separation studies. The structure of the glycolamic acids are shown in Figure 2. HDEHDGA exhibits superior selectivity towards

lanthanides and SHDEHDGA exhibits selectivity towards actinides. Extraction behaviour of a representative lanthanide,  $^{152+154}Eu(III)$  and a trivalent actinide,  $^{241}Am(III)$  was studied and the data on separation factors indicate that they are promising extractants for lanthanide-actinide separation. The extraction trend observed in HDEHDGA in the presence of DTPA as aqueous complexing agent shows that HDEHDGA can be employed for the An/Ln separation (Table 2). Unlike HDEHDGA, thio-derivative does not require the aqueous soluble complexing agent DTPA, for efficient separation. The distribution ratio of both  $^{152+154}Eu(III)$  and  $^{241}Am(III)$  increases with increase of pH as shown in Table 3.

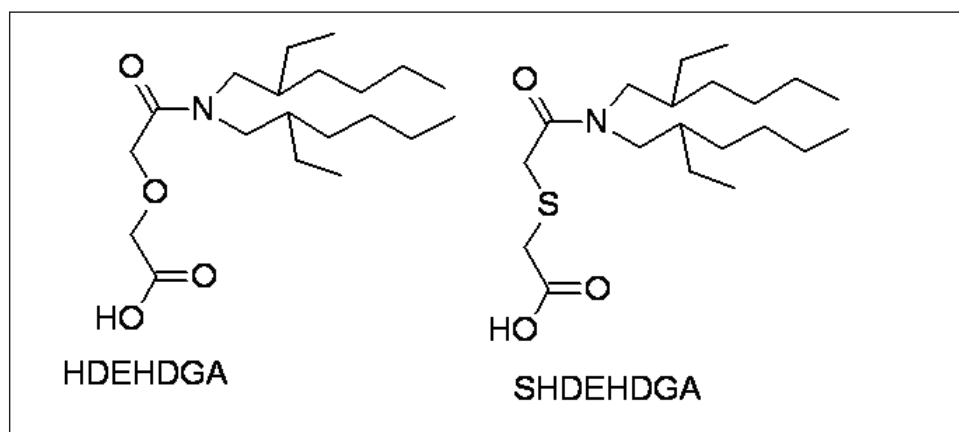


**Fig. 2** Structure of glycolamic acids

## IV.11 Liquid Chromatographic Studies of Lanthanides and Actinides on Monolith Support and their Application to Burn-up Measurement

In the recent past, chromatographic support material using monolith has been investigated for the separation of mainly organic compounds. Monolith column consists of a single piece of porous, rigid material containing mesopores and micropores, which provide fast analyte mass transfer. Silica based materials have become well

established supports in the field of chromatography. It was evident from Van Deemter plot that monolith silica provides significantly higher separation efficiency than particle-packed columns. A clear advantage of monolith is that it could be operated at higher flow rates but with lower back pressure. Higher operating flow rate results in higher

column permeability, which drastically reduces analysis time and provides high separation efficiency.

The major advantage of high performance liquid chromatography (HPLC) is its ability to provide rapid and high performance separations. Rapid and high performance separation with accurate estimation

of lanthanides and actinides such as uranium, plutonium and thorium is of great importance in the field of nuclear industry, such as burn-up measurement of nuclear reactor fuels, and high level liquid waste assay. Separation and determination of lanthanides and actinides in dissolver solution (FBTR spent fuel discharged at a nominal burn-up of 155 GWd/t) poses great challenge, as it involves handling high level of radioactivity associated with the discharged fuel. Hence the chromatographic procedure demands an efficient separation in shortest possible time.

In the dynamic ion-exchange technique, the ion-exchange surface is formed by passing water soluble modifier e.g. camphor-10-sulfonic acid (CSA) through hydrophobic stationary phase which is a <sup>18</sup>C support. Lanthanides can be separated by the exchange with the hydrogen ions present in the modifier, similar to the exchange behavior observed in conventional cation exchange resins.  $\alpha$ -Hydroxy isobutyric acid (HIBA) was used as the complexing reagent for the elution of metal ions. This technique was employed to determine lanthanide fission products such as Nd and La, uranium as well as

plutonium from dissolver solution for the determination of atom% fission.

**Separation of lanthanides**

A gradient elution procedure for isolation of individual lanthanides was developed using monolith support under the dynamic ion-exchange conditions. A large number of gradients were generated and employed by varying the concentrations of CSA  $\alpha$ -HIBA and pH of mobile phase. Based on these studies, a binary gradient elution method has been developed for the rapid separation of lanthanides, from La to Lu in about 2.8 min. In isocratic elution study, isolation of La from other lanthanide fission products such as Ce, Pr, Nd and Sm was investigated. La was separated from other lanthanides in about 1.77 min. These studies established that monolith supports could be operated at higher flow rates with low back pressure resulting into a higher column permeability, which drastically reduced separation time and also provided higher separation efficiency.

**Atom% fission determination using monolith support**

The direct injection of dissolver solution into the HPLC system was carried out and the results are shown

in Figures 1 and 2. The lanthanides present in the dissolver solution were mutually separated as well as resolved from uranium and plutonium under dynamic ion-exchange conditions from monolithic column. The concentration of La, Ce, Pr, Nd and Sm were determined in the dissolver solution using a calibration plot. Uranium and plutonium present in dissolver solution were estimated by both dynamic ion-exchange and reverse phase chromatographic techniques. The burn-up was determined using lanthanum as fission monitor and was found to be 16.1 atom%.

The development of fast separation HPLC technique using monolith, which leading to the isolation of lanthanum fission monitor from the dissolver solution in about 1.8 min, Pu(III) from other actinides and fission products in 1.18 min and that of  $UO_2^{+2}$  from other actinides and fission products in about 1.35 min resulted in the minimization of radiation exposure to the personnel. Though it is difficult to quantify at this stage, the reduction in separation times of U, Pu and La's achieved from the present work, would probably reduce the overall exposure by easily about 10 times. The overall reduction in separation time also reduces the waste that is generated during the course of the campaign.

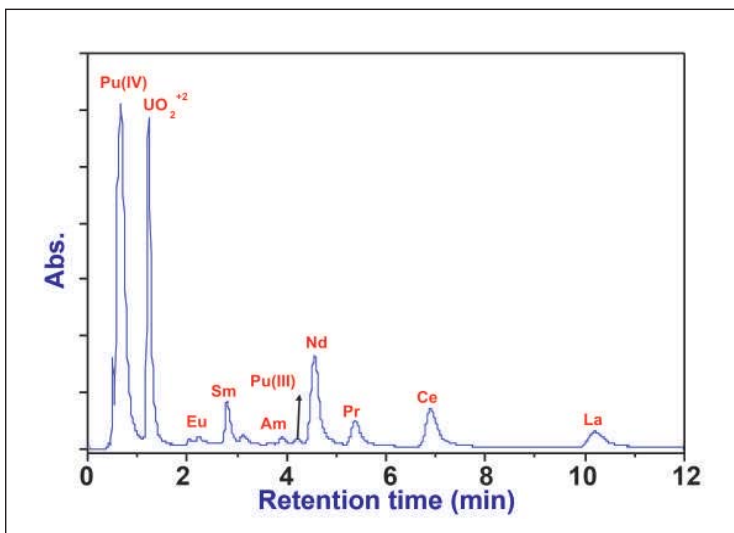


**Fig.1** Determination of U, Pu and lanthanide fission products present in dissolver solution (FBTR spent fuel discharged at ~155 GWd/t)

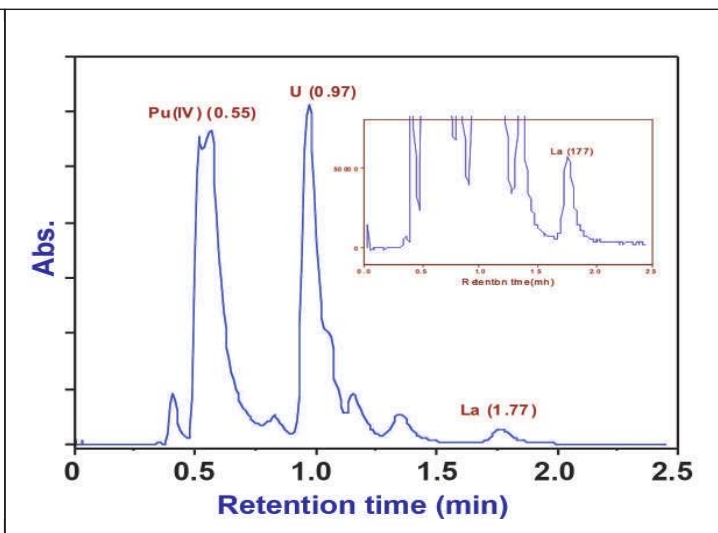


**Fig. 2** Separation and estimation of La from U and Pu present in dissolver solution in 1.8 min

## IV.12 Development of Special Gauntlets for Glove Boxes

Contamination and uncontrolled release of radioactive materials are prevented by confining the radioactive solutions in glove boxes. The gauntlets used in the glove boxes must resist permeation, degradation and penetration by the chemicals to which they are exposed to.

The gauntlets available in local markets have very short service life when they come into contact with the two chemicals, 30% TBP in NPH and 4 to 6 M nitric acid used in the aqueous reprocessing of FBR spent fuels by PUREX process. Hence, in collaboration with Indian Rubber Manufacturer's Research Association (IRMRA), Mumbai, a two stage developmental work was initiated to fabricate a product with better performance and longer service life in the most extreme conditions. In the first stage, rubber compound based on neoprene (CR), hypalon (CSM) and nitrile (NBR) elastomers having good resistance to the above chemicals was developed. In the second stage, gauntlet samples were fabricated by moulding technique, from each of the rubber compounds developed.

### Development of rubber compounds

For the development of rubber compounds, poly chloroprene rubber (Grade B-30) was the starting material. Mixing with the additives was done as per ASTM D-3182 practice in a laboratory two-roll mill using the mixing cycle for the required formulation. At the end of the mixing cycle, the compound was refined to ensure better dispersion of the compounding ingredients by

Property	Neoprene	Hypalon	Nitrile
Tensile strength, kg/cm <sup>2</sup>	173	175	191
Elongation at break (%)	342	347	393
300% Modulus, kg/cm <sup>2</sup>	138	110	120
Hardness, Shore A	56	52	62
Tear strength, kg/cm	32	25	40

doing several passing in the mill. Test slabs and buttons of the mixed compounds were obtained by compression-moulding technique as per ASTM D-3192 procedure and according to the optimum cure time got from rheometric studies.

The mechanical properties determined and listed in Table 1 for the three rubber compounds developed with suitable chemical formulation were found to be superior to those values determined for the commercially available gauntlets. The chemical resistance of the rubber compounds to organic solvents and nitric acid was evaluated by immersion test as per ASTM D-471 standard. The mechanical properties of the compounds before and after testing in the solvent and acid are compared in Table 2.

During immersion in organic solvents, rubber compounds

dissolve layer by layer resulting in the degradation of mechanical properties. The deterioration in the properties was more pronounced in neoprene and hypalon compounds. On the contrary, the increase in hardness value was found to be more in nitrile rubber and it should be considered that the extent of degradation in all the three compounds is more or less equal. The elongation at break of rubber compounds before and after testing in the solvent and acid is compared in Figures 1 (a) and (b) respectively as histograms.

After soaking in nitric acid, neoprene and hypalon rubber compounds showed a marginal increase in their mechanical properties, probably due to surface oxidation. However, the change in hardness was found to be insignificant. In the case of nitrile rubber compound, the hardness value had increased significantly (Table 2) and as the flexibility for its use as gauntlet decreases, it may not

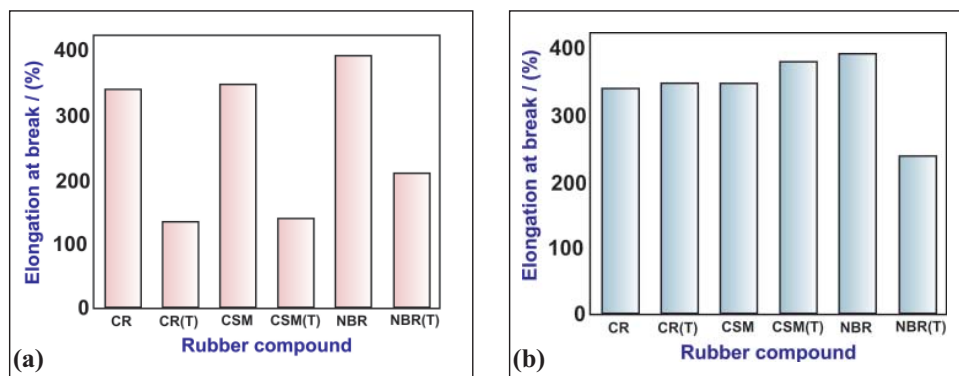


Fig. 1 (a) Plot of elongation at break of rubber compounds before and after immersion in solvent (b) Comparison of elongation at break of rubber compounds before and after testing in nitric acid (T) indicates after testing

**Table 2 : Degradation in mechanical properties of the rubber compounds after immersion test in organic solvent and nitric acid**

Chemical	Elastomer	Before immersion			After immersion		
		Tensile strength (kg/cm <sup>2</sup> ), (σ)	Elongation at break (%), (σ)	Hardness Shore A (σ)	Tensile strength (kg/cm <sup>2</sup> ), (σ)	Elongation at break (%), (σ)	Hardness Shore A (σ)
30% TBP in NPH	Neoprene	173 (7)	342 (9)	56 (2)	30 (3)	136 (10)	46 (3)
	Hypalon	175 (11)	347 (12)	52 (1)	29 (4)	142 (14)	42 (2)
	Nitrile	191 (8)	393 (10)	62 (2)	72 (3)	208 (8)	51 (2)
4 M nitric acid	Neoprene	173 (7)	342 (9)	56 (2)	187 (5)	351 (12)	57 (1)
	Hypalon	175 (11)	347 (12)	52 (1)	206 (7)	384 (9)	54 (2)
	Nitrile	191 (8)	393 (10)	62 (2)	96 (4)	240 (8)	77 (2)

be a proper choice in acid environment. The mechanical properties and chemical resistance of the rubber compounds were observed to improve by incorporating optimum quantity and proper grade of nano carbon. Using suitable curing agent and accelerators, the cross-link between the polymer chains can be controlled to yield compound with superior properties in order to resist the attack by chemical vapour. The developed rubber compounds in general, were found to be compatible with the chemicals, as the changes in mechanical properties are within allowable limits prescribed by ASTM standards. Fabrication by moulding process increases the density of the finished product. Therefore, in the second stage, gauntlet samples with

neoprene, hypalon and nitrile rubber as base materials were developed by moulding technique. Specimens cut from various locations of these gauntlets were tested for uniformity in mechanical properties and thickness. Visual and physical examination of the gauntlets for permeation and penetration yielded satisfactory results. For real time testing of the gauntlets, they were fitted to a glove box of the hot cell and their performance is being evaluated. After a period of six months, the gauntlets which were exposed to the vapour of solvent and nitric acid did not show any appreciable damage. For the sake of comparison, a pair of imported gauntlets was also attached to the

same glove box. Performance of the indigenously developed gauntlets was found to be equivalent or better than that of imported ones. As the mechanical properties of neoprene and hypalon gauntlets appeared to be better than those of nitrile rubber after immersion test, the former two rubber compounds will be selected for bulk production of gauntlets for service in corrosive and radiation environment.



Fig. 2 Photograph of neoprene gauntlet

### IV.13 Pyrolytic Graphite - Potential Candidate Material for Pyrochemical Reprocessing Applications

**M**etallic fuelled fast breeder reactors with pyrochemical reprocessing is chosen as the best option for future energy security. The most important part in implementation of the pyrochemical reprocessing technology involves identification, development and testing of corrosion resistant materials/coatings for service in

molten LiCl-KCl salt at high temperature for various unit operations. Graphite is one of the candidate materials for the fabrication of various crucibles and liners in salt purification and cathode processor operations involving high temperatures and molten chloride environment. The advantage of graphite includes easy fabrication

into containers of various shapes and good high temperature strength and thermal shock resistance. However, graphite undergoes degradation by forming intercalation compounds with molten salts and suffers from poor structural integrity. Due to limited life for application as containers and liners, often

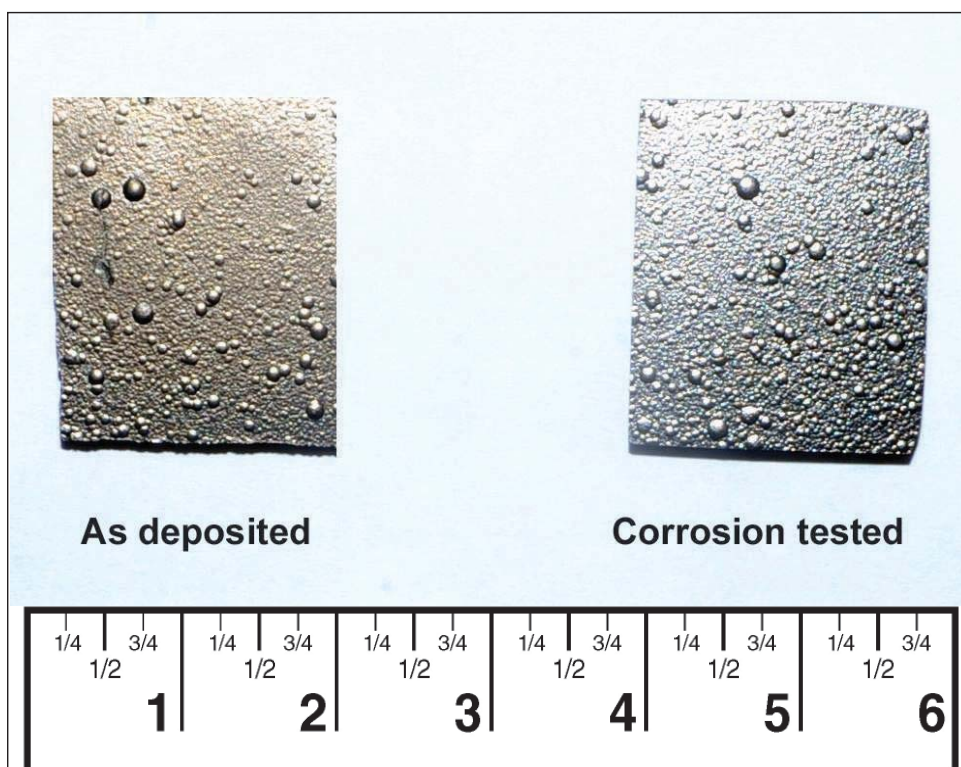


Fig. 1 Photographs of pyrolytic graphite sample

replacement necessitates and leads to accumulation of solid waste.

Pyrolytic graphite (PyG) and ceramic materials like  $ZrO_2$ ,  $Y_2O_3$ ,  $SiO_2$ ,  $Al_2O_3$ , and ceramic composites are proposed as candidate coating materials for corrosive molten salt environment. The strength of PyG increases with increasing temperature in contrast to most materials whose strength decreases with increasing temperature. The increase in strength of PyG with increasing temperature was attributed to the change in microstructure, layer order and preferred orientation. Pyrolytic graphite has greater oxidation resistance than normal graphite due to its impervious nature. Apart from this, PyG shows excellent strength, toughness, and ductility and is extremely resistant to corrosion in a wide range of environments. For pyrochemical reprocessing applications involving molten chloride environment, PyG has been proposed as a potential candidate material and efforts are being made to develop and test pyrolytic graphite

for molten chloride applications. Pyrolytic graphite can be deposited by pyrolysis of hydrocarbon gas as such as methane, propane and benzene at reduced pressure and at temperatures above 2273 K. Characterisation of PyG by XRD showed high preferred orientation along (002) plane with interlayer spacing ( $3.42 \text{ \AA}$ ) and crystal size

(24.94 nm) indicating that PyG has nearly ordered structure. Pyrolytic graphite plates of desired dimensions were cut and tested in molten LiCl (44.48 wt%)–KCl (55.52 wt%) eutectic salt in ultra high pure argon atmosphere at 873 K for 2000 h. The weight loss of the PyG samples were found to be insignificant and PyG samples exhibited no degradation or cracks increase in the surface brightness was also observed (Figure 1). The as deposited and corrosion tested samples were examined by optical microscopy, SEM and atomic force microscopy (AFM). The surface morphology of corrosion tested samples did not show any change and was similar to that of as-deposited surface of pyrolytic graphite (Figures 2a-d).

The results from this study clearly indicated that PyG has excellent corrosion resistance in molten LiCl-KCl eutectic mixture at high temperatures and is a potential candidate material for pyrochemical reprocessing applications.

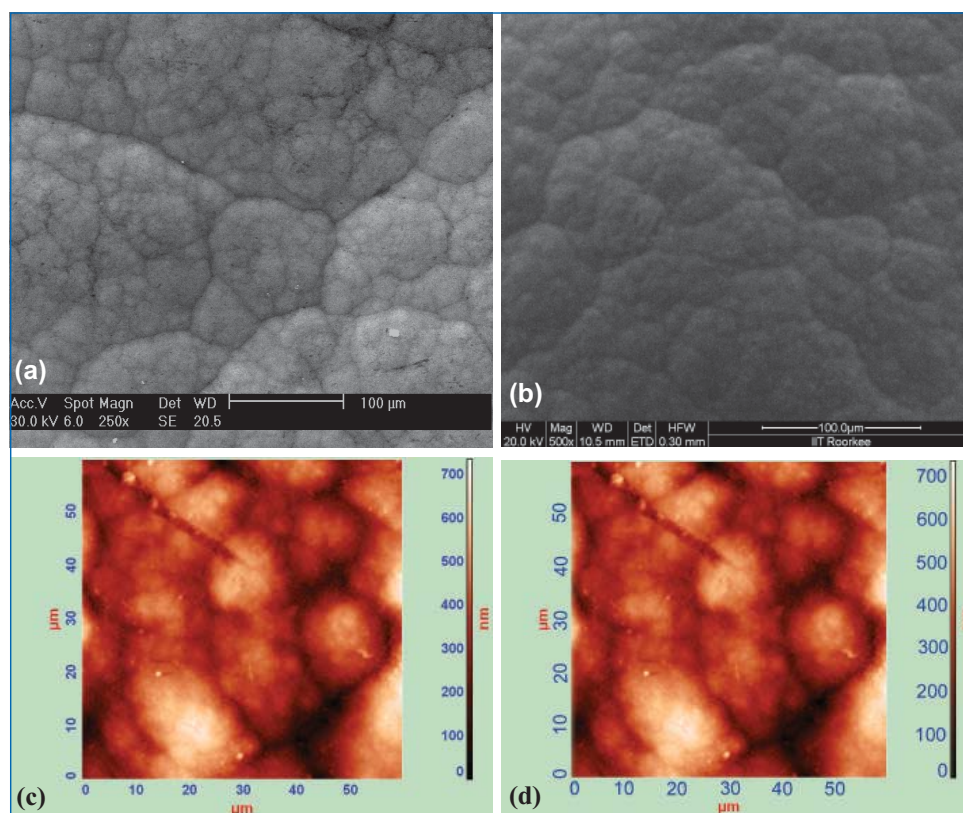


Fig. 2 SEM micrograph and AFM topography of pyrolytic graphite sample (a & c) as deposited (b & d) after corrosion test in molten salt at 873 K for 2000 hours

## IV.14 Studies on Pyrochemical Reprocessing

An engineering scale demonstration facility for carrying out studies on the molten salt electrorefining process on 1-2 kg of uranium alloys was commissioned. High purity of the argon gas with less than 50 ppm of oxygen and moisture was realized in this facility. The facility incorporates a pin chopper, an electrorefiner and a cathode processor. It is also provided with a crane and a power manipulator for enabling remote operations (Figure 1). A salt purification system was also commissioned and about 13 kg of LiCl-KCl eutectic salt mixture was purified from moisture by chlorination at 673 K. Purified salt loaded with 5 wt%  $\text{UCl}_3$  by adding stoichiometric amounts of  $\text{CdCl}_2$  to it and then equilibrating with uranium metal at 773 K was introduced in the electrorefiner. The completion of loading was checked by analysing the salt samples for Cd and U at periodic intervals. Then the first electrorefining experiment was carried out at 773 K using 1 kg of U metal as the anode and a steel rod as the cathode. During electrorefining, U metal was deposited on the solid rod cathode and it was occluded by the electrolyte salt. The deposit was scrapped from the cathode rod and collected (Figure 2). 5 kg of cadmium metal was charged to the electrorefiner which forms a liquid



Fig. 1 Engineering scale demonstration facility for pyroprocessing studies

pool at the bottom of the electrorefiner. It is intended to collect any uranium metal deposit falling off the cathode due to poor adherence. Electrorefining was carried out in galvanostatic mode for 96 hours. Samples of the cathode deposit, cadmium pool and the salt were analysed for their uranium contents. Amount of  $\text{UCl}_3$  in the salt was found to remain unchanged throughout the electrorefining run. Current efficiency was computed from these results to be 68%.

The DIFAC (DIFfusion of Actinides in EleCtrorefiner) computer code based on the diffusion layer at the electrodes has been developed to simulate the electrodeposition behaviour of actinides and fission products including zirconium in an electrorefining cell. The dissolution of U-Pu-Zr from the anode basket and the subsequent deposition of actinides at the cathode are assumed to be fast and in equilibrium. It is also assumed that the concentration of actinides and fission products are uniform in the salt and Cd phases except in the vicinity of the electrodes and the concentration gradient is approximated to be linear within a hypothetical layer called the diffusion layer. The modelling of the electrodeposition behaviour of

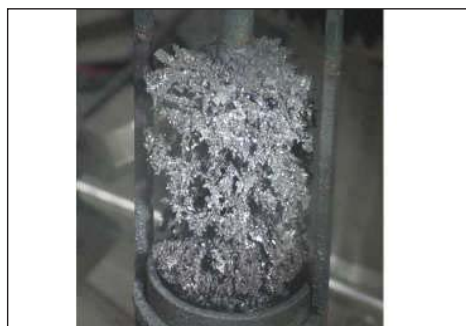


Fig. 2 Uranium metal deposited on solid rod cathode in the electrorefining cell

U-Pu-Zr in the electrorefining cell would require these diffusion layer thicknesses for each of the species. Polarization and constant current dissolution and deposition measurements were carried for various concentrations of uranium and zirconium in molten LiCl-KCl eutectic in the temperature range 762-837 K and the diffusion layer thickness for U and Zr were measured. Subsequently, the cell voltage and cell resistance during the anodic dissolution of U and Zr were modelled using the diffusion layer thickness. A typical polarization curve for Zr dissolution in molten LiCl-KCl eutectic at 807 K is shown in Figure 3.

Recently, it was discovered that metal oxides in the solid form could be directly reduced to metal by molten salt electrolysis. In this process, the metal oxide is used as the cathode, graphite or platinum as the anode and molten mixture of lithium chloride-lithium oxide or calcium chloride-calcium oxide as the molten electrolyte. The metal oxide cathode transforms itself to the metal by electrolysis and the oxygen released at the cathode discharges as carbon oxides on graphite or as oxygen gas on platinum anode. Currently, the process is being studied for the conversion of spent oxide fuels to

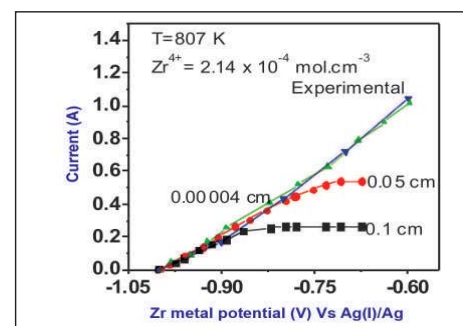


Fig. 3 Polarization curve for zirconium dissolution in molten LiCl-KCl eutectic

metallic form for consolidation and/or reprocessing in the pyrochemical method.

As a part of the study on this process, compacted and sintered pellets of niobium pentoxide were reduced in molten calcium chloride at 1173 K with graphite as the anode. The pellets (20 mm dia. x 3 mm thickness) were sintered at 1673 K and had an open porosity of ~ 4 %. Electrolysis was carried out at a constant current of 0.5 A for 40 hours. The results of a typical experiment are given below. SEM micrograph of the electrolysed product (Figure 4) and the XRD pattern show that the metal oxide was completely converted to Nb metal.

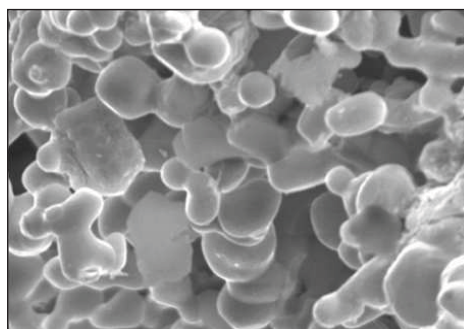


Fig. 4 SEM image of reduced pellet surface

Porous  $UO_2$  pellets too were reduced likewise, but with platinum as the anode. Unlike in the case of  $Nb_2O_5$ , the reduction was limited to a thick layer of uranium on the surface of the  $UO_2$  pellets. This typical behaviour was attributed to the sintering of uranium metal at the operation temperature of the cell (1173 K), which blocked the

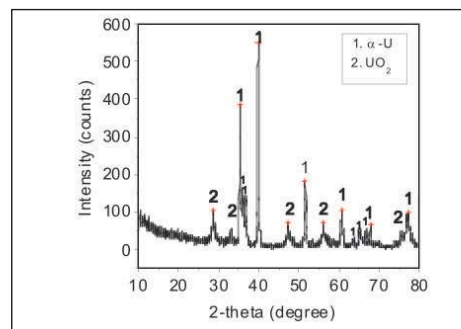


Fig. 5 XRD pattern of the polished surface of the  $UO_2$  pellet after electro-deoxidation

electrolyte access to the bulk of the pellet and hence, the bulk reduction (Figure 5). Further studies showed that  $UO_2$  in the form of thin discs (~ 1 mm thick) could be reduced in molten calcium chloride whereas porous preforms of higher thickness can be completely reduced in low-temperature lithium chloride-lithium oxide molten salt system (923 K).

## IV.15 Development of Solvent Regeneration Process by Vacuum Distillation

To recover uranium and plutonium from spent nuclear fuel, tri-butyl phosphate (TBP) diluted with *n*-dodecane (NDD) is used as a solvent in the PUREX process employed in fuel reprocessing plant (i.e. the solvent is a mixture of Tri-*n*-butyl phosphate and *n*-dodecane; 30%TBP+70% NDD). During the extraction, solvent is degraded under the influence of acid attack and radiation effect. The extent of degradation varies with the exposure of the organic extractant phase to radiation and reactive chemicals during the processing of the aqueous feed. The presence of degradation products even at concentrations of  $10^{-5}$  to  $10^{-3}$  M in the solvent influences extraction performance. The most significant single parameter which affects solvent extraction process operability

and product quality is the quality of the solvent. Hydraulic stability of the solvent extraction contactors and decontamination of the heavy metal from the fission products is directly traceable to the solvent quality. Hence, the solvent must be purified before it is recycled back to process. The primary degradation products of TBP are di-butyl-phosphate (HDBP), mono-butyl-phosphate ( $H_2MBP$ ), phosphoric acid and butyl alcohol and the diluent's primary degradation products include nitro alkanes, hydroxamic acids, carbonyls and alkyl nitrates.

A variety of methods have been proposed for cleanup of used solvent in the PUREX process to minimize the various problems encountered when the degradation products accumulate in the recycled solvent.



Fig.1 Pilot plant solvent purification system

The primary degradation products of the solvent can be removed by scrubbing with alkali solution, but secondary degradation products of solvent and diluent which are essentially surface tension-active

**Table 1: Results of a typical pilot plant run**

Stream	$\rho$ (g/cc)	Compositions %					
		TBP	NPH	C <sub>10</sub>	C <sub>11</sub>	C <sub>12</sub>	C <sub>13</sub>
Feed	<b>0.797</b>	27.12	72.88	15.64	21.03	<b>19.94</b>	16.20
Top Product	<b>0.741</b>	0.23	99.77	27.72	33.10	<b>26.14</b>	12.74
Bottom Product	<b>0.859</b>	47.50	52.50	2.79	12.06	<b>17.66</b>	20.15

agents and complexing agents of plutonium, zirconium and ruthenium, cannot be removed by alkali wash and they are accumulated in the solvent. A common method for purifying organics is distillation. Considerable effort has been devoted to the development of this method for solvent purification. The instability of tri-n-butyl phosphate at elevated temperature requires evaporator and distillation columns to be operated at reduced pressure.

A pilot plant scale solvent purification system (about 15 LPH capacity) based on vacuum distillation method was designed, developed and commissioned at Reprocessing Group, IGCAR. The photograph of the solvent purification setup developed is shown in Figure 1. Solvent recovery system is an integration of different liquid-vapour separation units. Spent solvent (degraded solvent) is first fed through alkali and then passed through a dehydration column, where water vapour is evaporated. Necessity of dehydration column arises from the fact that water will

behave as non-condensable vapour in the condenser of the main distillation unit owing to the low operating pressure of 1mm Hg. Dehydration is performed under reduced pressure (30 mm Hg) in a counter current evaporator.

The design of the purification process is based on the design of falling/wiped film evaporator and distillation column, which are operated at 10 and 1 mm Hg respectively. In the first step of the process, damaged solvent containing degraded products is passed through a wiped film evaporator, wherein the solvent is evaporated to the level of 95% and the 5% residue containing all the heavy compounds (degradation products of solvent) is discarded as waste product. The solvent vapours are then passed into a rectification column, where *n*-dodecane (99%) as top product and the bottom product of 60% TBP are obtained.

**Modeling and simulation of distillation column**

The mathematical modeling of distillation column for the separation

of the binary mixture of TBP-NDD system is based on mass balances and the equilibrium vapour-liquid equations. The model is based on the assumptions of constant flow rate for liquid and vapour, constant holdup, negligible vapour hold, total condenser, adiabatic column and theoretical trays. The experimental vapour-liquid equilibrium data of TBP-NDD system at 1 and 10 mm Hg pressure are shown in Figure 2. The mass balance equations for distillation column are solved numerically in order to obtain concentrations in stages.

The transient concentration profile are shown in Figure 3. From the simulation it was observed that a maximum of three theoretical stages are sufficient to obtain effective separation between the two. Based on the simulation results, dimensions of distillation column were arrived.

**Commissioning results of the pilot plant**

Initial trial run of the plant was conducted with 70 liter of 30 % TBP (diluent:n-paraffin hydrocarbon,NPH). The feed rate to the plant was maintained at 15 l/h. The performance of the process and auxiliary equipment were evaluated by monitoring the distillation column top product. About 30 liter of distillation column top product with 99.78% purity NPH and 20 liter of bottom product with 47.5% TBP concentration were obtained from the trial runs. Results of a typical run listed in Table 1 reveals the increase in C<sub>12</sub> to 26.14% from the feed value of 19.94% in the top product from the distillation column, whereas C<sub>13</sub> content increased from 16.2% in the feed to 20.15% in the bottom product. Detailed experimental runs with different operating conditions to optimize the process parameters are in progress.

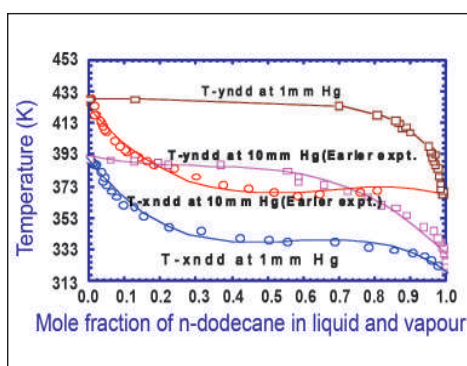


**Fig. 2** VLE data of TBP – NDD system

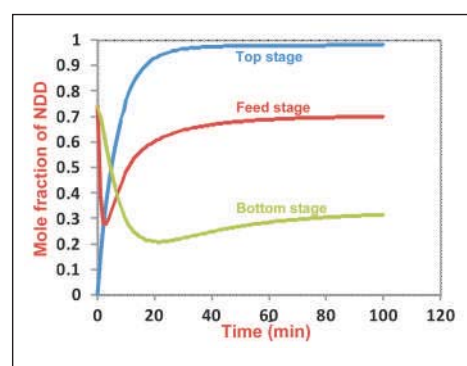


**Fig. 3** Transient concentration profile in column

## IV.16 Removal of Cesium From Simulated Waste: using AMP-PAN Resin Experiments and Numerical Analysis

One of the important goal of the radioactive nuclear waste treatment program is the selective removal of  $^{137}\text{Cs}$  from radioactive wastes. AMP is known as the best candidate for the removal of cesium from acidic waste. It has high selectivity and capacity for cesium and posses good mechanical strength to be used in large scale applications. Laboratory scale and pilot scale experiments has shown that cesium is being removed by ammonium molybdo phosphate in poly acrylo nitrile matrix (AMP-PAN) resin successfully in the presence of other ions. AMP-PAN resin and polymer coated resin were prepared and studied for absorption of cesium.

Numerical analysis has been carried out to determine the mass transfer coefficient of the resin-Cs system. The analysis results were validated with literature data and pilot scale experiments Figure 1. The values found form the analysis, can be used for the design of the column for large scale applications.

Equilibrium experiments were conducted with both coated and non coated resin to find out distribution coefficients ( $K_d$ ) in different concentrations of nitric acid. From the experimental results, it was seen that the  $K_d$  values decreases with increase in the Acidity of Nitric Acid Medium. The trend is given in the following graph (Figure 2).The  $K_d$  values for coated resin is slightly lower than the non coated resin, the resistance offered by the coating in



Fig.1 Pilot plant set up for cesium removal

the coated resin is higher compared to non coated resin. The same property is useful when the resin is used for repeated number of cycle of adsorption and elution of cesium.

The  $K_d$  values for coated resin is slightly lower than the non-coated resin, the coating offered the resistance and would be useful where resin is used for multiple cycles.

In order to find out the effective usage of the resin, repeated adsorption and elution of the resins were carried out. Initially, the Cs in 4 N nitric acid medium was loaded in the resin. Then, the loaded cesium was eluted using saturated

ammonium sulfate solution. The same procedure of loading and elution was repeated for 10 numbers of cycle .The amount of Cs loaded and eluted each cycle for both coated and non-coated resins were calculated. It was seen that the amount of cesium eluted increases up to five cycles and after that it reaches saturated value. Also, column experiments were carried out for coated AMP-PAN resin, as shown in Figure 3. The numerical analysis was carried out for determination of mass transfer coefficient of the cesium removal system using AMP-PAN resin.

The solute mass balance and rate equations were solved numerically using Finite Difference Method. The

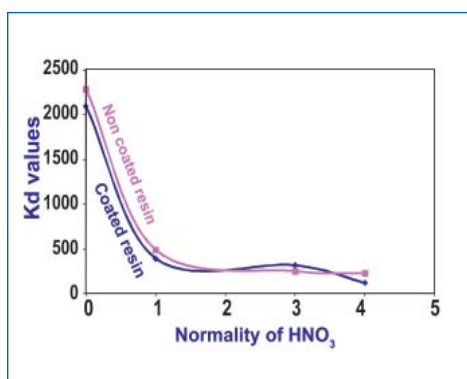


**Fig. 2** Variation of  $K_d$  under different concentration of Nitric acid for coated and non coated resin

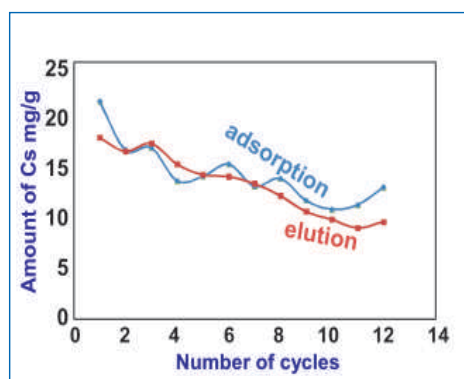


**Fig. 3** Adsorption and elution of Cs for coated resin by column experiments

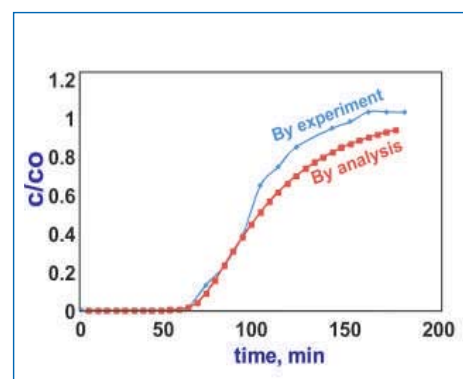


**Fig. 4** Comparison of experimental and analysis data

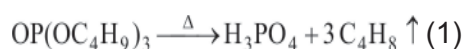
following parameters were taken for the analysis. diameter-2.52 cm, height =12 cm, porosity of 0.78. Since this adsorption follows Langmuir isotherm, the  $Q^0$  (maximum loading in the resin) 1.398 mole/cc, and Langmuir constant  $K_d=1E7$  cc/mole

were used. The outlet concentration of the solution from the column were predicted and the breakthrough was plotted. The results were compared with the experimental data and the mass transfer coefficient was determined, as shown in Figure 4.

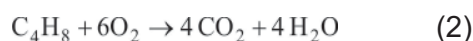
The effect of various parameters like, flow rate, bed porosity and bed height were also studied using this numerical model. The analytical results were validated with literature data and also with the pilot scale experimental data.

## IV.17 Thermal Stability of Extractants and Pressurization during Heating in Adiabatic Conditions

**T**ri-iso amyl phosphate (TiAP) is being proposed as an alternate extractant to TBP. The generally agreed thermal decomposition of TBP is listed as follows:



The product, butene is converted to combustion products in the presence of a metal as



Equation 2 predicts about 0.39 MPa/g of TBP pressurization at 523 K in a 1 litre autoclave. However, we could observe that pressurization was in excess of 3.45 MPa/g in a 1 litre metal autoclave. Therefore, the overall decomposition scenario is much more complex as compared to the simple set of equations 1 and 2. Decomposition route of TiAP is expected to be entirely different from equation 1. In this case, long chain

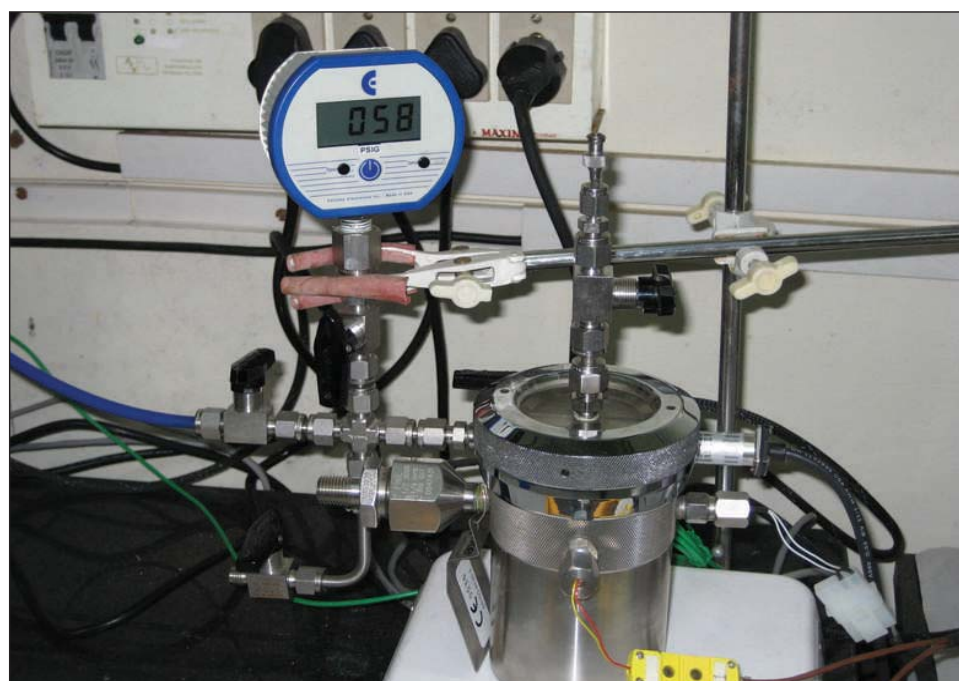
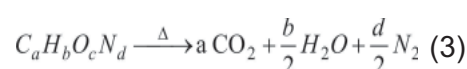


**Fig. 1** Adiabatic calorimeter setup

polyphosphates are supposed to be formed and absence of butene shall reduce the pressurization significantly. In the case of a CHON compound, following decomposition reaction may be assumed:



On the similar lines, one may write decomposition scheme for N, N, N',N'-tetraoctyl diglycolamide (TODGA) as follows:

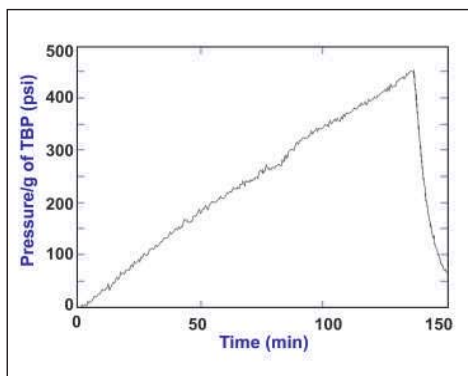


**Fig. 2** Pressure history for decomposition of TBP under adiabatic condition

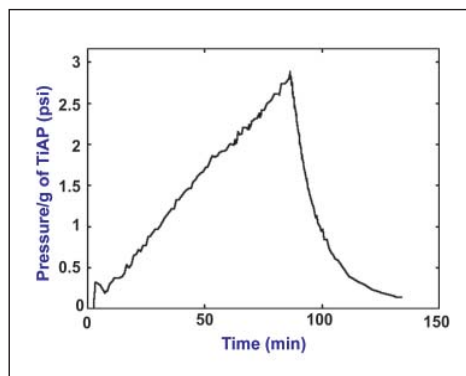
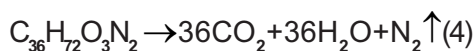


**Fig. 3** Pressure history for decomposition of TiAP under adiabatic condition



As per equation 4, at 523 K, the hypothetical pressurization owing to thermal decomposition of TODGA would be about 0.41 MPa/g of TODGA in a 1 litre autoclave. This value is marginally higher than that for TBP as predicted on the basis of equations 1 and 2. As there are no experimental data available in the open literature on thermal decomposition of extractants used in nuclear extraction, in the confined spaces and resulting pressurization, we have investigated the same in an adiabatic calorimeter in closed-vent conditions.

Adiabatic calorimeter setup (shown in Figure 1) consisted of a glass cell of 10 ml volume, a 24 Ω electrical band heater for heating, K-type thermocouple for sensing the temperature inside the cell and mineral wool insulation as well as encapsulation in aluminum foil for

minimizing the heat transfer with surroundings. The cell was put in a 350 ml high-pressure Paar Bomb, sealed and pressurized to 0.5-0.55 MPa to minimize evaporation during early heating. Agitation was provided by a powerful magnetic stirrer. A dedicated controller provided different modes of operation viz. free-run programmed ramp as well as DSC mode. Electronic pressure sensing module was calibrated in-situ at two points using digital pressure gauge mounted on the system. A weighed amount of the sample (~20 mg) was taken inside the glass cell and a 5-7 mm long piece of SS-316 3/16" wire was introduced into the cell to simulate the metal surface. After sealing and pressurization, the isolated cell was heated electrically at a rate of approximately two degree per minute in PID control mode. Temperature and pressure data were logged by system software at an interval of about 7 kPa as well as one

degree. For a 350 ml vessel, the pressurization was found to be approximately 3.45 MPa/g for TBP, 21 kPa/g for TiAP and 3.8 MPa/g for TODGA at 523 K as shown in Figures 2 to 4. In all the three cases, pressurization was much higher than the predicted values from equations 1-4 and the same is attributed to numerous side-reactions during heating as well as complex reaction network of decomposition. From Figures 2 and 3, it was observed that pressurization for TiAP was about two orders of magnitude lower than that for TBP. Thus, it appears that use of TiAP as a nuclear extractant may be safe even during accidental heating.

Role of diluents for pressurization incidents was also investigated. In an experimental run with 36% TiAP solvent and n-Dodecane as diluent, pressurization was studied and a peak pressure of about 2.76 MPa/g of diluted extractant was observed as shown in Figure 5. This pressurization is about 130 times the pressure generated under identical conditions for pure 100% TiAP. The excessive additional pressurization observed is due to the decomposition of C<sub>12</sub> n-alkane diluent to numerous smaller molecules. This experimental result confirms the positive role of diluent during thermal degradation and decomposition at elevated temperatures. The pressurization would be more severe in the presence of radiation.

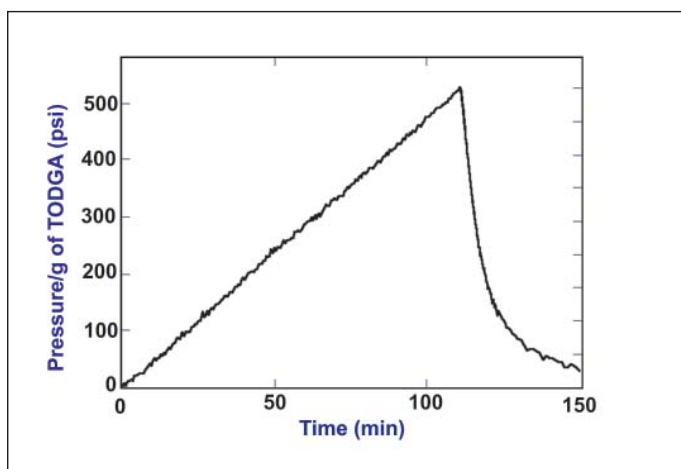


**Fig. 4** Pressure history for decomposition of TODGA under adiabatic condition

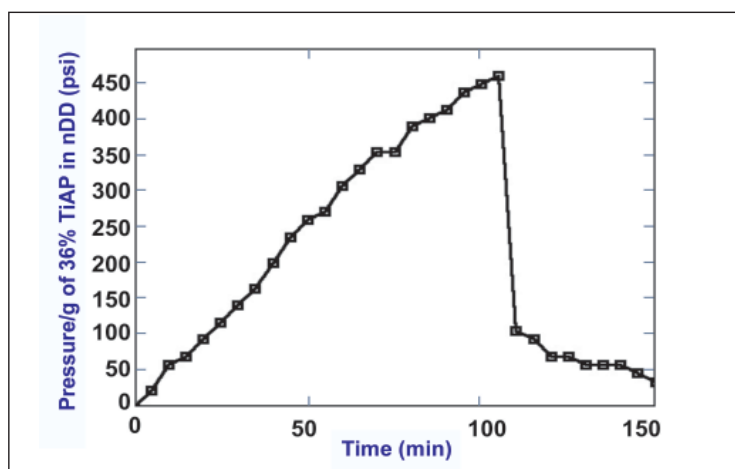


**Fig. 5** Pressure history for decomposition of 36% TiAP under adiabatic condition

## IV.18 Analytical Methods for Monitoring the Process Parameters during Reprocessing of Fast Reactor Fuels

### Spectrophotometric determination of Plutonium III, IV and VI in nitric acid solutions

The oxidation states of plutonium, which play an important role in adjusting the process conditions during the reprocessing of fast reactor fuels by PUREX process, are determined by double beam spectrophotometer. As radiation exposure is involved in analyzing active samples, fiber optic spectrometer can be used. There is a base line shift in this method due to the memory effects of the fiber optic tip. Hence, a base line correction method was established for the determination of the oxidation states of plutonium. In this method, absorbance at major peaks and subsequent troughs viz. 476–495 nm (Pu-IV), 560 – 640 nm (Pu-III) and 831–850 nm ( $[PuO_2]^{2+}$ ) from the spectrum were measured for all the three oxidation states of plutonium. The calibration plot generated from various measurements for the different oxidation states is given in Figure 1. The molar absorption coefficient calculated from the experimental absorbance for all the oxidation states at different peak-trough combination was employed for fitting into the following equations given in Table 1

Table 1: Determination of individual oxidation states of plutonium containing solution		
Species	Peak-trough combination for fitting into equations	Peak-troughs
Pu (III)	$0.02535 x_1 + 0.00492 x_2 - 0.000068 x_3$	$x_1 = 560-640 \text{ nm}$
Pu (IV)	$0.0129 x_2 - 0.001147 x_1 + 0.000763 x_3$	$x_2 = 476-495 \text{ nm}$
$[PuO_2]^{2+}$	$0.0021 x_3 - 0.00027 x_1 + 0.0000977 x_2$	$x_3 = 831-850 \text{ nm}$

for the determination of individual oxidation states of plutonium containing solution in the plant.

### Studies on the detection of third phase during reprocessing of fast reactor fuels

Spent nuclear fuels discharged from fast reactors are reprocessed by PUREX process utilizing 30% TBP as the solvent. In order to achieve high decontamination factor (DF) from fission products, higher loading of metal ions in the organic phase is necessary. During this operation, there is a possibility of formation of the third phase i.e. splitting of the single organic phase into two phases (third phase and diluent rich phase), if there is variation in the aqueous and organic flow rates. Once this third phase is formed, it may lead to criticality as well as operational problems such as ingress of organic to either aqueous

or organic phase. Hence, detection of third phase is essential in the fast reactor fuel reprocessing. Conductivity based pulsating sensor at our Centre developed by Innovative Instruments Section was employed for measuring the conductivity of the organic phases. Feasibility studies were carried out for the detection of third phase by extracting  $U^{4+}$  by 30 % TBP from 4 M nitric acid medium. Variation of conductivity of the different organic phases as a function of aqueous/organic phase ratio, shown in Figure 2 revealed that the increase in conductivity of third phase solution is appreciable when compared to the other organic phase (~100 to 300 times higher). Such a large change in the conductivity of the third phase with respect to the other organic phase can be used as a deciding parameter to get first hand information about the occurrence of third phase.

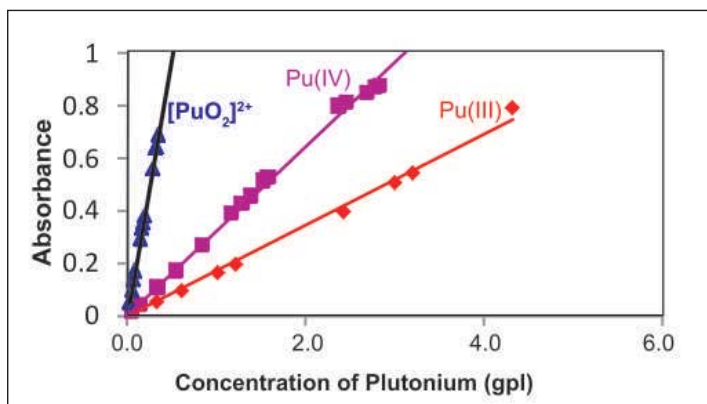


Fig. 1 Effect of the oxidation state of Pu in the feed on absorbance

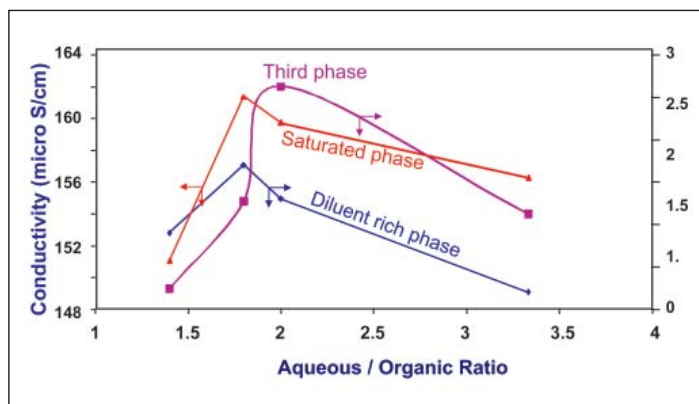


Fig. 2 Variation in conductivity as a function of A/O phase ratio

## IV.19 Application of Indigenous Nickel Alloys for Storage of Nuclear High Level Waste

Traditional austenitic stainless steels like 304L are widely used in the nuclear industries for storage of nuclear high level waste (HLW). However, they are susceptible to sensitization in the welded zones, which involves chromium depletion at grain boundaries. Additionally, these alloys also suffer from pitting corrosion and transgranular stress corrosion cracking (TGSCC) in chloride containing solutions. In order to minimize these problems, austenitic nickel based alloys are found to be good alternative to austenitic stainless steels. These alloys have a higher tolerance for alloying elements in solid solution than stainless steels but maintain good metallurgical stability. Nickel based alloys have good resistance

to a wide variety of corrosive environments in industrial processes such as chemical and petrochemical processing, marine engineering and nuclear industries. The present work was carried out to explore the possibility of using Ni based alloys for nuclear high level waste storage purpose.

The corrosion resistance of indigenous Ni 690 and Ni 693 manufactured at MIDHANI, Hyderabad, along with commercial Inconel 625 was investigated in 3 M HNO<sub>3</sub> and 3 M HNO<sub>3</sub> containing simulated high level waste at two different temperatures (298 and 323 K). The pitting corrosion resistance of these alloys at different concentrations of chloride ion (100, 250, 1000 and 2000 ppm) in 3 M HNO<sub>3</sub> were also investigated from

the potentiodynamic anodic polarization behaviour studies of the alloys. It is found that the corrosion behavior of Ni 690 and Ni 693 are in close proximity. Under ambient conditions, both the alloys possess very good corrosion resistance in both the media. These alloys were passivated spontaneously, and maintained a low passivation current density with wide passive range without exhibiting the active to passive transition peak. The passive film consisted of an oxide layer of Ni, Cr and Fe, which is characterized by XPS analysis after carrying out potentiostatic polarization in both the media. With the increase in solution temperature, the corrosion potential also increased and the passive range was decreased. This is attributed to

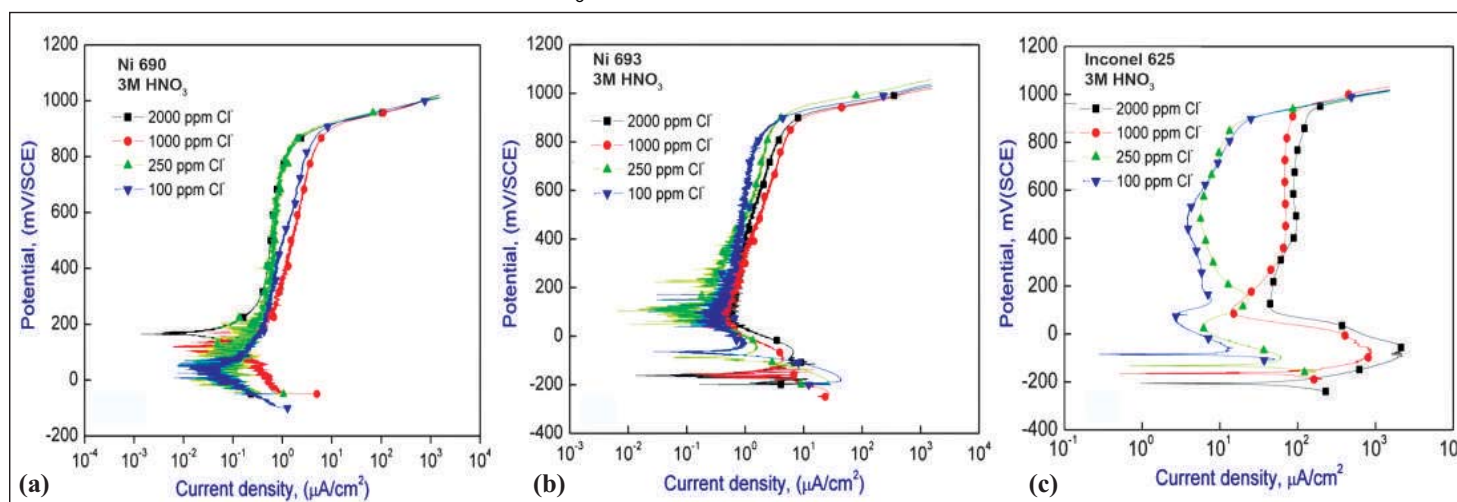


Fig. 1 Potentiodynamic polarization curves in 3M HNO<sub>3</sub> containing different concentrations of chlorides (a) Ni 690 (b) Ni 693 (c) Inconel 625

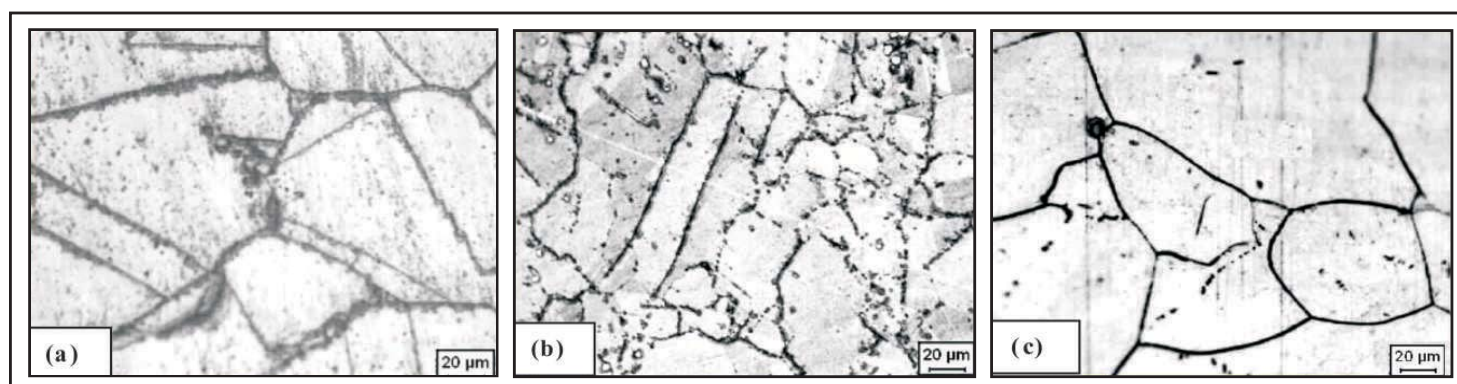


Fig. 2 Microstructure of (a) Ni 690 (b) Ni 693 (c) Inconel 625

the autocatalytic reduction of nitric acid, which has enhanced with temperature. In simulated HLW, the corrosion potential was found to be comparatively higher which is attributed to the additional cations present (that are available for reduction). Inconel 625 possesses a very high passivation current density compared to the other two alloys in both 3 M nitric acid as well as 3 M

nitric acid containing simulated HLW. Figure 1 provides the potentiodynamic anodic polarization behaviour of all the three alloys in 3 M HNO<sub>3</sub> containing different concentrations of chloride ions. Inconel 625 was found to possess an inferior pitting resistance as compared to the other nickel alloys. Though a few micro pits were found even at a concentration of 100 ppm chloride ions in the alloys

Ni 690 and Ni 693, they exhibit excellent resistance towards pitting corrosion. The microstructures of all the alloys in the as-received conditions are given in Figure 2 after etching with suitable etchants. All the alloys possess austenitic structure with clear grain boundaries. Twin boundaries were found for Ni 690, where as there were not observed in the case of Ni693 and Inconle 625.

## IV.20 High Nitrogen Nitric Acid Grade Type 304L Stainless Steel for Reprocessing Plant Applications

Type 304L austenitic stainless steel (SS) is extensively used in reprocessing and waste management plants owing to its good corrosion resistance in nitric acid medium. Corrosion investigation on high nitrogen stainless steels designated as 304LN1 (0.13%N), 304LN2 (0.19%N) and 304LN3 (0.41%N) was carried out in as-received (forged), hot rolled + heat treated (wrought) and welded conditions as per ASTM A262 Practice A, E and C tests, potentiodynamic anodic polarization in 1, 4 and 6 M HNO<sub>3</sub> at 298 K and 323 K and pitting corrosion studies in 0.5 M NaCl medium. Degree of sensitization was estimated for these stainless steels

subjected to heat treatment at 948 K for various durations ranging from 1 to 1000 hours. The addition of nitrogen showed increase in hardness as well as decrease in grain size, both of which indicate higher strength as well as wear resistance. Addition of 0.13% and 0.19% nitrogen showed better Inter granular corrosion resistance and further increase in nitrogen content resulted in deterioration due to chromium nitride precipitation. Onset of desensitization was faster for the alloys with 0.13% N as well as 0.41% N due to lower nitrogen content in the former case and finer grain size in the latter case (Figure 1). The corrosion results indicated that

there is no major difference in corrosion rate values in wrought and as-received conditions. These results were compared with those values for commercial and nitric acid grade 304L stainless steels. It is observed that the nitrogen containing 304LN1 is better than commercial 304L SS but not 304LN2 and 304LN3. The corrosion rate of nitrogen containing stainless steel particularly 304LN3 increases with test period. However the average corrosion rates of all the stainless steels were below 18 mil per year which is acceptable for reprocessing plant applications. The higher corrosion resistance of 304LN SS filler wire can be attributed to the

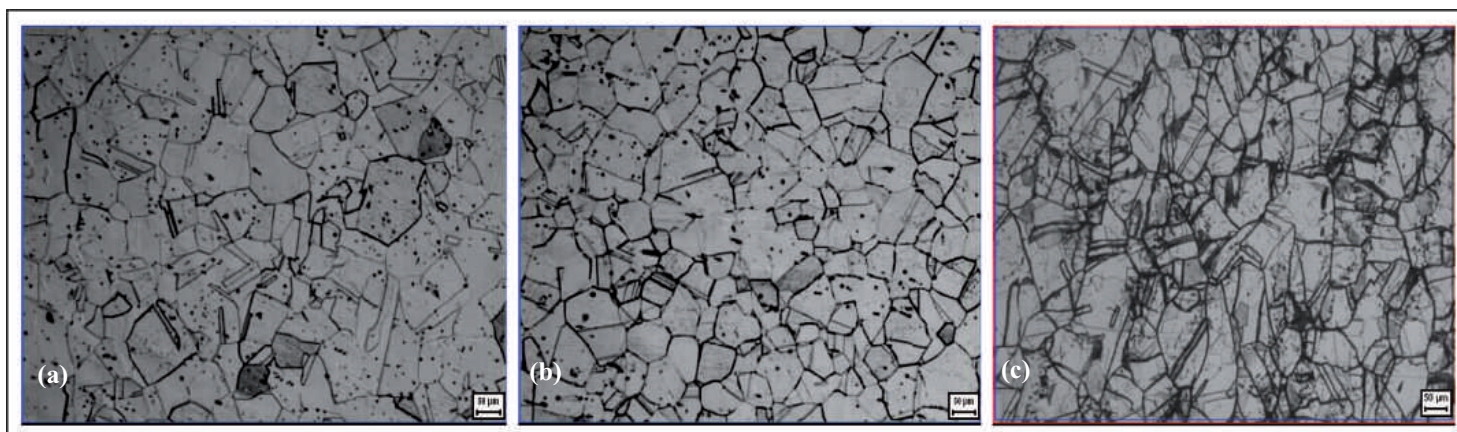


Fig. 1 Microstructure obtained in ASTM A 262 practice A test in the as received (hot rolled) conditions: (a) 304LN1, (b) 304LN2, (c) 304LN3 (575)

synergistic effect of high N, Cr and Ni content. Further, the corrosion rates of 304LN weld deposit and weldment were found to be marginally higher than the base metal.

The HNS alloys did not show any deleterious effect on corrosion resistance as the oxidizing condition was increased with increase in nitric acid concentration, and also with increase in test temperature. The beneficial role of nitrogen in enhancing the pitting corrosion resistance was observed when the nitrogen content was increased from 0.13 wt% to 0.19 wt% however, further increase to 0.406 wt %N was found to be detrimental owing to the presence of continuous network of chromium nitride and manganese

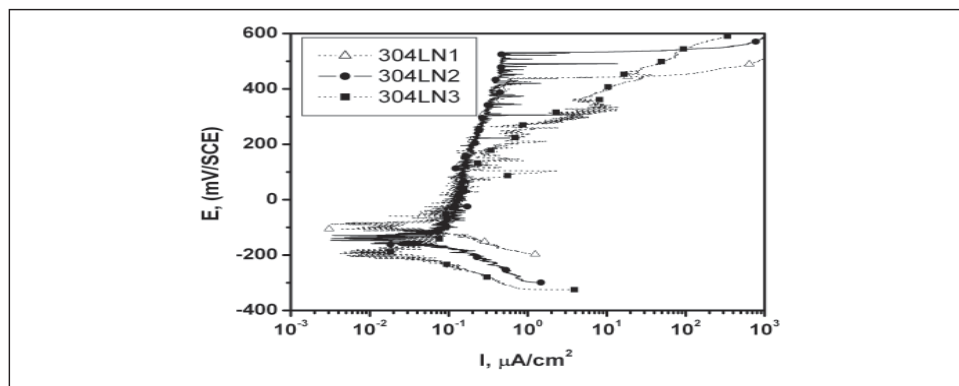


Fig. 2 Potentiodynamic polarization curves for the as-received high nitrogen stainless steel alloys in 0.5 M NaCl

rich precipitates along the grain boundaries. Nitrogen addition also showed marked effect on mechanical properties with significant increase in yield strength and very good elongation. Weldability was evaluated with filler wire drawn with the material (0.3%N) and the mechanical property evaluation showed increase in strength with nitrogen content.

Nitrogen alloying has been reported to improve the sliding wear resistance and cavitation erosion resistance of austenitic stainless steels. The outcome of the present study clearly revealed the good corrosion resistance of high nitrogen type 304LN SS coupled with improved hardness, fine grain size and wear resistance.

## IV.21 Evaluation of the Microstructure in an Explosive Clad Joint of Ti-5Ta-2Nb and 304L Steel

A titanium based alloy of nominal composition, Ti-5Ta-2Nb (Ti-Ta-Nb) is being considered as the candidate structural material for the electrolytic dissolver in reprocessing plants of fast breeder reactors due to its excellent corrosion resistance in boiling nitric acid environment. Other components of the plant are fabricated using 304L austenitic stainless steel (SS). Hence, dissimilar joint between Ti-Ta-Nb and 304L SS becomes unavoidable. Conventionally used fusion welding processes cannot be used for joining Ti-Ta-Nb and SS since it leads to the formation of Fe and Ti based intermetallic phases at the weld interface. Hence, explosive cladding, a solid state welding process was used which has been reported to give

diffusionless metallurgically bonded interface.

During explosive cladding, 304L SS was chosen as the base and Ti-Ta-Nb as the flyer plate respectively. Figure 1 shows optical microstructure and superimposed hardness profile of 'as received' explosive joints. The clad interface showed no observable change in the microstructure. However, shrinkage cavities and solidified melt zones which are characteristic features of an explosive clad were occasionally observed at the interface. Hardness profile showed high hardness of ~425 VHN very near the interface on 304L SS side of the clad. Average hardness values obtained on 304L SS base plate and Ti-Ta-Nb flyer

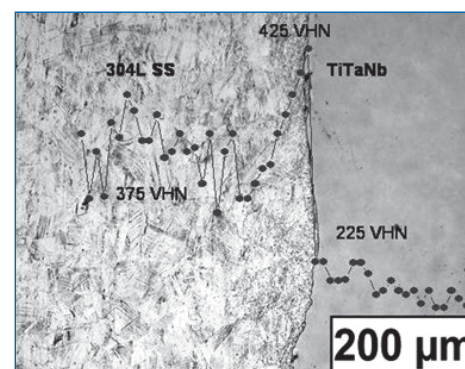


Fig. 1 Optical microstructure and superimposed hardness profile of 'as welded' explosive joints

plate were 375 and 225 VHN respectively.

To understand the increase in hardness, the base and flyer plate microstructures were more carefully examined. Figure 2 shows the optical microstructure obtained from 304L SS base plate. 304L SS normally has an equiaxed austenite structure with

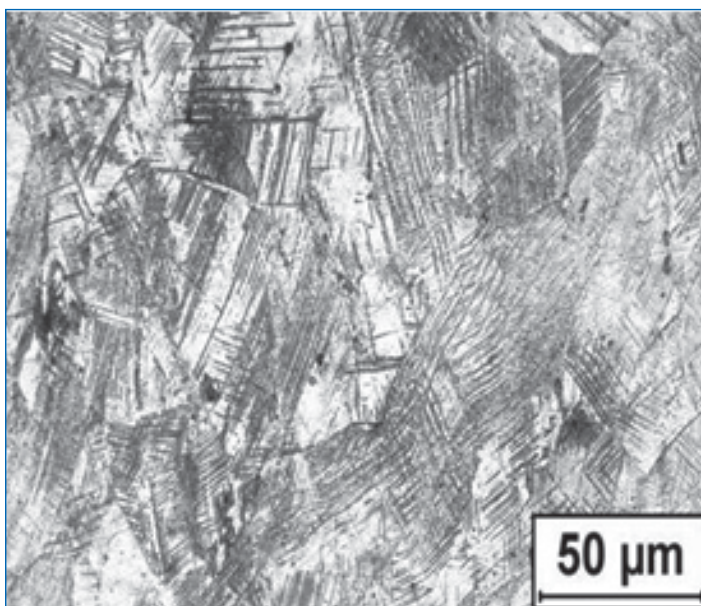


Fig. 2 Optical microstructure showing deformation twins

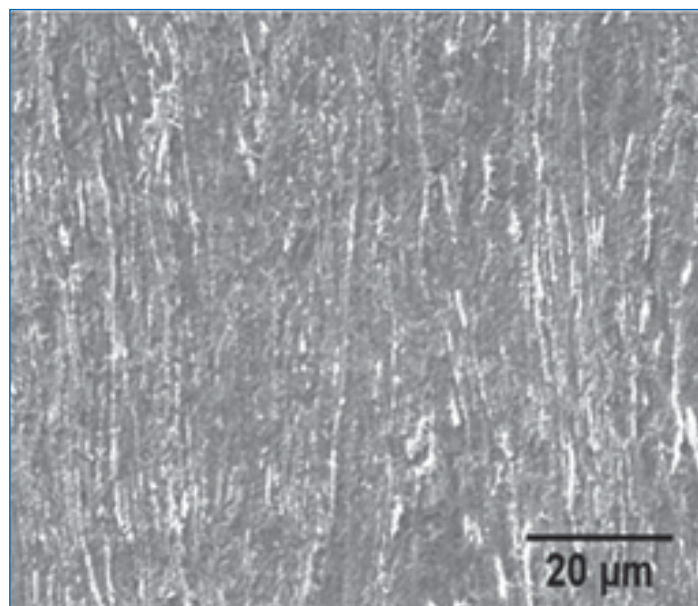


Fig. 3 Optical microstructure showing elongated grains

an average hardness of 230 VHN. From Figure 2, a severely deformed microstructure is seen after explosive cladding, which is consistent with the high hardness values obtained. XRD spectrum obtained from 304L SS indicated the presence of a bcc phase in addition to the expected fcc ( $\gamma$ ) phase. Detailed transmission electron microscopy (TEM) based investigations confirmed the formation of  $\alpha'$ (bcc) martensite phase in 304L SS. 304 SS which has a metastable austenite matrix is susceptible for strain induced martensitic transformation. From the present study, micro shear bands, shear band intersections and twin boundaries were identified as the nucleation sites for  $\alpha'$ (bcc) martensite. No evidence existed for the nucleation of  $\alpha'$ (bcc) martensite at the intersections of  $\epsilon$ (hcp) martensite phase.

Ti-5Ta-2Nb is an  $\alpha$ - $\beta$  alloy with Ta and Nb lean hcp  $\alpha$  phase and solute rich bcc  $\beta$  phase. Starting material has globular  $\beta$  particles distributed in an equiaxed  $\alpha$  matrix, which is identified from previous studies as the optimum microstructure having best corrosion resistance. Average hardness of Ti-Ta-Nb alloy was obtained as  $\sim$ 210 VHN. After exposure to explosive cladding conditions, the  $\alpha$  grains of the alloy

were found to have elongated in the detonation direction as shown in Figure 3. XRD spectrum obtained from Ti-Ta-Nb gave evidence for the formation of a metastable fcc phase in addition to the matrix phases. TEM based analysis shown in Figure 4 also confirmed the formation of fcc phase of titanium in Ti-Ta-Nb.

Observation of non equilibrium phases in both 304L SS base plate and Ti-Ta-Nb flyer plate must be a consequence of the passage of high pressure and high velocity shock waves during the explosive cladding process. Hence, explosive welding process was found to have modified the structure of both base and flyer plates possibly due to the increase in strain energy or by generating catalyzing defect sites for the phase transformation.

Elemental redistribution profiles obtained across the explosive clad interface using the electron

microprobe did not give evidence for the inter-diffusion of major alloying elements. XRD spectrum obtained from the clad interface also did not reveal the presence of Fe and Ti rich intermetallic phases. In direct fusion welded joints, due to inter-diffusion of alloying elements, intermetallic phases will form as separate zones parallel to the interface. In the case of explosive weldments, such zone formations are not expected since diffusion of alloying elements was avoided. However, intermetallic phases may be present as isolated pockets near the solidified melt zones which form due to jetting of the molten metals during the welding process. If the volume fraction and size of such isolated packets is less, it is possible that neither EPMA nor XRD detect their presence. Investigations are in progress for further confirmation. Property evaluation of these joints is also in progress.

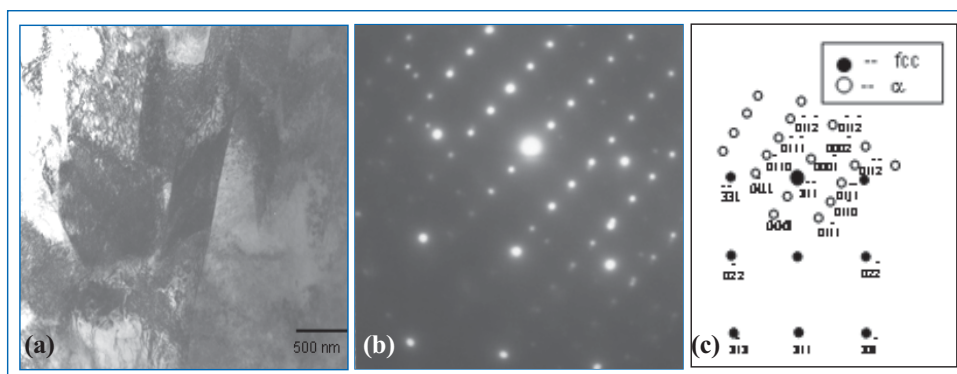


Fig. 4 (a) TEM bright field image (b) SAD pattern and (c) Key for the SAD pattern

## IV.22 Fissile Material Assaying of Waste Drums

Characterization and quantification of alpha bearing nuclear waste before disposal is mandatory. This is normally carried out using gamma based techniques like segmented gamma scanning or gamma tomography. However, as the fast reactor fuel cycle uses large amount of fissile material, mainly plutonium, the neutrons emitted by the spontaneous fission of the even-even plutonium isotopes can be used to estimate the amount of plutonium left behind in the waste. Depending on the type of sample, passive neutron based assay systems can utilize total neutron counting, neutron coincidence counting or neutron multiplicity counting.

As fast reactor fuels are associated with high gamma fields due to fission products, tracking fissile materials using neutrons is resorted to achieve the required minimum detection levels. The even-even isotopes of plutonium undergo spontaneous fission with reasonably low half-lives and release about 2.1 neutrons/fission on an average. These neutrons can be used to estimate the amount of plutonium if the isotopic composition of the sample is known. Waste drums for fissile material assaying based on passive neutron counting was manufactured at ECIL and is installed at CORAL facility of Reprocessing Group.

The system is of semi-circular in shape which encircles half of the drum to be assayed as shown in Figure 1. There are eight <sup>3</sup>He neutron detectors. These are embedded in HDPE moderating medium to ensure adequate thermalization of the neutrons. A 25 mm thick lead sheet

covering the front face enables the system to be used for reasonably high gamma field samples also. The system has a trolley on which the drum to be assayed is placed and moved in position for assay. All the detectors are identical with an active length of 900 mm, diameter of 50 mm and containing a fill gas of 75% <sup>3</sup>He and 25% Kr at 3 bar pressure. Each detector has a sensitivity of 130 cps/nv and a gamma tolerance of about 500 mR/h. The 25 mm thick lead sheet provided in the system limits the surface dose of the drum to less than 1 R/h for optimum detection. The positions of the detectors have been optimized using MCNP to obtain maximum sensitivity. The detectors are configured into two channels containing four detectors per channel to reduce the cumulative capacitance of the detectors with each channel covering a quadrant of 90 degree. The electronics processing system consists of a common low voltage power supply module, two independent high voltage detector bias supply units with two independent pulse amplifiers and a single micro controller module (MCM) to count both the channels. The current pulses from each channel are fed to a fast current amplifier followed by three stages of amplifier, discriminator, monoshot and TTL converter. The TTL pulses from each channel are counted in MCM depending on the time and iteration set from the software.

The statistical analysis of data revealed that the functioning of the system is satisfactory and summing up the counts in both the channels led to a total counting efficiency of



Fig. 1 Schematic view of assay including waste drum and detector assembly

8.5% as shown in Table 1. To determine the possible error arising out of a non-uniform sample distribution, the sample was kept at different locations in the drum and the count rate obtained. The efficiency reported in Table 1 was computed based on the total counts.

In actual practice, the drum will be assayed four times. After the first assaying, the drum will be rotated by 90 degrees and then assayed. This is to ensure that a non-uniform sample distribution would not lead to unacceptably high errors. The system is being calibrated and is getting ready to receive wastes generated in the glove boxes during the various campaigns of CORAL before disposal.

Table 1 : Total neutron counting data obtained for 1.5 g Pu sample (6% <sup>240</sup> Pu)	
Channel No.	Nett Counts / 30 s
1	140.6
2	94.2
Total	234.8
% Efficiency	8.5

## IV.23 Crystallization Studies on Cesium Iron Phosphate Glasses

Understanding the crystallization behaviour of glass enables to understand their glass forming ability. Crystallization can be classified as either surface crystallization or bulk crystallization. Bulk crystallization involves formation and growth of nuclei in the bulk whereas surface crystallization involves the formation and growth of nuclei on the surface. Though these two processes compete during the crystallization of the glass, one of them controls the crystallization. The present study involves understanding the crystallization behaviour of the cesium loaded iron phosphate glasses under non-isothermal conditions by employing differential scanning calorimetry (DSC).

$\text{Cs}_2\text{CO}_3$ ,  $\text{Fe}_2\text{O}_3$  and  $\text{NH}_4\text{H}_2\text{PO}_4$  were mixed in appropriate amounts, calcined at 873 K and melted in platinum crucible in air at temperatures ranging from 1263-1373 K and were air quenched. The air quenched samples were characterised by XRD and were found to be amorphous. The chemical composition of the glass was analyzed by XRF technique and the results are shown in Table 1. The glass samples were ball milled and the crystallization studies were carried out by using glass powders under flowing argon (50 ml/min) atmosphere by employing differential scanning calorimetry. Nearly 7 mg of the sample was taken in the Pt crucible and experiments were carried out at various heating rates like 5, 7, 10 and 15 K/min. The variation in the amount of sample

Sample code	Glass composition (mol %)			Upon Annealing	
	$\text{Fe}_2\text{O}_3$	$\text{P}_2\text{O}_5$	$\text{Cs}_2\text{O}$	T in K	Phases identified in addition to $\text{CsFeP}_2\text{O}_7$
IP8C2	34.5	53	12.5	913	$\text{Fe}(\text{PO}_3)_3$ and $\text{Fe}_2\text{O}_3$
IP7C3	33	46	21	913	$\text{FePO}_4$ and $\text{Fe}_2\text{O}_3$
IP6C4	29	44	27	878	$\text{Cs}_3\text{Fe}_4(\text{PO}_4)_5$ and $\text{Cs}_3\text{PO}_4$
IP5C5	26	38	36	858	$\text{Cs}_7\text{Fe}_7(\text{PO}_4)_8\text{O}_2$ and $\text{Cs}_3\text{PO}_4$

used in the DSC measurements was within  $\pm 2 \mu\text{g}$ . In order to identify the products of crystallization of the glass, the glass powders were annealed separately in the temperature range 853 to 913 K under flowing argon atmosphere. The weight of the sample was measured before and after the annealing, confirming that there was no weight loss during annealing. The phases identified from the XRD pattern of the annealed specimen are also shown in the Table 1. The major lines present in the XRD pattern of the annealed IP7C3 glass at 853 and 913 K were found to be similar. The pattern corresponding to 853 K showed the existence of both amorphous and crystalline phase.  $\text{CsFeP}_2\text{O}_7$  phase was found to be the major phase in all the ternary cesium loaded iron phosphate glasses, indicating pyrophosphate type of linkage in the glass. The minor phase varied depending on the composition of the glass. Generally alkali iron phosphate glasses crystallize to the pyro phosphate phase depending on the ratio of  $\text{Fe}^{2+}/\text{Fe}^{3+}$ . The glasses richer in  $\text{Fe}^{2+}$  content crystallizes to metaphosphate [ $\text{Fe}(\text{PO}_3)_2$ ] ferrous-

ferric pyro phosphate [ $\text{Fe}_3(\text{P}_2\text{O}_7)_2$ ] and ferrous ferric ortho phosphate [ $\text{Fe}_7(\text{PO}_4)_6$ ] whereas the iron phosphate glasses richer in  $\text{Fe}^{3+}$  content crystallize to ferric orthophosphate, ferric meta phosphate [ $\text{Fe}(\text{PO}_3)_3$ ] and ferric pyro phosphate [ $\text{Fe}_4(\text{P}_2\text{O}_7)_3$ ]. The glasses under present study were rich in  $\text{Fe}^{3+}$  (Mossbauer study) and thus crystallize to ferric phosphates rather than a mixture of ferrous ferric phosphates. A typical XRD patterns of the annealed IP7C3 glass is shown in Figure 1.

Differential scanning calorimetry was employed to determine the glass transition temperature of these glasses. Among the four glasses studied, the IP7C3 glass showed

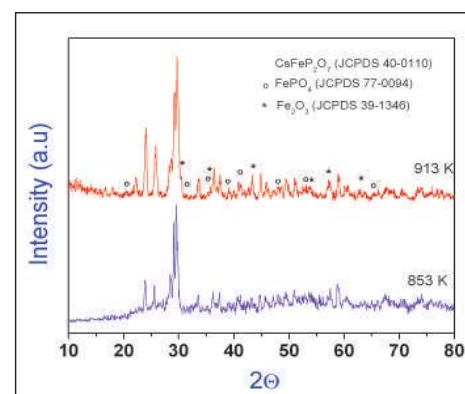


Fig. 1 XRD pattern of the annealed IP7C3 glass

better thermal stability ( $T_g$ : 810 K) than the other cesium loaded glasses. An attempt was made to explain the better stability of the IP7C3 glass by model free kinetic evaluation of the crystallization process by employing DSC. A typical DSC curve of the IP5C5 glass at various heating rates in the temperature range of 805-920 K is shown in Figure 2. From the DSC curve,  $\alpha$ , (fraction of crystallization) was determined.

The Kissinger-Akahir-Sunose (KAS) isoconversional method was employed to evaluate the activation energy of the crystallization process, which can be represented as,

$$\ln \frac{\beta_i}{T_{\alpha,i}^2} = \text{const} - \frac{E_{\alpha}}{RT_{\alpha,i}}$$

where the subscript 'i' denotes the various heating rates. The slope of the plot  $\ln[\beta_i/T_{\alpha,i}^2]$  vs  $1/T_{\alpha,i}$  gives the value of effective activation energy  $E_{\alpha}$ . The plot of  $E_{\alpha}$  as a function of  $\alpha$  for the crystallization of IP5C5 glass is shown in Figure 3. From this Figure, it is clear that the effective activation energy increases as a function of  $\alpha$  up to a value 0.1. For the  $\alpha$  value of 0.1-0.75, only a small increase was observed. The  $E_{\alpha}$  was found to increase beyond the  $\alpha$  value of 0.75. The  $E_{\alpha}$  plots as a function of  $\alpha$  were determined for other ternary cesium loaded iron phosphate

glasses also in a similar way and are shown in Figure 3. The  $E_{\alpha}$  was found to decrease with  $\alpha$  for the crystallization of IP6C4 and IP8C2 glasses. The dependence of  $E_{\alpha}$  on  $\alpha$  for IP7C3 was found to be different from that of other cesium loaded iron phosphate glasses under study.  $E_{\alpha}$  value increases up to the value of  $\alpha = 0.12$  and then decreases continuously with  $\alpha$ . During the initial crystallization period, i.e., up to  $\alpha = 0.12$ , an increase in activation energy was observed up to a value of 692 kJ/mol, which is very high. At a fixed  $\alpha$ , the activation energy evaluated for the IP7C3 glass was always higher than that of IP5C5, IP6C4 and IP8C2, indicating the higher resistance to crystallization and thus better thermal stability. Thus the isoconversional method of kinetic analysis could explain the better thermal stability of IP7C3 glass compared to other cesium loaded iron phosphate glasses.

Mechanism of crystallization (surface or bulk) can be explained only based on physical model dependent kinetic methods like Coats and Redfern, which can be represented as,

$$\ln \left[ \frac{g(\alpha)}{T^2} \right] = \ln \frac{AR}{\beta E_c} \left( 1 - \frac{2RT}{E_c} \right) - \frac{E_c}{RT}$$

where,  $g(\alpha)$  is the integral form of the conversion function, which is

dependent on the mechanism of the crystallization,  $\beta$  is the rate of heating,  $A$ , pre-exponential factor,  $E_c$ , the activation energy of crystallization,  $R$ , the gas constant and  $T$  is the absolute temperature. A plot of  $\ln(g(\alpha)/T^2)$  vs  $1/T$  gives a straight line when appropriate  $g(\alpha)$  function is used in this equation. The mechanism of the reaction is given by the  $g(\alpha)$  function. The best fit was obtained for  $g(\alpha) = [-\ln(1-\alpha)]^{1/4}$  (Figure 4). This  $g(\alpha)$  corresponds to Avrami – Erofeev nucleation and growth model (A4) with 'n' (Avrami-exponent) as 4 in the  $\alpha$  range of 0.1 to 0.75. Generally, the value of the Avrami-exponent 'n' is equal to  $m$  or  $m+1$ , where  $m$  denotes the dimension of the growth of the nuclei during crystallization. When the nuclei are formed prior to heat treatment then the value of  $m$  is equal to  $n$  and when the nuclei are formed during heat treatment at constant  $\beta$ , the value of  $n$  is equal to  $m+1$ . For the crystallization of IP5C5, the nuclei are formed during heating in the DSC hence,  $n=m+1$ . Thus the value of  $m$  is 3 indicating that growth occurs in all three dimensions in the bulk. Therefore, IP5C5 crystallization is dominated by bulk crystallization mechanism and not by surface crystallization. The studies on the mechanism of crystallization of other cesium loaded glasses are in progress.

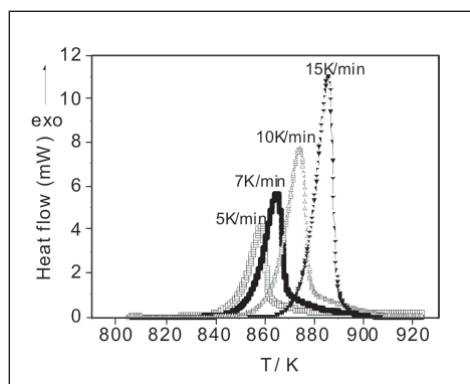


Fig. 2 DSC curves showing the crystallization of IP5C5 glass

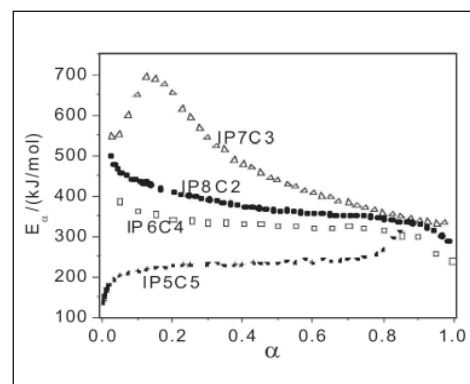


Fig. 3 Plot of  $E_{\alpha}$  as a function of fraction crystallized ( $\alpha$ )

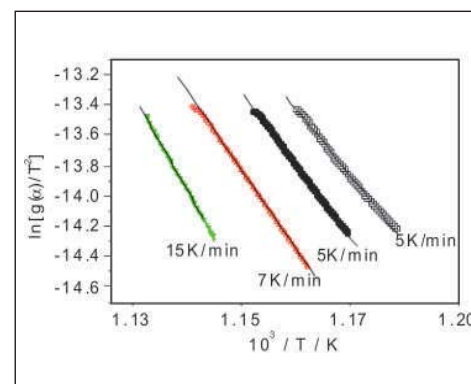


Fig. 4 Coats and Redfern fit for the crystallization of IP5C5 glass

## IV.24 Stability of Cesium Loaded Iron Phosphate Glass - Simulation for Nuclear Waste Immobilization: An FTIR Study

The disposal of radioactive wastes generated by the nuclear fuel cycle is among the most pressing and potentially important environmental problems facing the nuclear industry. Although borosilicate glasses are extensively used as a matrix material, the high processing temperatures and low waste loading capacities limit their use. Currently phosphate glasses are being explored as a potential matrix for high level nuclear waste immobilization owing to their higher waste loading capacity and lower processing temperatures. The highest chemical durability was exhibited by glasses having pyrophosphate (Q<sup>1</sup>) type of dimeric linkages with an O/P ratio of 3.5 and a Fe/P ratio of 0.67. It now becomes important to understand the structural changes in these glasses associated with the incorporation of waste streams in terms of these building units, that ultimately decides their durability and qualifies them as waste matrices.

Infrared spectroscopy is a very simple but excellent tool to probe the local structural aspects of phosphate glasses. The present study focuses

on the effect of incorporation of cesium as a simulated nuclear waste into the iron phosphate glass (IPG) matrix maintaining an Fe/P ratio of 0.67 and following the associated structural changes using far and mid infrared spectroscopy. Figure 1 shows the room temperature mid infrared spectra of the as prepared iron phosphate glass of composition 40Fe<sub>2</sub>O<sub>3</sub>.60P<sub>2</sub>O<sub>5</sub> along with the cesium doped samples in the 400-1500 cm<sup>-1</sup> range. The mid infrared spectrum of the undoped sample reveals broad and strong convoluted bands centered around 1300, 1200, 1100, 1050, 980, 920, 744, 680 and 515 cm<sup>-1</sup> which are characteristic of various vibrations of the phosphate tetrahedra in these glasses. The mode assignments depicted in Figure 1 for the undoped IP glass are based on earlier reports. On doping the IP glass with cesium, systematic changes in the mid infrared spectra can be seen on account of the reorganization process accompanying the addition of the modifier oxide. An evident depletion of the Q<sup>3</sup> and Q<sup>2</sup> units along with a corresponding increase in the Q<sup>1</sup> and Q<sup>0</sup> components are seen as one dopes the IP glass with cesium.

In order to gain detailed information regarding the variation of the constituent modes, these broad bands have been deconvoluted into their constituent features and the relative peak area of individual infrared bands evaluated and the data are presented in Figure 2. For initial doping levels (up to 21 mol% Cs) no appreciable changes are seen (Figure 2) in the constituent units. It is clearly evident that for doping beyond 21 mol% Cs, break down of the extended chain length (Q<sup>3</sup> and Q<sup>2</sup> units) of the phosphate linkages occurs leading to predominantly shorter chains dominated by Q<sup>1</sup> and Q<sup>0</sup> units inferring depolymerisation of the glass network (Figure 2). Based on the above, one would expect a weakening of the glass network on progressively loading the glass matrix with cesium but it is indeed surprising to note that the glass transition temperature shows a steady increase up to 21 mol% Cs (exhibits maximum thermal stability. T<sub>g</sub> = 810 K). This can be correlated to the maximum extent of cross linking for this composition as shown in Figure 2. It is to be mentioned here that the area under the bands of 400-600 cm<sup>-1</sup> (Figure 2) and the

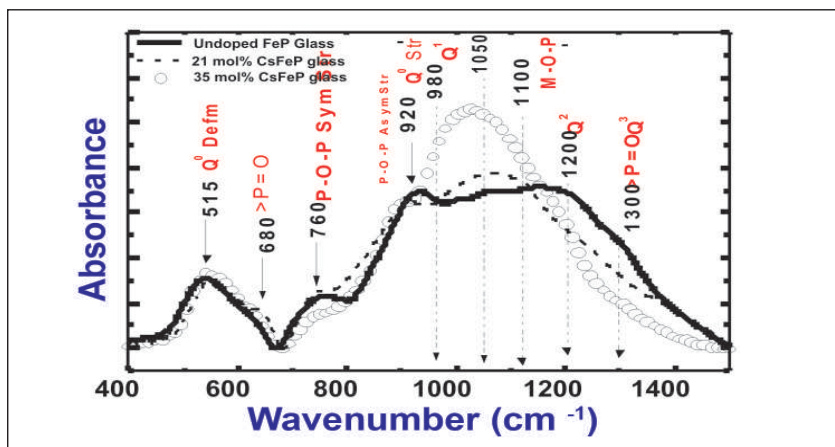


Fig. 1 Mid infrared absorption spectra of undoped and cesium doped iron phosphate glass

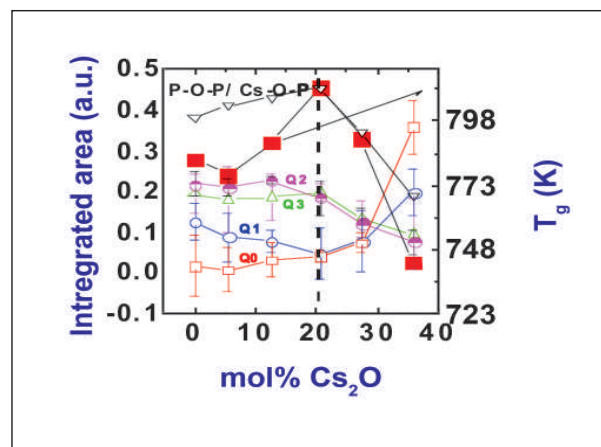


Fig. 2 Variation of integrated peak area of the constituent infrared modes and the glass transition temperatures as a function of cesium doping

intensity of the  $760\text{ cm}^{-1}$  (Figure 1) both characteristic of the extent of cross linking, exhibit a maximum for a critical doping of 21 mol% Cs. For doping beyond this composition the extent of cross linking shows a total collapse leading to a possible loss in the strength of these glasses. The above observations correlate excellently with the thermal stability exhibited by these glasses as reflected by the variation of the glass transition temperatures as a function of cesium doping (Figure 2). This behaviour can be understood as follows: The doped cesium is basically involved in two competing processes. On one hand it is involved

in the breaking of the existing P-O-P polymeric network and on the other hand it serves to form extensive cationic cross linking. During the initial phase of doping - up to 21 mol% Cs, cesium serves as a cationic cross link between nonbridging oxygen of neighbouring chains, thus enhancing the overall strength of the glass. On further doping the glass with higher amounts of cesium the incoming cesium now breaks the existing cross links thus enhancing the number of terminal oxygens resulting in the total collapse of the glass network. This is clearly evidenced by the enormous increase in isolated  $Q^0$  type of units beyond

21 mol% Cs doping (Figure 2). In addition, for samples containing higher amounts of cesium, a small well defined far infrared feature at  $\sim 79\text{ cm}^{-1}$  picks up (figure not shown), that corresponds to free Cs ions vibrating against the phosphate tetrahedra. The appearance of this new feature provides additional proof that the incoming cesium is no longer involved in cross linking but serves to terminate the linkages. Infrared spectroscopy has thus proved to be a valuable technique for help understanding the complex structural changes associated with cesium incorporation in iron phosphate glasses.

## IV.25 Design, Development and Implementation of Asset and Knowledge Management in DFRP

The demonstration fuel reprocessing plant (DFRP) at Kalpakkam has more than 250 process vessels and equipment of stainless steel 304L material and allied piping works of length around 62000 m with sizes varying from 8 NPS to 250 NPS with  $\sim 35000$  welds and over 70,000 radiographic exposures in about  $5000\text{ m}^3$  of concrete cell volume fabricated and installed with stringent quality requirements and critical quality assurance using conventional and advanced NDE put into place.

Documentation plays an important role during fabrication / construction, pre-commissioning and post commissioning activities of any nuclear plant. An effective and efficient quality management system (QMS) – “SMART (specific, measurable, achievable, robust and technologically innovative)” has been implemented in the plant. This QMS generates documents and assets like quality assurance plan

(QAP), procedures, inspection reports and as-built drawings. Since the plant is expected to operate for more than 20 years, to meet the statutory and regulatory requirements, the availability of right document at the right time over this period needs to be ensured. Apart from this, since more such plants are likely, it was also felt that the knowledge gained during the manufacture, fabrication and erection should be consolidated and be available for future generations so that innovative field practices can be adopted beneficially.

Asset management is primarily concerned with the collection, classification, manipulation and storage and retrieval of all documents related to the entire activities of a nuclear installation. The valuable documents will be a ready reference at any point of time in the future. Knowledge on the other hand takes time to acquire and mature. Mature knowledge is individual

specific and is not readily available in any text book. In any industry, this knowledge goes out with the individual unless the individual has trained his team like the teacher in a gurukul system. Documented knowledge of field practices with the experiences of seniors coupled with data base of important assets is the hallmark of the present asset and knowledge management system (AsKMe).

The structure of the AsKMe is like a tree starting with the brief over view of the nuclear plant and its objectives. The software provides the details of vessels, equipments and piping in a tree structure with a well defined hierarchy evolved after deep consideration from where an individual can navigate to the required drawing details or reports. The system has a base platform around which modules have been created and integrated together. The modules include data

management, record management, media management and knowledge management.

The data management module essentially consists of drawings, as built loop sketches, individual pipelines and joints. The record management module provides a secure digital archive of a variety of documents and reports of the entire project starting from the cradle, that is material identification up to the final integrity testing. It includes, material test certificates, corrosion test certificates, dimensional inspection reports, alignment reports, flow test reports, and conventional and non conventional NDE reports. Figure 1 shows a typical pipeline drawing.

Compared to the conventional asset management modules, it is the media management module and the knowledge management module that set this apart. The media management module essentially comprises a radiographic analysis and archiving management system. This module provides for evaluation, analysis and archiving of digitized radiographic images (Figure 2). Some of the salient features of this software system include :

- (a) Availability of a software magnifying glass for looking critically in the region of interest during radiographic evaluation
- (b) Dimensional measurement of features based on calibration of inherent features
- (c) Histogram analysis, line profiling of regions with varying densities
- (d) Image enhancement and analysis of features including selected widely used spatial filtering routines and
- (e) Simultaneous handling of multiple images features.

The specific and significant manufacturing and inspection procedures which are developed by the department are valuable for the future projects. The knowledge management module archives all these procedures. While generally it is a repeated statement that individuals are dispensable but a system is not, it is a well realized fact in strategic organizations that experiences and the tacit knowledge gained over years in a plant cannot be replaced unless there is an established documentation and strong mentoring which does not exist in a full fledged way. Thus, an important goal of knowledge management is capturing knowledge to reduce the impact of employee

attrition or retirement. The knowledge management module documents the field problems and the solutions arrived and also carries memoirs of senior managers and their experiences.

The system has been configured on a Server with 64 bit operating system with 64 GB RAM and 3 × 500 GB hard disc. Microsoft SQL Server 2005 Express Edition and .NET Framework 2.0 have been used for the development of this innovative software. The software has 4 levels of security. A user friendly and advanced search facility for the fast retrieval of the stored data /records has been provided for. Automatic backup of data has been provided for to ensure redundancy.

AskMe is an innovative and secure solution for improved project management, better regulatory compliance, improved knowledge sharing, enhanced digital retention and increased control of assets and expertise. As on date the system is a repository of about 40000 documents pertaining to DFRP. Loading of balance documents and development and integration of other modules such as ultrasonic data and signal management are in progress. While the present software is specific to DFRP, it can be personalized with minor modifications for asset management of other industrial or strategic plants also.

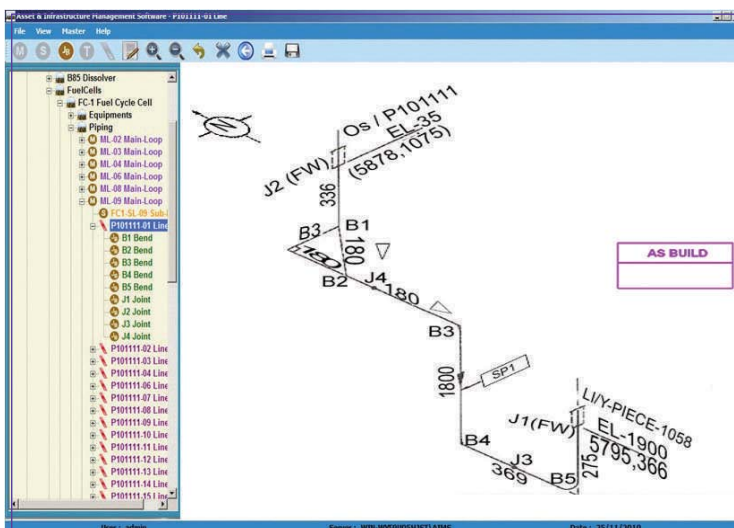


Fig.1 Typical pipe line drawing



Fig. 2 Screen shot of radiographic analysis and archiving software

## IV.26 Flight Trials of Time Domain Electromagnetic System

IGCAR is developing an airborne time domain electro-magnetic (TDEM) system, which is widely employed in the sub-surface exploration of minerals. The advantage of the airborne system is covering a larger survey area in a short time duration, irrespective of the terrain conditions. The system consists of an under slung transmitter coil and receiver coil assembly and onboard equipment, viz., power electronics and data acquisition system. The power electronics injects a pulsed current into the transmitter coil, which induces eddy currents in the conductive bodies present in the earth subsurface. The secondary field generated by the eddy currents is captured using the receiver coil as induced voltage and is acquired by

the on-board data acquisition system. The decay pattern represents the conductivity of the sub surface. The acquired data over the area is processed and a conductivity map is generated for interpretation of the sub-surface geology.

A non-metallic, near circular, light weight, semi rigid housing structure along with tow mechanism is used to house the transmitter coil, bucking coil and receiver coil. All the coils are concentrically hung from the helicopter. Aerodynamic stability of the entire structure under slung load at 100 K mph speed of the helicopter has to be ensured. Onboard TDEM equipment also need to be qualified as per the flight safety test standards, as recommended by the certifying agency. Hence, the flight trials were



**Fig. 1** Structural integrity testing of airborne time domain electro-magnetic under-slung assembly

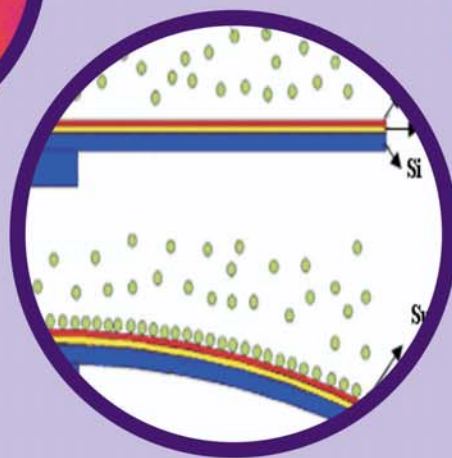
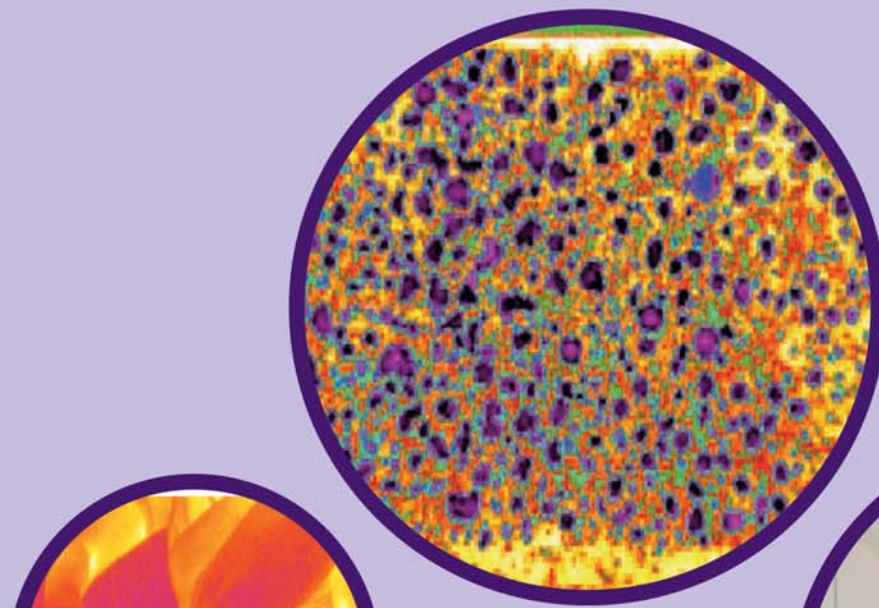


**Fig. 2** Phase-1 flight trials of the time domain electro magnetic system

planned in three phases using DHRUV helicopter.

The Phase1 flight trial is aimed to assess the aero dynamical stability and load assessment of under slung load. Prior to the flight trials structural integrity of the under-slung assembly was tested by lifting the entire assembly with a crane as shown in Figure 1. Accordingly, flight trials of the TDEM system with 16 meter diameter transmitter assembly weighing 450 kg were successfully conducted during the first week of September 2010. The system behaved with good aerodynamic stability. The underslung coil assembly with the helicopter in hovering condition is shown in Figure 2.

The Phase 2 flight trial is aimed to assess the EMI/EMC aspects of the entire TDEM system in power on condition. A 300 A current source, with pre-defined drop rate was already developed. Qualification tests are in progress.



# CHAPTER

## V

# Basic Research

## V.1 Plastic Deformation in Oxide Dispersion Strengthened Ferritic Alloys: A Three Dimensional Dislocation Dynamics Investigation

Oxide Dispersion strengthened (ODS) ferritic steels are fast becoming the prime candidates for nuclear reactor applications at high temperatures and irradiation doses. In spite of several experimental and computational research activities in this field, complete understanding of the micro-structural behavior of these materials is still lacking. For example, it is known that certain ODS alloys exhibit better post-irradiation ductility and hardening characteristics in comparison with their single phased counterparts, the microscopic origin of which is not fully understood. Discrete dislocation dynamics is one of the most important computational tools that aims to provide an understanding of the mechanical properties of the materials in terms of the dislocations. In this work, three-dimensional

discrete dislocation dynamics simulations are carried out to analyze pre and post-irradiation plastic deformation of ODS and non-ODS ferritic grains (Figure 1). The primary interest in these simulations was to compare and contrast the strain localization and hardening behavior of the ODS strengthened steel with the iron matrix, under tensile loading.

The ODS precipitates are modeled as impenetrable, hard particles of 20 nm size, uniformly spread over the simulation volume, with a volume fraction of 0.5%, yielding an inter-particle separation of 80 nm. The impenetrable nature of these precipitates implies that they are bypassed by mobile dislocations, whereby residual "Orowan" loops are left around each by-passed precipitate (Figure 2a). Critical stress of this mechanism is called the

Orowan stress, and is obtained from the elastic theory. When external load is applied, initial dislocation sources are activated and shear loops emitted, until dislocations are arrested by the hard precipitates and grain boundaries. Accumulation of Orowan loops (typically 1 or 2 loops) around the particles generates relatively high internal stress that helps for cross-slip activation. Repetition of this process can generate high density dislocation tangles, which can later act as pinning points for mobile dislocations. A primary feature of the irradiation is the formation of the irradiation induced defect loops. It is well known that, in iron based bcc materials, at high temperatures, these irradiation induced defect loops are sessile in character. Such defects are therefore modeled as

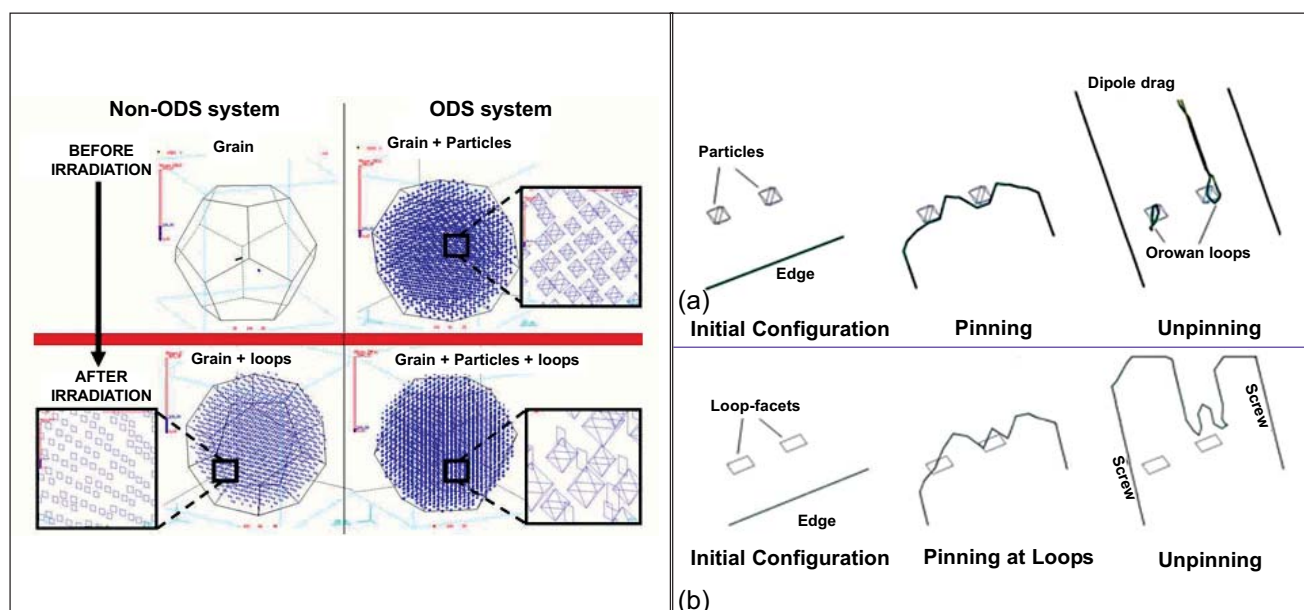


**Fig. 1** Tensile deformation studies corresponding to: The ferritic matrix, the matrix studded with 20 nm ODS precipitates, the irradiated matrix and irradiated ODS strengthened matrix respectively

**Fig. 2** Micro-level simulations are carried out to understand the interaction of the incoming edge dislocation with (a) The precipitates and (b) The irradiation loops

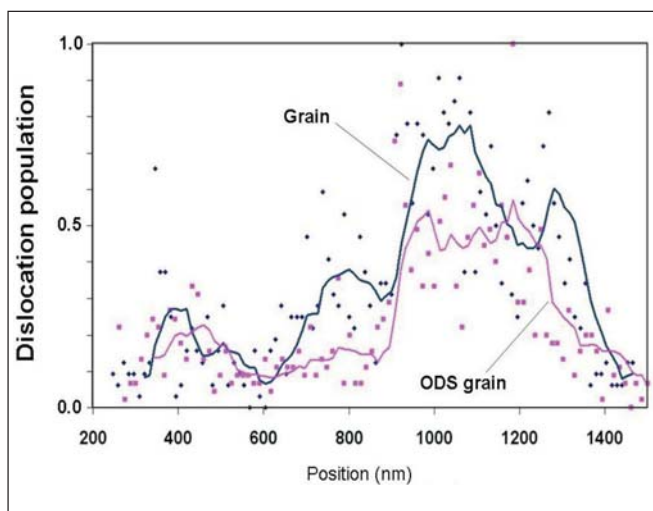


**Fig. 3** Dislocation population histogram of un-irradiated ODS and ferritic grains undergoing plastic deformation under tensile loading conditions. (Solid curves are running averages)

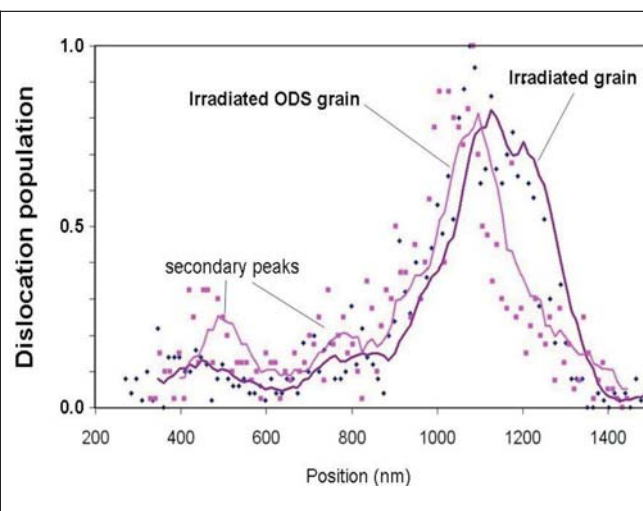


**Fig. 4** Dislocation population histogram of irradiated deformed systems. Presence of secondary peaks witnesses plastic strain spreading at long distance from the initial dislocation source slip plane. (Solid curves are running averages)

single immobile facets. Interaction of these single faceted loops with the incoming dislocations differ from the precipitates primarily in two aspects: The dislocation loops are penetrable by the incoming dislocation and the resolved shear stress required for shearing them depend on the nature of the incoming dislocation (edge or screw) (Figure 2b). Cross-slip mechanism is treated according to a specific procedure, where the glide plane of each screw segment is updated at each time step, depending on its physical selection probability.

These simulations show that in absence of irradiation defect loop clusters, ODS particles significantly reduce dislocation mean free path, leading to greater strain localization and significant hardening, by comparison with the same particle-free grain. In presence of irradiation defect loop clusters however, this trend is reversed. This effect is observed in certain ODS systems and clearly explained herein, in terms of particle/loop interplay. During tensile deformation indeed,

dislocations accumulate around ODS precipitates, generating high internal stresses. In these conditions, cross-slipped dislocations overcome irradiation defect cluster and as a result, irradiation-induced strain localization and hardening are reduced altogether.

Although it is clearly beyond the scope of model to predict the experimental ductility loss of actual specimens, trends can nevertheless be examined quantitatively, at the scale of individual grains, but understanding strain localization through examining the dislocation spreading in all the four cases is shown in Figure 1, at equal strain localization levels. The analysis are carried out as follows: Simulation volumes are first divided into  $N$  parallel sub-regions, parallel to primary slip plane. The  $i^{\text{th}}$  region is considered as being active if dislocation density is non-vanishing. Spatial coordinate of the  $i^{\text{th}}$  plane region,  $x_i$ , is the distance of the plane  $i$  taken from a reference grain boundary along a reference axis normal to slip planes. The reference axis is divided into finite spatial

intervals of 10 nm, and results are displayed in the form of dislocation population versus position histograms.

Before irradiation (see Figure 3) strain localization is significantly more pronounced in ODS grains than pure ferritic grains. This result is consistent with experimental data obtained on ODS steels containing 20 nm particles, where uniform elongation is less than in its precipitate-free counterpart. After irradiation (see Figure 4) however, such trend is reversed. Namely, strain localization is more pronounced in irradiated grain than in irradiated ODS grain. These predictions of the model are consistent with reported evidence that ODS alloys can be more resistant to post-irradiation loss of ductility than their non-ODS counterparts. A broader distribution is indeed considered as beneficial, in terms of residual ductility. This work can be regarded as a preliminary step towards predicting mechanical properties of metals in complex loading conditions, like fracture or fatigue.

## V.2 Lattice Kinetic Monte-Carlo Simulation of Yttria Nanoparticle Formation and Distribution in Model Oxide Dispersion Strengthened Steel

Nanostructured ferritic alloys derive their strength from the dispersion of yttria nanoclusters in the ferritic matrix. These alloys are prepared by ball milling, followed by a consolidation process at high temperatures which involves either hot extrusion or high temperature hot isostatic pressing. The size distribution of a fine dispersion of nanoparticles, which improves the mechanical properties, depends on the alloy composition and processing conditions. Data available in the literature shows that addition of minor alloying elements like titanium leads to refinement of the size of the oxide nanoclusters in the ferritic matrix. The details of the physical processes leading to formation of the nanoclusters are not clearly understood. Computer simulation plays a crucial role in elucidating the clustering phenomena and, in particular, the role of minor alloying elements and processing temperature. Lattice Kinetic Monte Carlo simulation technique was employed to understand the kinetics of formation and size distribution of

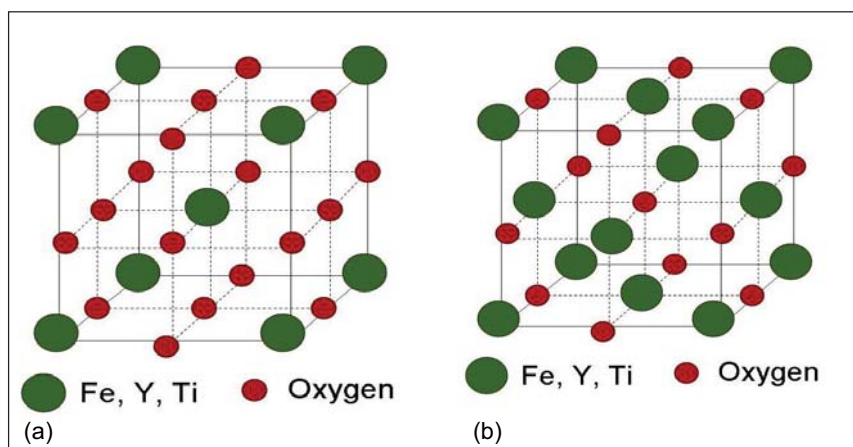


Fig. 1 Lattice model for (a) bcc and (b) fcc

yttria nanoclusters (NC) in iron and the role of titanium in refining the size of nano-precipitates. Lattice kinetic Monte Carlo codes are written to simulate the evolution of NC in fcc and bcc Fe matrix. Bond energies and migration energies used in Lattice Kinetic Monte Carlo simulations are calculated using Density Functional Theory (DFT). The lattice model used in our Lattice Kinetic Monte Carlo simulations is comprised of two rigid sublattices – the one encompassing the usual bcc or fcc lattice sites, and the other made of the octahedral interstitial sites (Figure 1).

Lattice Kinetic Monte Carlo simulations were performed on both bcc and fcc phase at corresponding temperatures. The Fe and substitutional solute atoms are assumed to diffuse via the vacancy mechanism while oxygen is assumed to diffuse via the interstitial mechanism. The vacancy can jump to any first neighbour site (in both bcc and fcc) and the oxygen atom can jump to any first neighbour octahedral site. The particles jump frequency  $\Gamma_i$  (which is also proportional to the jump probabilities) were calculated as

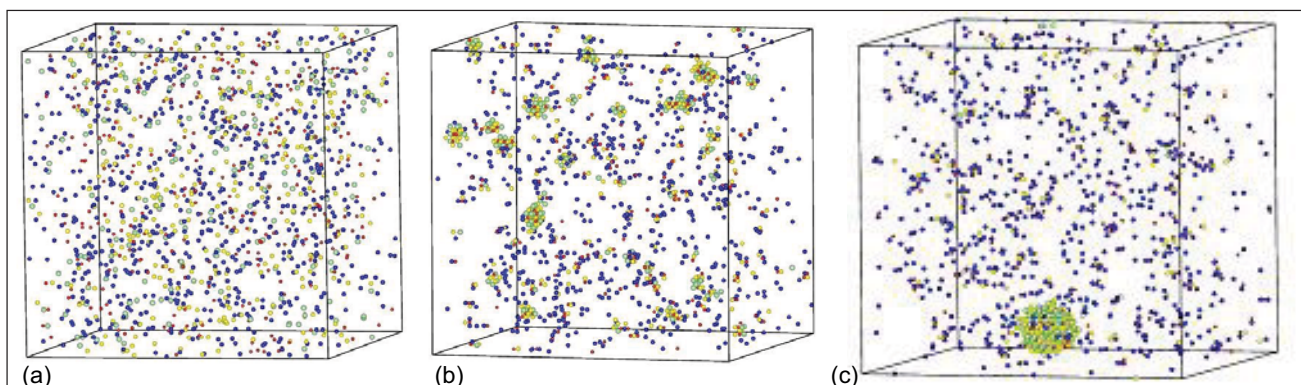
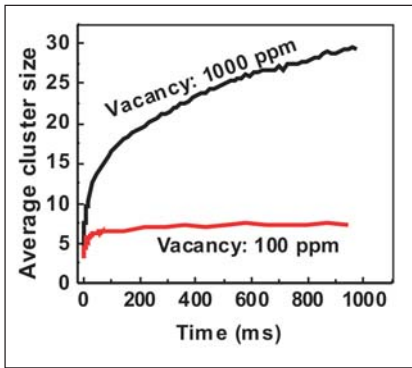
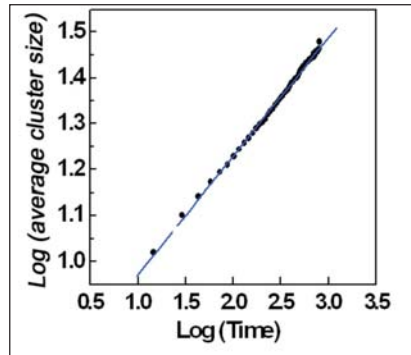


Fig. 2 A snapshot from the Lattice KMC simulation, showing Y-Ti-O nanocluster in  $42 \times 42 \times 42$  bcc Fe supercell at 1050 K, with the composition of Ti – 0.5at%;  $Y_2O_3$  – 0.3at%; Vac – 0.1at%. (Color: The green – Y atoms, yellow – vacancy and red – O atoms and blue – Ti.) (a) Random distribution (b) After 0.1 million MCS (c) After 5 million MCS



**Fig. 3** The growth of average cluster size at 1250 K



**Fig. 4** Straight line fit of log of average cluster size vs log of time, for 1250 K, with 1000 ppm vacancy

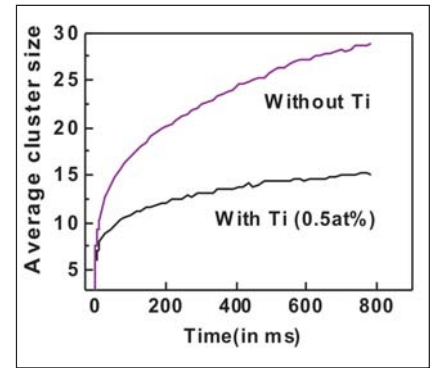


**Fig. 5** The effect of Ti on the cluster size distribution

$$\Gamma_i = \nu_x \exp [-(E_{sp} - E_{init})/k_B T]$$

where  $\nu_x$  is the attempt frequency,  $E_{sp}$  is the saddle point energy along the path connecting initial site and the final site  $i$ , and  $E_{init}$  is the energy before the jump. The equilibrium energies of atomic configurations are calculated considering pair-wise interactions between individual atomic species including vacancy (Bond Model approximation). The total crystal energy is approximated as

$$E = \sum_k \sum_{i,j} \varepsilon_{ij}(k) n_{ij}(k)$$

where,  $n_{ij}(k)$  is the number of bonds of the species. The saddle point energy can be written as

$$E_{sp} = E_m + \max(dE, 0)$$

where,  $dE$  is the difference between crystal energies of the initial and final configuration of the jump. The various energy parameters used in Lattice Kinetic Monte Carlo codes were obtained by fitting the formation energy and binding energy values obtained from ab initio calculations, employing density functional theory (using the package VASP). The ab initio calculations were done on several configurations of bcc or fcc iron together with alloying elements and vacancies. The ab initio simulations

were done on  $128 \times 128 \times 128$  supercell (relaxed configuration) with spin polarized formalism and using PAW pseudopotential. Lattice Kinetic Monte Carlo follows the residence time algorithm which uses the jump rates to move the vacancies and O atoms. One Monte Carlo Sweep (MCS) is said to be completed when all the vacancies and oxygen atoms are allowed to jump once. The snapshots of the simulation box in Figure 2 shows the formation of nanocluster ( $\sim 2$  nm) in bcc Fe after several million Monte-Carlo sweeps. Figure 3 shows the typical growth trends of the nanocluster observed at 1250 K for different vacancy concentrations in fcc iron. Similar trend is observed in bcc phase also.

The growth of nanoclusters is studied at different temperatures with different vacancy concentrations, and it is seen that the average cluster size (in terms of number of atoms) varies with time according to a power law  $t^\alpha$ ;  $N = N_0 t^\alpha$ . (Figure 4) In fcc phase  $\alpha \cong 0.25$  and in bcc phase,  $\alpha \cong 0.18$ . This means the growth is faster in the fcc phase. Further, in fcc phase, in the presence of titanium, the value of this exponent decreases to  $\alpha \cong 0.14$  which implies that Ti reduces the growth rate. The

composition of the nanocluster during its growth remains almost the same (i.e., Y/O ratio is  $\sim 1$ ) in both fcc and bcc phases. The nanocluster grows until the cluster size saturates and the size is large when the temperature or the vacancy concentration is high. Figure 5 shows the observed effect of Ti on the size distribution of the nanoclusters, which shows that presence of Ti refines the size of nanoclusters. This is in agreement with experimental results. Most of the clustered Ti atom is found to occupy the interface region between the yttria cluster and the iron matrix. Since Ti has higher binding with Fe, the bonding of Ti with Fe at the interface reduces interface energy and thereby refines the size distribution. In summary, the Lattice Kinetic Monte Carlo simulation on the formation of nanoclusters in the bcc and fcc phase of iron has led to the following results and insight: The effect of temperature and vacancy concentrations on the cluster size were observed in bcc and fcc phases. High temperature and high vacancy concentrations led to large cluster size. The growth rate of the nanoclusters is higher in the fcc phase as compared to the bcc phase. The presence of Ti refines the size of the nanoclusters.

### V.3 Multimode Non-destructive Evaluation for Corrosion Characterization

The need for advanced techniques for detection and evaluation of embedded corrosion and a class of sub-surface defects that require access only to one side of any material or structure relatively thick to be inspected has drawn attention to X-ray or gamma backscatter as a desirable choice. Moreover, in scattering, point-wise information can be obtained by focusing the field of view of the source and detector so that they interact around a point. Scattering also eliminates the need of accessing two opposing sides of the target object. Scanning of the object can be achieved by moving the source and detector and changing their relative positioning such that the area of interest is covered. Since both the source and detector are located on one side of the object, examination of extended structures becomes possible. This technique has been successfully used to produce a 2D map of the corrosion and the thickness profile of a MS plate with non-uniform corrosion and the results are correlated with those obtained from conventional

radiography imaging and thermography measurements.

The gamma scattering NDE method utilizes back-scattered gamma radiation for the detection of corrosion and the present experimental set-up is an indigenously designed PC controlled gamma scattering scanning system consisting of CNC controlled 6-axis source detector system and 4-axis job positioning system. The <sup>137</sup>Cs radioactive source of strength 155.4 GBq with a lead shielding and a collimated and shielded 50% efficiency coaxial HPGe detector providing high resolution energy dispersive analysis of the scattered spectrum are mounted separately on the source and detector sub assemblies of 6-axis system. Two MS plates (one corroded and another normal) of dimensions 23.5x15.5x1 cm were placed separately on the 4-axis sample platform. Scanning of the specimen was achieved by lateral movement of the MS plates across the source and detector collimators by computer commands. The pulse height spectrum of the detector

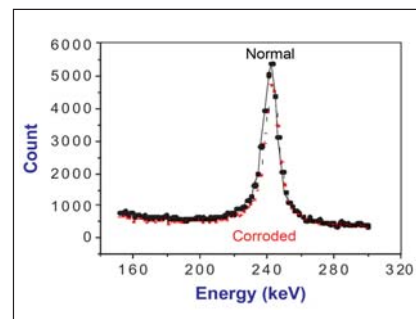


Fig.1 The scattered pulse height spectrum for normal and corroded MS plate

was displayed using a multichannel analyzer which was interfaced with a PC for data storage and analysis

Radiography of the MS plates was carried out using 160 KV X-ray machine. The thermography experimental setup consists of a focal plane array camera (Silver 420 M) and the 320 x 240 detectors array captures the IR radiation in the 3-5 μm spectral band at a frame rate up to 200 Hz.

The scattered intensity from eight different volume elements of the specimen was detected and intensity from one of the voxels is shown in Figure 1. The Monte Carlo (MC) numerical simulation of the phenomena is done using the MCNP

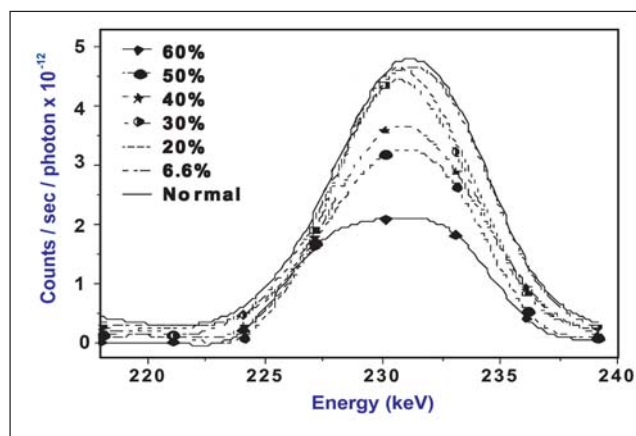


Fig. 2 The MC simulated spectra for different percentage of corrosion

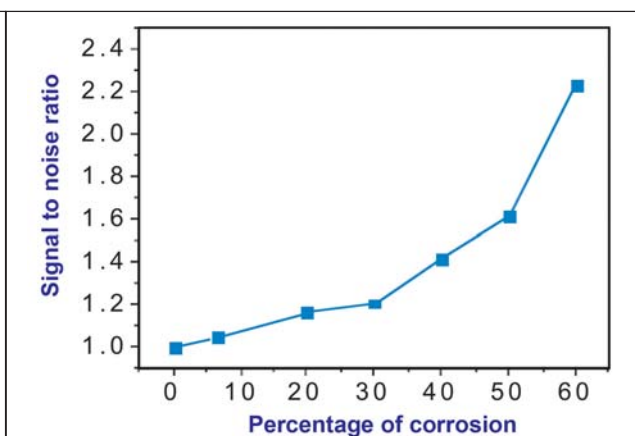


Fig. 3 The ratio between scattered intensities of normal and corroded MS plates

code (Figure 2) and the quantitative estimates of the values of Signal-to-Noise (S/N) ratio for different percentages of MS corrosion derived from these simulations are presented (Figure 3). The quantitative estimates of the values of S/N calculated from MC simulation of MS flat plate corrosion give an indication of the magnitude of S/N one can get in these type of investigations.

A detailed procedure to reconstruct the densities of the MS flat plates and an unambiguous interpretation of the signal  $I(P)$  as a function of material density at any point of the thick object being inspected is given. In this simple and straightforward method the density, ' $\rho$ ' of the target need not be known and only the knowledge of the target material's mass attenuation coefficients (composition) for the incident and scattered energies is enough to reconstruct the ' $\rho$ ' of each voxel of the specimen being studied. As the scattered intensity depends on the density and effective thickness of the sample, the magnitude of corrosion and loss in thickness are determined using iterated density from the known values of mass attenuation coefficients and the geometrical parameters.

The digitized radiographs (Figures 4a and 4b) with a resolution of 50 microns were processed for the

detection of corrosion damage in four different locations. Optical density of the film will vary with the change in thickness for a particular material which is radiographed and the calibrated values with known thickness variation (Figure 1).

The scattered pulse height spectrum for normal and corroded MS plate were taken as input for determination of corrosion damage at the unknown location.

Lock-in thermography based on the detection of infrared radiation has been successfully applied to study the corrosion damage in mild steel plates. Phase angle measurements were obtained for a range of thermal excitation frequencies (0.01Hz-0.6Hz) for each of the MS plates. Both the phase and the amplitude images were analyzed in lock-in thermography. Phase image of the corroded plate clearly maps the extension of corrosion damage that has occurred in the plate. The phase images of the two steel plates are shown in Figures 5a & 5b. It was observed from the phase image of the reference plate that the initialization of corrosion damages has occurred. Phase image of the already corroded plate clearly maps the extension of corrosion damage that has occurred in the plate. Phase values mapped on the sample can be correlated to the thickness

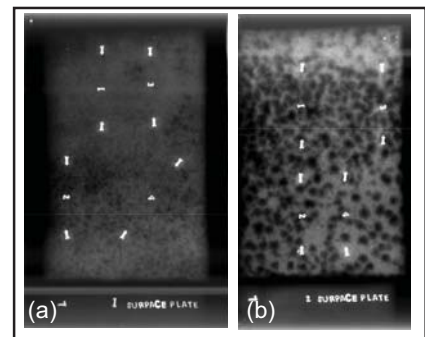


Fig. 4 Radiography images of (a) Normal and (b) Corroded MS plates

variation in the material with appropriate calibration.

The loss in thickness due to corrosion is compared with those values obtained from radiography technique. The percentage thickness loss estimated at different positions of the corroded MS plate varies from 17.78 to 34.78 by gamma scattering and 19.26 to 35.29 by radiography method.

The experimental and Monte-Carlo simulation results show that the scattering method is highly sensitive to changes in electronic and physical densities of the volume element under study and the magnitude of embedded corrosion can be clearly identified and quantified by monitoring single scattered events. An intercomparison of these results with those obtained by from conventional radiography imaging and thermography measurements show that the results are consistent and in line with each other.

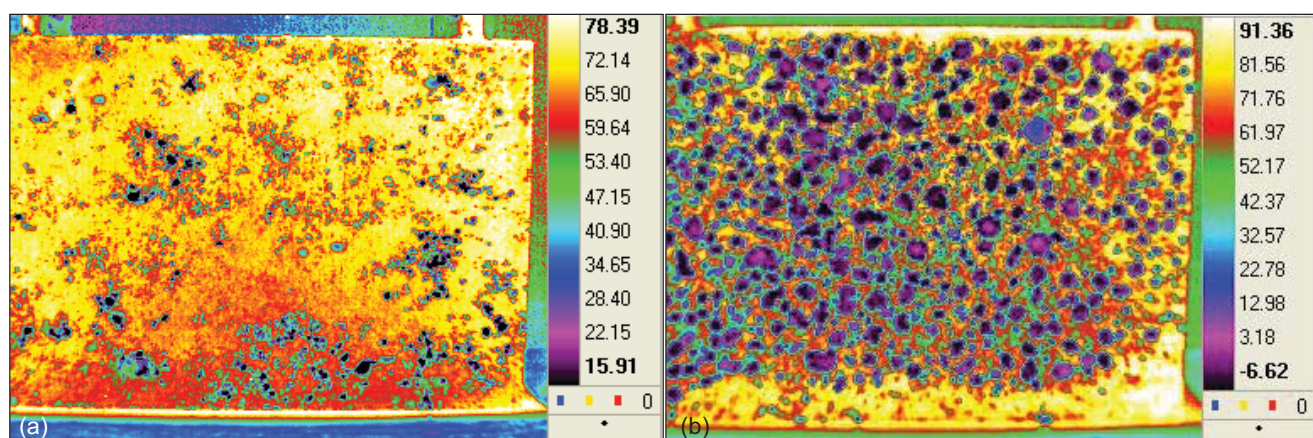


Fig. 5 Thermography (Phase) images of (a) Normal and (b) Corroded MS plates respectively

## V.4 Three-Dimensional Modeling and Array Sensor Development for Magnetic Flux Leakage NDE

Magnetic flux leakage (MFL) technique is widely used for non-destructive evaluation (NDE) of defects in ferromagnetic objects. Numerical modeling plays a vital role in predicting the MFL signals, studying the field/defect interactions and in optimizing the magnetizing unit and the test parameters. The understanding evolved during numerical modeling can be used to study inclined and interacting defects like slivers, closely situated fine cracks arising from excess grinding and defects (arising during low cycle fatigue) which are difficult to simulate experimentally.

Three-dimensional finite element (FE) modeling has been carried out to study the leakage flux from inclined and interacting defects in ferromagnetic material. The effect of inclined defects (inclination changed by 0°, 15°, 30°, and 45°) in 14 mm thick carbon steel plates on tangential ( $B_x$ ) and normal ( $B_z$ ) components of leakage fields have been predicted and validated experimentally.

Figure 1 shows the arrow plot of magnetic flux density of a 45° inclined surface-breaking slot of 6 mm deep

in 14 mm thick plate. As can be seen, the magnetic field is perturbed at the slot region and is leaked out of the slot surface. The predicted MFL signals are found to be asymmetric with increase in angle of inclinations. Further, the peak-to-peak signal amplitude is found to decrease with angle of inclination.

The influence of two interacting defects (6 mm deep slots separated by a distance of 4, 6, 8 and 10 mm) on the leakage fields was predicted by plotting the contour map of  $B_x$  component.

Figures 2a and 2b show the typical model predicted and experimentally measured contour plot of leakage fields arising from two 6 mm deep slots separated by 4 mm in 14 mm thick plates respectively. As can be seen, the shape of magnetic profile is dictated by the interacting defect geometries. It has been found that, when the slots are nearby, the intensity of the peaks gets reduced due to the dipole interaction between closely spaced defects. The effect of nearby slots with different depths on MFL signals have also been evaluated by model and experiments.

From the model predicted MFL signals, several useful features such

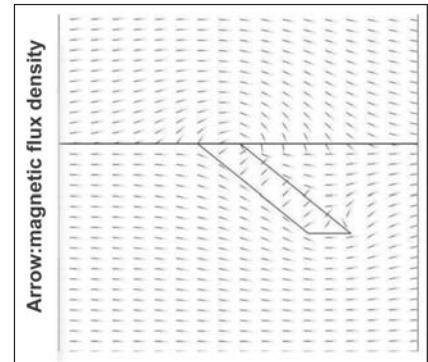


Fig. 1 The flux density arrow plot of a 45° inclined surface slot predicted by FE model

as signal amplitude, full width at half maximum, skewness and area under the signal have been determined for automated classification of inclined defects and for evaluating the spatial resolution of the MFL technique. The features predicted from model are found to be in good agreement with that obtained from experimental investigations.

Giant magneto-resistive (GMR) sensor array is a good candidate sensor to improve the performance of classical sensors due to its higher

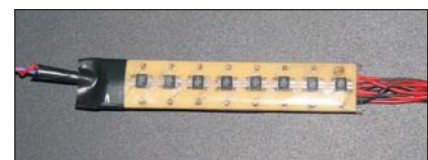


Fig. 3 Array GMR sensor

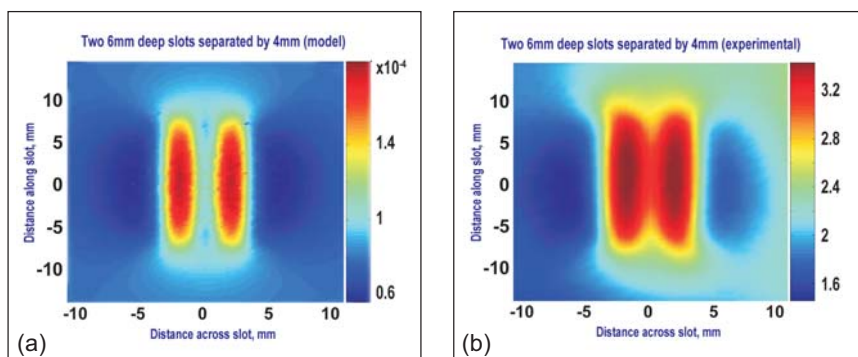


Fig. 2 a) Model predicted and b) Experimentally measured profile of  $B_x$  component from two slots separated by 4 mm in a 14 mm thick steel plate

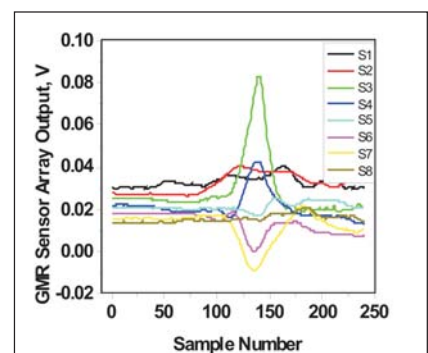


Fig. 4 Response of eight element array GMR sensor

sensitivity at low magnetic fields. For enhanced detection of defects with reduced inspection time, an array of eight GMR sensors (Figure 3) has been developed.

A software has been developed in LabView for acquisition of data from the eight GMR sensors, processing and producing on-line MFL image of defects during the scanning of the array

sensor over an object surface. The array sensor could detect and image defects as shallow as 0.5 mm deep in a 12 mm thick carbon steel plate and also defects located 6 mm below the surface (Figure 4).

## V.5 Short-time Fourier Transform Technique for Extracting Ultrasonic Signals Submerged in Back-Scatter Noise

An ultrasonic wave propagating through a polycrystalline material suffers spectral distortion due to high rate of attenuation of its high frequency components. This is particularly in the case of materials with coarse grain structure and high acoustic anisotropy. This results in a change in the central frequency of its power spectrum. Further, in case of high scattering materials, the back-wall/ defect reflection often gets submerged in high amplitudes of back-scatter signals and the signal to noise ratio is very poor. In the present study, a Short Time Fourier Transform (STFT) based methodology has been developed for extracting ultrasonic signals submerged in

back-scatter noise. The effectiveness of the methodology has been demonstrated for specimens of AISI type 316 stainless steel with large grain sizes.

A 6mm diameter, 25 MHz unfocused, immersion transducer and 35 MHz broadband ultrasonic pulser receiver were used to acquire ultrasonic data and were digitized at 500 MS/s. The A-scan (one dimensional) signals corresponding to different grain size specimens, normalized with respect to the peak amplitudes of the first back-wall echo signal, were windowed with a short Hamming window and their short time Fourier transforms were obtained for

analysis. Figure 1 shows a typical RF ultrasonic signal and its STFT obtained for a specimen with an intermediate grain size (121  $\mu\text{m}$ ). The back-scatter noise during the water path (before the front surface reflection) is very less. However, as the beam enters into the material, a sudden increase in the back-scatter noise can be observed clearly after the water-specimen interface echo. The amplitude of the back-wall echoes decreased and the spectrum shifted marginally towards lower frequency with increasing propagation distance. It is also seen that the peak frequency of the first back-wall echo is much lower as compared to the frequency content

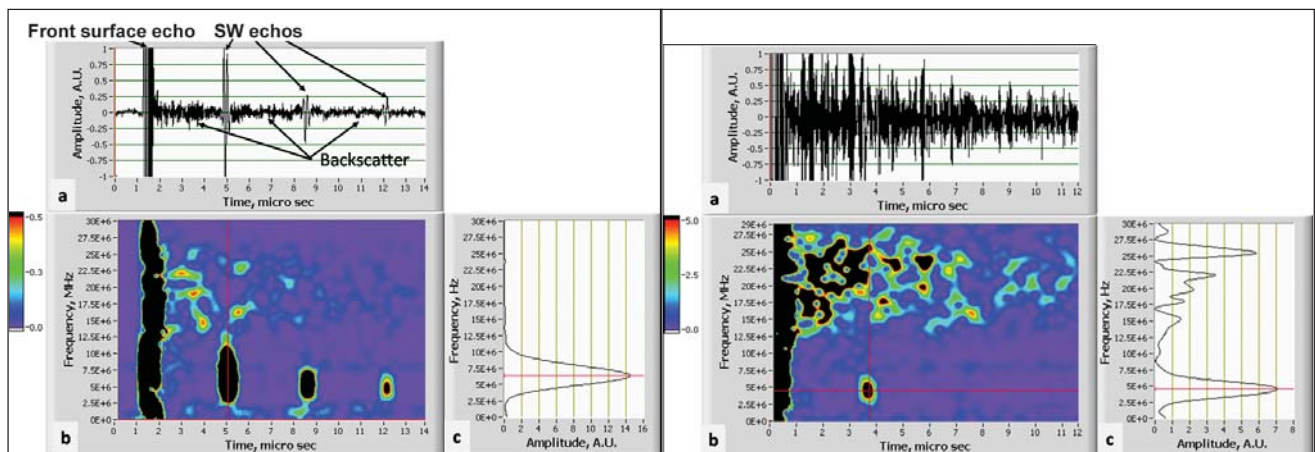


**Fig. 1** (a) Time domain signal from specimen of 121  $\mu\text{m}$  grain size (b) its spectrogram and (c) frequency content of the first back-wall echo

**Fig. 2** (a) A-scan, (b) spectrogram and (c) frequency transform of the first back-wall for 210  $\mu\text{m}$  grain size specimens

of the front surface reflection and the back scatter noise. The frequency content of the back-scatter signal obtained even after the first and the second back-wall echoes is much higher than that of the first back-wall echo. This is due to the higher scattering of the higher frequency components. The high frequency scattered energy keeps returning to the transducer due to multiple scattering and reflections of the originally scattered energy from the grains and the specimen boundaries in the direction of the transducer, until they are totally lost in the material due to absorption

phenomena. Based on this understanding of the frequency dependent scattering of ultrasonic waves in polycrystalline materials, it can be visualized that a back-wall reflection/ defect-echo can be differentiated from the back-scatter noise in the joint time frequency domain viz. the Short Time Fourier Transform analysis.

As can be seen in Figure 2, the back-wall echo is submerged in the back-scatter noise due to high scattering in the large grain size (210 μm) specimen. It could not be distinguished either in the time domain (A-scan) or in the

frequency spectrum. However, with even such a poor signal to noise ratio also, the back-wall echo stands out clearly with its low frequency component in the short time Fourier transform. The higher frequency peaks are from back-scatter noise. This demonstrates the advantage of the short time Fourier transform based approach over conventional frequency spectrum based analysis for extracting signals submerged in the back-scatter noise. The developed methodology will be very useful for defect detection and characterization in highly attenuating materials.

## V.6 Application of Advanced NDT for Quality Audit in DAE and other Strategic Sectors

**A**dvanced Ultrasonic examination technique like Phased array provides high speed electronic scanning without moving parts, improved inspection capabilities through software control of beam characteristics, inspection with multiple angles with a single electronically controlled probe, many configurations; P/E, T/R, TOFD and Tandem, and greater flexibility for inspection of complex geometries (optimized focusing and optimized beam angle).

Steam generator (Figure 1) is a vertical, countercurrent shell – and – tube type heat exchanger with sodium on shell side, flowing from top to bottom and water/steam on the tube side. The very high reactivity of sodium with water makes the steam generator a key component in determining the efficient running

of the plant and demand high integrity of steam generator weld joints. Advanced ultrasonic testing techniques like phased array has been applied to evaluate the shell side 12 mm thick butt welded joints as a part of quality audit. A total weld length of 6 meter from various seams has been subjected for ultrasonic examination. This is the first instance that a core nuclear component like steam generator has been evaluated by using phased array advanced ultrasonic examination technique. For this, a Phased array ultrasonic transducer of 5 MHz frequency having 16 elements with 0.6 mm pitches has been used.

During the scanning indications were noticed at various locations. The results were compared with the radiographic examination and found to be satisfactory. When compared

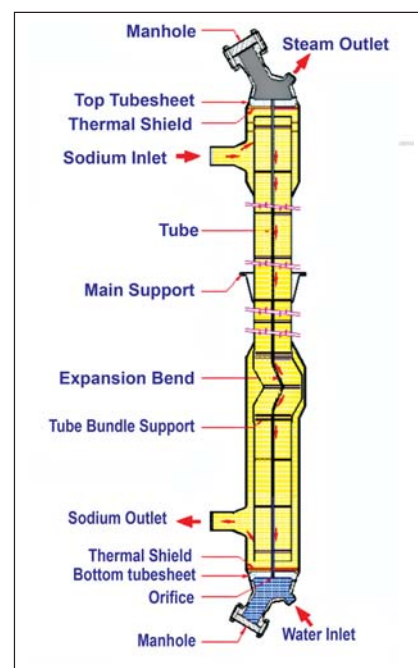


Fig. 1 Steam generator for 500 MWe PFBR

with the conventional pulse echo ultrasonic examination technique, it was found that there is a higher probability of detection and drastic reduction of scanning and evaluation

time with phased array ultrasonic technique.

Phased array ultrasonic examination technique has also been applied for the evaluation of Silicon steel Rocket Motor Casing (Figure 2) and Maraging steel Rocket Motor Casing (Figure 3) butt welded joints for Defence Metallurgical Research Laboratory (DMRL) and Advanced Systems Laboratory (ASL), Hyderabad.

DMRL and ASL are developing a rocket motor casing for their specific purpose. Rocket motor casing is being fabricated by M/s Walchandnagar Industries Limited (WIL), Walchandnagar at Pune. The material chosen was silicon steel and maraging steel based on their in house R&D activities carried out and several other considerations.

Each casing has seven weld joints and all are of pressurized type. Total length of weld scanned was 17 meter



**Fig. 2** Silicon steel rocket motor casing being evaluated at WIL, Pune

in each casing. Being a critical one, phased array advanced ultrasonic testing technique was also applied to evaluate these welds.

The calibration specimen used was a weld plate of same material and thickness with artificial notches as the reference defects. Two G-notches (1.2 mm depth, 0.26 mm width, 2.5 mm length) were used for the calibration purpose for the inspection of Maraging steel motor casing and two F-notches (0.76 mm depth, 0.26 mm width, 1.27 mm length) were used for the Silicon steel motor casing. These notches were



**Fig. 3** Maraging steel rocket motor casing being evaluated at WIL, Pune

on the weld of the calibration plate; one parallel and other perpendicular to the weld.

During the phased array ultrasonic examination, volumetric indications were noticed which were not picked up during the conventional ultrasonic testing. The reason is that conventional pulse echo ultrasonic testing utilizes only one angle at a time whereas in phased array ultrasonic testing, a range of angles can be used at a time. Also, there is a drastic reduction of scanning time and evaluation time was noticed with phased array technique with higher probability of detection.

## V.7 Microcontroller based Compact Solution Calorimeter for Alkali Metal Compounds

**D**etermination of thermal properties of compounds containing alkali metal as one of the constituents requires special type of solution calorimeter as most of the alkali metal compounds are moisture sensitive. In solution calorimeter, the heat of reactions of substances dissolved in appropriate solutions would result in a temperature change in the order of a few mK. For carrying out the studies on such compounds a compact indigenous solution calorimeter is designed. A double

walled glass vacuum vessel with a capacity to hold a solution of 150 ml, a thermal probe with a thermistor (range: 298 to 300 K) and a programmable precision Joule heater calibration source (maximum 4250 J) are developed. The integrating software in LabVIEW has been developed to conduct the experiments and calibration runs.

### Outline of the system

The schematic of the design is shown in the Figure 1. The Dewar

vessel holds the solution in which the reaction is carried out and the heat of reaction is measured. The vessel contains the temperature sensor, stirrer, joule heater and the sample injector. The change in resistance of the thermistor is measured by the customized thermometric method. A suitably configured microcontroller interfaces with the measurement system and logs the data. The controller also takes care of the Joule heater control circuit. Finally the

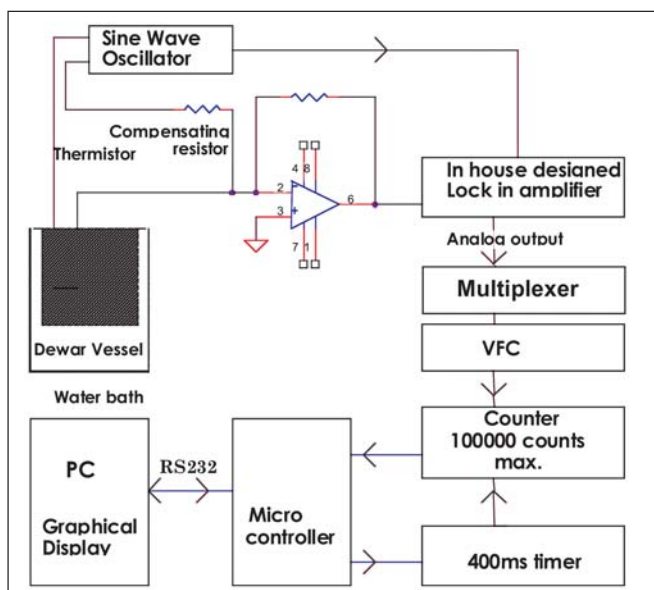


Fig. 1 Schematic of the calorimeter design

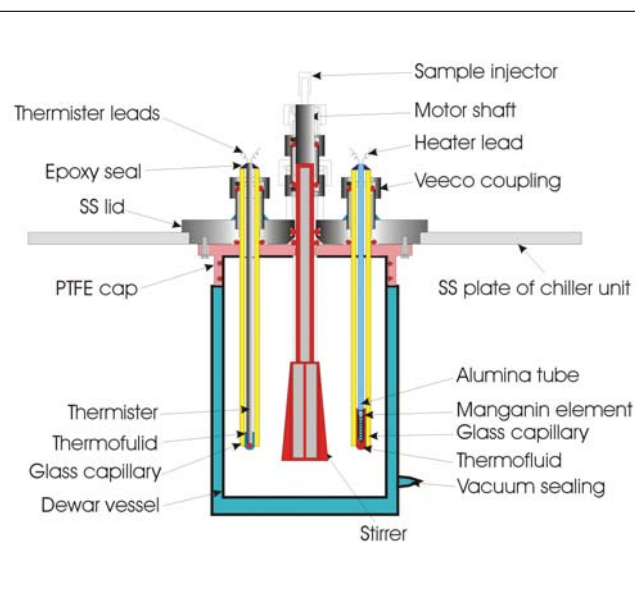


Fig. 2 Schematic of the double walled glass vacuum vessel

controller transmits the temperature and the heater data along with time of measurement to the PC through RS232 serial port. The software in PC processes the data and plots the same. The different blocks of the system are explained in detail in the following paragraphs.

### Double walled glass vacuum vessel

The schematic of the vessel is shown in the Figure 2. It consists of a double walled glass vacuum vessel to hold 150 ml of concentrated acid which can dissolve the sample of interest immediately. The glass vessel can be slipped in to a teflon lid that is provided with a silicone O-ring-liner, which provides a leak tight sealing between the teflon lid and dewar reaction vessel. The teflon lid is fastened to a stainless steel flange, which in turn is attached to the cover plate of a water bath. The stainless steel flange has a feed through to insert teflon stirrer, joules calibrator, a thermistor assembly and the sample injector. All these components are sealed from ambient by means of silicone 'O'-rings. Manganin wire wound over a 3 mm OD alumina tube serves as joules

heater which is used to calibrate the system with known amount of heat input. During experiments the water bath is maintained at  $298 \pm 0.01$  K. The Teflon stirrer is coupled with a DC motor and the speed is controlled by means of a regulator. A thermistor is concealed in a thin walled stainless steel tube which serves as thermal probe.

### Instrumentation details

The thermal probe is constructed using the YSI 44000 series thermistor that has  $10 \text{ k}\Omega$  at  $298 \text{ K}$  with a sensitivity  $\Delta R/R$  at  $298 \text{ K}$  as  $426 \times 10^{-4}$ . The change in resistance is effectively measured by using an operational amplifier circuit in which the base resistance of the thermistor is subtracted using another standard resistor. A sine wave oscillator of in-house built lock in amplifier circuit is adapted to supply the excitation signal to the thermistor and an anti-phase excitation signal to a standard resistor. The resulting differential signal is suitably processed in the synchronized demodulation method. The change in resistance signal is further converted into frequency and measured by a counting system and

the data is processed by a microcontroller.

### Measurement of resistance

As a calibration procedure, a set of standard resistances in the range of our interest ( $10$  to  $9 \text{ k}\Omega$  for the  $2 \text{ K}$  range) is used instead of thermistor and counts were measured. A linear curve fitting is done based on the data collected. The microcontroller uses the fitted values to compute the resistance from measured count data. The standard deviation is  $0.12 \Omega$  with the mean value  $9137.22 \Omega$ .

### Measurement of temperature

All the presently available resistance - temperature models are based on the experimentally established fact that the logarithm of a thermistor's resistance  $R$  relates to its absolute temperature  $T$  by a polynomial equation. Following the Steinhart Hart model the equation for the range of temperature from  $298$  to  $300 \text{ K}$  is simplified as given below:

$$T = 10^6 / [2567.134 - 1.232(\ln R) + 1.022(\ln R)^2] \quad (1)$$

The controller computes the temperature from the measured resistance value using the above

equation. The standard deviation deduced from the temperature data logged over 2 hours is  $6.3723 \times 10^{-4}$  K with the mean value at 299.2393K.

### Joule calibrator

The programmable Joule calibration source is integrated to generate known amount of heat energy in the solution in order to calibrate the thermal capacity of the calorimetric system. A highly stable (3 ppm stability) current source is used to heat the joule heater. The current and the period of heating are user selectable. By selection of appropriate parameters in commensurate with the solution under study, a precise amount of heat energy can be released to the calorimeter. The period of heat release can be set up to 1000 s. The actual voltage drop and current passing through the heater are measured by the controller to calculate the actual resistance. Thus the amount of Joule energy applied to the calorimetric

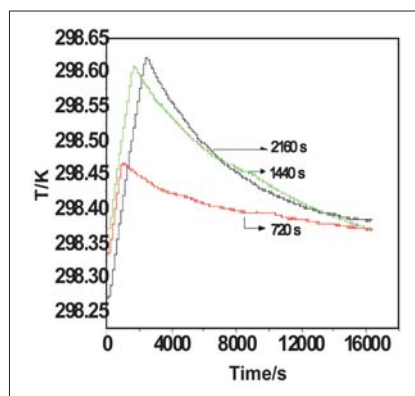


Fig. 3 Acquired plot of temperature for different heating times (Power = 174.135 mW)

vessel is computed and the corresponding rise in temperature is measured using the thermal probe. Three experiments were conducted delivering different amount of heat energy to the system and measured. The typical acquired plot is shown in the Figure 3. The change in temperature for the given amount of energy is plotted to verify the linearity of the system and is presented in the Figure 4. It is found to have good linearity.

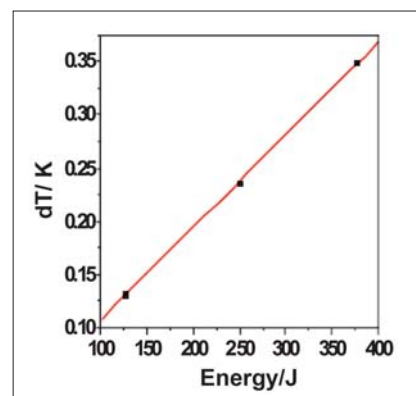


Fig. 4 Plot of Energy vs change in temperature

### User friendly Experimental procedure

The operational procedure is developed in LabView. The Procedure has two menus viz. Calibration and Experiment. The acquired temperature data is smoothed by five point moving average method and plotted in a graphical display. The display has auto scale feature and hence the thermal profile of the whole experiment in any given time can be assessed.

## V.8 Influence of Aggregation on Thermal Conductivity Enhancement in Stable and Unstable Nanofluids

Thermal conductivity (k) of nanofluids has been an area of interest during the last decade, owing to their applications in heat transfer and need for superior coolants with improved performance. Several studies show unusual enhancement of thermal conductivity of nanofluids. However, some of the recent studies show enhancement within the predictions of effective medium theory. Several possible mechanisms are proposed to explain the large spectrum of data. These include the Brownian motion of

nanoparticles, fluid convection at the microscales, liquid layering at the particle-fluid interface, cluster agglomeration or a combination of above mechanisms. Among these, Brownian motion induced convection and effective conduction through percolating nanoparticle paths are considered to be the two most probable mechanisms that cause the enhanced heat conduction in nanofluids.

Systematic investigation was carried out to understand the role of

clustering of nanoparticles (aggregation) on thermal conductivity and rheology of nanofluids. We follow the time dependant thermal conductivity, average particle size, microstructure and viscosity of a 'stable' (non-aggregating) and an 'unstable' (aggregating) nanofluid. Magnetite ( $Fe_3O_4$ ) nanoparticles of primary particle size of about 8.7 nm and copper oxide (CuO) nanoparticles of size 10 nm were prepared by chemical co-precipitation and precipitation techniques respectively. The

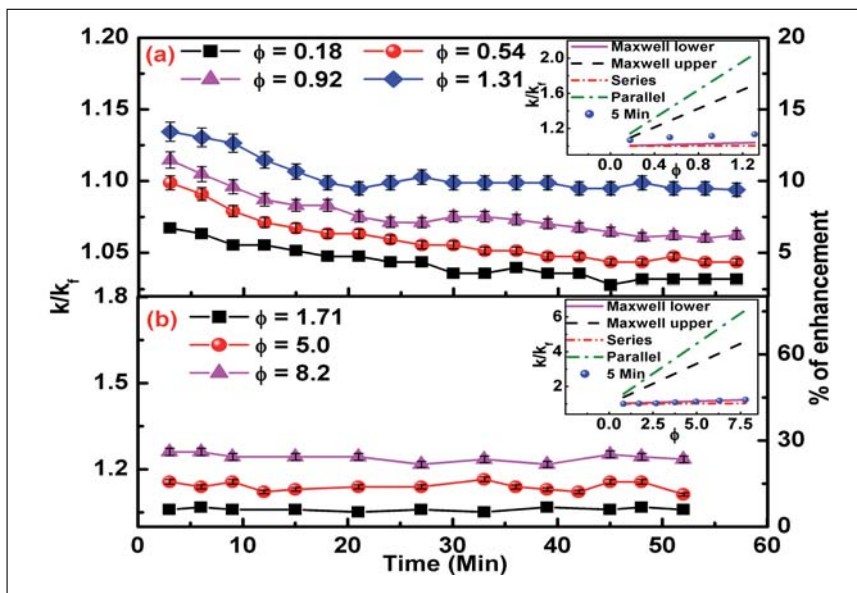


**Fig.1** The variation of  $k/k_f$  and the percentage of enhancement in  $k$  with time after sonication (a) for ethylene glycol based CuO nanofluids with  $\phi = 0.18, 0.54, 0.92$  and  $1.31$  (b) for kerosene based  $Fe_3O_4$  nanofluids with  $\phi = 1.71, 5.0$  and  $8.2$ . The inset shows the fit with Maxwell models

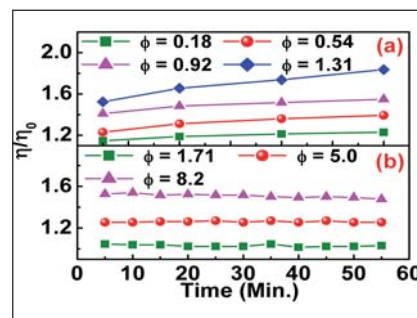
magnetite nanoparticles were functionalized with a surface active species of oleic acid that provides steric stabilization. Thermal conductivity was measured using a transient hot wire. A rotational rheometer with a cone and plate geometry was used for the viscosity measurements.

Figure 1a shows the variation of  $k/k_f$  and the  $k$  enhancement with time, after 20 minutes of sonication of ethylene glycol (EG) based copper oxide nanofluids at four different particle concentrations. The highest value of  $k/k_f$  is observed immediately after sonication. The  $k/k_f$  decreases with elapsed time and finally reaches an equilibrium value after a time interval of about 45 minutes. A systematic increase in  $k/k_f$  with particle loading is observed. Figure 1b shows the variation of  $k/k_f$  and the  $k$  enhancement with time after sonication in kerosene based  $Fe_3O_4$  nanofluids at three different particle concentrations. It can be seen that the  $k$  values are time independent, though the particle number density was much higher than that of CuO.

It is known that the fatty acids offer steric stabilization, and prevent the formation of agglomerates in dispersions. However in CuO nanofluids, the aggregation and the subsequent settling of agglomerates leads to a decrease in  $k$  with elapsed time.

For a nanofluid with non-interacting spherical nanoparticles, the effective-medium or mean field theory of Maxwell predicts a thermal conductivity ratio of

$$\frac{k_p}{k_f} = \frac{1 + 2\beta\phi}{1 - \beta\phi}$$



**Fig.2** The variation of  $\eta/\eta_0$  with time after sonication for (a) EG based CuO nanofluids and (b) kerosene based  $Fe_3O_4$  nanofluid

where  $\phi$  is the nanoparticle volume fraction,  $k_p$  and  $k_f$  are the thermal conductivities of the nanoparticle and the base fluid respectively.  $\hat{\alpha}$  is given by  $(k_p - k_f)/(k_p + 2k_f)$ . There are two limiting bounds for classical Maxwell theory that correspond to two geometrical configurations of the nanoparticles. The enhancement in the parallel mode can be much larger than that of the series mode if  $k_p \gg k_f$ . Since the parallel mode corresponds to a geometric configuration that allows the most efficient way of heat propagation, it represents the absolute upper limit for the effective thermal conductivity. The results show that the Maxwell lower and series bound lie slightly below the experimental data while the upper and parallel bounds fall well above in CuO nanofluid (insets of Figure 1a). On the contrary, the data fits well with Maxwell model for  $Fe_3O_4$  nanofluids (insets of Figure 1b).

Figure 2(a) shows the variation in viscosity ratio with time for EG based CuO nanofluids at different particle loading. The viscosity ratio was found to increase with time after sonication in all the nanofluids. The nanofluid with low particle loading shows least enhancement in viscosity with time and the extent of viscosity

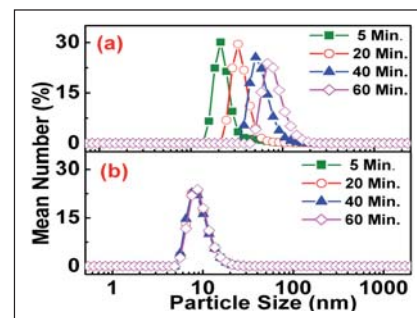


**Fig. 3** Mean number percentage as a function of particles size at different time intervals after sonication (a) EG based CuO nanofluids with  $\phi = 0.18$  and (b)  $Fe_3O_4$  nanofluids with  $\phi = 0.414$

enhancement was high for nanofluids with higher particle loading owing to the great degree of aggregation. Interestingly, the viscosity measurements in kerosene based magnetite nanofluids (Figure 2(b)) at different time intervals after sonication do not show any variation with time.

Figure 3 shows the variation in particle size distribution with time for copper oxide and iron oxide nanofluids with different particle loading. Interestingly, the average particle size was found to increase with time after sonication in CuO nanofluids, while the particle size remains constant for iron oxide nanoparticles. To obtain macroscopic evidence of the aggregation process, the phase contrast microscopic images of the nanofluids are taken at different time intervals. Figure 4 shows the microscopic images of EG

based CuO nanofluids taken at three different time intervals ( $t = 0, 30$  and  $60$  min) after sonication with  $\phi=0.54$  (a1-a3), and  $0.92$  (b1-b3) respectively. Figures (c1-c3) show the micrographs of  $Fe_3O_4$  nanofluid for a  $\phi = 5.0$ . The micrographs confirm that fractal like cluster formation takes place in CuO nanofluids with elapsed time after sonication and cluster size increases as a function of time. The  $Fe_3O_4$  nanofluid micrographs show no aggregation (with cluster size  $> 200$  nm) with elapsed time after sonication, probably due to sufficient repulsion through steric hindrance.

The thermal conductivity, viscosity and particle size were time independent and dependant in  $Fe_3O_4$  and CuO based nanofluids respectively. The phase contrast microscopic studies show particle clustering with time in CuO

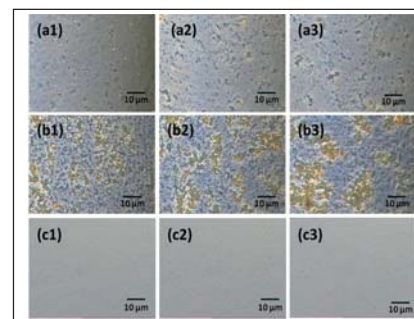


**Fig. 4** The phase contrast microscopy images taken immediately after sonication, after 30 minutes and 60 minutes of sonication of EG based CuO nanofluids  $\phi = 0.54$  (a<sub>1</sub>-a<sub>3</sub>),  $\phi = 0.92$  (b<sub>1</sub>-b<sub>3</sub>) and  $Fe_3O_4$  nanofluids of  $\phi = 5$  (c<sub>1</sub>-c<sub>3</sub>)

nanofluids while no clustering of nanoparticles is observed in  $Fe_3O_4$  nanofluids. These studies unambiguously confirm the prominent role of agglomeration on thermal properties of nanofluids and the importance of surface functionalization of nanoparticles for improved stability.

## V.9 Magnetocardiography Studies using 13 Channel SQUID based System – Tracing ‘His bundle’ Activity

Magnetocardiography signifies the non-invasive and non-contact measurement of the magnetic fields associated with the physiological activities of human heart and represents one of the most challenging applications of the Superconducting Quantum Interference Devices (SQUIDs). These magnetic fields ( $\sim 50$  pico-Tesla) are a million times weaker than the earth’s magnetic field and their measurement falls exclusively in the domain of SQUID technology. Since the ambient magnetic noise could be

as high as 100 nano-Tesla, a Magnetically Shielded Room (MSR) is essential for the measurement and characterization of biomagnetic fields (100 femto-Tesla to 100 pico-Tesla). As shown in Figure 1, a 13 channel SQUID system is currently operational at IGCAR inside a MSR designed to have a shielding factor of 70 dB at 1 Hz improving to 100 dB at 100 Hz.

The system consists of thirteen first order axial gradiometers arranged in a hexagonal close packed array inside a 130 mm diameter circle,



**Fig. 1** 13 channel SQUID based system for magnetocardiography

each connected to an individual SQUID sensor, and enables simultaneous measurement of magnetic fields at thirteen different locations at sampling rates upto 204 kHz per channel. The system

was operated at a gain setting of  $5V/\Phi_0$  and the typical noise was estimated to be under  $9 \text{ femto-Tesla}/\sqrt{\text{Hz}}$ .

The cryostat has a warm-to-cold distance of about 10 mm and enables measurements to be carried out with a high signal-to-noise ratio. Figure 2 shows the magneto cardiogram (MCG) recorded simultaneously at 13 locations on the chest and shows all the distinct features such as the P-wave (atrial depolarization), QRS peak (ventricular depolarization) and T-wave (ventricular repolarization). Using this data, iso-field contour maps have been generated and the direction of the equivalent current dipole has been inferred at different instants of the cardiac cycle. Such visual aids help recognize any abnormalities easily. It is often important for the clinician to locate the signal associated with 'His bundle' using an invasive catheter tip electrode in subjects suffering from cardiac arrhythmia. Clinicians use an invasive catheter based procedure for recording this as shown in Figure 3.



**Fig. 2** Thirteen Channel magneto-cardiogram recorded using the system

However, as shown in many of the cases, it was possible to recognize the 'His bundle' like feature in the signal averaged MCG. Development of a non-invasive technique for recording the 'His bundle' activity (Figure 3) is very significant and augurs well for the clinical management of arrhythmias.

'His bundle' is a fine structure surrounded by fibrous insulating tissue making the electric potential measurement relatively difficult unless the invasive catheter tip electrode is inserted very close to it. Since the magnetic measurements are less affected by the electrical conductivity of the surrounding

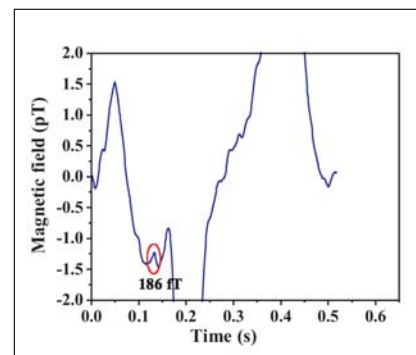


**Fig. 3** Signal averaged MCG showing the 'His bundle' activity marked by a red oval

tissues, experiments were carried out on five human subjects. Since the activity of the 'His bundle' is typically in the range of 100-200 femto-Tesla, it is essential to average a large number of nominally identical cardiac cycles using a fiducial reference point on the time axis to provide the necessary trigger. If  $N$  cardiac cycles are averaged, the uncorrelated noise is suppressed by a factor of  $\sqrt{N}$ , while any activity, which maintains a definite phase relationship with the fiducial reference, will stand out. In some subjects, the 'His-bundle' like feature could be seen in the P-R segment of the recorded magneto cardiogram even before averaging.

## V.10 Development of Borate based Tissue Equivalent Thermoluminescent Phosphors

Thermo luminescent material is widely used as a very sensitive detector for the estimation of absorbed radiation doses in human beings in nuclear industry and for clinical applications. Accurate measurement of the absorbed dose in human tissues should be performed using a dosimeter material which has energy absorption characteristics nearly same as that of soft biological tissue,

i.e. to be tissue equivalent. Ideally the effective atomic number ( $Z_{\text{eff}}$ ) of the dosimeter material should match as close as that of biological tissue ( $Z_{\text{eff}} = 7.42$ ) so the measurement becomes independent of the energy of the incident photons. The tissue equivalence becomes very important for the incident gammas or X-rays in the energy region between 20 and 100 keV, i.e. in the region which is

important in medical applications of radiation, especially diagnostic radiology. At this energy region the photoelectric interaction is predominant and depends on the third power of the atomic number of the Thermo luminescent material; so, at these energies there is an over-response for materials of high  $Z_{\text{eff}}$ .

The  $Z_{\text{eff}}$  for some of the popular TLD phosphors are as follows; LiF= 8.14,

$\text{CaSO}_4:\text{Dy} = 15.3$ ,  $\text{CaF}_2 = 16.3$ ,  $\text{Li}_2\text{B}_4\text{O}_7 = 7.3$  and  $\text{MgB}_4\text{O}_7 = 8.4$ . Among them detectors of lithium fluoride based are the most popular. Lithium borate based thermo luminescent dosimeters appeared to be attractive, especially after advances in the preparation procedure by a sintering technique, with an effective atomic number of 7.3 and is significantly superior to LiF. An additional advantage is its simple glow curve structure and consequent stability under various thermal treatments and its outstanding stability against radiation damage. In addition to X-ray and  $\alpha$ -ray radiation, lithium borate based dosimeters have an additional advantage of being sensitive to neutron radiation, since boron has a high neutron absorption cross-section. Recently, two types of borate based tissue equivalent and neutron sensitive thermo luminescent have been synthesized in the laboratory using the simple solid state diffusion methods. They are i) Mn doped lithium tetra borate and ii) Tb doped lithium magnesium borate. The dosimetric characteristics of these thermo luminescent phosphors are better than the existing borate based phosphors.

The first thermo luminescent material based on lithium borate which was introduced in radiation dosimetry was  $\text{Li}_2\text{B}_4\text{O}_7:\text{Mn}$  phosphor. The sensitivity of the phosphor has improved when it was doped with copper, silver, phosphorus, magnesium, indium or any combination of these dopants.

$\text{Li}_2\text{B}_4\text{O}_7:\text{Mn}$  phosphor used in this study are synthesized by solid state sintering, where stoichiometric compositions of  $\text{Li}_2\text{CO}_3$  and  $\text{H}_3\text{BO}_3$

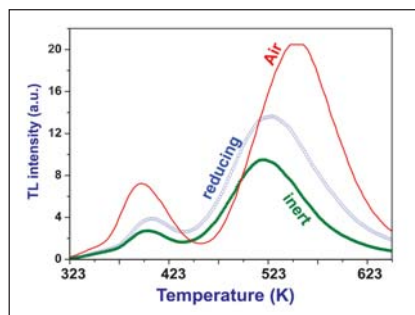


**Fig. 1** Thermo luminescent glow curves of gamma irradiated  $\text{Li}_2\text{B}_4\text{O}_7:\text{Mn}$  prepared in air, reducing and inert atmosphere

along with the required dopant ( $\text{MnCO}_3$ ) concentration are well mixed and sintered at  $1023 \pm 10$  K for 3 hours in an alumina crucible using a muffle furnace in air, inert or reducing atmosphere. The thermo luminescent glow curves of the  $\text{Li}_2\text{B}_4\text{O}_7:\text{Mn}$  phosphor prepared at different atmosphere are shown in Figure 1. The best phosphor sample with maximum sensitivity is obtained for the sintering in air atmosphere. This material has shown the main dosimetric thermo luminescent glow peak at 533 K, which is 50 K higher than the earlier reported thermo luminescent peak in  $\text{Li}_2\text{B}_4\text{O}_7:\text{Mn}$ . Thermo luminescent emission of the glow peak is observed in the orange region at 580 nm is shown in Figure 2. The main dosimetric peak occurs at a higher temperature and is found to exhibit negligible fading behavior upon storage. The response of this phosphor is linear upto a dose range of  $10^3$  Gy. The thermo luminescent sensitivity is nearly equal to tissue-equivalent TLD-100 (LiF).

Two major drawbacks reported in literature for  $\text{Li}_2\text{B}_4\text{O}_7:\text{Mn}$  in earlier preparation technique, hygroscopicity and, sensitivity to light and strong fading are overcome in our synthesis. This phosphor is found to be non-hygroscopic and chemically stable. Regarding the light induced thermo luminescent fading,



**Fig.2** Thermo luminescent emission of orange light from  $\text{Li}_2\text{B}_4\text{O}_7:\text{Mn}$  phosphor

irradiated  $\text{Li}_2\text{B}_4\text{O}_7:\text{Mn}$  powder on direct exposure to room light or sunlight for six hours showed no fading. In  $\text{CaSO}_4:\text{Dy}$  powder about 75% of the thermo luminescent signal is erased on exposure to sunlight for same duration. With regard to its applicability to neutron dosimetry, the thermo luminescent sensitivity is found to be comparable with that of TLD-100.

Magnesium borate is a near tissue equivalent material and doping of rare earth elements in this host are reported recently. A very sensitive  $\text{MgB}_4\text{O}_7:\text{Dy}$  ( $Z_{\text{eff}}=8.4$ ) thermo luminescent phosphor which is prepared through the solid state sintering is reported in literature. A mixed borate of lithium and magnesium ( $Z_{\text{eff}} \sim 8$ ) material with rare earth dopant can be ideally a better tissue-equivalent thermo luminescent phosphor of high sensitivity. Mixed lithium magnesium borate polycrystalline thermo luminescent phosphor powder doped with terbium is synthesized successfully in our laboratory by the high temperature solid state diffusion reaction.

Gamma irradiated LMB:Tb phosphor powder showed a very intense single thermo luminescent glow peak at 513 K (Figure 3). It showed thermo luminescent sensitivity about 10 times

that of tissue equivalent TLD-100 (LiF) phosphor. TL dosimetric properties of the LMB:Tb<sup>3+</sup> phosphor showed near linear thermo luminescent response versus gamma dose over wide range of six decades till the saturation dose of 10<sup>3</sup> Gy. Another advantage of this phosphor is simple annealing procedure followed for the reuse which keeps the glow curve structure and sensitivity stable for many cycles. Post- irradiation storage stability of LMB:Tb<sup>3+</sup> phosphor is comparable with other standard thermo luminescent phosphors. The thermo luminescent emission have shown a PMT sensitive broad green emission band

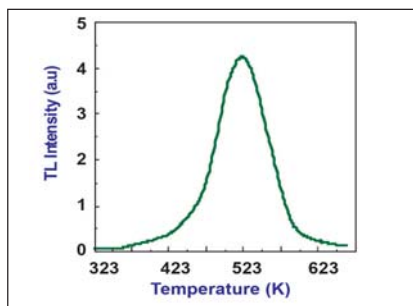


**Fig. 3** Thermo luminescent glow curves of gamma irradiated LMB:Tb phosphor



**Fig. 4** Thermo luminescent emission of pale green light from LMB:Tb phosphor

around 550 nm which consists of both Tb<sup>3+</sup> and host material emissions (Figure 4). PL spectra revealed the characteristic Tb<sup>3+</sup> lines and no redox process observed on irradiation. It is a very promising tissue equivalent thermo luminescent

dosimeter and due to the presence of large number of boron atoms in the phosphor compound it can be a good neutron dosimeter also and its neutron sensitivity can be enhanced by using <sup>6</sup>Li and <sup>10</sup>B enriched starting chemicals.

## V.11 Early Detection of Diabetic Neuropathy using Infrared Thermal Imaging

The prevalence of type 2 diabetes is rapidly rising worldwide. It has been recognized that the main causes of ulceration are diabetic neuropathy and vascular disease of both the macro and microcirculation. Uncontrolled diabetes leads to various complications affecting the eyes, kidneys, heart, nerves and feet. Indeed, foot complications are one of the most frequent problems of diabetes mellitus and key contributors to medical costs, as

50% of all inpatient admissions due to diabetes are due to foot complications. The main causes of diabetic complications are decreased blood supply and loss of sensation to the feet (neuropathy). For confirming the presence or absence of diabetic neuropathy, nerve conduction velocity measurements and alternating current perception threshold are used as the standard methods. The latter is used to assess the

quantitative level of severity of diabetic sensory neuropathy. Currently, there are equipments to measure these two parameters, i.e nerve conduction velocity and current perception threshold. Handheld dermal thermometers and liquid crystal thermography are being used for home temperature monitoring e.g. warmth or coldness of feet. High temperatures under the foot, coupled with reduced or complete loss of sensation can

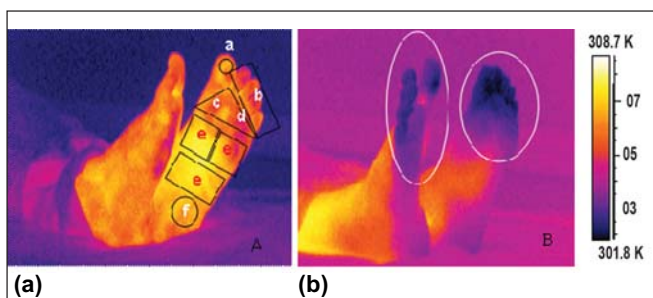


**Fig. 1** Typical thermal image foot with (a) Hot and (b) Cold regions

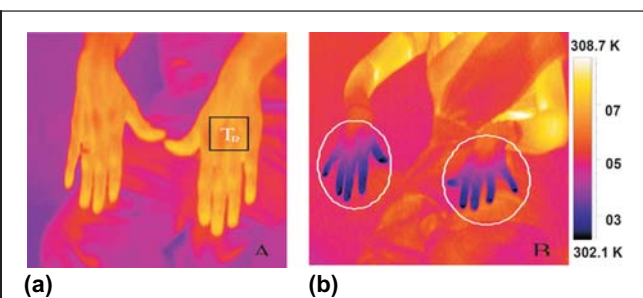


**Fig. 2** (a) Typical thermal image of dorsal view of hand of patients and (b) Cold spots in the both hands

predispose the patient to foot ulceration. Thermography has emerged as a potential tool for diagnostic as it enables remote and non contact mapping of thermal patterns. Infrared thermography (IRT) has been used to determine the temperature variations of the plantar surface of feet. The purpose of the present study is to see the correlation between foot temperature and neuropathy in subjects with type two diabetes.

The study subjects were randomly selected from Dr. Mohan's Diabetes Specialities Centre, Chennai. A total of 112 type 2 diabetic subjects underwent thermal imaging using infrared thermal system. The room temperature and humidity were maintained consistently with air conditioning. The skin temperatures of both feet and hands are imaged using infrared thermal imaging system. Thermal imaging of the patients was carried out using a Thermovision system. This is a compact lightweight focal plane array based system with a temperature resolution of 0.1K. A high-resolution color image is provided in real time, which can be viewed on the miniature screen provided with the system or using an external monitor. The image is captured and stored in the removable PC-card. The surface temperature profiles of the patients were recorded and later analyzed using IRWIN software. Neuropathy was assessed using biothesiometer. Vibratory perception threshold (VPT) of the great toes was measured in a standardized manner by a single observer. The biothesiometer probe was applied perpendicular to the test site with a constant and firm pressure and VPT was measured at the distal plantar surface of the great toe in

both legs. The voltage was slowly increased and the VPT was defined as the voltage value when the subject first felt the vibration. The mean value of three measurements of both legs was used for analysis. The mean + two standard deviations (SD) was used to derive the upper limit of normal for the non-diabetic study population aged 20–45 years, which was 19.7 V. Hence the cutoff point was derived as  $VPT \geq 20$  V. Vibratory perception threshold is largely meant to diagnose high risk patient of diabetic ulcers. However, several epidemiological studies have been done using vibratory perception threshold as a cut point because it is the simplest parameter of assessing neuropathy. In fact, peripheral neuropathy cannot be assessed by one test and it needs a battery of tests, each of which measures different parameters, e.g., small fiber, large fiber, myelinated and unmyelinated etc. Therefore, vibratory perception threshold is recognized as a simple screening tool. Data were expressed as mean  $\pm$  standard deviation. Pearson correlation analysis was carried out to determine the relation of mean foot temperature with other risk variables. All analyses were done using a windows-based statistical package for the social sciences (SPSS)  $p \leq 0.05$  was considered as significant. Where  $p$  is a significant coefficient.

Figures 1a and 1b show the typical thermal images of the foot. In Figure 1(a), the plantar thermal image was divided into six regions of interest. Sufficient care is taken for thermal equilibrium and the planar view of the plantar foot is taken in most of the specimens. The mean foot temperature is calculated from these six regions i.e. (a) hallux (big

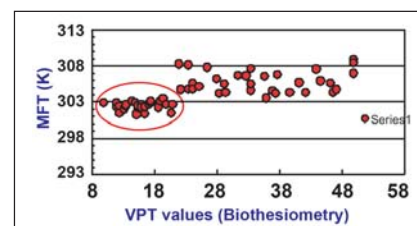


Fig. 3 Mean foot temperature (MFT) as a function of vibratory perception threshold values measured by biothesiometry

toe), (b) lesser toes, (c) arch, (d) lateral sole, (e) fore foot, and (f) heel. In Figure 1(b) cold regions in the toe regions are encircled. In the case of foot temperature imaging by infrared radiations, the important parameters such as mean foot temperature (MFT), temperature difference ( $\Delta T$ ) and the normalized temperature ( $T_N$ ) are calculated using equations 1, 2 and 3 respectively.

$$MFT = \frac{(T_a + T_b + T_c + T_d + T_e + T_f)}{6} \quad (1)$$

$$\Delta T = T_R - MFT \quad (2)$$

$$T_N = \frac{\Delta T}{T_R} \quad (3)$$

where  $T_a$  is the Hallux temperature,  $T_b$  is the lesser toes temperature,  $T_c$  is the arch temperature,  $T_d$  is the lateral sole temperature,  $T_e$  is the fore foot temperature and  $T_f$  is the heel temperature.  $T_R$  is the reference temperature. In our experiment is the average hand temperature (shown in Figure 2a). The patient of Figure 1a is a 44 year old non neuropathic male with a history of diabetics for 7 years and HbA1C value 9.6 and the patient of Figure 1b is a 61 year old non neuropathic female with a history of diabetics for 31.7 years and HbA1C value 6.6. In Figure 1b the average foot temperature in the circled region is 302.3 K.

Figure 2b shows the typical thermal image of dorsal view of hand of patients and marked area in the hand image corresponds to reference temperature ( $T_R$ ) (average

temperature in the marked area in K) and Figure 2b shows the thermal image of patient with cold spots in both the hands (encircled region). The patient of Figure 2a is a 38 year old non neuropathic male with a history of diabetes for 6 years of duration and HbA1C value 6.2. The average temperature of the marked area in Figure 2a is 309.8 K the patient of Figure 1b is a 26 year old non neuropathic female with a diabetic's history of 3.8 years and HbA1C value 11.2. In Figure 2b, the average finger temperature in the circled region is 303.1 K.

Figure 3 shows the mean foot temperature as a function of mean vibratory perception threshold value. The mean foot temperatures were higher for the patients with neuropathy. There were twenty eight patients with vibratory perception threshold values less than twenty at the great toe and they had foot temperature values within the band of 300-303 K. In contrast, there were thirty three patients with diabetes neuropathy (VPT values greater than twenty) and they showed higher foot

temperatures in the range of 303-310 K.

The study also revealed that patients with vibratory perception threshold values on biothesiometry greater than twenty show a higher foot temperature band compared to those patients without neuropathy. Diabetic subjects with neuropathy had higher mean foot temperature compared to non-neuropathic subjects. Mean foot temperature also showed a positive correlation with right great toe and left great toe vibratory perception threshold values.

## V.12 Formation of Periodic Surface Patterns during MeV Heavy Ion Irradiation in Silica

Ion beam sputtering is known to give rise to surface roughening and under certain conditions can result in the formation of self organized surface morphological features such as ripples and quantum dots. Such ordered patterns on ion irradiated surfaces could have wavelengths ranging from micrometers to a few nanometers, mostly controlled by irradiation parameters. Surface micro-roughening, by ion sputtering, leads to the instability of the plane surface against the formation of periodic undulations. The basic reason for the instability is the curvature dependant sputtering; the sputtering rate at valleys on the surface is higher than the sputtering rate at hills. In the absence of smoothing mechanisms all sinusoidal perturbations at the surface will grow and the growth rate will be maximum for the disturbances with the shortest wave length.

However several surface relaxation mechanisms like surface diffusion, irradiation induced viscous flow tend to smooth the surface irregularities giving rise to the reduction in the surface energy. Figure 1a illustrates the curvature dependant sputtering which gives rise to surface roughening. The elliptical contours represent how the energy of an ion is deposited inside the bulk in the Sigmund's sputtering model. Incoming ions strike normal to the surface at trough (positive curvature) at A, O and B and at a crest (negative curvature) at points A', O' and B'. The sputtering rate at any point is proportional to the sum of the energy deposited at that point due to the ions incident at all the neighboring points. At point like O in a positive curvature region (trough) the sputtering rate will be high due to the shorter distances to the energy deposition profiles of the ions incident at neighboring

points as compared to the corresponding point O' at crest (region of negative surface curvature).

The Figure1b shows the surface relaxation by diffusion which tends to smoothen the surface irregularities. The rate of the roughening and smoothening processes depend on the wave vector of the surface irregularities. The rate of surface roughening by

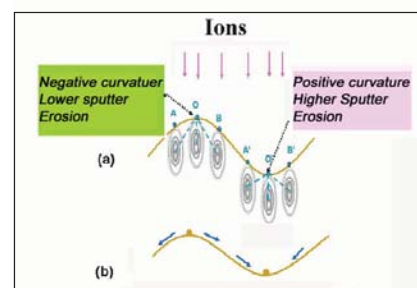


**Fig. 1** The schematic of the surface (a) Roughening by curvature dependant sputtering and (b) Smoothening by surface diffusion by transporting atoms from hills to valleys

curvature dependant sputtering is proportional to the square of the wave vector ( $k^2$ ) and the smoothening rate by surface diffusion is proportional to the fourth power of the wave vector( $k^4$ ). The competition between the roughening and smoothening processes results in the wave vector dependant growth rate  $R_k$  of the surface undulations of the form  $R_k = Ak^2 - Bk^4$ , where A and B are constants dependant on the irradiation conditions and the smoothening mechanisms involved. The dominating wave vector  $k^*$  with the highest growth rate given by,  $k^* = (A/2B)^{1/2}$ , will determine the periodicity of surface morphology observed during ion beam sputtering. In most of the previous studies on the surface pattern formation, irradiation with low energy noble gas ions at off-normal incidence was made use of. In the present study, surface pattern formation was observed during MeV energy heavy ion irradiation at normal incidence in silica. The silica samples were irradiated with

Indium, gold and silver ions in the energy range of 600 keV to 2 MeV, to various irradiation doses in the range of  $1 \times 10^{16}$  ions/cm<sup>2</sup> to  $3 \times 10^{17}$  ions/cm<sup>2</sup>. The irradiation flux was maintained at around  $8 \times 10^{12}$  ions/cm<sup>2</sup>/sec. Irradiations were carried out at room temperature with incoming ion beam normal to the sample surface. The surface morphological features which evolve during ion irradiation were examined by Atomic force microscope (AFM). Figures 2(a) to 2(c) show the AFM images of silica irradiated with 1.8 MeV gold ions to various doses from  $5 \times 10^{16}$  to  $2 \times 10^{17}$  ions/cm<sup>2</sup>. The insets show the FFT taken on respective images. The development of the periodic surface morphology as a function of irradiation dose is evident from figures. No noticeable surface pattern formation was observed in the Silica sample irradiated with Au+ ions to a lower ion fluence of  $5 \times 10^{16}$  ions/cm<sup>2</sup> (Figure 2a). However, clear evidence for the formation of self-organized surface patterns was

observed in the samples irradiated with Au+ ion to the higher ion fluences of  $1 \times 10^{17}$  ions/cm<sup>2</sup> (Figure 2b) and  $2 \times 10^{17}$  ions/cm<sup>2</sup> (Figure 2c). The spatial periodicity of such patterns was found to be around  $1.35 \mu\text{m}$ . The figures (d), (e) and (f) are the plots of Power Spectral Density (PSD) versus the wave vector k in log scale from AFM images shown in (a), (b) and (c) respectively. The appearance of a clear peak in Figures 2(e) and 2(f) around  $\log k = -3$  is indicative of the formation of periodic surface pattern with a spatial periodicity of  $1.35 \mu\text{m}$ . The surface patterns were also observed during irradiation with silver and indium ions of MeV energy. Systematic investigations, by varying the ion energy and irradiation dose rate(flux) have been carried out to understand the mechanisms responsible for surface relaxation. It was found that the spatial periodicity(wave length) of the patterns is flux independent. Further a linear increase of the wavelength with ion energy was also noticed. These two observations strongly suggest that irradiation induced

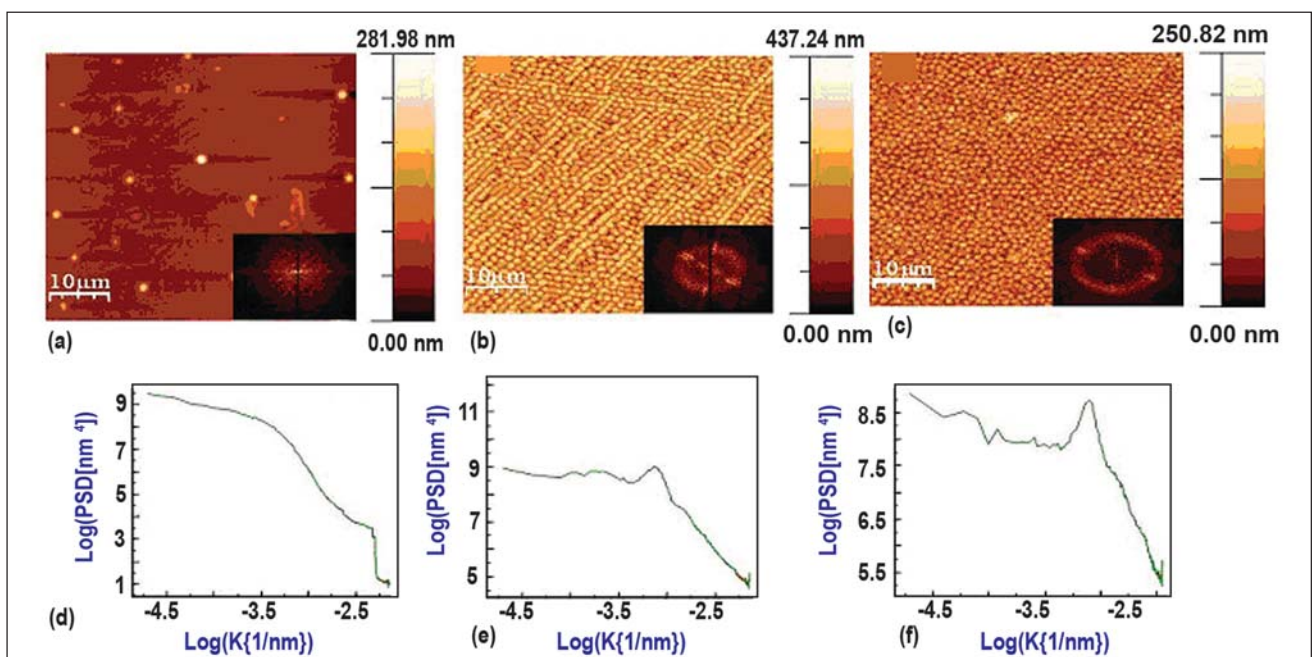


**Fig. 2** AFM image of silica sample irradiated with 1.8 MeV gold ions to fluences of (a)  $5 \times 10^{16}$  ions/cm<sup>2</sup> (b)  $1 \times 10^{17}$  ions/cm<sup>2</sup> and (c)  $2 \times 10^{17}$  ions/cm<sup>2</sup>. Insets show the FFT taken on respective images. (d), (e) and (f) are the plots of PSD verses k in log scale from AFM images shown in (a), (b), and (c) respectively

viscous flow, rather than surface diffusion is the most likely mechanism for surface relaxation. The mechanism for pattern formation hence should be the competition between surface roughening by curvature dependant sputtering and surface relaxation by viscous flow. However the growth rate of the surface morphological features calculated assuming curvature dependent sputtering and irradiation induced viscous flow was

found to be a few orders of magnitude lower than the experimentally observed growth rates. This suggests that the conventional models used in the context of pattern formation during low energy ion sputtering may not be adequate to explain the periodic surface morphology observed under the present experimental conditions. One important observation made during the study of surface morphology was that during

irradiation with metal ions there is surface segregation of metal atoms. The presence of the metal atoms in the surface and near surface region is expected to modify the kinetics of surface roughening. Surface stresses developed due to the accommodation of the metal atoms in the near surface region is expected play a major role in the formation of periodic surface morphology during ion irradiation.

## V.13 Development of Reduced Activation Ferritic Martensitic Steel and its Welding Consumable

Internationally developed reduced activation ferritic martensitic steel (RAFM) contain tungsten in the range 1-2 wt.% and tantalum in the range 0.02-0.18 wt.%. The development of India-specific RAFM steel aims to optimize the tungsten and tantalum contents for better combination of mechanical strength and fracture toughness. Four runs of RAFM steel with tungsten and tantalum in the ranges 1-2 wt.% and 0.06-0.14 wt.%, respectively, were melted through vacuum induction melting and vacuum arc remelting routes with strict control over the

radioactive tramp elements (Mo, Nb, B, Cu, Ni, Al, Co, Ti ) and on the elements that promote embrittlement (S, P, As, Sb, Sn, Zr, O).

### Mechanical Properties

The influence of tungsten and tantalum on the tensile and creep properties of RAFM steel has been studied. Figure 1 shows the variation of ultimate tensile strength of these steels with test temperature. In the investigated tungsten range of 1-2 wt.%, tensile strength was found not to depend on the tungsten content appreciably except in the

intermediate temperature range. Creep tests have been carried out at 823 K over a stress range of 180-260 MPa. The creep deformation of the steels was found to proceed with relatively shorter primary regime followed by an extended tertiary regime with virtually no secondary regime. The variation of minimum creep rate ( $\dot{\epsilon}_m$ ) of the materials with applied stress ( $\sigma$ ) followed a power law relation,  $\dot{\epsilon}_m = A\sigma^n$ , where A and n are constants. The onset of tertiary stage of creep deformation in the steel was found to be delayed with increase in tungsten content, as shown in Figure 2.

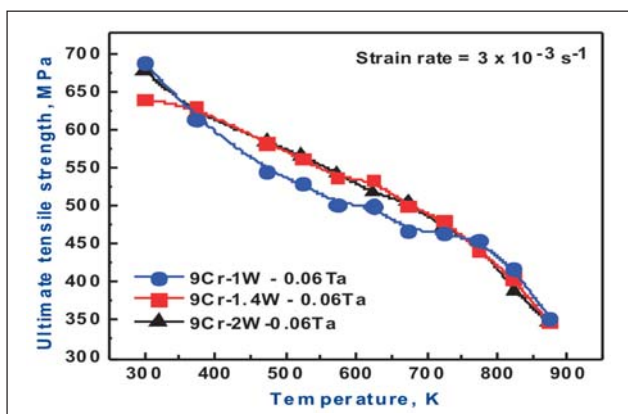


Fig. 1 Effect of tungsten on ultimate tensile strength of RAFM steel

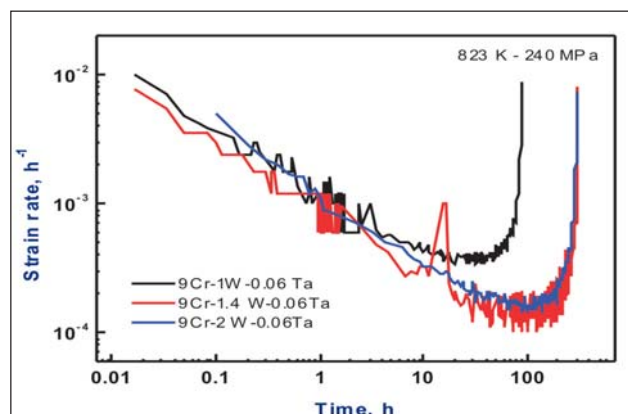


Fig. 2 Effect of tungsten on the onset of tertiary stage of creep deformation

The minimum creep rate decreased with increase in tungsten content. Creep-rupture strength of the steel increased with increase in tungsten content (Figure 3). The increase in tantalum content from 0.06 to 0.14 wt.% in RAFM steel having 1 wt.% tungsten was found to reduce the creep rupture strength and increase in creep rupture ductility.

**Welding Consumable**

As there is no commercially available welding consumable for RAFM steel, development of filler wires for joining of RAFM steel was undertaken. The filler wires are to be used for tungsten inert gas welding (TIG), narrow-gap TIG (NG-TIG) and hybrid laser welding of thick section joints of the RAFM steel. The essential feature of the consumable is that the weld metal microstructures should be resistant to effects of neutron irradiation to achieve the strength levels, fracture toughness, creep and fatigue resistance required to ensure adequate structural stability throughout the operating phase of International Thermo Experimental Reactor. The performance of ferritic-martensitic steel weld depends on various factors such as chemistry of the consumable, welding process and welding parameters. Based on the above, a detailed specification was prepared for the development

Table 1: Tensile Properties of RAFM steel base and weld metal						
Tensile Properties	at Ambient Temperature			at 773 K		
	Specified	Achieved	Base Metal	Specified	Achieved	Base Metal
Y S (Mpa)	560 (min)	<b>687</b>	504	390 (min)	<b>504</b>	399
UTS (Mpa)	660 (min)	<b>782</b>	635	420 (min)	<b>528</b>	420
% Elongation	15 (min)	<b>16.1</b>	21		<b>15.9</b>	20
% Reduction in Area		<b>64</b>	78		<b>61</b>	71

of these filler wires using the concept of weld metal composition matching with that of base metal to ensure the structural stability at high temperatures. TIG welding studies were carried out on 2.5 mm thick RAFM steel using different heat inputs and preheat temperature of 523 K followed by different post weld heat treatments (PWHT). The microstructure of the weld metal in most of these cases showed presence of some amount of delta-ferrite, which is not acceptable as this will seriously affect structural stability. As presence of delta-ferrite is strongly influenced by resultant cooling rate due to the imposed thermal cycle of the welding process, the welding parameters, including the preheat temperature, were suitably modified to avoid presence of delta-ferrite in the weld metal. Optimisation of PWHT parameters was carried out using the weld metal

hardness, after subjecting to various PWHT, as the indicative parameter for achieving the specified mechanical properties. The PWHT parameter that resulted in weld metal hardness very close to that of the normalized and tempered base metal hardness was chosen as the optimum PWHT parameter. After the above welding parameter and PWHT optimizations, the mechanical properties achieved in both ambient temperature and at 773 K (Table 1) are significantly better than that specified and are comparable to the base metal values for the Indian RAFM steel as well as International steels developed for similar applications. Further, the Ductile to Brittle Transition Temperature, using Charpy V-notch impact energy based on 68 J criteria, achieved for the weld metal was 192 K (Figure 4) against the specified value of 228 K.

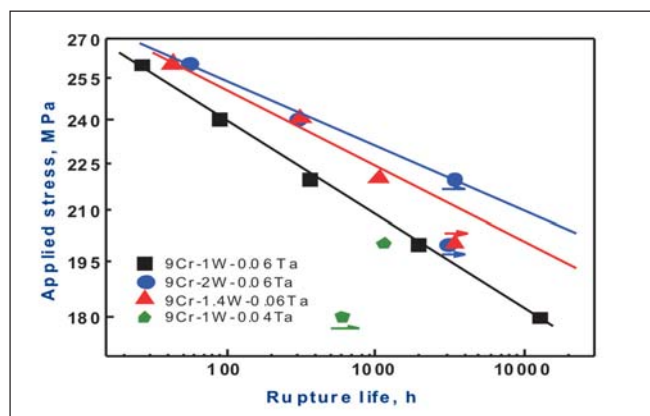


**Fig. 3** Effect of tungsten on the creep-rupture strength of RAFM steel at 823 K

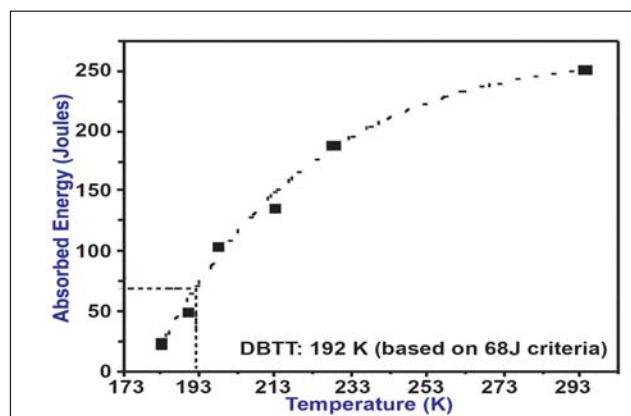


**Fig. 4** Charpy V-notch impact absorbed energy vs temperature for RAFM steel weld metal

## V.14 A Study of Phase Stability of Pulsed Laser Deposited Ceria / Zirconia Multilayers

Ceria stabilized zirconia films are widely used for structural materials due to numerous technologically important properties, such as heat resistance, high hardness, chemical durability and high oxygen ionic conductivity. Pure  $ZrO_2$  exhibits three structural modifications of which the high temperature phases (i.e. tetragonal and cubic which are stabilised in the temperature range 1443-2643 K and 2643-2953 K respectively) are important and are required to be stabilised down to room temperature. The main approach adopted for this purpose is to dope zirconia with trivalent or divalent cations such as  $CeO_2$ ,  $Y_2O_3$  or  $Al_2O_3$ .

Ceria – zirconia multilayers were synthesised by pulsed laser deposition (PLD) using a KrF excimer laser ( $\lambda=248$  nm) from sintered pellets of ceria and zirconia (99.99% purity) as targets. Prior to the deposition of the multilayers, the chamber was evacuated to  $2 \times 10^{-5}$  mbar and the oxygen partial pressure was kept constant at  $3 \times 10^{-2}$  mbar during deposition. Alternate nanoscale layers of ceria and zirconia were deposited on a Si(100) single-crystal

substrate at room temperature. One such multilayer sample was in situ heat-treated in a high-temperature X-ray diffractometer under vacuum of  $2 \times 10^{-5}$  mbar. Cross-sectional TEM (XTEM) studies were carried out in a transmission electron microscope operated at 200 kV. The XTEM micrographs from as deposited as well as thermally annealed specimen have been analysed to reveal the structural details of phase transformations. Figure 1 shows the as-deposited multilayer system where dark bands are from ceria and the bright bands correspond to zirconia nanolayers. The nanolaminates are observed to be well defined, of uniform thickness (ceria and zirconia layers are of 12 nm and 18 nm respectively) over large distances. Selected area electron diffraction pattern (inset) confirmed that ceria is of cubic structure and zirconia is of tetragonal structure. The high-resolution TEM micrograph imaged the lattice fringes corresponding to tetragonal phase of zirconia. After annealing, the interface remains no longer flat and continuous as observed from the HRTEM micrograph shown in Figure 2; grain boundaries near the interfaces are seen

to be reoriented and the position of the initial interface could not be easily identified. In addition, interfacial defects are also seen in the HRTEM micrograph shown in Figure 3. It is quite evident from the high resolution micrographs imaged from the interface region in annealed multilayer that interdiffusion has resulted the formation of  $CeO_2$ - $ZrO_2$  solid solution. The equilibrium  $CeO_2$ - $ZrO_2$  phase diagram also shows that a mixture of tetragonal  $ZrO_2$  and cubic  $CeO_2$  can exist under these conditions. Interdiffusion is also evident from the nanocrystalline grains, which are observed to be extended in both the neighboring nanolayers. The phase transformations occurring in the multilayers among room temperature and high temperature phases have a significant implication in designing novel  $ZrO_2$ -based nanostructures for wide range of technological applications such as solid oxide fuel cells. The present work allows a unique study on some of the issues related to the phase and chemical stability of the multilayers in the as-deposited and in the high-temperature annealed conditions.

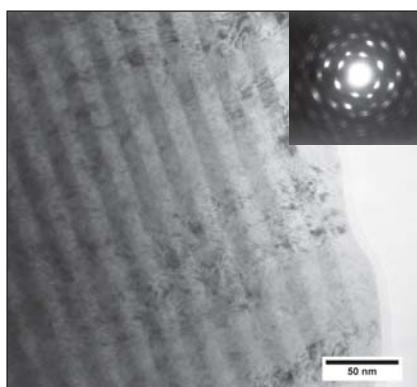


**Fig. 1** Low magnification image of ceria-zirconia multilayers

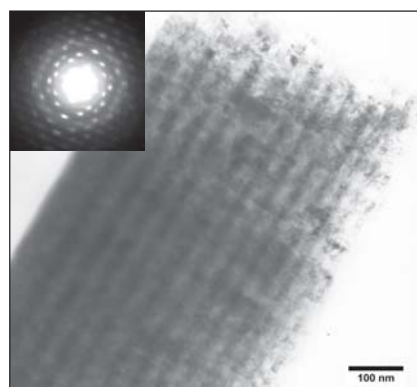


**Fig. 2** Low magnification bright field image after annealing

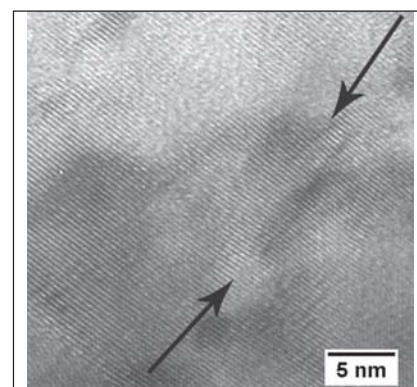


**Fig. 3** High-resolution image of the interface showing the defects generated after the thermal annealing

## V.15 Embedded Read-out Electronics Design for Microstructured Sensors

Piezoresistive microcantilever sensors, which embed a piezoresistor within the microcantilever surface are outstanding platforms for high throughput, highly sensitive of various chemical and biological phenomena. The greatest advantage of piezoresistive cantilevers is that they can be integrated with readout electronics. Molecular adsorption, when restricted to a single side of a deformable cantilever beam, results in measurable bending of the cantilever. Bending of the cantilever is reflected in terms of change in resistance of the piezoresistor, which can be detected by a highly sensitive Wheatstone bridge circuit.

Electronics plays a key role in accurately interpreting the change in resistance due to microcantilever bending and carrying this signal to the computer system without adding much noise, where the user can

control and monitor the phenomenon under consideration with required accuracy.

Design implementation of the read out electronics for a commercial piezoresistive microcantilever (PMC) sensor is described here. The basic idea is to detect the change in resistance of the sensor by means of a Wheatstone bridge, excited by a precision voltage supply. Then, the bridge output is processed by a signal conditioning circuit, which is digitized and communicated to a computer system through the latter's USB interface. A control program written in LabVIEW, a graphical programming language, which runs in the computer system provides a user interface and displays the acquired bridge output with a very good accuracy.

As an example, an attempt was made to study the response of the

sensor to a change in temperature in a non-contact way. The change in the bridge output could be seen very clearly upon the effect of placing the commercial microcantilever near a hot plate, set at a specified temperature. From this, the utility of the developed read out electronics to measure the phenomena detected by the sensor has been proved. The out put from the Wheatstone bridge formed with PMC sensor and its reference along with external resistance  $R_2$  and  $R_3$  (Figure1).

The bridge output is connected to an embedded single chip design, which has been programmed with signal conditioning modules, PGA (programmable gain amplifier), Analog-to-digital Converter (ADC) and Universal Asynchronous Receive Transmit (UART) block for serial communication.

The process of communicating with the embedded read-out electronics

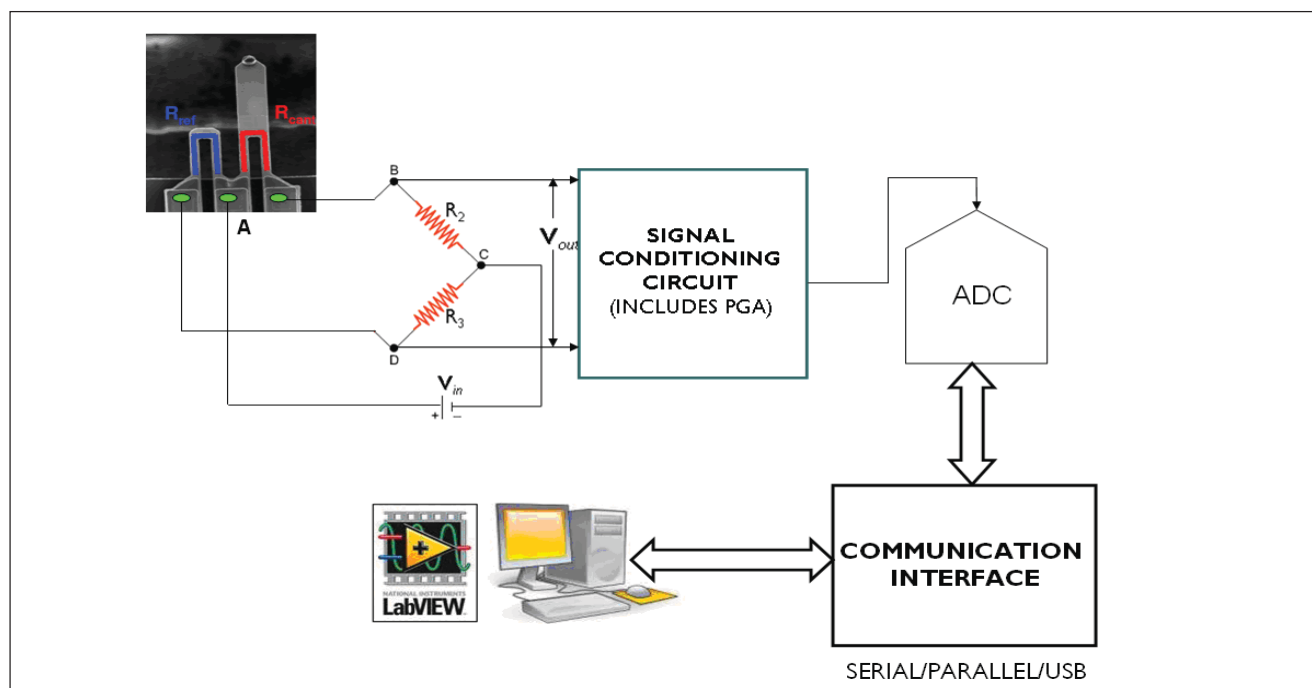
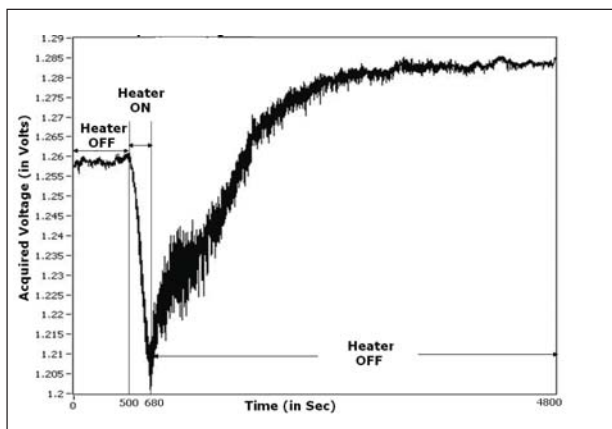


Fig. 1 Block diagram of embedded read-out electronics for commercial piezoresistive microcantilever (PMC) sensor



**Fig. 2** On-line data acquisition using embedded read-out design and its virtual instrument graphical language program of Pizeo-resistive Micro-cantilever (PMC) deflection measurement functionalized with temperature effect

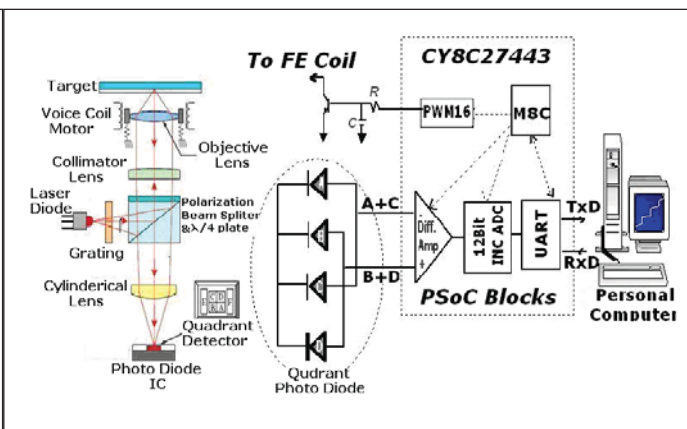
and acquiring the data from the design is done by means of a control program written in LabVIEW. The acquired bridge output signal is displayed with a very good accuracy to the user using graphical user interface (GUI) menu driven program developed with LabVIEW, the 'G' language. The functionality of the read-out electronics design was confirmed by deflecting the cantilever kept near a heat source.

Figure 2, shows the output voltage corresponding to the temperature change, in turn deflection of the cantilever. This study shows the functioning of a PMC and its corresponding recording of on-line data with the embedded design through a graphical control program which acquires the data and displayed on a PCs screen.

In an another design, development of a micro-displacement measurement system based on the commercial compact disk (CD) pickup head is described (Figure 3 & 4), which consists of an optical laser pickup head, as well as a holographic grating as a position reference and its focusing control coil (voice coil) and a quadrant photo diode for sensing the reflected back image. In

this design a Cypress Micro Systems Programmable System on Chip (PSoC) has been programmed in such a way to interface the CD's optical pickup head and control the focusing coil with the feed back from photo-diode array in the pickup head assembly for micro-position measurement. Our astigmatic detection system is based on modification of a commercial CD optical head to achieve a resolution better than 2 μm in detection of the displacement measurement of the object surface.

The PSoC design implementation an instrumentation amplifier (INSAMP) receives the photodiode signals (A+C) and (B+D), after amplifying fed into a 12 bit incremental ADC for digital conversion. The ADC output is sent to UART block by the M8C microcontroller in the PSoC internal for easy communication to the PC for further measurement and analysis. The proper focusing of the optical collimator lens, the focusing coil control has been implemented through a 16-bit PWM with an external R,C circuit, which functions as a 16 bit digital-to-analog converter (DAC) and a driver transistor.



**Fig. 3** PSoC based CD optical pick-up head read-out for micro-position measurement

The control program written in LabVIEW initially sense the image from the quadrant photodiode and drive the FE coil for its focusing with respect to the target object. With this initialization, accurate positional measurement has been carried out.

Since measurements of linear displacement is essential in a various application area, this position measurement is a promising design for applications, such as micro positioning, accelerometers, micro cantilevers, alignment of small objects, etc. Figure 4 shows the on-line measurement of micro-displacement of a target material using CDs optical pick-up head and embedded read-out design with PSoC single chip supported with the LabVIEW control program to acquire the displacement data in a PC screen.

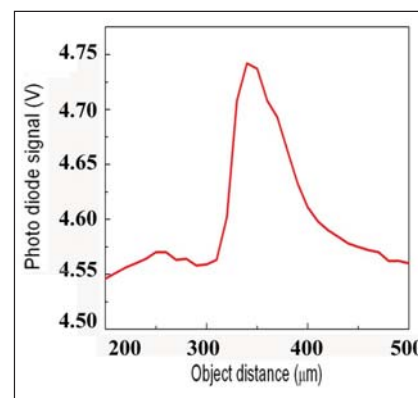


**Fig. 4** Non-contact micro-position measurement

## V.16 Micro Cantilever based Sensors

Micro cantilever sensors are the simplest micromechanical systems that can be mass-produced using conventional micromachining techniques. In recent years, these sensors have attracted much attention due to their potential as a platform for the development of numerous physical, chemical, and biological sensors. Micro cantilevers can be either used in dynamic mode by measuring the shift in natural frequency or in static mode where it undergoes bending due to molecular adsorption (see Figure 1). At IGCAR, these sensors are being explored for various novel applications. This report describes a simulation work where thermomechanical analysis of a bimaterial cantilever is studied and an experimental work using commercial AFM cantilevers for the possibility of gamma radiation detection.

Bimaterial microcantilever sensors, microscopic analogs of traditional bimetallic structures, have been extensively studied for uncooled infrared (IR) detection and micro calorimetry. Infrared detection with bimaterial microcantilevers have shown a temperature sensitivity

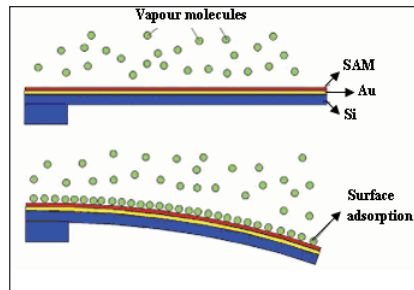


Fig.1 Micro cantilever bending due to molecular adsorption

down to  $10^{-5}$  K and heat flow measurements as small as femtoJoule.

These sensors are usually fabricated by coating a layer of metal like gold or aluminum on silicon cantilever. Performance of these sensors is highly dependent on the thickness of the metal layer. In the resent study, thermo-mechanical analysis of a bimaterial cantilever is performed using finite element analysis (FEM) for various thickness of the coated material. Dimension of bimaterial (Si & Au) cantilever simulated is 500  $\mu\text{m}$  length, 100  $\mu\text{m}$  width and 1  $\mu\text{m}$  thick with different gold thickness ranging from 0.01 to 1 $\mu\text{m}$  (see Figure 2). Mesh size was fixed at 3  $\mu\text{m}$  and one end of cantilever was fixed by boundary conditions. A uniform temperature load of 373 K was applied on the Au coated surface and static analysis was

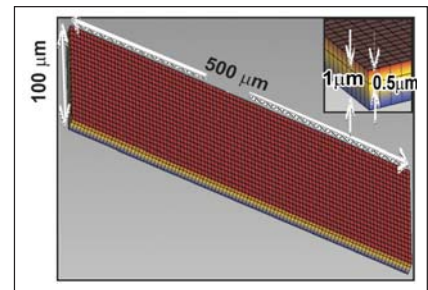


Fig.2 Thermomechanical analysis of bimaterial cantilever using finite element analysis

performed. For every thickness of the Au, simulations were repeated and thermomechanical sensitivity was estimated.

Figure 3(a) shows the variation of thermal sensitivity of the bimaterial cantilever for increasing thickness of Au on Si. This figure also shows the similar results for  $\text{Si}_3\text{N}_4$  cantilever coated with gold. From these results it is clear that thermal sensitivity of Si cantilever is greater than  $\text{Si}_3\text{N}_4$  cantilever; this is due to higher Young's Modulus of  $\text{Si}_3\text{N}_4$  compared to Si. In both the cases the sensitivity is maximum for a particular thickness of coating (0.5  $\mu\text{m}$  for Si 0.7  $\mu\text{m}$  for  $\text{Si}_3\text{N}_4$ ). It shows that thermal sensitivity is highly dependent on thickness of metal coating and the material of cantilever.

Now to study the effect of non-uniform thermal loading, the metal surface of the cantilever was designed with ten entities of 50  $\mu\text{m}$  each. Thermomechanical simulations were repeated by applying the temperature difference in the range of 5 to 35 K between extreme entities from free and fixed end. Figure 3b shows the maximum deflection of the cantilever for various temperature gradients on the cantilever surface. For comparison uniform temperature

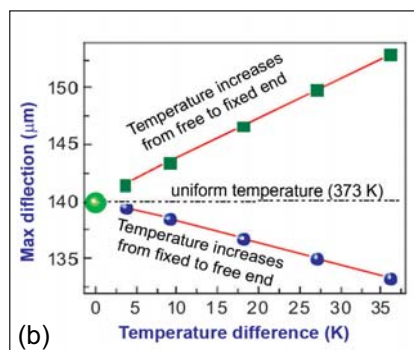
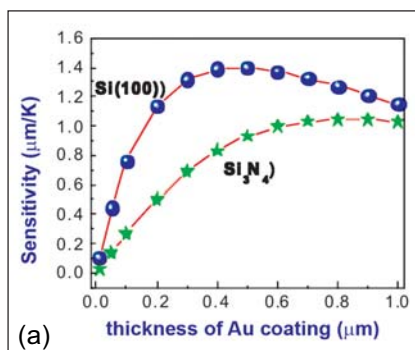
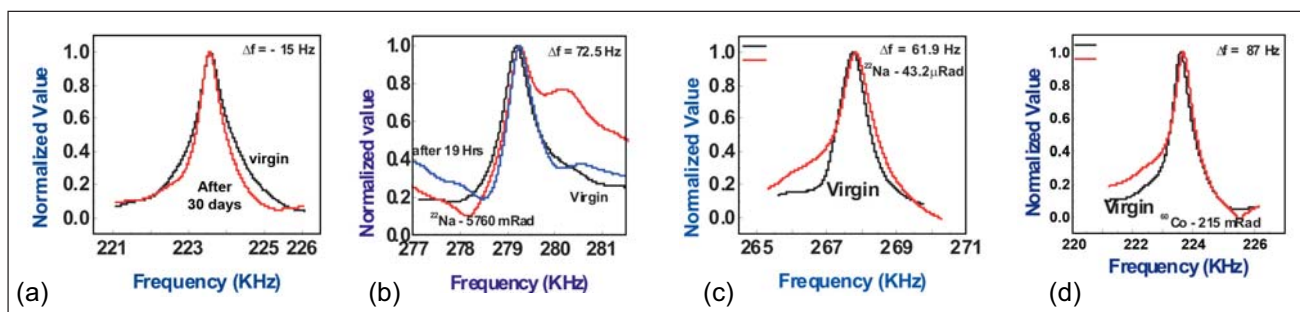


Fig. 3 (a) Comparison of thermal sensitivity between Si and  $\text{Si}_3\text{N}_4$  cantilever with Au coated (b) Effect of non-uniform temperature on maximum deflection of bimaterial cantilever



**Fig. 4** Shift in natural frequency of microcantilever due to gamma radiation exposure (a) Virgin case (b) <sup>22</sup>Na exposed (c) <sup>22</sup>Na exposed without gold (d) <sup>60</sup>Co exposed

point is also shown. From this figure it is clear that the deflection of a bimaterial cantilever due to non uniform temperature is higher when fixed end is at a higher temperature than free end.

In an experimental investigation, single crystal silicon micro cantilevers used in atomic force microscope (AFM) are exposed to different types of gamma radiation for the possibility of using these cantilevers as radiation detectors. Natural frequency of the cantilevers was measured using NT-MDT AFM

head before and after exposing to three types of gamma sources. Cantilever used are N-type single crystal Si with the dimensions of 95 μm (L) X 30 μm (W) X 2 μm (T) with gold coating. Figure 4 shows the shift in natural frequency of the cantilevers when exposed to <sup>22</sup>Na (with and without gold), <sup>60</sup>Co. For comparison an un-exposed cantilever (virgin case) is also shown where frequency shift is negative after 30 days. From these figures it is clear that due to radiation exposure natural frequency has increased (peak shifted in the

positive direction) in all the three cases and there is an extra peak at the higher frequency side for <sup>22</sup>Na exposure. But after some time the shape and natural frequency tend to return to its original value. The positive shift in natural frequency indicates the stiffening of the cantilever with radiation exposure. This can be due to bimaterial nature of the cantilever and or due to photo induced stress. These results indicate the possibility of using these cantilevers as radiation detectors and further investigations are underway to understand these results better.

## V.17 Room Temperature Capacitive and Resistive Sensor for Improved Selectivity in Nanostructured (Semiconducting) Materials

Ubiquitous uses of sensors have driven tremendous research interest with cutting edge nanomaterials for the benefits of health, safety and environments. Among the demands in sensor technology, selectivity and its operation at room temperature in a cost effective manner are the key factors that attracts considerable interest in applied sensor technology. One of the approaches for improved selectivity focuses to utilizaion of

multi parameter sensor responses e.g. capacitance, resistance and device parameters offering enhanced discriminatory signals for a set of analytes obtained from an array of samples.

Data acquisition plays a crucial role that should commensurate to low power consumption and sensible to weak signal for practical uses. Figure 1 shows a simple astable 555 based circuit and measurement set up that

eventually help in monitoring the sensor response. In this context, usefulness of astable 555 timer that effectively uses two resistances, R<sub>1</sub> and R<sub>2</sub> and a capacitance (C) in generating frequency (f) where time period (T) = 1/f = 0.69(R<sub>1</sub>+2R<sub>2</sub>)C. Here, a sample can act as 'C' in the capacitive mode while frequency is monitored with known resistances. Similarly, in the resistive mode, R<sub>2</sub> does act as sample. Thus, this read-out can allow measurements of both

capacitance and resistance even at low signals. Capacitance as low as 0.01 nF have been, reproducibly, measured.

Figure 2 details sensor responses measured using above circuit for the exposures to a set of organic vapors to an yttria stabilized zirconia (YSZ) thin films.

Nano structured YSZ films of 80 nm thick ( $T_{ox}$ ) were prepared by electron beam deposition technique. XRD pattern confirms the presence of tetragonal crystallites of 10 nm size. While the capacitance measurement of Al/YSZ/Al system provided dielectric constant ( $\epsilon$ ) = 19 from  $\epsilon_{ZrO_2} = T_{ox} C / \epsilon_0 A$ , where A is area. Using capacitive mode of the Astable measurement scheme, the frequency was recorded with the help of Agilent DSO 5012 Oscilloscope. All the analytes were exposed at room temperature 297K with the equilibrium vapor pressure in the atmospheric condition.

The recovery was studied by flowing commercial air. The observed trend in sensor response  $f$  as  $C_2H_5OH$  ( $\epsilon = 24$ ) >  $CH_3COCH_3$  ( $\epsilon = 21$ ) >  $CH_2Cl_2$  ( $\epsilon=10$ ). Under the constant humidity (~40%), there was no effect of water on the sensor response. The trend closely follows the variation of dielectric constant of analyte

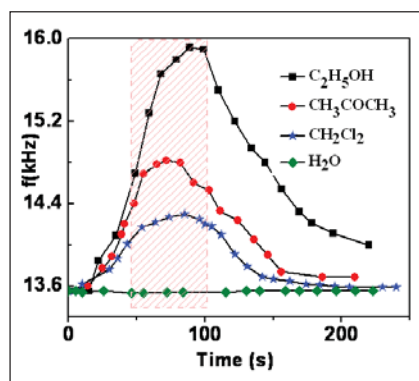


Fig. 2 Capacitive sensor response from Al/YSZ/Al

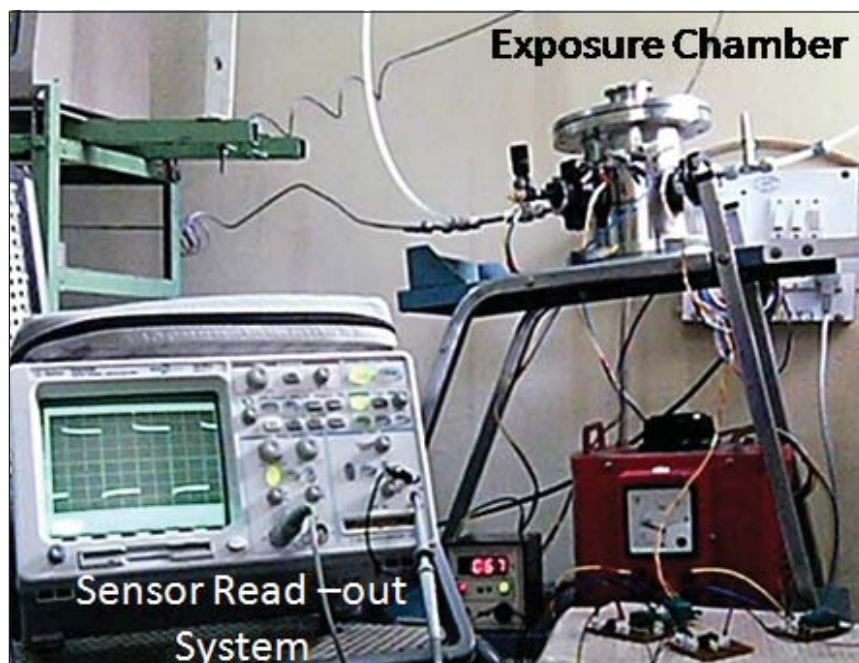


Fig. 1 Measurement set up used for capacitive and resistive responses

molecules. Figure 3 shows exposure of ammonia solution to the capacitive YSZ sensor. Ammonia is hugely used in fertilizer industry and also in nuclear technology for heavy water production. Ammonia sensor is also extremely important for automobiles and medical purposes. Metal oxides widely used for ammonia sensor work at high temperatures and suffers from selectivity. The selectivity has been achieved using capacitive mode as shown in Figure 3 at room temperature.

The shift in frequency contradicts the trend observed for a series of organic analytes. At a higher concentration, 5 to 30% (w/v) of ammonia solution

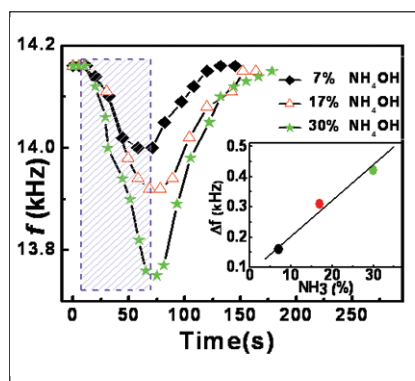


Fig. 3 Selective sensor response for ammonia from Al/YSZ/Al capacitor

is easily detected and linearly vary with responses. With a thick film of 300 nm, the recovery was found to be slow as opposed to sensor signal from 80 nm film. This observation as well as reported interaction for  $ZrO_2/WO_3$  with ammonia indicates a prevalent interaction with ammonia and YSZ responsible for shifting frequency. The decreasing frequency confirms enhancement in capacitance.  $C = Q/E \cdot T_{ox}$ , where Q is charge at the surface for electric field E. Effective electric field,  $E_{ef} = E - E_{pol}$  is modulated via  $E_{pol}$ , local electric field due to polarization of the material. Thus any interaction that locally shifts the polarization, can affect the capacitance. Hence, the interaction between ammonia and YSZ has changed the local polarization of the YSZ molecule and effectively increase the capacitance.

Figure 4 displays the result of frequency shift after an exposure of analyte to nano metric (7 nm)  $Al_2O_3$  film created from a 30 nm Al film by anodization process. The dielectric constant was determined to be 9.4. The effect of ammonia solution clearly produced orthogonal

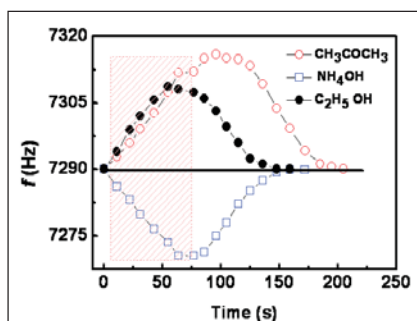


Fig. 4 Capacitive sensor response from Al/Al<sub>2</sub>O<sub>3</sub>/Al

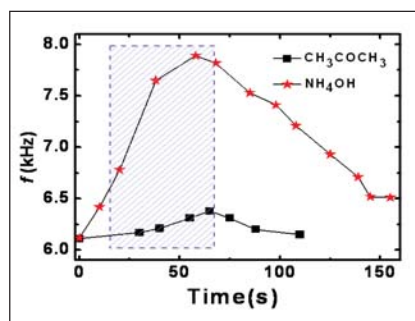


Fig. 5 Capacitive sensor response from Al/PTA-Al<sub>2</sub>O<sub>3</sub>/Al

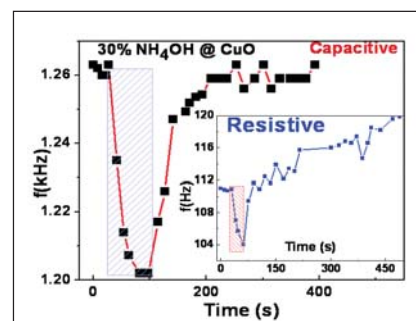


Fig. 6 Capacitive sensor response from Al/NP-CuO/Al. Inset is resistive response for ammonia solution

response in comparison to other analyte. However, the response was weak. For enhancing the response, a semiconducting polymer film, polytriarylamine (PTA) was spin cast from toluene solution. Figure 5 shows the response to ammonia solution. In contrast to other analytes, ammonia solution induced huge shift in frequency from its baseline contributing to higher sensitivity. Thus, using uncoated and coated polymer film with Al<sub>2</sub>O<sub>3</sub> layer, selectivity and sensitivity are modulated for ammonia solution.

Multi parameter sensor measurements like resistive as well as capacitive have also been studied using nano sized CuO (10 nm). These

semiconducting nanomaterials with band gap 3.3 eV and dielectric constant of 18 were synthesized by hydrothermal process from ammoniacal solution of Cu(NO<sub>2</sub>)<sub>2</sub> as precursor. These nano particles were embedded to silica for making pellets for sensor studies. Figure 6 displays effect of ammonia solution to NPs CuO @ silica. The capacitive measurement following the Astable measurement scheme showed a fast response (< 5 sec) and a recovery within 100 sec. It held repeatability at ambient condition. The inset shows resistive measurement of the sample taking advantage of 'R<sub>2</sub>' of the same measurement scheme. Resistive

mode also responded quickly, however, was short of recovery in maintaining a constant background as observed for the capacitive measurement. The sensor did not significantly respond to water and alcohols.

Therefore, using arrays of sensors made of semiconducting and nanomaterials like ZrO<sub>2</sub>, Al<sub>2</sub>O<sub>3</sub>, polymer and CuO, ammonia can be selectively and sensitively detected using a novel measurement algorithm based on a cost-effective electronic chip at low power. The measurement scheme offers both DC capacitance and resistance measurement of sensor signals.

## V.18 Unusually Large Structural Stability of Terbium Oxide Under High Pressure

The rare earth oxides are of scientific and technological importance. Recently there have been several studies in the area of radiation damage effects on a variety of rare earth oxides due to their potential application as nuclear waste host materials. Among other requirements, the nuclear waste host materials should be resistant to amorphization transitions induced by

self radiation damage and extreme pressure and temperature environment. Hence, it was interesting to study terbium oxide under pressure. Figure 1 shows a broad peak near the Tb<sup>3+</sup> (148.52 eV) and Tb<sup>4+</sup> (150.591 eV) which indicates the presence of both Tb<sub>2</sub>O<sub>3</sub> as well as Tb<sub>4</sub>O<sub>7</sub> in the starting material. The in-situ high-pressure

X-ray diffraction was carried out with a Mao-Bell type diamond anvil cell (DAC) in the angle dispersive mode using the high-pressure guinier diffractometer. The high-pressure X-ray diffraction patterns up to 35 GPa are shown in Figure 2. Above 27 GPa, the signature peaks of the parent fluorite phase slowly start to broaden out and split, indicating a phase

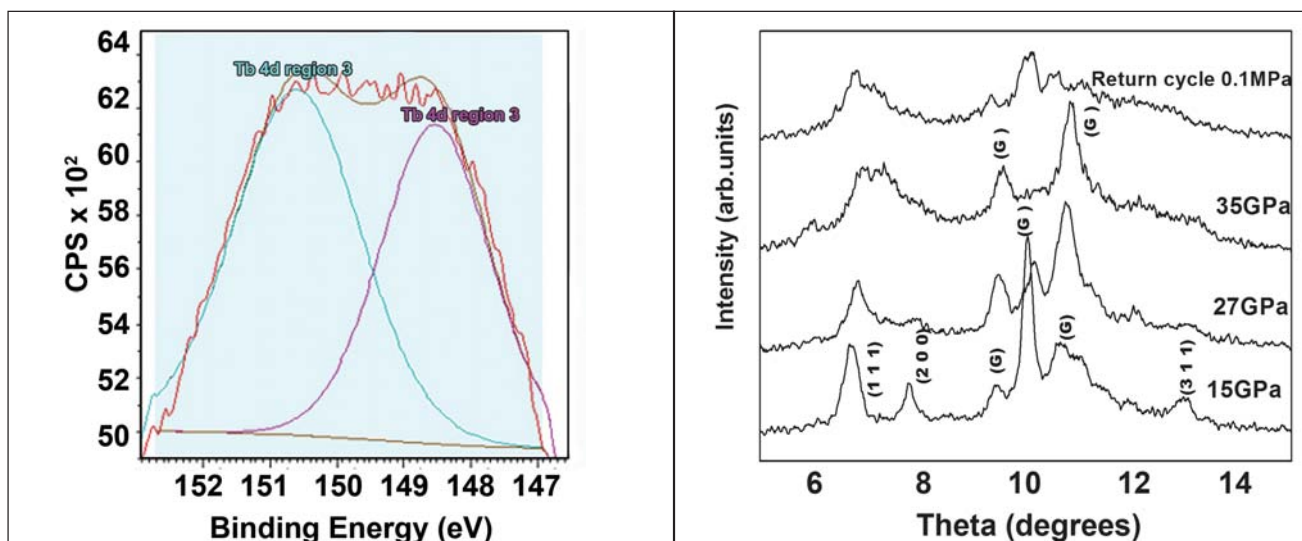


**Fig. 1** X-ray photoelectron spectroscopy of terbium oxide sample **Fig. 2** The X-ray diffraction pattern for  $Tb_4O_7$  at pressures up to 35 GPa along with the return cycle pattern at 0.1MPa

transition, probably to the cotunnite phase, which is the high pressure phase of fluorite structure. The peaks of the high-pressure phase obtained in this study are too broad to be considered for any meaningful analysis. This structural transition was found to be irreversible in nature, as can be seen from the XRD pattern of the return cycle at 0.1MPa in Figure 2. The transition pressure of 27 GPa for terbium oxide is much higher than that generally found in other oxides (<15 GPa).

In  $Tb_4O_7$ , the different cation sites in the fluorite lattice are occupied by trivalent and tetravalent Tb ions, which are coordinated by 6 and 8 oxygen atoms respectively. X-ray absorption spectroscopy studies reveal that the  $f^8$  ground state configuration of terbium is well localized in the trivalent oxide while in the case of tetravalent oxide, the last 4f electron delocalizes in the valence band and the remaining seven-4f electrons remain localized. This indicates that

the last f electron participates in a partial type covalent bonding. Since our sample mostly consists of  $Tb^{4+}$  ions due to the presence of  $Tb_4O_7$ , this may probably be one of the reasons for the large stability seen here.

The reported transition pressures for the other oxides at room temperature are all below 15 GPa as in most of the cases the bonding is ionic in nature. The large structural stability and high bulk modulus make the oxide an ideal choice for the nuclear waste immobilization.

## V.19 Local Structure of Wide Band Gap Tunable Mixed Crystals of $Cd_{1-x}Ca_xO$

Variation of band gap of semiconductors by alloying is being actively pursued, since such alloys find a wide range of applications as transparent conducting semiconductors, solar panel elements, matrix in spintronics, UV-emitting diodes etc. In many systems, the band gap tunability range is restricted due to the limited solubility between end members with

different crystallographic structure. This is partially overcome by resorting to thin film deposition, a non-equilibrium process. In this context, important to identify an alloy system wherein band gap can be varied over a wide range in its bulk form.

$CdO$  and  $CaO$  crystallize in NaCl-type structure with  $Fm\bar{3}m$  space group, with a lattice parameter of 4.6950 Å

and 4.8123 Å respectively. The lattice mismatch being only ~7%, complete solubility is expected. As such,  $Cd_{1-x}Ca_xO$  alloy offers a definite possibility to tune the band gap from 2.2 eV ( $CdO$ ) to 7 eV ( $CaO$ ). Indeed, we have observed complete solubility between  $CdO$  and  $CaO$ . However, both lattice parameter and fundamental band gap exhibit negative deviation from Vegard's law.

The deviation was best described by quadratic dependence with negative curvature, defined by bowing parameter  $\beta=0.03088 \text{ \AA}$ . This signifies deviation(s) in the local atomic structure from average cubic crystal structure, as determined by regular X-ray diffraction studies. A detailed local structure study which is sensitive to length changes at atomic level is adequate to understand. Extended X-ray absorption fine structure spectroscopy (EXAFS) is not only sensitive but it also probes local environment around a given (absorbing) atomic species.

Figure 1 shows the absorption spectrum of  $\text{Cd}_{1-x}\text{Ca}_x\text{O}$  system for  $0 \leq x \leq 0.9$ , measured at the Cd-K absorption edge. Necessary data reductions, normalization, pre- and post-edge background subtraction were carried out to the individual absorption spectrum to obtain EXAFS signal,  $|\chi|$ . In Figure 2, EXAFS signal, weighted by  $k^3$  to enhance the signal at higher photoelectron momentum  $k$ , is plotted as a function of  $k$ .

Figure 3 is the Fourier transformed  $|\chi|$  signal plotted as a function of distance from the absorbing atom, cadmium. The first peak centered

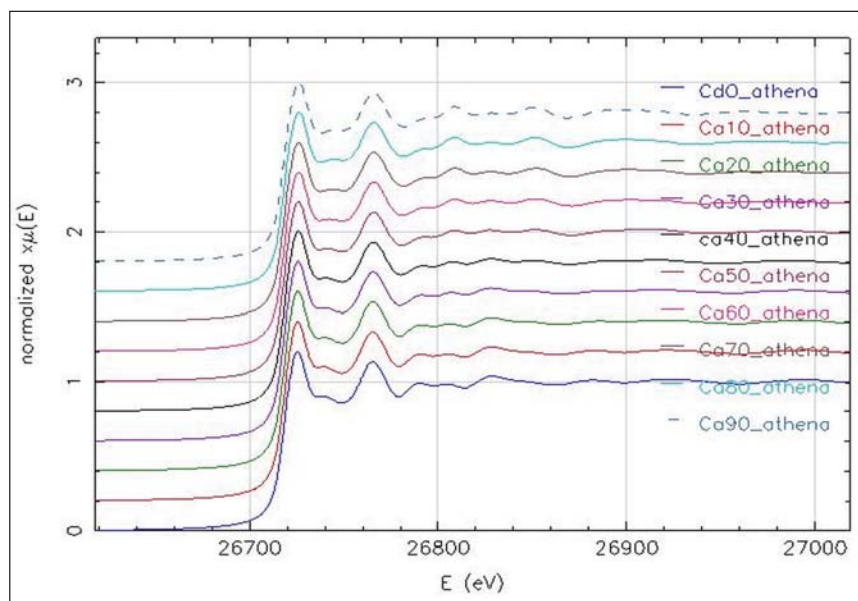


Fig. 1 Absorption spectra of  $\text{Cd}_{1-x}\text{Ca}_x\text{O}$  system (for  $0 \leq x \leq 0.9$ ) as a function of Ca concentration

about  $2.3 \text{ \AA}$ , corresponds to Cd-O distance, which is half the lattice parameter. Even without further analysis, first peak position is seen to linearly increase, with  $x$  at half the rate expected from Vegard's law. This clearly implies that the oxygen surrounding the cadmium systematically deviates from a cubic environment. A linear increase in Cd-O distance against the quadratic increase of the lattice parameter with negative curvature implies a decrease in one or more bond lengths, other than Cd-O. In order to estimate the relevant bond lengths, EXAFS

signal in real space was fitted to standard EXAFS equation.

From the analysis it is seen that the second nearest neighbour distance  $r_{(\text{Ca-Cd/Cd})}$  also increases with Calcium concentration, though at a lower rate compared to that of first nearest neighbour  $r_{(\text{Cd-O})}$  distance. Thus our studies indicate that the first and second nearest neighbour distances about cadmium increase linearly.

Considering the nonlinear variation of the lattice parameter, it is inferred from our studies that one or more relevant bond lengths around oxygen or/and calcium should decrease.

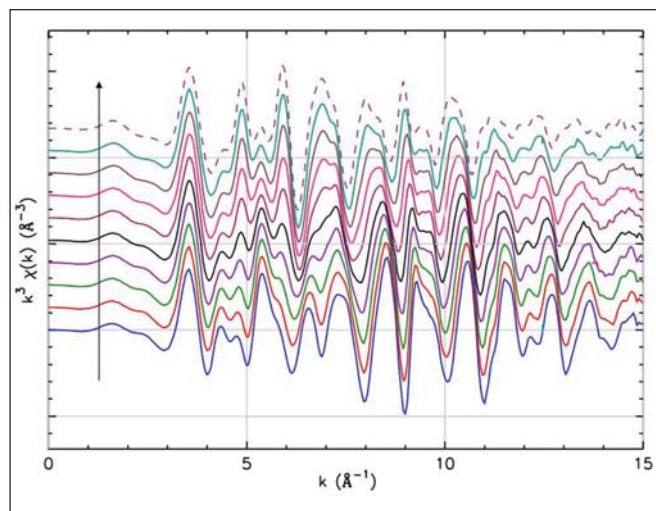


Fig. 2  $k^3$  weighted EXAFS spectrum of  $\text{Cd}_{1-x}\text{Ca}_x\text{O}$  for  $0 \leq x \leq 0.9$ . The spectra were shifted vertically for clarity. Arrow in the figure indicates the direction of increasing calcium concentration

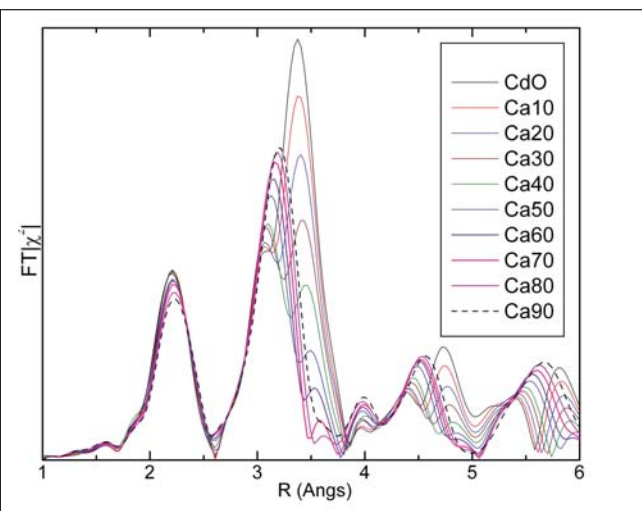


Fig. 3 Fourier transformed EXAFS spectrum as a function of distance from the absorbing atom cadmium

## V.20 Two-phase Coexistence and Hysteresis of Ferroelectric Transition in Sodium Niobate

Ferroelectric materials exhibit interesting phase transitions and have applications in piezoelectric, electro-optic, high density optical data storage.  $\text{NaNbO}_3$  based ferroelectric systems such as  $(\text{Li}, \text{Na})\text{NbO}_3$ ,  $(\text{K}, \text{Na})\text{NbO}_3$  with ultrahigh piezoelectric response comparable to  $\text{Pb}(\text{Zr}_x\text{Ti}_{1-x})\text{O}_3$  has evoked considerable interest as next generation ecofriendly lead free piezoelectric ceramics. NN exhibits a transition from paraelectric to antiferroelectric and then to ferroelectric phase and therefore is of particular interest from the point of view of sequence of phase transitions.  $\text{NaNbO}_3$  exhibit a transition from anti-ferroelectric to ferroelectric phase transition accompanied by the change in structure from orthorhombic to rhombohedral at 180 K.

In order to understand the nature of this transition, detailed Raman spectroscopic studies of  $\text{NaNbO}_3$  in the temperature range 10–300 K both in cooling and heating cycles were carried out. Raman spectra were recorded in the back-scattering geometry using 350 mW power of the 488 nm line from an argon ion laser. Spectra were recorded using a closed cycle helium refrigerator during cooling and heating cycles. Scattered light was analyzed using a double monochromator detected using a photomultiplier tube operating in the photon counting mode. Figure 1 shows the Raman spectra of  $\text{NaNbO}_3$  at various temperatures during the cooling cycle. At room temperature, a total

of 19 distinct Raman modes were identified in the frequency range 30–950  $\text{cm}^{-1}$ . The observed modes are less than the actually predicted which could be either due to accidental degeneracy of phonon frequency or due to the insufficient intensities arising from small polarizabilities of several modes. On the other hand, at 10 K only 12 distinct Raman modes could be found in that frequency range.

The less number of modes at 10 K is due to higher symmetry of the rhombohedral phase. The bands appearing in the low-wave number range 50–100  $\text{cm}^{-1}$  have been assigned to the external vibrations of Na ion and while in the range 100–180  $\text{cm}^{-1}$  to the librations (rotational vibrations) of  $\text{NbO}_6$  octahedra. The wave number regime 160–950  $\text{cm}^{-1}$  is associated with the internal vibrations of  $\text{NbO}_6$  octahedra. The Raman spectra shown in Figure 1 exhibit significant

changes upon passing through the anti-ferroelectric ferroelectric transition in the temperature range 10–300 K during cooling and also across the reverse transition in the heating cycle. The intensities of several modes gradually decrease initially upon cooling and exhibit a marked change at 180 K. During heating cycle, spectral features begin to exhibit marked changes at 260 K. These observations indicate that the phase transition from antiferroelectric to ferroelectric phase occurs at 180 K on cooling while the reverse transition at 260 K upon heating. The normalized integrated intensities of the modes are investigated to understand the temperature range of coexistence of antiferroelectric and ferroelectric during cooling and heating cycles. The integrated intensities of the modes are normalized against the intensity of the mode at 601  $\text{cm}^{-1}$ . This mode is associated with the symmetric stretching vibration of the

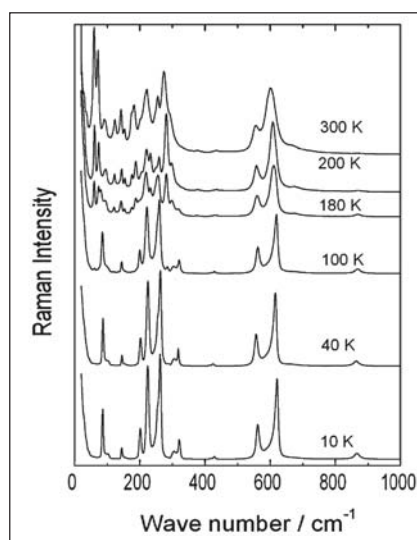


**Fig. 1** Raman spectra of  $\text{NaNbO}_3$  at different temperatures during cooling cycle

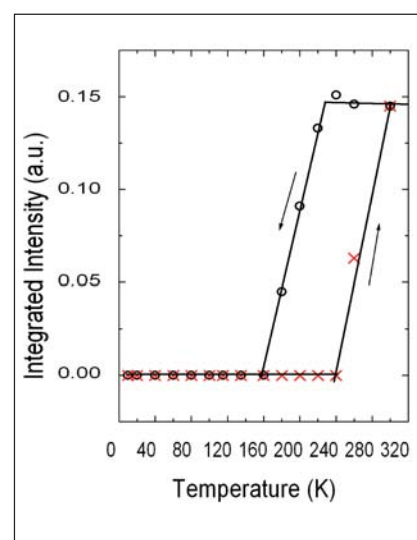


**Fig. 2** Temperature variation of integrated intensity of 182  $\text{cm}^{-1}$  mode during cooling (O) and heating cycle (X)

$\text{NbO}_6$  group and it persists both in cooling and heating cycle over the complete temperature range without much change in its intensity. Hence we use the intensity of this peak for normalization of the intensities of other modes. The intensity of the  $182\text{ cm}^{-1}$  mode shown in Figure 2 begin to exhibit a sharp decrease in the temperature range of 220-180 K. However, in the heating cycle,

$182\text{ cm}^{-1}$  mode begin to show a sharp increase in the temperature range 240 – 300 K. These findings suggest that both anti-ferroelectric and ferroelectric phases coexist between 220 and 160 K during cooling cycle and between 240 and 300 K during heating cycle. This mode attain same intensity in the heating cycle at 300 K, which suggest complete transfer into anti-

ferroelectric system. The analysis of the Raman data indicated that the transition from antiferroelectric to ferroelectric phase occurs at 180 K during cooling and the reverse transition at 260 K during heating. The transition is found to be a two step process involving coexistence of both phases in the temperature range 220-160 K during cooling cycle and 240–300 K during heating cycle.

## V.21 Conductive Atomic Force Microscopy of Ultra-thin High-k Dielectric Oxides

**A**  $\text{SiO}_2$  gate dielectric by thermal oxidation provides a very stable, superior electrical isolation property, hard electrical breakdown and high quality of Si-SiO<sub>2</sub> interface. Nowadays, the dielectric layer thickness is in the range of 1.2 nanometers, which is very close to the physical limit. Further scaling down of the gate dielectric leads to large leakage currents beyond the acceptable limits. To overcome these problems, dielectrics with high permittivity (high-k) have become the promising alternative to replace the existing silicon based CMOS and are undergoing intensive studies with respect to their potential applications as gate dielectrics. Hence it is important to study the dynamic mechanism of the dielectric degradation and breakdown (BD) process of the high-k materials at nanometer scale.

Among many alternatives to  $\text{SiO}_2$ ,  $\text{HfO}_2$  and  $\text{Al}_2\text{O}_3$  are the two promising candidates. Although these high-k materials can lead to a reduction of the leakage current by 2 to 3 orders of magnitude, many critical problems

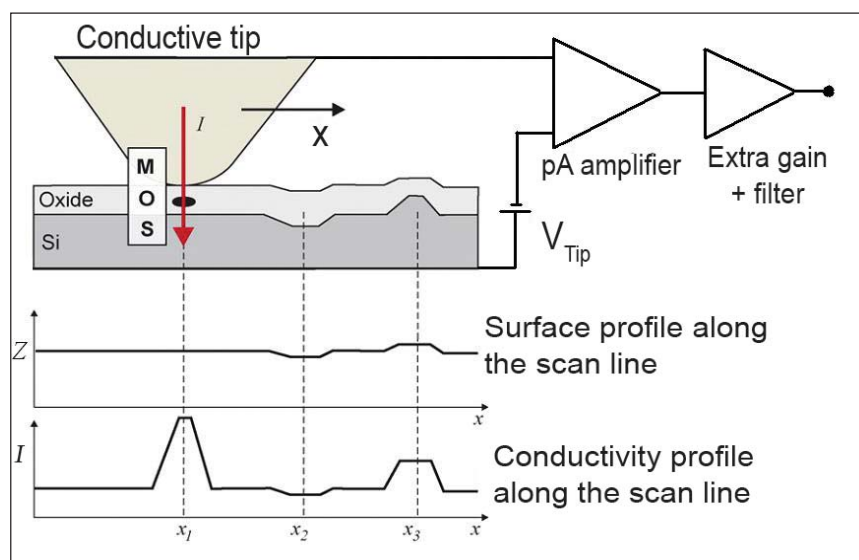


**Fig. 1** Schematic representation of the conductive atomic force microscopy setup

are yet to be addressed before employing in device fabrication. Also owing to extremely low thickness, these materials undergo degradation and breakdown due to electrical stress induced leakage currents. Characterizing the dielectric integrity and reliability of ultrathin dielectric films has become extremely challenging due to the difficulty in detecting breakdown of soft and noisy breakdown behavior in the current/voltage versus time characteristics of the test sample.

The conductive atomic force microscopy (C-AFM) study of dielectric degradation / breakdown behavior of ultra thin  $\text{Al}_2\text{O}_3$  films with nominal thickness of 0.4 and 2 nm coated by atomic layer deposition (ALD) technique is described. This technique enables simultaneous acquisition of topography and conductivity of the thin films. Since dielectric breakdown is a local phenomenon and it occurs at very small area  $\sim 10^{-14}$  to  $10^{-12}\text{ cm}^2$ , conventional electrical methods

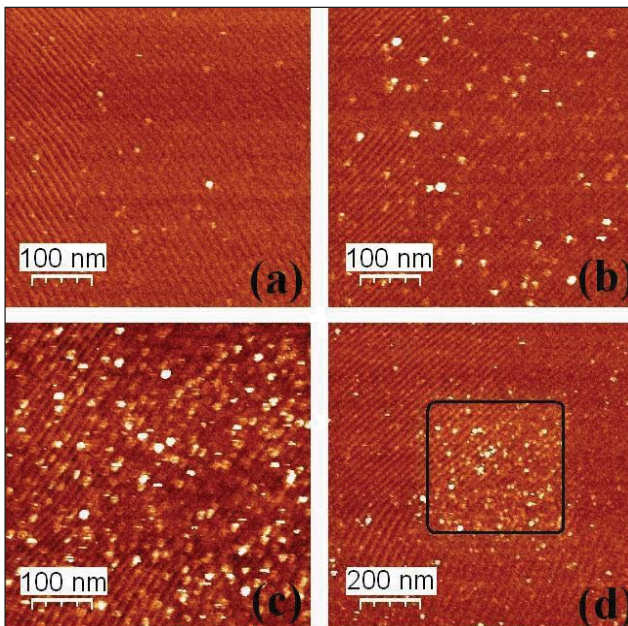


**Fig. 2** Current images at different bias voltages (a) 0.2V, (b) 0.4V (c) 0.8V (scan area  $500 \times 500 \text{ nm}^2$ ) and (d) 0.8V (scan area  $1000 \times 1000 \text{ nm}^2$ ). The inner stressed area of  $500 \times 500 \text{ nm}^2$  show large leakage current spots in comparison to the outer area (unstressed) (film thickness 0.4 nm)

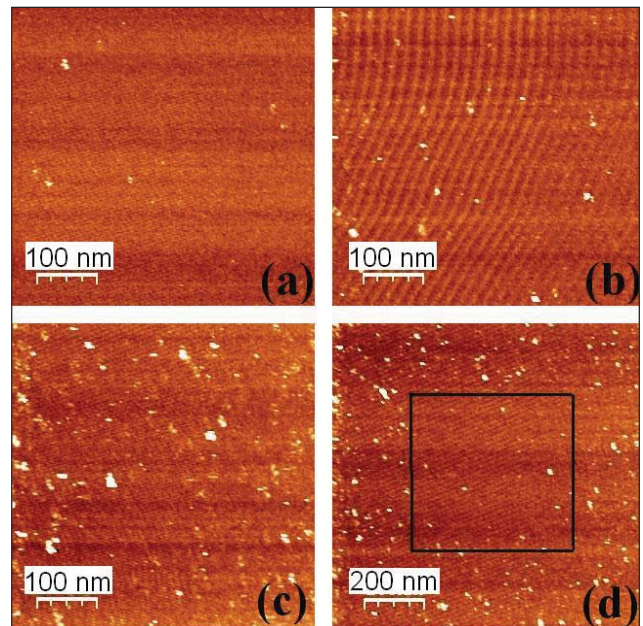


**Fig. 3** Current images at different bias voltages (a) 0.4V, (b) 0.8V (c) 1.2V (scan area  $500 \times 500 \text{ nm}^2$ ) and (d) 1.2V (scan area  $1000 \times 1000 \text{ nm}^2$ ). The inner stressed area of  $500 \times 500 \text{ nm}^2$  show reduced leakage current spots in comparison to the outer area (unstressed) (Film thickness 2nm)

which are usually based on macroscopic test structures, fail to locate and to characterize single electrically weak sites or defects. C-AFM has been proved to be an appropriate technique to address this problem. Figure 1 shows the experimental setup where the conducting tip, oxide film and silicon substrate form a metal-oxide-semiconductor (MOS) system. Using C-AFM, the conductivity of the sample is recorded by scanning the tip over an area of  $500 \times 500 \text{ nm}^2$  while keeping the tip voltage constant. The images thus obtained shows smooth surface with out any topographical features. However, the conductivity images show a few bright spots indicative of high currents for scans employing higher bias voltages. These bright spots originate due to the conductive paths along the defects and traps. This current is called stress induced leakage current and is shown in Figures 2 and 3. To further examine the nature of stress induced degradation and its dynamics,

sequence of images are acquired at constant bias mode with increment in bias voltage in the range 0-2 V over a specific region of  $500 \times 500 \text{ nm}^2$ . In addition, to understand the extent of electrical stress we also performed a  $1000 \times 1000 \text{ nm}^2$  scan encompassing the previously stressed region. This larger area scans show the pronounced distinction between the cumulative effects of electrically stressed region from the less stressed region around it. The experimental results show that the repeated voltage stress progressively

increase number of leakage spots on both samples. However, for a given range of electrical stress, stress induced leakage current in 0.4 nm film increases in contrast to 2 nm film. (See Figures 2 and 3).

The mechanism of the dielectric breakdown in 0.4 nm thin film can be modeled using percolation theory. According to this model, when charges are injected by the AFM tip into the dielectric medium there exist a possibility of these charges get trapped at the trap

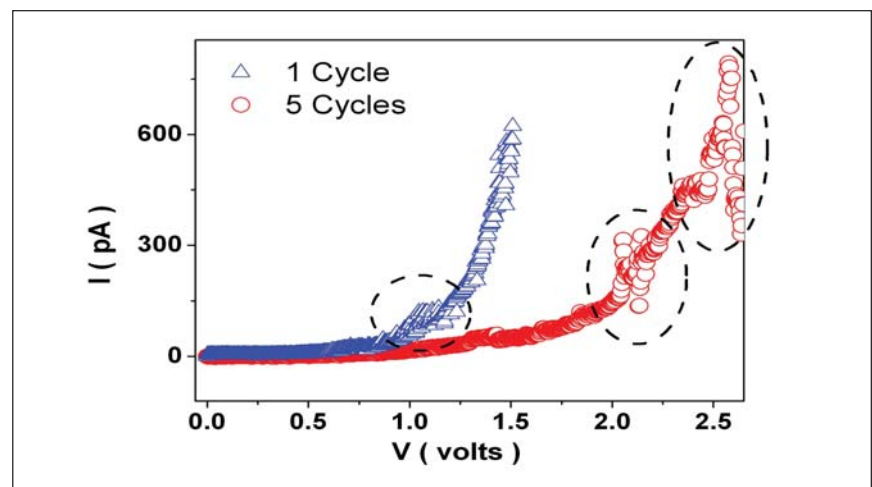


**Fig. 4** Typical I-V curves for the 0.4 and 2 nm thin ALD grown samples

centers. These traps introduce additional energy levels between the valence and conduction bands. Such energy levels aid the tunneling of charges under high electric field. When the number of such traps increase to a critical trap density, then a conductive path get established between the anode and cathode which eventually lead to the dielectric breakdown (Figure 2d). However, in the case of 2 nm thick film cathode field lowering effect due to the formation of positive traps near the anode prevents the formation of percolation path between the electrodes, even at high bias voltage, when compared to 0.4 nm thin film. Hence, the reduction of stress induced leakage currents is observed upon electrical stress as shown in Figure 3d.

Figure 4 shows the I-V curves obtained with Pt tip with 15 nN applied force. The I-V measurement is made at different regions of the specimen.

A voltage ramp is applied with step size of 5 mV at a ramp rate of 1 V/s.

This technique enables quick determination of an oxide intrinsic reliability and also provides information on defects. The I-V curves fit well with the modified Fowler-Nordheim tunneling equation. From this fit, the thickness and the barrier height of the dielectric films can be estimated. Using the barrier height for the bulk  $\text{Al}_2\text{O}_3$ , the nominal thickness of the films are estimated about 1.5 and 2 nm respectively for 0.4 and 2 nm. The deviation of the estimated oxide thickness for 0.4 nm film is mainly attributed to ambient conditions where water and/or hydrocarbons can lead to poor tip contact with oxide film. Also, estimation of oxide thickness depends not only on the physical thickness but also on the electrical properties.

Hence a noise free data acquisition is essential. However, when the amplifiers are used to measure in the lowest measurable currents specified, the possibility of the inaccuracy in determination of thickness can not be ruled out. In the I-V curves noticeable

oscillations in the current indicates trapping and detrapping of charges in the dielectric film. By calculating the derivative, the sharp deviation in the current vs voltage slope can be identified as the onset of breakdown. We estimated the breakdown field for these 0.4 and 2 nm films and found to be about 20 and 10 MV/cm, respectively. This is much above than the breakdown field of 8 MV/cm specified for bulk  $\text{Al}_2\text{O}_3$ .

From this C-AFM investigation, it may be concluded that the stress induced dielectric degradation is thickness dependant in  $\text{Al}_2\text{O}_3$  films. The result shows that the stress induced leakage current and degradation of thick film (> 1 nm) differs significantly from thin film due to formation of injection barrier. The current oscillations in the I-V measurement is found large for thick films due to charge trapping and detrapping. The low stress induced leakage current is an encouraging aspect of this material to employ them as a gate dielectric with breakdown field as high as 20 MV/cm.

## V.22 HCP and FCC Structures in Thermo-Responsive Microgel Crystals

Colloidal crystals (nanoparticle crystalline arrays) are ordered arrays of spherical particles with lattice constants of the order of the wavelength of visible light. Hence, static light scattering and confocal laser scanning microscopy are the appropriate tools to investigate their structure in reciprocal space and real-space, respectively. Colloidal crystals are being studied with considerable

interest as they serve as model systems for fundamental studies in various fields.

There is yet another colloidal system consisting of soft gel particles, where the size as well as the interparticle interaction is a strong function of temperature,  $T$ . Thermo-responsive Poly(N-isopropylacrylamide) (PNIPAM) microgel particles dispersed

in aqueous medium constitute the best example for such a soft sphere system. At  $\sim 305.4$  K, these microgel particles undergo a sudden volume change known as volume phase transition (VPT) which is reversible. The microgel particle size before and after the VPT is shown schematically (Figure 1). At sufficiently high concentrations these particles exhibit crystallization with lattice constants in

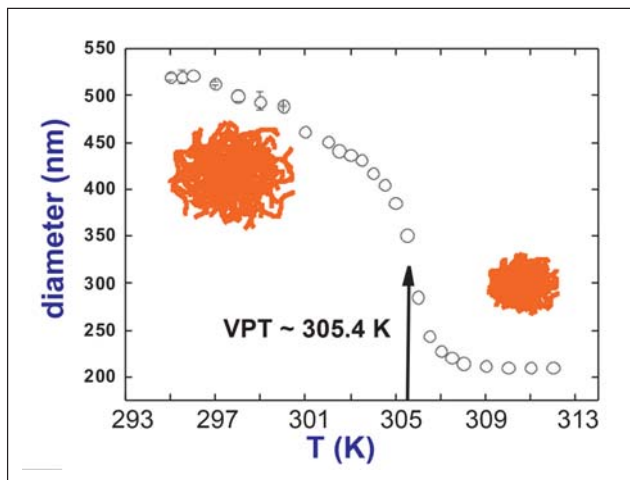


**Fig. 1** Hydrodynamic diameter as a function of temperature. Arrow indicates the VPT temperature

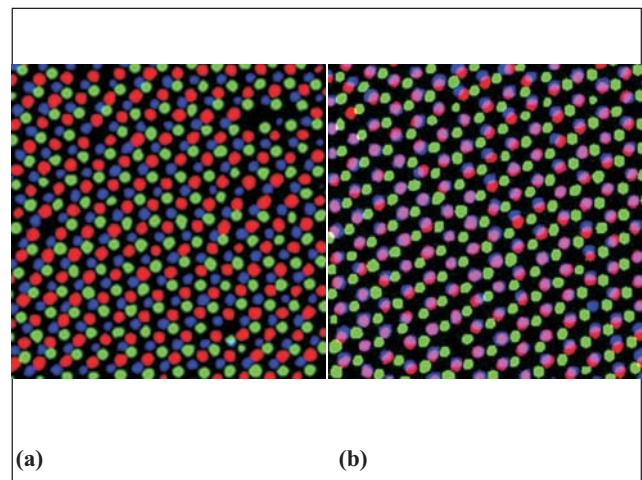


**Fig. 2** Micrographs revealing (a) the ABC stacking and (b) ABA stacking. The scale bar corresponds to  $1\mu\text{m}$

the visible range. We employ a confocal laser scanning microscope (CLSM) to investigate the real space three-dimensional (3D) structure and stacking disorder of PNIPAM microgel crystals and show that the structure of the PNIPAM microgel crystals depends upon the way they are prepared. We have synthesized monodisperse PNIPAM microgel particles having a diameter of 520nm in aqueous medium. The real space structures of these two samples having a volume fraction of  $\phi = 0.43$  are determined using a CLSM. CLSM images of several regions of the

microgel crystals are analyzed for determining the 3D pair-correlation functions,  $g(r)$  and the stacking sequence for both the crystals. The stacking disorder in the PNIPAM microgel crystals is quantified by analyzing the stacking sequence of the crystalline planes along the  $z$ -direction. From the stacking sequence the stacking probability,  $\alpha$  is determined. The consecutive three images in a region are assigned pseudo colours RGB (red, green and blue) for A, B, C planes and then merged these images. If the RGB colors are seen distinctly (Figure 2a) after merging, then the stacking is

identified as fcc-type; whereas if two of the colors merge (Figure 2b) then it is hcp-type of stacking. The as-prepared sample is found to have stacking disorder with an average stacking probability  $\alpha = 0.42$  which along with the analysis of 3D pair-correlation function,  $g(r)$  (Figure 3a) revealed the structure of microgel crystals in this sample to be random hexagonal close packing (rhcp). Further, for the first time a split second peak is observed in the 3D  $g(r)$  (arrows in Figure 3a) of the as-prepared sample. A split second peak is observed usually in glasses but we show here that it can also appear in a

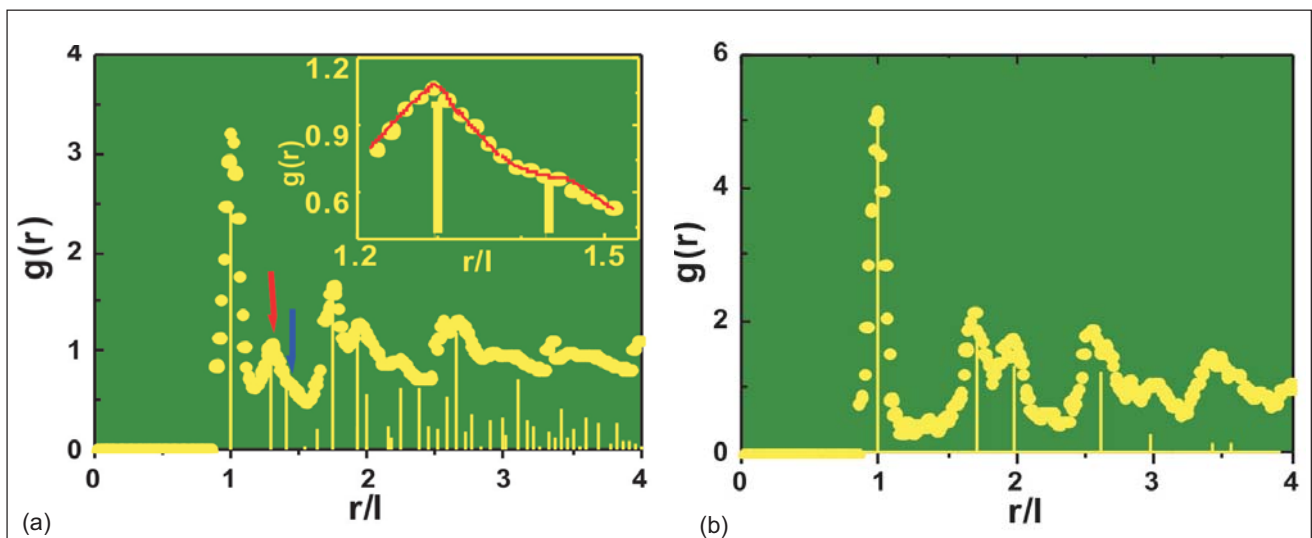


**Fig. 3** Experimental (dots) 3D  $g(r)$  for the PNIPAM microgel crystals of (a) as-prepared sample, lines represent the  $g(r)$  for an ideal hcp lattice with 57% of the B-planes displaced along the  $y$ -direction. The red and blue arrows marked at  $1.29l$  and  $\sqrt{2}l$  respectively indicates the split second peak which is shown in an Inset. (b) re-crystallized sample, lines represent the  $g(r)$  for an ideal fcc lattice

crystalline sample and whose origin is through simulations. The split second peak in PNIPAM microgel crystals with RHCP structure arises due to the displacement of 57% of the B-planes from the ideal hcp positions. The as-prepared sample is melted into a colloidal liquid state by heating it above VPT and recrystallized it at a cooling rate of 0.15 degree per minute.

The recrystallized sample is subjected to CLSM studies similar to that mentioned above. Surprisingly, the split second peak disappeared and the peaks in the  $g(r)$  (Figure 3b) matched with that of the simulated ideal fcc structure and the crystals are found to be free from stacking disorder. The fcc structure with almost no stacking disorder arises due to dual crossing

of the sample through a crystal-fluid phase transition and slow cooling. The rhcp structure occurs in the as-prepared sample due to the sudden withdrawal of shear on the shear melted liquid. Present studies suggest that tailoring the shear rate or cooling rate can help in tuning the stacking disorder and the structure in PNIPAM microgel crystals.

## V.23 Magnetic and Transport Characteristics of Nanoscale Systems from Ab-initio Methods and Green's Function Modeling

Nanowires, nanojunctions and hybrid nanostructures are the systems that are of interest in the data storage, read/write and sensor applications. Experimental investigation of the variation of the magnetic and transport characteristics of these systems with respect to the geometry, structure and chemical composition are essential in the identification of the systems required for the desired application and hence substantial effort is being spent in this direction. These efforts can be aided

by the modeling of the magnetic and transport properties of these systems and hence it has acquired considerable importance.

Large magnetic anisotropy energy and magnetoresistance are two important properties that are desired in storage and sensor applications. The large magnetic anisotropy is the energy required to deflect the magnetic moments from the easy axis of magnetization to the hard axis. Large magnetic anisotropy is thus desired to keep the orientation

of the magnetization. We have studied the large magnetic anisotropy energy in FeM (M=Pt,Co) nanowires and FeCo superlattices using the ab-initio (VASP) method. FePt nanowires are found to exhibit large magnetic anisotropy values as large as 102 meV/atom. The large magnetic anisotropy of  $Fe_{1-x}Co_x$  nanowires at different Co concentration obtained from our studies are shown in Figure 1.

Large magnetic moment is another quantity of importance in the above

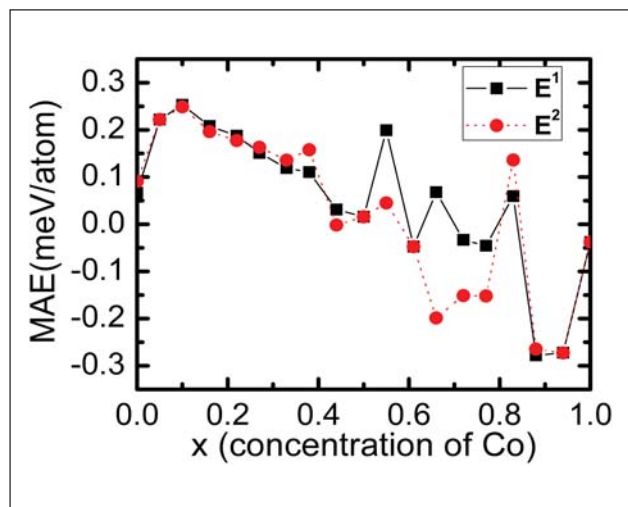


**Fig.1** MAE of  $Fe_{1-x}Co_x$  nanowires as a function of the cobalt concentration.  $E^1$  and  $E^2$  corresponds to nanowires with bcc (100) and (110)

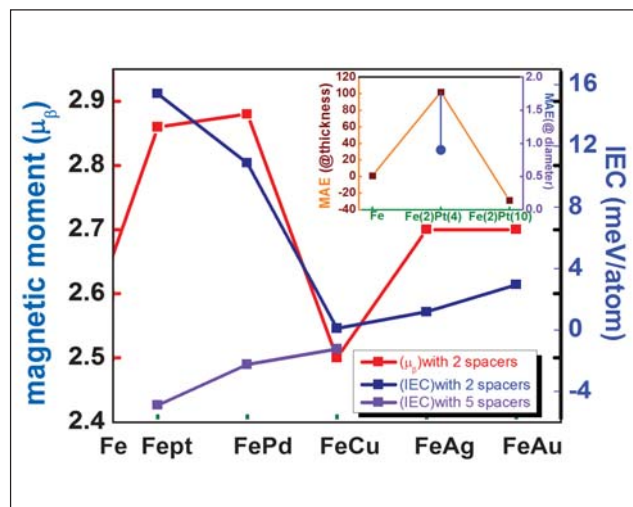


**Fig.2** Magnetic moments and IEC in FeM (M=Pt,Pd,Cu,Ag,Au) nanowires. The inset shows the MAE in Fe and FePt nanowires

said applications. The magnetic moment enhancement in several bimetallic nanowires and multilayers were studied using the ab-initio method. Figure 2 shows the magnetic moments of different nanowires obtained from our calculations. Maximum enhancement is found in FeNi nanowires and the value of the Fe magnetic moment in these nanowires is  $3 \mu_B$ . FeCo multilayers also show significant magnetic moment enhancement. The interlayer exchange coupling (IEC) in these nanowires were also studied using the ab-initio methods and the IEC obtained from our calculations are shown in Figure 2.

Ab-initio studies are useful in predicting the geometry and structure of nanoscale systems too. The equilibrium structure of the above mentioned nanowires, superlattices and multilayers were obtained from the ab-initio calculations through the energy minimization consideration and it is used in obtaining the above mentioned properties. The structure of FePt nanowire obtained from our studies is shown in Figure 3a.

Transport characteristics of these systems were studied using two approaches. The first approach that combines the Landauer method with the ab-initio electronic structure calculations (SMEAGOL, TRANSIESTA) is used to study the transport in nanowires and hybrid nanostructures. The second approach that is based on the Green's function modeling is used to study the magnetoresistance of magnetic tunnel junctions. A schematic diagram of the magnetic tunnel junction with ferromagnetic coupling between the electrodes is shown in Figure 3b.

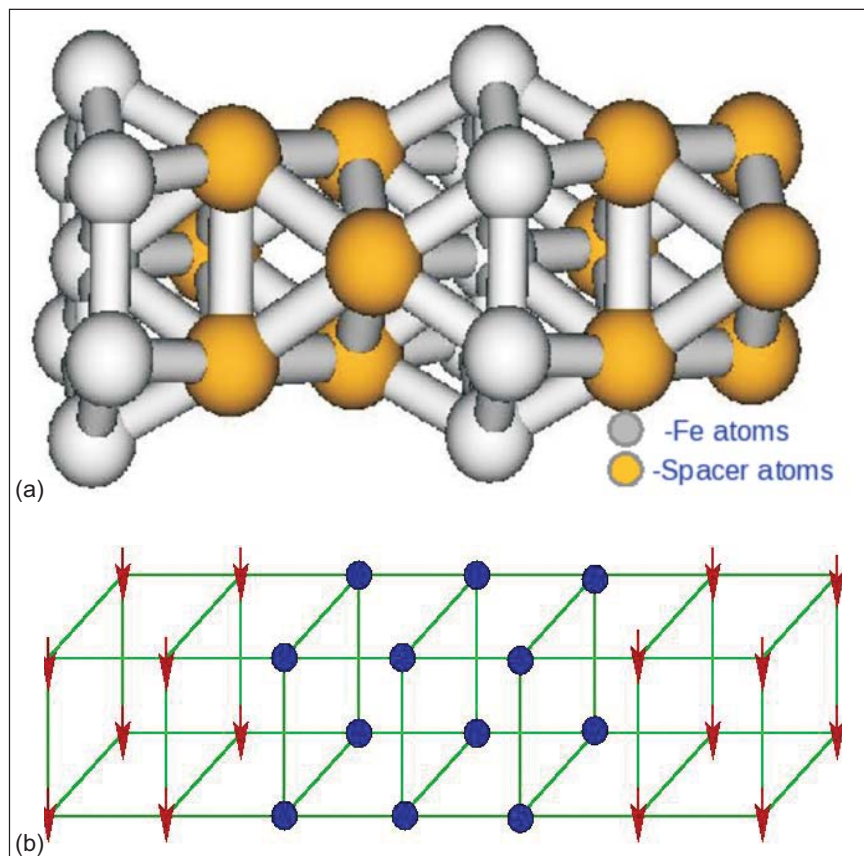


**Fig. 3** (a) Structure of the FePt nanowire obtained from ab-initio calculations (b) Schematic diagram of a magnetic tunnel junction

The magnetoresistance of the MTJ Expand is defined as

$$MR = \frac{I^P - I^{AP}}{I^{AP}}$$

$I^P$  and  $I^{AP}$  are the currents corresponding to the parallel and antiparallel configuration of the magnetization of the electrodes. The aim of our study is to investigate the crucial material characteristics that are important in deciding the magnetoresistance of magnetic tunnel junctions. The non-equilibrium Green's function formulation that we developed for this purpose is capable of taking into account the quasiparticle electronic structure of the magnetic tunnel junction as well as the multiple barriers present in the central region. We find from a model study that the band occupation of the electrodes play a significant role in deciding the tunnel magnetoresistance of the magnetic tunnel junction. The

tunnel magnetoresistance of a magnetic tunnel junction as a function of the applied bias at different values of the band occupation of the electrode is shown in Figure 4. Our studies on the magnetic and transport characteristics of these nanoscale systems can be further developed to obtain results that will be of aid in the device development.

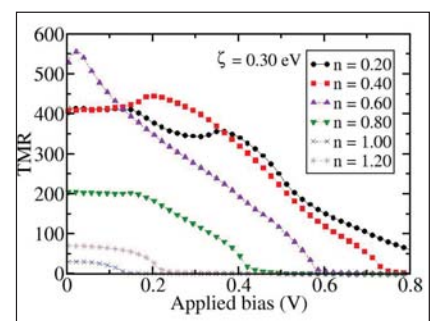


**Fig. 4** Tunnel magnetoresistance of a magnetic tunnel junction as a function of the applied bias at different values of the band occupation ( $n$ ) of the electrodes.  $\zeta$  is the conduction electron - local moment exchange coupling strength

## V.24 Study of Incongruent Decomposition of Calcium Carbonate by Transpiration Thermogravimetry

The transpiration thermogravimetric studies on systems such as CsI, Te, TeO<sub>2</sub> and H<sub>3</sub>BO<sub>3</sub> are successful. However, similar studies on Ru-Te as well as Mn-Te systems are not useful, as they are known to undergo incongruent vaporization. Studies on such systems require a systematic investigation on samples that vaporizes incongruently and the products do not condense. In this context, the temperature and flow dependence measurements on the solid CaCO<sub>3</sub>(s) was performed as there was no data reported in literature on solid CaCO<sub>3</sub>. The sample CaCO<sub>3</sub>(s) upon heating releases CO<sub>2</sub>(g) by incongruent decomposition. The measurements involved use of argon as the carrier gas for the transport of CO<sub>2</sub>(g) and derivation of its pressure in the temperature range from 650 to 790 K through many flow dependence runs (four at 720 K, five at 740 K, and three at 760 K) and thirteen temperature dependence runs.

Table 1. Thermodynamic parameters for the decomposition of calcium carbonate	
Reaction	CaCO <sub>3</sub> (s) = CaO(s) + CO <sub>2</sub> (g)
Temperature dependence of partial pressures	log [p(CO <sub>2</sub> )/Pa] = - (9074 ± 555)/(T/K) + (12.91 ± 0.71), T = 650 to 1177 K
Δ <sub>r</sub> H <sup>o</sup> <sub>m</sub> (298.15 K)	180.7 ± 11.0 kJmol <sup>-1</sup>
Δ <sub>r</sub> S <sup>o</sup> <sub>m</sub> (298.15 K)	161.6 ± 8.3 Jmol <sup>-1</sup> K <sup>-1</sup>

Figure 1 show some typical results of flow dependence runs, dm/dt vs. flow rate as well as the corresponding p(CO<sub>2</sub>) vs. flow rate. Figure 2 shows some typical results of dm/dt as well as the p(CO<sub>2</sub>) deduced from them as a function of temperature.

The decomposition pressures of CaCO<sub>3</sub>(s) obtained in this study represent the first results from dynamic measurements at low

temperatures and are in reasonable accord with those from the previously reported studies at relatively higher temperatures (dynamic method: from (950 to 1161 K); static method: (722 to 1177 K). The results from all three studies are combined to recommend the thermodynamic parameters pertinent to the decomposition reaction is shown in Table 1.

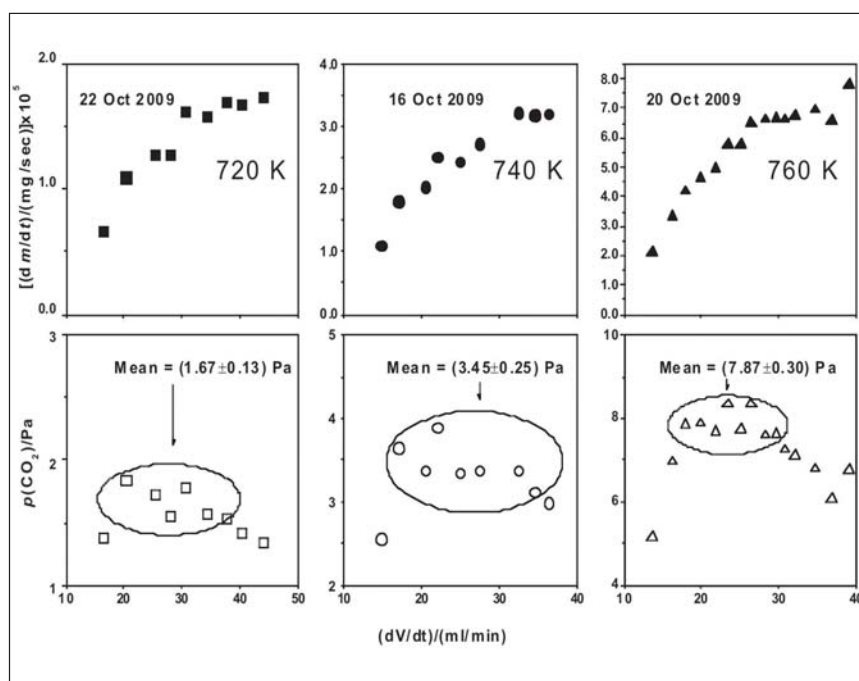


Fig. 1 Results of typical flow-dependence transpiration experiments on CaCO<sub>3</sub> decomposition

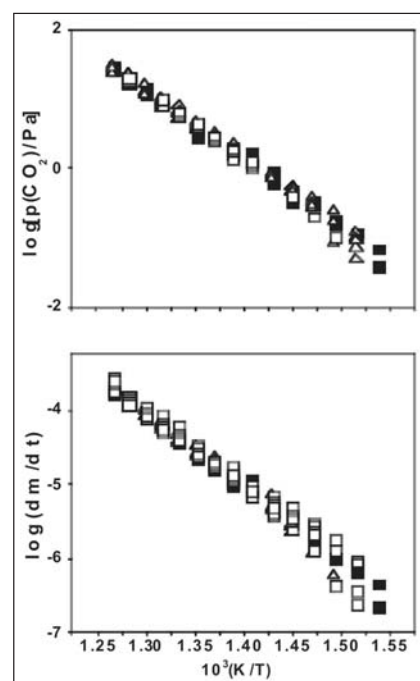
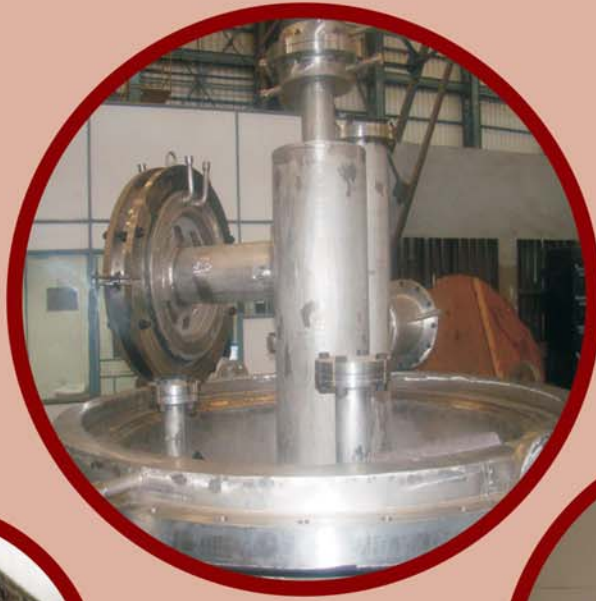


Fig. 2 Results of temperature-dependence transpiration experiments



# CHAPTER VI

## Infrastructure Facilities

## VI.1 Manufacture of Components

The content of this article highlights the varied experiences gained by central workshop in the manufacture of various components such as thermal striping test vessel (TSTV), electrochemical hydrogen meter (ECHM) for steam generator test facility (SGTF) and sampling vent pots (SVP) for demonstration fuel reprocessing plant (DFRP) with stringent dimensional and geometrical tolerances meeting the requirements of ASME Section VIII, Div I.

### Thermal striping test vessel

The test vessel was designed and fabricated to study the phenomenon of thermal striping in the vicinity of structural elements of sodium cooled fast breeder reactors. In thermal hydraulic phenomenon, random mixing of fluids induced by turbulence and jet instability in the vicinity of structural element causes random temperature fluctuations. These thermal fluctuations induce repeated thermal stresses which results in initiation and growth of crack and eventually leads to failure of the structure. Previously, similar studies were carried out with water as stimulant and was found to be inadequate due to its higher thermal conductivity compared to sodium. Hence, the test vessel was manufactured with the objective of conducting experiments for the study using sodium as stimulant for temperature variation from 373 to 423 K.

Thermal striping test vessel as shown in Figure 1 with OD 600 mm and height of 1000 mm was

fabricated using austenitic stainless steel grade AISI 316 L material. It consists of a cylindrical shell, tori-spherical dished end, ring flange, cover flange, nozzles, rings, guide mechanism for instrumentation, bellows, level probes and accessories. The tori-spherical dished end (ID 600 mm, crown radius 600 mm, knuckle radius 60 mm, straight face 40 mm and thickness 8 mm) was fabricated by progressive cold forming process and subsequently it was heat treated to relieve residual stress developed during forming process. The dish end was also subjected to surface treatment by shot blasting. Both ring flange of size OD 840, ID 612 and 35 mm thickness and cover flange of size OD 840 and 35 mm thickness were machined and 100 % dimensional inspection was carried out. The dish end and ring flange were welded with the cylindrical shell by GTAW process.

The nozzles were welded with dish end and care was taken to achieve the perpendicularity. Then guide mechanism for instrumentation and continuous level probes were assembled over the cover flange. An internal baffle plate arrangement was made and assembled from the bottom side of the cover flange. The external baffle plates were fillet welded on the outer periphery of the shell. Sequential welding technique was adopted to minimize distortion and to achieve geometrical tolerances within 0.5 mm. The thermal striping test vessel after fabrication was pneumatically tested at 7 bar and also subjected to helium leak test. The achieved leak rate was



**Fig.1** Thermal striping test vessel assembly

$10^{-8}$  std-atm-cc/sec. Machining of flanges, nozzles, guide plates, level probes and their welding with cylindrical shell along with dish end and fabrication of test vessel were a challenging task due to stringent dimensional and geometrical tolerances. With expertise and adoption of best methodology at different stages, the test vessel was manufactured successfully to ensure its functionality.

### Electrochemical hydrogen meter for steam generator test facility

Electrochemical hydrogen meter as shown in Figure 2 was fabricated to measure the hydrogen concentration in liquid sodium at high temperatures. It works based on the principle of electro chemical cell. The emf output produced in the cell is directly proportional to log of hydrogen concentration in liquid sodium. The

electrochemical hydrogen meter is compact in size. It consists of a central tube, cooling fins, knife edge flange, top cup, bottom cup, thermo well, spark plug for level detection and pipes for sodium inlet/outlet. For machining of twenty numbers of cooling fins of size 100 mm OD, 29.1 mm ID and 1.6 mm thickness from AISI - 316L material, round blanks were cut, two sets consisting of ten blanks each were made by stacking, tack welded and machined together. This has reduced the production time. Two sets were machined separately. The central tube of 29 mm OD and 215 mm length was pre-machined with 2 mm finish machining allowance on ID to take care of shrinkages during welding and to ensure final dimension after finish machining. The machined fins, each having four holes equally spaced on 55 mm PCD were assembled with equal distance on central tube and welded such that every alternative fin could be rotated by 15°. A special fixture was designed and fabricated to control distortion during GTA welding of the fins with central tube. The twenty cooling fins were welded in close distance of 5 mm and longitudinal and transverse shrinkage were measured to be within 3 mm and 0.5mm respectively. After welding the fins, the central tube was machined to achieve the required dimensional and geometrical tolerances. The thermo well, top and bottom cups were machined in 3-axis CNC machine and achieved the stringent geometrical tolerances. The inlet and outlet pipes for sodium, thermo well, top and bottom cups were welded using GTAW process and all weld joints were subjected to radiography examination. For ensuring leak tightness, electrochemical hydrogen meter was subjected to pneumatic

test at 50 bar pressure with nitrogen medium and helium leak test (HLT). A leak rate of  $10^{-9}$  std-atm-cc/sec was achieved.

### Sampling vent pots for demonstration fuel reprocessing plant (DFRP)

Seventy five numbers of sampling vent pots, as shown in Figure 3, were fabricated to separate gases from the liquid samples in Demonstration Fuel Reprocessing Plant. The vent pot consists of a main body, end cap, end plate, 15 NB top pipe, 8 NB pipe and pad. The overall size of sampling vent pot is 88.9 mm diameter and 535 mm length and is made of SS 304 L material. The bottom end of vent pot is connected with liquid collection tank and top end is connected with stack through which gases are discharged to atmosphere after passing through various stages of filters.

The end caps of dimensions OD 88.9 mm and 60 mm length were precisely machined in CNC Lathe and edges were beveled to 37.5 degrees for butt weld joint. Counter boring with 1 degree tapered face in the end cap and drilling of  $\phi$  13 mm hole with the inclination of 125 degree on main body were critical features of machining and could be achieved successfully.

The main body was machined from 80 NB pipe and half segmental pads with internal diameter 88.9 mm were formed from 3 mm thick SS 304L sheet in hydraulic press. The end plate was machined from SS 304L sheet plate of 6 mm thickness. 100 % dimensional inspection was carried out for each component. For ease of fabrication and inspection, the sampling vent pot was divided into two sub assemblies namely upper and lower subassemblies.



**Fig. 2** Electrochemical hydrogen meter

For the fabrication of upper sub assembly, a special fixture was designed and fabricated for welding of main body with 8 NB pipe at an angle of 125 degree with reference to centre axis of main body. In the lower sub assembly, the end plate was welded with 15 NB pipe. End cap was butt welded with upper sub assembly. Then both upper and lower sub assemblies were welded together. Finally, the pad was fillet welded with main body. All weld joints were welded by GTAW process.

Segmental welding technique with argon back purging was adopted to minimize the distortion and oxidation. A damper was provided to minimize purge gas consumption during welding. Pickling and passivation for both subassemblies were carried out, assembled and welded. All weld joints were subjected to liquid penetrant examination and ultrasonic examination.



**Fig. 3** Sampling vents pots

## VI.2 Development of a Universal Platform for Radiological Instrumentation

In any radiochemical facility, portable radiation monitors play a major role in ensuring safety of occupational workers from the standpoint of radiation protection.

### Basic structure of radiation monitors

Generally radiation monitors consist of a detector (sensor) operating in two basic interaction mechanisms namely ionization and excitation. In ionization based detectors (reverse biased p-n junction diodes or gas filled detectors), radiation interacts with the detector medium and produces ion pairs which flow as current. In excitation based detectors (scintillation detectors), a transducer converts light output into electrical signal. Both types of detectors require a high voltage bias to operate. Output from the detector is either current or voltage pulses which are converted to generate pulse signal either by preamplifier, current/voltage or charge sensitive or combination of the above. These pulses are counted and displayed in required unit. Detector, bias voltage and converting electronics combined together can be treated as transducer.

The data from all the field monitors (dose and alarm) are continuously and remotely logged in the radiation data acquisition system (RADAS) by communication channel (RS485 / ethernet network loop).

### Constraint in nuclear instrumentation

As radiological instrumentation is an emerging field in India, the requirement is being met by only few

suppliers. Though the sensor part being the same, for engineering conversion the communication electronics supplied by these suppliers greatly differ from each other. Thus, it is not possible to interchange the electronics, thereby making them indirectly proprietary in nature. It is also cumbersome to implement the monitors manufactured by different suppliers into a common monitoring and recording system in a huge nuclear facility.

### Development of a common platform

Keeping the analogy with process instrumentation which has reached maturity, an attempt is made to develop a common platform for radiological instrumentation. The flowchart of the process is given in Figure 1. For this, the radiation sensors are combined with that of standard HIO modules (mini PLC with IO) which are widely used in process instrumentation. The same HIO can be used in different types of monitors just by changing the configuration. Advantages of the above concept are

1. Maintenance of large number of different spares is avoided
2. Since these HIO modules come with industrial standard test certificates, their failure rate is less thereby improving the reliability
3. In the wide process instrumentation market, owing to competition, high quality modules with reasonably less cost can be purchased
4. Integration with the standard modules for data monitoring and

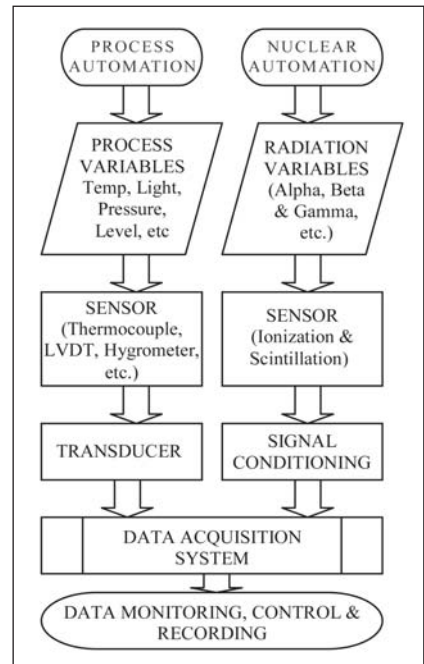


Fig. 1 Flowchart of the process

logging via standard protocols and channels (RS-485 / Ethernet communication loop) will be like plug and play

5. Power required for the monitoring system is a standard 24 volt with bare minimum current

Block diagram of radiation detectors developed based on nuclear automation principle is shown in Figure 2.

Using the above concept, standard HIO modules were configured to

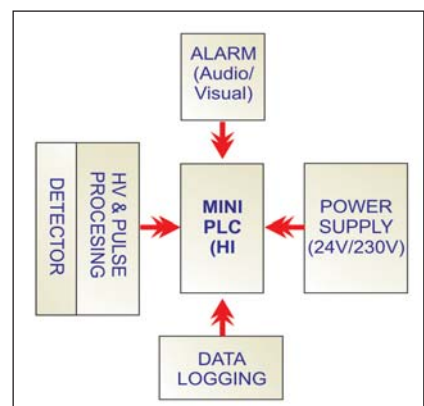


Fig. 2 Block diagram of radiation detectors



**Fig. 3** Alpha and beta hand cloth monitor

function as radiation monitors like AGM, CAM and AHM.

### Alpha and beta hand cloth monitor

Figure 3 shows the combined alpha and beta hand monitor. In this detector ZnS (Ag) scintillation is used for alpha particle detection and plastic scintillator is used for beta particle detection.

These two scintillators are sandwiched together and coupled to a PMT and the assembly acts as a transducer which is combined with biasing HV and pulse processing circuits. Mini PLC with in-built I/O is used to monitor and control the hand monitor functionality. The complete monitor works with 24 V, 600 mA power.

### Area gamma monitor

For area gamma monitor (Figure 4), commercially available mini PLC with



**Fig. 4** Area gamma monitor

in-built I/O is used in which a conventional AGM external probe is connected. Data from the PLC is logged in the centralized data logging system (RADAS).

### Kr air monitor

The release of <sup>85</sup>Kr through stack is monitored by passing the air through a cylindrical chamber in which a GM tube is fitted coaxially. A parallel pulse output from sensor is directly fed to the Mini PLC with in-built I/O and the data are logged in a standard paperless recorder connected in LAN. Logged data can be viewed and analysed via a desktop PC connected in the LAN. Data from conventional air monitor (Figure 5) were compared with the data obtained from the PLC and was found to be in good agreement.

### Special nuclear material monitor

At CORAL entry, the SNM monitor was connected to Mini PLC with in-built

I/O. The output of all the eight detectors were integrated and given to a window discriminator and the counts in the window region (fissile material region) and above the window region (fission product region) are counted in the PLC. Individual presetting is done for the two regions. Two different audio and visual alerts provided for the two regions of alarm are logged in the standard paperless recorder and viewed from any desktop PC connected in the LAN.

The nuclear instrumentation can be made robust by separating the detecting mechanism as a transducer and the measuring mechanism linked to the available global process automation equipment. Thus, the proposed (nuclear automation) strategy enhances the system reliability, improves the flexibility and reduces the cost.



**Fig. 5** Krypton air monitor

## VI.3 Contribution Towards Titanium Sponge Production

India is endowed with large quantity of Titanium (Ti) ore, mainly in the form of Ilmenite ( $\text{FeTiO}_3$ ) along the sea coast near Kerala, Tamil Nadu, Andhra Pradesh and Orissa. Hitherto, the Titanium industry in the country has been confined to beneficiation and export of Ilmenite or more significantly, in the production of Titanium tetrachloride intermediate, purification, and conversion back to titanium dioxide which is used as white pigments in paint industry. The deposits of titanium ore in the country are equivalent to about 140 million tons of titanium.

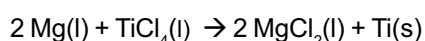
The technology for extraction of Ti metal from the intermediate titanium tetrachloride ( $\text{TiCl}_4$ ) has now been established in the batch size of 3000 kg at Defence Metallurgical Research Laboratory (DMRL), Hyderabad. The technology was developed in collaboration and co-operation with our Centre and Nuclear Fuel Complex, Hyderabad. This technology is currently being transferred for large scale production with installed capacity of 500 tons per annum of titanium sponge to start with, at M/s Kerala Minerals and Metals Ltd. (KMML),

Sankaramangalam, Kerala with complete funding by Vikram Sarabhai Space Centre, Department of Space.

KMML is responsible for construction and operation of the plant based on the technology transferred and training of O&M by DMRL. Providing the mechanical design, resolving the manufacturing issues during manufacture of the retorts and associated high temperature piping and quality assurance of the retort are the responsibilities of IGCAR.

### Process requirement for design

$\text{TiCl}_4$  is reduced to virgin Ti, called as Ti sponge in the presence of Mg at a temperature of about 1120 K and subsequent purification of the sponge is done by pyro-vacuum distillation at a temperature of about 1250 K to remove Mg and  $\text{MgCl}_2$  locked up in its pores.



The reactor is made with SS 304 as base material which is clad with SS 430 (Figure 1). The reactor is designed based on the mechanical strength of SS 304 and inside was lined with SS 430 to prevent contact

of SS 304 with Mg, as Ni bearing SS 304 is not compatible with Mg.

The reactor operates under controlled argon pressure of 0.25 kg/cm<sup>2</sup> during reduction and maximum internal pressure during  $\text{MgCl}_2$  transfer is 0.85 kg/cm<sup>2</sup>. During vacuum distillation the absolute pressure is about 0.014 mm of water column.

### Design challenges

The combined process unit developed at DMRL comprises two stations, furnace and condenser, in each of which an identical reactor is housed, which are connected together with interconnecting pipe. The reactor measures approximately 1.5 meter in diameter and about 5 m in height with a wall thickness of about 30 mm (Figures 2 & 3). The reduction is carried out in the reactor kept in the furnace station and during distillation the Mg and  $\text{MgCl}_2$  from the Ti sponge pass through the inter connecting pipe and gets collected in the adjacent reactor externally cooled with water kept in the condenser station. The reactor in the condenser station has to be mounted on trolleys for mobility to allow thermal expansion of inter-connecting pipe conveying Mg and  $\text{MgCl}_2$  vapor from one reactor to the other at 1170 K, the reactor in the furnace being stationary.

A dual flange design has been developed for the reactor. A flexible flange, welded below the top of the reactor, serves to support the reactor on the flange of the eight zoned, 480 kW pit type furnace and ensuring leak tightness of the furnace for maintaining the vacuum



Fig. 1 Clad reactor for titanium sponge production.

in the furnace at the same time. When the retort (Figure 4) is under vacuum during distillation, vacuum in the furnace will minimize the differential pressure. These flanges are water cooled ensuring safety of the vacuum seals and the flanges have to withstand the stress due to internal heat radiation and also allow radial expansion at high temperature.

A 450 mm nozzle at the bottom of the reactor was designed with a capped closure, amenable for de-welding of the cap after every batch run to enable ejection of the sponge cake from the top of the reactor, using a ram operating through this nozzle, vertically with a hydraulic press. The cap had to be welded with high reliability to the nozzle before restart of every batch operation, as any failure of this weld can be of safety concern due to leakage of molten magnesium and air ingress causing metal fire. The procedure for qualification of this important weld had been developed at our Centre. A perforated carbon steel, 150 mm thick plate located within the reactor near the bottom of the reactor, completely immersed in liquid Mg/MgCl<sub>2</sub>, was designed to retain and support 3,000 kg sponge cake produced during the process.

### Quality assurance and fabrication process development

As the temperature of operation of the SS retort reaches 1250 K, the quality



**Fig. 2** Top dished end of reactor

control is of great importance and quite extensive. The reactors are fabricated conforming to ASME Section VIII Division 1 with special requirements, in terms of improved chemical composition of SS plates and welding consumable and stringent manufacturing tolerances.

As part of technology development for various components, trials were conducted to finalize the die and punch for bottom dished end and semicircular pipe (Figure 3). A procedure had been developed for the fabrication of tapping pipe assembly with minimum welding distortion. A maximum of 0.5% Ni was allowed at the top of 4 mm SS 430 overlay. The condition was put as Mg preferentially leaches out Ni from the surface which leads to embrittlement of the austenitic SS (Table 1). The main challenges faced were in terms of more stringent radiographic acceptance criteria, control of distortion during welding of tapping pipe and thermowell to the retort shell ID, difficulties in hot forming the



**Fig. 3** Bottom dished end, after first stage hot forming

clad bottom dished end while minimizing scale formation and problems in achieving interchange ability of parts due to weld distortion in achieving tolerances on critical distances between the support flange and top flange and between cover flange and nozzle connecting to interconnecting pipe.

The quality assurance team of IGCAR at Mumbai is now carrying out quality assurance and complete stage inspection for sixteen reactors being manufactured for KMML by L&T, Ranoli. Three reactors were successfully manufactured and dispatched to KMML.

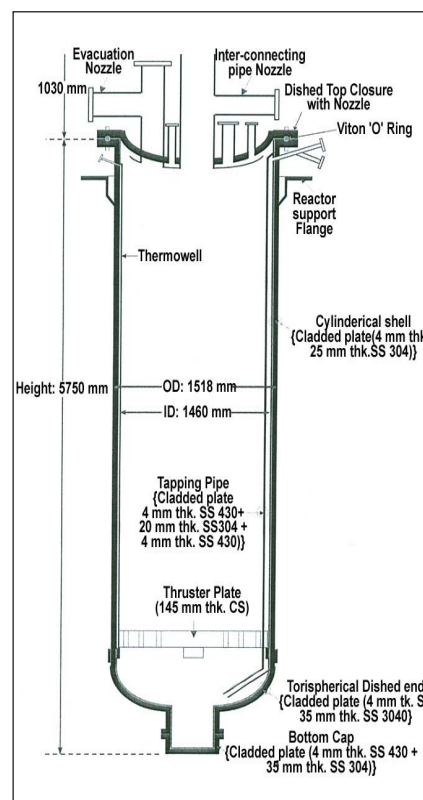


**Fig. 4** Schematic sketch of the retort

**Table 1: Nickel Dilution during overlaying.**

Diameter of electrode used in overlaying, mm.			Height from fusion line. (Mm)	Chemical composition of weld pad at qualifying height.			
Barrier layer.	2 <sup>nd</sup> run.	3 <sup>rd</sup> run.		Ni	C	Cr	Mo
2.5	3.15	4	2.5	0.725	0.10	16.939	0.063
2.5	3.15	4	3.0	0.573	0.111	17.038	0.063
2.5	3.15	4	3.5	0.615	0.101	16.921	0.063
2.5	3.15	4	4.0	0.342	0.103	17.469	0.063

## VI. 4 Automation of Cooling Tower Operation at CWCP

The central water chilling plant operates round the clock, all through the year to ensure uninterrupted and reliable chilled water supply for air conditioning and ventilation requirements of IGCAR. The installed capacity of the plant is 3100 TR (Figure 1). Six numbers centrifugal chillers are provided to cater the air conditioning loads with the operating strategy of four working, two standbys. Two to four units are operated continuously on rotational basis to meet the demand. There are two cooling towers which comprise sixteen cells of each 250 TR heat removal capacity. The required number of cooling tower cells were operated manually based on the heat load. In order to optimize the operation of cooling towers as well as to maintain the chiller condenser

cooling water inlet temperature at  $305\pm 1$  K, the operation of cooling tower fans has been automated using cooling tower manager.

The cooling tower manager (CTM) regulates the operation of cooling tower fans based on cooling tower approach and wet bulb temperature. It consists of temperature and relative humidity sensor to measure the ambient wet-bulb temperature, step controller to regulate the number of fans, temperature sensor to measure the cooling tower sump/outlet temperature and a water flow switch to monitor cooling tower water flow.

The cooling tower manager computes the actual approach (difference between cooling tower sump temperature and ambient wet-



**Fig. 1** Cooling tower

bulb temperature) and compares it with the set value (set at 3 to 4 K approach) and automatically switches ON / OFF the required number of fans to maintain the cooling tower sump temperature.

The automation of cooling tower operation is unique and the first of its kind in IGCAR. This feature has enabled in minimizing the operating time of cooling towers fans, reduction in man hours and considerable saving in energy of 25,550 units/annum.

## VI.5 Biometric Attendance Recording System - Successful Operation and its Development

Biometric attendance recording system (BARS) consisting of 37 numbers of hand geometry cum RFID readers throughout IGCAR, which are connected to two servers (redundant configuration) in Administration building via campus backbone, was installed in March 2006.

The BARS software consists of two modules : 1. Hand geometry reader program, which is part of the reader and 2. Server program consisting of (a) Transactions collection program, (b) Attendance processing program, (c) User interface for viewing reports, (d) User interface for modifying

database and (e) Leave updating program. During the last four and half years of successful operation of the system, various issues were addressed and several developments were made on the system. The various developments / enhancements carried out on the system are described as follows:

### Hand geometry reader module

The system was designed such that the employee's hand template is stored in the memory of the Identity card and thus the employee's hand template is static till the ID card is reprogrammed with the new

template. This had resulted in lot of rejection of daily attendance because for verification, the latest template generated by the reader depends on the environmental condition, health state etc. To overcome this problem the reader program was modified, such that the system generates a new template based on previous template stored and the new template generated by the hand geometry reader. This enabled the system to generate a dynamic template (stored in memory) unlike static template in the ID card. The modified system was installed in EID on experimental basis and it was

found that the rejection has drastically reduced to zero. In view of this successful achievement, it is planned to update firmware of all the readers of our campus.

### **Installation of new biometric cum RFID readers**

Initially there were 37 biometric cum RFID readers installed throughout IGCAR. During the last four and half years, requirements were received from different groups for installation of new biometric cum RFID readers. The software in the server was modified for accepting new readers and thus 6 numbers of additional readers were installed in different groups / locations.

### **Server Module**

#### **Transaction collection program**

Transaction collection program collects user transactions and synchronizes time. The program was modified to accept all 32 bit card serial numbers along with Identity card preparation program and data entry program for feeding card serial numbers.

#### **User interface for viewing reports**

The server program was modified for generating various reports as and when required by administration and user departments. The following are some of the modified reports / new reports made as per requirement.

1. Monthly attendance report lists the attendance codes of employees with leave details.
2. Shortfall or extra hours report calculates the cumulative shortfall or extra hours.
3. Reader status report shows the current status of all readers.
4. Absent, single entry, Irregular entry report gives the number of days an employee is absent or made single entry or irregular entry.
5. Today's present and absent report lists the employees present and absent respectively.
6. Card flash report and monthly report gives all the transactions of employees.

#### **User interface for modifying database**

Database modification is required on 1. Recruitment, 2. Promotion, 3. Transfer, 4. Expiring validity of identity card etc. Comprehensive user interface is developed for modifying database.

Many patterns of round the clock shifts are followed in IGCAR. General shift employees are asked to come in round the clock shift on need basis. A Universal interface is developed in ASP.Net to feed all patterns of shift information.

### **Integration with leave management system and workflow system**

Biometric attendance recording system (BARS) is integrated with leave management system. Software is developed to read Leave data periodically from leave management system and update in BARS.

Attendance details of employees to workflow system for the calculation of salary, overtime etc. are provided by BARS.

### **System administration**

Database backup is scheduled to run every day and the backup data is stored in CD. Regular maintenance of servers is being carried out. Assistance is provided to solve the day to day technical problems of admin operators.

The Biometric attendance system is being used successfully for the last four and half years. The system was integrated with online leave management system and workflow system. Also various other enhancements were carried out for better usage and fault free operation. The system was also extended to all the employees of SRI/AERB and it is being maintained in-house for better maintainability and availability.

## **VI.6 Ichthyologic Diversity Studies in Coastal Waters of Kalpakkam**

**A**nthropogenic impacts have reported to diminish biodiversity in all milieus Ichthyological diversity (variety of fish species) is no exception. Site-specific reports are essential because biodiversity profile

varies regionally. Considering the importance of Kalpakkam coast, it is imperative to collect benchmark data on fish diversity as part of long term studies on ecology of coastal milieu. Hence, an attempt has been initiated

to study the diversity pattern of marine fishes in and around Kalpakkam coast.

Samples were collected from the fishermen along the coast at regular

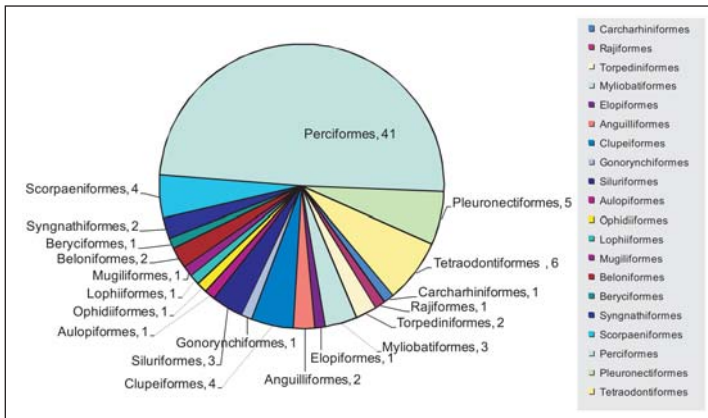


Fig. 1 Order wise family population

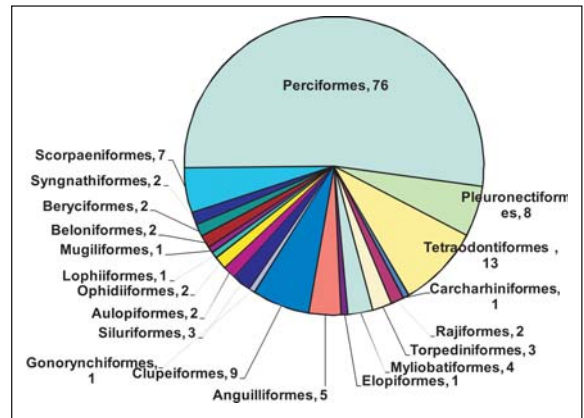


Fig. 2 Order wise genus composition

intervals for a period of three years from May 2007 to April 2010. The specimens were cleaned and brought to the laboratory. The morphometric and meristic characters like colour, spots and other important characters were noted for proper identification purpose.

A total of 203 species under 145 Genera, 83 Families and 20 Orders were collected. Cartilaginous fishes occupied only 6.4% of the total collection. The Family and Genus composition given in Figures 1 and 2 respectively give the taxonomic structure of the ichthyo-fauna available at Kalpakkam coast.

In the first sampling unit itself, 35 species were encountered. To know the accumulation pattern, species accumulation curve was plotted (Figure 3) against sampling unit. A steep increase on the 15<sup>th</sup> sampling

effort was observed with about 67 new species encountered in a period of 10 days during July, 2008.

Thirty five species were commonly available all throughout the year. Cartilaginous fishes like *Rhinobatus obtusus*, *Dasyatis bennetti*, *Dasyatis kuhlii*, *Himantura imbricate*, *Rhinoptera adspersa* and *Gymnothorax meleagris* were found at random between December to June. The period between June to October was found to be a period of high diversity. Demersal (bottom dwelling) fishes like *Paraplagusia bilineata*, *Trachinocephalus myops*, *Synodus indicus*, *Ophichthus apicalis*, *Lagocephalus inermis* and *Takifugu oblongus* were found in large numbers. About 65 species were found to be commercially important species.

A few of the species appeared to be new to the Indian coast were

encountered during this study period. Two of them viz *Brachysomophis cirrocheilos* (Bleeker) (Figure 4a) and *Torquigener brevipinnis* (Regan) (Figure 4b), common to the Indo-West Pacific waters comprising Papua New Guinea, Indonesia and Australia, were observed for the first time in Indian waters. Possibly, the mega 2004 Tsunami which originated from Indonesia, could have brought these species to the Indian coastal waters. Fifteen more species still remain unidentified, of which one is believed to be a totally un-described species, and has attracted the curiosity of scientists from Australia and South Africa.

Deep-sea fishes like *Amphotistius imbricate*, *Torpedo marmorata*, *Gymnura poecilura* (near-threatened species), *Carcharias menisorrh* (vulnerable to over-fishing) and *Rhinobatus granulosus* (vulnerable to over-fishing) were also available. Dominant groups such as flat fishes, puffer fishes, croakers, clupeids and carangids are abundantly available and help in enriching the resources. The results of last three year study in fish diversity indicated that Kalpakkam coastal water is rich in fish diversity. A digital monograph describing the ichthyo-fauna of Kalpakkam coastal waters is under preparation.

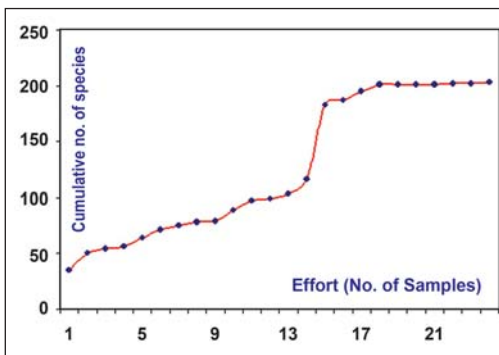


Fig. 3 Species accumulation curve

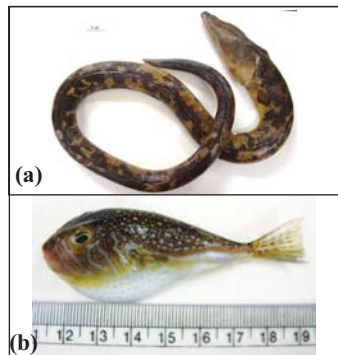


Fig. 4 (a) *Brachysomophis cirrocheilos* (Bleeker)  
(b) *Torquigener brevipinnis* (Regan)

**CHAPTER  
VII**

Awards /  
Publications /  
News & Events /  
Organisation

## AWARDS & HONOURS

**Dr. Baldev Raj**, has been awarded the

- **INSA Prize for Materials Science**, Indian National Science Academy (2010).
- **Betz - Dearborn - Professor C.N.R. Rao Medal and Chemcon Distinguished Speaker Award**, Indian Institute of Chemical Engineers (2010).
- **IIM Platinum Medal**, Indian Institute of Metals (2010).

**He has been invited to be:**

Member of the committee for selecting the Australia India Science & Technology Research Award on “Energy Generation in a Low Carbon Future” instituted by Australian Academy of Technological Sciences and Engineering in association with Australian Government’s Australia India Council.

**He has been nominated as a :**

- Member, R&D Advisory Council of Bharat Heavy Electricals Ltd. to enhance performance multifold based on science based technologies.
- Co-Chair, Editorial and Scientific Committee of International Journal of Nuclear Energy Science and Technology.
- Member, Governing Body of J&K State Council for Science & Technology.
- Member, Research Council, Institute of Minerals & Materials Technology, Bhubaneswar.
- Member, Advisory Council, Great Lakes-Bauer Energy Executive MBA Programme.
- Chairman, Research Advisory Board of PSG Institute of Advanced Studies, Coimbatore.
- Member, Editorial Advisory Board, Bulletin of Materials Science.
- External Expert, Peer Review Committee for the Cluster – Chemical Sciences, Group I: Chemical Materials & Energy, Council of Scientific & Industrial Research, New Delhi (2010).

**He has been elected as :**

- President, International Institute of Welding, which has a membership of fifty one countries.
- Fellow of ASM International, USA.
- President, Indian National Academy of Engineering.

**Dr. P. Chellapandi**, Nuclear & Safety Engineering Group, has received **Distinguished Alumnus Award** of IIT-Madras, 2010.

**Dr. P. Swaminathan**, Electronics & Instrumentation Group, was awarded **INS 2009 Award** in “High Technology Nuclear Related Areas” for his R&D contribution in development of strategic Instrumentation and Control system for FBR program.

**Shri R. Natarajan**, Reprocessing Group, has been elected, **Fellow of the Indian National Academy of Engineering** (INAE) in recognition of his contributions to “Engineering Sciences”.

**Dr. T. Gnanasekaran**, Chemistry Group, has been awarded the **MRSI medal and the Life time Achievement Award of the Thermal Analysis Society**.

**Dr. M. Sai Baba**, Scientific Information Resource Division and Strategic & Human Resources Planning Section has been invited to be a **member of the Editorial and Scientific Committee** of the International Journal of Nuclear Knowledge Management published by the World Council of Nuclear Workers (WONUC).

**Dr. A. K. Bhaduri**, Metallurgy & Materials Group has been awarded **Sir LP Mishra Memorial Lecture Award – 2010** from Indian Institute of Welding.

**Shri J. Jayapandian, Shri K. Prabakar, Shri C.S. Deepak and Smt. Usharani Ravi** from Materials Science Group, have received the '**Design Award**' for 'Measuring micro displacements using CD's Optical pickup Head from Idea for 'Design pages of Electronic Design' in May 2010.

**Dr. Rani P. George**, Metallurgy & Materials Group, has been awarded the **Corrosion Awareness Award 2009-10** from NACE INTERNATIONAL Gateway India Section on September 24, 2010 at CORCON2010, in Goa.

**Dr. R. Mythili, Dr. Saroja Saibaba and Dr. M. Vijayalakshmi**, Metallurgy & Materials Group, authored a paper, "Study of Strain Induced Martensite formation in a Ti Modified 316 Stainless Steel Bellow by Transmission Electron Microscopy", that appeared in Transactions of the Indian Institute of Metals, 62 (2009) 573-579, received the Indian Institute of Metals-**SAIL Gold Medal 2010** during 48<sup>th</sup> National Metallurgist Day (NMD) and the 64<sup>th</sup> Annual Technical Meeting of Indian Institute of Metals, November 14-17, 2010, Indian Institute of Science, Bengaluru.

**Ms. Dipti Samantaray**, Metallurgy & Materials Group, has received **Best M.Tech. Thesis-INA Innovative Student Project Award - 2010**.

**Ms. J. Brijitta**, Materials Science Group, has received the **Best Thesis Award** for her thesis titled "Phase Behaviour of Thermo Responsive Nanogel Dispersion: A Light Scattering and Confocal Microscopic Study" during the DAE-BRNS-National Laser Symposium (NLS-19) held at Raja Ramanna Centre for Advanced Technology, Indore during December, 2010.

## DAE AWARDS

Department of Atomic Energy has instituted annual awards for excellence in Science, Engineering and Technology in order to identify best performers in the area of Research, Technology Development and Engineering in the constituent units (other than Public Sector Undertakings and Aided Institutions). The Young Scientist, Young Engineer, Young Technologist, Homi Bhabha Science and Technology Award and Scientific and Technical Excellence Award fall under this category. Group Achievement awards for recognition of major achievements by groups have also been instituted. Life time Achievement Award is awarded to one who has made significant impact on the DAE's programme. They are the icons for young scientists and engineers to emulate. The awards consist of a memento, citation and cash prize.

**The recipients of the Awards from IGCAR for the year 2009 are:**

<b>Homi Bhabha Science &amp; Technology Award</b>	: Dr. K. Ananthasivan, CG
<b>Young Applied Scientist &amp; Technologist Award</b>	: Shri Sudheer Patri, FRTG
<b>Scientific &amp; Technical Excellence Award</b>	: Dr. Shaju K. Albert, MMG, Smt. R. Vijayashree, N&SEG Dr. B. Prabhakara Reddy, CG, Shri S. Raju, MMG Dr. Anil Kumar Sharma, N&SEG
<b>Meritorius Award</b>	: Shri S. K. Goverdhan, ESG Shri T. D. Sundarakshan, Director's Office Shri P. V. Sellaperumal, N&SEG Shri M. Arumugam, MMG
<b>Special Achievement Award</b>	: Shri P. Ramakrishnan, CAO

### Group Achievement Awards

**Design, manufacture and deployment of radiation and corrosion resistant compact custom designed motor for centrifugal extractors**

**Shri R. Natarajan, RpG, Group Leader**

Shri A. Sriramamurthy, Shri P. Vijayasekaran, Shri S. Sundaramurthy, Shri Felix Lawrence, Shri A. Palanivel from RpG and Shri P. Perachi Selvam from ESG

### Design, Development and Commissioning of Unique Engineering Facility for Sodium Fire Studies

#### Shri E.H.V.M. Rao, SED, N&SEG, Group Leader

Shri Sanjay Kumar Das, Shri S. S. Ramesh, Shri P. Mangarjuna Rao, Shri S.S. Murthy, Shri M. Kumaresan, Smt G. Lydia, Shri C. Lobomissier, Shri S. Srinivasan, Shri K. E. Jebakumar, Dr. D. Ponraju, Smt B. Malarvizhi, Shri Ramakrishnan, Shri J. Harvey, Shri B. K. Nashine from SED, Shri Siva Kumar, Shri Raghavendran from N&SEG, Shri K. Velusamy, Ms. R. Thilakavathy, Shri T. Johnson, Shri M. Sundar, Shri Trinathvas Gopi, Shri Rahul, from CED, Shri S. Balagurunathan, Shri S. Nagbhushanam, Shri N. Ramkumar, from ESD, Shri M. Nagamani, from ACVSD, Shri G. Kempulraj, Shri S. George from CWD, Shri C. Muniyandi, Shri P. Narayana Rao, Ms. M. Menaka, Shri Elumalai, Shri Hensan Raj, from QAD, Shri Kandasamy, Shri N. Ramesh from E&ISD

### Design, Construction, Commissioning and Operation of SADHANA Loop for Demonstration of Natural Convection in SGDHR Circuit of PFBR

#### Shri K. K. Rajan, STG, FRTG, Group Leader

Shri G. Padmakumar, Shri G. Madhusoodanan, Shri P. L. Valliappan, Shri V. Vinod, Shri K. Jayagopi, Shri Vivek Nema, Shri Gautam Kumar Pandey, Shri P. Mohanraj, Shri A. Rajan, Shri A. Chandran, Shri R. Rajendran, Shri Rafiq Basha, Shri J. Prem, Shri K. Palani from SE&HD, Shri C. Meikandamurthy, Shri V. Ramakrishnan, Shri R. K. Mourya, Shri P. Vijayamohana Rao, Shri P. Madan Kumar, Shri M. Anubuchelian, Shri A. Kolanjiappan, Shri R. Ramalingam, Shri P. Bakthavachalam from C&IDD, Shri S. Chandramouli, Shri R. Rajendra Prasad, Shri S. Krishnakumar, Shri R. Punniyamoorthy, Shri D. Laxman, Shri D. Muralidhar, Shri S. Ravishankar, Shri S. Alexander Xavier, Shri C. Rajappan, Shri R. Iyyappan, Shri L. Eagambaram, Shri N. Sreenivas, Shri G. Anandan, Shri K. Karunakaran, Shri P. R. Ashokkumar, Shri V. Kumaraswamy, Shri M. Karthikeyan, Shri K. Ganesh, Shri Ashish Tiwari, Shri G. Vijayakumar, Shri J. Prabhu from DD&RSD, Shri M. Shanmugasundaram, Shri P. Rajasundaram, Smt. Sundari Madasamy, Shri T. Chandran, Shri J. Vincent, Shri S. Nagajothi, Shri Vijay Tirkey, Shri S. Rangasamy from STG

### Selection and Development of Hardfacing Technology for PFBR

#### Dr. Arun Kumar Bhaduri, MTD, MMG, Group Leader

Dr. Shaju K. Albert, Shri Chitta Ranjan Das, Shri Harish Chandra Dey, Shri Hemant Kumar, Shri V. Ramasubbu from MTD, Shri S. Mahadevan, Shri Govind Kumar Sharma from NDED, Shri R. Sritharan, Shri P. Puthiya Vinayagam, Shri V. Rajan Babu from RCD, Shri V. Balasubramaniyan from HTSD, Shri S. Ragupathy, Smt. R. Vijayashree, Shri Jose Varghese from CH&MD, Shri C. Meikandamurthy, Shri V. Ramakrishnan from C&IDD, Shri S. Parivallal from CWD, Shri P. Jaganathan from QAD

### SQUID based Measurement of Biomagnetic Fields

#### Shri M.P. Janawadkar, CMPD, MSG, Group Leader

Dr. K. Gireesan, Smt. C. Parasakthi, Shri S. Sengottuvel, Shri Rajesh Patel, Shri N. Mariyappa from CMPD, MSG

### Design & Development of Small & Large Rotatable Plugs

#### Dr. P. Chellapandi, N&SEG, Group Leader

Shri Sriramachandra Aithal, Shri P. Puthiya Vinayagam, Shri V. Rajan Babu, Shri P. V. Sellaperumal, Shri S. Saravanan, Ms. P. Swetha from RCD, Shri V. Balasubramaniyan from HTSD, Shri S. Raghupathy from CH&MD, Shri N. Vijayan Varier, Shri Vimal Kumar from TC&QCD, Dr. K. Velusamy, Shri S. Jalaldeen, Shri T. Selvaraj, Shri S. D. Sajish, Shri Juby Abraham, Shri Ramkumar Maity, Shri A. Sivakumar, Shri C. Raghavendran, Shri Gagan Gupta, Shri S. K. Rajesh, Shri M. Babu Rao, Shri R. Manu, Shri G. Venkataiah from MHD, Dr. S. Venugopal from RIRD, Shri R. Veerasamy, Shri R. Dhanasekaran, Shri S. Suresh Kumar, Shri J. Saravanan, Shri A. Gururajan from C&IDD, Shri A. Babu from RMD,

Shri A.Venkatesan, Shri N. Subramanian from PPCD, Shri N. K. Sinha from IDEAS, Shri S. Chandramouli, Shri R. Puniamoorthy from DD&RSD, Shri Utpal Borah, Shri R. Nagarajan from MTD, Shri A. Govindarajan from SE&HD, Shri M. Venkatesan from CH&MD

### Development of Diverse Safety Rods Drop Time Measurement System Using Acoustic Technique

#### Shri V. Prakash, CT&VDD, FRTG, Group Leader

Shri R. Veerasamy, Shri S. C. S. P. Kumar Krovvidi, Shri T. Logaiyan from C&IDD, Smt. R. Vijayashree from CH&MD, Shri M. Thirumalai, Shri M. Anandaraj, Shri Ranga Ramakrishna, Shri P. Anup Kumar, Shri P. Adithan, Shri K. Tamilselvan, Shri A. Kanagaraj, Shri J. Jaikanth from CT&VDD, Shri C. Asokane, Ms. P. Anitha, Shri M. R. Jeyan from DD&RSD

## QUALITY CIRCLE AWARDS

The Quality Circle annual meet held at Kalpakkam during August 16-17, 2010, the following teams received trophies as indicated.

- Dr. Placid Rodriguez Memorial Trophy in the Mechanical and Manufacturing Category awarded to team from Civil Engineering, ESG (Leader: Shri S. Satheesh Kumar, Facilitator: Shri M.Krishnamoorthy).
- Shri M.K.Ramamurty Memorial Trophy in Plant Operation and Services Category awarded to team from Chemical Technology and Vibration Diagnostic Division, FRTG (Leader: Shri S. Suresh, Facilitator: Shri G. Mohanakrishnan).
- Dr. Sarvepalli Radhakrishnan Memorial Trophy in Schools Category awarded to team from Atomic Energy Central School-No.2, Kalpakkam (Leader: Ms. S.R. Nandini, Facilitator: Ms. S. Jayasree).

Six quality circles from IGCAR : **MOON** (FRTG), **SAMURAI** (ESG), **EXCEL** (FRTG), **STAR** (ESG), **SAKTHI** (GSO) and **RAINBOW** (FRTG) participated in the Quality Circle State Level Convention (CCQCC-2010) during September 4-5, 2010 at Meenakshi Sundararajan Engineering College, Chennai along with 135 other QC teams and bagged Gold (**MOON** and **SAMURAI**), Silver (**EXCEL** and **STAR**) and Bronze (**SAKTHI** and **RAINBOW**) medals.

**MOON** QC (Facilitator: Shri B. Krishnakumar, Components & Instrumentation Division, FRTG) has bagged the PAR EXCELLENCE PRESENTATION Award (The Highest in Quality Circle Competitions) at National Convention for Quality Circle at AMC Engineering College.

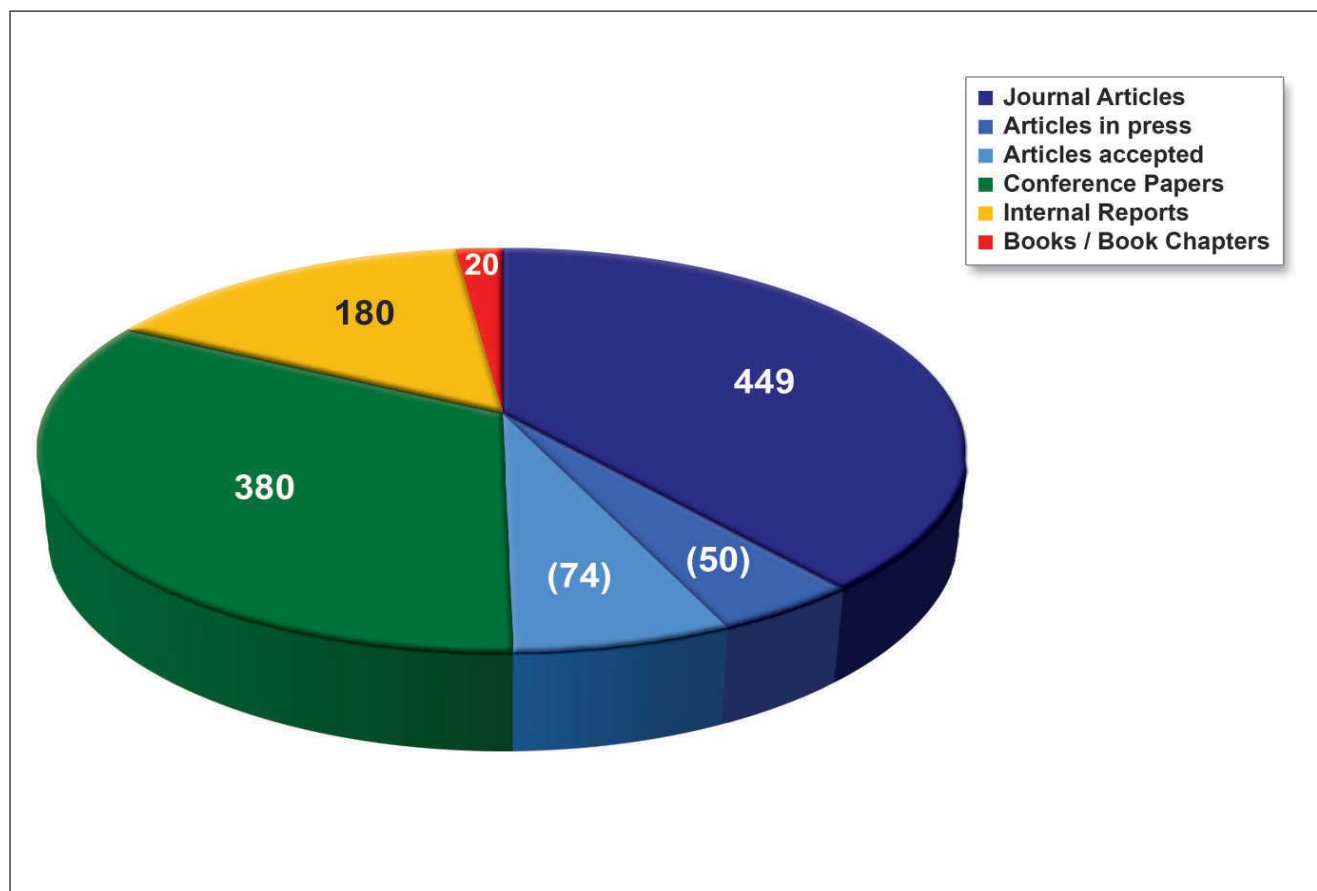
Three QC teams of IGCAR (**EXCEL**, **STAR** & **MOON**) have participated in the International Convention on Quality Concept Circle (ICQCC-2010) held at Hyderabad during October 12-15, 2010. All the three QC teams secured "GOLD AWARD".

Shri S. Suresh, Shri Joby Joseph, Shri V. Nanda Kumar, Shri R. R. Shridharan, Shri R. Kannan, Shri D. Alagar and Shri G. Mohanakrishnan from **EXCEL** QC, Chemical Technology and Vibration Diagnostic Division, FRTG.

Shri T. V. Maran, Shri K. Mohanraj, Shri A. T. Loganathan, Shri A. Ramamurthy, Shri D. Kuppaswamy, Shri A. Anthuvan Clement from **MOON** QC, Zonal Workshop, FRTG.

Shri M. Krishnamoorthy, Shri C. Subramanian, Shri G. Narendra Reddy, Shri K. M. Natarajan, Shri A. Padmanaban, Shri V. Kodiarasan from **STAR** QC, Central Workshop, ESG.

## IGCAR Publications during the year 2010



### EMINENT LECTURE SERIES

1. *"Graphene and beyond"* by Prof. C.N.R. Rao, JNCASR, Bengaluru on March 12, 2010 (Homi Bhabha Eminent Lecture Series).
2. *"Nuclear tools for agricultural transformation"* by Prof. M. S. Swaminathan, MSSRF, Chennai, on April 8, 2010 (Homi Bhabha Eminent Lecture Series).
4. *"Homeopathy: The need of modern world"* by Dr. A.U. Ramakrishnan, Chennai, on July 7, 2010 (Vikram Sarabhai Memorial Lecture Series).

### SPECIAL LECTURES AND COLLOQUIA SERIES

1. *"Tensioned Metastable Fluid Technology by Transformational Nuclear Particle Sensors, Materials Synthesis and Actinide Transmutation"* by Dr. Rusi P. Taleyarkhan, Professor, Nuclear Engineering, Purdue University, USA.
2. *"The Mini Bang and The Big Bang"* by Dr. Bikash Sinha, former Director, VECC, Kolkata, organised by Indian Physicist Association, Kalpakkam on February 11, 2010.
3. *"Superphenix: The Real Story"* by Dr. Andre Phillippe Maisseu, President, World Council of Nuclear Workers(WONUC) on March 8, 2010.
4. *"A Celebration of Chemistry"* by Prof. C.N.R. Rao, National Research Professor, JNCASR, Bengaluru on March 13, 2010.
5. *Seborg Memorial Lecture - "Nuclear Forensics"* by Dr. V. Venugopal, BARC, Mumbai. on April 4, 2010
6. *Curie Memorial Lecture - "Rapid Radiochemical Separations and their Applications to Neutron Activation Analysis"* by Dr. Z.R. Turel, Mithibai College, Mumbai organised by IANCAS on May 3, 2010.
7. *"An overview of ISRO Launch Vehicle Solid Motor System"* by Shri V. Srinivasan, Deputy Director, VSSC, Trivandrum organised by ISNT on August 31, 2010.

**SEMINARS, WORKSHOPS AND MEETINGS**

1. International conference on "External Flooding Hazards at Nuclear Power Plants Sites", January 11-15, 2010.
2. Seminar on "Instrumentation & Control Systems for Radioactive Laboratories" (ICRL 2010), January 29, 2010.
3. One Day Workshop on "Materials Characterisation using NDE Techniques" (MCNT-2010), February 10, 2010.
4. "8<sup>th</sup> International Conference on Barkhausen Noise and Micromagnetic Testing" (ICBM8), February 11-12, 2010.
5. Theme Meeting on "Challenges in Thermal Hydraulics of Nuclear Reactors" (CHITHOR 10), February 18-19, 2010.
6. Seminar on "Modern Trends in Nuclear Technology" in Hindi, February 24, 2010.
7. Seminar on "Emerging Trends in Separation Science and Technology" (SESTEC-2010), March 1-4, 2010
8. Meeting on "Robust Instrumentation & Control Systems for FBR Program", May 20, 2010.
9. Discussion Meeting on "Emerging Technologies for Clean Water", May 21-22, 2010.
10. Workshop on "Latest Trends on Virtual Instrumentation" and "Hands on Training" in LabView, June 10-11, 2010.
11. Seminar on "Recent advances in PIE & Remote Technologies for Nuclear Fuel Cycle" (RAPT 2010), September 23-24, 2010.
12. Silver Jubilee Commemoration of FBTR & RML, October 10, 2010.
13. Seminar on "Emerging Techniques, Tools and Probes in Radiobiology (ETTPR-2010)", November 18, 2010.
14. Theme meeting on "Chemistry in Back End of Fuel Cycle (CBFC 2010)", November 25-26, 2010.
15. Annual Theme Meeting on "Structure and Thermodynamics of Emerging Materials (STEM 2010)", November 25-26, 2010.

**NURTURING ACTIVITIES FOR STUDENTS/EMPLOYEES**

1. "Awareness Programme for Women Employees", January 27, 2010.
2. "Radiation Awareness Programme", organised by Indian Women Scientists Association, Kalpakkam, February 17, 2010.
3. "Women and Mental Health" by Ms. Porkodi, Director Community Mental Health, Chennai organised by Indian Women Scientists Association, Kalpakkam, March 8, 2010.
4. "How to Handle Adolescents", by Dr. P. Vineetha, DAE Hospital, organised by Indian Women Scientists Association, Kalpakkam, May 5, 2010.
5. "Heart Attack: Causes, Symptoms and Prevention Stem Cell Therapy and its Applications" by Dr.S. Balaji, Frontier Life Line, Chennai organised by AARCO, May 25, 2010.
6. "Summer Practice School of BITS Pilani and Goa" during May 24 - July 16, 2010.
7. "Summer Training Programme in Physics and Chemistry (STIPAC 2010)" during May 24 - July 6, 2010.
8. Workshop on "Handling Adolescents" organised by Indian Women Scientists Association, Kalpakkam, August 14, 2010.
9. "Quality Circles Annual Meet 2010", August 16-18, 2010.
10. "Prof. Brahm Prakash Memorial Materials Quiz 2010" organised by The Indian Institution of Metals, Kalpakkam Chapter, September 17-18, 2010.
11. "Defensive Driving Technique" by Institute of Road Transport, September 17, 2010.
12. "Chronic Pain" by Dr. Ramnarayan, Apollo Speciality Hospital, Chennai organised by AARCO, November 23, 2010.

## Graduation Function of 4<sup>th</sup> batch of BARC Training School at IGCAR

September 02, 2010



Dr. T. Ramasami, Secretary, Department of Science and Technology addressing the gathering, Dr. S. Banerjee, Chairman, AEC and Secretary, DAE, Dr. Baldev Raj, Director, IGCAR and Dr. M. Sai Baba, Head, BARC Training School at IGCAR are seated on the dias

The fourth batch of forty eight TSOs from the BARC Training School at IGCAR have successfully completed their training and were graduated in a special ceremony that took place on September 2, 2010 at 10.30 hours in the Sarabhai Auditorium, Homi Bhabha Building, IGCAR. Distinguished Academician, Dr. T. Ramasami, Secretary, Department of Science and Technology was the Chief Guest. Dr. S. Banerjee, Chairman, AEC and Secretary, DAE presided over the function. Dr. M. Sai Baba, Head, BARC Training School at IGCAR welcomed the gathering. Dr. Baldev Raj, Distinguished Scientist and Director, IGCAR gave an enlightening address to the gathering. Dr. S. Banerjee released the souvenir featuring the training school programme in the previous academic year and Dr. T. Ramasami received the first copy. Dr. Banerjee also gave a very inspiring and thought provoking lecture to the graduates passing out. Dr. T. Ramasami gave away the prestigious 'Homi Bhabha Prize' comprising of a medallion and books worth Rs.5000 to the meritorious toppers from all the disciplines. He also gave away the course completion certificates to the graduates TSOs. A few of the Trainee Scientific officers passing out, shared their experience on the academic programme and their stay at hostel. Dr. T. Ramasami gave a very inspiring and motivational lecture to the students. Dr. Vidya Sundararajan, S&HRPS proposed the vote of thanks.



Fourth Batch of Graduates of BARC Training School at IGCAR with Dr. T. Ramasami, Secretary, Department of Science and Technology (Chief Guest), Dr. S. Banerjee, Chairman, AEC & Secretary, Dr. Baldev Raj, Director, IGCAR and Senior Colleagues of the Centre and members of S&HRPS

## 400<sup>th</sup> Meeting of IGC Scientific Committee

April 12, 2010



Dr. Baldev Raj, Director, IGCAR & Chairman, IGCS releasing the CD containing the compendium of minutes and presentations

The 400<sup>th</sup> IGC Scientific Committee meeting was held on April 12, 2010 at Sarabhai Auditorium. The special programme was aimed to reminisce the past performances and to look into the future. The programme was aptly named as I4V5 (IGCS 400 & Vision for 500).

During the 395<sup>th</sup> IGCS meeting Dr Baldev Raj, Director, IGCAR and Chairman IGCS suggested that the 400<sup>th</sup> IGCS can be conducted as a special event. A small team comprising Dr. T. Jayakumar, Shri S. A. V. Satya Murty, Shri A.S.L.K. Rao, Dr. M.D. Mathew, Shri K.V. Sureshkumar, Dr. M. Sai Baba and Shri R.G. Raghavan, was formed to plan and organise the event.

Dr. Baldev Raj, Distinguished Scientist, Director, IGCAR/GSO and Chairman, IGCS, Dr. Prabhat Kumar, Project Director, BHAVINI, Shri K. Ramamurthy, Station Director, MAPS, all the Group Directors of IGCAR, Project Director, FRFCF, IGCS members, Heads of Sections, Senior officers of IGCAR/GSO in the grade of SO/G and above, Officers from Administration and Accounts of IGCAR, Principals of the Schools of Kalpakkam and Commandant of CISF, Kalpakkam attended the meeting.

The first ever meeting of the Reactor Research Centre Scientific Committee (RSC) was conducted on May 9, 1972. The first RSC comprised of : Shri N. Srinivasan, Chairman, RSC, Shri K. Chakravarthi, Shri N.L. Char, Shri B. S. Iyengar, Shri S.R. Paranjpe, Shri A.R. Parthasarathy and Shri N. Swaminathan. RSC was renamed as IGCS in January 1986. Currently, there are sixty one members of the IGCS and a Secretary.

The meeting started with Shri R. G. Raghavan, Secretary, IGCS welcoming the gathering. Dr. Baldev Raj, Director, IGCAR and Chairman IGCS gave the opening remarks and released the compendium of the minutes of the IGCS meetings held so far i.e. upto 399. He also inaugurated the PFBR model kept on display at the entrance of the ground floor of Homi Bhabha Building.

### Programme on this special occasion consisted of :

- Presentations by the Group Directors and Project Director, Fast Reactor Fuel Cycle Facility
- Presentations by the Young Officers of IGCAR - about their views on what is the vision for future of the domains of R&D in the Centre.

### Presentations were also made on a wide range of topics which included:

- |   |  |
|---|--|
| √ Collaborations, Human Resources Development, Publications and Citations | √ Improvements in Administration and Accounts                |
| √ Patents, Intellectual Property Rights and Technology Transfer           | √ Civil & Electrical Maintenance including Horticulture      |
| √ Expertise of IGCAR extended to other organizations                      | √ Vision for meeting the growing medical needs               |
| √ Overall budget – Growth and current scenario                            | √ Challenges in meeting the growing educational requirements |
| √ Township Amenities and Neighbourhood Development Programme              | √ Environment and Safety                                     |
|   | √ Industrial Security in current scenario                    |

Dr. Baldev Raj, Director, IGCAR and Chairman, IGCS gave the concluding remarks and Shri R.G. Raghavan, Secretary, IGCS proposed the vote of thanks.

## Eminent Lecture Series



Prof. C.N.R. Rao, National Research Professor, Honorary President and Linus Pauling Research Professor, Jawaharlal Nehru Centre for Advanced Scientific Research and Honorary Professor, Indian Institute of Science, Bengaluru while delivering the Dr. Homi J. Bhabha eminent lecture

**Prof. C.N.R. Rao**, National Research Professor, Honorary President and Linus Pauling Research Professor, Jawaharlal Nehru Centre for Advanced Scientific Research and Honorary Professor, Indian Institute of Science, Bengaluru visited the Centre during **March 12-13, 2010** accompanied with his wife, Mrs. Indumati Rao, Honorary Coordinator, Multimedia Group, Education Technology Unit, JNCASR. Prof. C.N.R. Rao delivered the “Eminent Lecture” as a part of the lecture series organised to commemorate the birth centenary of Dr. Homi J. Bhabha, on the topic “Graphene and Beyond”. This talk was well attended and appreciated.

Prof. C.N.R. Rao, with his keen passion to inspire the young minds, presented an interesting lecture on “A Celebration of Chemistry” followed by an equally inspiring interactive session on “Understanding Chemistry” by Mrs. Indumati Rao to the students from the schools of Kalpakkam. The students relished the lecture and were happy to have had an opportunity to interact with such eminent scientists. Prof. C.N.R. Rao and Mrs. Indumati Rao later visited laboratories in Electronics and Instrumentation Group, Materials Science Group and the construction site of PFBR.



Prof. C.N.R. Rao and Mrs. Indumati Rao with Dr. Baldev Raj, Director, IGCAR, senior colleagues of the Department and children from schools of Kalpakkam



Prof. M.S. Swaminathan, Member of Parliament (Rajya Sabha), UNESCO Chair in Eco-technology, M.S. Swaminathan Research Foundation & former Chairman, National Commission on Farmers, Government of India delivering the eminent lecture

**Prof. M.S. Swaminathan**, Member of Parliament (Rajya Sabha), UNESCO Chair in Eco-technology, M. S. Swaminathan Research Foundation & former Chairman, National Commission on Farmers, Government of India visited the Centre on **April 8, 2010** and delivered an Eminent Lecture on the topic, "Nuclear tools for agricultural transformation" as a part of the commemorative celebrations on the occasion of birth centenary of our founder father Dr. Homi J. Bhabha. During the visit, Prof. M.S. Swaminathan visited Rice Fields (salt tolerant varieties) being grown in the Centre, Plantation site and restoration of lake at Site which are being pursued by the Centre in collaboration with the M.S. Swaminathan Research Foundation.



Dr. A. U. Ramakrishnan, Honorary Homeopathic Physician to the President of India while delivering the talk along with Dr. Baldev Raj, Director, IGCAR

**Dr. A.U. Ramakrishnan**, Honorary Homeopathic Physician to the President of India visited the Centre on **July 28, 2010** to deliver the "6<sup>th</sup> Vikram Sarabhai Memorial Lecture" at Sarabhai Auditorium on "Homeopathy-The Need of the Modern World". Earlier he has also visited the Fast Breeder Test Reactor and the Magnetoencephalography Facility at the Materials Science Group. Dr. Ramakrishnan was accompanied by his wife.



Prof. R.K. Ray, Visiting Scientist TATA STEEL R&D, Jamshedpur, addressing the students during the interactive session

**Prof. R.K. Ray**, Visiting Scientist, TATA STEEL R&D, Jamshedpur and Dr. Satyam Suwas, Associate Professor, Indian Institute of Science, Bengaluru visited the Centre on **November 26, 2010**. Prof. R.K. Ray and Dr. Satyam Suwas gave an inspirational address and interacted with the Trainee Scientific Officers and Research Scholars in the Centre.

## News and Events

### Meeting of Scientific Advisory Committee to Prime Minister

February 12, 2010

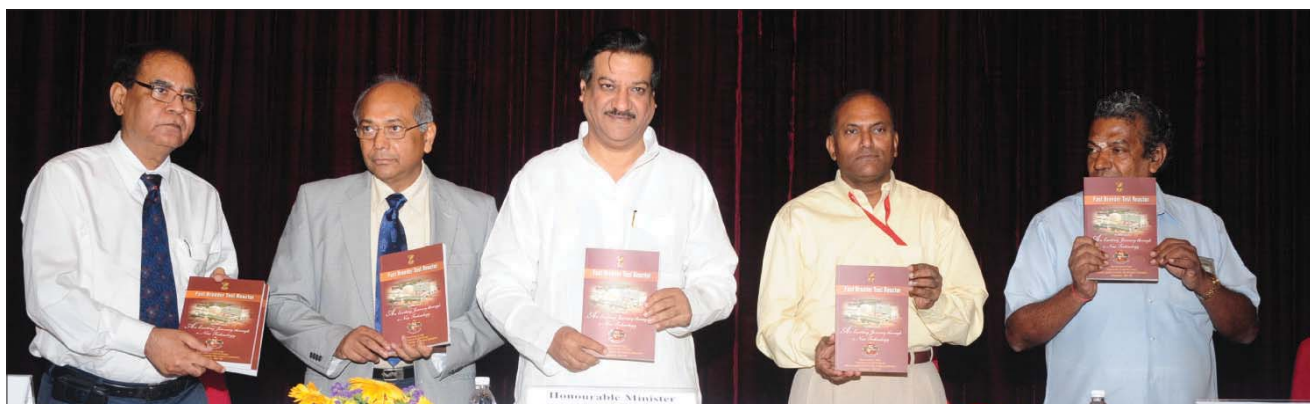


Prof. C.N.R. Rao, Chairman, Scientific Advisory Committee to Prime Minister, National Research Professor, Honorary President & Linus Pauling Research Professor, JNCASR, Dr. T. Ramasami, Secretary, Department of Science and Technology, Dr. Srikumar Banerjee, Chairman, AEC & Secretary, DAE and other members of the Scientific Advisory Committee to Prime Minister with Dr. Baldev Raj, Director, IGCAR

The meeting of the Scientific Advisory Committee to Prime Minister was held at IGCAR, Kalpakkam on **February 12, 2010**. The meeting was chaired by, Prof. C.N.R. Rao, Chairman, Scientific Advisory Committee to Prime Minister, National Research Professor, Honorary President & Linus Pauling Research Professor, JNCASR. Distinguished members, Dr. P. Rama Rao, Dr. Srikumar Banerjee, Prof. P. Balaram, Dr. M.K. Bhan, Dr. A.K. Sood, Prof. Bikash Sinha, Dr. T. Ramasami, Dr. Vijay Kumar Saraswat, Prof. Sujatha Ramadorai, Prof. B.K. Thelma, Prof. D.V. Khakhar, Prof. Mustansir Barma, Prof. M.M. Sharma, Dr. Ashok Jhunjhunwala, Prof. V.K. Singh and Dr. K. Vijayaraghavan attended the meeting. The expert committee meeting for combustion was also conducted prior to the meeting. The dignitaries visited various facilities of the Centre and construction site of PFBR.

## Silver Jubilee Commemoration of Fast Breeder Test Reactor and Radiometallurgy Laboratory

October 10, 2010



Dr. Baldev Raj, Director, IGCAR, Dr. S. Banerjee, Chairman, AEC and Secretary, DAE, Shri M.S. Ramanujan, Postmaster General, Chennai City Region, Chennai and Shri G. Srinivasan, Director, Reactor Operations and Maintenance Group with the then Honourable Minister for Science & Technology, Shri Prithviraj Chavan, during the release of commemorative volume on FBTR as a part of the silver jubilee celebrations

Fast Breeder Test Reactor, the flagship of the Centre, has performed exceedingly well without any major incidents. Every passing year has seen a new milestone being achieved for FBTR, in terms of reactor power, sodium temperature, fuel burn-up and so on. The unique high plutonium carbide fuel has seen a burn-up of 165 GWd/t without any clad failure. Radiometallurgy laboratory, was designed primarily to be a robust companion of FBTR, as a Post-Irradiation Examination Laboratory. Development of robust and innovative Non-Destructive Evaluation Methodologies and Robotics have made a significant impact on the success of Fast Reactor programme. A glittering ceremony was organized on October 10, 2010 to commemorate 25 years of the successful operation of Fast Breeder Test Reactor and the commencement of Radiometallurgy Laboratory at the Centre. The programme commenced with a power point presentation on the history and growth of Fast Breeder Test Reactor and the Radiometallurgy Laboratory, indicating significant milestones. Dr. Baldev Raj, Director, IGCAR and one of the pioneers involved in commissioning of the Radiometallurgy Laboratory, welcomed the gathering. Dr. S. Banerjee, Chairman, Atomic Energy Commission and Secretary, Department of Atomic Energy delivered a very inspirational address. The then Honorable Minister for State for Science and Technology, Earth Sciences, Personnel, Public Grievances, Pensions and Parliamentary Affairs, Shri Prithviraj Chavan, in his address, elaborated on the achievements of Department of Atomic Energy. On this memorable occasion, commemorative volumes on the history, growth and achievements of Fast Breeder Test Reactor and Radiometallurgy Laboratory were brought out. Indian Nuclear Society brought out a special issue on "Fast Breeder Test Reactor". One book in Hindi on the history of IGCAR and two books on the environmental studies carried out in the campus were also released on this occasion. A special postal cover was released by Shri M.S. Ramanujan, Postmaster General, Chennai City Region to mark the occasion. Dr. M.R. Srinivasan, Member and former Chairman, AEC, Dr. R. Chidambaram, Scientific Advisor to Government of India and former Chairman, AEC, Dr. P.K. Iyengar, former Chairman, AEC, Dr. Frank Carre, CEA, France and Dr. Yuri Sokolov, Deputy Director General, IAEA presented their experiences with FBTR and felicitations on the occasion. The programme concluded with a vote of thanks by Shri G. Srinivasan, Director, Reactor Operations and Maintenance Group.

Eminent Visitors To IGCAR

**Dr. M.R. Srinivasan**, former Chairman and Member, AEC visited the Centre on **January 6, 2010**. During the visit he went around the Virtual reality center, Simulator and High end computing facilities at Computer Division, Safety Grade Decay Heat System(SADHANA) at Fast Reactor Technology Group, Sodium fire facility at Safety Group and construction site of PFBR.



Shri S.A.V. Satyamurthy, Head, Computer Division giving details to Dr. M.R. Srinivasan, former Chairman and Member, AEC



Team from University of North Texas with Dr. Baldev Raj, Director, IGCAR and other senior colleagues of the Centre

A team of academicians from the University of North Texas led by **Dr. Rajarshi Banerjee**, visited the Centre on **January 7, 2010**. The team held discussions with Dr. Baldev Raj, Director, IGCAR and other senior colleagues from the Metallurgy & Materials and Materials Science Groups. They visited the laboratories in Metallurgy & Materials and Materials Science Groups.

A team of academicians from United Kingdom, comprising of **Dr. Timothy James Abram**, Professor in Nuclear Fuel Technology, University of Manchester, **Dr. Michael Edward Fitzpatrick**, Chair, Materials Fabrication and Engineering, The Open University, Milton, Dr. Robin William Grimes, Director, Centre for Nuclear Engineering and Professor of Materials Physics, Imperial College and Mr. Richard Nicholas Buttrey, Diplomat, Second Secretary, Science and Innovation, British High Commission and Dr. Hajime Hatano, Chairman, ISO TC/SC 135 and Professor, Department of Applied Electronics, Tokyo University of Science, Japan visited the Centre during **January 7-8, 2010**. The team held discussions with DAC members of the Centre and visited Fast Breeder Test Reactor, Hot Cells and Non-Destructive Evaluation Division and the construction site of PFBR.



Dr. Baldev Raj, Director, IGCAR with the visitors from United Kingdom and Dr. Hajime Hatano, Chairman, ISO TC/SC 135 and Professor, Department of Applied Electronics, Tokyo University of Science, Japan

**Dr. Luc Vanden Durpel**, Scientific Director and Mr. Patrick Tuyssier, Director, Marketing and Strategy, AREVA visited the Centre on **January 7, 2010**. After meeting Dr. Baldev Raj, Director, IGCAR and holding discussions with the DAC members they were taken around to visit the Fast Breeder Test Reactor, the construction site of PFBR and Nuclear Desalination Development Plant.



Dr. Baldev Raj, Director, IGCAR with Dr. Luc Vanden Durpel, Scientific Director and Mr. Patrick Tuyssier, Director, Marketing and Strategy from AREVA

**Dr. Rusi P. Taleyarkhan**, Professor, Nuclear Engineering, Purdue University visited the Centre on **January 8, 2010** and gave a lecture on “Tensioned Metastable Fluid Technology for Transformational Nuclear Particle Sensors, Materials Synthesis and Actinide Transmutation”. He later visited the Fast Breeder Test Reactor, laboratories in the Materials Sciences Group and the construction site of PFBR.



Dr. Rusi P. Taleyarkhan, Professor, Nuclear Engineering, Purdue University with Dr. Baldev Raj, Director, IGCAR



Dr. Eberhard Diegle, Fusion for Energy, Barcelona along with a senior colleague of the Centre

**Dr. Eberhard Diegle**, Fusion for Energy, Barcelona, Spain visited the Centre on **January 8, 2010**. After meeting Dr. Baldev Raj, Director, IGCAR and other senior colleagues from the Metallurgy and Materials Group, he visited the construction site of PFBR.

A delegation from Fermilab led by **Dr. Piermaria Oddone**, Director, Fermilab visited the Centre on **January 16, 2010**. After holding discussions with the DAC members, the team visited the Accelerator & Low temperature laboratories in the Materials Sciences Group, laboratories in the Safety Group, the Fast Breeder Test Reactor and the construction site of PFBR.



Delegation from Fermilab at FBTR Control Room along with colleagues of the Centre



Prof. Eberhard Roos, Dr. Andreas Klenk and Dr. Xaver Schueler from MPA, Stuttgart, Germany with Dr. Baldev Raj, Director, IGCAR and Dr. T. Jayakumar, Director, Metallurgy and Materials Group

**Prof. Eberhard Roos, Dr. Andreas Klenk and Dr. Xaver Schueler** from MPA, Stuttgart, Germany visited the Centre on **January 22, 2010**. After meeting Dr. Baldev Raj, Director, IGCAR the team visited Structural Mechanics Laboratory and construction site of PFBR. The team also had discussions with colleagues from Metallurgy & Materials and Reactor Engineering Groups on the status of collaborative projects.

**Dr. Shchedrovitskiy Petr, Dr. Alexandar Bychkov and Dr. Igor Leshukov** from ROSATOM, Russia visited the Centre during **February 2-4, 2010**. After meeting the DAC members, the visitors were taken around to visit Fast Breeder Test Reactor, Laboratories in Metallurgy and Materials, Chemistry, Safety, Electronics & Instrumentation, Materials Science and Reactor Engineering Groups. They also visited the construction site of PFBR.



Dr. Baldev Raj, Director, IGCAR, with the visiting delegation from ROSATOM and other colleagues from the Centre



Shri Y. S. Mayya, Chairman and Managing Director, Electronics Corporation of India with Dr. Baldev Raj, Director, IGCAR during the signing of MoU

**Shri Y.S. Mayya**, Chairman & Managing Director and a team from Electronics Corporation of India visited the Centre on **March 6, 2010**. After meeting Dr. Baldev Raj, Director, IGCAR, they discussed with senior colleagues of the Centre. A memorandum of understanding was signed for collaboration between IGCAR and ECIL. They later visited the facilities in the Computer Division.

**Dr. Andre Phillippe Maisseu**, President, World Council of Nuclear Workers(WONUC) & Chief Editor, International Journal of Nuclear Engineering Science and Technology, undertook a visit to our Centre on **March 8, 2010**. After meeting the Director and DAC members, Dr. Maisseu visited the Fast Breeder Test Reactor and laboratories in the Fast Reactor Technology Group. Dr. Maisseu gave a special lecture to the colleagues of the Centre.



Dr. Tomas Huner, leader of Czech Nuclear Power delegation with Shri S. C. Chetal, Director, REG

A delegation from the Czech Nuclear Power visited the Centre during **March 9-10, 2010**. The team visited the Fast Breeder Test Reactor, Laboratories in Non-Destructive Evaluation Division and Hot cells, laboratories in Fast Reactor Technology Group and Structural Mechanics Laboratory at IGCAR. The team also visited the Madras Atomic Power Station and the construction site of PFBR.



Prof. Arvind P. Kudchadker, Emeritus Professor, IIT-Bombay, Mumbai and Dr. Shanti Kudchadker along with the students of the Training School

**Prof. Arvind P. Kudchadker**, Emeritus Professor, IIT-Bombay, Mumbai visited the Centre along with his wife, Dr. Shanti Kudchadker and gave a special lecture to the students of Training School on **April 5, 2010** at Ramanna Auditorium on the topic, "Research and innovation ecosystem" and interacted with the students.

**Shri Sriprakash Jaiswal**, Hon'ble Minister of State for Coal, Government of India visited the Centre on **April 6, 2010**. During the meeting with the DAC members of the Centre he was briefed about the Fast Reactor Programme in India by Shri S. C. Chetal, Director, REG and on the status of PFBR by Dr. Prabhat Kumar, PD, BHAVINI. Shri Sriprakash Jaiswal visited the Fast Breeder Test Reactor, Laboratories in the Non-Destructive Evaluation Division, Hot cells, Madras Atomic Power Station and the construction site of PFBR.



Shri Sriprakash Jaiswal, Hon'ble Minister of State for Coal, Government of India with Shri S. C. Chetal, Director, REG, along with other officials of the visiting team from the Ministry of Coal



Delegates from United Kingdom with Dr. P. R. Vasudeva Rao, Director, CG and Dr. M. Sai Baba, Head, S&HRPS

A delegation from United Kingdom led by **Dr. Richard Nicholas Buttrey**, Second Secretary, Science and Innovation Network, British High Commission, **Dr. Daniel Jonathan Rham**, Incumbant Second Secretary, **Dr. Christopher Fitzgerald**, VVIP Programmes and **Dr. Mathew Donald Kennedy Chalmers**, Physics World visited the Centre during **July 29-30, 2010**. After a brief meeting with the Director, IGCAR and deliberations with collaborators of the projects, the team visited the Fast Breeder Test Reactor, Laboratories in Materials Science, Metallurgy & Materials and Chemistry Groups.



Delegates from CEA with Shri S. C. Chetal, Director, REG along with other participants of the CEA-DAE Review Meeting

A delegation from CEA comprising of **Mr. Phillip Delaune**, Deputy Director for International Cooperation, International Affairs Division, **Mr. Dominique OChem**, Special Advisor to the Director for International Cooperation, Nuclear Energy Division, **Mr. Thierry Forgeron**, Group for Innovation and Nuclear Support, **Mr. Sunil Felix**, Nuclear Energy Division and **Mr. Hugues De Longevialle**, Counsellor, Energy and New Technologies, French Embassy in India visited the Centre during **July 8-9, 2010** for participating in the Mid-term Annual Review Meeting of CEA-DAE cooperation. After deliberations with participants from DAE, the team visited Fast Breeder Test Reactor, Hot Cells, Laboratories in Non-Destructive Evaluation Division, Fast Reactor Technology Group, Chemistry Group, Materials Science Group, Safety Group, Structural Mechanics Laboratory and the construction site of PFBR.



Dr. Baldev Raj, Director, IGCAR, Dr. S. Banerjee, Chairman, AEC and Secretary, DAE, Shri Prithviraj Chavan, the then Honorable Minister of State for Science and Technology and Shri G. Srinivasan, Director, Reactor Operations and Maintenance Group during visit to Fast Breeder Test Reactor

Honourable Minister for Science & Technology, Minister of Earth Sciences, Minister of Personnel, Public Grievances and Pensions, Minister of Parliamentary Affairs, **Shri Prithviraj Chavan**, visited the Centre on **October 10, 2010** to participate in the silver jubilee commemoration of the Fast Breeder Test Reactor, the flagship of the Centre. The dignitaries later visited the Fast Breeder Reactor and Radiometallurgy Laboratory.



Honourable Minister of Power and Energy, Government of Sri Lanka, Shri Patali Champika Ranawaka with Dr. S. Banerjee, Chairman, AEC and Secretary, DAE and Dr. Baldev Raj, Director, IGCAR

Honourable Minister of Power and Energy, Government of Sri Lanka, **Shri Patali Champika Ranawaka**, **Shri Vidya Dilruk Amarapala**, Chairman, Ceylon Electricity Board, **Shri Merrille Godfery Abeywickrama Goonetilleke**, Director (Technical), Minister of Power and Energy, **Shri V. Krishnamoorthy**, Deputy High Commissioner for Sri Lanka in Southern India and **Shri M.K. Pathmanaathan**, Minister Counsellor & Head of Chancery, Deputy High Commission of Sri Lanka in Southern India visited the Centre on **October 30, 2010**. After meeting **Dr. Baldev Raj**, Director, IGCAR, **Dr. S. Banerjee**, Chairman, AEC and Secretary, DAE and other senior colleagues of the Centre the team visited the Fast Breeder Test Reactor, Hot Cells, Non-Destructive Evaluation Division, Madras Atomic Power Station, Nuclear Desalination Development Plant and construction site of Prototype Fast Breeder Reactor.



Delegation from CEA with Dr. Baldev Raj, Director, IGCAR and other senior colleagues of the Department

A Delegation from CEA led by **Mr. Christophe Behar**, Director for Nuclear Energy which included **Mr. Frederic Mondoloni**, Director for International Affairs, CEA, **Mr. Philippe Delaune**, Deputy Director for International Affairs, International Affairs Division, **Mr. Dominique Ochem**, Special Adviser to the Director for International Cooperation, Directorate of Nuclear Energy and **Mr. Alain Porrachia**, Director for Innovation and Nuclear Support at the Directorate for Nuclear Energy visited the Centre during **December 6-7, 2010**. The delegation met **Dr. Baldev Raj**, Director, IGCAR and other senior colleagues of the Centre and visited Fast Breeder Test Reactor, Hot Cells, Laboratories in Non-Destructive Evaluation Division, Laboratories in Nuclear and Safety Engineering Group, Materials Science Group and Chemistry Group. The team also visited the construction site of Prototype Fast Breeder Reactor.

## Conference/Meeting Highlights

### Instrument and Control Systems for Radioactive Laboratories (ICRL)

January 29, 2010



Shri R. Natarajan, Director, RpG and Shri K. V. Kasi Viswanathan, AD, GRIP during the meeting

One day meet on Instrumentation & Control systems for Radioactive Laboratories (ICRL 2010) was held on January 29, 2010, in Raja Ramanna Auditorium, Kalpakkam, under the auspices of Post Irradiation Examination Division (PIED), GRIP, MMG.

Welcome address and genesis of ICRL 2010 was given by Shri K.V. Kasiviswanathan, AD, GRIP. The one day meet was inaugurated by Shri R. Natarajan, Director, RpG and Shri N.G. Muralidharan, PIED proposed the vote of thanks.

Shri R. Natarajan in his inaugural address stressed the need and importance of the instrumentation in the reprocessing and other radioactive laboratories. Since there are going to be more number of reactors (thermal and fast) in the coming years, to enhance the contribution of nuclear energy, the quantity of fuel to be reprocessed would be more (in tonnes). The reprocessing plant will handle more fuel in complex pipe lines inside the hot cell which will have high activity and high gamma dose the need of instrumentation control has become a vital and important one. For example monitoring of Plutonium in air, neutron monitoring system with less error, computer based system for plants and Plutonium monitoring system for on line monitoring in the pipe lines are the some of the areas where the instrumentation and control system plays a vital role. He also stressed the need for details required for obtaining the clearance from the safety authorities. At present no standard is available for such equipments and all are under development. Further he said that this one day meet is only a start and ignition to have big events in future to discuss and to have more deliberation with more participants working in the areas of instrumentation and control in our Department.

Seven invited talks by the Instrumentation & Control experts in various radioactive facilities of IGCAR and BARC were presented during the one day meet. About sixty five participants including the young engineers involved in instrumentation and control of radioactive laboratories were attended the one day meet. Forenoon session was chaired by Shri P. Kalyanasundaram, AD, FRTG where invited talks were presented.

### One Day Workshop on Materials Characterisation using NDE Techniques (MCNT- 2010)

February 10, 2010

A pre-conference workshop on 'Materials Characterisation using NDE Techniques (MCNT-2010)' was organised jointly by IGCAR, Board of Research in Nuclear Sciences, Atomic Energy Regulatory Board and Materials Research Society of India, Kalpakkam chapter on February 10, 2010 at SRI Convention Centre, Anupuram. This workshop was part of the eighth International Conference on Barkhausen Noise and Micromagnetic Testing (ICBM8) which was held at Anupuram during February 11-12, 2010. During the inaugural function of MCNT-2010, Dr. T. Jayakumar, Chairman, MCNT-2010 and Director, MMG, IGCAR gave the welcome address. Dr. G. Dobmann, Deputy Director, Fraunhofer-IZFP, Saarbrücken, Germany inaugurated the workshop. During the inaugural address, he highlighted the lead role played by NDE techniques during manufacturing stages and towards assessment of damage in



Dr. D.K. Bhattacharya, Acting Director, Central Glass Ceramic Research Institute, Kolkata releasing the proceedings of MCNT-2010 in the presence of Dr. G. Dobmann, IZFP, Germany and Dr. T. Jayakumar, Chairman, MCNT-2010 and other colleagues of the Centre

operating components. Dr. D.K. Bhattacharya, Acting Director, Central Glass and Ceramic Research Institute (CGCRI), Kolkata, released the workshop proceedings and addressed the delegates. Dr. B.P.C. Rao, Co-Chairman, MCNT-2010, explained about the workshop. Dr. C.K. Mukhopadhyay, Convener, MCNT-2010 proposed the vote of thanks.

There were nine lectures in this workshop covering various aspects of materials characterisation using NDE techniques like, micromagnetic, ultrasonic, eddy current, acoustic emission, positron annihilation, X-ray diffraction, infrared thermography and in-situ metallography for characterization of microstructures, residual stresses, deformation, damage and fracture, in addition to a lecture on 'Importance of microstructure and residual stress for materials characterization' delivered by Dr. D.K. Bhattacharya. The faculty of MCNT-2010 was drawn from IZFP, Germany; CGCRI, Kolkata, IPR, Gandhinagar and IGCAR, Kalpakkam. The workshop was attended by seventy scientists and engineers from R&D organizations and industry including delegates one each from Tampere University of Technology and University of Oulu, Finland; Iwate University, Japan and Comision Nac de Energia Atomica, Argentina.

## Eighth International Conference on Barkhausen Noise and Micromagnetic Testing (ICBM8)

February 11-12, 2010



Dr. Baldev Raj, Director, IGCAR, inaugurating the International Conference on Barkhausen Noise and Micromagnetic Testing on February 11, 2010

Eighth International Conference on Barkhausen Noise and Micromagnetic Testing (ICBM8) was organised jointly by IGCAR, BRNS and AERB during February 11-12, 2010. During the inaugural function, Dr. T. Jayakumar, Chairman, ICBM8 and Director, MMG, gave the welcome address and Mr. Lasse Suominen, Chairman, ICBM Organisation and President, Stresstech Oy, Finland spoke about ICBM serial conference. Dr. Baldev Raj, Director, IGCAR, inaugurated the conference and in his address during which he stressed the need for increased use of Barkhausen noise and micromagnetic techniques by the industry for materials evaluation and stress measurement applications. He emphasized the need for evolving standards for magnetic Barkhausen emission techniques for different applications and forging international collaborations among different research groups working in this field. Dr. B.P.C. Rao, Co-Chairman, ICBM8 explained about the conference and Dr. C.K. Mukhopadhyay, Convener, ICBM8 proposed the vote of thanks.

The conference was attended by fifty scientists, engineers and scholars from various DAE units, IIT Madras, BHU-IT, SERC, DMRL, NML, CPRI, Mercantile Marine Department etc., and sixteen foreign delegates from nine countries including Stresstech Oy, Finland; Fraunhofer-IZFP, Germany; University of Defence and Institute of Physics, Czech Republic; Tampere University of Technology and University of Oulu, Finland; Iwate University, Japan; Atomic Energy Research Institute, Hungary; Comisión Nac de Energía Atómica, Argentina and Newcastle University, UK. In the conference, six eminent international experts including Dr. G. Dobman, IZFP, Germany, Dr. B.A. Shaw, Newcastle University, UK and Dr. Evan Thomas, Institute of Physics, Czech Republic delivered invited lectures covering various aspects of Barkhausen noise and micromagnetic testing. A total of twenty two contributory papers covering microstructural characterization; residual stress measurements; damage assessment and industrial applications were presented in six technical sessions. A technical visit to FBTR and NDED was organized for the ICBM delegates.

The concluding session of ICBM was held on February 12, 2010. A panel consisting of Dr. T. Jayakumar, Dr. G. Dobmann, Dr. S. Sitaramu, Director, CPRI, Bengaluru, Dr. B.A. Shaw and Mr. Lasse Suominen summed up the deliberations in ICBM8 and highlighted the need for round robin tests; separation of stress and microstructure effects on MBE signal; consideration of material properties and probabilistic fracture for better understanding of MBE signals; increased use of multi-parameter approaches and neural networks. Mr. Lasse Suominen announced that the ICBM9 would be held in Czech Republic in 2011.

## Mid-Year meeting of the Materials Research Society of India Council

April 3, 2010



Dr.T. Ramasami, Secretary, Department of Science and Technology, members of the Materials Research Society of India Council with Dr. Baldev Raj, Director, IGCAR and other senior colleagues of the Centre

The Mid-Year meeting of the Materials Research Society of India (MRSI)- Council, to deliberate on the formulation of a five year Road Map for MRSI was held on Saturday, April 3, 2010, at IGCAR, Kalpakkam. The meeting was chaired by Dr. T. Ramasami, Secretary, Department of Science & Technology and President, MRSI, with several senior functionaries present: Dr. Baldev Raj, Director, IGCAR and Vice-President MRSI, Prof. S.B. Krupanidhi, General Secretary MRSI, Council members and Chairmen of various MRSI Subject groups and Regional Chapters. Several senior materials scientists from IGCAR also participated in the day-long meeting.

Dr. Ramasami elicited the viewpoints of Council members and invitees, both on the content of current activities and on the Structure of MRSI, to take this important Professional body forward towards facilitating front-ranking research in the important area of Materials Science. Several suggestions on, new initiatives to be taken up, starting of new subject groups, merger of a few related subject groups and conduct of thematic workshops, were made. An important recommendation of the meeting pertains to the formation of new task forces with the explicit purpose of enhancing the MRSI linkage with Industry, Academic Institutes, Research laboratories and for Societal benefits.

Dr. Ramasami, indicated that based on these deliberations, an action plan for implementation by MRSI would be prepared, which would serve as a valuable scientific input towards the formulation of XII- plan proposals. The MRSI- Council members also visited the PFBR site and some of the research laboratories, and expressed their appreciation for the nice hosting of the meet at Kalpakkam.

## Robust Instrumentation & Control Systems for FBR Program

(May 20, 2010)



Dr. P. Swaminathan, Director, EIG, Shri B. Krishnakumar, Head, Components and Instrument Development Division, FRTG, Shri S. Ilango Sambasivan, Head, Electronics and Instrumentation Division, EIG & Shri S.A.V. Satya Murty, Associate Director, EIG, during the inaugural session of the meeting

A theme meeting on 'Robust Instrumentation and Control Systems for FBR Program' was held on May 20, 2010, in Ramanna Auditorium, IGCAR, Kalpakkam, under the auspices of EIG. Shri B. Krishnakumar, Head, Components and Instrument Development Division, FRTG welcomed the participants and gave the genesis of the theme meeting. Dr. P. Swaminathan, Director, EIG, in his inaugural address, outlined the importance of Instrumentation and Control Systems in Nuclear Power Plants, regulatory requirements, design and development and qualification methodology currently adopted for Instrumentation and Control Systems of PFBR. He further stressed the need for security aspects also to be addressed in design and development of instrumentation and control systems, since future Instrumentation & Control Systems will be computer based. There were seven invited talks covering the areas of Quality Assurance in Design and Manufacturing phase, Quality Assurance in Operation & Maintenance phase, Information Security in Nuclear Facilities, Challenges in Neutronic instrumentation, Operator Training Simulator and Gap areas for R&D. About sixty participants working in the areas of instrumentation and control system of IGCAR and BHAVINI attended the meeting. Shri G. Kishore, Electronics and Instrumentation Division, EIG proposed the vote of thanks.

## Discussion Meeting on Emerging Technologies for Clean Water

(May 21-22, 2010)



Dr. R. Chidambaram, Principal Scientific Advisor, Government of India, addressing the gathering during the inaugural session. Dr. Baldev Raj, Director, IGCAR, Prof. T. Pradeep, IIT-M, Dr. C. Anand Babu, Head, Separation Technology and Thermal Hydraulics Division, FRTG are seated on the dais

A two day discussion meeting on "Emerging Technologies for Clean Water" was organized at SRI Guest House, Anupuram, during May 21-22, 2010. About thirty six participants and experts from premier academic institutes, national laboratories and industries, actively involved in various aspects of research and product development in diverse areas related to clean water were invited to participate. This focussed meeting was organized under the auspices of the 'Office of the Principal Scientific Advisor, Government of India' and was supported by the Department of Science & Technology, New Delhi. Dr. R. Chidambaram, Principal Scientific Officer, Government of India in his inaugural address highlighted the tasks that have been completed, challenges ahead and the

perspective and vision towards providing clean water solutions to the nation. Dr. Prasada Raju, Department of Science & Technology highlighted the importance of this activity in terms of various funding mechanisms for worthy research and product realization initiatives. On the first day, the delegates made brief presentations of their work and gave suggestions on specific areas of activity that could be undertaken towards achieving the objective of clean water for all. On the second day, three specialist/theme group meetings were conducted (i) nanostructured and related materials (ii) membranes, related materials and contaminants (iii) industries and product development for clean water. These specialist groups had intense discussions to arrive at specific recommendations. These recommendations were consolidated in the final session, under the chairmanship of Dr. Baldev Raj, Director, IGCAR to identify the thrust areas and a comprehensive roadmap for implementation by the National Water Mission, Government of India.

## BITS Practice School

May 24 - July 16, 2010



BITS PS I Students and guides with Shri S.C. Chetal, Director, REG interaction session

Twenty five students from BITS Pilani (Pilani and Goa campuses) underwent BITS practice School for seven weeks at our Centre. Dr. P.R. Vasudeva Rao, Director, Chemistry group inaugurated the BITS practice School at IGCAR on May 24<sup>th</sup> 2010. The BITS practice school bridges the professional world with the educational world. The course aims at exposing the students to industrial and research environments, on how the organizations work, to follow and maintain work ethics, study the core subjects and their application in the organization, participate in some of the

assignments given to them in the form of projects. The students were from various engineering disciplines like, Mechanical Engineering / Computer Science / Electrical & Electronics / Electronics & Instrumentation and Electronics and Communication Engineering. Students carried out challenging projects at various Divisions in line with their discipline. During their period of stay they visited various facilities at IGCAR, BHAVINI and MAPS. Group discussions, seminars, project work presentation and report writing formed the practice school curriculum. On completion of the practice school, Dr. P. Chellapandi, Director, Safety Group and AD, NEG, distributed certificates to the students during their valedictory function. Shri S.C. Chetal, Director REG, had an interaction session with the students on one of the days during practice school.



BITS PS I Students and guides with Dr. P. Chellapandi during Valedictory Function

## Quality Circles Annual Meet (QCAM- 2010) at IGCAR

August 16-17, 2010



STAR QC team receiving Dr. Placid Rodriguez memorial Trophy (Mechanical and Manufacturing Category)



EXCEL QC team receiving Shri M.K. Ramamurthy memorial Trophy (Plant Operation & Services Category)

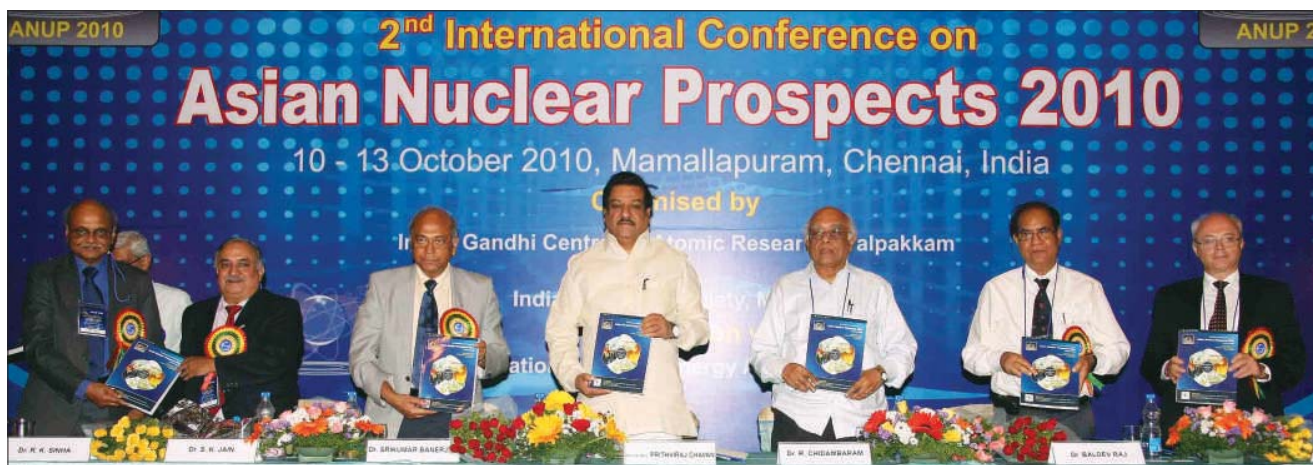
Quality Circles Annual Meet (QCAM) is being conducted every year by Apex Steering Committee on Quality Circles (ASCQC) at IGCAR. The aim of this convention is to provide a common platform for working group people to share the knowledge gained by them in applying new ideas to solve their work related problems. This year, QCAM was conducted during August 16-17, 2010. The programme was inaugurated by Shri S.C. Chetal, Director, REG. Dr. P.R. Nakkeeran, Director, Tamil Virtual Academy, Chennai delivered the key note address. Thirty-six Quality Circles (about 300 members) from IGCAR, GSO, MAPS and Schools at Kalpakkam had presented their QC case-studies under Mechanical & Manufacturing Category, Plant Operation & Services and Schools Category. A quiz programme on QC concepts, QC tools & techniques was conducted to propagate the QC concepts. Professionally qualified judges from Quality Circle Forum of India, Chennai chapter assessed the case-studies presented in parallel sessions at Sarabhai Auditorium and Ramanna Auditorium. The Valedictory address was given by Shri G. Srinivasan, Director, ROMG. He also gave away the Memorial Trophies to successful QC groups.



LOTUS QC team receiving Dr. Sarvepalli Radhakrishnan memorial Trophy (Schools Category)

## Second International Conference on Asian Nuclear Prospects 2010 (ANUP 2010)

October 10- 13, 2010



Dr. R.K. Sinha, Vice President INS & Director, BARC, Dr. S.K. Jain, CMD, NPCIL & BHAVINI, Dr. Srikumar Banerjee, Chairman, AEC and Secretary, DAE, Shri Prithviraj Chavan, the then Honourable Minister of State for Science & Technology and Earth Sciences, Government of India, Dr. R. Chidambaram, Principal Scientific Advisor to Government of India, Dr. Baldev Raj, Chairman, Organizing Committee and Director, IGCAR, Dr. Y. Sokolov, Deputy Director General, IAEA while releasing the souvenir during the inauguration

The Second International Conference on Asian Nuclear Prospects 2010 (ANUP 2010) was organized by the Indira Gandhi Centre for Atomic Research and the Indian Nuclear Society, in co-operation with the International Atomic Energy Agency (IAEA) during October 10-13, 2010, at Radisson Resort Temple Bay, Mamallapuram. The aim of the Conference was to bring about increased interaction between Asian countries which are having nuclear energy programmes and the developed countries of the world where nuclear energy has reached a level of maturity. The scope of ANUP 2010 included all aspects of nuclear energy and related technology. The format of the Conference included invited talks by eminent experts, poster presentation by participants (contributed papers), and a few oral presentations by young researchers.

The Conference evoked excellent response from the international nuclear community. Three hundred and thirty delegates from different parts of the world including about sixty from overseas, and about fifty from the industry attended ANUP 2010. There were nine plenary talks, forty one invited talks and one hundred thirteen contributed papers among which eight were young researcher oral presentations. Twenty seven speakers were from foreign countries. Among the contributed papers, twenty were from abroad, and the rest from Indian atomic energy units, national laboratories, universities and industry.

The Conference was inaugurated in the evening of October 10, 2010, by Dr. Srikumar Banerjee, Chairman, Atomic Energy Commission of India. The function was presided over by Shri Prithviraj Chavan, the then Honourable Minister of State for Science & Technology and Earth Sciences, Government of India. Dr. Baldev Raj, Chairman, Organizing Committee and Director, IGCAR welcomed the gathering, Dr. R.K. Sinha, Vice President INS & Director, BARC and Dr. Y.Sokolov, Deputy Director General, IAEA addressed the gathering, and Dr. S.K. Jain, CMD, NPCIL & BHAVINI released the Souvenir and inaugurated the Exhibition. Dr. P.R. Vasudeva Rao, Director, CG, delivered the vote of thanks.

Three days were devoted to intensive technical discussions in three plenary sessions, and six technical sessions in parallel. The topics ranged from atomic minerals exploration to nuclear waste disposal, materials development and associated technologies. Eight young researchers gave short oral presentations on their R&D work in an impressive session chaired by Dr. Anil Kakodkar, Member, AEC and former Chairman, AEC. There was also an industrial forum, chaired by Dr. R. Chidambaram, Principal Scientific Advisor to Government of India, in which several leaders of the nuclear and related industries from India and abroad (AREVA India, Cameco India, Nuvia India, Westinghouse, BHEL and L&T) presented their perspectives on sustainable growth of nuclear energy in Asia and the rest of the world. There was an exhibition with ten pavilions showcasing the strengths and achievements of several industries allied to nuclear energy and was kept for all three days of the meeting. The Conference ended in the evening of

October 13, 2010 with a panel discussion on the topic, “Engines of robust and sustainable nuclear energy growth” chaired by Dr. Anil Kakodkar. The panel consisted of senior nuclear programme leaders from almost all countries with major nuclear energy projects. At the end of the Conference, the feedback received from delegates and other observers uniformly referred to the high technical content and professional conduct of the event.

## Workshop on Structure and Thermodynamics of Emerging Materials (STEM-2010)

November 25-26, 2010



Dr. Baldev Raj, Director, IGCAR addressing the gathering, Dr. M. Vijayalakshmi Head, Physical Metallurgy Division Dr. T. Jayakumar, Director, Metallurgy and Materials Group, Professor R. K. Ray, Visiting Scientist, Tata Steel, and Dr. Saroja Saibaba, Head, Nuclear Materials Microscopy Section, Physical Metallurgy Division and Convener, STEM 2010 during the inaugural function

The BRNS sponsored two-day workshop STEM-2010 on the theme “Advanced Methods in Characterisation of Texture and Microtexture of Materials” was organized jointly by Indira Gandhi Centre for Atomic Research and The Indian Institute of Metals – Kalpakkam Chapter during November 25-26, 2010 at Convention Centre, Anupuram. Dr. T. Jayakumar, Director, MMG welcomed the participants and emphasized the role of crystallographic texture in the development of various nuclear materials. Dr. M. Vijayalakshmi, Head, Physical Metallurgy Division briefed upon the genesis of STEM annual meetings on a focused theme to foster professional knowledge, the recent advancements in texture characterisation and its potential for improving material performance. Dr. Baldev Raj, Director, IGCAR inaugurated the meeting, and stressed the importance of research collaborations and modeling studies for tackling various challenging problems in materials at a shorter time. The plenary lecture “Crystallographic texture in understanding material behavior” by Professor R.K. Ray, Visiting Scientist, Tata Steel, provided an excellent overview of the theme of the workshop. He provided a historical glimpse on texture studies, different representations of texture data and the role of texture in improving material properties through illustrative examples. Dr. Saroja Saibaba, Head, Nuclear Materials Microscopy Section and Convener, STEM-2010 delivered the vote of thanks.

Invited lectures were delivered by eminent scientists from leading national R&D institutions and academia covering aspects of texture characterization techniques (electron back scattered diffraction, X-ray diffraction, transmission electron microscopy), mechanisms of texture formation and evolution, grain boundary engineering, texture-property correlations in nuclear and automotive industries and the recent developments. About one hundred and ten delegates from various institutes such as Indian Institute of Science, IITs, DMRL, NIT, IMMT, IPR, and other engineering/science colleges, and from DAE units of BARC, NFC and IGCAR participated in the two-day deliberations. Young research scholars presented their work as posters. The technical program was appreciated by the participants, and valuable inputs for further discussions were provided during the feedback session at the end of two day workshop.

## IGC COUNCIL

## Chairman



**Dr. Baldev Raj**, BE, Ph.D; Member, German National Academy of Sciences, International Nuclear Energy Academy, Fellow, Third World Academy of Sciences, Fellow of all Engineering and Science Academies in India and Distinguished Scientist & Director, Indira Gandhi Centre for Atomic Research. His specializations include materials characterization, testing and evaluation using non-destructive evaluation methodologies, materials development and performance assessment and technology management. He has steered and mentored large, multi and cross-disciplinary domains and multi-institutional teams to earn for India an eminent and esteemed position in high technology domain of sustainable clean energy system; sodium cooled fast spectrum reactor with closed fuel cycle. This energy system has the capacity to deliver large clean energy to the country and the world for centuries. He has more than 760 publications in leading refereed journals and books. He has been invited to contribute to 26 times for contributions in Handbooks and Encyclopedia. He has co-authored and co-edited 58 books and special journal volumes. He has 5 Indian Standards and 21 patents to his credit. He is on the editorial boards of national and international journals. He is Editor-in-Chief of three series of books: one related to NDE Science & Technology second related to Metallurgy & Materials and third related to Corrosion Science & Technology. He has guided 20 Ph.D. students. He has taught courses in eminent institutes in India and abroad. He has delivered more than 300 honour, plenary, keynote and invited talks in some of the most eminent forums related to his fields of specialization. These achievements establish him as an eminent and prolific researcher in domains of his expertise. He is acclaimed in India and world for his excellent and sustained contributions. He has been responsible for starting, nurturing and enhancing international collaborations of high merit of relevance and eminence with Germany, United Kingdom, France, Russia, Japan, Singapore, China, South Africa, USA, etc. He is the past-President of International Committee on NDT. He is President of Indian National Academy of Engineering, Vice President, Materials Research Society of India, Vice President, Academia NDT International and President-elect, International Institute of Welding (a member body of more than 50 countries with affiliation to United Nations and International Standards Organization). He has won many awards and honours, notable among them during the last five years include: Padma Shri from Govt. of India (a Civilian honour - 2006), Distinguished Alumni Award (2007) of Indian Institute of Science, Prof. Jai Krishna Memorial Award-2008 of Indian National Academy of Engineering, Distinguished Materials Scientist for the year 2009 from Materials Research Society of India, Federation of Indian Chamber of Commerce and Industries Annual Award for Outstanding Research in Materials Science (2007-08), Pandit Jawaharlal Nehru National Award from Department of Science & Technology, Govt. of Madhya Pradesh (2007), Indian National Science Academy Prize for Materials Science (2010), Portevin Lecture of International Institute of Welding (2011), etc. He is member, Global Energy International Prize Committee, Russia (considered parallel to Nobel Prize in the domain of Energy), Nano Mission Council of Department of Science & Technology, India, National Nanotechnology Advisory Board of South Africa; Chairman of India-Brazil-South Africa Initiative on Nano Science & Technology, Scientific Advisory Council to Prime Minister, Scientific Advisory Committee to Cabinet, etc. He is Adjunct Professor of Institute of Chemical Technology, University of Mumbai, PSG College of Technology, Coimbatore, Department of Electrical and Computer Engineering, Michigan State University, USA, INAE-AICTE Distinguished Visiting Professor of Vellore Institute of Technology and Indian Institute of Technology Madras, Chennai. His expertise is acclaimed by research, academia and industry and thus he has been requested to build strategic capacities of high significance and enriching specific domains of expertise of high importance to the country. His holistic management of two townships with more than 10,000 residents with six schools, two hospitals and many unique facilities such as zero solid waste, entertainment, sports, etc. is exemplary in ensuring inspiring and quality living. His other interests include science and technology of cultural heritage and theosophy. He has passion for teaching, communications and mentoring.

## Members



**Dr. Ratan Kumar Sinha** graduated in Mechanical Engineering from Patna University in 1972, standing first in the University. After completing the one year Course of BARC Training School he joined Reactor Engineering Division of BARC in the year 1973. At present he is serving as Director, Bhabha Atomic Research Centre. Dr. Sinha has been guiding the programmes for new advanced reactors under design and development at BARC to utilise thorium. These include, the Advanced Heavy Water Reactor, which produces most of its power from thorium, and has several innovative passive safety systems. He is also responsible for the design and development of the Indian High Temperature Reactor intended for hydrogen generation. As a part of the work, he has guided the design of the Compact High Temperature Reactor, which will serve as a

technology demonstrator for future larger high temperature reactors. Dr. Sinha is a nationally and internationally recognised expert in the area of nuclear reactor technology. He has represented India in several important forums of the International Atomic Energy Agency. These include the Steering Committee of the IAEA's International Project on Innovative Nuclear Reactors and Fuel Cycles (INPRO), of which he was chairman for four years. Dr. Sinha has received several awards and honours. These include the Homi Bhabha Science and Technology Award, VASVIK Award, Indian Nuclear Society Award and the DAE Special Contributions Award. He was elected a Fellow of the Indian National Academy of Engineering in 1998. Dr. Sinha was conferred the honorary Doctorate of Science (D.Sc.) degree by the University of Mysore.

**Shri S.C. Chetal,**



graduated in Mechanical Engineering from Delhi College of Engineering in 1970. After graduating from the 14<sup>th</sup> Batch of BARC Training School, he joined IGCAR in 1971. Since then, he has been engaged in the field of fast reactor engineering. He has made contributions towards design of FBTR sodium systems and components. At present, he is Distinguished Scientist & Director, Reactor Engineering Group, IGCAR. He is the principal design engineer of PFBR. He has made outstanding contributions towards the material selection, manufacturing technology, R & D design and construction of 500 MWe Prototype Fast Breeder Reactor. He is member of many professional institutions and fellow of Indian National Academy of Engineering. He is a recipient of Indian Nuclear Society INS Award 2003 for contributions towards nuclear related high technology, National Design Award-2007 by Institution of Engineers, 2003 VASVIK Award, Agni Award for Excellence in self-reliance by DRDO for titanium sponge production, and Certification of Appreciation by IAEA towards fast reactor technology. His interests include pressure vessel and materials technology. He is on the Board of BHAVINI.

**Dr. P. Chellapandi** is an Outstanding Scientist and Director, Nuclear and Safety engineering Group & Associate Director of



Nuclear Engineering Group. He is from 22<sup>nd</sup> batch of BARC training school with First Rank. He joined IGCAR in 1979 and since then, he is working for the design and development of 500 MWe Prototype Fast Breeder Reactor (PFBR), over a wide spectrum of design, viz., conceptualization, development of sophisticated computer codes, detailed analysis, design validation, preparation of preliminary safety analysis reports, execution of R&D activities involving national academic institutions and R&D establishments in the country. He got his B.E (Hons) in Mechanical Engineering with First Rank from Madras University in 1978, and M.Tech in Engineering Mechanics (Gold Medalist with CGPA 10) and Ph.D in Applied Mechanics from IIT Madras. He is a senior professor of Homi Bhabha National Institute. He has played a key role to establish a state-of art structural mechanics laboratory at IGCAR, for successful erection of safety vessel in June 2008 and for getting the safety clearance recently from Project Design Safety Committee. He is also the convener of Task-force which is co-ordinating for the manufacture and erection of reactor assembly components for PFBR. He has provided significant design support for Fast Breeder Test Reactor, high temperature design of reduction retort for titanium sponge plant for DMRL, Hyderabad and thermo-mechanical analysis of scramjet engine to DRDL, Hyderabad. He has guided 50 Post Graduate students and published about 420 papers in journals, national and international conferences. He is a Fellow of Indian National Academy of Engineering. He has received the Homi Bhabha Science and Technology Award for the year 1997, Indian Nuclear Society Award and National Design Award in Mechanical Engineering in 2006, DAE Group achievement award for Design of PFBR Main Vessel and Safety, 2006, and DAE Group Achievement Award for Seismic Design and Qualification of PFBR Components, 2007 for his outstanding contributions in the design of Fast Breeder Reactor Components and Agni Award for Excellence in Self-reliance from DRDO, 2007 and DAE Group Achievement Award for Design and Manufacture of Grid Plate of PFBR (2008).

**Dr. A.K.Ghosh,**



joined the Bhabha Atomic Research Centre in 1971 after graduating in Mechanical Engineering from Indian Institute of Technology, Kharagpur, India. He obtained his Ph.D from Indian Institute of Technology, Bombay. Currently, he is the Director, Health, Safety and Environment Group of BARC. Dr. Ghosh has been carrying out R&D work in the field of reactor safety and his area of work includes both thermal-hydraulic safety and structural safety. He has carried out some pioneering work on the hazards due to earthquakes and tsunamis. Presently, he is also associated with various programmes on radiation safety. He has published more than 100 papers in International Journals and Conferences. He is a Chairman/Member of various Safety Committees of BARC and Atomic Energy Regulatory Board (AERB) for Siting and Design Safety Review and has made significant contribution in the preparation of various Safety Codes and Guides on these subjects.



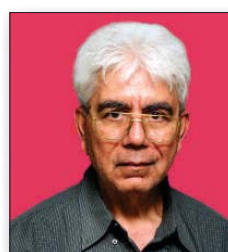
**Dr. T. Jayakumar**, B.Tech.(Metallurgy, REC Warangal), M.S (Metallurgy, IIT Madras), Ph.D (Engineering, University of Saarland, Germany) is currently Outstanding Scientist & Director, Metallurgy and Materials Group at IGCAR. Since 1978, he has been engaged in the field of Non-destructive Evaluation. Over the years he has carried out and steered innovative research and development programmes in the areas of Non-Destructive Evaluation, Failure Analysis and Structural integrity of Nuclear Components specifically for the Fast Breeder Reactor components. He is a Fellow of the Indian National Academy of Engineering. He has

been a recipient of several awards such as National NDT Award from ISNT, Metallurgist of the Year award from IIM, Homi Bhabha Science and Technology Award from DAE. He has co-authored 3 books, co-edited 3 books and has published over 250 papers in International Journals. He also has 6 patents to his credit.



**Shri R.N. Jayaraj**, presently the Chief Executive of Nuclear Fuel Complex (NFC), Hyderabad, is a Mechanical Engineer from Osmani University, Hyderabad. Shri Jayaraj, after obtaining the Bachelors Degree in Mechanical Engineering in the year 1973, joined the 17<sup>th</sup> batch of BARC Training School, Mumbai, India for one-year orientation course in Nuclear Engineering. At BARC, he has carried out development and manufacturing of metallic fuels for thermal research reactors. Shri Jayaraj joined NFC in 1978 and was responsible for establishing a facility for the fabrication of core sub-assemblies for the Fast Breeder Test Reactor (FBTR).

After successful completion of the first core requirement, he was assigned the responsibility of fabricating fuels for all the Power Reactors in India. Shri Jayaraj has played a pioneering role in standardizing the processes and manufacturing fuel bundles required for 540 MWe Pressurised Heavy Water Reactors (PHWRs) for the first time in the country. Presently he is engaged in the expansion activities of fuel fabrication capacities to meet the enhanced fuel demands. Shri Jayaraj has received many prestigious awards including the Indian Nuclear Society (INS) Award and The Indian Institute of Metals (IIM) SMS Damage Excellence Award-2009 (Gold Medal). He is a Fellow of Indian National Academy of Engineering (INAE), Fellow of Andhra Pradesh Akademi of Sciences (APAS) and Honorary Fellow of Indian Institute of Chemical Engineers. Shri Jayaraj, besides being a Member of IGC Council, is on the Board of Directors of Uranium Corporation of India Limited (UCIL) and Indian Rare Earths Limited (IREL). He is also the Council Member of Indian Institute of Metals (IIM), Kolkata and the Chairman of Indian Nuclear Society, Hyderabad Chapter.



**Prof. P.K. Kaw**, Ph.D (Physics) from IIT Delhi, is the Director of Institute for Plasma Research, Gandhinagar since 1986. The Institute has pioneered plasma physics research in India which includes design, development and fabrication of two tokamaks, ADITYA and SST 1, research work on a large number of fundamental plasma physics experiments and work on industrial applications of plasma physics. ADITYA was the first tokamak to discover intermittency in edge and SOL turbulence. The Institute also spearheaded India's case for participation in ITER and is now the nodal domestic agency for ITER. Prof. Kaw's personal research work in this period includes physics of intermittency, drift waves and anomalous transport, MARFES, solitons, laser fusion, anomalous stopping effects, dusty plasmas, nonneutral plasmas, quark gluon plasmas, etc. Earlier he had held positions like Princeton University Plasma Physics Laboratory Research Staff and Professor at Physical Research Laboratory, Ahmedabad before taking over as Director, Plasma Physics Program in 1982. He played a key role in initiating tokamak physics program in India. He has more than 305 research papers to his credit in international journals. He has several honours to his credit and has delivered important lectures: Artsimovitch Memorial lecture at the IAEA Fusion Energy Conference in 1992, Invited talk on International Energy Research at the APS Centennial celebrations (1999) in Atlanta, Georgia and a presentation on the International impact of USDOE Fusion Theory Program to the NSF-NRC Panel Chaired by C F Kennel, San Diego are just a few of them to name. Prof Kaw was also the Chairman of the International Fusion Research Council (IFRC) of IAEA from 2000 to 2007 and was the Chairman of the Science & Technology Advisory Committee [STAC] of the ITER Governing Council till December 2009. He was awarded the TWAS Prize in Physics during 2008, by the TWAS Council of the Academy of Sciences for the developing world.



**Dr. P. Kalyanasundaram** obtained his Bachelor of Engineering from University of Madras and MS (by research) from IIT Madras. He joined Indira Gandhi Centre for Atomic Research, Kalpakkam in 1974. He is presently an Outstanding Scientist and Director of Fast Reactor Technology Group, IGCAR. He has been steering a multidisciplinary program in the areas of Sodium Technology, design and development of electronics & instrumentation and sensors, testing of components for Prototype Fast Breeder Reactor, R&D in reactor engineering and developments related to Under Sodium Examination. He has specialized in the areas of signal analysis, artificial intelligence and neural networks for NDT and engineering applications and has devised innovative methodologies for detection and characterization of defects in materials and condition monitoring of components. He has led several inservice inspection campaigns for PHWRs and also to the life extension programme of defence air crafts. He has been involved in modeling, design and testing of sensors for high temperature sodium applications, vibration and modal analysis etc. He is the recipient of the NDT Man of The Year Award 1994, AEWG (I) gold medal (2002), Kalpakkam Science and Technology Award and Sir C.V.Raman Award on two occasions. He has more than 120 publications in both national and international journals, authored 2 books, one on Acoustic Emission and the other on Practical Digital Signal Processing, and has eight patents to his credit.



**Shri Y.C. Manjunatha**, Director, Engineering Services Group of Indira Gandhi Centre for Atomic Research, Kalpakkam, is a M.Tech. in Electrical Engineering from IIT, Madras and graduated from the 16th batch of BARC Training School. He steers one of the largest multidisciplinary groups in the Centre which focuses on providing reliable and robust services through cutting edge technologies and methodologies. The Group comprises of AC&VSD, CWD, CED, ESD & QAD and infrastructural divisions of GSO. Some of his major contributions are development and sustenance of infrastructural works of IGCAR & GSO involving civil, electrical, air conditioning and ventilation, communication, workshop and QA activities. He has published more than twelve papers. He has nurtured and mentored the quality circle activities of the Group. He has a significant contribution in making the project site and townships more green and presentable. Introduction of a systematic domestic solid waste management system at GSO is being appreciated by all. The present focus is on establishment of 2 MGD desalination plant, water treatment plants and provision of common services features to FRFCF. He is a fellow of Institution of Engineers, patron of ISHRAE and Chairman of Kalpakkam Chapter of Indian Society of Non-Destructive Testing.



**Shri S.D. Misra**, B.E (Electrical & Mechanical Engineering) is presently the Director of Nuclear Recycle Group at BARC. He is from 13<sup>th</sup> Batch of BARC Training School and has been involved in the Back End activities of Nuclear Fuel Cycle. He was a member of the team that pioneered setting up of the first Vitrification Plant in the country. Shri Misra was responsible for design and construction of vitrification plants at Trombay & Kalpakkam. He was also instrumental in solving all the problems faced in the first resin fixation facility at Narora Atomic Power Project and made it operational. Shri Misra has participated in a number of symposia and seminars on radioactive waste management and has also worked as an expert on various technical committees of International Atomic Energy Agency. Presently he is a Member of International Radioactive Waste Technical Committee (WATEC) of IAEA. He has also served as Director, Purchase & Stores, DPS. In this capacity, he has successfully overcome the problems of technology control regime and made available some of the critical stores for the programmes of the Department. Presently, as Director, Nuclear Recycle Group, he is holding the responsibility of setting up and operation of Reprocessing and Waste Management Plants at various sites in the country.



**Shri R. Natarajan**, a Chemical Engineer from the 19<sup>th</sup> batch of BARC training school, joined the Department of Atomic Energy in 1975. He is presently the Director of Reprocessing Group in IGCAR. Under his leadership, the CORAL facility, for establishing the process technology for the reprocessing of fast reactor fuels, was designed, erected and commissioned. He led the team which has successfully completed the reprocessing of fast reactor spent fuel, with a burn-up of as high as 155 GWd/t with plutonium rich fuels, for the first time in the world. As Director of Reprocessing Group, he is responsible for the R&D activities of fast reactor fuel reprocessing and setting up of demonstration as well as the commercial PFBR fuel reprocessing plants. His specialisation is in the design process flow sheets and plant design. He has also experience in the design and operation of Thorium-Uranium cycles. He has participated in the irradiated thorium fuel reprocessing campaigns at the Reprocessing Development Laboratory and the <sup>233</sup>U recovered is used as fuel for the reactor KAMINI. He has interests in solvent extraction process modeling, extraction equipment design, design of feed clarification systems of high active solutions, acid recovery systems, system designs of radioactive offgas circuits and ventilation design of radiochemical plants. He has over hundred technical presentations and publications to his credit. He has won prestigious NOCIL Award for Excellence in Design and Development of Process Plant and Equipment for the year 2005 for his contribution in the development of fast reactor fuel reprocessing. He is also the recipient of Indian Nuclear Society's INS award for the year 2006 for his contributions in Nuclear Fuel Cycle technologies.



**Dr. G.J. Prasad**, Outstanding Scientist, Associate Director (P), Nuclear Fuels Group BARC, graduated from Training School 14<sup>th</sup> batch (Metallurgy) obtained BSc (Metallurgical Engineering.) from NIT Rourkela and PhD (Technology) from University of Mumbai & has main area of work in the development and fabrication of research and test reactor fuels. He was responsible for the development and fabrication of <sup>233</sup>U plate fuels for the KAMINI Reactor & currently LEU plate fuel for the modified core of APSARA reactor. His area of interest also includes fuels for thermal and fast reactors for nuclear power. He is a Senior Professor in HBNI. He has received MRSI medal in 2001 and DAE special contribution award in 2006.



**Dr. Prabhat Kumar**, Distinguished Scientist and Project Director, BHAVINI is responsible for construction and commissioning of India's first Prototype Fast Breeder Reactor which has been designed indigenously and launched as a precursor to commercial exploitation on a large scale. This advanced technology reactor requires understanding of various disciplines of science, multidisciplinary capability of engineering and management skills to achieve the success. In his career, he has worked on nuclear system and component design, indigenisation of critical nuclear equipment, participated in erection of the equipment and their commissioning. He has headed Quality Assurance Group of Kudankulam project during formative years, later he worked for Coolant Channel Life Management, Remote Tooling for reactor inspection and maintenance and started R&D centre for NPCIL. He has steered many programmes of vital importance for Indian nuclear power plants and has broad vision of the issues involved. With large exposure of Pressurized Heavy Water Reactor and Pressurized Water Reactor technologies, he has been chosen to construct the India's prestigious Prototype Fast Breeder Reactor, PFBR.



**Smt. Revathy Iyer**, is from the Indian Audit & Accounts Services of the 1980 batch. She is a Post Graduate in Chemistry from Delhi University. After joining the Services, initially she was posted to Office of AG, Maharashtra, Mumbai. She has worked in various capacities in Audit offices in Hyderabad, New Delhi and Bhopal. During May 1990 to May 1994, she was on deputation to Department of Personnel & Training, New Delhi. From April 2003 to March 2005, she was posted as Principal Director of Audit in High Commission of India, London, UK and thereafter (2005-2007) as Principal Director of Commercial Audit & ex-officio Member Audit Board, Mumbai auditing Public Sector Units in oil & aviation sector. From October 2007, she is on Central deputation to Department of Atomic Energy as Joint Secretary in-charge of Industrial units, Public Sector Undertakings, IR&W matters, training activities, etc. From July 2010, she has taken over charge of R&D wing of DAE which deals with units like BARC, IGCAR, RRCAT, VECC and all Aided Institutions under DAE.



**Dr. K.L. Ramakumar** did his post graduation from Sri Venkateswara University, Tirupati and joined Bhabha Atomic Research centre (BARC), Mumbai in 1975 after successfully completing one year orientation course in Chemistry discipline from 18<sup>th</sup> batch of BARC Training School. He is Outstanding Scientist and is currently Associate Director, Radiochemistry & Isotope Group and also Head, Radioanalytical Chemistry Division, BARC. He is a specialist in Analytical Chemistry, trace elemental analysis employing mass spectrometry, chromatography and optical spectrometry. He has been peer reviewer for International Science Foundation, USA for financial grant to Russian scientists. Dr. Ramakumar was also on expert assignment to the IAEA for mass spectrometry measurements.

Dr. Ramakumar was a member of Indian negotiating team for concluding (i) civil nuclear cooperation agreements with the USA and France, (ii) India's safeguards agreement and additional protocol with the IAEA, and (iii) agreement with the USA on arrangements and procedures for reprocessing of safeguarded spent fuel. He has also vast experience in nuclear safeguards and nuclear material accounting and control. He was one of the coauthors of NUMAC Manual for Indian nuclear facilities. He is also actively involved in the preparation of standard analytical methodology for chemical quality control measurements. Dr. Ramakumar is a recognised Ph.D. guide for Mumbai University and HBNI for Chemistry and also strategic studies (HBNI). Dr. Ramakumar has more than 300 publications.



**Shri A.L.N. Rao**, B.E. (Electrical), is presently the Chairman & Chief Executive of the Heavy Water Board. He joined Bhabha Atomic Research Centre as 15<sup>th</sup> batch trainee in the year 1971. He was awarded Junior License Certificate in 1974 and took independent charge of the unit consisting reactor, turbine, generator and associated utilities and control systems of TAPS. Shri A.L.N. Rao participated in the first refuelling operations which consisted of transferring the irradiated fuel bundles from the reactor core to fuel storage pool and loading the fresh fuel bundles from storage pool into the reactor under 60 feet of water. He had also replaced the core components which was a challenging task. In the year 1978, he obtained Senior License Certificate and took independent charge of the complete plant in shifts.

Shri A.L.N. Rao moved from Nuclear Power Board to Heavy Water Board in the year 1984. He closely followed up the project activities of the Captive Power Plant of Heavy Water Plant (Manuguru). In the year 1987 he took over as Operation Manager of Captive Power Plant having capacity to generate 265 x 3 T/ hr of superheated steam and 3 x 30 MWe of electricity generation. He assumed charge as General Manager of the complete Heavy Water Plant (Manuguru), which is the largest heavy water producing plant in India, in the year 1998. He became Associate Director (Projects/Energy & Services) in the year 2003 at the Central Office and took charge as Director (Energy & Services/Operation) in the year 2004. In 2005 he was designated as Executive Director (Projects/Energy & Services). During this period, he formed Energy Cells at every Plant with common monitoring at Corporate office. The Specific Energy Consumption had come down to 32 GJ/Kg. of Heavy Water produced during this period. He discharged the duties as the Secretary of the Heavy Water Board. He coordinated all activities related to export of Heavy Water to South Korea and the Republic of China. As Management Representative for Quality Management Systems as per ISO 9001, he followed up all the activities and obtained ISO 9001 Certificate for Board Office.



**Dr. P. Swaminathan**, graduated with honours degree in Electronics & Communication Engineering from Regional Engineering College, Tiruchirapalli in 1971. He is the Gold medalist of University of Madras. After undergoing one year course in Nuclear Science & Engineering from BARC Training School, Dr. P. Swaminathan joined IGCAR in 1972. He further underwent one year training course in Main frame computer system from International Honeywell Bull Training Institute, Paris. Dr. P. Swaminathan is the main architect for the design, development, installation and commissioning of Fault Tolerant Safety Critical Real Time Computer System for FBTR and library INFO service committee As Director of Electronics & Instrumentation Group, Dr. P. Swaminathan is actively engaged in the

development of Safety Instrumentation, Pulsating sensors, Distributed Digital Control System, Full scope Training Simulator and Knowledge Management System for Fast Breeder Reactor Programme. Dr. P. Swaminathan is a Fellow of Institution of Engineers. He also holds Master Degree in Management Science and Doctorate degree in electronics engineering. He has brought out Indian standards for the usage of computers in Nuclear Installations. He has over 50 publications in International journals/seminars. Also as Chairman, Hospital Management Committee, Dr. P. Swaminathan ensures smooth functioning of the Health Care System and flow of campus wide networked library & scientific information.



**Shri G. Srinivasan** is a mechanical engineer from the 18<sup>th</sup> batch of BARC Training School. He joined FBTR project as a designer in 1975, and participated in the design, fabrication and installation of Reactor Assembly Components. He moved over to O&M in 1983. After holding the positions of Senior Engineer (Planning) & Senior Engineer (Technical), he took over as Technical Services Superintendent and later as AD (O&M). He is Director, ROMG since September 2008.



**Dr. C.S. Sundar**, obtained his Masters degree in Physics from the University of Delhi in 1972, and a Ph.D in Physics from the University of Madras in 1983. He heads the Materials Science Group at IGCAR with a comprehensive research programme on basic research in materials science. Dr. Sundar's research contributions, spanning over three decades, has been on the investigation structure, defects and phase transitions in novel materials using the techniques of positron annihilation and infrared spectroscopy, and has over 100 journal publications. He is a recipient of the Materials Research Society of India Medal, 1994 and the MRSI-ICSC superconductivity and Materials Research Annual Prize 2007.

He is a Fellow of the Indian Academy of Sciences, Bangalore and the National Academy of Sciences, Allahabad. Dr. Sundar is a member of the DST-Programme Advisory Committee on Condensed Matter Physics and Materials Science and the Nano Science Advisory Group of Department of Science and Technology. He is on the Editorial Board of PRAMANA and Solid State Communications.



**Shri Umesh Chandra** is Senior Executive Director (Safety and Knowledge Management) in NPCIL. His areas of responsibilities include Reactor Safety & Analysis of design, Health, Safety & Environment of nuclear power plants in operation and construction, Software Quality Assurance, Training Simulators, Knowledge Management, IT infrastructure and Communications. He has been responsible for establishing R&D infrastructure and activities in NPCIL, including setting up an R&D Centre at Tarapur and a computer based C&I lab at NPCIL HQ. He has been responsible for design of Control and Instrumentation of 540 MWe PHWRs at Tarapur. Earlier at BARC, he has been a developer of computer

based control and monitoring systems of several nuclear power plants. He has also been responsible for establishment of a group engaged in Independent Verification and Validation of Digital Systems in NPCIL. He has contributed in preparation of safety guides of AERB for safety systems and computer based I&C systems and also in safety reviews of projects. Shri Umesh Chandra is a Distinguished Scientist and a graduate of IIT, Kanpur.



**Dr. P.R. Vasudeva Rao**, is a Distinguished Scientist and presently Director of Chemistry Group in IGCAR. He obtained his Doctorate degree in Inorganic Chemistry from Bombay University in 1979. He has played an active role in shaping the Radiochemistry Programme of IGCAR to its current status. His research interests cover a wide range of areas such as development of alternate extractants and resins for actinide recovery solvent extraction, third phase formation, thermodynamics, applications of photochemistry in actinide separations, development of pyrochemical and other non-aqueous processes for recovery of actinides and rare earths, thermochemical studies on nuclear materials, fuel behaviour in reactors, burn-up measurements and non-destructive assay. He has published more than 150 papers in reputed international journals apart from guiding several research scholars for their doctorate degrees. He is a life member of Indian Nuclear Society, Materials Research Society of India, Society for Advancement of Electrochemical Science and Technology and Indian Association of Nuclear Chemists and Allied Scientists (IANCAS). He has been awarded the MRSI Medal in 1998 and the INS award for the year 2007. He is also a Fellow of Tamil Nadu Academy of Sciences.

## MEMBERS OF IGCSC AND ACTIVITIES OF VARIOUS GROUPS

## Chairman

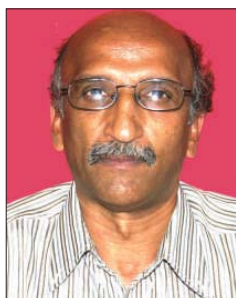


**Dr. Baldev Raj**  
Director, IGCAR

## Chemistry Group



**Dr. P.R. Vasudeva Rao**  
Director



**Dr. T. Gnanasekaran**  
AD, CG &  
Head, LM&SCD



**Dr. V. Ganesan**  
Head, MCD



**Dr. K. Nagarajan**  
Head, FChD



**Shri G. Ravishankar**  
Head, CFD

The Chemistry Group is responsible for carrying out R&D to provide inputs with respect to all the chemistry aspects of the fast reactor and its fuel cycle. Besides the R&D activities, the Chemistry Group also provides extensive analytical support using a wide range of analytical techniques to all the programmes at Kalpakkam. The areas of R&D in Chemistry Group include sodium chemistry, chemistry of un-irradiated as well as irradiated fuel materials, development of fuel cycle, high temperature chemistry, analytical chemistry, spectroscopy and boron chemistry. Chemistry Group also has been developing instrumentation and facilities in support of the R&D programme. Development of sensors for PFBR and sensors for environmental applications, cover gas purification system for PFBR, development of radionuclide traps for PFBR, development of cleaning and decontamination techniques for fast reactor components, development of Laser Induced Breakdown Spectroscopy and X-ray absorption based techniques for on-line monitoring of plutonium streams in reprocessing plants, development of technology for production of plutonium rich fuels and minor actinide containing fuels through sol-gel route and development of sodium bonding for metallic fuels are some of the R&D programmes on the anvil. Recent achievements include successful testing of the electrochemical hydrogen sensor in Phoenix reactor in France, trial fabrication of fuel pins containing uranium dioxide micro spheres, production of enriched elemental boron, mixer settler demonstration of partitioning of minor actinides and lanthanides from fuel solution in hot cells, demonstration of sodium bonding of U-Zr slug with SS316 pin and lab scale separation of <sup>89</sup>Sr from yttrium irradiated in FBTR.

## Electronics and Instrumentation Group



**Dr. P. Swaminathan**  
Director



**Shri S.A.V. Satya Murty**  
AD, EIG & Head, CD



**Shri. B. Krishnakumar**  
Head, EID



**Shri N. Murali**  
Head, RTSD



**Dr. M. Sai Baba**  
Head, SIRD



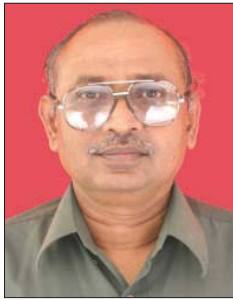
**Dr. A. Vijaya**  
Head, MD

The Electronics and Instrumentation Group is actively engaged in the development of Strategic Instrumentation Systems for Fast Breeder Reactor and Fuel Reprocessing Programme such as Real Time Computer Systems, Safety Logic Systems, Expert Systems, Distributed Digital Control Systems, Wireless Sensor Network etc. Unique Instrumentation Systems such as Electromagnetic Time Domain Survey System is also being developed to detect deeply buried uranium ore. Highly reliable instrumentation systems are being developed using modern VLSI design tools, thermal design tools, EMI/EMC design tools etc. Application software packages are being developed using powerful CASE TOOL. The development process is ISO certified. A Full Scope Replica type Training Simulator is being developed for training the operators of Prototype Fast Breeder Reactor. Walk-through of different areas of the reactor is being developed using PDMS package. State of the art visualisation center with stereoscopic projection is set up. Intranet based Knowledge Management System is being effectively managed. Simplicity in instrumentation is being realised through the innovative programme on creation of pulsating sensors for diverse parameters, enabling development of completely indigenous plant monitoring and surveillance systems, rapid analytical and diagnostic tools. Security electronics systems are constantly being updated for Kalpakkam site. Biometric hand geometry based attendance system is commissioned and is operating satisfactorily. The group has Scientific Information Resource Division which is in pursuance of its objective of providing efficient and effective information service to the Scientists, Engineers, TSOs and Research Scholars at Kalpakkam Campus. The group is also responsible to ensure satisfactory health services to the residents of Kalpakkam and Anupuram Townships.

## Engineering Services Group

Engineering Services Group is responsible for providing quality services pertaining to Civil engineering, Electrical Engineering, Voice Communication Systems, Air-conditioning & Ventilation Systems, Material Handling Equipments, Central Workshop activities. The group also coordinates the telecommunication requirements of the Centre. The group has a mandate to establish additional infrastructure requirements so as to meet Design, R&D and operational objectives of IGCAR. The group has expert teams with capability to design, engineer and execute systems under their jurisdiction. Electricity, water, quality-air and other services are being extended to other units of DAE located at Kalpakkam. The nature of work involves interaction with several State Government and Central Government Organisations.

**Engineering Services Group.....**



**Shri Y.C. Manjunatha**  
Director



**Shri A.S.L.K. Rao**  
AD, ESG(M) & Head, PD



**Shri C. Sivathanu Pillai**  
AD, CEG



**Shri C. Chandran**  
Head, ACVSD

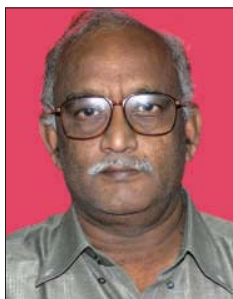


**Shri A. Jyothish Kumar**  
Head, ESD



**Shri K. Manoharan**  
Deputy Director, GSO

**Fast Reactor Technology Group**



**Shri P. Kalyanasundaram**  
Director, FRTG



**Shri K.K. Rajan**  
AD, STG



**Dr. C. Anand Babu**  
Head, CT&VDD



**Shri B. Babu**  
Head, CIDD



**Shri B.K. Nashine**  
Head, DDRSD



**Shri G. Padmakumar**  
Head, SE&HD

The Fast Reactor Technology Group is responsible for development and testing of FBR components, design validation through experiments and design, development and manufacture of sodium sensors and devices for in-sodium examination, Process development for enrichment of boron and separation technologies. The group has developed expertise in sodium handling, design, construction, commissioning and operation of high temperature sodium systems. FRTG has set up major sodium facilities such as 5.5 MWt Steam Generator Test Facility, the Large Component Test Rig, INSOT facilities for creep and fatigue studies and SADHANA loop for demonstrating natural convection in safety grade decay heat removal system. The other facilities available The Fast Reactor

Technology Group is responsible for development and testing of FBR components, design validation through experiments and design, development and manufacture of sodium sensors and devices for in-sodium examination, Process development for enrichment of boron and separation technologies. The group has developed expertise in sodium handling, design, construction, commissioning and operation of high temperature sodium systems. FRTG has set up major sodium facilities such as 5.5 MWt Steam Generator Test Facility, the Large Component Test Rig, INSOT facilities for creep and fatigue studies and SADHANA loop for demonstrating natural convection in safety grade decay heat removal system. The other facilities available in the group are the SAMRAT model and the Sub assembly test rig for water studies and the Cover gas Purification system (CGPS) and the Boron Enrichment Plant (BEP). Development of sodium purification systems, discrete and continuous sodium level sensors, sodium flow measuring sensors and different types sodium leak detectors are some of the important achievements. In short, the Group is working on all Engineering aspects of FBRs.

## Metallurgy and Materials Group



**Dr. T. Jayakumar**  
Director, MMG  
& Head, NDED



**Dr. S. Venugopal**  
AD, GRIP &  
Head, RIRD



**Dr. A.K. Bhaduri**  
Head, MTD



**Shri Jojo Joseph**  
Head, PIED



**Dr. U. Kamachi Mudali**  
Head, CSTD



**Dr. M.D. Mathew**  
Head, MMD



**Dr. M. Vijayalakshmi**  
Head, PMD

Metallurgy and Materials Group pursues a wide range of Research Programmes of the Centre that encompass both basic and applied aspects of the structural materials development for Fast Breeder Reactors and associated fuel cycle facilities. The key areas of research and development have been broadly classified and addressed in the dedicated administrative Divisions. They include the areas of 1. Materials Design and Manufacturing Technology, 2. Materials Mechanics and Properties, 3. Physical Metallurgy and Characterisation, 4. Nondestructive Evaluation and In Service Inspection, 5. Irradiation Experiments and Post-Irradiation Examination, 6. Robotics, Innovative design, Engineering and Synthesis and 7. Corrosion Science and Technology. The current activities of importance being pursued are: development of special materials like Oxide Dispersion Strengthened (ODS) Ferritic Steels and Reduced Activation Ferritic - Martensitic (RAFM) Steels, development of welding consumables, optimisation of thermo mechanical treatments and other fabrication processes, characterisation of microstructures and mechanical properties and their interrelationship, modeling of micro structural stability and phase evolution, corrosion and bio-fouling studies, development and application of specialised NDE techniques and advanced mechanical property measurements like impression creep testing, irradiation experiments and development of technologies for robotics and remote handling. The group also has several novel technology development missions for meeting the requirements of future FBRs such as the development of hard facing procedures for critical components, studies on leak detection in sodium circuits using Raman distributed optical fiber sensor, development of Ferro fluid based seals for sodium pump applications and development of advanced shielding materials. The Group also is getting geared towards the National requirement of advanced high temperature power plant materials.

## Materials Science Group



**Dr. C.S. Sundar**  
Director



**Dr. A.K. Arora**  
Head, CMPD



**Dr. A.K. Tyagi**  
Head, SND



**Shri M.C. Valsakumar**  
Head, MPD

The Materials Science Group, comprising of three Divisions, has the mandate of pursuing high quality basic research on topical problems in Materials Science, to work towards ion beam and computer simulation of radiation damage and to pursue research on innovative sensors accruing from basic research in superconductivity and nanomaterials. The Condensed Matter Physics Division focuses on the investigation of physical properties of novel materials under temperature, pressure and magnetic fields. Active research programs on Raman spectroscopy studies of vibrational properties, Dynamic light scattering and Confocal Microscopy studies of soft condensed matter, Laser heated diamond anvil cell facility for synthesis and study of materials under high pressure and high temperature and investigation of material properties at low temperatures under high magnetic fields and pressures are being pursued. The indigenously built SQUID sensors and control electronics have been translated into SQUID based measuring systems such as a high field magnetometer, a SQUID based set-up for Non-Destructive Evaluation (NDE), and SQUID based Magnetoencephalography (MEG). The activities of Materials Physics Division pertain to studies on Ion beam simulation of radiation damage using a 1.7 MV tandem accelerator; in depth studies on defects using Positron Annihilation Spectroscopy and Computer simulation of material properties. The Surface and Nanoscience Division focuses on studies on thin films using a variety of techniques such as Secondary Ion Mass Spectrometry and Scanning Probe Microscopy. Studies on controlled growth of nanometric multi-layer films for increased hardness and exploration of nanomaterials micro-machined cantilevers and MEMS as sensors are being actively pursued.

## Nuclear & Safety Engineering Group



**Dr. P. Chellapandi**  
Director



**Shri. B.K. Nashine**  
Head, SED



**Shri P. Puthiyavinayagam**  
Head, RCD



**Shri S. Raghupathy**  
Head, CH & MD



**Shri P. Selvaraj**  
Head, MHD

### Nuclear & Safety Engineering Group.....

NSEG is responsible for the design and development of reactor assembly components including core, shutdown and handling mechanisms for the sodium cooled fast reactors (SFR) and getting safety clearance from Atomic Energy Regulatory Board (AERB). The group also executes R&D in the domain of structural mechanics, thermal hydraulics and safety engineering, involving national and international institutions. It provides design support to the construction and commissioning of 500 MWe Prototype Fast Breeder Reactor (PFBR), which is under construction at Kalpakkam. It also provides analysis supports to other groups in the centre including fast breeder test reactor (FBTR) as well as for other strategic and high end technologies in the country. The responsibility of group includes developing high quality human resource for the design and analysis of SFRs in the country. It is currently engaged in conceptualizing as well as detailing the innovative reactor components for the reactor assembly of future SFRs.

The group has about 100 scientists and engineers, who are relatively younger. They are organized under four divisions viz. Reactor Components Division (RCD), Component Handling and Mechanism Division (CHMD), Mechanics and Hydraulics Division (MHD) and Safety Engineering Division (SED). These apart, it has a modern design office with many advanced modeling and analysis softwares, Structural Mechanics Laboratory (SML) having state-of-art facilities for carrying out tests on large components, high temperature structural integrity and seismic tests with large size shake tables and safety engineering laboratory for carrying out tests in the domain of severe accidents and science & technology of sodium fires and fire extinguishers.

The group has high quality expertise in the domain of design of mechanisms operating in sodium, mechanical design and analysis of components as per the American (ASME) and French (RCC-MR) design codes, thermal hydraulics of liquid metal, plant dynamics, etc.

## Reactor Operations and Maintenance Group



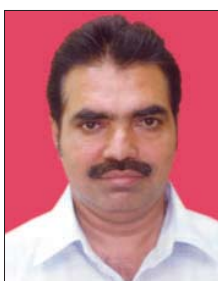
**Shri G. Srinivasan**  
Director



**Shri B. Ananthapadmanaban**  
Head, RMD



**Shri N. Kasinathan**  
Head, RAD



**Shri K.V. Suresh Kumar**  
Head, ROD



**Shri PR. Swaminathan**  
Head, PPD



**Kum. S. Usha**  
Head, TSD

ROMG is responsible for safe operation of Fast Breeder Test Reactor (FBTR) and KAMINI reactor within the limits given in technical specification documents. The group also takes part in the operational safety review of PFBR Project documents. The Training section of the group, besides training O&M staff of FBTR and KAMINI, is also responsible for training the O&M staff of PFBR and future FBR's. Progressive modifications in FBTR to increase its availability and for gaining newer experience in operation, utilizing the reactor for irradiation of advanced fuels and materials for fast reactors and conducting safety related experiments form a major part of ROMG's activities.

## Reactor Engineering Group



Shri S. C. Chetal  
Director



Dr. P. Mohanakrishnan  
AD, RPhG & Head, RPD



Shri C. Sivathanu Pillai  
AD, CEG



Shri B. Venkatraman  
AD, RSEG& Head, RSD



Shri B. Ananthapadmanaban  
Head, QAD



Shri V. Balasubramanian  
Head, HTSD



Dr. R. S. Keshavamurthy  
Head, RSSD



Shri K. Madhusoodanan  
Head, PPCD



Dr. K.K. Satpathy  
Head, EISD



Shri N. Vijayan Varier  
Head, TC&QCD

The Reactor Engineering Group (REG) comprising of Reactor Physics Group, Radiological and Environmental Safety Group, Heat Transfer System Division, Power Plant Control Division, Technical Co-ordination and Quality Control Division and Civil Engineering Design Division is responsible for the design of fast reactor physics, heat transport system, plant layout, steam water system, instrumentation & control systems and civil structures of fast reactors. It has carried out the design of above systems for 500 MWe Prototype Fast Breeder Reactor (PFBR) and has obtained the statutory / regulatory clearances from AERB. Along with BHAVINI, REG engineers are responsible for getting the heat transport and instrumentation & control system components of PFBR manufactured by the Indian industries. REG also provides necessary design support to FBTR. REG is presently engaged in design of above stated disciplines for future 500 MWe FBRs to provide enhanced safety and improved economics. As a spin off, the expertise acquired in mechanical design is being provided to a number of organizations for non-reactor activities. The Group is also responsible for providing quality assurance / quality control services for all the major projects being undertaken by IGCAR through the ISO 9001-2008 certified Quality Assurance Division. The Radiological Safety Division of the Group is responsible for R&D activities in the areas of radioactivity transport and improving the radiation detection and measurements through advanced techniques. This Division provides health physics and radiation safety services for the radioactive facilities in IGCAR. Environmental and Industrial Safety Division provides industrial safety services to all the facilities at IGCAR. This Division also carries out R&D in the domain of aquatic and terrestrial biodiversity and sediment characterization. The Group organizes public awareness programs on radiation safety and nuclear energy in addition to training and awareness programs on industrial, radiation and fire safety to occupational workers.

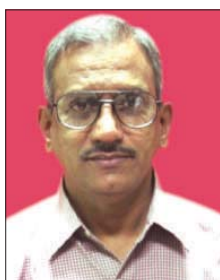
## Reprocessing Group



**Shri R. Natarajan**  
Director



**Dr. U. Kamachi Mudali**  
Head, RRDD



**Shri P. Ramkumar**  
Head, RPSD



**Shri A. Ravishankar**  
Head, RPDD



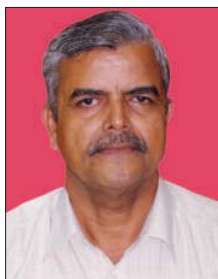
**Shri V. Sundararaman**  
Head, FRPD



**Shri M. Venkataraman**  
Head, RPOD

The success of Indian Fast Breeder Reactor (FBR) programme depends on the closure of fuel cycle within a short period. The Reprocessing Group (RpG) of IGCAR is responsible for the development of fast reactor fuel reprocessing technology as well as design, construction and operation of the reprocessing plants. Various R&D activities are being carried in the Reprocessing Development Laboratory (RDL). Extensive, engineering scale testing of equipment and systems are carried out before installation in hot cells. Chopper, dissolver, feed clarification equipment, centrifugal extractors and different types of pulse columns are few of the important equipment being developed at RDL. Apart from equipment development, research is undertaken for understanding and solving various process and chemistry problems of fast reactor fuel reprocessing such as, process flow sheet studies to improve the plant performance for higher recoveries and reduced waste generation, mathematical modeling of solvent extraction of the complex U-Pu system, solvent management, development of alternate solvent-diluent systems, development of online monitoring of Pu for process control, liquid flow metering in high radioactive fields, development of material handling equipment inside the hot cells, etc. In one of the hot cell facilities at RDL,  $^{233}\text{U}$  was recovered from irradiated thorium rods using THOREX process which is used as fuel in KAMINI reactor and in FBTR (as PFBR test fuel). The other hot cell facility, called CORAL (Compact facility for Reprocessing Advanced fuels in Lead cells) commissioned in 2003, is being deployed as a versatile test bed for validating the process flow sheet and scaling up of equipment designs for fast reactor fuel reprocessing, by processing the FBTR spent fuel. This experimental facility has been used for reprocessing several batches of mixed carbide fuels irradiated in FBTR with 25, 50, 100 and 155 GWd/t burn-ups. This has provided valuable experience to the design of Demonstration Fast Reactor Fuel Reprocessing Plant (DFRP) in which all the types of FBTR fuels, namely the mixed carbide and oxide of different compositions, will be reprocessed on a regular basis. DFRP is also designed to reprocess PFBR fuel subassemblies also for demonstrating the reprocessing of irradiated PFBR oxide fuels. In addition to these activities, RpG is also carrying out the design of the reprocessing plant, FRP, for reprocessing spent fuels of PFBR on commercial basis

## Fast Reactor Fuel Cycle Facility



**Shri P.V. Kumar**  
Project Director

Fast Reactor Fuel Cycle Facility Project Group is entrusted with the work of planning, designing and constructing the Fast Reactor Fuel Cycle Facility (FRFCF) to close the fuel cycle of PFBR. The Group carries out all interactions with the design consultants. The Group coordinates the work on the design of the plants in FRFCF with participating Groups from BARC, NFC and IGCAR. Preparation of the detailed project report, processing for obtaining financial sanction, development of infrastructure at the project site, and obtaining regulatory and other statutory clearances is part of the mandate of this group

## Strategic and Human Resources Planning Section



**Dr. M. Sai Baba**  
Head, S & HRPS

The section has the mandate of planning for the Strategic and Human Resource needs of the Centre which involve: Planning and running the training school programs at Training School; Collaborative projects with various R&D organizations and academic institutes; Compilation of technical reports on important activities of the Centre; Interacting and coordinating with national and international delegations; Assessing and projecting the human resource needs of the Centre for effective deployment and utilization; Interacting with the research scholars at the Centre; Planning and organizing meetings related to human resources, personality development and co-ordinating M. Tech. programmes in Nuclear Engineering of various universities.

## Madras Regional Purchase Unit



**Shri K. Balachander**  
Regional Director,  
MRP

Material Management activities for IGCAR and General Services Organisation are taken care by Madras Regional Purchase Unit which comes under Directorate of Purchase & Stores of Department of Atomic Energy. Procurement and payment to suppliers are carried out at Chennai and inventory and accounting are carried out by Central Stores at Kalpakkam. E-Tendering was implemented successfully and more than 200 files were processed by e-Tendering mode. Total expenditure for purchase of material and equipment in the calendar year 2010 has crossed 180 crores. Some of the major equipment for which orders have been placed are Laser Raman Spectrometer, Digital Holographic Microscope, XRD with High Temperature attachments, HPC Cluster System, Tri-Junction Forged Rings and Neutronic Channels. Timely action taken by MRP has resulted in excellent compliance of expenditure budget targets.

## Administration and Accounts



**Shri. P. Ramakrishnan**  
Chief Administrative Officer



**Shri C.G.S. Nair**  
Joint Controller  
(Finance & Accounts)

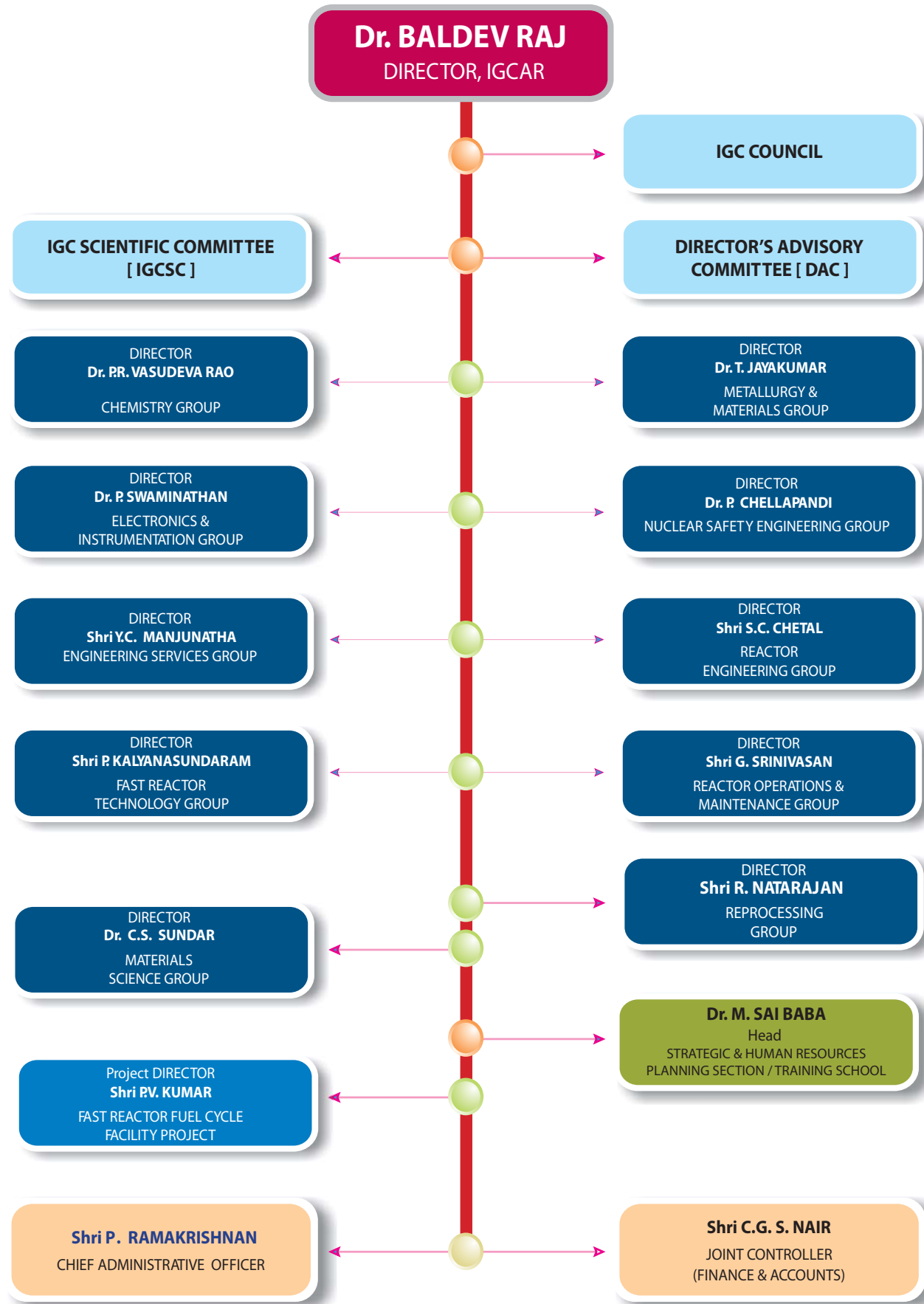


**Smt. Saroja Gopal**  
AO(R&SR)  
Secretary, IGSC

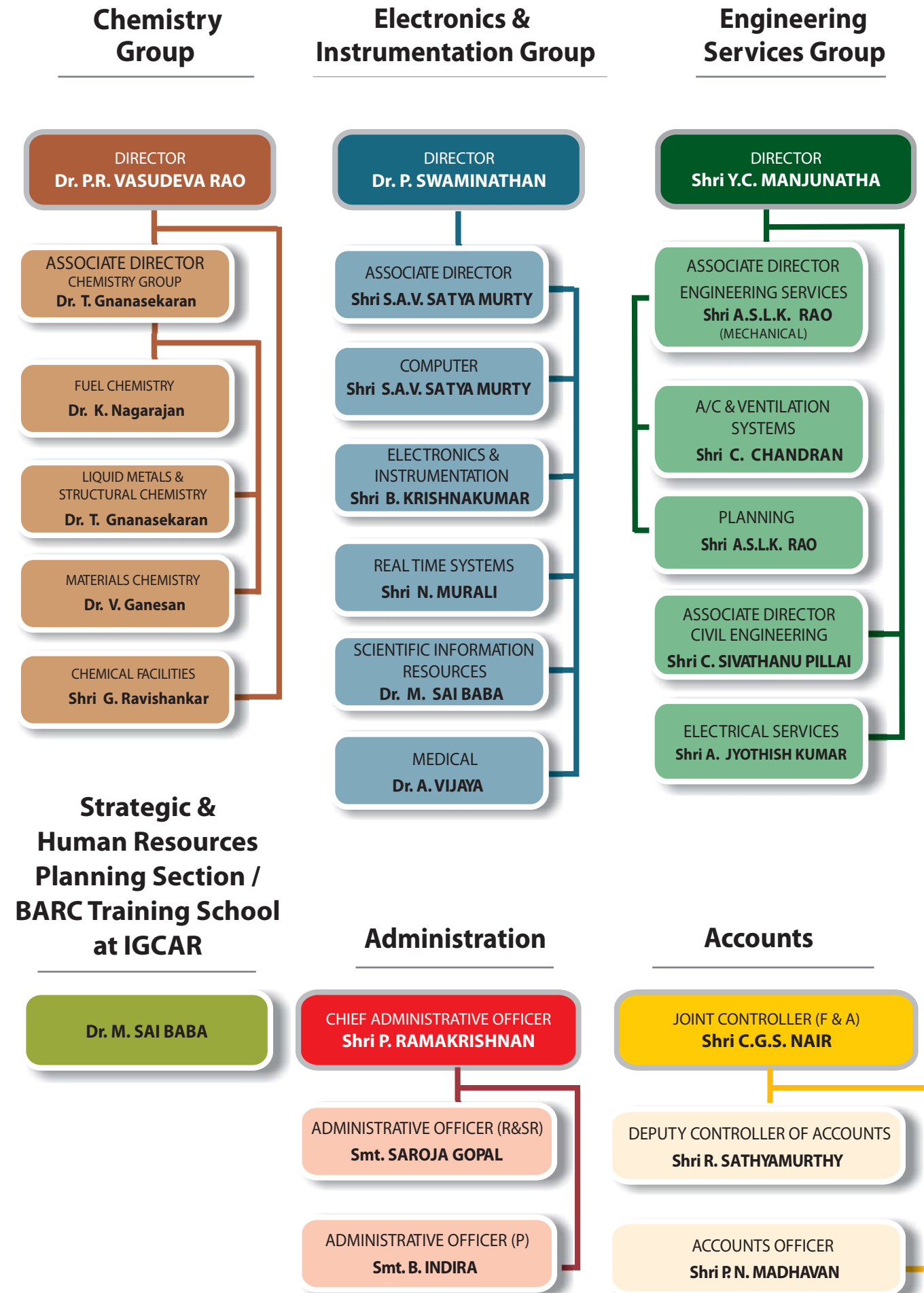
## LIST OF IMPORTANT ABBREVIATIONS

AC&VSD	Air Conditioning and Ventilation System Division	MMG	Metallurgy and Materials Group
AERB	Atomic Energy Regulatory Board	MPD	Metal Physics Division
BARC	Bhabha Atomic Research Centre	MRPU	Madras Regional Purchase Unit
BARCF	Bhabha Atomic Research Centre Facilities	MSG	Materials Science Group
BHAVINI	Bharatiya Nabhikiya Vidyut Nigam Limited	MTD	Materials Technology Division
CD	Computer Division	NDED	Non-Destructive Evaluation Division
CDPS	Central Data Processing System	NFC	Nuclear Fuel Complex
CEG	Civil Engineering Group	NICB	Nuclear Island Connected Building
CERMON	Continuous Environmental Radiation Monitoring Network	NPC	Nuclear Power Corporation
CFD	Chemical Facilities Division	NSEG	Nuclear and Safety Engineering Group
CG	Chemistry Group	NSSS	Nuclear Steam Supply System
CH&MD	Components Handling & Mechanism Division	PD	Planning Division
CIDD	Components and Instrumentation Development Division	PFBR	Prototype Fast Breeder Reactor
CMPD	Condensed Matter Physics Division	PHWR	Pressurized Heavy Water Reactor
CORAL	COmpact facility for Reprocessing Advanced fuels in Lead cell	PIED	Post Irradiation Examination Division
CSTD	Corrosion Science and Technology Division	PMD	Physical Metallurgy Division
CT&VDD	Chemical Technology and Vibration Diagnostics Division	PPCD	Power Plant Control Division
CWD	Central Workshop Division	PPD	Project Planning Division
DDRSD	Device Development and Rig Services Division	RAD	Reactor Analysis Division
ED	Electronics Division	RCD	Reactor Components Division
EID	Electronics and Instrumentation Division	REG	Reactor Engineering Group
EIG	Electronics and Instrumentation Group	RIRD	Remote Handling, Irradiation Experiments and Robotics Division
ESD	Electrical Services Division	RMD	Reactor Maintenance Division
ESG	Engineering Services Group	ROD	Reactor Operation Division
FBR	Fast Breeder Reactor	ROMG	Reactor Operation and Maintenance Group
FBTR	Fast Breeder Test Reactor	RPD	Reactor Physics Division
FChD	Fuel Chemistry Division	RPDD	Reprocessing Plant Design Division
FRFCF	Fast Reactor Fuel Cycle Facility	RpG	Reprocessing Group
FRPD	Fuel Reprocessing Process Division	RPhG	Reactor Physics Group
FRTG	Fast Reactor Technology Group	RPOD	Reprocessing Plant Operations Division
GRIP	Group for Remote Handling, Robotics, Irradiation Experiments and PIE	RPSD	Reprocessing Projects & Services Division
GSO	General Services Organisation	RRDD	Reprocessing Research and Development Division
HTSD	Heat Transport Systems Division	RSD	Radiological Safety Division
IAEA	International Atomic Energy Agency	RSDD	Reactor Shielding and Data Division
IIT	Indian Institute of Technology	RSEG	Radiological Safety & Environmental Group
IMSc	Institute of Mathematical Sciences	RTSD	Real Time Systems Division
LMFBR	Liquid Metal Cooled Fast Breeder Reactor	SED	Safety Engineering Division
LM&SCD	Liquid Metals and Structural Chemistry Division	SE&HD	Sodium Experiments & Hydraulics Division
MAPS	Madras Atomic Power Station	SGTF	Steam Generator Test Facility
MCD	Materials Chemistry Division	S&HRPS	Strategic & Human Resources Planning Section
MD	Medical Division	SIRD	Scientific Information and Resource Division
MHD	Mechanics & Hydraulics Division	SND	Surface and Nanoscience Division
MMD	Mechanical and Metallurgy Division	SOWART	Sodium Water Reaction Test facility
		SRI	Safety Research Institute
		STG	Sodium Technology Group
		TC&QCD	Technical Coordination & Quality Control Division
		TSD	Technical Services Division

# INDIRA GANDHI CENTRE FOR ATOMIC RESEARCH

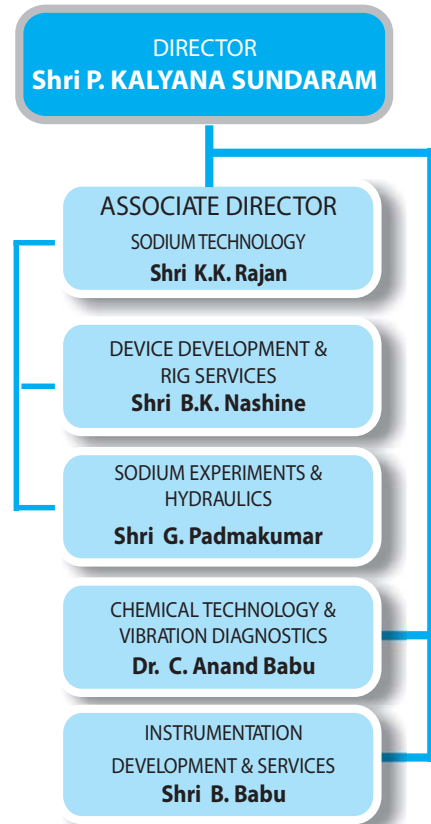


## GROUPS / DIVISIONS / HEADS

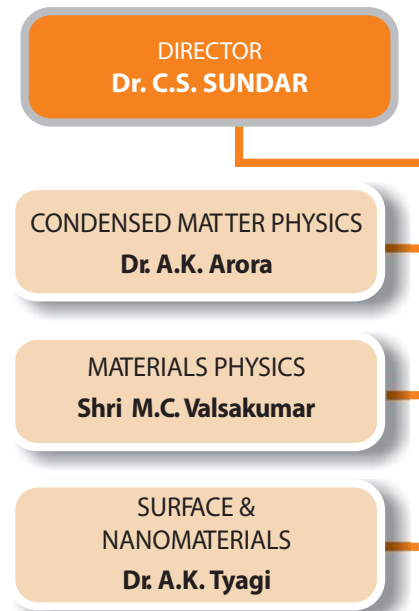


# GROUPS / DIVISIONS / HEADS

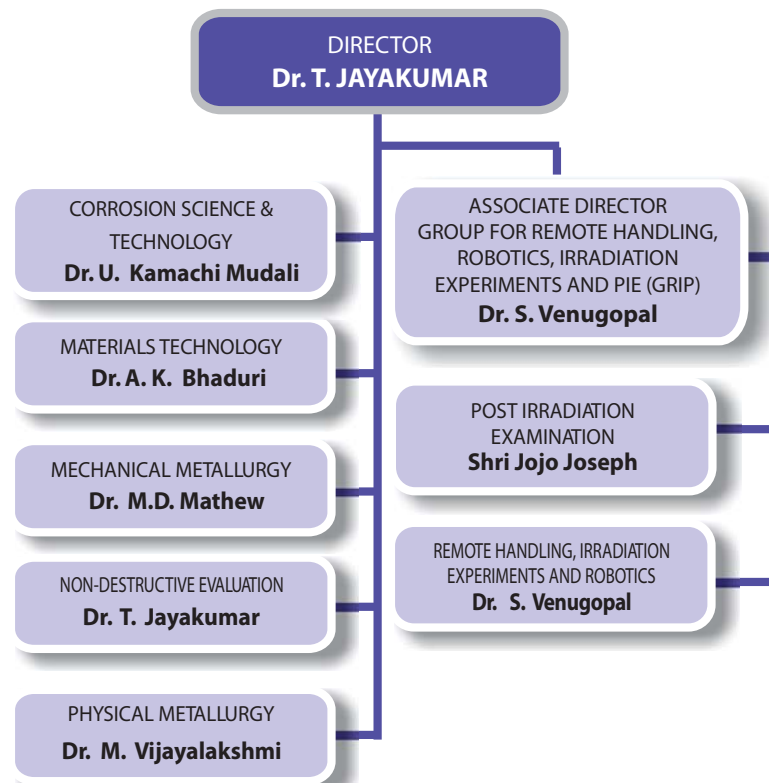
## Fast Reactor Technology Group



## Materials Science Group



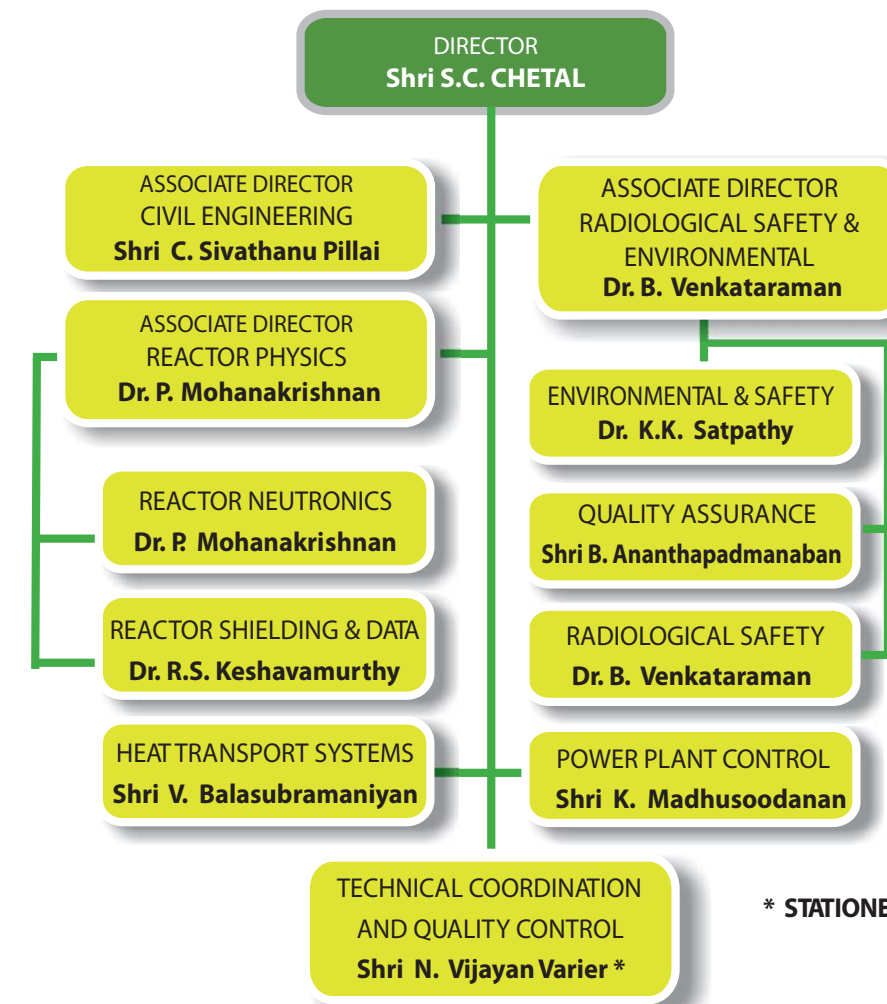
## Metallurgy & Materials Group



## Nuclear & Safety Engineering Group



## Reactor Engineering Group



\* STATIONED AT MUMBAI

## Reactor Operations & Maintenance Group



## Reprocessing Group

